

UNIVERSITY COLLEGE LONDON

DEPARTMENT OF ELECTRONIC AND  
ELECTRICAL ENGINEERING

*Target recognition  
techniques for  
multifunction phased  
array radar*

**Andrew French**

A thesis submitted for the degree of Doctor of Philosophy  
of the University College London

January 2010

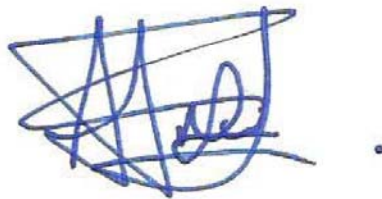
*Supervisor:* Dr Karl Woodbridge. University College London.  
Peter Tait. BAE Systems  
Prof. Chris Baker. Australian National University.

## DECLARATION

I, Andrew French

Confirm that the work presented in this thesis is my own. Where information has been derived from other sources, I confirm that this has been indicated in the thesis.

Signed



Dorchester, January 2010

To my Parents

*Est unusquisque faber ipsae suae fortuna*  
- Appius Claudius Caecus

# Contents

0.1	Acknowledgements . . . . .	1
0.2	Glossary . . . . .	1
0.3	Parameter list with typical values . . . . .	6
<b>1</b>	<b>Introduction</b>	<b>7</b>
1.1	Chapter summary . . . . .	7
1.2	The operational need for target recognition . . . . .	7
1.2.1	Target recognition ‘at a glance’ . . . . .	7
1.2.2	Recognizing objects of military importance via remote sensing . . . . .	7
1.3	Target recognition methods using Radar . . . . .	8
1.3.1	The Radar sensor . . . . .	8
1.3.2	The hierarchy of Radar derived target intelligence: from recognition to identification . . . . .	9
1.3.3	A summary of target recognition methods using Radar . . . . .	11
1.3.4	MESAR2 . . . . .	12
1.4	Overall aims of this thesis . . . . .	14
1.4.1	Scope . . . . .	14
1.4.2	Problem statement . . . . .	14
1.4.3	Fundamental research aims & key questions . . . . .	15
1.5	Thesis structure and chapter summaries . . . . .	17
1.6	Literature survey . . . . .	18
1.6.1	Stepped frequency methods . . . . .	18
1.6.2	Doppler processing and Jet Engine / Propeller Modulation . . . . .	22
1.6.3	Feature extraction and classification methods . . . . .	24
<b>2</b>	<b>Background theory</b>	<b>29</b>
2.1	Chapter summary . . . . .	29
2.2	Classical stepped frequency High Range Resolution profiling . . . . .	30
2.2.1	The stepped frequency concept . . . . .	30
2.2.2	The practical need for stepped frequency waveforms . . . . .	31
2.2.3	‘Classical’ method stepped frequency processing . . . . .	32
2.2.4	Limitations of Classical stepped frequency processing . . . . .	33
2.2.5	Motion compensation . . . . .	34
2.3	Hybrid stepped frequency High Range Resolution profiling . . . . .	36
2.3.1	Requirements . . . . .	36
2.3.2	Previous work . . . . .	36
2.3.3	Recent developments of the Hybrid technique . . . . .	36
2.3.4	Overall method . . . . .	37
2.3.5	Mitigation of the problem of aliases . . . . .	37
2.4	Doppler processing and Jet Engine Modulation . . . . .	44
2.4.1	The Doppler Filter & its associated ambiguities . . . . .	44
2.4.2	Sources of target Doppler: HERM & JEM . . . . .	46
2.5	Feature extraction methods . . . . .	53



2.5.1	Effect of target aspect and elevation . . . . .	53
2.5.2	Use of target kinematics . . . . .	53
2.5.3	Radar Cross Section . . . . .	54
2.5.4	Length from HRR profiles . . . . .	54
2.5.5	Scattering center extraction using HRR profiles . . . . .	54
2.5.6	dfrac and efrac from Doppler spectra . . . . .	58
2.5.7	Major peaks in Doppler . . . . .	58
2.6	Methods of target classification . . . . .	60
2.6.1	Choice of classifier . . . . .	60
2.6.2	Bayesian classifier . . . . .	63
2.6.3	Fuzzy logic classifier . . . . .	65
2.6.4	k-means classifier . . . . .	65
2.7	Features & limitations of an S-band multifunction phased array Radar used for NCTR . . . . .	67
2.7.1	Multi-function phased array Radar . . . . .	67
2.7.2	Frequency stability . . . . .	67
2.7.3	Beam position, scanning losses & true time delay . . . . .	69
2.7.4	Stretch processing - an alternative to stepped frequency . . . . .	75
<b>3</b>	<b>NCTR experiments using MESAR2</b>	<b>77</b>
3.1	Chapter summary . . . . .	77
3.2	Trials rationale . . . . .	77
3.3	Waveforms . . . . .	79
3.4	Overall extent of data . . . . .	80
3.5	NCTR signal processing . . . . .	84
3.5.1	Flow diagram of analysis methodology . . . . .	84
3.5.2	NCTR signal processing . . . . .	88
3.6	On & off boresight trials . . . . .	97
3.6.1	Trials description . . . . .	97
3.6.2	Waveforms and dipole spacing . . . . .	99
3.6.3	Summary of results . . . . .	100
3.7	Pod & Falcon trials . . . . .	103
3.7.1	Trials description . . . . .	103
3.7.2	Summary of results . . . . .	105
3.8	Targets of opportunity . . . . .	109
3.8.1	Trials description . . . . .	109
3.8.2	Summary of results . . . . .	109
3.9	Conclusions . . . . .	115
<b>4</b>	<b>Target classification using HRR profiles</b>	<b>117</b>
4.1	Chapter summary . . . . .	117
4.2	Target data sheets of six aircraft types . . . . .	117
4.3	Range sidelobes resulting from low frequency propeller modulations . . . . .	119
4.4	Target classes based on scalar HRR profile features . . . . .	124
4.4.1	Long or short (length) . . . . .	124
4.4.2	Four lengths (length) . . . . .	124
4.4.3	Pod vs Falcon (SCM compare) . . . . .	124
4.4.4	Six aircraft types (SCM compare) . . . . .	124
4.5	Variation of length feature measurements . . . . .	125
4.6	Classification performance via range profiles of six aircraft . . . . .	129
4.7	Conclusions . . . . .	137

<b>5</b>	<b>Range-Doppler profiling &amp; Doppler spectra classification</b>	<b>138</b>
5.1	Chapter summary . . . . .	138
5.2	Prop, JEM and NNSD classes discriminated by the dfrac feature . . . . .	139
5.3	Classification performance using the dfrac feature . . . . .	140
5.4	Range-Doppler profiles from stepped frequency waveforms . . . . .	146
5.4.1	Classical stepped frequency model including JEM . . . . .	146
5.4.2	Range-Doppler profiles from targets of opportunity . . . . .	151
5.5	Conclusions . . . . .	159
<b>6</b>	<b>Relationship between characteristics of stepped frequency methods and overall air target classification performance</b>	<b>160</b>
6.1	Chapter summary . . . . .	160
6.2	Variation of $\xi$ with $P, Q$ and length and Doppler fraction feature thresholds . . . . .	160
6.3	Variation of $\xi$ with carrier frequency jitter . . . . .	170
6.4	Classification using combined length and Doppler fraction features . . . . .	174
6.5	Conclusions . . . . .	181
<b>7</b>	<b>NCTR waveform design recommendations</b>	<b>182</b>
7.1	Chapter summary . . . . .	182
7.2	Operational requirements of an NCTR waveform . . . . .	182
7.3	NCTR waveform design chart . . . . .	185
7.4	Conclusions . . . . .	196
<b>8</b>	<b>Conclusions &amp; Recommendations</b>	<b>198</b>
8.1	Revisit scope of thesis . . . . .	198
8.2	Summary of research achievements . . . . .	198
8.3	Summary of results presented in this thesis . . . . .	200
8.4	Recommendations for further study . . . . .	203
8.5	List of publications arising from this thesis . . . . .	205
<b>A</b>	<b>The radiation pattern of a phased array Radar</b>	<b>214</b>
<b>B</b>	<b>The Radar Equation</b>	<b>217</b>
<b>C</b>	<b>The <math>\chi(x, z)</math> function</b>	<b>219</b>
<b>D</b>	<b>Fourier transform of a linear chirp waveform</b>	<b>222</b>
D.1	Definition of a linear chirp signal . . . . .	222
D.2	Fourier Transform of a linear chirp . . . . .	226
<b>E</b>	<b>The Martin &amp; Mulgrew model of Jet Engine Modulation</b>	<b>229</b>
E.1	Derivation of the Martin & Mulgrew model of JEM . . . . .	229
E.2	A "cartwheel" model of JEM & amplitude modulation due to blade pitch. . . . .	235
<b>F</b>	<b>The benefits and limitations of stretch processing</b>	<b>238</b>
F.1	Overview . . . . .	238
F.2	The stretch mixer . . . . .	238
F.3	Benefits & limitations of stretch processing . . . . .	240

<b>G Radar Cross Section measurements of aircraft</b>	<b>242</b>
G.1 All aircraft Max RCS of Classical HRR profiles . . . . .	242
G.2 All aircraft Max RCS of Hybrid HRR profiles . . . . .	246
G.3 Six aircraft Max RCS Waveform A Classical . . . . .	249
G.4 Six aircraft Max RCS Waveform A Hybrid . . . . .	251
G.5 Six aircraft Max RCS Waveform B Classical . . . . .	253
G.6 Six aircraft Max RCS Waveform C Classical . . . . .	255
<b>H Importing MESAR2 data: DRAS, M2DATS &amp; MEROS import_data_gui</b>	<b>257</b>
<b>I k-means classification</b>	<b>260</b>
I.1 Clustering the training data . . . . .	260
I.2 Classifying features . . . . .	261
<b>J Alternative Bayesian method of computing the confusion matrix</b>	<b>266</b>
<b>K Target data sheets (Range profiles): wfc2 <math>\Delta f=3.2\text{MHz}</math> P=8 Q=128 (Waveform A).   Classical method</b>	<b>269</b>
<b>L Target data sheets (Range profiles): wfc2 <math>\Delta f=3.2\text{MHz}</math> P=8 Q=128 (Waveform A).   Hybrid method</b>	<b>276</b>
<b>M Target data sheets (Range profiles): wfc3 <math>\Delta f=0.8\text{MHz}</math> P=8 Q=128 (Waveform B).   Classical method</b>	<b>283</b>
<b>N Target data sheets (Range profiles): wfc3 <math>\Delta f=3.2\text{MHz}</math> P=8 Q=128 (Waveform C).   Classical method</b>	<b>290</b>
<b>O Target data sheets (Doppler): 6 aircraft inbound</b>	<b>297</b>
<b>P Target data sheets (Doppler): 6 aircraft outbound</b>	<b>304</b>

# Abstract

This thesis, submitted for the degree of Doctor of Philosophy at University College London, is a discussion and analysis of combined stepped-frequency and pulse-Doppler target recognition methods which enable a multifunction phased array radar designed for automatic surveillance and multi-target tracking to offer a Non Cooperative Target Recognition (NCTR) capability. The primary challenge is to investigate the feasibility of NCTR via the use of high range resolution profiles. Given stepped frequency waveforms effectively trade time for enhanced bandwidth, and thus resolution, attention is paid to the design of a compromise between resolution and dwell time. A secondary challenge is to investigate the additional benefits to overall target classification when the number of coherent pulses within an NCTR waveform is expanded to enable the extraction of spectral features which can help to differentiate particular classes of target. As with increased range resolution, the price for this extra information is a further increase in dwell time. The response to the primary and secondary challenges described above has involved the development of a number of novel techniques, which are summarized below:

- Design and execution of a series of experiments to further the understanding of multifunction phased array Radar NCTR techniques
- Development of a ‘Hybrid’ stepped frequency technique which enables a significant extension of range profiles without the proportional trade in resolution as experienced with ‘Classical’ techniques
- Development of an ‘end to end’ NCTR processing and visualization pipeline
- Use of ‘Doppler fraction’ spectral features to enable aircraft target classification via propulsion mechanism. Combination of Doppler fraction and physical length features to enable broad aircraft type classification.
- Optimization of NCTR method classification performance as a function of feature and waveform parameters.
- Generic waveform design tools to enable delivery of time costly NCTR waveforms within operational constraints.

The thesis is largely based upon an analysis of experimental results obtained using the multifunction phased array radar MESAR2, based at BAE Systems on the Isle of Wight. The NCTR mode of MESAR2 consists of the transmission and reception of successive multi-pulse coherent bursts upon each target being tracked. Each burst is stepped in frequency resulting in an overall bandwidth sufficient to provide sub-metre range resolution. A sequence of experiments, (static trials, moving point target trials and full aircraft trials) are described and an analysis of the robustness of target length and Doppler spectra feature measurements from NCTR mode data recordings is presented. A recorded data archive of 1498 NCTR looks upon 17 different trials aircraft using five different varieties of stepped frequency waveform is used to determine classification performance as a function of various signal processing parameters and extent (numbers of pulses) of the data used. From analysis of the trials data, recommendations are made with regards to the design of an NCTR mode for an operational system that uses stepped frequency techniques by design choice.

## 0.1 Acknowledgements

I would like to thank all at BAE Systems for funding this work and providing access to world class engineering and Radar equipment. In particular, the support and contribution of Peter Tait, Robert Miller, Gordon Richards & Martin Widgery from BAE and Karl Woodbridge and Chris Baker from UCL is most appreciated. I would also like to record the efforts of Cambridge University students Neil Campbell and Mark Scott who worked with me on aspects of NCTR at BAE Systems Integrated System Technologies during the summers of 2005 and 2006.

## 0.2 Glossary

- **Azimuth  $\phi, \gamma$  (antenna coordinates)** Bearing angle of target relative to Radar system measured clockwise from the perpendicular to the antenna face
- **Bayesian classifier** A means of target classification by computing the *posterior* probability of obtaining a class distinction given a set of observed data. This is computed from a (typically Gaussian) *likelihood* distribution which defines the probability of set of measured data given a class distinction.
- **Burst** A set of coherently transmitted pulses, i.e. a continuous measurement of phase is measurable during times when the burst pulses are received. In this document, all transmitted pulses within each burst will use the same carrier frequency.
- **Carrier frequency  $f_{Tx}$**  All transmitted pulses, with spectral bandwidth  $B$  and duration  $\tau$ , are mixed with a radio-frequency (RF) sinusoidal carrier  $f_{Tx}$ . For an S-band system,  $f_{Tx} \approx 3\text{GHz}$  whereas the instantaneous pulse bandwidth  $B$  is typically  $< 20\text{MHz}$  for a phased array system. Received pulses are usually mixed down to ‘baseband’ (often in several stages) prior to digital sampling. In order to observe the Shannon-Nyquist sampling theorem, the sample rate of receiver Analogue to Digital Converters (ADCs) must exceed the instantaneous bandwidth of the pulse.
- **Chirp** Describes a pulse with a linear frequency coding. The frequency variation of the pulse is proportional to the transmission time. A chirp with bandwidth  $B$  and duration  $\tau$  will have a (frequency,time) gradient  $\frac{df}{dt} = \frac{B}{\tau}$ .
- **Classical method** Refers to the conventional method of forming High Resolution Range (HRR) profiles of targets illuminated by stepped frequency waveforms. In essence, a single measurement of target phase is determined for each frequency step and the inverse Fourier Transform of the set of these measurements yields the HRR profile. In this document, the ‘Classical’ technique also means the use of chirp waveforms. Target phase (and amplitude) samples are taken from the pulse compressed receiver samples.
- **Confusion Matrix** Square matrix  $\mathbf{C}$  which describes the performance of a classification scheme based upon a finite number of classes. If a set of feature measurements is obtained from known source classes, element  $[\mathbf{C}]_{ij} \equiv C_{ij}$  corresponds to the number of features assigned to class  $i$  (which are actually from class  $j$ ) divided by the total number of features which are sourced from class  $j$ . Perfect classification will result in an identity matrix of size equal to the number of classes.

- **dB** Decibels. If a signal power is  $x$  and a reference power  $x_0$  the signal power in dB of  $x$  relative to  $x_0$  is given by  $10 \log_{10} \left( \frac{x}{x_0} \right)$ . dBm( $x$ ) is a special case when  $x_0 = \max(x)$ .
- **Doppler filtering** In general, receiver samples resulting from a burst of identical pulse transmissions can be combined in such a way as to weight the relative gain of spectral components of a signal. In this document, a weighted Discrete Fourier Transform is applied over samples from each of the within-burst pulses. This is done for every HRR range cell. Doppler filtering is applied after the effects of bulk target motion have been subtracted from the receiver samples, so the distribution of power in the ‘Doppler domain’ gives an indication of the internal target motion projected in the look direction.  $P$  pulses transmitted at a pulse repetition frequency of  $f_{PRF}$  will give ‘Doppler bins’ of frequency width  $\frac{f_{PRF}}{P}$ . A range-rate of  $\dot{R}$  will give rise to a Doppler shift of  $f_D = -\frac{2\dot{R}}{c} f_{Tx}$  where  $f_{Tx}$  is the transmitted frequency and  $c$  the speed of light. Doppler shifts outside the range will be ‘folded’ in; i.e. any measured Doppler shift will be ambiguous by  $Z f_{PRF}$  where  $Z$  is an integer which defines the ambiguity.
- **DRAS** Software written by Roke Manor designed to interface with the MESAR2 data logger and allows track data to be extracted.

- **Dwell** Total time required to transmit (and receive) the stepped-frequency train of pulses in order to form a HRR profile of a target. If the pulse repetition interval is  $f_{PRF}$ , the number of pulses per burst is  $P$  ‘real’ pulses and  $G$  ‘guard’ pulses, and the number of frequency steps is  $Q$

$$T_{dwell} = \frac{(P + G) Q}{f_{PRF}} \quad (1)$$

- **Elevation (antenna coordinates)** Vertical angle (relative to the antenna face normal) that a beam must be steered to intersect a target, following alignment in azimuth.
- **Falcon** Commercial jet aircraft manufactured by Dassault.
- **FFT Fast Fourier Transform** This is an efficient implementation of a Discrete Fourier Transform. A (suitably weighted) FFT of a set of time samples is often an acceptable approximation of the Fourier Transform of the analogue signal being sampled.
- **fproc** Processing software for MESAR2 NCTR data written for the MATLAB environment by the author.
- **FTG False Target Generator** This is a mechanism for delaying the reflection of incident electromagnetic radiation upon a target, such that the target appears (to the observing Radar) to be at a much longer range. For experimental systems this might practically consist of dipoles separated by several kilometers of cable, wrapped up in a portable container.
- **Fuzzy Logic classifier** A simple implementation of a scalar discriminant based classification scheme. The classifier consists of a set of pre-defined discriminant functions of target feature measurements; (e.g. single input, single output or many inputs, single output). A different function is defined for each class of a (usually finite) set. For a given set of feature measurements, a class is assigned which corresponds to the largest value of the discriminants evaluated for each of the classes.

- **Guard pulses** Prior to the ‘Classical’ or ‘Hybrid’ processing described in this document, some form of Clutter filtering will likely be applied by combining receiver samples from consecutive pulses within each burst. For example, three consecutive pulses can be combined (with suitable weightings) such that signal frequency components near to zero are suppressed. (This would be an example of a ground clutter filter). In order to give filter outputs with the same clutter content contributing to each pulse, additional ‘guard’ pulses must be transmitted first. Conventionally one assumes clutter is present up to a maximum range. The number of guard pulses is chosen so each processed pulse has clutter returns (from previous pulses) up to the maximum clutter range.
- **HRR profile** High Range Resolution profile of a target. This usually means range cell widths of less than a metre.
- **Hybrid method** An improvement upon the ‘Classical’ signal processing scheme of generating HRR profiles of targets using stepped-frequency waveforms being developed at BAE Systems Integrated System Technologies. In essence a wide bandwidth pulse is ‘synthesized’ from an ensemble of modest bandwidth chirps, with each of these transmitted with a linearly stepped carrier.
- **ISAR** Inverse Synthetic Aperture Radar. Equivalent to SAR but utilizes the rotational motion (and aspect change) of a target instead of motion of the sensor antenna.
- **k-means** A popular data clustering algorithm applied in this thesis to yield a *non-parametric* alternative to the Bayesian classifier.
- **Look** The transmission and subsequent reception of target reflections from a particular azimuth and elevation. To achieve maximum gain a Radar beam is typically steered (mechanically and/or electronically) to the desired location.
- **M2DATS** Data processing software written by Graham Biggs of BAE Systems to convert DRAS outputs into text files that can be human read and imported into MATLAB via Meros.
- **MATLAB** Comprehensive computer aided mathematics tool supplied by The Mathworks Inc. Nearly all figures<sup>1</sup> and processing schemes described in this document have been created within the MATLAB environment.
- **Meros** Processing and modelling tool developed at BAE Systems Integrated Systems & Technologies designed to implement and investigate performance of ‘Classical’ and ‘Hybrid’ HRR methods using data from MESAR2.
- **MESAR2** Experimental multi-function phased array Radar system designed and currently sited at BAE Systems Integrated Systems & Technologies, Cowes, Isle of Wight. MESAR2 was developed as the technological testbed for the Sampson Multi-Function Radar and is currently part of the ARTIST joint programme between US DoD and UK MoD.
- **Motion compensation** Manipulation of Radar receiver samples to remove the effects of bulk target motion. This requires an accurate estimation of target range rate, obtained either directly from data or in conjunction with external information; e.g. from a track extractor.

---

<sup>1</sup>Xara X, Microsoft Excel and Microsoft Draw are used for the remainder.

- **MTD** Moving Target Detection. Use of a bank of clutter filters to detect targets with a characteristic range-rate and thus Doppler frequency.
- **MTI** Moving Target Indication. Doppler (or ‘clutter’) filter designed to admit Doppler contributions close to the range-rate of a target.  $P$  pulses-worth of receiver samples gives one clutter-filtered pulse at the output of the MTI filter.
- **NCTR** Non Cooperative Target Recognition.
- **NCTR scaling** Calibration coefficients that take account of the phase shift from the Radar to the ‘average’ target range, (i.e. the range obtainable from a conventional plot extractor) plus any internal system phase effects. If  $Q$  carrier frequencies are transmitted, receiver data for each of these will be multiplied by one of  $Q$  coefficients. Calibration coefficients are derived from stepped frequency illumination of a static point target, in conjunction with the ‘average’ target range.
- **Off Diagonal Extent (ODE)** Measure of misclassification  $\xi$ . This is defined to be  $\xi = 1 - \frac{\text{Tr}[\mathbf{C}]}{\sum_{i=1}^N \sum_{j=1}^N [\mathbf{C}]_{ij}}$  where  $\mathbf{C}$  is the Confusion matrix and  $N$  is the number of classes.  $\mathbf{C}$  has dimensions  $N \times N$ . For perfect classification  $\xi$  is zero, for total misclassification  $\xi$  is unity.
- **Phased array** Ensemble of Radar transmit & receive elements. Each element has a controllable phase shift which means a net radiation field can be formed with a principal lobe that points in a desired look direction; i.e. a phased array Radar can potentially offer electronic beam steering.
- **Pod** Refers to a ‘repeater’ or False Target Generator (see above) carried by an aircraft such a Dassault Falcon.
- **Polarimetry** The use of a variety of planes of electric field vector to yield information about the scattering mechanisms that form a high resolution target image e.g. obtainable using SAR or ISAR techniques.
- **PRF** Pulse Repetition Frequency  $f_{PRF}$
- **Pulse** Radio frequency Radar transmission. In a Pulse-Doppler Radar that employs pulse compression, frequency coded pulses (or waveforms) of duration  $\tau$  and bandwidth  $B$  are transmitted at repetition frequency  $f_{PRF}$ .
- **Pulse compression** Receiver samples are convolved with a stored set of weights generated from the receiver samples of a reflection from a static point target. If a frequency coded waveform of bandwidth  $B$  is used, range resolution  $\delta R$  can theoretically be as good as  $\delta R = \frac{c}{2B}$ .
- **RCS** Radar Cross Section. Effectively the electromagnetic scattering area of a target. Typically defined in  $\text{m}^2$  or  $\text{dBm}^2$ .
- **Rx** Radar receiver.
- **SAR** Synthetic Aperture Radar. A means of imaging a ground scene using an airborne or spaceborne sensor that forms a wide aperture via sensor bulk translation rather than having a physically large antenna.



- **Scattering center Model (SCM) compare classifier** Scattering centres are extracted from the ‘major’ peaks of HRR profiles and their ranges compared (via a barcode matching algorithm<sup>2</sup>) to the radial projections of scattering centres which are marked upon the plan views of the aircraft drawings. Classification is assigned based on the nearest barcode match.
- **Signal processor** Sequence of processes that take raw Radar signals and transform these into a form that enables useful features to be extracted. In this document the signal processing chain described in the ‘Classical’ and ‘Hybrid’ methods begins with in-phase and quadrature digital samples and ends with the generation of a HRR profile.
- **SNR** Ratio of Signal to Noise power. Usually expressed in decibels (dB)
- **Spectral stitching** Method critical to the ‘Hybrid’ HRR technique which involves the assembly of the spectra of receiver samples corresponding to consecutive frequency steps. This is used to ‘synthesize’ the receiver samples of a wide bandwidth chirp.
- **Stepped frequency** A waveform consisting of an ensemble of identical pulses, but with the carrier frequency of each pulse stepped by (in this document) a constant amount.
- **tsee** Visualization software for MESAR2 NCTR data written for the MATLAB environment by the author.
- **Tx** Radar transmitter.
- **Waveform A** Linear chirp waveform of pulse length  $25.6\mu\text{s}$  and bandwidth  $\sim 4.5\text{MHz}$  transmitted in bursts of 8 pulses for 128 frequency steps of  $3.2\text{MHz}$ , starting with a carrier of  $2724.2\text{MHz}$ . A PRF of  $2.5\text{kHz}$  is used.
- **Waveform B** Non-linear chirp waveform of pulse length  $20\mu\text{s}$  and bandwidth  $\sim 5\text{MHz}$  transmitted in bursts of 8 pulses for 128 frequency steps of  $0.8\text{MHz}$ , starting with a carrier of  $2953\text{MHz}$ . A PRF of  $2.5\text{kHz}$  is used.
- **Waveform C** Non-linear chirp waveform of pulse length  $20\mu\text{s}$  and bandwidth  $\sim 5\text{MHz}$  transmitted in bursts of 8 pulses for 128 frequency steps of  $3.2\text{MHz}$ , starting with a carrier of  $2724.2\text{MHz}$ . A PRF of  $2.5\text{kHz}$  is used.
- **Waveform D** Non-linear chirp waveform of pulse length  $20\mu\text{s}$  and bandwidth  $\sim 5\text{MHz}$  transmitted in bursts of 32 pulses for 32 frequency steps of  $0\text{MHz}$ , starting with a carrier of  $2999.4\text{MHz}$ . A PRF of  $2.5\text{kHz}$  is used.
- **Waveform E** Linear chirp waveform of pulse length  $25.6\mu\text{s}$  and bandwidth  $\sim 4.5\text{MHz}$  transmitted in bursts of 32 pulses for 32 frequency steps of  $3.2\text{MHz}$ , starting with a carrier of  $2708.2\text{MHz}$ . A PRF of  $2.5\text{kHz}$  is used.

---

<sup>2</sup>The nearest aircraft is selected based upon the maximum value of the peak power of the cross-correlation of the projected scattering centre barcode (i.e. a binary vector) for each item in a database of aircraft, and the barcode derived from HRR profile scattering centre extraction.

### 0.3 Parameter list with typical values

$f_{Tx}$	Carrier frequency	GHz
$f_{PRF}$	Pulse repetition frequency	kHz
$f_s$	Receiver sample frequency	MHz
$f_{JEM}$	Jet Engine Modulation frequency	few kHz
$\Delta f$	Frequency step of NCTR waveform	few MHz
$B$	Bandwidth of pulses transmitted	few MHz
$\tau$	Duration of transmitted pulse	$\mu s$
$P$	Processed pulses per burst	8, 32 ... 1024
$Q$	Frequency steps	32 ... 128 ...
$G$	Guard pulses	1 ..10
$\sigma$	(Target) Radar Cross Section	0.1 .. 30 dBm <sup>2</sup>

# Chapter 1

## Introduction

### 1.1 Chapter summary

The context and motivation for this research is firstly described with the aim of taking the reader from the *operational need for target recognition* through to a discussion of the applicable attributes of the *Radar sensor*. The aims and content of the research reported in this thesis is then summarized followed by an outline of the thesis structure. Finally a *survey of published literature* is presented relating to the major topics discussed in this thesis.

### 1.2 The operational need for target recognition

#### 1.2.1 Target recognition ‘at a glance’

One of the most potent of human skills is the ability to rapidly recognize and classify environmental stimuli, often when such signals are severely corrupted. Of this toolkit of sensors and processing, the method of visual facial recognition is perhaps the most impressive. Typically, a successful recognition will occur in 120 ms [93], with cruder classifications (for example classification of a species group from a background) in as little as 50ms. Not only is the latency of this process sufficiently small as to be negligible on the typical timescales of human communication; from an early age most humans have an extensive library of faces which they not only can recognize as a class (e.g. man or woman, child or adult) but assign an identification, a name. The triumph which is human visual facial recognition is perhaps the utopia that any machine<sup>1</sup> designed for target recognition must aspire to. A credible system must be able to recognize broad object classes against a cluttered background with a latency which is small on the timescales of the expected engagement with the object. Ideally the system must possess an extensive library of profiles which can be rapidly correlated with input sensory data; the ultimate goal of identification being conditional on the fidelity of such a database.

#### 1.2.2 Recognizing objects of military importance via remote sensing

Modern warfare relies heavily on the effective use of environmental information returned from sensors mounted upon military platforms. Radar, Sonar, thermal imaging technologies (to list but a few) can, jointly, allow an operator to survey the battlespace far beyond the limits of human sensors, both in terms of range and external environmental conditions such as weather. However, to quote Dr René van der Heiden of NATO Consultation Command & Control Agency: “One of the most serious problems in

---

<sup>1</sup>See [6], [102] for a description of machines that aspire to perform visual face recognition.

today's military capability is the lack of rapid and reliable identification of objects in the battlespace." [103].

The current trend is that of the asymmetric engagement: a highly mobile, dispersed army of enemy combatants pitted against a large scale, complex force with armaments designed primarily to defend platforms against weaponry similar to their own. [29]. The suicide bomber riding in a car, rigid inflatable boat or underground train is a tragically regular threat, one which contemporary defence systems are somewhat ill posed to counter. The challenge is to enhance military sensors to be aware of the small, mobile, but potentially lethal objects in the battlespace without mass physical incursions into the lives of civilians whose liberty belligerents often exploit as camouflage. The issue is not confined to the problem of urban or littoral waters terrorism. In ballistic missile defence, identification of the warhead amongst a cloud of delivery vehicle parts and chaff is a major challenge, and crucial to the success of an anti-missile defence system such as Patriot.<sup>2 3</sup> Beyond visual range missiles such as BVRAAM are being adopted by the UK Royal Air Force as part of the armory of the Typhoon aircraft.<sup>4</sup> However, current rules of engagement require a positive target identification prior to launch. Until a viable non-visual Non-Cooperative Target Recognition (NCTR) capability has been proven, the extra range of BVRAAM cannot be fully exploited.

Awareness is not just detection, but recognition; ultimately to obtain sufficient information that military resources can be intelligently deployed. Unfortunately it is often the case that the only defence against modern threats is the swift application of lethal force. Here there is clearly no room for error. Mistaken identity will lead to likely death of innocent individuals and widespread public condemnation, as in the case of the shooting down of the Iranian Airbus flight IR655 in 1988 by USS Vincennes stationed in the Persian Gulf.<sup>5</sup> In addition to the correct recognition of a terrorist threat, a large and complex military force must also be able to recognize its own personnel and platforms. During the 1991 Gulf War 35 of the 148 U.S. fatalities were as a result of fratricide, or 'friendly fire.' [103] Cooperative systems such as Identify Friend or Foe (IFF) radio transponders<sup>6</sup> are fallible, both mechanically and subject to human error.<sup>7</sup> IFF systems could potentially be set with the incorrect codes, be accidentally turned off, jammed and even used to masquerade a real threat. In all cases there is a clear operational need to possess an NCTR capability to, at minimum, check the validity of the intelligence received via a cooperative system.

## 1.3 Target recognition methods using Radar

### 1.3.1 The Radar sensor

Radar is a contraction of RAdio Detection And Ranging. It is a particular example of a wide class of sensors that detect the presence of a physically remote object via the reception and processing

---

<sup>2</sup><http://www.raytheon.com/products/patriot>

<sup>3</sup>[http://www.theregister.co.uk/2004/05/20/patriot\\_missile/](http://www.theregister.co.uk/2004/05/20/patriot_missile/)

<sup>4</sup><http://www.eurofighter-typhoon.co.uk/common/AA/bvraam.html>

<sup>5</sup>[http://news.bbc.co.uk/onthisday/hi/dates/stories/july/3/newsid\\_4678000/4678707.stm](http://news.bbc.co.uk/onthisday/hi/dates/stories/july/3/newsid_4678000/4678707.stm)

<sup>6</sup>The civil equivalent of military IFF is known as Air Traffic Control Radar Beacon System (ATCRBS). Both IFF and ATCRBS employ an electronic dialogue of the form: Interrogator: "Who are you?" Target transponder: "I am a friend and my identity reference is .... "

<sup>7</sup>A Royal Air Force (RAF) Board of Inquiry investigating the destruction of an RAF Tornado GR.4A by a US Army Patriot missile during the March 2003 invasion of Iraq concluded that the aircraft's identification friend-or-foe (IFF) system had failed. However, it also criticised the missile-classification criteria used by the Patriot system, and the US Army's Patriot rules of engagement, firing doctrine and crew training.

[Jane's Missiles and Rockets - 28 June 2004]

of backscattered electromagnetic waves. Unlike optical systems, (which are responsive to frequencies  $\approx 10^{15}$  Hz), Radar is typically associated with frequency bands ranging from a few MHz (High Frequency or HF band) up to hundreds of GHz (mm wave). Radar is somewhat useful for the following reasons:

- Most targets of interest (especially those constructed from metal) are highly reflective at Radar frequencies.
- Radar can be used in darkness and can penetrate haze, fog, snow and rain.
- Atmospheric propagation attenuation is much less severe for Radar than higher frequency electromagnetic disturbances. This means Radar can be used for long range surveillance. A military air defence system may have an operational range of hundreds of kilometers. At the extreme end, Radar has been used to successfully measure the distance between the Earth and other planets in the solar system. [103]
- The technology to generate, receive and process Radar signals has been continuously refined for nearly 100 years. Military and civilian air traffic control have employed Radar as a key sensor extensively since the Second World War. Magnetron transmitters, which are stable sources of microwaves (0.1 - 100 GHz approximately) are ubiquitous as a fundamental element of modern domestic ovens. Given the size of a Radar antenna roughly scales with the wavelength it transmits/receives, Radars (with modest directivity, i.e. a beamwidth of a few degrees) tend to be of dimensions well suited to human use i.e. of the order of a few metres.

### 1.3.2 The hierarchy of Radar derived target intelligence: from recognition to identification

As alluded to in section 1.2.1, there is an important difference between recognition and identification of targets. Although no general standard exists, in this thesis a convention based on the definitions in Skolnik [96] pp370 will be used. These statements describe a four part breakdown of target recognition, with the ultimate goal being full identification.

1. *Recognition of general nature of target.* Broad class distinction such as aircraft, ship, motor vehicle, land clutter, sea clutter etc.
2. *Recognition of target type.* Initial division of broad class. e.g. ‘aircraft’ can be subdivided into missile, propeller driven, jet, helicopter. At limits, distinction of targets such as a multi engine commercial airliner from a fighter jet. It is the methodology of such *perceptual classification* on which this thesis focuses.
3. *Recognition of target class.* This is essentially a species identification. For ‘aircraft’ it would reveal ‘Airbus A380’, ‘Boeing 747-400’...
4. *Full target identification.* Determination of name or other unique identifier of object being interrogated. For example: ‘Airbus A340, Acme Airlines flight AM42 from London Heathrow to New York.’

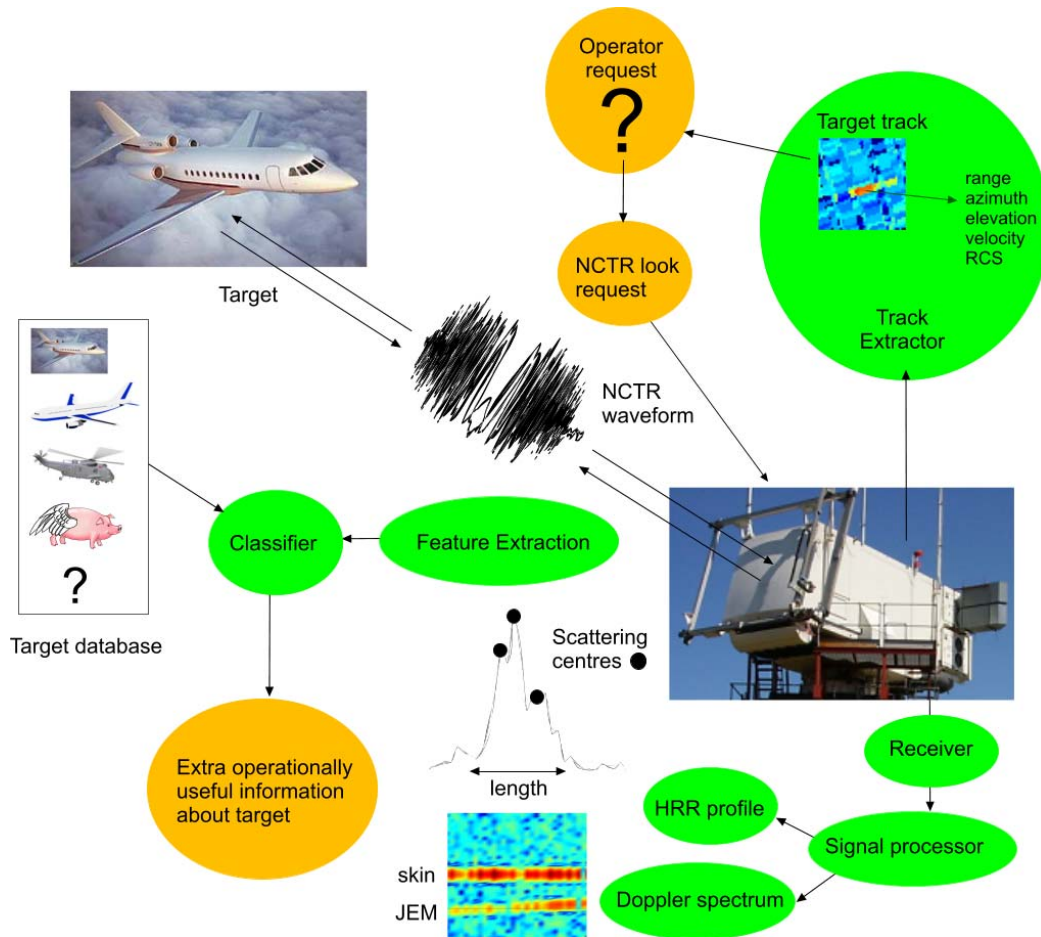


Figure 1.1: Description of a generic Radar based system for Non-Cooperative Target Recognition (NCTR). In this example we focus on the generation of High Range Resolution (HRR) profiles and Doppler spectra of targets. Features such as length, distribution of scattering centres and presence of Jet Engine Modulation (JEM) can be used to classify a set of radar returns and thus associate a target with one example from a defined set of objects. In this thesis we will principally explore *broad* classes such as “long or short”, “propeller, jet engine or no visible rotating parts”, rather than jump straight to the more difficult challenge of aircraft type classification e.g. 747,757,A340...

### 1.3.3 A summary of target recognition methods using Radar

Radar technology can initially be subdivided into two broad categories. ‘Active’ Radar transmits an electromagnetic disturbance and then listens for reflections. The time delay between transmission and reception can be used as an accurate estimator of range, if indeed the clock used is sufficiently accurate and stable. Interrogation systems such as IFF are active and also cooperative since target identification information is encoded into the returning signal if a successful dialogue is set up. ‘Passive’ systems aim to interpret electromagnetic emissions from external sources. For example, transmissions from other active Radars or emissions from a target aircraft.

Radar, like any other sensor, is in essence an information gathering machine. The received electromagnetic signals from active or passive devices will contain a wealth of information imparted upon them via their interaction with the external environment, as well as the effect of the receiver and signal processing chain. To achieve target recognition, a basic minimum amount of information must be distilled from a received signal. For level 1 recognition (as defined in the previous subsection), a target must firstly be detected and discriminated from reflections from thermal noise and unwanted objects (clutter) such as mountains, rain and birds. In addition particular features must be extracted from the signal, which are correlated with a distinct target class such that some form of classification can be inferred. It is this latter statement of a requirement of *additional information* which differentiates a target recognition system from a Radar which simply reports detections of wanted objects, and perhaps their location in one or more geometric coordinate. A summary of such additional information is best aligned to particular technologies, which are tabulated below.

Radar technology	Measured quantities	Possible information obtainable
Active normal Radar	Signal to noise ratio Time delay Phase	Range Bearing Elevation Radar Cross Section
Doppler & Interferometric Radar	Phase change of a sequence of returning signals	Range rate Signal modulations from moving parts
Polarimetric Radar [94]	Signal strengths in various polarizations	Indications of the target scattering mechanisms
Plot & Track extractor	History of target coordinates + uncertainty	Estimate of target position and velocity vectors
Synthetic Aperture Radar (SAR)	As Doppler Radar + accurate (moving) Radar position	Reflectivity map of surface illuminated by Radar
Inverse SAR (ISAR)	As Doppler Radar (assumes change of target aspect angle)	Target image, with major scatterers highlighted

Table 1. Summary of Radar based technologies and corresponding measured quantities and target information obtainable.



Figure 1.2: The MESAR2 S-band experimental multi-function phased array Radar designed and installed at Cowes, Isle of Wight, United Kingdom.

### 1.3.4 MESAR2

MESAR2 (fig 1.2) is the second iteration of an experimental phased array Radar developed by BAE Systems at Cowes on the Isle of Wight. It is the prime demonstrator of technology used in the Sampson Multi-Function Radar (fig 1.3) which forms a key sensor in the UK Navy Type 45 platform.(fig 1.4). A third iteration is now being developed as part of the ARTIST programme funded jointly by the UK MoD and US DoD.

MESAR2 has the ability to electronically steer a Radar beam to any desired azimuth and elevation within a defined operational sector (approximately 90 degrees in azimuth and elevation, subject to angular transmission restrictions at a given site). It can therefore be used to interleave wide area surveillance activities with tracking functions. The latter are specially designed waveforms transmitted at the estimated angular position of detected objects designated by the system as targets of interest. The NCTR waveforms discussed in this thesis are transmitted by MESAR2 upon targets that are already being successfully tracked. Whereas tracking estimates the bulk position and velocity (plus associated uncertainties) of a target, the NCTR mode aims to determine additional information such as length and other inferred parameters from the position and within-target motion of the constituent scatterers which compose the target as viewed by the Radar.





Figure 1.3: The Sampson multi-function phased array radar mounted in its antenna test facility at Cowes, Isle of Wight, UK. Unlike MESAR2, Sampson is a full production system which rotates continuously and contains two opposing faces fully populated with Transmit-Receive modules.



Figure 1.4: Artistic impression of the Sampson Multi-Function Radar mounted atop the principal mast of the UK Navy Type 45 Anti Air Warfare Destroyer class warship.

## 1.4 Overall aims of this thesis

### 1.4.1 Scope

This study is largely based upon Non Cooperative Target Recognition (NCTR) research conducted using the S-band multifunction Radar technical demonstrator MESAR2.<sup>8</sup> The practical elements of the research are based upon a discussion and analysis of the following:

1. A suite of stepped frequency High Range Resolution (HRR) NCTR waveforms automatically transmitted upon targets being tracked by MESAR2, interleaved between surveillance & tracking functions.
2. Multi-pulse *bursts* at fixed frequency and pulse repetition frequency (PRF) to enable Discrete Fourier Transform (DFT) based Doppler filtering. Short bursts are used to filter Jet Engine Modulation (JEM) from range profiles, whereas longer bursts are used to identify JEM frequencies.
3. Fully catalogued and accessible target data set (1498 looks upon 54 different target trajectories). 17 different target classes from four sets of experimental trials: (i) On and (ii) Off boresight static trials; (iii) Moving point target (Falcon & pod); (iv) Targets of opportunity (commercial aircraft).
4. A development suite of NCTR signal processing, feature extraction & analysis, and classification software written as part of this research.

### 1.4.2 Problem statement

A multifunction phased array Radar (MFPAR) such as MESAR2 operates via the scheduling of distinct remote sensing activities directed against a potential multitude of targets. Indeed this facility of ‘simultaneous engagement’ is one of the key discriminators against the majority of systems which claim target recognition capabilities (which typically can only maintain a limited number of simultaneous target tracks due to the need to mechanically orient an antenna to coincide with the estimated position of the target). The inevitable compromise conceded by the MFPAR to achieve its desirable qualities is two-fold: an NCTR waveform will have a *limited transmitted pulse bandwidth* and a *limited dwell time*.

Electronic beam scanning (E-scan) is typically applied to improve upon the latencies associated with a purely mechanical antenna orientation system. A cost effective and typical implementation of this is a phased array. At S-band, the bandwidth required to yield target range profiles<sup>9</sup> is a significant proportion of the carrier frequency. This implies significant beam squint during the transmission of a HRR waveform.<sup>10</sup> To limit the squint to within a beamwidth (typically a small number of degrees), the S-band phased array imposes a limit on the maximum bandwidth which can be associated with any transmitted pulse. For MESAR2 this is of the order of 5MHz, which is insufficient for target

<sup>8</sup>The technical content of this thesis is intended to be generic and of an unclassified nature. Where specific reference is made to MESAR2 (which is in part a UK Restricted and UK Secret programme), references are limited to the scope agreed with the UK Ministry of Defence (MoD) Defence Science & Technology Laboratories (DSTL) in 2006, which is the series of experiments described in this thesis. Trials results alluded to in this thesis refer to non-military aircraft only.

<sup>9</sup>Sub-metre range resolution requires in excess of 150MHz of bandwidth

<sup>10</sup>See Background theory section.

recognition. A means of getting round this constraint is to transmit an ensemble of pulses which are stepped in frequency. When combined, the ‘synthesized’ waveform is of the required bandwidth. However, this solution impacts upon the second MFPAR compromise, which is time. To provide a continuous wide area surveillance, multiple target tracking and NCTR functions, the amount of time allocated to any given task is inevitably bounded by a time window functionally dependent on the typical speeds of objects being tracked and the number of objects under consideration. For aircraft targets, ‘looks’ of more than a few hundred milliseconds are likely to be unacceptable operationally.<sup>11</sup>

The primary challenge is to determine whether stepped frequency waveforms can be used for NCTR purposes with an S-band multifunction phased array system. A secondary challenge is to understand the benefits and limitations of making use of multiple pulse bursts, rather than single pulses at each frequency step. Although the extra pulses will cause a further erosion of the schedule as a consequence of increased dwell, these waveforms can provide clutter cancellation as well as further target characterization via identification of Doppler domain signatures such as Jet Engine Modulation.

### 1.4.3 Fundamental research aims & key questions

The overall aim of the thesis is to understand the relationship between the characteristics of stepped frequency methods which can be applied using multifunction phased array Radar, and the resulting air target classification performance. As a sub-aim, we shall seek to improve classification performance via optimization of the signal processing and feature extraction methods used. Specifically, we shall address the following list of fundamental research aims and key questions.

#### Fundamental research aims

1. Conduct a literature survey of the following topics relating to NCTR using phased array Radar: stepped frequency high range resolution waveforms; Doppler processing (with specific relevance to Jet Engine Modulation and Propeller modulation); feature extraction and classification methods using range and Doppler profiles.
2. Use MESAR2 to deliver NCTR waveforms upon static and moving aircraft targets. Implement signal processing algorithms to obtain range and Doppler profiles from raw receiver samples obtained from stepped frequency waveforms consisting of coherent bursts of frequency coded pulses. In the first instance use ‘conventional’ algorithms such as the Classical stepped frequency methods described in the background theory section.
3. Develop improved signal processing techniques for stepped frequency waveforms which enable the ‘Classical’ link between HRR profile extent and HRR resolution to be broken; i.e. which enable extended aircraft such as a Boeing 747 to be captured unambiguously and a measure of its length measured directly from a HRR profile. Construct software to apply the required processing to large numbers of data files automatically. Also construct visualization and analysis tools to enable interrogation (and testing) of the processing chain at all stages.
4. Conduct trials which enable an incremental understanding of the capabilities and limitations of the NCTR techniques applied using S-band multifunction phased array Radar (as exemplified using MESAR2). Start with static trials with two point targets separated in range. Then repeat

---

<sup>11</sup>Based upon practical experience with systems such as MESAR2.

this in a scenario where the Radar beam is required to be electronically scanned off-boresight. What is the effect upon the HRR profile? Next conduct controlled aircraft trials consisting of a ‘point’ target co-moving with a (range separated) small aircraft. Can NCTR waveforms be successfully interleaved with other scheduled activities such as surveillance and tracking? How does a moving point target HRR profile compare to its static equivalent? What does the ‘point target response’ tell us about the range profile of the small aircraft? How successful are ‘conventional’ motion compensation algorithms? Finally conduct an uncontrolled aircraft trial using ‘targets of opportunity’ with a mechanism for providing independent identification of each target via collaboration with a nearby air traffic control. Ideally collect profiles of aircraft whose length is beyond ‘Classical’ HRR windows, and aircraft which exhibit Jet Engine Modulation or Propeller Modulation.

5. Implement post processing algorithms which enable the extraction of ‘physical’ scalar features such as Radar Cross Section (RCS) and target length, plus detection of rotational motion induced modulation effects.
6. Implement classifier methods which allow for an exploration of: (i) methods which assume an *a priori* feature distribution with pre-defined parameters (such as mean and standard deviation); (ii) an *a priori* feature distribution with parameters estimated from training data; (iii) methods which make no assumption of the feature distribution; (iv) methods which allow for a natural extension to multi-dimensional feature vectors.
7. Analyze classifier performance as a function of signal processing and feature extraction parameters. To make initial progress against this somewhat generic statement, choose ‘physical features’ such as target length<sup>12</sup> and well known classifiers such as Gaussian Bayes, Fuzzy logic or k-means. Parameters consist of numbers of pulses per burst, number of frequency steps, feature thresholds and carrier frequency jitter.
8. Investigate to what extent combined range and Doppler profiles (using multi-pulse burst stepped frequency waveforms) can yield useful target information, and model the various associated ambiguities and coupling phenomena resulting from the use of an S-band multifunction phased array Radar.
9. Model wider the operational constraints which impact upon the design of NCTR waveforms and suggest mechanisms for parameter selection such as Pulse Repetition Frequency (PRF).

### Key questions

1. Can MESAR2 (and by inference other S-band multifunction phased array radars) be used to record robust range (and Doppler) profiles of air targets?
2. How robust are feature measurements taken from the trials data set? Do feature measurements naturally segment into classes? Should certain features be combined, and are they correlated?
3. Can we achieve acceptable classifier performance based upon the extraction of various target features? How does the crudeness of class definition affect this result and how does performance

---

<sup>12</sup>Instead of abstracted features such as those resulting from a dimensionality reduction process such as a Karhunen Loeve transform (see Literature Survey)

depend upon: (i) the proportion of total pulse cycles used to form the target data set; (ii) thresholds used in feature measurement, and (iii) the features used (and their possible combination)?

4. Based upon the learning obtained in conducting this research, what are the recommendations regarding the design of future NCTR modes?

## 1.5 Thesis structure and chapter summaries

### 1. Introduction

The operational need for target recognition, Target recognition methods using Radar, MESAR2. Scope, problem statement, fundamental research aims and key questions. Literature survey (stepped frequency methods, Doppler processing & Jet Engine Modulation, feature extraction & classification methods).

### 2. Background theory

Classical stepped frequency High Range Resolution (HRR) methods: requirement, theory, limitations. Bulk target motion compensation. Hybrid stepped frequency HRR method. Alias mitigation. Doppler processing. Jet Engine Modulation (JEM), Helicopter & Propeller modulation. Target feature extraction: Kinematics, Radar Cross Section (RCS), length, scattering center extraction, Doppler fraction (dfrac). Methods of target classification (Bayes, Fuzzy logic, k-means). S-band multifunction phased array Radar (beam position, scanning losses, frequency stability).

### 3. NCTR experiments using MESAR2

Waveforms. Overall extent of trials data. NCTR signal processing chain. On & Off boresight static trials. Pod & Falcon aircraft trials. Targets of Opportunity trial.

### 4. Target classification using HRR profiles

Target data sheets. Range sidelobes from low frequency propeller modulation. Long or Short, Four Lengths & Pod or Falcon class definitions. Variation of length features. Six aircraft (Pod, Falcon, Dash8, B747, B757, B777) classification performance via length and 'Scattering center Model (SCM) compare' features.

### 5. Range-Doppler profiles & Doppler spectra classification

Prop, JEM or No Non Skin Doppler (NNSD) classes discriminated by dfrac. Six aircraft classification performance via dfrac. Range-Doppler profiles using multi-pulse burst stepped frequency waveforms. Classical stepped frequency model + JEM. Range-Doppler profiles of Targets of Opportunity.

### 6. Relationship between characteristics of stepped frequency methods and overall air target classification performance

Variation of confusion matrix off diagonal extent (ODE,  $\xi$ ) with: Pulse per burst  $P$ , frequency steps  $Q$ , length and dfrac thresholds, carrier frequency jitter. Classification via combined length & dfrac features.

## 7. NCTR waveform design recommendations

Generic operational requirements for a (stepped frequency) NCTR waveform. NCTR waveform design chart.

## 8. Conclusions & Recommendations

Reiteration of problem statement. Summary of research achievements and scientific contributions. Summary of specific results. Recommendations for further study. List of publications arising from this thesis.

### References

**Appendices A-P** are split into two broad categories:

- Theory sections on the main topics discussed in the thesis (phased arrays, Radar equation,  $\chi(x, z)$  function, linear chirp waveforms, JEM, stretch processing, k-means and Bayesian classification).
- MESAR2 trials data sheets for Pod, Falcon & Targets of Opportunity (maximum RCS, Range profiles, Doppler profiles).

## 1.6 Literature survey

The subject of Non-Cooperative Target Recognition using Radar is an active research area with many hundreds (if not thousands) of relevant research papers and textbooks. (e.g Tait [103]). In this thesis I will not attempt to survey the entire subject but instead focus on a subset relevant to three key areas which align to the main research aims. These are:

- Stepped frequency methods
- Doppler processing & Jet Engine Modulation
- Feature extraction and classification methods<sup>13</sup>

### 1.6.1 Stepped frequency methods

#### Overview

Following an overview of the terminology and hierarchy of target recognition, Skolnik [96] pp372 -375 effectively states the goal of the stepped frequency HRR method: the generation of a profile in range of sufficient resolution to discern individual scattering centres. Radial profiles of a commercial 757 airliner and the (now out of service) US Navy Gun Cruiser USS Baltimore are provided as illustrations. The latter is generated using an X-band system with a resolution of about 30cm i.e. an intrinsically wide bandwidth waveform is used. Clark [19] discusses the use of stepped frequency HRR waveforms in the detection of ballistic missiles. Particular reference is made to the problems associated with the bulk motion compensation of tumbling objects. In this thesis the bulk acceleration (and rotation) of targets, which are typically commercial aircraft, is ignored, i.e. a constant range-rate model is assumed for each look.

---

<sup>13</sup>With particular reference to classification of airborne targets using radar.

## Stepped frequency HRR profiling

What will be referred to as the Classical method in Chapter 2 is well documented in Wehner [111] pp200 - 237. The theoretical HRR profile for a point reflector is derived and the effects of target motion are alluded to. Wehner also discusses the use of pseudorandom frequency steps, i.e. rather than a one-way progression of carrier frequencies, (for example in a linear fashion up or down) a jumbled sequence is used. This can help to remove range-Doppler coupling effects resulting from target motion. This scheme is somewhat similar to the Costas waveforms described in Richards [88] pp222. In this case the frequency steps are chosen to yield an *Ambiguity diagram* for the waveform which has very low sidelobes in range and Doppler away from the central spike at the origin. Richards gives a summarized account of stepped frequency HRR. Like Wehner, he uses a fixed frequency pulse and alludes to the details of the resulting ambiguity diagram derived in the 2004 book by Levanon & Mozeson. Two key papers are of particular interest and are most likely source material for the book. The first by Levanon 2002 [58] describes the stepped frequency method in general terms. Similar papers are presented by Gill & Huang [34] and Kai [50], with the latter discussing the use of phase coding in the constituent pulses of the stepped frequency train. The second, coauthored by Mozeson [59] considers a scheme for the reduction of ‘grating lobes’ processing artifacts. Several papers consider this topic and add further colour to the theoretical exposition of the stepped frequency HRR method: Rabideau [87] and Gladkova [37],[38] consider the use of non-linearly stepped frequencies and the effect of this scheme upon the ambiguity function of the overall waveform.

## ‘Hybrid’ techniques

A further refinement of the stepped frequency method is to code in frequency the individual pulses that constitute the stepped frequency waveform. As applied in the Classical method, this allows for a more accurate means of identifying the ‘target sample’ at each carrier since the returns from each pulse can be pulse compressed in the conventional way to yield a (low resolution) range profile. M<sup>c</sup>Groary & Lindell [65] describe the theoretical frequency domain synthesis of samples from two  $\tau = 1 \mu\text{s}$ ,  $B = 75\text{MHz}$  chirps spaced in frequency such that the central section of each chirp forms a continuous bandwidth. Schimpf, Wahlen & Essen [92] describe a similar ‘bandwidth synthesis’ technique using 100MHz or 200MHz linear FM chirps transmitted using the 35 or 94GHz MEMPHIS mm-wave Radar operated by FGAN. Lord & Inggs [62] start from 347.5MHz (using 8 non-overlapping steps of 15MHz) but otherwise describe a very similar method, with some insight how to provide phase continuity between the frequency steps.

Ching Tai Lin and Cantrell [17] report similar results with three 100MHz linear FM chirps. Chirps are combined via an ‘inverse filter’ which appears to account for the fact the combined spectrum of three chirps of 100MHz bandwidth is different from a single chirp of 300MHz bandwidth. It is possible that the ‘frequency domain weighting’ proposed in the ‘Hybrid’ method discussed in this thesis are functionally similar to the application of the ‘inverse filter’. However, it is unclear whether the method properly accounts for HRR profile aliases in the manner proposed in this thesis.

Berizzi [12], provides extensive analysis of bandwidth synthesis via short pulse CW, linear FM pulses and phased coded pulses stepped in carrier frequency. The method appears to be closer in technique to the Classical processing described above. Rather than synthesize a wide-bandwidth waveform in the frequency domain, the HRR profiles formed for each receiver range cell are combined with an appropriate range offset. This could be viewed as an extension of the Classical method described in this thesis. The latter involves an initial pulse compression step to identify the range

cell of the target. Following motion compensation, the HRR profile is formed from the inverse FFT of these target samples, one for each frequency step. The Berizzi method could be summarized as a time domain combination of Classical HRR profiles. It is not totally clear from [12] how the Berizzi method deals with targets who range extent is beyond the Classical HRR window  $\frac{c}{2\Delta f}$ . A time domain synthesis of Classical profiles should cause ‘aliases’ wrapped into each profile to superpose. (See Background theory chapter). Although methods for grating lobe suppression (via careful choice<sup>14</sup> of frequency step  $\Delta f$  and pulse bandwidth  $B$ ) are discussed, it is not clear whether this is totally effective for alias reduction of extended targets.

An alternative to the subsequent “transmit, receive, shift frequency, repeat” of the stepped frequency waveforms described above is to break down a single transmission into sub-pulses of different frequency. This type of waveform is known as ‘frequency jump burst’ and is described by Maron [66].<sup>15</sup> There are clearly drawbacks with this approach. By transmitting a longer pulse train, the minimum range is increased and maximum pulse repetition frequency is reduced to achieve a sensible duty cycle. The benefit of pulse-Doppler processing between frequency steps (or indeed between frequency jump bursts) is therefore not fully exploitable. However, using a single transmit mode may well reduce the overall waveform dwell time which would be amenable to a multi-function Radar. (See Chapter 7). This could be doubly beneficial if the target is accelerating as a longer dwell assuming a constant range rate model may become less appropriate, resulting in a corrupted HRR profile.

The idea of removing the edges of the spectra of each chirp prior to bandwidth synthesis is outlined by Walbridge & Chadwick [109] and more recently Miller, Shepherd & Newman [70]. The term ‘Hybrid’ originates from the latter. The research in this document aims to continue from this work, principally to document the delivery and subsequent processing of Hybrid & Classical waveforms using an S-band phased array Radar.

### Impact of target motion

A number of recent papers consider methods for the mitigation of target motion induced effects associated with stepped frequency methods applied in phased array Radar. Zeng & Long [116] present a description of the implementation of a stepped frequency method using a phased array Radar, particularly the phase shifts required to maintain focus upon a target. Haiying & Ruliang [61] then derive a theoretical model to quantify the impact of uncompensated target range rate upon the HRR profile. Haotian *et al* [115] present a scheme for the automatic motion compensation of a stepped frequency waveform which appears to work without the need for a independent range-rate estimate. The method is based on a waveform which comprises of ‘positive’ and ‘negative’ frequency step ‘styles’ rather than the conventional fixed step linear increase. An alternative method considered by Bai Jin Liang *et al* [5] makes use of a ‘Fractional Fourier Transform’ (FRFT) and associated matrix based parameter estimation technique to remove the effects of bulk target motion. In this method there is no requirement for positive and negative frequency steps and, according the authors, the practical implementation of the method is comparable in computational efficiency to the Fast Fourier Transform (FFT). These methods might be useful if a single pulse is used per frequency step and each pulse has poor range resolution. (e.g. ‘modest’ pulse length CW rather than frequency coded pulses which yield

<sup>14</sup>By setting the pulse bandwidth  $B$  such that the nulls of the pulse temporal autocorrelation at intervals of  $\frac{c}{2B}$  correspond to the stepped frequency aliases separated by  $\frac{c}{2\Delta f}$ .

<sup>15</sup>The theoretical analysis of stepped frequency waveforms, in particular the ambiguity function presented by Levanon & Mozeson [59] are probably best described as Frequency Jump Burst. i.e. a single transmission of stepped frequency pulses.



(via pulse compression) range accuracies of a few tens of metres<sup>16</sup>). For the waveforms discussed in this thesis, motion compensation in the absence of a range-rate estimate from the tracking system could be achieved by firstly estimating a target range rate from the peaks of the pulse compressor outputs plotted against pulse number. Given the PRF is known (and fixed) for each waveform, the range rate could be obtained from the gradient of a linear regression of this data. Improvements upon the crude estimate are then made by considering the skin return deviation in the target Doppler spectra, which is incoherently summed over all frequency steps. (See section 3.5.2).

## Practical applications

In the majority of the examples cited, any practical implementation is typically using an X-band or millimetric Radar. Walbridge & Chadwick [109] provide an isolated example and discuss the use of 5MHz bandwidth pulses stepped by 3.2MHz, which matches one of the waveforms applied in MESAR2. (See Chapter 3). The S-band (3GHz) BYSON Radar installation at QinetiQ (formerly DERA) in Malvern, UK was used in this instance. However, results which demonstrate the practical application of stepped frequency waveforms in an operational context at S-band are not well represented. It is the practical demonstration of the use of stepped-frequency waveforms for NCTR, using a multifunction phased array Radar (with the prime example at S-band), that represents the main contribution to ongoing research captured in this thesis.

Stepped frequency Radar finds an application in sub-surface remote sensing, in particular buried object detection. The remote (and therefore safe) detection of explosive devices such as landmines is a pressing requirement for military & civilian personnel who live and work in regions undergoing current or recent conflict. Cattin [15] states that the generation of a (typically centimetre resolution) range profile (to a depth of a few metres) might be more optimally achieved using a stepped frequency approach than via an intrinsically wideband waveform as generated by an ‘impulse Radar.’ Cattin states: “Sensitivity, dynamic and investigation depth are improved. Moreover perturbations due to the antenna or material properties can be corrected for each frequency.” The latter concept is considered by Cherniakov [16] who derives weighting functions for the signal contributions at each frequency step prior to the Inverse FFT processing which yields the range (or depth) profile.<sup>17</sup> A theoretical discussion relating to the detection of buried spherical objects using stepped frequency Radar is presented by Freundorfer and Iizuka [32]. Based upon measurements of two 6.6cm dielectric spheres, a recommendation is made to use the ‘anti resonance mode’ since the backscattered signal is largest. Stickley *et al* [98] employ a system with carrier frequencies ranging from 10 to 620MHz with penetration to approximately 9m.<sup>18</sup> Sorensen [97] explicitly reports upon landmine detection using a 3.8-3.9GHz system with 100 steps of 3MHz, i.e. relatively similar to the waveforms described in this thesis. The method appears to successfully detect non-metallic anti-personnel mines as well as metallic variants.

Another novel application of stepped frequency Radar is in the remote mapping of ocean currents. Traditionally, ocean currents are detected remotely via HF band systems (3-30MHz) which tend to be large structures (i.e. several tens if not hundreds of metre arrays of antennae) to enable sufficient azimuth resolution for mapping purposes.<sup>19</sup> However Popstefanija *et al* [84] demonstrate a

<sup>16</sup>i.e. sufficient to detect the bulk position of the target in range but not infer any great detail about the position of scatterers, overall length etc.

<sup>17</sup>In all the references relating to stepped frequency methods applied to ground penetrating radar, a “Classical” technique is used.

<sup>18</sup>A delay of 60ns is quoted.

<sup>19</sup>Although HF radars require large antennae, they also offer the possibility of over-the-horizon marine surveillance

stepped frequency microwave Radar operating between 5.62GHz to 5.92GHz with 16 pairs of frequencies separated by between 2MHz and 40MHz can be employed to achieve an acceptable result. The HF frequency ‘Bragg’ spectrum, (which is used to quantify the ocean current magnitude and direction) can be derived via a cross correlation of each pair of signals followed by a power sum of these correlations. The method works because “the energy in the resonant peak in these cross products is correlated because the HF separation frequency of the transmitted microwave signals is the same. However, the energy of the cross products at other frequencies is uncorrelated so the averaging results in a spectrum having enhanced energy in the  $\Delta K$  (wavenumber) peak compared to energy in the background spectrum.”

## 1.6.2 Doppler processing and Jet Engine / Propeller Modulation

### Overview

There are numerous classic texts which describe the coherent processing of bursts of receiver samples obtained using a pulse-Doppler Radar. Skolnik’s *Introduction to Radar Systems* [96] provides a general introduction, although the discussion is mostly focussed on analogue systems which use delay lines to achieve signal processing effects. Skolnik’s *Radar handbook* [95] is a much more complete reference and provides useful pictorial examples relating to digitized receiver samples. An excellent, and modern, reference is by Richards [88]. Much of the discussion of Jet Engine Modulation (JEM) is summarized from Tait [103] which in turn provides a summary of the (open<sup>20</sup>) literature relating to JEM.

The theoretical model presented in section 2.4.2 is due to Martin & Mulgrew [67],[68] who derive the JEM spectrum from a simple electromagnetic model of rotating line antennas. Their model represents a propeller rather than a jet engine but is thought to be applicable at S-band [103] where it is less likely more than one engine stage will be resolved. A number of other papers present models of varying fidelity, but all come to the same basic conclusion: A rotating blade modulation will (principally) manifest as a set of spectral lines separated by a Doppler frequency shift equal to the product of the number of propeller blades and the propeller spool rate. Revelation of further spectral structure depends on wavelength and Doppler resolution.

### Helicopter modulation

Anderson [1] and Green [39] refer to helicopter modulation observed using HF band (3-30MHz) Radar. Anderson describes the spectral discrimination of two helicopters in a 1983 experiment using the Australian Jindalee skywave system. However, he reports a tough requirement of 60dB SNR to detect modulation lines for jet aircraft using this system.<sup>21</sup> Green derives theoretical models for the backscatter of HF frequency radio waves from rotating blades using a similar ‘rotating wires’ model as employed by Martin & Mulgrew. This model is compared to idealized experiments using 3000RPM rotors mounted upon scale models which are positioned in an anechoic chamber to minimize clutter. To account for the reduction in physical scale, frequencies are increased to 3.4GHz. Misiurewicz *et al* [73],[72] & Kulpa *et al* [56] present an analysis of Radar signal backscatter from a Russian MI-2 helicopter with 14.6m diameter blades rotating at 246RPM. A 4kHz PRF, S-band coastal surveillance

---

due to the possibility of surface and skywave propagation modes; i.e. the range extent for a HF radar is potentially far greater than an equivalent altitude microwave system.

<sup>20</sup>Previous (classified) work during the 1970s by W. Bardo of the UK Ministry of Defence Royal Signals & Radar Establishment is also credited in Tait [103].

<sup>21</sup>Which are predicted to appear 50dB below the skin return associated with the aircraft fuselage

Radar is used in these experiments. Kulpa states that the ‘shelf’ in spectra resulting from the rotating hub is more easily detectable if the fuselage skin return is removed from the spectra.

Pouliguen *et al* [85] present the most detailed theoretical description of the RCS of a rotating helicopter blade using Physical Optics (PO) methods combined with Method of Equivalent Currents (MEC) techniques to model diffraction effects from the edge of the blades. He Sisan *et al* [44] offers an alternative perspective by considering the detection of sinusoids in a stack of consecutive HRR profiles resulting from rotating structures. However, the method presented is possibly of limited practical use given the time domain signals resulting from propeller modulation typically appear to manifest as a series of regular impulses (‘blade flashes’) rather than a smoothly varying oscillation. Yoon [114] outlines techniques for exploiting the blade flash effect via use of a stacked Discrete Fourier transform. The time variation of the Doppler spectrum is used (as it is for propeller aircraft in this thesis) to estimate the blade flash rate.

## Jet Engine Modulation

Tong *et al* [105] describe a simple physical model of JEM where the engine air intake is represented as a cylindrical waveguide. Assuming ideal conductors, a scattering matrix is computed incorporating the effect of rotating blades. Bell & Grubbs [10] refer to previous work by Gardner, Hynes & Mensa (1967) and describe a parametric model based upon the periodic modulation of the scattered return. Their analysis is based upon experiments using a Hughes X-band Radar with a PRF of 25kHz, a pulse bandwidth of 1MHz and  $P = 1024$  pulses per burst. Piazza, Pellegrini, Cuomo & Pardini discuss models of JEM and its possibility to enable classification of civilian aircraft in a series of papers. [80] identifies JEM in the Doppler spectra of civilian aircraft and presents the finding that energy in JEM could be up to 20% higher than the skin return.<sup>22</sup> The paper also reports JEM effects “disappear for the transverse aspect” above 30° from nose on to the aircraft. [24]&[25] describe the details of a classification approach based upon a neural network. Data was gathered on five different civilian target classes and 5 target profiles (a mixture of raw signal and spectral) were used in classification. The Radar used a 32 pulse burst with a PRF of 1kHz. Training data proportions ranged from 3 in 5 to 12 in 76, and average confusion matrix diagonals ranged between 36% and 51% which implies that mis-classification is predicted to occur between 2 in 3 and 1 in 2 occasions. [79]&[83] describe the validation of the Martin & Mulgrew model against target spectrum data acquired using the S and L-band ATC radars at Fiumicino (Rome) and Linate (Milan) airports.

Miller, Shepherd & Newman [70] combine stepped frequency and Doppler processing to form range-Doppler images of targets where JEM lines can be localized in range. The research in this thesis is a continuation of this theme with the major difference being the use of an S-band phased array system with correspondingly different pulse lengths, bandwidths and sample rates. In [70] a sequence of 25 bursts (stepped in frequency by 4MHz) of 50 linear chirp pulses with a bandwidth of 270MHz and pulse length  $1\mu\text{s}$  were used. By contrast, MESAR2 uses a more modest bandwidth of 5MHz<sup>23</sup>.

<sup>22</sup>This observation is the motivation for the energy fraction (efrac) and Doppler fraction (dfrac) feature measurements discussed in section 2.5.6.

<sup>23</sup>It seems somewhat strange that the actual bandwidth of the transmitted waveform (250MHz) is higher than the entire bandwidth (100MHz) of the 25 x 4MHz frequency steps. In MESAR2, frequency steps of 0.8MHz and 3.2MHz were used using pulses of bandwidths between 4.5 and 5MHz. Hence the synthesized bandwidth is indeed significantly higher than it is possible to transmit for any given pulse.

### 1.6.3 Feature extraction and classification methods

#### Overview

The *classification* of remotely observed objects via features extracted from Radar data is a sub-field of the broad topic of *pattern recognition*. As outlined in the introductory chapter of the classic textbook by Duda [27],<sup>24</sup> the overall goal is to determine the *decision boundary* within a *feature space* such that feature measurements can be correctly assigned to their true class. In [27] the example is given of the classification of two classes of fish (sea bass and salmon) based upon a two dimensional feature vector comprising, respectively, of measures of fish width and skin lightness. The decision boundary is determined via a model of expected width and lightness for each class of fish. Techniques for the formulation of the boundary (for generic, non-fish specific problems!) form a major part of the field of pattern recognition, in particular when considering *decision theory*. In this literature survey we shall firstly consider the sort of features derived from Radar which are typically used for classification experiments. We shall then discuss references to methods of classification (classifiers) which, in essence, generate the decision boundary between feature measurements. Lastly we shall survey reports of classification experiments using Radar.<sup>25</sup>

#### Features used for target classification

Tait [103] provides a discussion of feature based classification vs template matching, the latter being the correlation of target profiles (either in range or Doppler, or both) with reference profiles. The theory of predicted classification performance via correlation based template matching is discussed in depth by Haspert [41]. The inherent variability (‘speckle’) of target profiles<sup>26</sup> with very small changes in aspect is considered both by Tait and Hudson [46]. They suggest that very large databases of range or Doppler profiles corresponding to many angular steps is required for this method to be robust. Van der Heiden [106] outlines additional problems associated with range profiles; a profile formed using a Discrete Fourier Transform (DFT) technique (see Classical method in Background theory) will have an unknown circular range shift. Hwang [47] proposes an additional matching algorithm where an incremental phase shift is added to the DFT of each range profile, thus enabling the profile under test to be ‘aligned’ to the database entry. Van der Heiden proposes a ‘Smoothed zero phase representation’ (SZPR) which achieves a similar effect. All profiles are aligned based upon a moving average DFT phase shift corresponding to the phase of the maximum correlation of profiles in range. In this thesis, all range profiles are generated such that the maximum power corresponds to the middle range cell. Further alignment techniques (based on maximum or start range) are then considered for the purposes of range profile combination. Hudson [46] considers the benefits of averaging range profiles. Using an 0.5m resolution S-band Radar<sup>27</sup> he defines an ‘encounter’ of 100 profiles sub-divided into ‘frames’ of 8 profiles. Using 119 encounters of 24 aircraft he is able to report significant improvements in classification performance based upon template matching when encounters are used rather than frames or indeed individual ‘looks.’ Zyweck & Bognor [121] add to this sentiment by noting that  $\sqrt{N}$

<sup>24</sup>Alternatively Webb [110] or Jain [49].

<sup>25</sup>The overall structure of this thesis is, in essence, an expanded version of the style typically adopted by papers which report classification experiments. i.e. theory section, choice of features, classification performance (possibly as a function of some property of the feature generation process and/or classification method).

<sup>26</sup>Zyweck & Bognor [120] propose that specular reflection, as oppose to diffractive scattering, is the dominant contributor to target RCS at typical radar frequencies using the example of ISAR imagery of a Mirage III aircraft observed at  $\approx 9\text{GHz}$ .

<sup>27</sup>Air Force Rome Air Development Center

signal to noise ratio improvement can be achieved via *coherent* combination of range profiles i.e. those formed from a burst of phase coherent pulses, relative to a non-coherent power sum over different looks.<sup>28</sup>

A practical alternative to template matching is to instead extract a number of features from the target profile which are themselves less sensitive to changes in aspect angle, as discussed by Nieuwoudt [78] who compares feature vs correlation based classifiers<sup>29</sup>. Zyweck & Bogner [118], [119] present a practical classification scheme (evidenced using recordings of several commercial aircraft leaving Adelaide airport) based upon ‘dimensionality reduction’, which is to collapse a large number of features (effectively samples of the target Doppler spectrum) into a feature space with much fewer dimensions. Stove & Sykes [100],[101] employ a similar ‘PCA’ technique<sup>30</sup> for reducing the Doppler spectra of personnel, wheeled or tracked vehicles into two dimensional feature vectors. Atrouz [3] also employs PCA in a less dramatic fashion, reducing 64 sample range profiles to 26 element vectors. Alternatively, Mitchell [74] demonstrates that (Rician) probability distributions can be estimated for the amplitude associated with each range bin. He forms a classification process by combining the probabilities of each (measured) range bin amplitude given the estimated distribution for each class. This is an example of classifier combination rather than feature combination.<sup>31</sup> In this thesis we use ‘physical’ features (i.e. length and a shape characteristic of the Doppler spectrum) since the focus is to understand the underlying causes of changes to classification performance when profile resolution is degraded and feature measurement thresholds are varied. (Which would be harder to understand if a scalar output Karhunen Loeve transform was used, for example). It is also more obvious how to define *a priori* feature distributions using physical observables, a necessity in this thesis given the lack of adequate training data. Whether this physical approach is less optimal in an operational context (with the possibility of human-in-the loop classification and the obvious need for meaningful features) compared to training data driven dimensionality reduction techniques, is outside the scope of this thesis.

## Classification methods

In addition to textbook references such as those by Webb [110] and Duda [27], Kotsiantis [54] provides a review of ‘supervised’ machine learning<sup>32</sup>, which he defines as follows:

“Supervised machine learning is the search for algorithms that reason from externally supplied instances to produce general hypotheses, which then make predictions about future instances. In other words, the goal of supervised learning is to build a concise model of the distribution of class labels in terms of predictor features. The resulting classifier is then used to assign class labels to the

<sup>28</sup>A coherent sum of  $N$  pulses will yield an increase in signal to noise ratio by a factor  $N$ . An incoherent sum (i.e. a sum of magnitudes or powers) can be shown (see any Radar textbook such as Skolnik [95]) to only offer an improvement of  $\sqrt{N}$ . The relative SNR improvement going from incoherent to coherent is therefore  $\sqrt{N}$ .

<sup>29</sup>Nieuwoudt [78] classifies four different aircraft types ranging from a 7.3m ‘Arrow’ to a 41.5m B727-200 using simulated HRR profiles created from plan drawings. Range profiles are reduced to a smooth ensemble of peaks using Burg and MUSIC super-resolution algorithms. Classifier performance is then evaluated against target aspect and range resolution. A similar analysis of classification performance (via HRR template matching) vs range resolution is presented by Rosenbach [90].

<sup>30</sup>PCA stands for Principal Component Analysis. A covariance matrix is formed from a set of training data vectors. The eigenvectors of the covariance matrix, ordered by size of associated eigenvalue, are used as basis vectors for a new set of dimensions. For example, if a feature vector (e.g. a HRR profile) has 128 elements, this can be ‘dimensionality reduced’ to two elements by outputting the scalars resulting from the projections using the first two eigenvectors. (Which will also be 128 element vectors). This projection by covariance matrix eigenvectors is also known as the Karhunen Loeve transform. An expanded discussion of PCA and its application to target classification using radar is provided by Borrión [13].

<sup>31</sup>Kahler [51] describes the use of both feature and decision level fusion.

<sup>32</sup>Which includes Bayesian, Neural networks, Nearest neighbour, Support Vector Machine and other classifier methods.

testing instances where the values of the predictor features are known, but the value of the class label is unknown.”

Webb essentially defines unsupervised learning as the automatic assignment of classes via a clustering algorithm applied to a data set, i.e. the class alphabet (and associated characteristics) are not defined *a priori*.

Fuzzy logic methods initially proposed by Zadeh are presented as a comprehensive tutorial by Mendel [69]. A practical Radar classification example and theory summary is provided by Colin & Moruzzis [22] who make the distinction between ‘Possibility’ (which corresponds to the maximum value of the fuzzy membership function over classes for a given feature measurement) and ‘Necessity’ (which considers the distribution of a particular feature measurement). In this thesis the fuzzy logic classifier includes ‘Possibility’ but not ‘Necessity’ (the inclusion of which could be a potential refinement).

Bayesian Gaussian classification is briefly described by Tait [103], Vespe [108] and in greater detail by Duda [27], Webb [110], Krieg [55], Das, [26], Heckerman [42] and Murphy [76],[77].<sup>33</sup> This is a well established technique and typically forms the point of departure for any serious discussion of parametric classifiers. The Friedman Regularized Discriminant (FRD) method employed in this thesis is described by Webb and is in essence based upon the assumption of Gaussian probability distributions of feature measurements deriving from a particular class. The FRD recipe allows for the estimation of the feature mean and covariance matrices for each class if training data is provided. A slightly different approach for estimating these parameters is presented by El-Matouat *et al* [28] who use the concept of the ‘optimal histogram;’ i.e. the quality of the estimation of the underlying feature probability distribution per class is dependent of the histogram bin size; too large or too small and no structure is revealed for a finite data set.

The *k-means* classifier is a popular *non-parametric method* which is based upon the iterative Generalized Lloyd algorithm (Karayiannis 1995). The version described here (see section 2.6.4 and the Appendix) is an application of the methods of Bezdeck, Ehrlich & Full cited in Bowden [14] and Wong [113]. *k-means* classification is widely referenced, although perhaps more as a data clustering algorithm rather than a classification scheme. Vespe [108] provides a very clear introduction to this method. Pham [82] describes a novel use of *k-means* clustering to help reduce the database size for a template matching scheme, i.e. clustering regions of aspect angle where the range profile is moderately invariant.

Van der Walt [107] reviews general characteristics of data which determine classifier performance and compares parametric and non-parametric classifiers. The effect of noise is compared independently of the natural distribution of features and the amount of feature data is related to classifier dimensionality.

## Target classification experiments

A thorough application of a Bayesian classifier<sup>34</sup> using target feature data of a similar nature proposed in this thesis is presented by Leung & Wu [60]. Target identity from an Identify Friend or Foe (IFF) system, elevation measurement from Radar and target speed & target acceleration from a tracker are used as features to classify targets into broad categories based upon permutations of ‘hostile’, ‘friendly’, ‘commercial’, ‘military’, ‘unknown’ and ‘clutter.’ This type of classification of physical at-

<sup>33</sup>There are a large number of references describing Bayesian classifiers and Bayesian Networks. A recommended website is <http://www.cs.berkeley.edu/~murphyk/Bayes/bayes.htm> which provides an overall summary and plenty of links for further reading.

<sup>34</sup>and an alternative ‘Dempster-Shafer’ methodology.

tributes into general categories that are of operational significance is the methodology adopted in this thesis. A comprehensive scheme for target classification is presented by Bastiere [9]. The MILORD system deployed upon the BEM MONGE measurement & test vessel operated by the French Navy deploys Bayesian and fuzzy logic classifiers using features taken from kinematic, HRR, Doppler and ISAR Radar measurements.

Rosenbach [91], like Zyweck & Bogner [118], [119] devise a practical feature processing and classification scheme for aircraft targets. Following a thresholding and normalization process, range profile features are extracted via Kohonen-net dimensionality reduction of Zernike moment magnitudes. The latter is a rotation invariant transformation of the range profile. Zyweck & Bogner by contrast opt for a DFT of range profile magnitude which corresponds to a translation invariant transform. Rosenbach then compares Bayes, Neural network<sup>35</sup> and k-nearest-neighbour classifiers. Hu [45] presents a paper along similar lines. HRR profiles are used “to avoid the complexity of ISAR” and are reduced to a nine dimensional feature vector corresponding to various statistical characteristics such as length, maximum, asymmetry etc. A Mellin transform is applied to the data to circumvent scale variations due to aspect angle change, and dimensionality reduction via the Karhunen Loeve method is also considered. Neural network and nearest neighbour classifiers are applied and compared to a simple correlation filter (template matching) approach.

Jahangir [48] and Stove & Sykes [100],[101] discuss classification of land based targets divided into personnel, wheeled or tracked classes using Doppler spectra measurements. Using a 15.75GHz, 4kHz PRF Radar, Jahangir claims the profiles are “invariant to aspect angle and speed” and therefore form the basis of a robust identification system. Jahangir develops a ‘Hidden Markov Model’ (HMM) to predict the evolution of (dimensionality reduced) feature vectors over time. Classification is determined via the most probable dynamic model based upon a measured time series of Doppler spectra. Stove & Sykes describe classification experiments using the AMSTAR battlefield surveillance Radar and employ dimensionality reduction via PCA and classification using a Fisher linear<sup>36</sup> discriminant. The Doppler frequencies associated with the AMSTAR experiments are of the order of a kilohertz which enable the Radar spectrum to be replayed to an operator as an audible tone. Stove & Sykes remark that automatic classification (which requires typically less than 100ms dwell) can proceed faster than human classification which, even for trained operators, can take several seconds.

Miller, Shepherd & Newman [70] present graphs of classification performance (although not a full confusion matrix) using 58 data sets consisting of 6 different aircraft types. Performance is evaluated using feature measurements (length and presence of JEM are mentioned) and correlation of HRR profiles with a database of 612 range profiles of aircraft. Both measures are plotted as a function of additive noise and range resolution. A similar method is presented in this thesis using data obtained using MESAR2. In addition to a change of sensor, in this thesis we also explore a variation of waveforms (frequency step size, and numbers of pulses per burst), consider a much larger dataset (1498 NCTR looks upon 17 distinct target types) and compute full confusion matrices using k-means, Fuzzy Logic and Bayesian classifiers. A variety of class distinctions are considered; from all aircraft types to some very general discriminators such as ‘long’ and ‘air-breathing’ (e.g. contains a jet engine or propeller). The robustness of feature measurements (for example the statistical variation of length measurement) are considered as a data quality check. Classification performance results can then be better understood by virtue of a comparison of the estimated probability density functions of feature

<sup>35</sup>For a more comprehensive analysis of neural network based classification using turntable data see Abbott [2].

<sup>36</sup>Note: A Gaussian Bayes method such as FRD is a *quadratic* discriminant - i.e. the discriminant function varies as the square of the elements of the feature vector.

measurements between classes.



# Chapter 2

## Background theory

### 2.1 Chapter summary

The purpose of this chapter is to provide a theoretical foundation from which research topics discussed in later chapters are based. As stated in the Introduction, (and indeed the title) the topic of this thesis is primarily concerned with target recognition modes applied using multifunction phased array Radar. To consider the practical realization of such systems we shall refer to attributes of MESAR2, which shall naturally constrain our discussion of target recognition to the subset of methods applied in its operation. Note inferences made following analysis of the NCTR modes applied using MESAR2 are of course generally applicable to any form of sensing system adopting similar waveforms and processing techniques. This argument is founded on the basis that MESAR2 has been designed as an experimental multifunction radar “technological testbed” rather than a tightly specified production system.

For reasons of cost and historical design preference, the NCTR modes in MESAR2 are implemented as bursts of phase-coherent pulses (allowing for the possibility of determining the target’s internal motion induced Doppler spectrum) and ensembles of bursts, each stepped in carrier frequency by a fixed amount. Each pulse is coded in frequency with an instantaneous bandwidth which can be at most 5MHz. There are of course in general many other ways of performing target recognition, as described in Table 1, such as polarimetry, SAR and ISAR techniques. [103]. None of these are applied in MESAR2.<sup>1</sup> Other waveform choices which can lead to viable high range resolution modes such as very short, high energy ‘impulse’ pulses or wide bandwidth *stretch* waveforms<sup>2</sup> were also not implemented in MESAR2 by design choice.

In this chapter, the ‘Classical’ method of stepped frequency High Range Resolution profiling, as deployed in MESAR2, is discussed first. The successes, and limitations, of this technique are highlighted using examples from the (static) trials data set. An alternative processing scheme, the ‘Hybrid’ method, is presented to improve upon the (literal!) shortcomings of the Classical method. Doppler processing is then discussed and ‘Skin’ and JEM line features of a target Doppler profile are defined from a theoretical standpoint. After a discussion of feature measurement (length, scattering centres and RCS from HRR profiles, Doppler fraction (dfrac) from Doppler spectra), three methods of target classification (k-means, Fuzzy logic and Bayesian) are described, leading to a recipe for

---

<sup>1</sup>ISAR may be possible using a manoeuvring target with a continually changing aspect angle to the radar, totalling a significant angular change over the duration of an NCTR look. However, since most of the experiments were based upon targets of opportunity which in the main followed linear trajectories, this technique was not explored. Indeed most targets were chosen based upon a radially inbound trajectory.

<sup>2</sup>See Appendix and section 2.7.4 for a discussion of the benefits and limitations of stretch processing.

computing classification performance. Lastly we discuss the practical features and limitations of an S-band multifunction phased array Radar used for NCTR. In particular, the differences between the stepped frequency techniques applied in MESAR2 and methods deployed in other Radar sensors such as Stretch Processing and use of True Time Delay.

## 2.2 Classical stepped frequency High Range Resolution profiling

### 2.2.1 The stepped frequency concept

Define a waveform consisting of  $Q$  single pulse transmissions (or  $Q$  bursts of  $P$  coherent transmissions) with each being radiated using a different carrier frequency  $f_{Tx}(q)$ . The pulses are transmitted by a monostatic Radar which generates a set of complex receiver samples  $\{\psi_{q,p,k}\}$  between the transmission of pulses.  $k$  is the range cell number of the  $K$  receiver samples for each pulse  $p$  of burst  $q$ . Consider for simplicity  $P = 1$  and a simple rectangular pulse of constant frequency and duration  $\tau$ . The carrier frequencies are linearly stepped by interval  $\Delta f$  and begin with frequency  $f_1$ . Let a Radar illuminate a static reflector at range  $R_T$  which corresponds (approximately) to range cell  $k_*$ . The  $Q$  (mixed down) signal samples at range cell  $k_*$  corresponding to the target reflection are

$$\psi_q = \psi_0 e^{-i\phi} \quad (2.1)$$

where phase

$$\phi = 2\pi f_{Tx}(q) \frac{2R_T}{c} = \frac{4\pi R_T f_{Tx}(q)}{c} \quad (2.2)$$

and carrier frequency

$$f_{Tx}(q) = f_1 + (q-1)\Delta f \quad (2.3)$$

i.e. it is assumed each sample has the same phase reference, which could be achieved via calibration between frequency steps and phase locking during a burst.

Hence

$$\psi_q = \psi_0 e^{-i \frac{4\pi R_T}{c} (f_1 + (q-1)\Delta f)} \quad (2.4)$$

$$= \psi_0 e^{-\frac{4\pi i R_T (f_1 - \Delta f)}{c}} e^{-\frac{4\pi i R_T \Delta f}{c} q} \quad (2.5)$$

Let us compute the Discrete Inverse Fourier Transform<sup>3</sup> (DIFT) of these samples to generate a  $Q$  component vector with elements  $\{y_n\}$ . For a derivation of the last step, see the Appendix.

$$y_n = \frac{\psi_0}{Q} e^{-\frac{4\pi i R_T (f_1 - \Delta f)}{c}} \sum_{q=1}^Q e^{\frac{2\pi i (q-1)(n-1)}{Q} - \frac{4\pi i R_T \Delta f}{c} q} \quad (2.6)$$

$$= \frac{\psi_0}{Q} e^{-\frac{4\pi i R_T (f_1 - \Delta f)}{c} - \frac{2\pi i (n-1)}{Q}} \sum_{q=1}^Q e^{\frac{2\pi i q}{Q} \left( n-1 - \frac{2R_T Q \Delta f}{c} \right)} \quad (2.7)$$

$$= \frac{\psi_0}{Q} e^{-\frac{4\pi i R_T (f_1 - \Delta f)}{c} - \frac{2\pi i (n-1)}{Q}} \left( \frac{e^{ix} \sin \left\{ \left( 1 + \frac{1}{Q} \right) x \right\}}{\sin \left( \frac{x}{Q} \right)} - 1 \right) \quad (2.8)$$

where  $\frac{x}{\pi} = n - 1 - \frac{2R_T Q \Delta f}{c}$ . If range cells are defined

$$R(n) = \frac{c}{2Q\Delta f} (n - 1)$$

---

<sup>3</sup>A Discrete Inverse Fourier Transform (DIFT) is a linear filter of the form  $y_n = \sum_{q=1}^Q w_{n,q} \psi_q$  where  $\{\psi_q\}$  are the set of signal samples and  $w_{n,q} = \frac{1}{Q} e^{\frac{2\pi i (q-1)(n-1)}{Q}}$  are the filter weights.

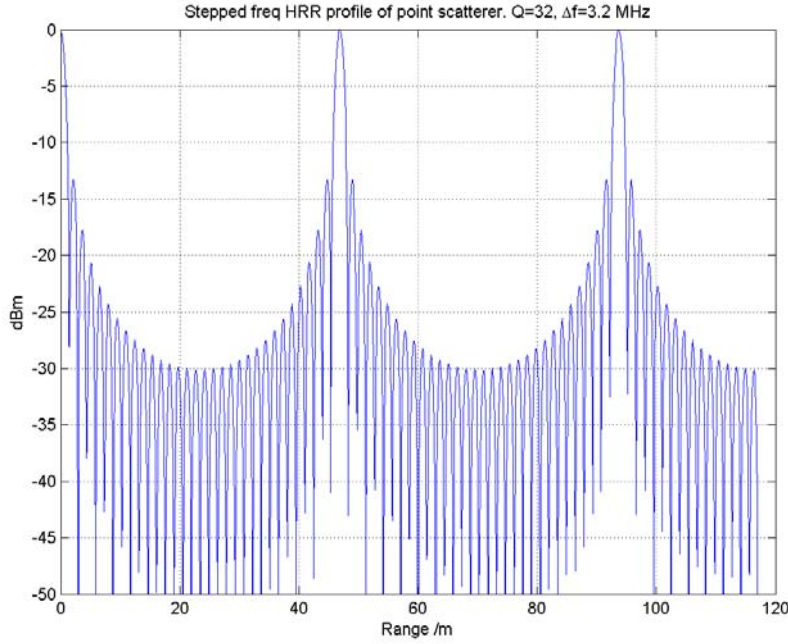


Figure 2.1: Stepped frequency HRR profile of a static point reflector using  $Q = 32$  frequency steps of  $\Delta f = 3.2\text{MHz}$ . No windowing has been used to reduce sidelobes. Peaks have range width of  $\delta R \approx \frac{c}{2Q\Delta f}$  and are aliased at intervals of  $\Delta R = \frac{c}{2\Delta f}$  (46.8m).

then

$$\begin{aligned} x(n) &= \pi \left( \frac{2Q\Delta f}{c} R(n) - \frac{2R_T Q\Delta f}{c} \right) \\ &= \frac{2\pi Q\Delta f}{c} (R(n) - R_T) \end{aligned}$$

Since the complex numbers  $\{\psi_q\}$  amount to frequency domain samples of the reflector, the DIFT of these is an approximation to its temporal signature, and since Radar range is proportion to signal delay, the filter output power  $\Psi = |y_n|^2$  can be thought to be a *range profile*. (See figure 2.1) The peak of this repeats periodically when  $x = \pi QZ$ , where  $Z$  is an integer, and has value at the peak(s) of  $Q^2$ . The peak half width of  $\Psi(R)$  can be shown to be  $\frac{c}{2Q\Delta f}$  [88].

In summary, the power of the DIFT of a set of samples of a point reflector, (where each sample derives from a transmission whose carrier is stepped in frequency by  $\Delta f$ ) is a function with periodicity in range  $R$  of  $\frac{c}{2\Delta f}$  and peak width  $\frac{c}{2Q\Delta f}$ . We can infer from this the  $Q$  length vector output of the DIFT will be spaced in frequency by  $\frac{c}{2Q\Delta f}$  and occupy the range window  $\left[0, \frac{c}{2\Delta f}\right]$ . Hence if the parameters are chosen appropriately, one can achieve a sub-metre resolution range profile of a target, albeit ambiguous at integer multiples of  $\frac{c}{2\Delta f}$ . The problems of forming profiles of targets with range extents longer than  $\frac{c}{2\Delta f}$  will be discussed in section 2.2.4 below.

### 2.2.2 The practical need for stepped frequency waveforms

The range resolution of a Radar system which uses waveforms defined over bandwidth  $B$  can be at most

$$\delta R = \frac{c}{2B} \quad (2.9)$$

i.e.

$$\delta R/m = \frac{149.9}{(B/\text{MHz})} \quad (2.10)$$

where  $c = 2.998 \times 10^8 \text{ ms}^{-1}$  is the speed of light and  $B$  is the bandwidth of the waveform transmitted.<sup>4</sup> A modern system is likely to employ a digital signal processor which requires the sample rate  $f_s$  to be at minimum equal to  $B$  by the Shannon-Nyquist criterion. (See Richards [88] pp27). For sub-metre resolution, the waveform bandwidth must therefore be greater than 149.9 MHz and the receiver sample rate must be greater than or equal to this. This is well within the capabilities of modern tracking Radar systems [103] which often operate at X band (9-10 GHz) and fix all of their attention upon a single target. Tracking Radars are typically cued from another surveillance sensor. Modern analogue to digital converters can run at a sample rate in excess of 100 Mega-samples per second at 14 to 16 bits per sample.<sup>5</sup> However, for a number of design choice reasons, the S-band multi-function system MESAR2 can only sample at 5 MHz. In MESAR2 the limitations upon  $f_s$  are twofold. Firstly, the relatively low transmission duty cycle<sup>6</sup> (pulse length divided by pulse repetition interval) implies a very high time fraction of continuous data sampling. Data processing has to introduce minimal latency in order to keep up with this near ceaseless torrent of data. Unlike a tracking Radar, in surveillance mode all range cells are processed. Secondly, a phased array system will naturally have a degree of loss resulting from the scanning of a beam as the pulse bandwidth is swept. (See section 2.7). For lower carrier frequencies, the fractional change of  $\approx 150$  MHz becomes more significant. Hence the amount of inter-pulse scanning of an S-band system will be greater than an equivalent X-band sensor. Note this is not so much of an issue with reflector antennas, which do not squint as phased arrays do. Phased array squint can be corrected for using True Time Delay techniques (see section 2.7.3) or equivalently sub-microsecond changes to the phase shifters to account for deviations in instantaneous frequency of the transmitted pulse from the carrier. However, these corrections can add significant extra cost, and possibly weight, to a Radar.

In summary: since MESAR2 is limited to sample rates of the order of 5 to 10 MHz, to achieve sub-metre range resolution one requires a stepped frequency waveform approach since True Time Delay or sub-microsecond phase shifter changes are not implemented.<sup>7</sup>

### 2.2.3 ‘Classical’ method stepped frequency processing

Stepped frequency high range resolution profiling, as described in section 2.2.1 can be practically achieved by transmitting frequency coded pulses which are mixed with a carrier whose frequency is stepped between bursts. The frequency coding is used to enable the range resolution achieved with each set of receiver samples to be better than  $\frac{1}{2}c\tau$  where  $\tau$  is the pulse length. This is achieved by cross-correlating the combined in-phase and quadrature representations of the received signal (i.e. as a complex number) with a static point target reference.<sup>8</sup> This method is commonly known as *Pulse*

<sup>4</sup>Unless super-resolution algorithms [117] have been applied, obtaining extra resolution while trading signal to noise ratio. [103]

<sup>5</sup>[www.analog.com](http://www.analog.com). October 2006.

<sup>6</sup>Even if it were to rise to say 50%, a surveillance sensor will process everything received (i.e. 50% of total Radar time) which will still equate to an overall high data rate.

<sup>7</sup>If the within-pulse squinting problem can be resolved, *stretch* techniques (see section 2.7.4) can yield high range resolution using a wide bandwidth waveform (i.e. not stepped in frequency) but without the need to sample at frequency equal to or above the waveform bandwidth. However, stretch techniques have their own limitations and require major changes to the receiver hardware.

<sup>8</sup>The static point target reference is typically weighted by an amplitude taper. This has the effect of reducing the range sidelobes of the pulse compressor output, albeit at the expense of a slight broadening of the range resolution (set by the main lobe width) beyond  $\frac{c}{2B}$

*Compression* (Richards [88] pp43) and can achieve a theoretical range resolution of  $\delta R = \frac{c}{2B}$  where  $B$  is the swept bandwidth of the coded pulse. Applying pulse compression to an ensemble of stepped frequency receiver samples can enable the most appropriate range cell to be chosen for the target. This is clearly desirable since the Classical method requires a single complex sample per frequency step. In this thesis we will refer to two popular frequency coding schemes. *Linear chirp* waveforms employ a constant rate of change of frequency within the pulse length. These are required by Hybrid spectral stitching method described in in section 2.3 below. A common alternative to linear chirp coding is to use a non-linear frequency sweep<sup>9</sup>, such that the autocorrelation function of the pulse has intrinsically low range sidelobes without having to resort to a weighting function. In Chapter 3 we demonstrate that non-linear chirp waveforms can, compared to linear chirp waveforms, offer a slight improvement in Classical HRR profile sidelobe levels.

As illustrated in figure 2.2,  $Q$  bursts of linearly swept ‘chirp’ pulses are alternately transmitted and received, with the carrier frequency of each burst<sup>10</sup> stepped by a constant interval  $\Delta f$ . All transmissions are steered at a target already being tracked (i.e. its range and range-rate are known) and the opening time of the receiver is set such that the anticipated reflection can be fully captured. Following a mix-down to baseband, digital sampling at rate  $f_s$  results in sets of  $Q$  complex receiver samples. These are pulse-compressed to yield a stack of  $Q$  target range profiles with range cells of width  $\frac{c}{2f_s}$ , where  $c$  is the speed of light. If the target is well defined, i.e. resulting in a dominant single peak in the range profile, a set of  $Q$  peak ranges can be determined. These measurements, in conjunction with the target range-rate supplied by the tracking system, can be used to take  $Q$  complex samples at the range of the target. Further motion compensation is applied by subsequently correcting each sample by subtracting the phase resulting from any change in propagation distance to the target as a result of target motion during the illumination period.

The  $Q$  complex numbers can be thought of as being the frequency domain samples of the target since each corresponds to a carrier stepped in frequency by  $\Delta f$ . Application of an inverse Fast Fourier Transform to the target samples yields a set of time (and therefore range) samples bounded by a ‘window’ of  $\frac{c}{2\Delta f}$ . The range interval is thus  $\delta R \approx \frac{c}{2Q\Delta f}$ . The range resolution obtainable following pulse compression of a chirp of bandwidth  $B$  is  $\delta R \approx \frac{c}{2B}$ <sup>11</sup> i.e. effectively limited by the instantaneous bandwidth of transmission and thus the receiver sample rate. In an S-band system one is practically limited to values of 5 to 10 MHz, which gives a range resolution of between 15 and 30 metres. The corresponding resolution of a ‘Classical’ range profile is not bound by such restrictions as long as the Radar can transmit over a much larger spectral domain, albeit in small segments during any one transmission, and sufficient time is available to deliver the stepped frequency waveform. Sub-metre range resolution is therefore obtainable with an S-band Radar. For example,  $Q=100$  frequency steps of  $\Delta f=3\text{MHz}$  gives a resolution of  $\approx 50\text{cm}$ .

### 2.2.4 Limitations of Classical stepped frequency processing

The range window provided by the Classical method of HRR processing is limited to  $\Delta R = \frac{c}{2\Delta f}$ . A frequency step of 3MHz will give a window of length  $\approx 50\text{m}$ . A large aircraft such as a Boeing

<sup>9</sup>This can be approximated by an arctanh function  $f(t) = \frac{B}{\tau} \tanh^{-1}(\frac{2t}{\tau})$  given variables time  $t$ , frequency  $f$ , pulse length  $\tau$  and bandwidth  $B$ . The rate of change of frequency at the centre of the pulse ( $t=0$ ) is the same as a linear chirp. i.e.  $\frac{df}{dt}|_{t=0} = \frac{B}{\tau}$ .

<sup>10</sup>A set of coherently transmitted pulses; i.e. a continuous measurement of phase is measurable during times when the burst pulses are received. In this document, all transmitted pulses within each burst will use the same carrier frequency.

<sup>11</sup>The receiver sample rate must exceed the Shannon-Nyquist criterion to avoid aliasing of target returns i.e.  $f_s > B$ . The width of a target response following pulse compression will therefore span one or more range cells.

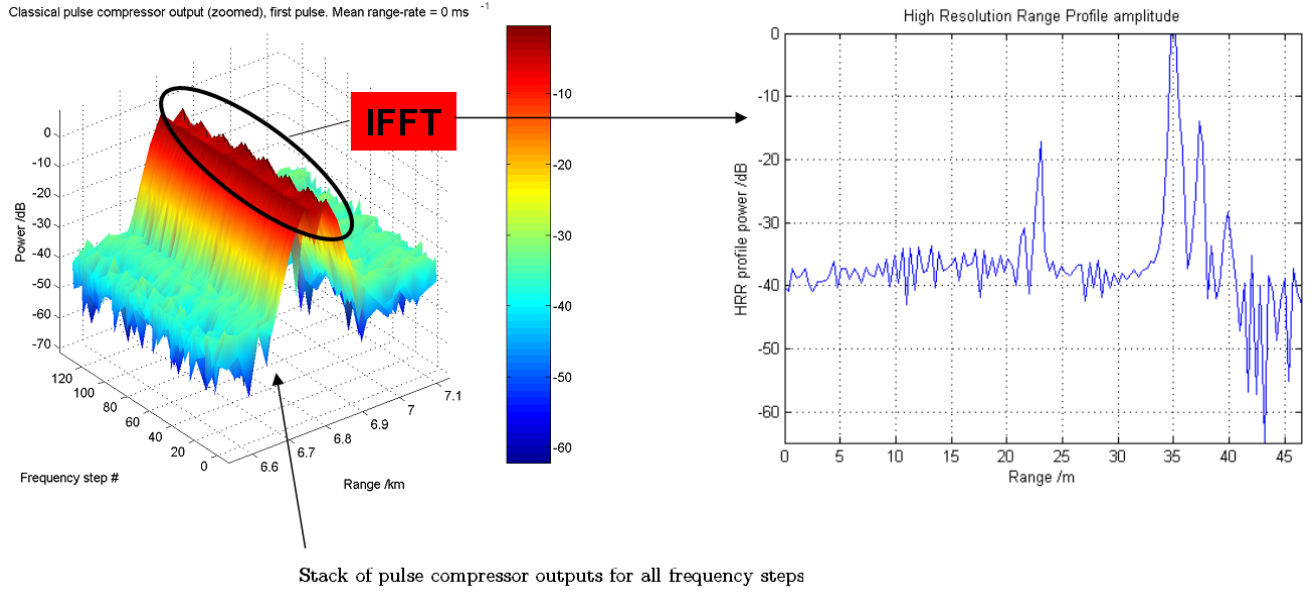


Figure 2.2: Classical method explained in pictures.  $Q$  complex samples are taken from the pulse compressor output, (following motion compensation) at the range cell corresponding to the target position. A HRR profile is formed from the output power of a Discrete Inverse Fourier Transform (DIFT) of the complex samples.

747 (70.7m) or Airbus A380 (80m) will exceed this for many look orientations and yield a profile of principal returns (‘scattering centres’) from, say, the nose, main engines and tail-fin out of their actual range order, as illustrated in figure 2.3. Since any peak in the Classical profile will be *a priori* range ambiguous by integer multiples of  $\frac{c}{2\Delta f}$ , this presents a significant challenge in post-processing to disentangle the data set in order for the processes of feature extraction and ultimately, non-cooperative target recognition, to work.

There is a additional problem. As target scattering centres become further separated, their gain relative to those well within the  $\frac{c}{2\Delta f}$  window about the ‘range’ of the target will rapidly reduce. This is because all the scattering centres which comprise the target contribute to a single complex sample interpolated from the pulse compressor output of each of the  $Q$  frequency steps. If the separation of the target’s scattering centres exceed the Radar compressed pulse width, the component scatterers will be resolved by the pulse compressor. As a result, the method of ‘target sampling’ will tend to ignore much of the target structure. Both these effects were observed during the MESAR2 static trials described in Chapter 3. Figure 2.2 shows the Classical HRR profile of two dipoles separated by 58m. In this example a frequency step of 3.2MHz was used which gives rise to a HRR window which is less than the separation, causing wrapping and loss of gain effects. The latter is clearly evidenced by the resolution of the two dipoles in the pulse compressor output and the target samples taken at a significant separation from the second dipole.

### 2.2.5 Motion compensation

If the motion of a target is not corrected for prior to HRR processing, the resulting profile will be corrupted. General effects may involve combinations of peak broadening (and resulting loss of resolution), range shifting of peaks and loss of dynamic range. To explain the source of these corruptions let us consider a point reflector moving at (constant) range rate  $v$ . Between frequency steps (which occur

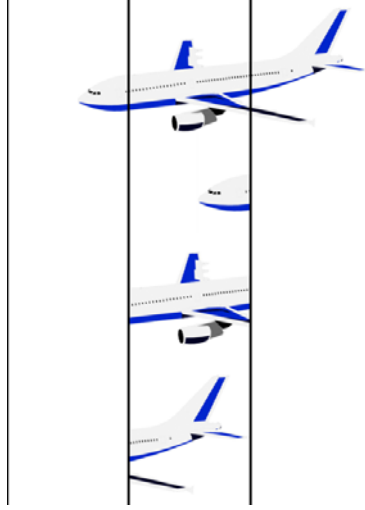


Figure 2.3: Extended range targets (such as a Boeing 747) will ‘wrap’ into the Classical window if the actual range extent is longer than  $\frac{c}{2\Delta f}$ .

at equal intervals  $\Delta t$ ) the target moves in range by  $v\Delta t$  and thus contributes extra phase  $4\pi f_{Tx}v\Delta t/c$  to target samples  $\psi_q$

$$\psi_q = \psi_0 e^{-\frac{4\pi i}{c}(R_T + (q-1)v\Delta t)(f_1 + (q-1)\Delta f)} \quad (2.11)$$

$$= \psi_0 e^{-\frac{4\pi i R_T \{f_1 - \Delta f + v\Delta t(\Delta f - f_1)\}}{c}} e^{-\frac{4\pi i \{R_T \Delta f + v\Delta t(f_1 - 2\Delta f)\}}{c}} q e^{-\frac{4\pi i}{c}v\Delta t\Delta f q^2} \quad (2.12)$$

The linear term  $e^{-\frac{4\pi i}{c}\{\dots\}q}$  is now shifted by the transformation  $R_T\Delta f \rightarrow R_T\Delta f + v\Delta t(f_1 - 2\Delta f)$  which results in a range shift of the HRR peak formed from the Inverse Discrete Fourier Transform of  $\{\psi_q\}$ .

The quadratic term  $e^{-\frac{4\pi i}{c}v\Delta t\Delta f q^2}$  results in a corruption of the profile. If  $v$  is modest the quadratic term results in peak broadening.

## 2.3 Hybrid stepped frequency High Range Resolution profiling

### 2.3.1 Requirements

The ‘Hybrid’ technique presented in this thesis is an attempt, via modified signal processing, to yield range profiles obtained using stepped frequency waveforms<sup>12</sup> which are not subject to the Classical limitations discussed above. The requirements for the Hybrid technique might be summarized as follows:

1. Yield identical range profiles within the range  $\pm \frac{c}{4\Delta f}$  (about the profile maximum) as returned via the Classical method for aircraft of Radar lengths  $\leq \frac{c}{2\Delta f}$
2. Extend the HRR profile to the full range available during conventional pulse compression. If there are  $K$  receiver samples obtained with frequency  $f_s$  this means a range<sup>13</sup> of  $\frac{Kc}{2f_s}$ .
3. Scatterers resolvable in the conventional pulse compressor output (i.e. are separated by more than  $\frac{c}{2f_s}$ ) should not incur a loss in magnitude as a result of Hybrid processing, as observed in the Classical method.
4. Offer a range resolution of  $\frac{c}{2Q\Delta f}$  throughout the Hybrid HRR profile.
5. Will not impart any processing artefacts which degrade the HRR profile significantly more than the Classical method when subject to realistic motion compensation errors, frequency jitter etc; i.e. must be shown to work with real targets.

### 2.3.2 Previous work

Initial development of the Hybrid technique, which culminated in an IEEE Radar 2006 conference paper [31], was conducted during a BAE Systems research programme into Phased Array target recognition techniques during 2004 and 2005. The static and Pod & Falcon experiments were conducted during this time. The Hybrid concept was fleshed out from earlier work (circa 1990) conducted at the BAE Systems Advanced Technology Centre at Great Baddow, Chelmsford, UK by Kite, Tait *et al* and more recently by Miller, Shepherd & Newman [70]. The term ‘Hybrid’ originates from the latter. Outside of BAE Systems, M<sup>c</sup>Groary & Lindell (1991) [65] describe the theoretical frequency domain synthesis of samples from two  $\tau = 1 \mu s$ ,  $B = 75 \text{MHz}$  chirps spaced in frequency such that the central section of each chirp forms a continuous bandwidth. Further refinements (i.e. the idea of removing the edges of the spectra of each chirp) are described in the method outlined by Walbridge & Chadwick of DERA, Malvern in 1999. [109]. Additional references are discussed in the Literature Survey.

### 2.3.3 Recent developments of the Hybrid technique

Below is a summary of work conducted by the author relating to the Hybrid technique. Details are described in section 3.5.2.

<sup>12</sup>i.e. based upon a frequency coded waveform of bandwidth  $B$  and duration  $\tau$  transmitted in coherent bursts of  $P$  pulses.  $Q$  bursts are transmitted using a frequency step of  $\Delta f$ .

<sup>13</sup>In the experiments conducted with MESAR2 described in this thesis,  $K$  is typically 150 and  $f_s = 5 \text{MHz}$ . This yields a range extent of 4.5km, i.e. significantly higher than the Classical range windows quoted in this thesis, which are 47m ( $\Delta f = 3.2 \text{MHz}$ ) and 187m ( $\Delta f = 0.8 \text{MHz}$ ).



- Implementation of a signal processing scheme based upon the concepts described in the previous section such that MESAR2 receiver samples could be processed using the Hybrid technique.
- Motion compensation algorithms (applied to Classical as well as Hybrid methods) which exploit the Doppler spectra obtainable from each burst in addition to range walk and phase correction based on prior knowledge (e.g. from the Tracking sub-system) of target range rate.
- Hybrid range profile alias minimization via frequency domain scaling using weights derived from the Fourier Transform of a synthesized linear chirp of bandwidth  $Q\Delta f$  and duration  $\tau$ .
- Hybrid de-aliasing via HRR power subtraction.

### 2.3.4 Overall method

Rather than applying pulse compression and then taking a set of ‘target samples’, receiver samples are combined, following motion compensation, in the frequency domain to synthesize a ‘psuedo-chirp’ of bandwidth  $B = Q\Delta f$ . (See fig 2.4). This is converted back into the time domain and correlated with the equivalent ‘spectrally-stitched’ receiver samples of a single static point target. The result of this pulse compression is a range profile of resolution  $\frac{c}{2Q\Delta f}$ , i.e. the same as the ‘Classical’ technique. However, because the entire set of receiver data is used, the range extent is only limited by the duration of the receiver opening. This is typically several kilometers and thus the Hybrid technique offers significantly greater unambiguous (high resolution) range coverage than the Classical method. The waveform architecture which enables Hybrid processing is identical to that of the Classical technique, but with the additional constraint that the frequency sweep  $B$  of consecutive transmitted chirps overlap such the central portions of their spectra (of width  $\Delta f$ ) form a continuum over the total stitched bandwidth  $Q\Delta f$ .

### 2.3.5 Mitigation of the problem of aliases

Fig 2.5 compares the Hybrid HRR profile of two static dipoles separated by 58m using a 3.2MHz stepped frequency waveform with the corresponding Classical profile. The Hybrid profile unambiguously resolves the dipoles with the correct separation and without the loss of gain experienced with the Classical method. However, even in this static example<sup>14</sup>, aliases are clearly present at intervals of  $\frac{c}{2\Delta f}$  at around 20dB below the main peak.

A three-fold mechanism has been devised to reduce the effects of aliasing:

1. Improved motion compensation
2. Frequency domain scaling
3. Hybrid de-aliasing via HRR power subtraction

Step 1 is discussed in section 3.5.2, but is obviously irrelevant for static targets. Step 2 involves the scaling of the stitched spectrum by the ratio of a wideband chirp<sup>15</sup> spectrum to the stitched spectrum of a static point target. Hybrid processing of a static point target will therefore become

<sup>14</sup>Aliasing can be described as a (weighted) convolution of the range profile with a periodic ‘comb’ function spaced by  $\frac{c}{2\Delta f}$ . If motion compensation is imperfect there will be periodic disturbances in the stitched spectrum of interval  $\Delta f$ . Hence one would expect aliasing to be worse for targets in motion than for genuinely static targets.

<sup>15</sup>of bandwidth  $Q\Delta f$  and duration  $\tau$

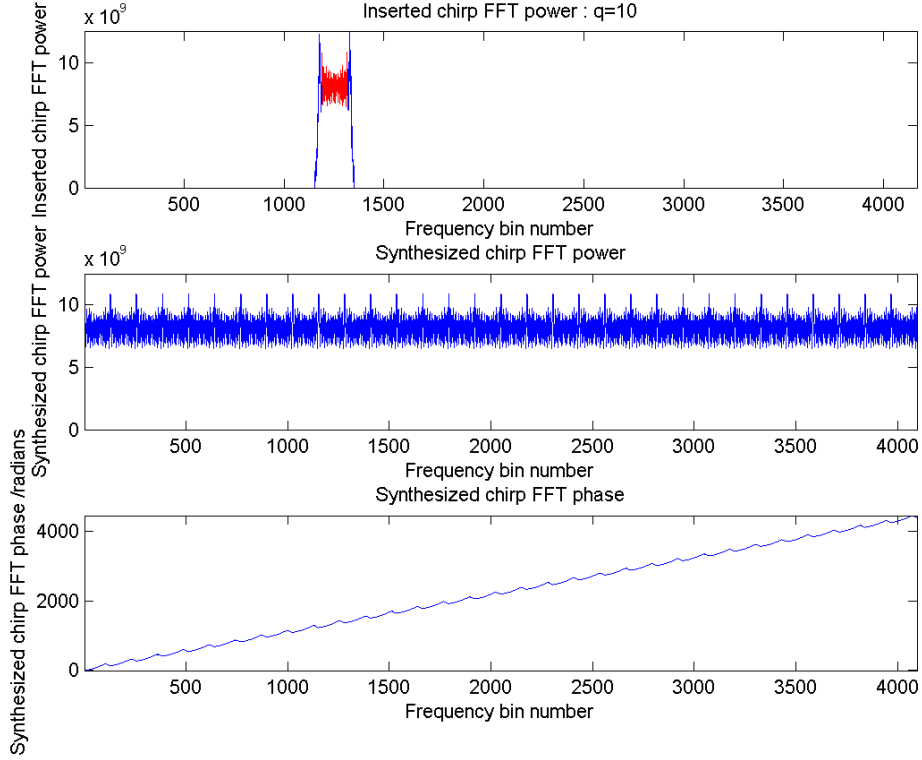


Figure 2.4: Graphical representation of the ‘spectral stitching’ employed in the Hybrid method. In this example a linear chirp waveform is transmitted upon a static point target and receiver samples are stored for a range of carrier frequencies stepped by a constant amount, such that the central (red) region of the spectra shown in the uppermost graph form a continuous bandwidth (shown in the middle graph). Despite the ‘ears’ being removed from the spectrum, the stitching method yields periodic amplitude (and phase) disturbances. These yield the aliases as shown in fig 2.5 , which can be minimized (as shown in fig 2.8 and fig 3.14) by a combination of scalings in the frequency domain and power subtraction in the time domain.

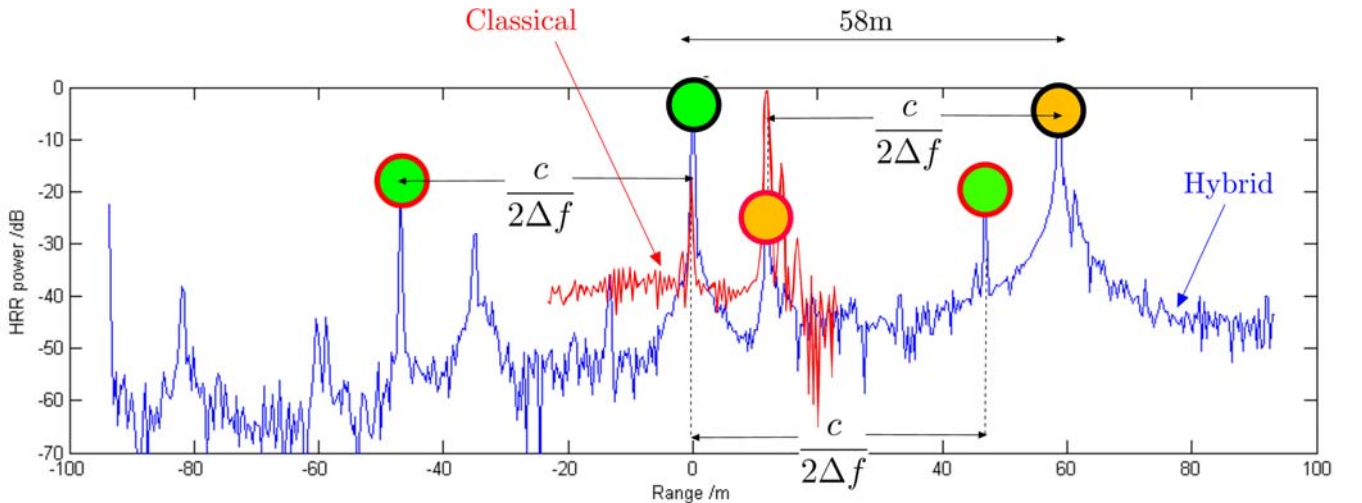


Figure 2.5: Hybrid and Classical HRR processing of two point targets separated by 58m. Aliases separated by HRR window  $\frac{c}{2\Delta f}$  are indicated. Black rings indicate principal return and red rings indicate aliases. The two targets are highlighted by orange and green filled circles. The limited HRR window causes the Classical stepped frequency method to wrap the dipole into this window, therefore underestimating its range by  $\frac{c}{2\Delta f}$ . The gain of first dipole is also reduced.

the autocorrelation of the wideband chirp and therefore, by definition, yield the desired result. To understand how this mechanism is applicable in the general case of multi-scatterer targets let us firstly define a number of quantities.

- $\psi_q(t)$  is the time domain complex signal which represents the transmitted waveform. This is a linear chirp of bandwidth  $B$  and duration  $\tau$  transmitted using carrier frequency  $f_{Tx}(q) = f_1 + (q-1)\Delta f$ .
- $\Psi_q(t)$  is the received signal (for frequency step  $q$ ) resulting from the reflection of the transmitted waveform off a target. Assuming a scattering center decomposition of this signal we may construct  $\Psi_q(t)$  from  $\psi_q(t)$  and the ranges  $\{R_n\}$  and reflectivities  $\{a_n\}$  of the  $N$  scatterers.

$$\Psi_q(t) = \sum_{n=1}^N a_n \psi_q\left(t - \frac{2R_n}{c}\right) \quad (2.13)$$

- $\Theta_q(f) = \mathcal{F}[\Psi_q]$  is the Fourier Transform of the receiver samples from frequency step  $q$ .

$$\Theta_q(f) = \mathcal{F}[\Psi_q] = \sum_{n=1}^N a_n \mathfrak{F} \left[ \psi_q\left(t - \frac{2R_n}{c}\right) \right] \quad (2.14)$$

By the Fourier Shift theorem  $\mathcal{F}[y(t-a)] = e^{-2\pi i a f} \mathcal{F}[y(t)]$ , the expression above can be written as

$$\Theta_q(f) = \sum_{n=1}^N a_n e^{-\frac{4\pi i R_n}{c} f} \mathcal{F}[\psi_q(t)] \quad (2.15)$$

- $\Xi(f)$  is the stitched spectrum

The stitched spectrum is thus defined as

$$\Xi(f) = \sum_{q=1}^Q \Lambda_q \quad (2.16)$$

where

$$\Lambda_q = \begin{cases} \Theta_q(f) & f_{Tx}(q) - \frac{1}{2}\Delta f \leq f < f_{Tx}(q) + \frac{1}{2}\Delta f \\ 0 & \text{otherwise} \end{cases} \quad (2.17)$$

which yields

$$\Lambda_q = \begin{cases} \mathcal{F}[\psi_q(t)] \sum_{n=1}^N a_n e^{-\frac{4\pi i R_n}{c} f} & f_1 + (q - \frac{3}{2})\Delta f \leq f < f_1 + (q - \frac{1}{2})\Delta f \\ 0 & \text{otherwise} \end{cases} \quad (2.18)$$

Since the non-zero regions of  $\Lambda_q$  form a continuous frequency range without gaps or overlaps, we can therefore write  $\Xi(f)$  as the product of a term involving the scattering center decomposition, and a term which involves the transmitted waveform.

$$\Xi(f) = \underbrace{\sum_{n=1}^N a_n e^{-\frac{4\pi i R_n}{c} f}}_{\text{Scattering center term (SCT)}} \times \underbrace{\sum_{q=1}^Q \begin{cases} \mathcal{F}[\psi_q(t)] & f_1 + (q - \frac{3}{2})\Delta f \leq f < f_1 + (q - \frac{1}{2})\Delta f \\ 0 & \text{otherwise} \end{cases}}_{\text{Waveform term (WFT)}} \quad (2.19)$$

or

$$\Xi(f) = \begin{cases} \text{SCT} \times \text{WFT} & f_1 - \frac{\Delta f}{2} \leq f < f_1 + (Q - \frac{1}{2})\Delta f \\ 0 & \text{otherwise} \end{cases} \quad (2.20)$$

The spectrum for a wide bandwidth chirp  $\psi_{WB}(t)$  (see fig 2.6) with carrier  $f_{Tx} = f_1 + \frac{Q}{2}\Delta f$  (i.e. a single scatterer at range  $R_0$ ) and central bandwidth<sup>16</sup>  $Q\Delta f$  can be written as

$$\Xi_{WB}(f) = \begin{cases} a_0 e^{-\frac{4\pi i R_0}{c} f} \mathcal{F}[\psi_{WB}(t)] & f_1 - \frac{\Delta f}{2} \leq f < f_1 + (Q - \frac{1}{2})\Delta f \\ 0 & \text{otherwise} \end{cases} \quad (2.21)$$

whereas the stitched spectrum for the same target is

$$\begin{aligned} \Xi_{PT}(f) &= e^{-\frac{4\pi i R_0}{c} f} \sum_{q=1}^Q \begin{cases} \mathcal{F}[\psi_q(t)] & f_1 + (q - \frac{3}{2})\Delta f \leq f < f_1 + (q - \frac{1}{2})\Delta f \\ 0 & \text{otherwise} \end{cases} \\ &= e^{-\frac{4\pi i R_0}{c} f} \begin{cases} \text{WFT} & f_1 - \frac{\Delta f}{2} \leq f < f_1 + (Q - \frac{1}{2})\Delta f \\ 0 & \text{otherwise} \end{cases} \end{aligned} \quad (2.22)$$

If we define spectral scalings

$$W(f) = \frac{\Xi_{WB}(f)}{\Xi_{PT}(f)} \quad (2.23)$$

then for a point target at range  $R_0$ ,  $\Xi(f)W(f) = \Xi_{WB}(f)$ . Because of the decomposition of target and waveform terms in  $\Xi$ , for multi-scatter targets we should obtain  $\Xi(f)W(f)$  equal to the SCT multiplied by the band-limited  $\mathfrak{F}[\psi_{WB}(t)]$ , i.e. the Fourier Transform of the wide bandwidth waveform  $\psi_{WB}(t)$  multiplied by a ‘top hat’ of width  $Q\Delta f$ . In the time domain this is the convolution of the wide bandwidth chirp, a sinc function of periodicity  $\frac{c}{2Q\Delta f}$  and a comb of unit impulses which correspond to the scattering center decomposition. If this result is sampled with range cells of  $\frac{c}{2Q\Delta f}$  then this result is effectively the receiver samples one would obtain using a wide-bandwidth waveform.

Figures 2.7 & 2.8 illustrate the application of the Hybrid method with spectral scaling. Compared to fig 2.8, the 58m dipole result has almost non-existent aliases.<sup>17</sup> In both examples the experimental results are compared to (idealized) synthesized receiver samples, which assume no noise.

<sup>16</sup>In practise this means the actual bandwidth  $B_{WB}$  would likely exceed  $Q\Delta f$

<sup>17</sup>The return at -37dB is likley to be a genuine target reflection resulting from imperfections in the False Target Generator setup since it doesn't match up in range with any alias of the two dipoles

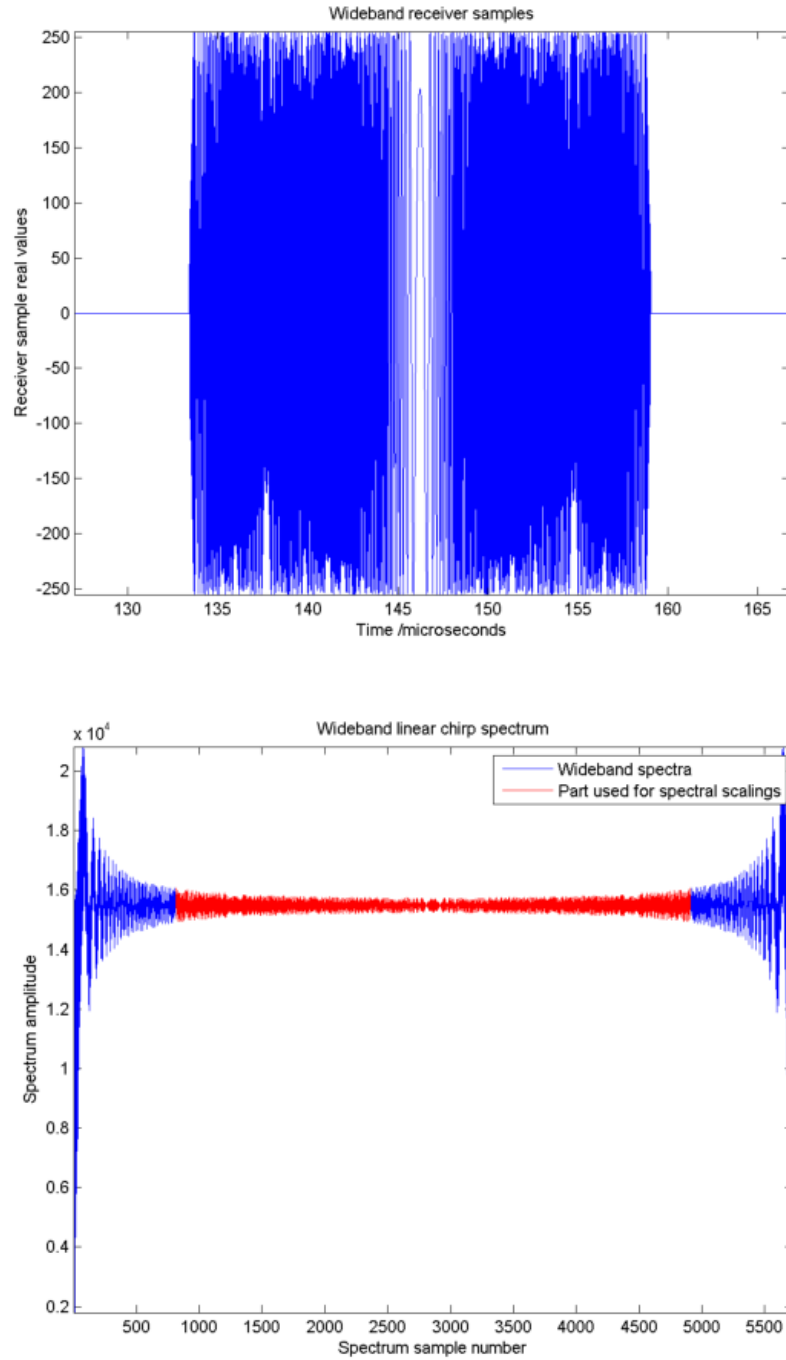


Figure 2.6: The principle goal of the stepped frequency method is to yield a comparable range profile to that which could be obtained with a pulse whose bandwidth equates to the total bandwidth covered by the stepped frequency waveform. In this figure we show a wide bandwidth waveform in the time and frequency domains. The red region corresponds to the stitched spectrum of a corresponding stepped frequency variant. To minimize aliases caused by stitching periodicity, we scale the stitched spectrum by the stitched spectrum of a point target reference and multiply by the corresponding region of the wideband waveform (which is synthesized from a model). A point target (as shown in fig 2.7) should correspond perfectly to the wideband result. More realistic targets should have minimal aliases unless motion compensation or other receiver effects cause additional distortion.

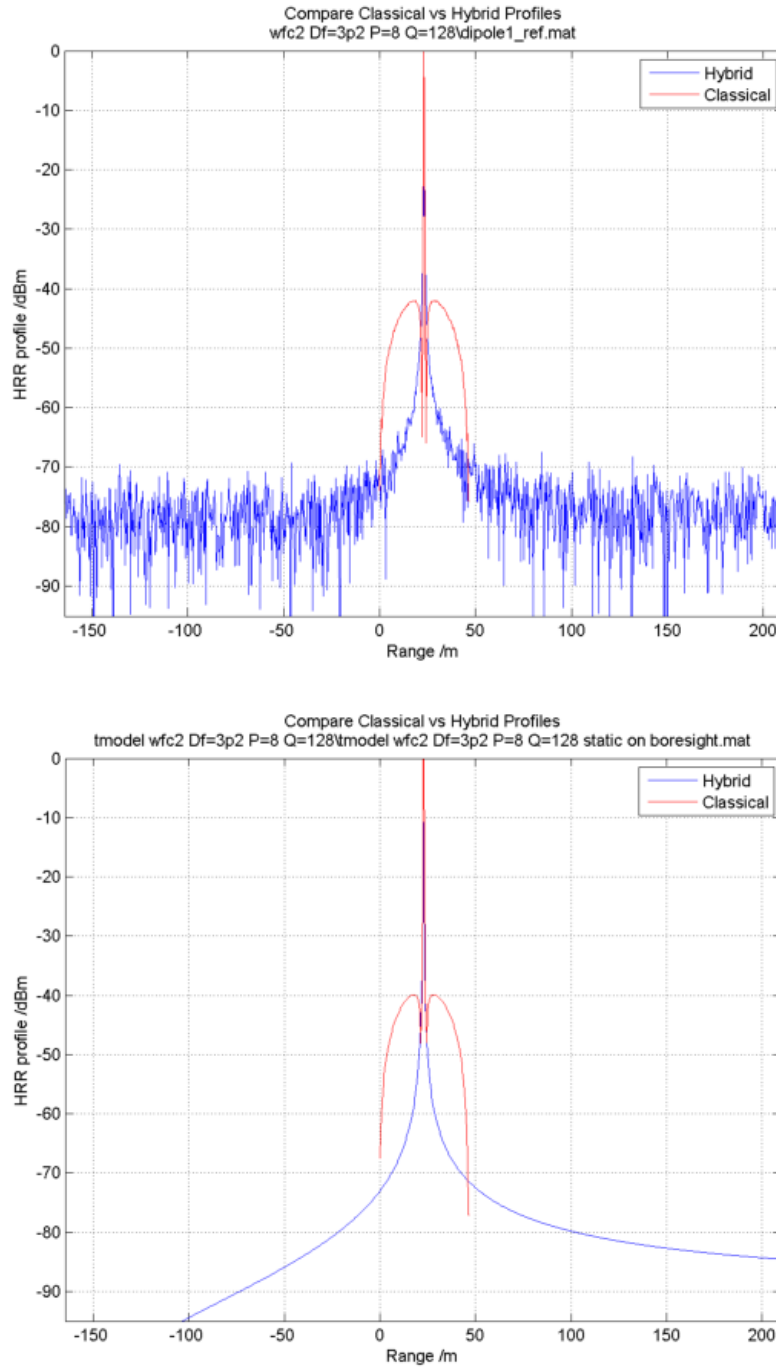


Figure 2.7: (Above) Overlay of the HRR profiles of a single dipole reflector obtained using a waveform of 128 linear chirps of bandwidth  $-4.5\text{MHz}$  stepped in frequency by  $3.2\text{MHz}$ . The red trace is generated using the Classical method described in the previous section. The blue trace is generated by the Hybrid method using the same data. For this calibration target, the Hybrid technique has significantly lower sidelobes than the those of the Classical technique (where a  $40\text{dB}$  Dolph-Chebyshev amplitude taper has been applied prior to application of the IFFT). (Below) Noiseless modelled data is fed into the same Classical and Hybrid signal processing, yielding very similar traces. Notice the Hybrid technique yields range asymmetric profiles below  $-80\text{dB}$ . (i.e. below the noise floor of the above example which may explain why it cannot be observed here).

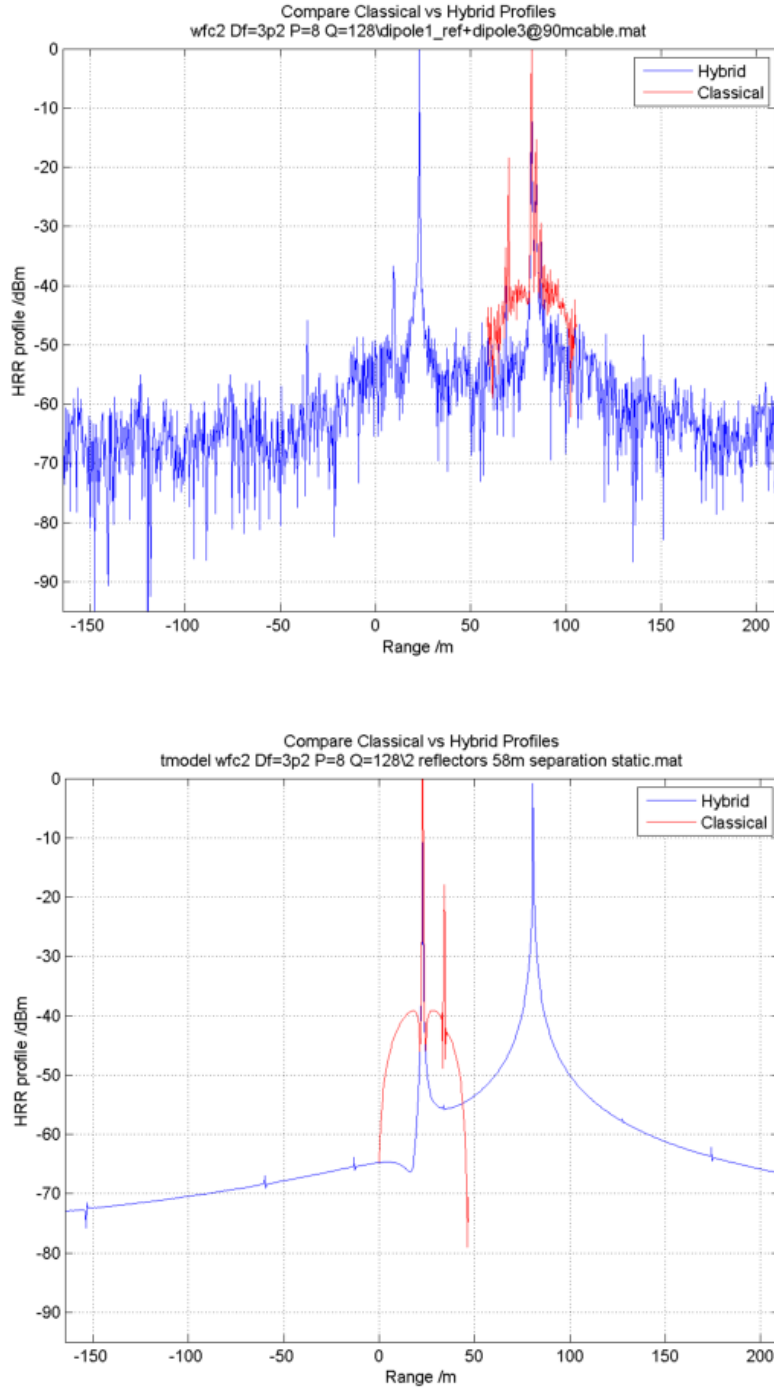


Figure 2.8: (Above) Overlay of the HRR profiles of two static dipoles spaced by 58m obtained using a waveform of 128 linear chirps of bandwidth -4.5MHz stepped in frequency by 3.2MHz. The red trace is generated using the Classical method described in the previous section. The blue trace is generated by the Hybrid method using the same data. Unlike the Classical technique, the Hybrid method can unambiguously separate both targets at the correct range. (Below) Noiseless modelled data is fed into the same Classical and Hybrid signal processing. The aliases at  $\frac{c}{2\Delta f}$  are almost non existent in the modelled example, compared to 10dB in height above the main trace for the above example, which was generated using trials data obtained via MESAR2. Interestingly, the experimental dipole profiles are actually sharper at -50dB than the ideal profile.

## 2.4 Doppler processing and Jet Engine Modulation

### 2.4.1 The Doppler Filter & its associated ambiguities

A coherent Radar alternately transmits and receives a burst of  $P$  pulses using a common phase reference. This effectively means no jumps in signal phase are introduced by the mixing down process in the receiver. Let us assume a reflector is initially placed at range  $R$  and is illuminated using a pulsed Radar which operates at pulse repetition frequency  $f_{PRF}$  and carrier  $f_{Tx}$ . The phase shift of a received reflection from what was transmitted is  $\phi = 2\pi f_{Tx} t_{delay}$  where  $t_{delay} = 2R/c$  is the time of flight between transmission and reception, i.e.

$$\phi = \frac{4\pi f_{Tx} R}{c} \quad (2.24)$$

Let us now assume the reflector is moving with range rate  $\dot{R}$ . Between consecutive pulses the difference in phase  $\Delta\phi$  will be accounted for by the change in target range. If the target is moving with uniform range rate, the range change during the pulse repetition interval is  $\dot{R}/f_{PRF}$  hence

$$\Delta\phi = \frac{4\pi f_{Tx} \dot{R}}{c f_{PRF}} \quad (2.25)$$

The instantaneous frequency of a signal of general form  $s(t) = \cos(2\pi f_{Tx} t - \phi(t))$  is given by

$$f(t) = f_{Tx} - \frac{1}{2\pi} \frac{d\phi}{dt} \quad (2.26)$$

Hence we can assign a Doppler Shift  $f_D$  of frequency resulting from (constant range rate) target motion

$$f_D = -\frac{1}{2\pi} \frac{\Delta\phi}{1/f_{PRF}} = -\frac{2\dot{R}}{c} f_{Tx} \quad (2.27)$$

In summary, a moving target in range will result in a non-zero rate of change of phase in the received signal. This is equivalent to a physical frequency shift of the carrier by the Doppler Frequency  $f_D = -\frac{2\dot{R}}{c} f_{Tx}$ . This result allows one to discriminate a target reflection from potentially larger returns that do not have the same Doppler frequency by application of a filter. The simplest design is one which combines  $P$  subsequent sets of receiver samples  $\{\psi_p\}$  in a linear fashion to produce a single output  $y = \sum_{p=1}^P \psi_p w_p$ . The weighting of each set  $\{w_p\}$  is set to either suppress signals with Doppler frequencies characteristic of clutter (as in MTI) or maximize the target to clutter ratio (as in an MTD system).

The frequency response of a filter is the frequency dependence of the output power given a pure tone as the input. Let samples of the input be  $\psi_p = e^{2\pi i t_p f}$  where  $t_p$  are the sampling times corresponding to each of the  $P$  receiver intervals. The frequency response is therefore

$$|y(f)|^2 = \left| \sum_{p=1}^P w_p e^{2\pi i t_p f} \right|^2 \quad (2.28)$$

with a corresponding phase response

$$\arg[y(f)] = \tan^{-1} \left\{ \sum_{p=1}^P w_p e^{2\pi i t_p f} \right\} \quad (2.29)$$



For example, the frequency response of an MTI filter designed to suppress ground clutter may have weights similar to  $\{w_p\} = \{1, -2, 1\}$ . If no stagger is used (i.e. the pulse repetition interval is uniform at  $f_{PRF}$ ) then the frequency response of the filter is

$$|y_{GCF}(f)|^2 = \left| e^{\frac{2\pi i(1-1)f}{f_{PRF}}} - 2e^{\frac{2\pi i(2-1)f}{f_{PRF}}} + e^{\frac{2\pi i(3-1)f}{f_{PRF}}} \right|^2 \quad (2.30)$$

$$= \left| 1 - 2e^{\frac{2\pi i f}{f_{PRF}}} + e^{\frac{4\pi i f}{f_{PRF}}} \right|^2 \quad (2.31)$$

The most basic form of an MTD system uses a bank of filters and utilizes the filter with the maximum gain to provide the input to a target signal threshold detector. The filter weights are defined such that the bank of filter outputs are the Discrete Fourier Transform (DFT) of a vector of signal samples from the  $P$  contiguous pulses. This is a good idea as the DFT of a vector of complex numbers can be efficiently coded (a Fast Fourier Transform) if  $P$  is an integer power of 2. The DFT filter weights (for output  $k$ ) are

$$w_{p,k} = e^{-\frac{2\pi i(p-1)(k-1)}{P}} \quad (2.32)$$

The frequency response using a uniform PRF is

$$|y_k(f)|^2 = \left| \sum_{p=1}^P e^{-\frac{2\pi i(p-1)(k-1)}{P} + \frac{2\pi i f(p-1)}{f_{PRF}}} \right|^2 \quad (2.33)$$

$$= \left| e^{2\pi i \left\{ \frac{k-1}{P} + \frac{f}{f_{PRF}} \right\}} \sum_{p=1}^P e^{\frac{2\pi i p}{P} \left\{ 1-k + \frac{fP}{f_{PRF}} \right\}} \right|^2 \quad (2.34)$$

$$= \left| \sum_{p=1}^P e^{\frac{2\pi i p}{P} \left\{ 1-k + \frac{fP}{f_{PRF}} \right\}} \right|^2 \quad (2.35)$$

$$= \left| \frac{e^{ix} \sin \left\{ \left( 1 + \frac{1}{P} \right) x \right\}}{\sin \left( \frac{x}{P} \right)} - 1 \right|^2 \quad (2.36)$$

where<sup>18</sup>  $\frac{x}{\pi} = 1 - k + \frac{fP}{f_{PRF}}$ .

This has a maximum of  $P^2$  when  $1 - k + \frac{fP}{f_{PRF}} = 0$  i.e.

$$f_{\max} = \frac{k-1}{P} f_{PRF} \quad (2.37)$$

The  $k^{\text{th}}$  filter bank therefore has a frequency response that peaks at the fraction of the PRF defined by the ratio of  $k$  to the number of input samples  $P$ . One can therefore use the output of this filter bank as an approximation to the Fourier Transform<sup>19</sup> of the input signal if  $k = 1 \dots P$ , albeit that we restrict the spectrum to frequency extent  $[0, f_{PRF}]$ . Note that the frequency response is periodic in  $f_{PRF}$ , i.e. the transformation  $f \rightarrow f + Zf_{PRF}$  where  $Z \in \mathbb{Z}$  has no effect on the frequency response.

<sup>18</sup>  $\sum_{n=1}^z e^{\frac{2\pi i n x}{z}} = \frac{e^{ix} \sin((1+z^{-1})x)}{\sin(z^{-1}x)} - 1$  where  $z$  is integer. This result is proved in the Appendix.

<sup>19</sup> The Fourier Transform  $\tilde{\psi}(f)$  of a signal  $\psi(t)$  is defined as  $\tilde{\psi}(f) = \int_{-\infty}^{+\infty} \psi(t) e^{-2\pi i f t} dt$ . The output of a Fourier Transform is the spectrum (frequency content) of the signal. A pure tone  $\psi(t) = e^{2\pi i f_* t}$  has a delta function Fourier Transform at frequency  $f_*$  i.e. a frequency content at  $f_*$  only and zero elsewhere.

$$y_k(f + Zf_{PRF}) = e^{2\pi i \left\{ \frac{k-1}{P} + \frac{f}{f_{PRF}} \right\} + 2\pi i Z \sum_{p=1}^P e^{\frac{2\pi i p}{P} \left\{ 1-k + \frac{fP}{f_{PRF}} \right\} + 2\pi i p Z}} \quad (2.38)$$

$$= e^{2\pi i \left\{ \frac{k-1}{P} + \frac{f}{f_{PRF}} \right\}} \sum_{p=1}^P e^{\frac{2\pi i p}{P} \left\{ 1-k + \frac{fP}{f_{PRF}} \right\}} \quad (2.39)$$

$$= y_k(f) \quad (2.40)$$

since  $p$  is also integer and  $e^{2\pi i J} = 1$  when  $J$  is any integer. This means any characteristic frequency inferred from the DFT will be ambiguous by  $f_{PRF}$ .

Armed with this bank of filters (which we shall call a Doppler Filter from now on), let us consider the effect of a the received signal  $\psi_p$  being represented as a complex number  $I + iQ$  and take the form  $\psi_p = \psi_0 e^{-i(p-1)\Delta\phi}$  where  $\Delta\phi = \frac{4\pi f_{Tx} \dot{R}}{c f_{PRF}} = -2\pi f_D / f_{PRF}$ . The envelope  $\psi_0$  is the part of the signal return which is unchanging between pulses, i.e. in this example we shall neglect for the moment the effect of clutter and focus purely on the target. Comparing this to the samples of a pure tone used to define the frequency response above we have

$$\begin{aligned} \psi_p &= \psi_0 e^{\frac{2\pi i (p-1) f_D}{f_{PRF}}} && \text{Signal from uniformly moving target} \\ \psi_p &= \psi_0 e^{\frac{2\pi i (p-1) f}{f_{PRF}}} && \text{Pure tone} \end{aligned} \quad (2.41)$$

Since these take the same functional form, by substituting  $f$  by the Doppler Shift  $f_D$  in the frequency response we derive the variation of the filter output  $y_k$  with  $f_D$ , or equivalently for a given target range rate  $\dot{R}$ , we determine the signal Doppler spectrum ‘measured’ by the filter by considering the variation of filter amplitudes vs  $k$ .

Of course we could dispense with the concept of a discrete set of filters and

- Use a continuous variable  $f = \frac{k-1}{P} f_{PRF}$  and plot an interpolated Doppler spectrum

$$y(f) = \sum_{p=1}^P \psi_p e^{\frac{-2\pi i (p-1) f}{f_{PRF}}} \quad (2.42)$$

This would be useful for visual analysis of the frequency content of a sampled signal.

- Design a filter with a single output that has its maximum response when the signal has a tone component of the Doppler frequency. This occurs when  $f_D = \frac{k-1}{P} f_{PRF}$ . The filter weights are therefore

$$w_p = e^{\frac{-2\pi i (p-1) f_D}{f_{PRF}}} \quad (2.43)$$

This would be useful in adapting signal processing to a target whose range-rate is already well known; e.g. a tracking waveform which follows surveillance and range rate estimation from analysis of the Doppler spectrum of the received signals.

## 2.4.2 Sources of target Doppler: HERM & JEM

In the previous sections we have discussed how bulk target motion can lead to an effective frequency shift  $f_D$  resulting from a continuous change in the propagation distance, and therefore change in phase of the returning waveform from pulse to pulse. In addition, internal motions superposed upon bulk

movement can lead to detectable signal modulations which, if correctly interpreted, can assist classification of the overall target. Significant research (for example by Martin & Mulgrew [103],[67],[68]) has been conducted on the signal variations (and resulting Doppler spectrum) resulting from rotating blades. This has applications to propeller driven aircraft as well as jet engines<sup>20</sup>, helicopters and wind turbines. Indeed, the absence of rotating blade effects can also help to distinguish other flying objects such as missiles, ballistics and gliders from their ‘air breathing’ counterparts.

In the Appendix a model of JEM (which is equally applicable to all other single stage<sup>21</sup> rotating blade systems) is derived and is essentially the Martin & Mulgrew result described in [67] & [68].

$$\psi(R, t) \approx \frac{\psi_0 (L_2 - L_1)}{R^2} e^{2\pi i f_{Tx} t - \frac{4\pi i R}{\lambda}} \sum_{n=0}^{N-1} \zeta_n e^{\frac{1}{2} i (L_1 + L_2) \xi_n} \text{sinc} \left( \frac{1}{2} (L_2 - L_1) \xi_n \right) \quad (2.44)$$

$$\Omega_n = 2\pi \left( f_{rot} t + \frac{n}{N} \right) \quad (2.45)$$

$$\zeta_n = -\frac{a}{R} (\mathbf{z}_E \cos \phi_P + (\mathbf{y}_E \sin \Omega_n - \mathbf{x}_E \cos \Omega_n) \sin \phi_P) \cdot \mathbf{R} \quad (2.46)$$

$$\xi_n = -\frac{4\pi}{R\lambda} (\mathbf{y}_E \cos \Omega_n + \mathbf{x}_E \sin \Omega_n) \cdot \mathbf{R} \quad (2.47)$$

$\psi$  is the JEM modulation of the original signal  $\psi_0$ ,  $R$  is the target range,  $f_{Tx}$  is the carrier frequency,  $\lambda$  is the corresponding wavelength,  $L_1$  is the radius of the blade root,  $L_2$  is the radius of the blade tip,  $N$  is the number of blades,  $\theta$  is the angle between the Radar look vector  $\mathbf{R}$  and the plane of blade rotation  $\{\mathbf{x}_E, \mathbf{z}_E\}$ ,  $\phi_P$  is the pitch angle of the blades and  $f_{rot}$  is the blade rotation or ‘spool’ rate.

Martin & Mulgrew consider the special case of  $\mathbf{R} = -R(\mathbf{z}_E \sin \theta + \mathbf{x}_E \cos \theta)$  i.e. the Radar line of sight is in a plane which is at right angles to the plane of blade rotations.

$$\zeta_n = \frac{a}{2} [\sin(\theta + \phi_P) + \sin(\theta - \phi_P)] (1 - \cos \Omega_n) \quad (2.48)$$

$$\xi_n = \frac{4\pi}{\lambda} \sin \Omega_n \cos \theta \quad (2.49)$$

*Assumptions are:*

- Each engine blade acts as a homogeneous, linear, rigid antenna.
- The jet engine is in the far-field of the Radar, i.e.  $R \gg \frac{L_2^2}{\lambda}$
- The only significant contributions to the received signal derive from reflections off the equi-spaced engine blades at the inlet. Hence the analysis is identical to that of a propeller. Reflections from the housing and rotating shaft are not considered since they will not result in any time varying effects, assuming the received signal is compensated for the bulk motion of the jet engine (i.e. the motion of the aircraft that bears it).
- The aspect ratio of each blade is such that the length is much greater than the width.

<sup>20</sup> Although jet engines are just one type of rotating blade system that give rise to detectable modulation of microwaves, the generic term for this effect is Jet Engine Modulation (JEM). The exception are helicopters which have their own Helicopter Rotor Modulation (HERM). The physical effect is the same however, although the rotation speed and number of stages are very different in a typical jet engine.

<sup>21</sup> Actual jet engines may have two or more stages of blades. However, at S-band frequencies, penetration beyond the first stage is more difficult than at K-band (or higher). Hence a single stage JEM model is thought to be quite appropriate at S-band for a wide set of aero-engines.

The major results of the Martin & Mulgrew model are as follows

- Major spectral lines at Doppler frequencies  $f_{JEM} = Zf_{rot}N$  where  $Z$  is an integer. These are known as ‘JEM lines.’ See figures 2.9 & 5.11. Note a practical Doppler filter using a pulsed Radar will be ambiguous by integer multiples of the PRF. Hence the actual position of JEM lines will be

$$f_{JEM} = Zf_{rot}N + Yf_{PRF} \quad (2.50)$$

where both  $Y$  and  $Z$  are integers. The even or oddness of the number of blades  $N$  further constrains the JEM lines. Tait [103] explains that  $Z$  can be effectively any integer (subject to bandwidth envelope  $B_{JEM}$ ) for an even bladed system whereas a rotor with an odd number of blades will have JEM lines only when  $Z$  is even.

- The spectral extent or bandwidth  $B_{JEM}$  of the JEM envelope is bounded by the Doppler frequencies resulting from the motion of the blade tips, which are the fastest moving surface upon the blade relative to the Radar.

$$B_{JEM} = \frac{8\pi f_{rot}(L_2 - L_1) \cos \theta}{\lambda} \quad (2.51)$$

- Blade pitch will cause asymmetry in the JEM spectrum, and this asymmetry varies with aspect angle  $a = \frac{\pi}{2} - \theta$ . To investigate the detailed changes, a MATLAB program `jem_plot.m` has been constructed. Fig 2.11 gives a screen shot.

In addition the Radar Cross Section (RCS) of the blade will strongly peak when the blade is fully face on to the illuminating beam. If the blade projected area in the direction of the Radar beam is  $L$  long and  $W$  wide, Tait [103] pp 186 shows the RCS to be

$$\sigma_{blade} = \frac{4\pi L^2 W^2}{\lambda^2} \left[ \frac{\sin\left(\frac{2\pi L}{\lambda} \sin a\right)}{\frac{2\pi L}{\lambda} \sin a} \right]^2 \cos^2 a \quad (2.52)$$

which confirms blade flashes to occur with a peak width of approximately  $\frac{\lambda}{L}$  radians about  $a = 0$ .

In summary, the effect of rotating blades upon microwave Radar is measurable by computing the Doppler spectrum resulting from a burst of coherent pulse returns from the range cell which contains the target. The resulting separation of JEM lines, bounded by bandwidth  $B_{JEM}$ , can be used to infer the product of blade number and spool rate  $Nf_{rot}$  which is likely to be a useful characteristic to aid classification, especially if it is zero. Figure 2.9 demonstrates what is possible to achieve using a much higher (36 GHz) carrier than discussed in this thesis. In addition to the JEM lines it is possible to resolve lines at integer multiples of the spool rate. Hence in this case both  $N$  and  $f_{rot}$  could be inferred from the spectrum. An S-band example (using MESAR2) is provided in fig 5.11.

Examining the JEM spectrum over time, i.e. from burst to burst, can yield additional information notably another estimate of the spool rate, and whether more than one rotors are contributing (in the case of a Chinook helicopter, where the spectrum will alternate between ‘towards’ and ‘away from’ Doppler spectrum biases). The blade flash effect causes quite a severe amplitude modulation which in turn will modulate the spectrum. In fig 2.9 one can clearly determine the period of blade flash from the variation in spectrum between bursts (whose individual Doppler spectra are stacked). So what would be a practical waveform to determine a JEM spectrum? A typical jet aircraft has a first stage spool rate of around 12 - 13,000 RPM  $\approx 200$  Hz. Many of the A380 engines (some of the largest in

service) use the Rolls Royce Trent 900 design<sup>22</sup> which has a first stage fan diameter of 2.94m. If a carrier of 3 GHz is used,  $\lambda \approx 10$  cm, which should be small enough to resolve features in the first stage of the jet engine. If  $N=25$  blades are used, JEM line spacings are  $Nf_{rot} = 5\text{kHz}$  with a maximum bandwidth of  $B_{JEM} \approx 74$  kHz. So to faithfully represent the entire spectrum unambiguously one requires a PRF of in excess of 74 kHz. This is unlikely to be practical because a PRF this high limits the unambiguous range<sup>23</sup> to be just over 2 km.<sup>24</sup> A compromise solution which allows the first few JEM lines to be recorded might require a PRF of 5 - 10 kHz. In addition, the number of pulses  $P$  per burst must be sufficient to resolve the JEM lines. 16 to 32 pulses are thought to be a minimum to achieve this based on practical experiments with MESAR2.  $P = 32$  pulses with a PRF of 10kHz yields a burst repetition frequency of  $10,000/32 = 300$  Hz which might be just sufficient to resolve the spectral periodicity resulting from blade flash if one expects an effect once a revolution.

---

<sup>22</sup>See Trent 900 specification. [www.rolls-royce.com](http://www.rolls-royce.com).

<sup>23</sup> $\frac{c}{2f_{PRF}}$

<sup>24</sup>It is possible to use PRFs which result in ambiguous ranges - see Chapter 7.

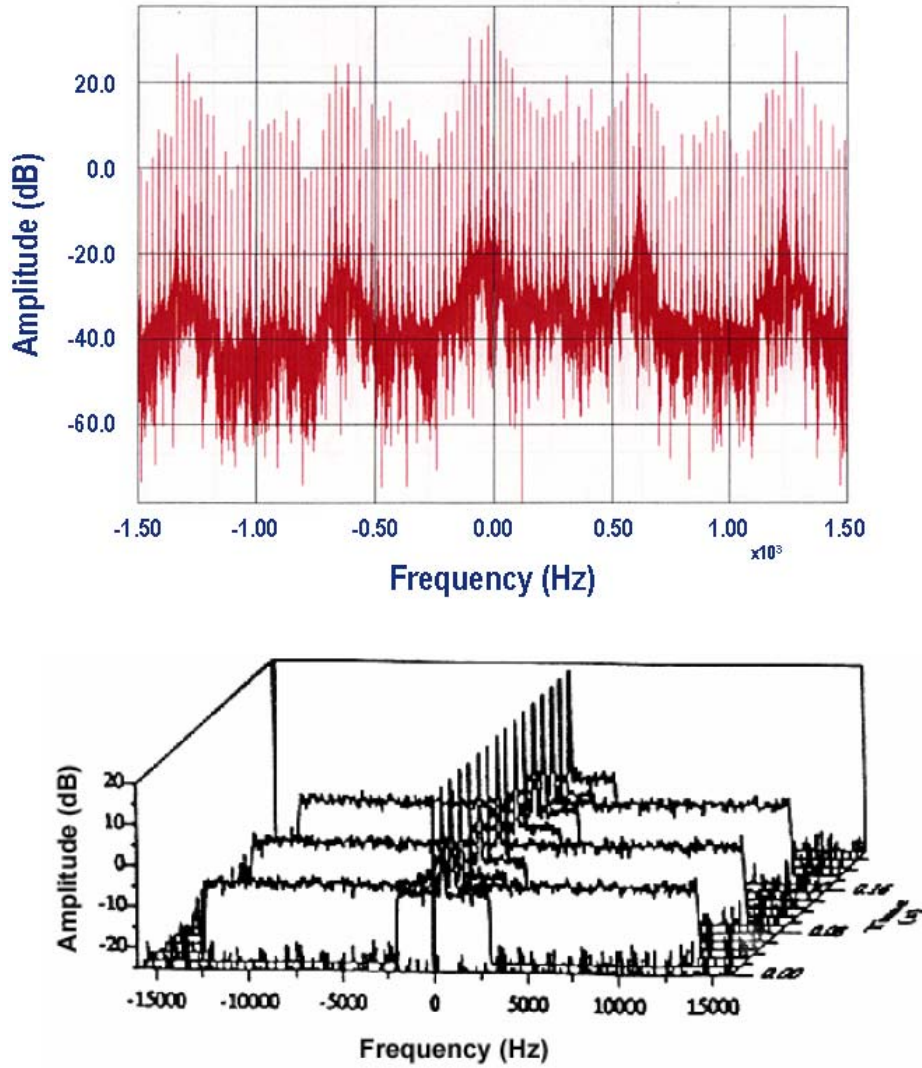


Figure 2.9: (Above) Spectral power of 36 GHz microwaves reflected off a rotating propeller. The principal JEM (Jet Engine Modulation) lines are spaced by  $Nf_{rot}$  where  $N$  is the number of engine blades in the (first fan stage typically) and  $f_{rot}$  is the rotation or ‘spool’ rate of this engine stage. The smaller spaced lines are at the spool rate. In this case the JEM lines occur at approximately 600Hz and there are about 25 spool lines between consecutive JEM lines. This means the propeller has 25 blades and rotates at  $600/25 = 24 \text{ Hz} = 1440 \text{ RPM}$ . (Below) Helicopter Rotor Modulation. (HERM). A Short-Time Fourier Transform (STFT) is displayed of Radar returns from a helicopter. This is achieved by processing bursts of coherent pulses and stacking the result burst by burst. The resulting surface oscillates at the burst level as the blade RCS varies relative to the area, peaking in a ‘blade flash’ when the blade surface is perpendicular to the incoming wavevector. From the Tutorial notes of Cohen [20].

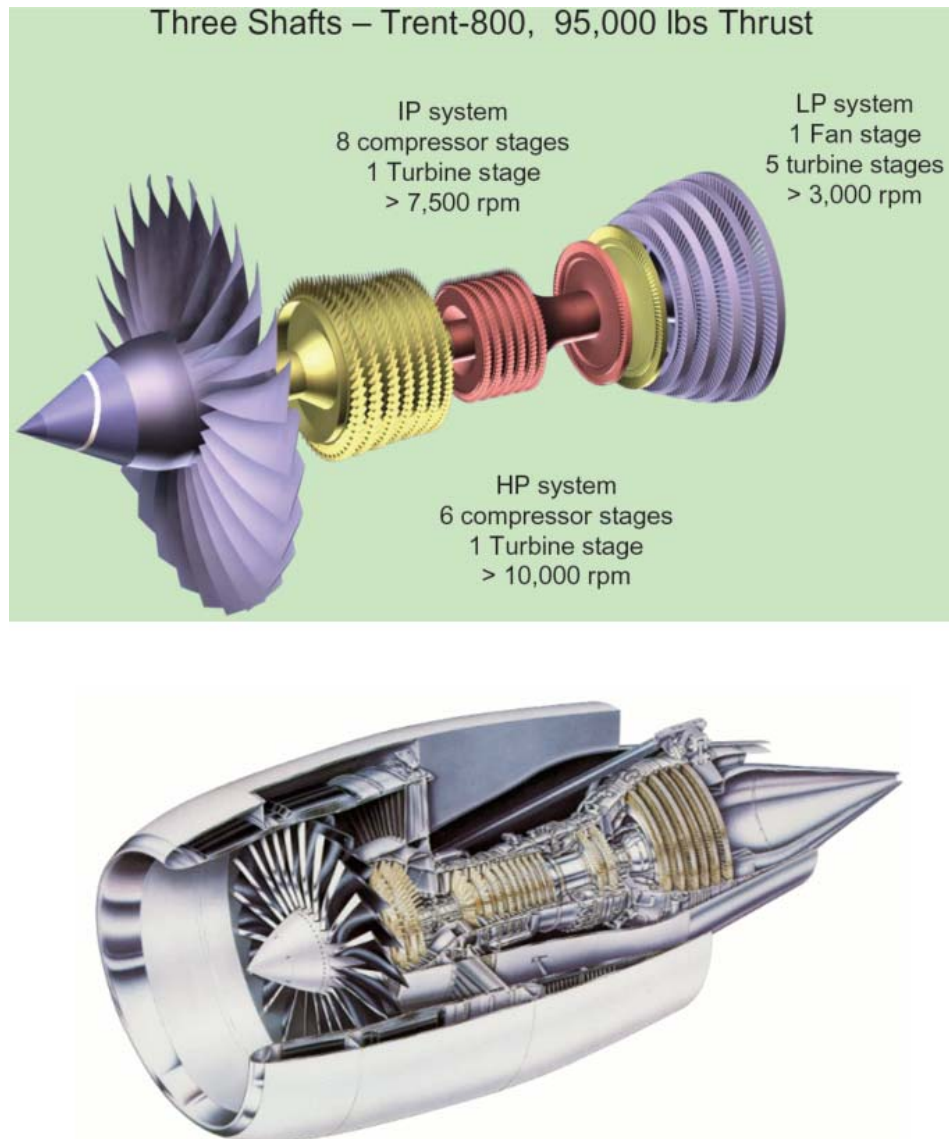


Figure 2.10: (Above) Three stage jet engine typified by the Rolls-Royce Trent-800. Each shaft can rotate or spool independantly at its own optimum rate. Illustration from <http://www.brunel.ac.uk/338/cem/cem3/seminar110106Main.pdf>. (Below) Artists impression of a Jet engine. In this example the fan main stage has  $\approx 25$  pitched blades. If the spool rate  $f_{rot} = 200\text{Hz}$  this implies JEM lines spaced by 5kHz.

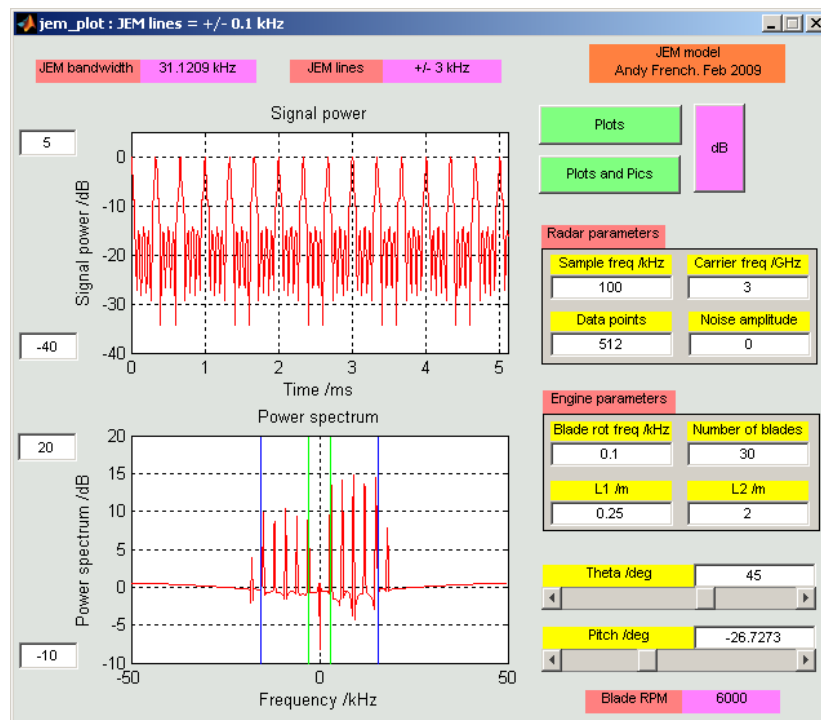


Figure 2.11: Screenshot of a MATLAB utility used to plot the signal modulations predicted by the Martin & Mulgrew model of Jet Engine Modulation (JEM). The signal is represented in both time and frequency domains.



## 2.5 Feature extraction methods

### 2.5.1 Effect of target aspect and elevation

Azimuth  $\phi$ , elevation  $\varepsilon$  and altitude  $h$  are computed from the U,V target coordinates determined from monopulse [88] measurements and target range  $R$ . The conversion is made for MESAR2 using the following parameters:

- Antenna tilt in degrees  $\delta = 15^\circ$
- U,V scaling factor  $S = 32768$ ,
- Antenna height  $h_a = 10\text{m}$
- Antenna base altitude  $h_b = 57\text{m}$ ,
- Radius of Earth  $R_E = 6.37 \times 10^6\text{m}$

and the following series of formulae:

$$\begin{aligned}
 U &\rightarrow U/S \\
 V &\rightarrow V/S \\
 A &= \sqrt{1 - U^2 - V^2} \\
 \delta &\rightarrow \frac{\pi\delta}{180} \\
 a &= R^2 - 2(R_E + h_a + h_b)R \cos\left(\varepsilon + \frac{\pi}{2}\right) \\
 \phi &= \tan^{-1}\left(\frac{-U}{A \cos \delta - V \sin \delta}\right) \\
 \varepsilon &= \sin^{-1}(A \sin \delta + V \cos \delta) \\
 h &= \sqrt{a + (R_E + h_a + h_b)^2} - R_E
 \end{aligned} \tag{2.53}$$

### 2.5.2 Use of target kinematics

Target range rate is supplied by the track extraction system in MESAR2. Additional motion compensation is employed (see section 3.5.2) to refine this value based upon the observed peak position of the skin return in the target Doppler spectra. Target aspect angle is also supplied and is quantized in intervals of  $10^\circ$ . In this thesis the focus is upon radially inbound trajectories; such that the Targets of Opportunity recordings can be readily compared to the Pod & Falcon data (which were all radially inbound). Range rate, and possibly its rate of change, could be used as feature measurement independent of length and Doppler fraction.<sup>25</sup> This possibility is not considered any further in this thesis, but shall be reiterated in the recommendations.

---

<sup>25</sup>Although one might expect a correlation with Doppler fraction; Jet aircraft are typically faster than Propeller driven aircraft).

### 2.5.3 Radar Cross Section

After formation of the HRR profile (via either Classical or Hybrid methods), the constituent complex signal samples are firstly converted to powers and then scaled using a calibration function based upon the *Radar Equation*. (See section 3.5.2). The calibration function was originally designed to be consistent with the pulse compressor output, hence an empirically determined RCS offset in  $\text{dBm}^2$  has been determined for each waveform to yield the same peak RCS for Classical, Hybrid and pulse compressor range profiles. During the trials there was unfortunately no direct calibration using a target of known RCS. Hence all RCS figures quoted are likely to be systematically in error by an unknown, but constant, number of decibels. To add a degree of realism to the RCS figures quoted, the point target references used for each waveform are all set at  $10\text{dBm}^2$ .

In the Appendix the maximum RCS values are plotted against target range for Classical & Hybrid HRR profiles, using waveforms A,B & C. The first set of graphs contrast the max HRR power in dB against the RCS measurements produced upon application of the calibration function. Although one can see the inverse fourth power of range correlation is not present in the calibrated data, there is still significant variability (some  $20\text{dBm}^2$ ) within the measurements. This observation is perhaps more clearly evident in the latter set of figures which plot (calibrated) RCS against range for each waveform and for a variety of class distinctions using recordings from six aircraft types, i.e. aircraft type, Long or Short and Four Lengths. (See Chapter 4). All targets are significantly variable, and indeed many targets of opportunity profiles have very small RCS values compared to the Pod and Falcon results. A possible inference, which is based upon the kinematic data evidenced in the Target data sheet section of the Appendix, is that the overall RCS is very sensitive (i.e. up to  $20\text{dB}$ ) to relatively small deviations in target aspect angle. An alternative hypothesis is that the absolute signal values which emerge from the MESAR2 receiver are also subject to significant variation. Whether the truth is explained by either (or both) these explanations is beyond the scope of this thesis. For the purposes of classification analysis, maximum RCS measurements obtained in the trials are deemed too variable to be of use. Instead we will focus on HRR length, scattering center range and Doppler spectral features.

### 2.5.4 Length from HRR profiles

Length measurements are computed from HRR profiles (in  $\text{RCS} / \text{dBm}^2$ ) via a threshold crossing; i.e. length is defined to be the range distribution of all HRR profile RCS values above the threshold. Given the variability of RCS measurements, coupled with the observation of relative stability in profile shape in the trials data set, a below-maximum threshold is employed.<sup>26</sup> Fig 2.12 demonstrates length feature extraction using a HRR profile of a Falcon jet aircraft.

### 2.5.5 Scattering center extraction using HRR profiles

Scattering centres are extracted from HRR profiles and their ranges compared (via a barcode matching algorithm<sup>27</sup>) to the radial projections of scattering centres which are marked upon the plan views of the aircraft drawings, as illustrated in fig 2.14. In this thesis the library of profiles is restricted to the set of aircraft under test. Scattering centres are selected from the HRR profile via the following

<sup>26</sup>e.g. if the peak of a particular HRR profile is  $10\text{dBm}^2$  and the threshold is set at  $20\text{dB}$ , the absolute threshold for length measurement is an RCS of  $-10\text{dBm}^2$ .

<sup>27</sup>The nearest aircraft is selected based upon the maximum value of the peak power of the cross-correlation of the projected scattering centre barcode (i.e. a binary vector) for each item in a database of aircraft, and the barcode derived from HRR profile scattering centre extraction.

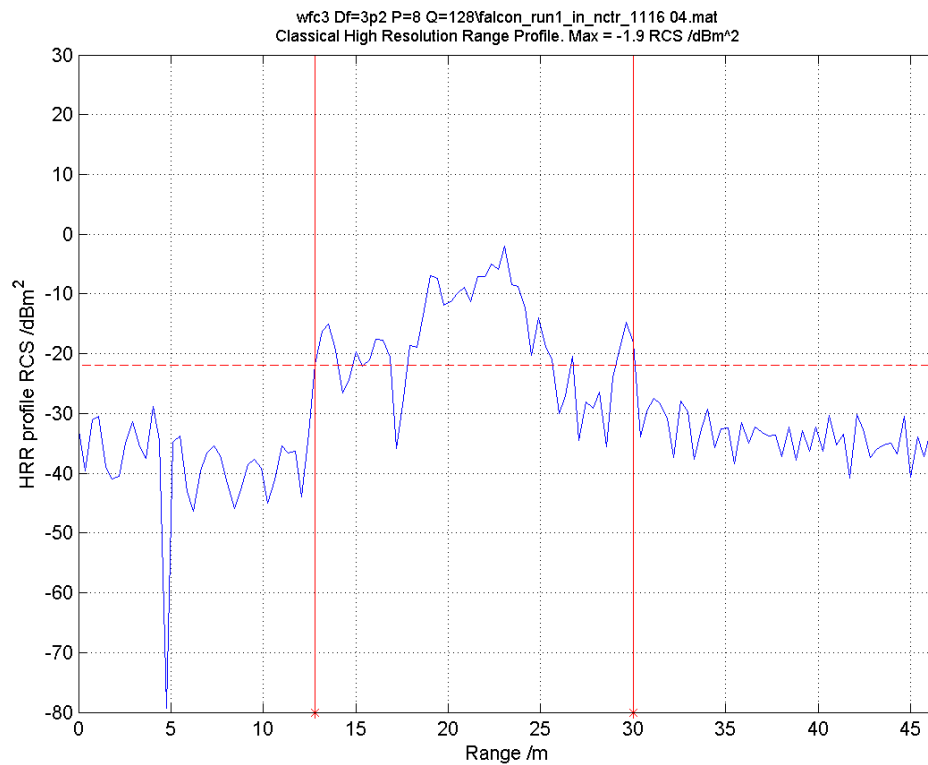


Figure 2.12: Classical HRRP of a radially inbound Falcon aircraft using a 5MHz non linear chirp waveform transmitted in 128 bursts of 8 coherent pulses, with each burst stepped in carrier frequency by 3.2MHz. The physical length of  $\approx 17\text{m}$  matches the radar length, which in this case is defined to be the extent of the profile 20dB below the maximum. Distinct front and back scatterers of the Falcon aircraft, coupled with the low sidelobes of the non-linear chirp, are likely to be the major factors in this positive agreement of radar and optical measurements.

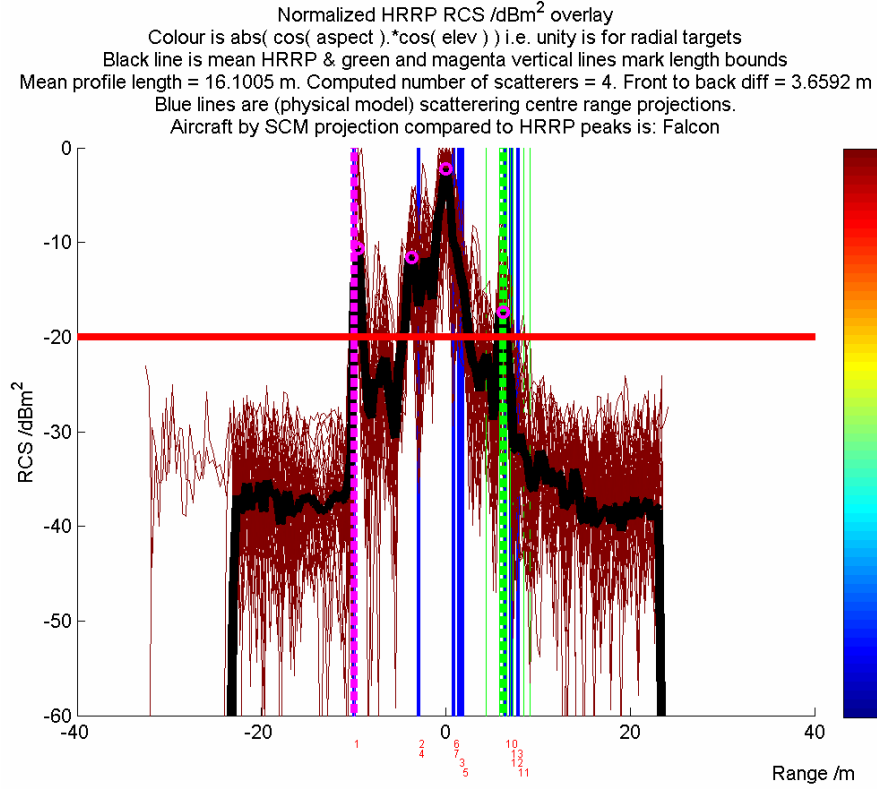


Figure 2.13: Overlay of 42 Classical HRRP profiles of a radially inbound Falcon aircraft. Profiles are normalized such that the maximum power is 0 dB and aligned in range to the start of the range profiles (i.e. the first range where the profile exceeds the relative threshold, -20dBm in this case). Magenta circles indicate the positions of major peaks. These can be related to the ranges of scattering centres (indexes are printed at various projected ranges below the range axis). The latter are defined manually based upon a plan view of the Falcon aircraft (see fig 2.14)

method:

1. Determine HRRP profile power peaks based upon selecting samples  $y(n)$  whose power is greater than the previous sample  $y(n - 1)$  and the following sample  $y(n + 1)$ .
2. Filter these to those peaks which exceed the length threshold.
3. Using a rolling window of  $\Delta R_{\min}$ , select the maximum peak value and pass this to the final set of scattering centres. This last step prevents a single peak being fragmented into many closely spaced peaks due to the effects of signal processing artifacts and noise. In this thesis a  $\Delta R_{\min}$  of 3m has been chosen.

Fig 2.13 represents an overlay of normalized HRRP profiles of a Falcon aircraft. The (four) scattering centres are marked with magenta circles at the corresponding peaks. Below the graph are the (numbered) locations of the radial projections of the scattering centres, which are defined in fig 2.14. In this example these elements match up. One may speculate that the rear pair of scattering centres are actually ensembles of scattering centres at the same range. Only the first scatterer is unique, which is most likely that of the nose cone.

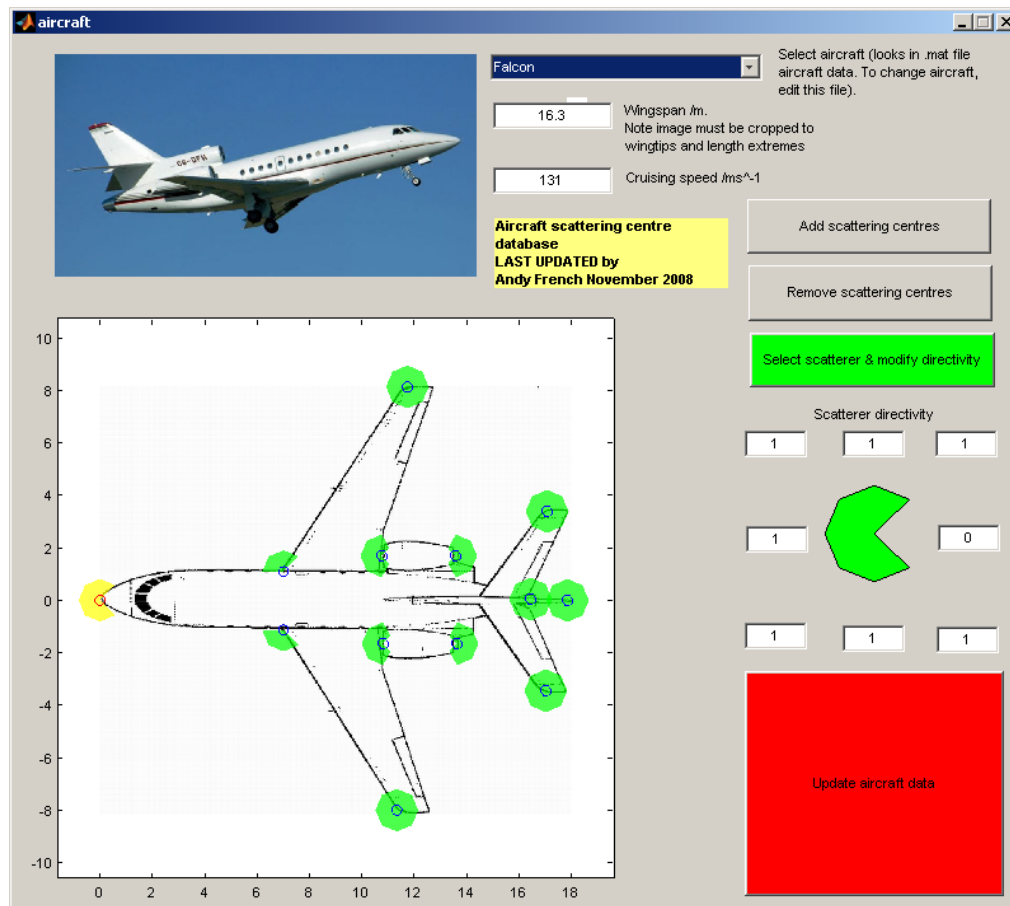


Figure 2.14: Scattering centre models of all the aircraft discussed in this thesis are defined using the tool illustrated. This is done by eye using plan views of each aircraft. The tool is also the entry point to set the anticipated range rate and physical length of each aircraft, which can be used in classification methods. Although not used in this thesis, crude (eight sector) values for directivity can be set to help generate more realistic model profiles.

### 2.5.6 dfrac and efrac from Doppler spectra

The Doppler fraction (dfrac) feature is defined as the fraction of samples of the (normalized<sup>28</sup>) target Doppler spectra which exceed a fixed threshold. In fig 2.15 a threshold of -25dBm is set which gives a dfrac value of 0.35 for the Boeing 777 aircraft, which appears to display a clear set of JEM lines.

An alternative Doppler Energy Fraction (efrac) feature is defined to be the ratio  $\epsilon$  of integrals

$$\epsilon = 1 - \frac{\int_{-\frac{f_{PRF}}{P}}^{\frac{f_{PRF}}{P}} \Theta(f) df}{\int_{-\frac{f_{PRF}}{2}}^{\frac{f_{PRF}}{2}} \Theta(f) df} \quad (2.54)$$

$\Theta(f)$  is the Doppler filter output power sum over frequency steps<sup>29</sup> and  $f$  is the Doppler frequency. This is computed numerically from an array of  $\{\Theta(f), f\}$  using the methods of Duane & Hanselman [40]. Coefficients of cubic splines are computed for each  $\Theta(f)$  data point and frequency pair and the resultant series of splines are integrated exactly over the integral range desired in the denominator and numerator of the above fraction. This feature may help to distinguish aircraft which have a broad Doppler spectrum, but no clear JEM, from those exhibiting very little motion (beyond bulk velocity) in the radial direction.

### 2.5.7 Major peaks in Doppler

This feature is the Doppler domain equivalent to scattering center extraction in the HRR profile. The same algorithm has been used to determine the peaks (represented by the magenta circles in fig 2.15). The rolling window is set at 2.5/16 kHz, i.e. two Doppler bins for a 32 pulse waveform with a PRF of 2.5kHz. Doppler peaks could be used to infer the position of JEM lines. However, since the PRF is much lower than the expected JEM bandwidth for typical aircraft (see section 2.4.2), JEM lines are likely to be highly ambiguous. Hence ‘spectral shape’ features rather than JEM line spacing is used for classification in this thesis.

<sup>28</sup>i.e. maximum spectrum power is set at 0dBm.

<sup>29</sup>This should increase the signal to noise ratio since post motion compensation one would expect the Doppler filter output powers to be very similar for each frequency step.

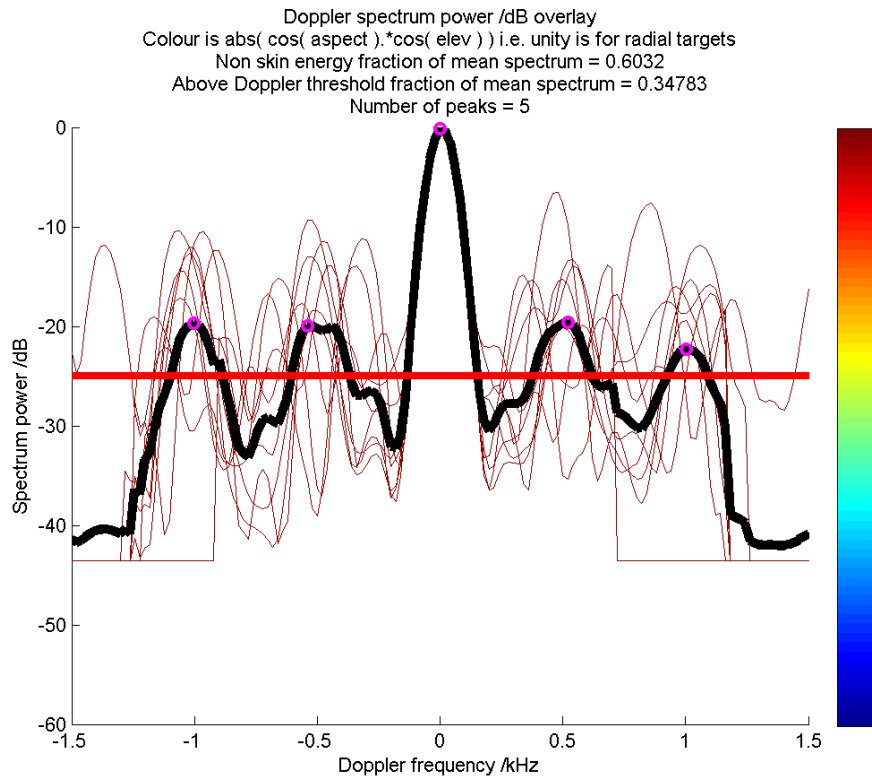


Figure 2.15: Overlay of 10 (normalized) Doppler power spectra of a Boeing 777 aircraft using a 32 pulse waveform of -4.5MHz linear chirps of duration  $25.6\mu\text{s}$ . The black trace is the mean spectra. Jet Engine Modulation (JEM) can be clearly observed at intervals of approximately 500Hz. For the mean spectrum, the fraction of total power above -25dB is 34% and the ‘non skin energy fraction’ is 60%. Moderate values allow JEM to be distinguished from No Non Skin Doppler (which might result from a missile or obscured engine) and Propeller modulation (which tends to result in a broader doppler spectra) using a simple three class, scalar parameter classifier.

## 2.6 Methods of target classification

One of the goals of this research is to investigate what classification performance is achievable using features taken from NCTR mode recordings of airborne targets using MESAR2. To provide a mechanism for this, three well established schemes will be used. Each scheme employs the same fundamental logic. A *discriminant function*  $g_i(\mathbf{x})$  is computed from each feature vector  $\mathbf{x}$  (i.e. a single feature such as length or an ensemble of features such as length & Doppler fraction) for each class  $w_i$  of a defined finite alphabet  $\{w_1, \dots, w_N\}$  of length  $N$ . The assigned class  $w_j$  to  $\mathbf{x}$ , where  $w_j \in \{w_1, \dots, w_N\}$ , corresponds to the maximum discriminant  $g_j(\mathbf{x})$  such that  $g_j(\mathbf{x}) = \max [g_1(\mathbf{x}), \dots, g_N(\mathbf{x})]$ .

In the Pod & Falcon and Targets of Opportunity aircraft trials described in this thesis, the class origin of every measurement is known; i.e. a length measurements may derive from either a Pod, Falcon, Boeing 747, 757, 777 or Dash 8 aircraft. We can therefore compute a statistical measure of classification performance by comparing the number of features which are correctly classified to those which are not. Let us define a (square) *confusion matrix*  $\mathbf{C}$  where element  $[\mathbf{C}]_{ij} \equiv C_{ij}$  corresponds to the ratio of the number of features  $n_i$  (sourced from class  $w_j$ ) and classified as class  $w_i$  to the total number of features  $m_j = \sum_i n_i$  which are sourced from class  $w_j$ . Perfect classification is when

$$C_{ij} = \frac{n_i}{m_j} = \begin{cases} 1 & i = j \\ 0 & i \neq j \end{cases} \quad (2.55)$$

i.e. when  $\mathbf{C}$  is an identity matrix. A scalar performance metric can therefore be sensibly defined as the ‘off diagonal extent’  $\xi$  of the confusion matrix.<sup>30</sup> This has value 0 when classification is perfect and value 1 when there are no correct classifications.

$$\xi = 1 - \frac{\text{Tr} [\mathbf{C}]}{\sum_{i=1}^N \sum_{j=1}^N [\mathbf{C}]_{ij}} \quad (2.56)$$

Fig 2.16 describes the spreadsheet used in the analysis described in the following chapters. As illustrated, a set of target data is assigned a ‘truth’ classification (based upon knowledge of aircraft type, physical length, knowledge of engine type...) using class sets (defined in the following two Chapters)

- Aircraft type
- Long or Short Four Lengths
- Prop, JEM or No-Non Skin Doppler (NNSD).

Classifier performance is assessed against these assignments.

### 2.6.1 Choice of classifier

A major aim of this thesis is to investigate the variation of classification performance with key parameters of the signal processing and feature extraction methods applicable to measurements made using a multifunction phased array Radar. The emphasis is not the assessment of novel classification algorithms. To this end the classifiers employed to determine performance are very well known and have been chosen for their simplicity. Three types of scheme are alluded to (with the classifiers used in brackets):

---

<sup>30</sup>Similar to the ‘error rate’ described in many publications.



	A	B	C	D	E	F	G	H	I	J	K	L	M
1		Class assignments spreadsheet created by Andy French on 22-Feb-2008				JEM is Jet Engine Modulation	means No Non skin Doppler	Prop means propeller modulation					
2		Number of data files	13							Number of classes	2	2	4
3													
4		Target data	Look class name (elements of input data)	Aircraft type class name	Wingspan /m	Long or short class name	Four lengths class name	Prop, JEM or NNSD class name	Aircraft type by airspeed class name	Look class name	Aircraft type classes	Long or short classes	4 length classes
5	1	falcon_run1_in_nctr_1116	Falcon	Falcon	16.3	Short	S	NNSD	Falcon	Falcon	Falcon	Long	VS
6	2	falcon_run3_in_nctr_1039	Falcon	Falcon	16.3	Short	S	NNSD	Falcon	Pod	Pod	Short	S
7	3	falcon_run4_in_nctr_1157_1237	Falcon	Falcon	16.3	Short	S	NNSD	Falcon				L
8	4	falcon_run5_in_nctr_1121_1193	Falcon	Falcon	16.3	Short	S	NNSD	Falcon				VL
9	5	falcon_run6_in_nctr_1030	Falcon	Falcon	16.3	Short	S	NNSD	Falcon				
10	6	falcon_run7_in_nctr_1136	Falcon	Falcon	16.3	Short	S	NNSD	Falcon				
11	7	falcon_run8_in_nctr_1015	Falcon	Falcon	16.3	Short	S	NNSD	Falcon				
12	8	pod_run1_in_nctr_1127	Pod	Pod	1.5	Short	VS	NNSD	Pod				
13	9	pod_run3_in_nctr_1101	Pod	Pod	1.5	Short	VS	NNSD	Pod				
14	10	pod_run4_in_nctr_1173_1204	Pod	Pod	1.5	Short	VS	NNSD	Pod				
15	11	pod_run5_in_nctr_1017	Pod	Pod	1.5	Short	VS	NNSD	Pod				
16	12	pod_run6_in_nctr_1112	Pod	Pod	1.5	Short	VS	NNSD	Pod				
17	13	pod_run8_in_nctr_1019	Pod	Pod	1.5	Short	VS	NNSD	Pod				
18	14												
19	15												
20	16												
21	17												
22	18												

Figure 2.16: Screenshot of spreadsheet used to assign classes to radar data from known aircraft types. The performance of the classification methods is assessed by the proportion of classifications automatically made by the classifier which agree to those assigned in this spreadsheet.

1. *Expert parametric classifier* (Bayesian Gaussian, Fuzzy logic). Prior knowledge regarding the parameters and functional form of the underlying feature probability distribution is assumed, rather than inferred from a training subset of the feature data set. For the Gaussian classifier this corresponds to a definition of the mean and standard deviations of each class distribution. For the fuzzy logic classifier this corresponds to a definition of the membership function of each class.
2. *Data driven parametric classifier* (Bayesian Gaussian). In this case the parameters of each classifier are derived from a training subset of the recorded data. However, an overall functional form of the underlying feature distribution is assumed (e.g. a two parameter Gaussian probability distribution).
3. *Data driven non-parametric classifier* (k-means). Classifier inputs are derived from a clustering of training data; i.e. no assumption regarding the functional form of the underlying feature distribution is assumed.

In Chapters 4 and 5, classification performance using scalar features is assessed via Bayesian and Fuzzy Logic classifiers which are constructed from ‘Expert’ training data established using the tool described in fig 2.17. This decision was made for two reasons:

1. The features chosen were ‘physical’ in nature and therefore could be easily characterized. e.g. expect Radar length to be strongly correlated with physical length. Dash8 has a propeller, a B747 has jet engines etc.
2. The number of feature measurements obtained from the MESAR2 trials are relatively small, i.e. insufficient data to train a classifier and assess its performance.<sup>31</sup>

<sup>31</sup>How many looks do you need to construct a viable training data set? This is a difficult question to answer from a

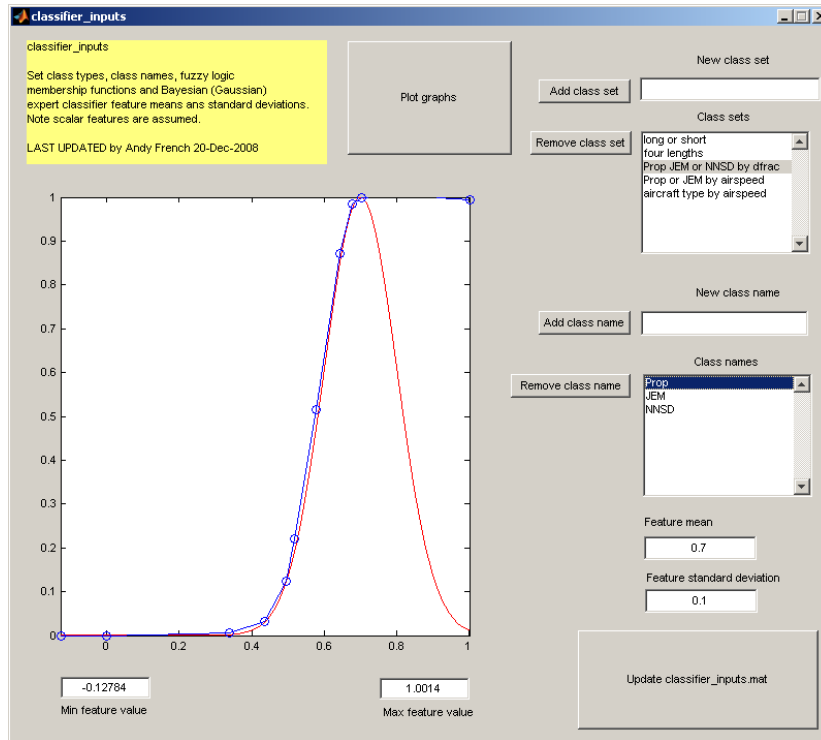


Figure 2.17: Inputs to the scalar Bayesian & Fuzzy logic classifiers are set using the tool illustrated. In this example, the (unnormalized) Gaussian probability density function used to define the ‘expert’ training data in the Bayesian classifier, and the Fuzzy Logic ‘membership’ function are overlaid. In this example, the (scalar) feature is the fraction of Doppler spectrum power above a defined threshold. One might expect subtle differences in performance between Fuzzy Logic and Bayesian classifiers in this case given the difference in their function forms.

The (Expert) Bayesian Gaussian classifier is adopted as the parametric classifier of choice due to its simplicity and formulation using feature vectors of arbitrary dimensions.<sup>32</sup> To check its implementation the highly intuitive but crude ‘Fuzzy logic method’ is also employed for classification of scalar features. In Chapter 6 a two-parameter feature vector is considered (length and Doppler fraction) for aircraft type classes. Classification performance in this case is considered using the (Expert) Bayesian Gaussian method.

In the recommendations of this thesis it is suggested that further experiments be conducted to enable a training data set to be constructed. A simple extension might be an further day of ‘targets of opportunity’ trials. If the original data set (collected in 2006) is used as training data then one could argue quite a strong case for independence of training and measurement data! If this extra experiment is conducted then the Bayesian Gaussian and k-means methods described below could be fully exploited in their ‘data driven’ rather than ‘Expert’ form.

---

theoretical standpoint in general terms. An empirical approach based upon previously reported successful experiments is probably the best point of departure. Regular data gathering and analysis of target recognition algorithms applied in an operational system will surely improve upon this estimate. Zyweck & Bognor [118] present a classification analysis comparing Boeing 727 and Boeing 737 aircraft. Approximately 40% of the data collected was used for classifier training. (48 looks for B727 and 66 looks for B737. Measurement data was 96 looks for each aircraft type). In the experiments reported in this thesis, around 50 looks is the maximum per (inbound) aircraft type per waveform. Hence the decision to use an ‘expert’ classifier and classify all the looks rather than take a training subset.

<sup>32</sup>i.e. the method is readily extensible to include multiple dimension features such as length & Doppler fraction (dfraction).

### 2.6.2 Bayesian classifier

Friedman (1989) proposed *Regularized Discriminant Analysis* (RDA) (see Webb [110] pp37) which is a mixture of linear and quadratic terms (in feature vector  $\mathbf{x}$ ) in the expression of the discriminant  $g_i(\mathbf{x})$ . This derives from the assumption of a Gaussian distribution of  $M$  dimensional features  $\mathbf{x}$  for each class  $w_i$

$$p(\mathbf{x} | w_i) = \frac{1}{(2\pi)^{\frac{M}{2}} |\mathbf{\Xi}_i|^{\frac{1}{2}}} \exp \left\{ -\frac{1}{2} (\mathbf{x} - \boldsymbol{\mu}_i)^T \mathbf{\Xi}_i^{-1} (\mathbf{x} - \boldsymbol{\mu}_i) \right\} \quad (2.57)$$

where  $\boldsymbol{\mu}_i$  is the feature mean and  $\mathbf{\Xi}_i$  the covariance matrix. The discriminant function is defined to correspond to the logarithm of the posterior probability  $p(w_i | \mathbf{x})$ , i.e. classification based on the largest discriminant corresponds to the highest probability of the chosen class, given the feature measurement. Applying Bayes rule  $p(w_i | \mathbf{x})p(\mathbf{x}) = p(\mathbf{x} | w_i) p(w_i)$ , noting  $p(\mathbf{x})$  is independent of class  $w_i$ , yields the discriminant

$$g_i(\mathbf{x}) = \log(p(w_i)) - \frac{1}{2} \log(|\mathbf{\Xi}_i|) - \frac{1}{2} (\mathbf{x} - \boldsymbol{\mu}_i)^T \mathbf{\Xi}_i^{-1} (\mathbf{x} - \boldsymbol{\mu}_i) \quad (2.58)$$

Given a training data set  $\{\mathbf{t}_1^{(i)} \dots \mathbf{t}_{Z_i}^{(i)}\}$ , Webb [110] pp35 shows that maximizing the *Likelihood function*

$$L\left(\{\mathbf{t}_1^{(i)} \dots \mathbf{t}_{Z_i}^{(i)}\} | \boldsymbol{\mu}_i, \mathbf{\Xi}_i\right) = \prod_{z=1}^{Z_i} p(\mathbf{t}_z^{(i)} | w) = \prod_{z=1}^{Z_i} \frac{1}{(2\pi)^{\frac{M}{2}} |\mathbf{\Xi}_i|^{\frac{1}{2}}} \exp \left\{ -\frac{1}{2} (\mathbf{t}_z^{(i)} - \boldsymbol{\mu}_i)^T \mathbf{\Xi}_i^{-1} (\mathbf{t}_z^{(i)} - \boldsymbol{\mu}_i) \right\} \quad (2.59)$$

i.e. finding solutions to  $\frac{\partial \log(L)}{\partial \boldsymbol{\mu}_i} = 0$  and  $\frac{\partial \log(L)}{\partial \mathbf{\Xi}_i} = 0$ , yields the following estimates for the mean and covariance matrix

$$\begin{aligned} \boldsymbol{\mu}_i &\approx \mathbf{m}_i = \frac{1}{Z_i} \sum_{z=1}^{Z_i} \mathbf{t}_z^{(i)} \\ \mathbf{\Xi}_i &\approx \mathbf{\Sigma}_i = \frac{1}{Z_i} \sum_{z=1}^N (\mathbf{t}_z - \mathbf{m}_i) (\mathbf{t}_z - \mathbf{m}_i)^T \end{aligned} \quad (2.60)$$

where  $\mathbf{m}_i$  is the sample mean and  $\mathbf{\Sigma}_i$  is the sample covariance. Using the assignment of the prior probability to be  $p(w_i) = \frac{Z_i}{Z}$  where  $Z = \sum_i Z_i$ , one arrives at the *Gaussian classifier*

$$g_i(\mathbf{x}) = -\frac{1}{2} (\mathbf{x} - \mathbf{m}_i)^T \mathbf{\Sigma}_i^{-1} (\mathbf{x} - \mathbf{m}_i) - \frac{1}{2} \log(|\mathbf{\Sigma}_i|) + \log\left(\frac{Z_i}{Z}\right) \quad (2.61)$$

Friedman improves upon this with RDA using the parameters  $0 \leq \mu, \lambda \leq 1$  to account for situations when  $\mathbf{\Sigma}_i$  becomes singular, i.e.  $|\mathbf{\Sigma}_i| \rightarrow 0$ . RDA apparently offers superior performance (for suitably chosen  $\mu, \lambda$ ) than a linear approximation<sup>33</sup> for higher dimensional features and smaller sample sizes, when there is danger of singular  $\mathbf{\Sigma}_i$ . Note  $\mu, \lambda = 0$  yields the (quadratic) Gaussian classifier and  $\mu, \lambda = 1$  yields the linear version. In this thesis we will use  $\mu, \lambda = 0.01$  to guard against possible singularity, but in the main approximate the Gaussian discriminant function. The full RDA recipe is as follows:

<sup>33</sup>i.e.  $g_i(\mathbf{x}) = -\frac{1}{2} \mathbf{m}_i^T \mathbf{S}_W^{-1} \mathbf{m}_i + \mathbf{x}^T \mathbf{S}_W^{-1} \mathbf{m}_i + \log\left(\frac{Z_i}{Z}\right)$  where the ‘within class pooled covariance’  $\mathbf{S}_W = \sum_i \frac{Z_i}{Z} \mathbf{\Sigma}_i$

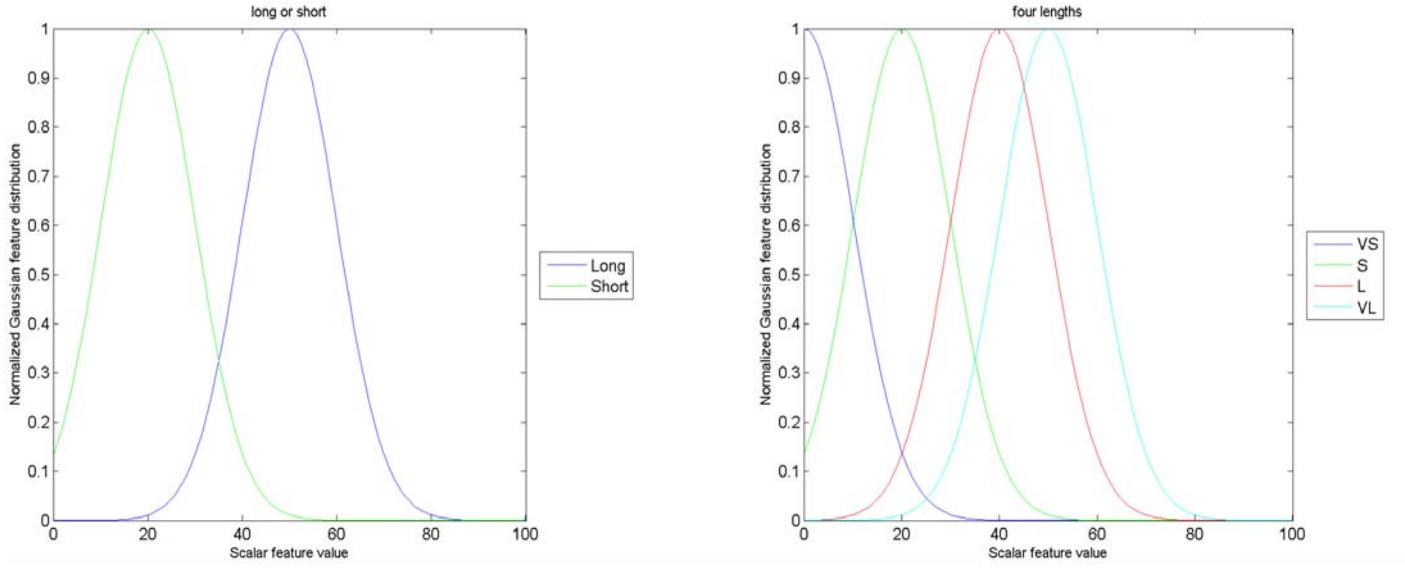


Figure 2.18: Overlay of the (unnormalized) probability density functions for the Long or Short classes, and the Four Lengths classes. These are used to generate ‘expert’ data for use in the Bayesian classifier. In both examples, a fixed standard deviation but variable mean is used.

$$\begin{aligned}
 g_i(\mathbf{x}) &= -\frac{1}{2}(\mathbf{x} - \mathbf{m}_i)^T [\boldsymbol{\Sigma}_i^{\lambda, \gamma}]^{-1} (\mathbf{x} - \mathbf{m}_i) - \frac{1}{2} \log \left( |\boldsymbol{\Sigma}_i^{\lambda, \gamma}| \right) + \log \left( \frac{Z_i}{Z} \right) \quad (2.62) \\
 \boldsymbol{\Sigma}_i^{\lambda, \gamma} &= (1 - \gamma) \boldsymbol{\Sigma}_i^{\lambda} + \gamma c_i(\lambda) \mathbf{I} \\
 c_i(\lambda) &= \frac{\text{Tr}(\boldsymbol{\Sigma}_i^{\lambda})}{M} \\
 [\mathbf{I}]_{ij} &= \delta_{ij} \quad i, j = 1, \dots, M \\
 \boldsymbol{\Sigma}_i^{\lambda} &= \frac{(1 - \lambda) \mathbf{S}_i + \lambda \mathbf{S}}{(1 - \lambda) Z_i + \lambda Z} \\
 \mathbf{S}_i &= Z_i \boldsymbol{\Sigma}_i \\
 \mathbf{S} &= Z \mathbf{S}_w \\
 \mathbf{S}_w &= \sum_{i=1}^N \frac{Z_i}{Z} \boldsymbol{\Sigma}_i \\
 \boldsymbol{\Sigma}_i &= \frac{1}{Z_i} \sum_{z=1}^N (\mathbf{t}_z - \mathbf{m}_i) (\mathbf{t}_z - \mathbf{m}_i)^T
 \end{aligned}$$

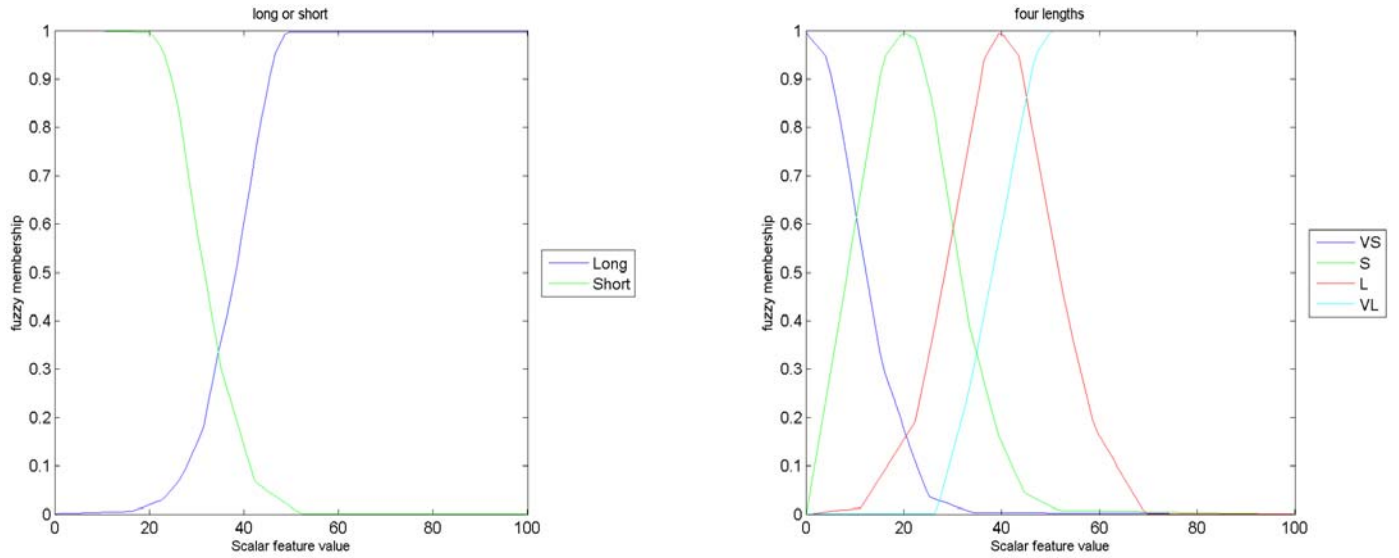


Figure 2.19: Overlay of the (unnormalized) probability density functions for the Long or Short classes, and the Four Lengths classes. These are used to define the membership functions used in the Fuzzy Logic classifier. In this example, the form of the membership functions has been designed to match those of the Bayesian probability density functions illustrated in fig 2.18.

### 2.6.3 Fuzzy logic classifier

This method (Moruzzis 1998 [75]) relies on the form of the discriminant function to be user defined, as illustrated in fig 2.19. For scalar features this is implemented as an interpolation of a *membership function*  $\Omega(x)$  defined over the likely feature range, whose values are constrained to be in the range  $[0,1]$ . For multidimensional feature vectors a multi-value discriminant is used. For simplicity we will define this to be the product of the scalar membership functions for each feature, and assume these are independent.

$$g_i(\mathbf{x}) \equiv g_i([x_1 \dots x_M]) = \prod_{j=1}^M \Omega_j^{(i)}(x_j) \quad (2.63)$$

### 2.6.4 k-means classifier

The *k-means fuzzy classifier* is a popular *non-parametric method* which is based upon the iterative Generalized Lloyd algorithm (Karayiannis 1995). The version described here is an application of the methods of Bezdek, Ehrlich & Full cited in Bowden [14] and Wong [113] and clearly described (in the context of other clustering and classification techniques) in the textbooks by Webb [110] and Duda [27]. Unlike Bayesian methods, the k-means technique does not depend upon knowledge of the underlying likelihood probability distributions of the feature measurements.

*k-means* is an  $M$  dimensional non-parametric classifier based upon  $K$  hyperspheres of radius  $R_k^{(i)}$  and origin vector  $\mathbf{c}_k^{(i)}$  determined to optimally cluster feature training data for each class  $w_i$ . The algorithm for this clustering approach is described in the Appendix. The discriminant function  $g_i(\mathbf{x})$  is computed from the clusters formed from the training data set using the following formula:

$$g_i(\mathbf{x}) = \max_k \left\{ \exp \left( - \frac{|\mathbf{x} - \mathbf{c}_k^{(i)}|^2}{2R_k^{(i)} R_k^{(i)}} \right) \right\} \quad (2.64)$$

---

i.e. find the maximum association  $\exp\left(-\frac{\|\mathbf{x}-\mathbf{c}_k^{(i)}\|^2}{2R_k^{(i)}R_k^{(i)}}\right)$  of the feature vector with each cluster hypersphere  $k$  (of  $K$ ) defined by radius  $R_k^{(i)}$  and origin vector  $\mathbf{c}_k^{(i)}$ , as illustrated in (Appendix) fig I.4.

## 2.7 Features & limitations of an S-band multifunction phased array Radar used for NCTR

In this section the physical characteristics of the S-band multifunction phased array Radar MESAR2 are summarized, in particular those attributes which can constrain NCTR performance. Although MESAR2 is a unique experimental sensor, the discussion below should be generally applicable to most S-band phased array systems.

### 2.7.1 Multi-function phased array Radar

A phased array Radar such as MESAR2 is one that possesses an antenna composed of an ensemble of radiating elements. The net electric field is shaped by the phase and amplitude relationship between each component part. If these relationships can be controlled this can allow for a steering and re-shaping of the main beam produced by the antenna without having to mechanically rotate or deform its shape. If electronic control is possible, this can allow for rapid functional changes. This key attribute allows systems such as MESAR2 to act as multifunction Radars; for example, enabling the simultaneous tracking of targets with wide area surveillance. An important feature of MESAR2 is an automatic scheduler which effectively maintains a dynamic prioritized ‘to do’ list of activities. The stepped frequency NCTR waveforms described in this thesis were added to the scheduler alongside the other waveforms representing the tracking and surveillance functions. Each activity in the schedule is assigned a priority rating which depends on a number of user defined factors<sup>34</sup> as well as increasing in urgency with delay since the last update. Since the schedule at any one time is dependant on the status of the environment, (i.e. a large number of targets being tracked may reduce the ‘occupancy’, or schedule time available for NCTR looks) this means the rate of particular looks is governed by a probability distribution rather than being deterministic, as indicated in figure 2.20.

### 2.7.2 Frequency stability

If the standard error in carrier frequency (‘jitter’) is  $\sigma_{f_{Tx}}$ , a HRR profile will be severely affected if the jitter results in a phase change between signal transmission and reception of around  $\pi$  at the range of interest  $R$ . The logic behind this stems from the qualitative statement that a stepped frequency HRR technique effectively assesses the phase change of a signal reflected from a target at fixed range<sup>35</sup> between frequency steps<sup>36</sup>.

Therefore in order not to corrupt a HRR profile with random phase errors:

$$2\pi\sigma_{f_{Tx}}\frac{2R}{c} \ll \pi \Rightarrow \sigma_{f_{Tx}} \ll \frac{c}{4R} \quad (2.65)$$

Hence if a target is at  $R = 100\text{km}$ , carrier frequency jitter  $\sigma_{f_{Tx}} \ll 750\text{Hz}$ . Since carrier frequencies are of the order of a few GHz at S-band, this requires frequency stability of better than 1 part in  $10^6$ .

<sup>34</sup>for example one can set a fast moving inbound target, which might be a missile, to have a high priority (which is likely to result in a high tracking update rate).

<sup>35</sup>i.e. motion compensation assumed.

<sup>36</sup>Which are required to be constant if a Discrete Fourier Transform method is used to compute the HRR (as is the case with both Classical and Hybrid methods).

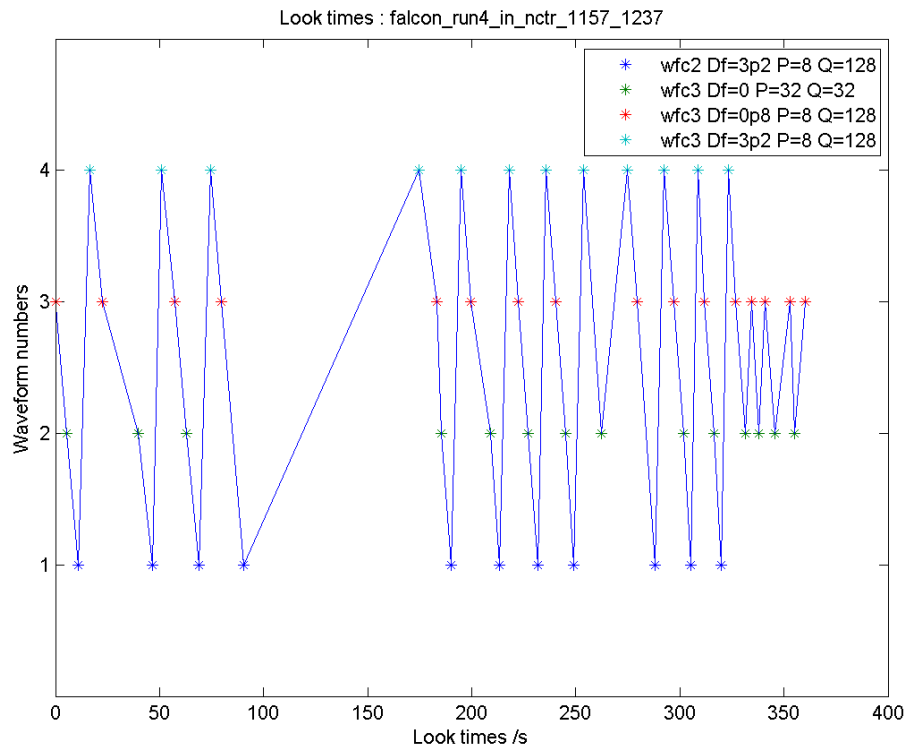


Figure 2.20: Times /s of NCTR looks (four waveforms) delivered by MESAR2 on 14th October 2005 against a Falcon trials aircraft. Note periodicity between NCTR looks is not constant since MESAR2 is a multi-function radar which operates with an adaptive scheduler.



### 2.7.3 Beam position, scanning losses & true time delay

In this section we briefly summarize the practical constraints applicable to phased array radars such as MESAR2. In Appendix A we show that one can steer the main beam of a phased array to angle  $\phi$  using an inter element phase shift of

$$\Delta\Omega = -\frac{2\pi f}{c} \left( \frac{L}{N-1} \right) \sin \phi \quad (2.66)$$

where  $f$  is the transmitted frequency,  $L$  is the antenna length,  $N$  is the number of elements,  $c$  is the speed of light. For optimal beamshapes, i.e. without excessive sidelobes and grating lobes, the inter-element spacing must be half a wavelength i.e.

$$\frac{L}{N-1} = \frac{c}{2f}$$

If the transmitted signal comprises of a swept bandwidth of  $B$  then this will result in a squint  $\delta\phi$  of the peak if  $\Delta\Omega$  is fixed during the transmit of the pulse, which is typical.<sup>37</sup> If the carrier frequency is  $f_{Tx}$  and instantaneous frequency is  $f \in [f_{Tx} - \frac{1}{2}B, f_{Tx} + \frac{1}{2}B]$

$$\delta\phi(f) = \sin^{-1} \left( \frac{f_{Tx}}{f} \sin \phi_{peak} \right) - \phi_{peak} \quad (2.67)$$

There is also a change in directivity<sup>38</sup> with frequency and a reduction in the projected antenna area radiating in the look direction. Balanis [7] pp273 shows the directivity of a large<sup>39</sup> planar array antenna to be

$$D = \pi \cos \phi D_x D_y \quad (2.68)$$

where  $D_{x,y}$  are the directivities of broadside linear arrays in orthogonal directions  $x, y$ . Balanis pp234 gives<sup>40</sup>

$$D_{x,y} = \frac{2Nd_{x,y}}{c} f \approx \frac{2L_{x,y}f}{c} \quad (2.69)$$

where  $d_{x,y}$  are the inter-element spacings in (respectively)  $x$  and  $y$  directions. Hence one expects a one-way scanning loss<sup>41</sup> proportional to the cosine of the look angle, since this is the reduction in projected area. In practice this is the minimum loss since mutual coupling between elements can result in directivity nulls. These can result in disastrous consequences if the beam is steered to these directions; the radiated power is reflected back upon the antenna face and can result in the destruction of the radiating elements. The reduction in directivity with scan angle also has the effect of broadening the beam, so angular resolution will degrade. Scanning loss is mediated by a gain proportional to frequency  $f$  (for a linear array) and  $f^2$  (for a planar array).

<sup>37</sup>i.e.  $\Delta\Omega = -\pi \sin \phi_{peak}$  and  $\frac{L}{N-1} = \frac{c}{2f_{Tx}}$ .

<sup>38</sup>Directivity is the distribution of radiated power in an angular sense. In a particular azimuth  $\phi$  and elevation  $\varepsilon$  the directivity gives the fraction of total radiated power per unit solid angle  $d\Omega = \frac{\mathbf{R} \cdot d\mathbf{S}}{R^3} = \cos \varepsilon d\varepsilon d\phi$ . Directivity is effectively the angular variation of antenna gain  $G$ .

<sup>39</sup>The number of elements is such that the distance between elements is much smaller than the overall array size.

<sup>40</sup>Note end fire arrays can have greater directivities than this. The Hansen-Woodyard design is greater by  $1.789 \times 2$ .

<sup>41</sup>The loss on receive is of course two way. This will be the square of the one way losses. Skolnik [95] pp2.56 states squinting loss to be

$$L_{sqint} \approx \frac{1}{\cos^2 \phi_{peak}} \quad (2.70)$$

which is consistent with the result from Ballanis, but does not include the effects of frequency. The latter is conventionally incorporated in the gain terms of the Radar equation.

Perhaps more serious than a loss in directivity is the possibility that the scanning of the beam due to the frequency sweep will cause the target not to be illuminated. This effect can be mediated to a certain extent if the frequency sweep causes a squint which opposes the rotation of the antenna, an effect exploited in the AR327 (Commander) series of Air Defence slotted waveguide Radars manufactured by BAE Systems. To illustrate squinting effects, (see figures 2.21 to 2.24) consider a linear phased array of length  $L = 0.948$  m with  $N = 20$  elements delivering a linear chirp of bandwidth 400MHz about a carrier of  $f_{Tx} = 3\text{GHz}$ . The far field beam pattern of the linear array power, including directivity, (see Appendix) is proportional to

$$|\psi(\phi)|^2 \propto \frac{Lf}{c} \cos \phi \left| \frac{e^{i\omega} \sin((1+N^{-1})\omega)}{\sin(N^{-1}\omega)} - 1 \right|^2 \quad (2.71)$$

where

$$\omega = \frac{\pi N f L}{c} \left( \frac{c \Delta \Omega}{2\pi f L} + \frac{\sin \phi}{N-1} \right) \quad (2.72)$$

$$\Delta \Omega = -\frac{2\pi f_{Tx}}{c} \left( \frac{L}{N-1} \right) \sin \phi \quad (2.73)$$

The losses inherent in a phased array architecture can be overcome by using ‘True Time Delay’ elements rather than phase-shifters. To synthesize a wavefront at a particular angle from the array face the waveform supplied to each of the constituent elements is time delayed by the difference in time of flight from the element to the wavefront. If the distance from the array<sup>42</sup> centre to the wavefront is  $R$  then the distance  $R_D$  to the wavefront from an element at a distance  $D$  from the array centre is  $R - D \sin \phi$  where  $\phi$  is the angle of the wavefront from the normal to the array face. (See fig 2.25). The time delay for element at  $D$  is therefore

$$\Delta T_D = \frac{D \sin \phi}{c} \quad (2.74)$$

Implementation of True Time Delay (TTD) is described in Tait [103]pp 293 and Skolnik [95] pp7.56. Optical delay line components are one means of achieving TTD. Given the time accuracy required so not to introduce additional phase shifts, and the desire to scan at a variety of angles of boresight, this solution is far from simple and as a result an expensive modification with current technology.

---

<sup>42</sup>assumed to be planar

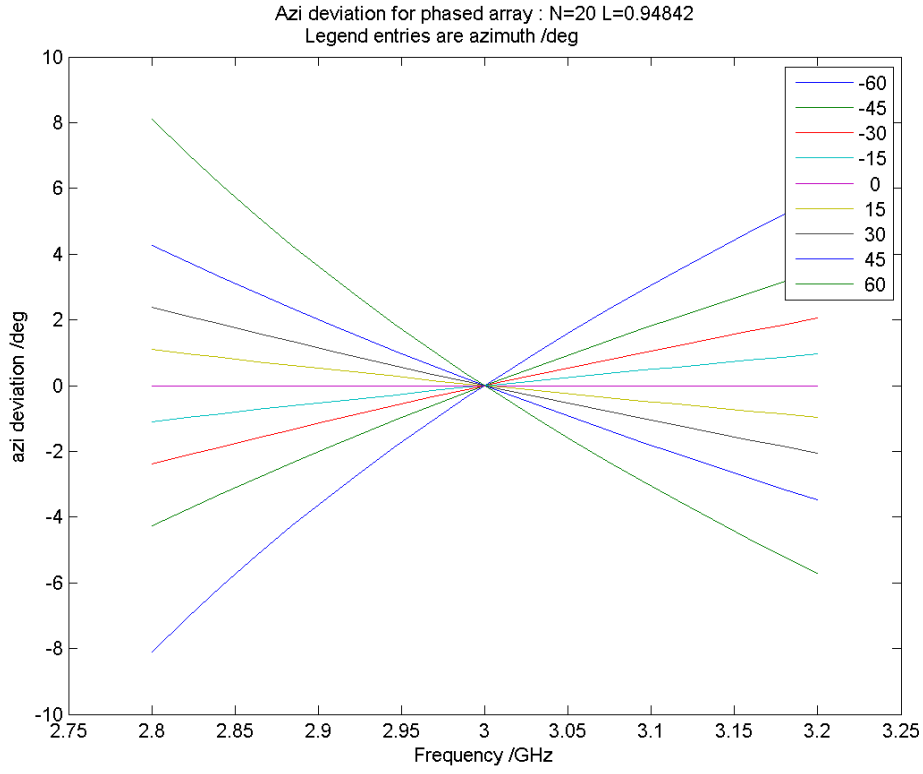


Figure 2.21: Azimuth deviation from initial look direction as a function of frequency for a linear phased array  $L = 0.948$  m,  $N = 20$ ,  $f_{Tx} = 3\text{GHz} \pm 200\text{MHz}$ .

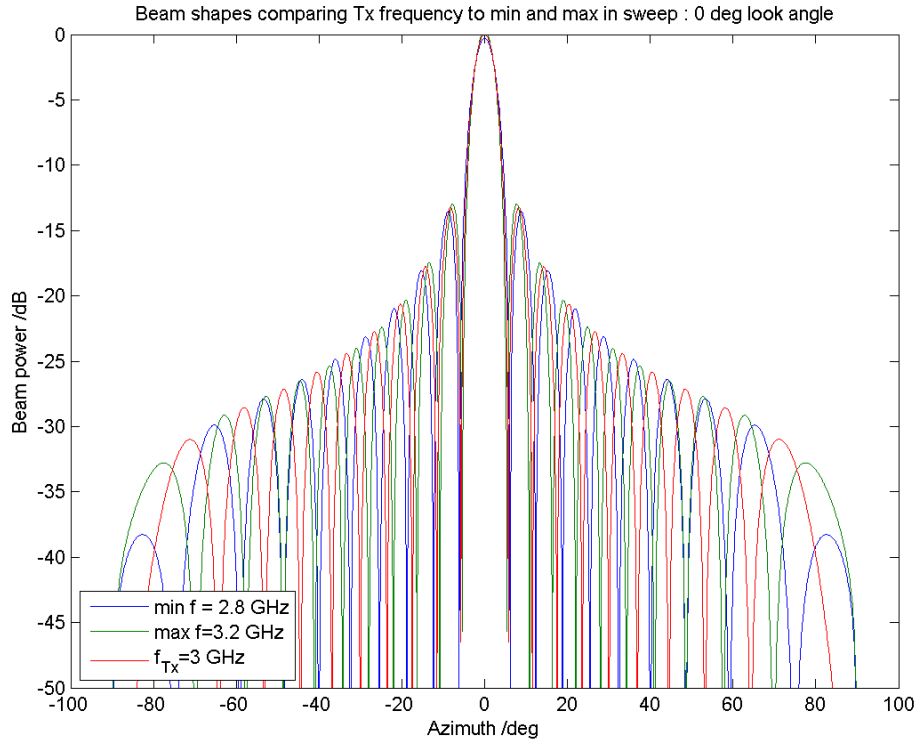


Figure 2.22: Beam power (including frequency proportional directivity) for a linear phased array computed as a function of azimuth.  $L = 0.948$  m,  $N = 20$ ,  $f_{Tx} = 3\text{GHz} \pm 200\text{MHz}$ . Phase shifters are set to give a look angle  $\phi = 0$ .

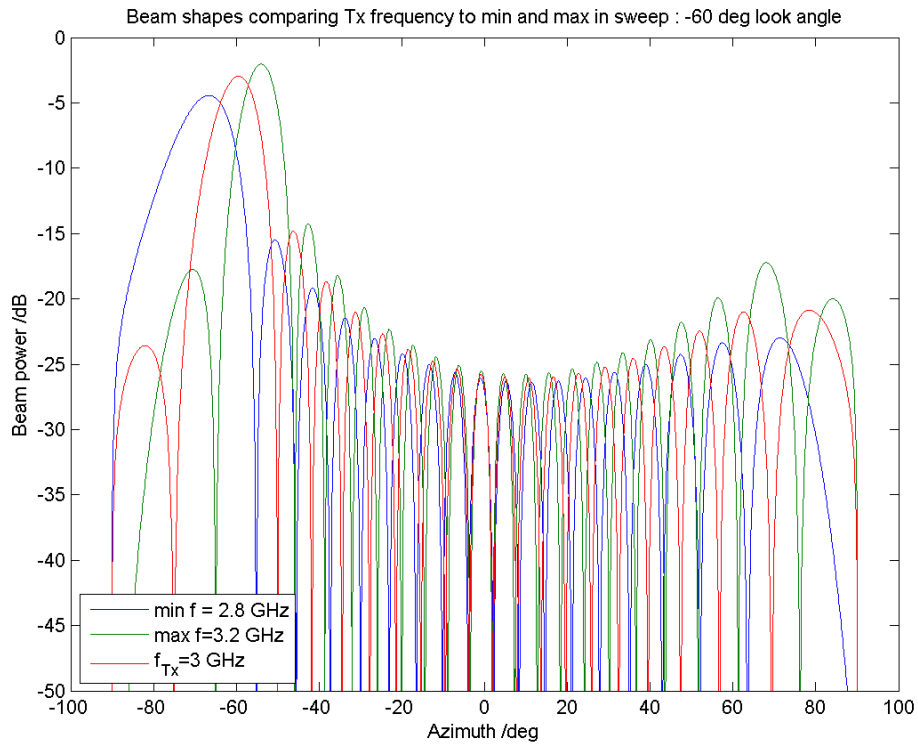


Figure 2.23: Beam power (including frequency proportional directivity) for a linear phased array computed as a function of azimuth.  $L = 0.948$  m,  $N = 20$ ,  $f_{Tx} = 3\text{GHz} \pm 200\text{MHz}$ . Phase shifters set to give a look angle of  $\phi = -60^\circ$ .

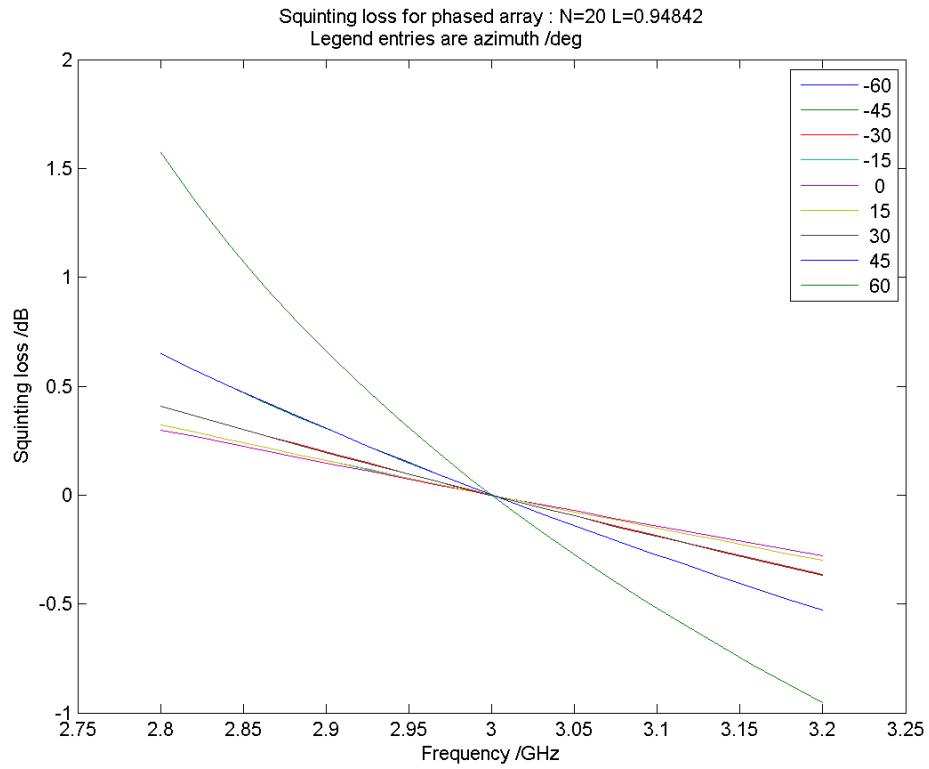


Figure 2.24: One way squinting loss (including frequency proportional directivity) computed as a function of frequency and initial look direction for a linear phased array  $L = 0.948$  m,  $N = 20$ ,  $f_{Tx} = 3\text{GHz} \pm 200\text{MHz}$ .

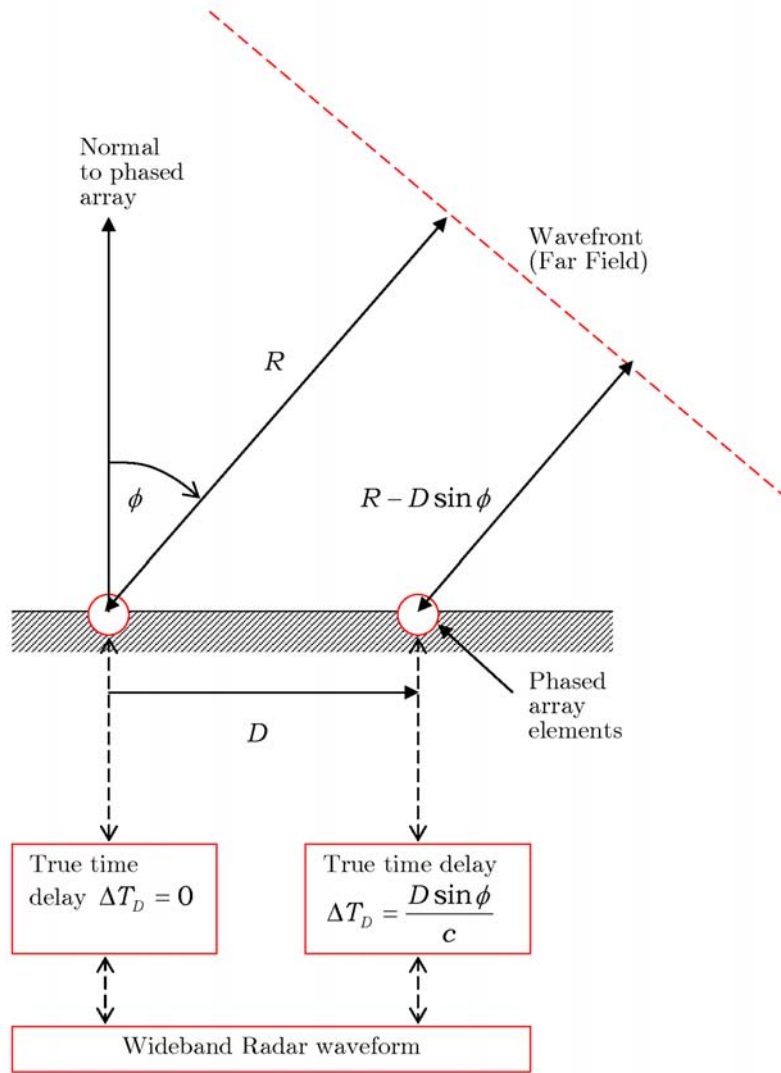


Figure 2.25: The time of flight difference between elements on a phased array and the wavefront is explicitly accounted for in a True Time Delay (TTD) system. In many non-TTD systems a phase shift is used instead. This is ambiguous by integer multiples of  $2\pi$  radians and subject to quantization errors whose size depend on the number of bits in the phase shifter. For example, a 12 bit device will have intervals of  $2\pi/4096$  radians.

### 2.7.4 Stretch processing - an alternative to stepped frequency

An alternative to stepped frequency methods is the use of stretch processing. Rather than sampling the (mixed down) signal directly, the mixer itself is modified to be a replica of what was transmitted. The differential time delay (and thus range) between scatterers relative to some central reference point on the body of a target can be shown to be proportional to a frequency modulation of the ‘stretch’ mixer output, if a linear frequency modulated waveform is used. If samples of this are taken and then processed using a Discrete Fourier Transform, the result will be a HRR profile of the target. In Appendix F the beat frequency (for target scattering center at range  $R_n$ ) of the output of the stretch mixer is shown to be

$$f_{sm} = \frac{2B(R_0 - R_n)}{c\tau} \quad (2.75)$$

where  $\tau$  is the transmitted pulse length and  $B$  is the pulse bandwidth. Let us define the HRR range window to be  $R_0 \pm \frac{1}{2}L$ . In order for peaks of the Fourier Transform of the stretch mixer output to appear correctly within this window; by the Shannon-Nyquist criterion, the output must be sampled at a rate greater than or equal to the frequency difference between the component beats. Hence:

$$f_s \geq \frac{2B(R_0 + \frac{1}{2}L)}{c\tau} - \frac{2B(R_0 - \frac{1}{2}L)}{c\tau} \quad (2.76)$$

$$\geq \frac{2BL}{c\tau} \quad (2.77)$$

Note also that the stretch mixer must sweep for  $2L/c + \tau$  in order to collect the signal contributions from all scatterers in the HRR window prior to the computation of the Fourier Transform of the mixer output samples. This means the mixer must be physically able to sweep through a bandwidth of

$$B_{sm} = \left(1 + \frac{2L}{c\tau}\right) B \quad (2.78)$$

In summary, stretch processing allows for the production of a HRR target profile without necessarily having to sample at the bandwidth of the transmitted signal, as in conventional pulse compression. It therefore allows for high range resolution to be obtained from a single burst rather than having to wait for the transmission of an ensemble of burst stepped in frequency. To achieve  $\delta R = 1\text{m}$  range resolution, the bandwidth  $B = 149.9\text{MHz}$ . If a maximum sample rate of  $5\text{MHz}$  is possible, since  $L \leq \frac{c\tau}{2B}f_s$  this means the HRR window must be less than  $100\text{m}$  using a chirp pulse length of  $20\mu\text{s}$ . Setting  $L = 100\text{ m}$  gives a mixer sweep of  $B_{sm} = 154.9\text{ MHz}$ . The outputs of the stretch mixer begin at time since transmission

$$t_{start} = \frac{2(R_0 - \frac{L}{2})}{c} \quad (2.79)$$

and finish at time

$$t_{stop} = \frac{2(R_0 + \frac{L}{2})}{c} + \tau \quad (2.80)$$

The potential limitations of stretch processing are:

1. Require modification to RF hardware to implement mixer. Mixer must be adaptive to changes in  $R_0$  which would vary as the target moves. The mixer must also be able to sweep over bandwidth  $(1 + \frac{2L}{c\tau}) B$ . The time variable in the mixer must be aligned with precision to that of the Radar clock which starts at the time of transmission; i.e. the mixer is phase locked to the transmitted signal.

2. Given a practical sample rate, to achieve finer range resolution will restrict the size  $L$  of the HRR window.
3. A separate mixer channel must be provided for each target, if separations are greater than  $L$ .
4. Since a stretch waveform is intrinsically wide bandwidth, an S-band phased array will sweep the beam significantly within the pulse. To alleviate this effect (and mitigate resulting losses of energy on target) true time delay corrections must be applied during pulse transmission and reception. This could be an expensive modification to the antenna



## Chapter 3

# NCTR experiments using MESAR2

### 3.1 Chapter summary

Four NCTR trials (on and off boresight static, Falcon&Pod and Targets of Opportunity) are described, including a detailed account of the waveforms used, leading to a statement of the extent of the trials data collected. This is supplemented by a tour of the software suite used to process the trials data. The journey of a target data recording is charted from the MESAR2 data logger, through signal processing and finally to the extraction of features and classification. The implementation of stepped-frequency HRR and Doppler processing is described in addition to other practical aspects such as calibration, data visualization and testing.

### 3.2 Trials rationale

A four stage trials programme (summarized in fig 3.1) was devised to test out whether NCTR waveforms could be successfully applied against aircraft, ultimately in an experimental context which is operationally realistic. This is assessed via analysis of HRR and Doppler profiles and overall classification performance. The following two chapters describe the latter. In order to help characterize processing artifacts, each stage of the trials programme represented a gradual evolution in target complexity and/or environmental context.

Trials began with single point target positioned on-boresight. This would serve as calibration reference for subsequent experiments and could be used as a check that the NCTR signal processing

	MESAR2 NCTR trials	Key tests
1	Static, on boresight	Point target calibration. Processing check. Fundamental test of stepped frequency method. Limitations of classical method.
2	Static, off boresight	Assess effect of electronic scanning of beam upon HRR profiles.
3	Moving point target trials	Test motion compensation algorithms. NCTR mode applied in a 'real' scenario, interleaved with the surveillance and tracking functions of MESAR2. Opportunity to collect profiles of a Falcon jet aircraft during the same trial. Test out feature extraction mechanisms.
4	Targets of opportunity	Collect data on a number of targets. Perform classification experiments. Investigate effect of long targets compared to classical HRR window size.

Figure 3.1: Description of the four trials using MESAR2 alluded to in this thesis.

was correctly implemented. A second set of experiments involved two dipoles spaced in range between 0 and 60m. The aim of this was to investigate whether the stepped frequency waveforms transmitted could be used to deliver a sub-metre range resolution and thus resolve the dipoles when this was not possible (at least for separations less than 30m) using the conventional pulse compressor output for each frequency stepped burst.<sup>1</sup> The longer separation dipoles (which *could* be resolved using conventional pulse compression) were used to probe the limitations of the Classical method (see section 2.2.4 above) and assess the potential benefits of the Hybrid technique described in section 2.3. The on-boresight experiment was repeated with the dipoles moved  $-45^\circ$  in azimuth off-boresight in order to assess the effect of electronic beam scanning upon the target profiles obtained using the stepped frequency methods.

The next logical progression was to illuminate a moving point target with the NCTR waveforms that had been proven upon static targets. In this case the NCTR mode would be cued from the surveillance and then target tracking functions of MESAR2 and therefore would also be an operational test of the NCTR mode in conjunction with the other functions of MESAR2. The moving point target would test the motion compensation algorithms as well as providing further confirmation of the results of the static trials. Since the practical mechanism for flying a point target was decided to be a repeater pod mounted upon a trials aircraft, the moving point target experiment also yielded a large number of recordings of a (small) jet aircraft, a Dassault Falcon. The signature of this was compared to the point target and an initial assessment made of target features (such as length, maximum Radar cross section). This experiment also investigated whether NCTR waveforms could be automatically delivered upon multiple targets, which is not often possible for conventional tracking radars.

Finally, a series of ‘Targets of Opportunity’ were illuminated using the NCTR mode. This was done automatically by MESAR2, although targets of interest were manually chosen (and later extracted from the data logger). The experiment was conducted by operators at MESAR2 and at the National Air Traffic Service (NATS) at Swanwick working jointly to record track numbers and corresponding identities of aircraft. These experiments would build upon the previous trials and serve as a data set to enable classification experiments to be performed. It was hoped this data set would additionally yield (i) evidence of Jet Engine Modulation and (ii) signatures of aircraft with range-projected length in excess of the classical range window set by the waveform frequency step. Processing of the latter would be a further test of the ‘Hybrid’ method, as well as comparing the performance of different stepped frequency waveforms; i.e. a 3.2MHz frequency step and 0.8MHz frequency step.

---

<sup>1</sup>The bandwidth of individual waveforms employed in NCTR modes was in all cases  $\approx 5\text{MHz}$ , yielding a resolution of 30m.

Waveform	Parameters	Notes
"A" (wfc2 3.2MHz)	$f_{PRF}=2.5\text{kHz}$ , $P=8$ , $Q=128$ , $K=152$ , $\Delta f=3.2\text{MHz}$ , $B=-4.5\text{MHz}$ , $\tau=25.6\mu\text{s}$ , $f_{Tx}(q=1)=2724.2\text{MHz}$	'Hybrid' waveform. Linear chirps with a stepped-frequency carrier such that the central $\Delta f$ portion of the waveform spectrum forms a continuum when the spectra are 'stitched' together.
"B" (wfc3 0.8MHz)	$f_{PRF}=2.5\text{kHz}$ , $P=8$ , $Q=128$ , $K=174$ , $\Delta f=0.8\text{MHz}$ , $B\approx 5\text{MHz}$ , $\tau=20\mu\text{s}$ , $f_{Tx}(q=1)=2953\text{MHz}$	Original 'Classical' NCTR waveform using a non-linear chirp to give lower range sidelobes. ( $\approx 5\text{MHz}$ in linear region). A smaller frequency step is used to extend the Classical HRR window.
"C" (wfc3 3.2MHz)	$f_{PRF}=2.5\text{kHz}$ , $P=8$ , $Q=128$ , $K=174$ , $\Delta f=3.2\text{MHz}$ , $B\approx 5\text{MHz}$ , $\tau=20\mu\text{s}$ , $f_{Tx}(q=1)=2724.2\text{MHz}$	Other original 'Classical' NCTR waveform using a non-linear chirp to give lower range sidelobes. ( $\approx 5\text{MHz}$ in linear region).
"D" (wfc3 0MHz)	$f_{PRF}=2.5\text{kHz}$ , $P=32$ , $Q=32$ , $K=174$ , $\Delta f=0\text{MHz}$ , $B\approx 5\text{MHz}$ , $\tau=20\mu\text{s}$ , $f_{Tx}(q=1)=2999.4\text{MHz}$	32 pulse per burst, single frequency waveform, but otherwise the same as waveforms B & C. This is used to give improved Doppler resolution.
"E" (wfc2 3.2MHz)	$f_{PRF}=2.5\text{kHz}$ , $P=32$ , $Q=32$ , $K=152$ , $\Delta f=3.2\text{MHz}$ , $B=-4.5\text{MHz}$ , $\tau=25.6\mu\text{s}$ , $f_{Tx}(q=1)=2708.2\text{MHz}$	32 pulse per burst, 32 frequency step version of waveform A.

Figure 3.2: Description of the five NCTR waveforms transmitted by MESAR2

### 3.3 Waveforms

During the trials programme, five different NCTR waveforms were used. These are described in fig 3.2.

MESAR2 NCTR experiments	Waveforms
On & Off boresight static trials	A
Pod & Falcon aircraft trials	A,B,C,D
Targets of Opportunity trials	A,B,C,E

Four different NCTR waveforms were used in each of the aircraft trials. They were added to the MESAR2 scheduler like any other activity (such as surveillance and tracking looks) so one would not expect an exact cycle of A,B,C.. as illustrated in fig 2.20. The 'Hybrid' waveform used in the static trials (Waveform A) was used in addition to three waveforms used in previous NCTR experiments with MESAR2. Waveform B was designed to yield a wide (Classical) range window (187m) by virtue of the 0.8MHz frequency step. Compared to waveforms A (and C) resolution is traded to achieve this extra window size.

Waveform	Resolution $\frac{c}{2Q\Delta f}$ /m
A	0.37
B	1.46
C	0.37
D	1.46

Waveforms B, C & D employ non-linear chirps (see fig 3.3) rather than the linear chirps used in waveforms A & E. This is to achieve a lower sidelobe level following pulse compression. [88]. However, this does not allow for the spectral-stitching required of the Hybrid method, hence Hybrid processing is restricted to waveforms A & E. All waveforms were Classically processed. Waveform C ( $\Delta f = 3.2\text{MHz}$ ) was the forerunner of Waveform A, prior to the requirement to enable Hybrid processing. Waveform D was initially designed as a Doppler waveform. The higher number of pulses (32) was chosen to give a four-fold increase in spectral resolution compared to the 8 pulse bursts used in waveforms A,B & C. It was initially planned that each of the 32 burst should be stepped in frequency, hence the resulting High Range Resolution range-Doppler profile (see fig 3.4) could present target length and Doppler information in a single image. Unfortunately this was not implemented prior to the trial and the end result was all 32 burst being at the same frequency. In the targets of opportunity trial (see below), this waveform was changed to the linear chirp waveform (E) to enable Hybrid processing but with 32 frequency steps of 3.2MHz and 32 pulses per burst. For pure Doppler processing Waveforms D and E are equivalent, which enables the Pod & Falcon and Targets of Opportunity Doppler results to be directly compared. (See Chapter 5). For each look (of 1024 pulses), a PRF of 2.5kHz was used.

### 3.4 Overall extent of data

A total of 1498 NCTR looks using five stepped frequency waveforms (A,B,C,D & E) were recorded relating to 17 distinct aircraft. Many targets were captured in multiple (radially inbound) runs.<sup>2</sup> During processing of the trials data (which amounts to an archive size of 56.8GB including processed .mat files, M2DATS output ASCII text files and original DRAS files) the pulse compressor power is used to assess whether the data is ‘good’ or not. (See section 3.5.2). Overall 83% of data was deemed to be ‘good’ based on a peak to median pulse compressor power ratio of 30dB or higher.

Fig 3.5 describes the distribution of recordings amongst targets and waveforms. Note that the number of outbound and inbound looks is somewhat comparable to the number of ‘crossing looks’ for the targets of opportunity recordings. Typically this reduces the number of looks per aircraft to between 10 and 40 per waveform. This is an order of magnitude less than the number of signatures used in classification analysis by Zywek & Bognor [118] and therefore one must make our conclusions with an appropriate degree of uncertainty. However, one might argue that a more modest number of looks (prior to the need for some form of classification) is more relevant in an operational context. In this thesis we shall focus upon the inbound data for the purposes of understanding classification performance relating to length and Doppler feature measurements, since this represents the best case for obvious signatures, and then contrast this with outbound data.

The trials data can be re-processed and classification analysis completed using the automated tools described in the following section in approximately five hours using a PC laptop<sup>3</sup>. This requires user

<sup>2</sup>The Falcon aircraft was captured in seven inbound runs, a total of 243 looks.

<sup>3</sup>3GHz Pentium 4 with 1GB RAM, accessing data from a 250GB 7200 RPM external USB2 hard-drive

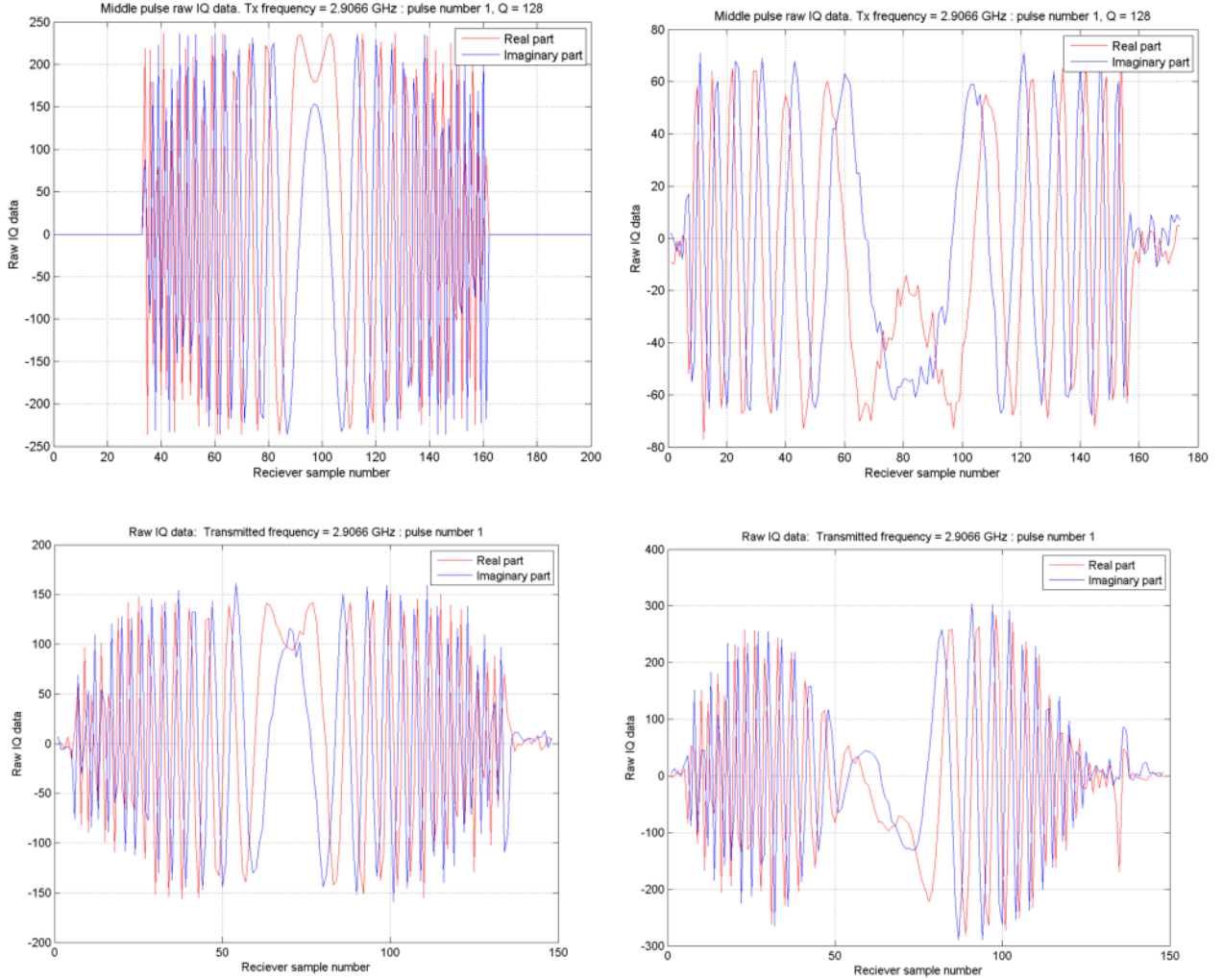


Figure 3.3: Phase (real) & Quadrature (imaginary) parts of the transmitted waveforms deployed in the MESAR2 trials. The upper plots illustrate the difference between the -4.5MHz,  $25.6\mu\text{s}$  linear chirp (wfc2, model generated) and the 5MHz,  $20\mu\text{s}$  non-linear chirp (wfc3, from Pod) waveforms. The bottom left plot is the wfc2 result from the single dipole reference target. The bottom right plot is the wfc2 result for two dipoles separated by 58m in range. The interference between the two reflections is clearly manifested in the distorted receiver  $I, Q$  values. In all cases, a sample rate of 5MHz was used.

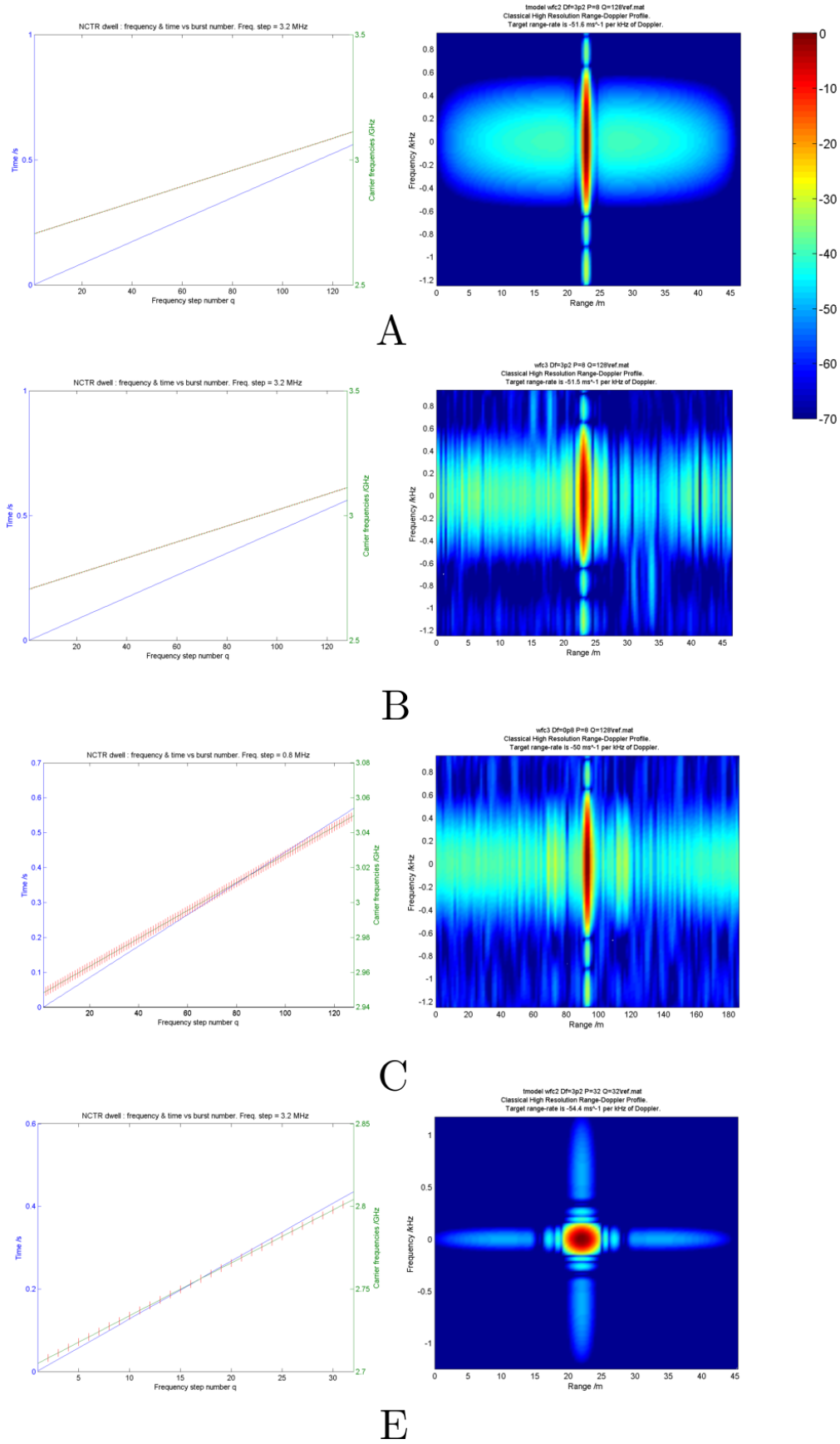


Figure 3.4: Variation of carrier frequency and duration of the stepped frequency waveforms A,B,C & E is shown against the corresponding (Classical) High Range Resolution Range-Doppler profiles obtained using static point target references. Waveforms A,B,C offer cruder resolution in Doppler (on account of the broad sidelobes) than Waveform E because the latter has 32 pulses per burst compared to 8 for the former three. A pulse repetition frequency of 2.5kHz is used in all examples. Note: In the frequency vs frequency step plots, the vertical red bars represent the bandwidth of the waveforms transmitted and hence illustrate the overlap in frequency between steps for waveforms A & E.

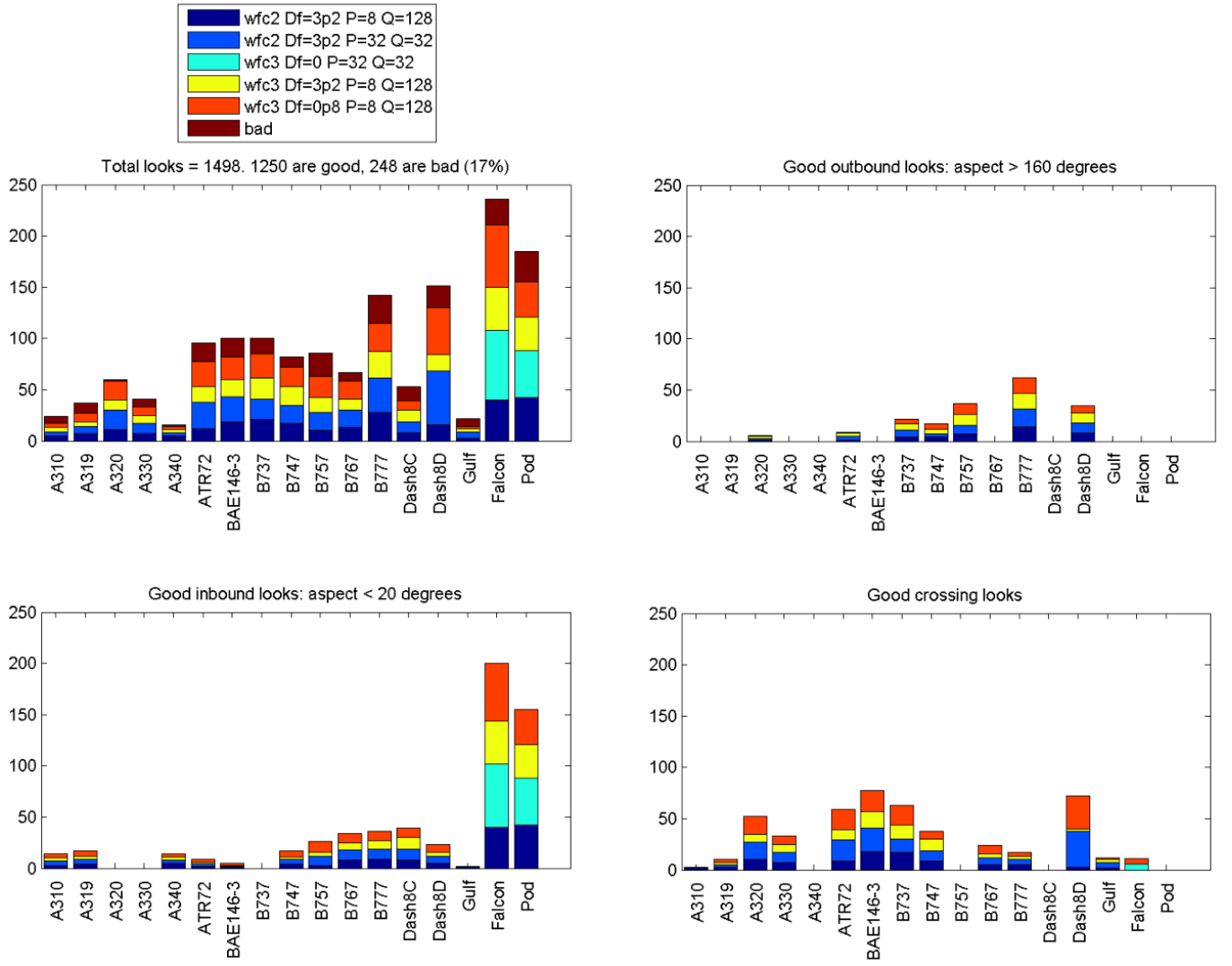


Figure 3.5: Extent of NCTR looks scheduled upon aircraft via MESAR2 during the trials described in this thesis. Data was deemed to be ‘good’ based on a peak to median pulse compressor power ratio of 30dB or higher. Histograms are colour coded by waveform (and ‘bad’ looks) and further subdivided into inbound, outbound and crossing via aircraft aspect angle. Inbound corresponds to an aspect  $\leq 20^\circ$  and outbound  $\geq 160^\circ$ .

intervention for the first ten minutes and then for another ten, forty five minutes before the end, to set the classification settings. The time taken to extract data from the MESAR2 data logger, filter in DRAS<sup>4</sup>, convert to ASCII using M2DATS and then import into MATLAB compatible files was considerable (estimate several weeks full time). Given the difference in effort to access data at various stages of post-processing and the relative abundance of storage capacity, it was decided to retain copies of the data at the DRAS, ASCII, MATLAB imported and MATLAB processed stages. Although the same information is effectively stored four times, the speed of access and the ability to implement changes in final processing vastly outweighed the cost of data duplication.

<sup>4</sup>See following section for a description of the NCTR processing.

### 3.5 NCTR signal processing

#### 3.5.1 Flow diagram of analysis methodology

MESAR2 was designed as an experimental system and was equipped with a mass storage data logging facility. A trials record could be fully captured consisting of:

- Screenshots of the display (as in fig 3.21)
- Recordings of all plot and track messages (via the CADS system)
- $I, Q$  data direct from the output of the analogue to digital converter + all associated system parameters associated with a particular look.

In the experiments described in this thesis, receiver samples<sup>5</sup> were captured for each pulse repetition interval (PRI) for every look issued by MESAR2 upon a target being tracked.<sup>6</sup> Data was actually captured at the sub-array level for sum, difference and sidelobe-blanking receive beams. As described in Appendix H and in fig 3.6, recordings were extracted from the data logger using the Roke Manor DRAS software and then converted into ASCII files (one per look) using a Visual Basic tool called M2DATS<sup>7</sup>. From this point onwards data is manipulated using the MATLAB environment, using a series of bespoke tools devised by the author which enable automated:

- Formation of low resolution range profiles via pulse compression
- Formation of High Range Resolution profiles using Classical (and where possible) Hybrid stepped frequency methods
- Formation of Doppler spectra and range-Doppler profiles
- Extraction of length, scattering centres and Doppler spectrum features
- Assembly of range, Doppler and kinematic profiles into a set of target data sheets for each aircraft
- Classification analysis

This process is illustrated in fig 3.6. In addition to the target data sheet and classification statistic outputs, data viewing tools have been constructed to display the output of the signal processing stage; i.e. load data files (representing individual looks) that have yet to be combined for feature extraction and classification analysis. `cvview` (figs 3.8, 3.9) and `tsee` (fig 3.7) have proved to be important diagnostic tools as well as a convenient means of generating illustrations.<sup>8</sup>

<sup>5</sup>The In-Phase and Quadrature signal samples following mix down, analogue to digital conversion and beamforming.

<sup>6</sup>Surveillance activities such as Normal radar, MTI and MTD looks could also be captured in the same way, but these are not discussed in this thesis.

<sup>7</sup>Written by Graham Biggs, formerly of BAE Systems Integrated System Technologies.

<sup>8</sup>In the target Doppler spectrum display of `tsee.m` one can see JEM lines if (a) the target possesses unshielded rotating reflectors which will give rise to JEM and (b) the number of pulses per burst and PRF are both high enough to resolve JEM lines from the Doppler filter sidelobes. To assist in the automatic capture of target features a JEM line estimation function `tjem.m` is used by `tsee.m`. The lines highlighted (in black) can be seen in figure 3.28 This operates by sequentially subdividing the Doppler spectrum in to finer and finer bins. For each binary division, the Doppler frequencies of the maximum signal values are recorded. In a method similar to track initiation and update algorithms [95], new JEM lines are only initiated if these peaks exceed a minimum frequency difference from already established peaks. The minimum distance is set to be twice the Doppler resolution of the filter, that is  $2f_{PRF}/P$ . Note the actual Doppler spectrum is interpolated to have distinct spectral samples of number greater than  $P$  (typically 100) so the position of each JEM line can be estimated to a greater precision than  $f_{PRF}/P$ . Finally, only JEM lines which correspond to peaks which exceed a defined threshold in dB below the skin return are returned by the function.



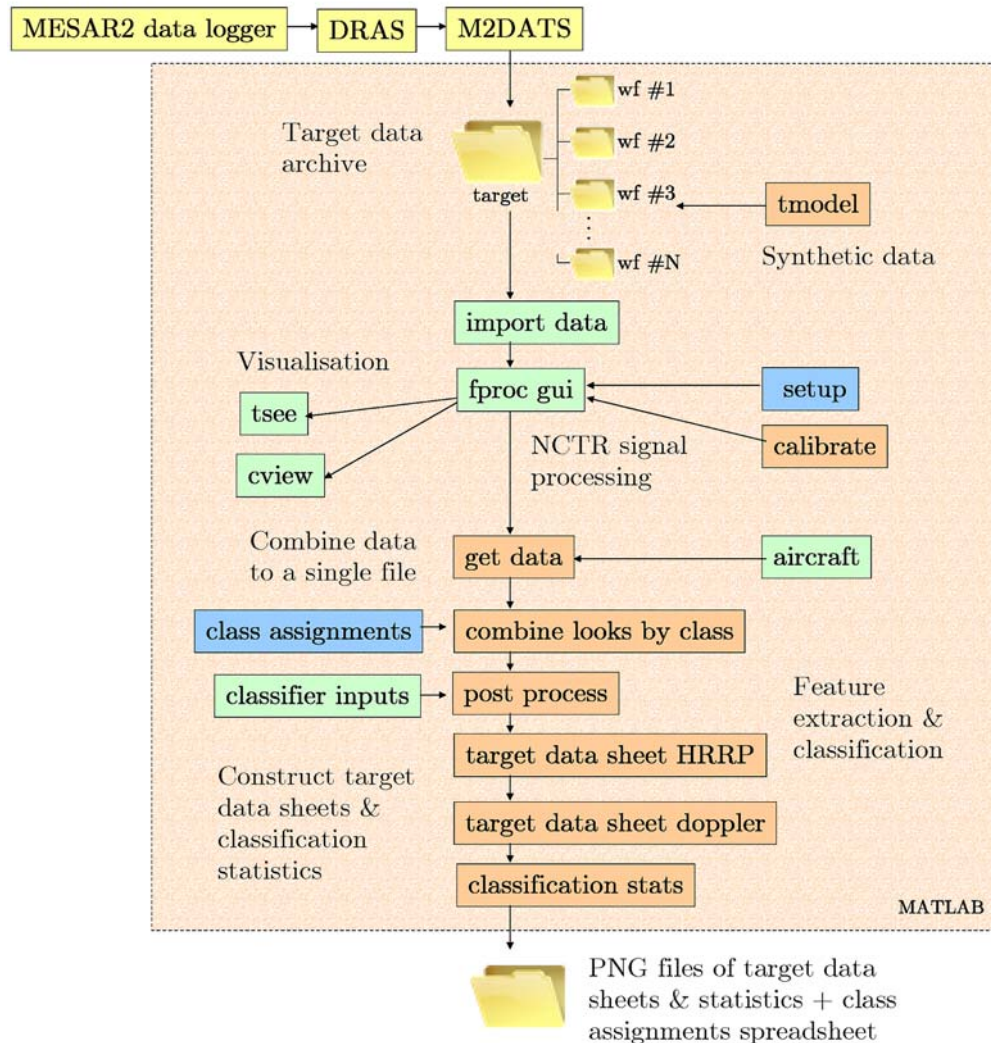


Figure 3.6: Diagram describing the processing chain which begins with data stored on the MESAR2 data logger and ends with a series of target data sheets containing montages of Range and Doppler profiles of aircraft alongside relevant kinematic parameters. Feature data from a defined subset of trials data (e.g. six aircraft, as in this thesis) are then used to feed a classifier, whose outputs are recorded and plotted graphically as colour coded confusion matrices. **tsee** and **cview** allow for individual looks to be analysed visually. **tmodel** allows for synthetic data to be generated as an alternative to experimental data. All methods within the apricot coloured box have been written by the author in the MATLAB environment. Green boxes denote the use of graphical user interfaces. Blue boxes denote setup files, which are constructed using Microsoft Excel.

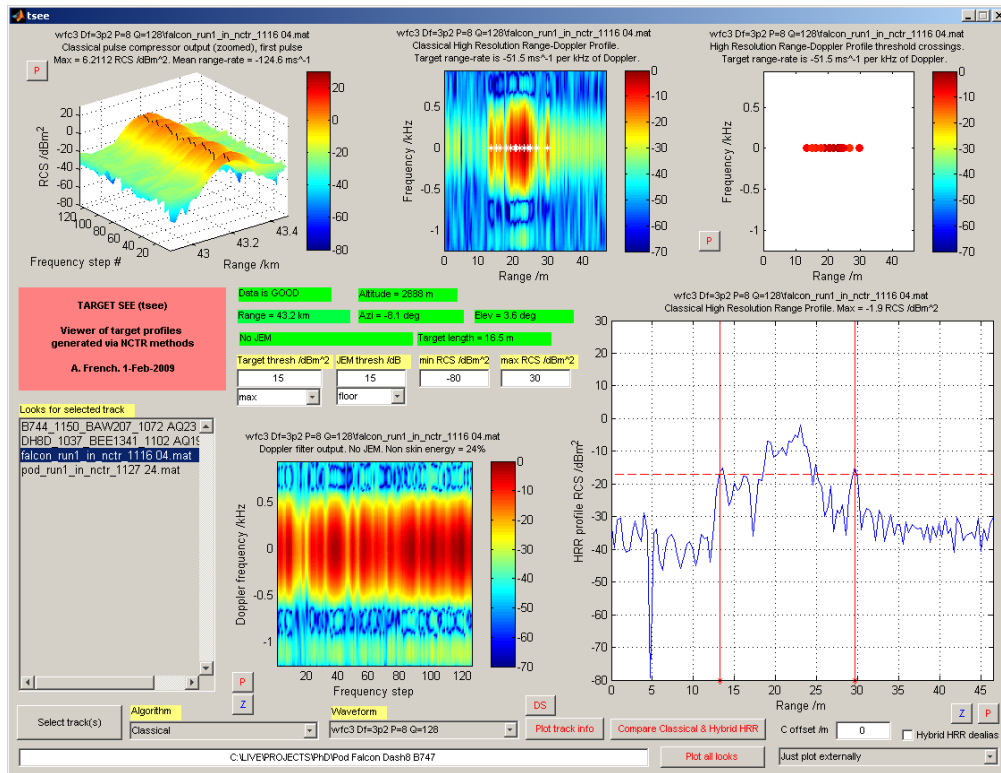


Figure 3.7: Screen capture of the visualisation software **tsee** ('Target See') implemented in MATLAB. The data displayed are processed recordings of the returns from a Falcon aircraft.

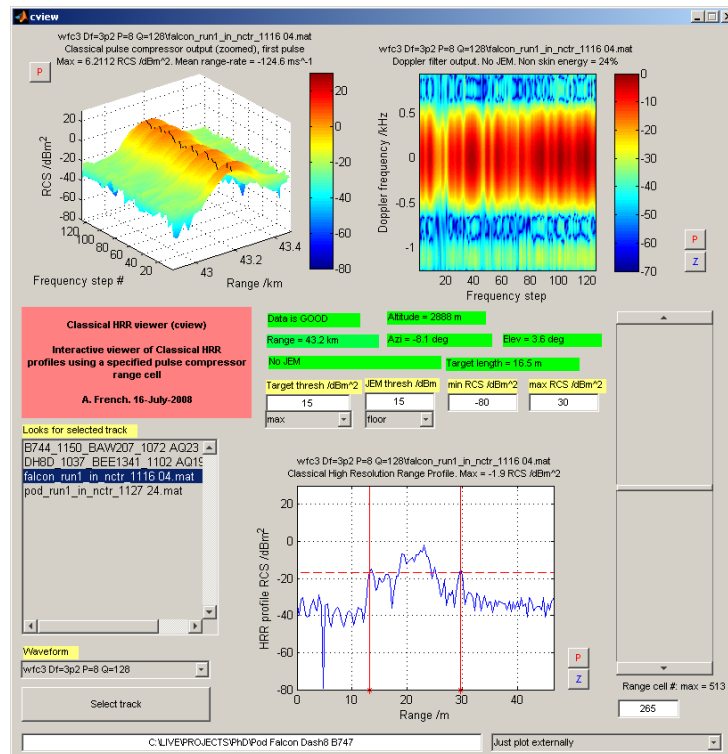


Figure 3.8: Alternative look data viewing tool to **tsee**. **cview** "Classical Viewer" includes the algorithms for Classical HRR processing and allows the user to dynamically change the range of the pulse compressor output that the 'target samples' are taken from.

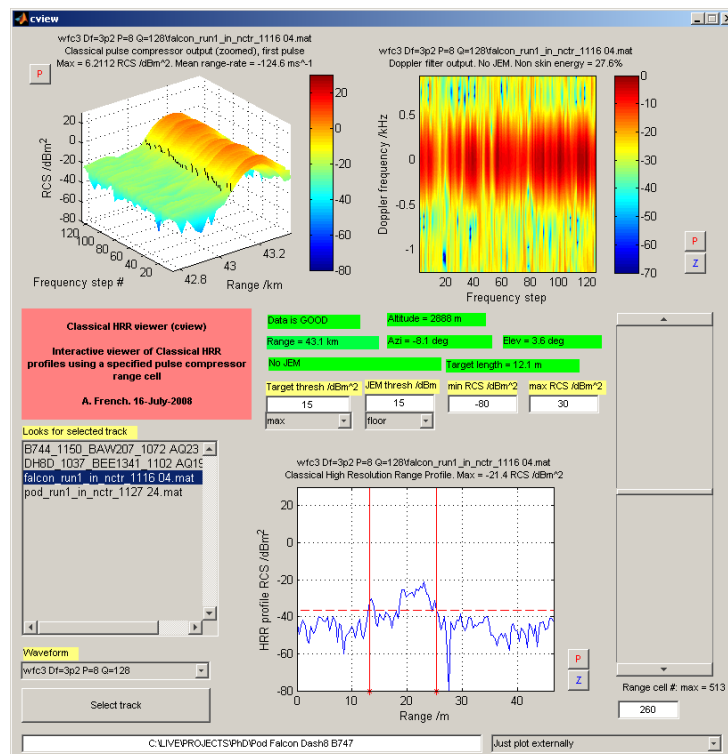


Figure 3.9: This this figure, target samples are taken 5 range cells (150m) away from the main peak, resulting in 20dB degradation of the Falcon range profile. This is exemplific of one of the flaws of the Classical method: if a target has structure on the pulse compressor scale, scatters away from the peak will contribute to the resulting HRR with a lower signal to noise ratio.

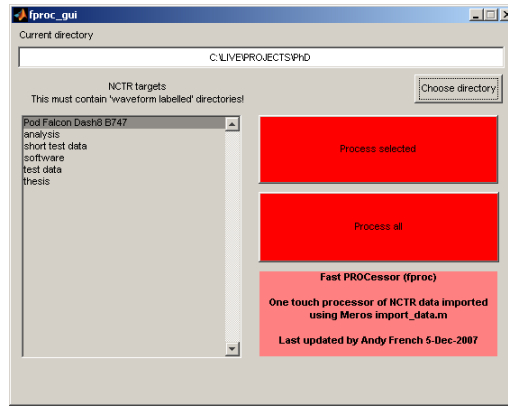


Figure 3.10: Graphical user interface to MATLAB code `fproc`, which converts  $I, Q$  receiver samples to Classical & Hybrid High Range Resolution profiles. `fproc` can be applied to any number of files with a single button click since it is designed to operate on a defined directory structure labelled by (defined) waveforms. Once general settings are applied a large data set can be processed without further intervention. This is useful in the context of this research, where the 58GB trials data set takes about four hours to process. The effect of signal processing settings (upon HRRP quality, and ultimately classification performance) can be practically investigated using overnight batch processing runs.

### 3.5.2 NCTR signal processing

The NCTR signal processing chain has been encoded as a MATLAB function `fproc` and is applied via a graphical user interface which enables batch processing of data of arbitrary size, so long as the data is firstly deposited in a defined directory structure which matches the names of waveforms that appear in a setup document written using Microsoft Excel. Processed data are stored in a structured array `processed_data`, which is appended to the same MATLAB `.mat` file created upon conversion from ASCII to the MATLAB domain.<sup>9</sup> Each time `process_data_gui` or `fproc_gui` updates a file, the `imported_data` part is left untouched. Although this increases the file size by retaining earlier steps in the processing mechanism, it means signal processing modifications can be tried out on the same files without worry of overwriting the source data. `fproc_gui` is, as the name suggest, an interface to `fproc`. The key stages of NCTR signal processing are illustrated in figures 3.10, 3.11 & 3.12 and can be summarized as the following:

#### INITIAL PROCESSING

1. **Pulse compression.** The three dimensional array of complex receiver samples (rows being pulses, columns being frequency steps and pages being receiver samples for a given pulse) are cross correlated in the page ( $3^{\text{rd}}$ ) dimension with the corresponding receiver samples of the calibration measurement for the waveform. In the case of waveform A, the calibration target was the static single dipole positioned on-boresight. By the convolution (and Wiener-Khinchine) theorems [112] this can be efficiently implemented as a multiplication in the frequency domain of the Discrete Fourier Transform (DFT) of the receiver samples and the DFT of the conjugate of the calibration reference, followed by an inverse DFT to convert back to the time (or range) domain.

<sup>9</sup>Currently, conversion from ASCII to MATLAB is a slow process, up to a minute per look. Once in the MATLAB domain, signal processing can be completed in a matter of seconds. In `cview`, the Classical processing stage can be achieved in near real time.

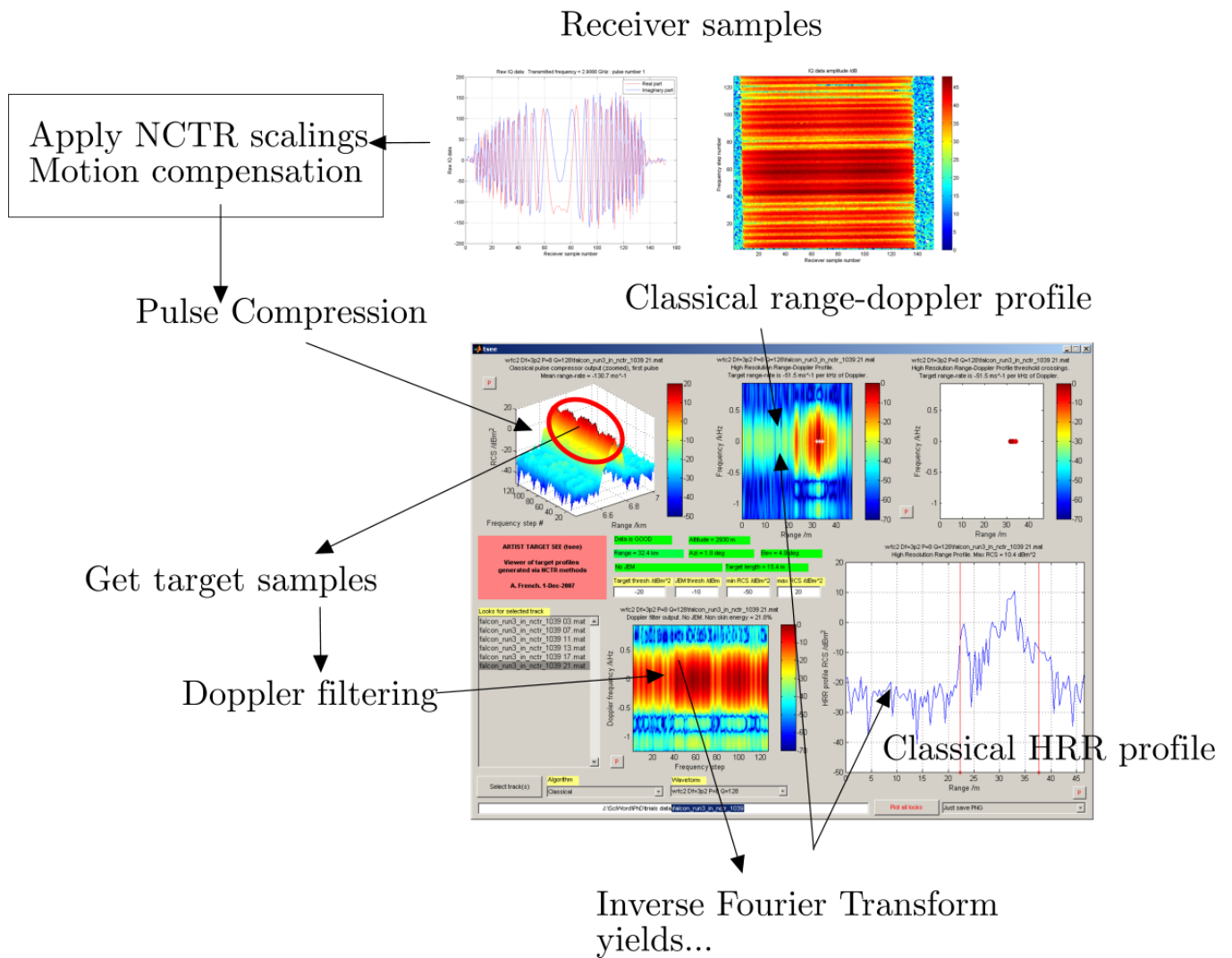


Figure 3.11: The (Classical) NCTR signal processing applied in **fproc** is described pictorially using recording taken from a Falcon jet aircraft. The waveform is A.

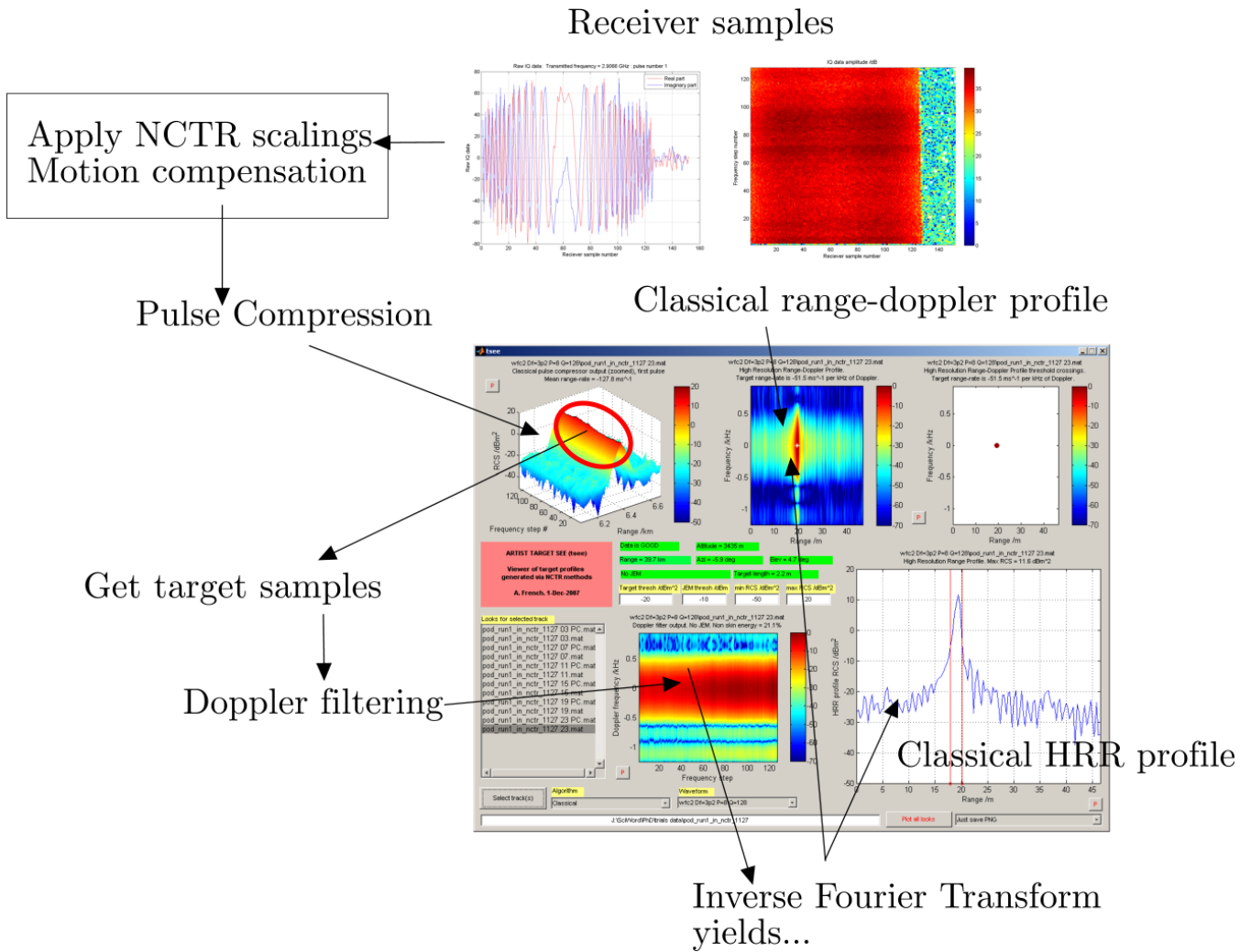


Figure 3.12: The (Classical) NCTR signal processing applied in `fproc` is described pictorially using example data taken from a ‘pod’ moving point target. The waveform is A.

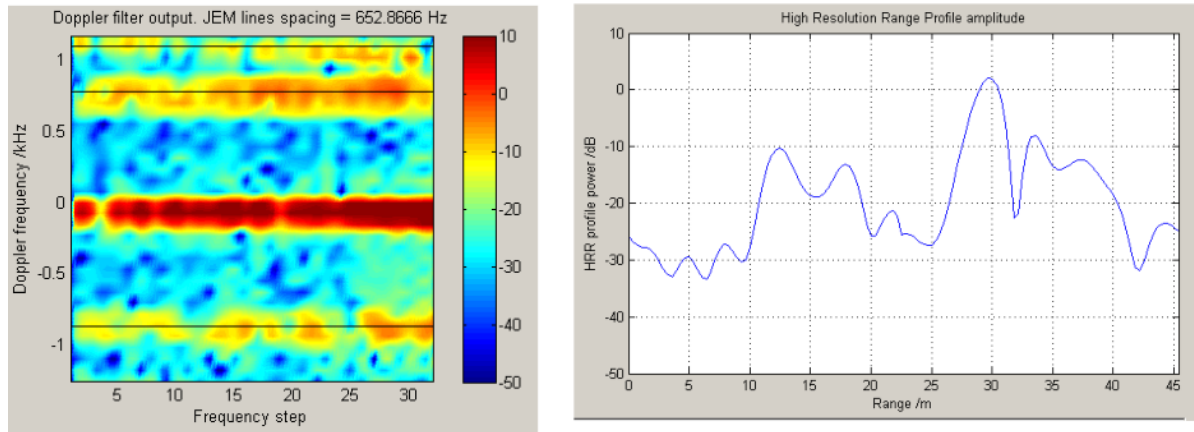


2. **Apply NCTR scalings.** The pulse compressed receiver samples are then divided by the amplitude and phase corresponding to the (burst averaged) complex samples corresponding to the peak of the pulse compressed calibration reference. This division corresponds to a complex sample for each frequency step. These NCTR scalings are computed in advance from the calibration reference (using automated calibration software written as part of `fproc`) and are normalized to prevent excessive signal size change, i.e. the mean scaling amplitude is unity. Additionally, the scalings are modified by a unit magnitude phase factor which corrects for the difference in phase between the start range of the target and the range of the calibration reference.
3. **Estimate range rate.** In most cases the MESAR2 tracker provides a good estimate of the target range rate to an accuracy of a few  $\text{ms}^{-1}$ . However, occasionally this estimate is not sufficiently correct to yield a focussed range profile. (See fig 3.13). To perform a fine correction, the pulse compressor outputs are firstly put through motion compensation, ‘get target sample’ and Doppler filtering stages. The Doppler filter output is averaged over frequency steps and the peak frequency determined via interpolation in the region  $\left[-\frac{2f_{PRF}}{P}, \frac{2f_{PRF}}{P}\right]$ . This restricted region is to avoid contamination from JEM which may be present. The peak is assumed to correspond to the skin return and therefore the Doppler frequency of the peak can be used to determine a range rate correction  $\Delta v \approx \frac{-c\Delta f}{2f_{Tx}}$  where  $\Delta f$  is the Doppler shift of the skin return. This method only works well when the tracker range rate is near to the correct result. Practically, if the velocity deviation exceeds the magnitude  $\frac{cf_{PRF}}{2Pf_{Tx}}$  then the corrective mechanism will not work.<sup>10</sup> This corrective mechanism can be applied iteratively. The Hybrid method aliasing effects appear to be somewhat sensitive to errors in range rate<sup>11</sup>. It was found that modifying the number of iterations from one to five significantly reduced the aliasing effects. In contrast, the Classical result was more robust, only requiring a single iteration. In `fproc`, additional options allow for data with corrupted tracker range rate to be processed. In this case the peak positions of the pulse compressor output are used to estimate the range rate using (respectively) curve fitting and regression of the peak ranges. Provision is made to estimate the target acceleration in range as well as range rate to allow the software to cope with non uniform motion. Although this modification was made in anticipation of ballistic targets, experiments by Neil Campbell (2005) using data with known, constant range rate seemed to suggest that (incorrect) small estimated accelerations can have drastic effects upon the resulting range profile. Hence it was recommended to apply the linear approach described above rather than attempt to guess an acceleration via polynomial curve fitting.
4. **Apply motion compensation.** The best estimate of target range rate is used to remove (i) the additional phase to the targets between pulses and (ii) the shift in (fractional) range cells of the target samples between pulses. (i) is achieved via a complex multiplication of  $\exp\left(\frac{4\pi if_{Tx}}{c}t_{pq}\dot{R}\right)$  where  $t_{pq}$  the time of pulse  $p$  of  $P$  and frequency step  $q$  of  $Q$  since the start of the look. (ii) is achieved by application of the Fourier shift theorem [112]; i.e. multiplying the DFT of receiver samples by a phase ramp corresponding to the target range shift  $\frac{1}{2}t_{pq}\dot{R}$ , then converting back to the time (range) domain, results in ‘range walk’ correction that is not limited to whole range cells.

<sup>10</sup>For a carrier frequency of 3GHz,  $f_{PRF}$  of 2.5kHz and  $P = 8$  this is of the order of  $16 \text{ ms}^{-1}$ .

<sup>11</sup>Experiments conducted by the author seem to indicate  $> 1\text{ms}^{-1}$  motion compensation errors may result in significant aliasing which can cause erroneous length measurements from the Hybrid HRR profiles.

## After Doppler correction



## Before Doppler correction

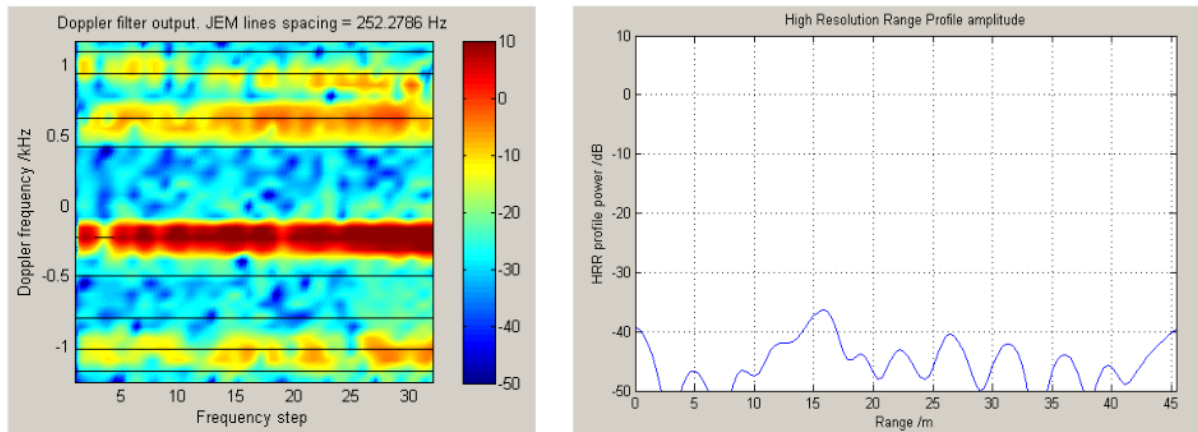


Figure 3.13: For certain looks the range-rate supplied from the tracker is insufficient to correctly account for bulk target motion. The lower profile shows the Doppler filter output and Classical HRR profile using a 32 pulse and 32 frequency step Waveform E. Since the skin return is offset from 0Hz, the resulting HRR profile is significantly degraded. The range rate correction is determined using this Doppler offset. The upper figure demonstrates the application of this method, resulting in a much improved range profile.



## CLASSICAL HRR PROCESSING

5. **Get target samples.** The range cell is determined which corresponds to the maximum (motion compensated) pulse compressor output power. The maximum is taken over all pulses, frequency steps and receiver samples to account for the possibility of interference effects between multiple scatterers which may result in a null at a particular frequency step. For each pulse and frequency step a complex number is taken from the vector of receiver samples at this particular range cell.<sup>12</sup>
6. **Apply Doppler filter.** The  $P \times Q$  matrix of complex samples is passed through a  $P$  pulse Doppler filter, with outputs at Doppler frequencies from  $-\frac{1}{2}f_{PRF}$  to  $\frac{1}{2}f_{PRF}$  spaced by  $\frac{f_{PRF}}{P}$ . This is mathematically implemented as a Discrete Fourier Transform preceded by multiplication by a low sidelobe (40dB) Dolph-Chebyshev windowing function.
7. **Apply weighted inverse Fourier Transform to form Classical HRR profile.** The  $Q$  complex samples corresponding to the zero Doppler output of the filter are weighted by a 40dB Dolph-Chebyshev weighting function and inserted into an inverse DFT. The magnitude of this result is the Classical HRR profile. Filter outputs away from 0Hz can be processed in an identical fashion to form a HRR range-Doppler profile.
8. **Interpolation.** `fproc` interpolates in range and Doppler dimensions (in magnitude and phase) to yield profiles that clearly show up sidelobe features that could otherwise be confused with genuine target signatures. For the trials data processed, 128 range and Doppler values were chosen for all waveforms.
9. **Determine whether data is ‘good’.** Data is deemed corrupted if the conventional pulse compression process does not yield distinct peak(s). Average peak to noise floor ratios (in dB) are computed and compared to a set threshold. (30dB for the trials data processed). If the threshold is not exceeded then data is deemed corrupt. The noise floor is defined as the median pulse compressor signal power, averaged over pulses within each burst. The average peak to noise floor ratio is computed jointly as the mean of the ratios computed for each frequency step, and the ratio of the mean target sample values and the mean noise floor values (which are averaged over all frequency steps). When both means exceed the threshold, the data is deemed ‘good.’ The peak values are taken to be the complex samples used for Classical HRR processing (i.e. a single sample for each frequency step). Goodness of data is indicated by a binary flag appended to the processed data file.

---

<sup>12</sup>In `fproc` there is the potential to apply a non-linear (Lorentzian) curve fitting algorithm to determine the fractional range cells corresponding to the peak, then use spline interpolation in magnitude and phase to yield the peak samples. However, very little refinement to the resulting HRR profiles has been observed as a result of this extra effort!

## HYBRID HRR PROCESSING

10. **Pad receiver samples.** The bandwidth segment  $\Delta f$  corresponding to the  $N_{stitch}$  samples extracted from the central portion of Discrete Fourier Transform of the (motion compensated and NCTR scaled) receiver samples must form a continuous (linear) progression; otherwise the Hybrid range profile shall suffer aliasing resulting from periodic discontinuities in the frequency domain. To achieve this the number of receiver samples  $K$  must satisfy the following conditions:

$$\begin{aligned} N_{stitch} &= \frac{K\Delta f}{f_s} \in \mathbb{Z}^{\pm} \\ N_{overlap} &= \frac{1}{2}(K - N_{stitch}) \in \mathbb{Z}^{\pm} \end{aligned} \quad (3.1)$$

where  $N_{stitch} + 2N_{overlap} = K$  and  $\mathbb{Z}^{\pm}$  represents the set of positive integers. In **fproc** these criteria are met in the general case of a non-compliant<sup>13</sup>  $K$  by padding the receiver samples with  $m$  zeros until  $K \rightarrow K + m$  satisfies the above criteria.

11. **Spectral stitching and scaling.** As alluded to in the previous step, the receiver samples are firstly transformed to the frequency domain. The central  $N_{stitch} = \frac{K\Delta f}{f_s}$  samples are then extracted and added to the correct slot in an array of length  $QN_{stitch}$  appropriate to the frequency step. After applying this process for all  $Q$  frequency steps the array will be filled and the wide bandwidth spectrum (of bandwidth  $Q\Delta f$ ) will be stitched together. (Recall fig 2.4). These complex samples are then multiplied element-wise by a set of spectral scalings specially created for the waveform. These are spectral samples of a synthetic wideband chirp of bandwidth  $Q\Delta f$  divided by the stitched spectrum of the point target reference for the waveform. The stitched spectrum of a point target reference will therefore be a perfect wideband chirp. (See fig 2.6). For more complex targets, the effect of the scalings helps to reduce aliases in the resulting Hybrid range profile. A mechanism for the latter is discussed in section 2.3 above. Following stitching, the array of samples are converted back into the time domain via an inverse Discrete Fourier Transform.
12. **Hybrid pulse compression.** The Hybrid HRR profile is computed by determining the cross correlation between the time domain samples of the stitched spectrum and the corresponding samples derived from the point target reference. For display purposes, **fproc** truncates the end result to a defined number of Classical HRR windows either side of the maximum power in the Hybrid profile.<sup>14</sup>
13. **Hybrid dealias.** Aliases in the Hybrid method at intervals of  $\frac{c}{2\Delta f}$  appear to result from periodic disturbances which result from stitching spectra at intervals of  $\Delta f$ . Modelling suggests this can

---

<sup>13</sup> In the model code, which generates synthetic receiver samples,  $K$  is chosen to satisfy the criteria for spectral stitching. It is computed using the iterative padding and integer criteria checking as described and starts from an initial value set to include maximum target extent  $\Delta L$ , the range equivalent to the pulse length  $\tau$  plus  $\frac{\tau}{2}$  as a safety factor; i.e.  $K = \text{ceil}(f_s(\frac{3}{2}\tau + \frac{2\Delta L}{c}))$ . If the overall range of the target is  $R_0$ , the receiver opening times can be computed as

$$\begin{aligned} t_{open} &= \frac{\text{round}(f_s(\frac{2R_0}{c} - \frac{1}{4}\tau))}{f_s} \\ t_{close} &= t_{open} + \frac{K-1}{f_s} \end{aligned}$$

<sup>14</sup>  $\frac{5c}{2\Delta f}$  either side of the Hybrid HRRP maximum power seems to be sufficient to investigate the progression of aliases that may manifest. Clearly this should also exceed the target maximum range window  $\Delta L$  if the waveform has been designed (and receiver opening times chosen) in the manner discussed above.

occur due to imperfect motion compensation plus any receiver distortions which cause deviation from calibration. Aliases which manifest following Hybrid signal processing can be minimized by subtracting copies of the central  $\frac{c}{2\Delta f}$  power from subsequent (and prior, in range) intervals of  $\frac{c}{2\Delta f}$ . The central region is multiplied by the maximum power within the aliases region and divided by the maximum power in the central region. As demonstrated in fig 3.14 for a Hybrid profile of a Pod moving point target (the green and red regions were the original Hybrid profile), power subtraction can be effective as long as the central region contains well defined peaks, which lead to obvious aliases, and a ‘distant’ scatterer does not fall close to an integer multiple of  $\frac{c}{2\Delta f}$  in range from the highest peak. In summary:

- (a) Start with a high resolution range profile (power vs range) produced via the ‘Hybrid’ technique. Determine the range  $R_{\max}$  corresponding to the maximum power  $P_{\max}$ .
- (b) Define the  $n^{\text{th}}$  alias region to be  $\pm \frac{c}{4\Delta f}$  about  $R_{\max} + n\frac{c}{2\Delta f}$ , where  $n \neq 0$ . Let the maximum power in the  $n^{\text{th}}$  alias region be  $A_{\max}^{(n)}$ .
- (c) Apply ‘de-aliasing’ by subtracting the region  $R_{\max} \pm \frac{c}{4\Delta f}$ , scaled by  $\frac{A_{\max}^{(n)}}{P_{\max}}$  from the alias regions.

#### 14. Determine Radar cross section (RCS) of pulse compressor output and HRR profiles.

The profile power is passed through a function which applies the *Radar Equation* (See Appendix) to estimate RCS  $\sigma$  from the signal to noise power ratio, thermal noise and estimates of various system gains and losses.

$$\sigma = \frac{4\pi c^2 L k_B T_0 N_f R^4}{A^2 \eta^2 n E_i(n) \tau P_t f_{Tx}^2 |F_t F_r|^2} (S/N) \quad (3.2)$$

where  $S/N$  is the signal to noise power ratio  $k_B$  is Boltzman’s constant,  $R$  is the target range,  $A$  is the antenna aperture area,  $\eta$  is the ‘antenna effectiveness’,  $f_{Tx}$  is the carrier frequency,  $T_0$  is the ambient temperature,  $N_f$  is the receiver noise figure,  $L$  is the product of system loss factors (and reciprocal of any processing gains)  $F_t, F_r$  are (respectively) transmission and reception propagation factors,  $\tau$  is the pulse length,  $n$  is the number of integrated pulses,  $E_i(n)$  is the integration efficiency and  $P_t$  is the transmitter power.

An empirically determined calibration factor (a constant in dB) is added to the result to ensure consistency between waveforms and between pulse compressor and Classical HRR profiles. In the absence of any absolute calibration, the point target reference RCS was set to be 10dBm<sup>2</sup> for each waveform. The deviation between this and the computed RCS for the reference target yields the calibration factor for each waveform and profile type. The benefit of this empirical approach is that the Radar equation can be used to correct for differences in range between measurements, but accuracy in computing the loss factors is not required.

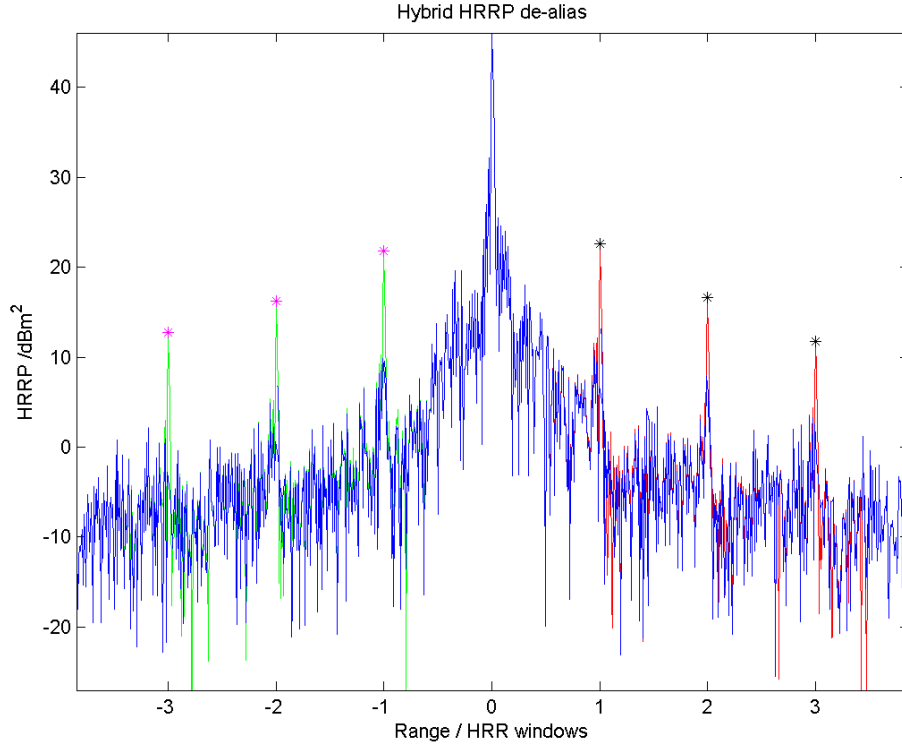


Figure 3.14: Aliases in the Hybrid method at intervals of  $\frac{c}{2\Delta f}$  appear to result from periodic disturbances which result from stitching spectra at intervals of  $\Delta f$ . Modelling suggests this can occur due to imperfect motion compensation plus any receiver distortions which cause deviation from calibration. Aliases which manifest following Hybrid signal processing can be minimized by subtracting copies of the central  $\frac{c}{2\Delta f}$  power from subsequent (and prior, in range) intervals of  $\frac{c}{2\Delta f}$ . The central region is multiplied by the maximum power within the aliases region and divided by the maximum power in the central region. As demonstrated for a Hybrid profile of a Pod moving point target (the green and red regions were the original Hybrid profile), power subtraction can be effective as long as the central region contains well defined peaks, which lead to obvious aliases, and a ‘distant’ scatterer does not fall close to an integer multiple of  $\frac{c}{2\Delta f}$  in range from the highest peak.

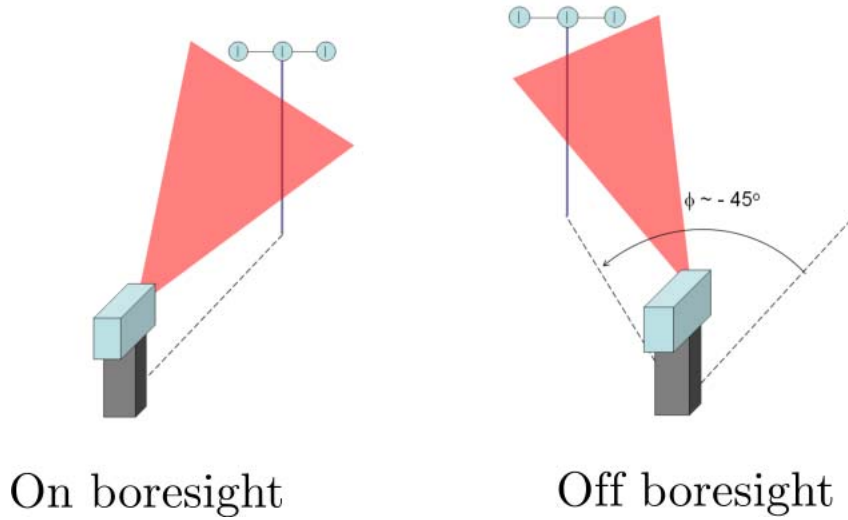


Figure 3.15: Cartoon descriptions of on and off boresight static trials using MESAR2.

### 3.6 On & off boresight trials

#### 3.6.1 Trials description

Trials proceeded by illuminating (using a stepped-frequency waveform) a set of three dipoles mounted on a mast (fig 3.16) some 100m directly in front of the MESAR2 antenna. RF energy is only permitted to enter the central dipole, from which a delay (equivalent to a cable length of several tens of kilometers) is connected. After propagation through this, the signal is split between the outer dipoles with one of these attached to a variable extra length of cable. The net result of this setup is the provision of two point targets at an effective distance of many tens of kilometers separated in range between 0 and 60m.

The mast was positioned by eye on-boresight, using as a guide the four vertical lightning conductors mounted on each corner of the MESAR2 antenna. (You know you are on-boresight when you cannot see the two lightning conductors behind). The off-boresight ( $-45^\circ$  in azimuth) position was determined using a theodolite sited next to the antenna face, and confirmed using a handheld Global Positioning System (GPS) receiver. MESAR2 was run in Experimental (X) mode and the beam was configured electronically (from a computer terminal within the control cabin) to point at the on and off boresight positions, illustrated by fig 3.15. The on-boresight trials were conducted during August 2004 and off-boresight trials during October 2005.

Uncompressed In-phase  $I$  and Quadrature  $Q$  data for the  $P$  (pulses)  $\times$   $Q$  (frequency) sets of receiver samples comprising each look, plus additional ‘header’ waveform parameters, were extracted from the MESAR2 data logger and transferred to a PC for analysis using the software described in the previous section.

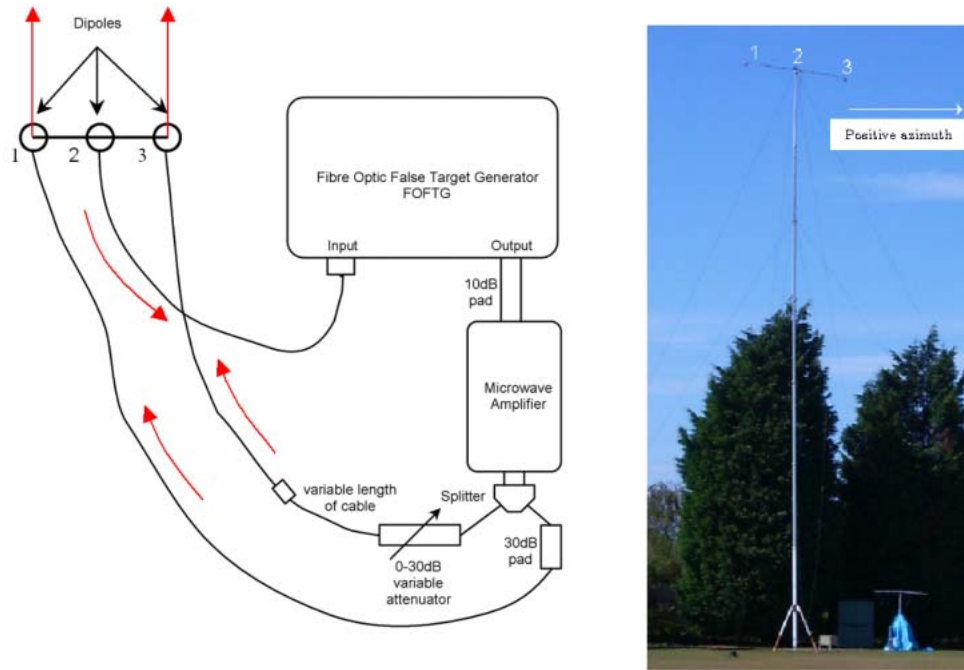


Figure 3.16: (Left) Schematic of the False Target Generator (FTG) used in the On & Off boresight MESAR2 trials. RF is permitted to enter dipole 2 from which it is allowed to propagate through several kilometers of cable. After this the signal is split between two paths to dipoles 1 & 3, whereupon the RF exits in the direction from where it originated. The path to dipole 3 can be lengthened using extra cable to generate two reflections spaced in range. In the trials, separations between 0 and 58m were used. (Right) Pump-up mast used in On & Off boresight trials using MESAR2. The mast was placed approximately 100m in front of the antenna. The three dipoles used in the experiment are mounted behind plastic windows on the horizontal bar at the top of the mast. The cabling used in the False Target Generator (FTG) is contained in the green shed to the right of the mast.

Physical cable length /m	Dipole separation on boresight /m	Dipole separation off boresight (on boresight calibration) /m	Dipole separation off boresight (off boresight calibration) /m	Average relative permittivity
0	0.4	0.7	0.0	
3	2.9	3.3	2.2	3.6
6	4.4	4.4	3.3	1.8
12	8.1	8.8	8.1	1.9
30	19.4	18.3	17.2	1.5
60	38.8	39.2	38.1	1.7
90	58.2	58.9	57.8	1.7

Figure 3.17: Table of added cable lengths and corresponding effective dipole range separations used in the on & off boresight static trials.

### 3.6.2 Waveforms and dipole spacing

In both on and off boresight experiments, Waveform A, (a  $B = -4.5\text{MHz}$ <sup>15</sup> linear chirp waveform of duration  $\tau = 25.6\mu\text{s}$ ) was transmitted in bursts of  $P = 8$  pulses +  $G = 2$  guard pulses.  $Q = 128$  bursts stepped in frequency by  $\Delta f = 3.2\text{MHz}$  constituted each look. The carrier frequency was 2.705 GHz for the first activity and 3.1114 GHz for the last. A uniform PRF of 1kHz was used which meant each look was composed of 1280 transmit-receive cycles containing 1024 processed pules with overall duration 1.92s. Although the total duration is likely to be excessive for operational use (see Chapter 7) the other parameters were chosen to maximize the possibility of resolving the two dipoles. Following High Range Resolution (HRR) processing over all 128 frequency steps, the theoretical range resolution was  $\Delta R \approx \frac{c}{2Q\Delta f} = 0.37\text{m}$ . The pulse compression ratio of each chirp was  $\approx B\tau = 20.6\text{dB}$  which was expected to be sufficient to extract a clear target sample, using the Classical method described in section 2.2.1.

The simulated target range<sup>16</sup> corresponding to the fixed dipole path (MESAR2 to dipole2 to FTG optic fibre to dipole 1) was set at  $R_0 = 23.384\text{km}$ . Extra cable was added in the split between the False Target Generator (FTG) and dipole 3. As described in fig 3.17, cables at lengths 0, 3,6,12,30,60 & 90 metres were used, resulting in target separations between 0 and 58m. Given the unambiguous length of the HRR profile for the waveform used was  $\frac{c}{2\Delta f} \approx 46.8\text{m}$ , the 90m cable (58m dipole separation) experiment would allow the Hybrid method to be tested out in a situation where the Classical result would yield an erroneous result for dipole separation. In addition to the two dipole experiments, separate recordings were made using the fixed range dipole (dipole 1), and also the variable range dipole (dipole 3) for each cable length.

<sup>15</sup>A ‘down’ chirp was transmitted. Over the  $25.6\mu\text{s}$  duration the instantaneous frequency varied from +2.25MHz to -2.25MHz about the main carrier (which was stepped by 3.2MHz between the 128 bursts from 2.705GHz to 3.1114 GHz).

<sup>16</sup>Propagation time in homogeneous cable of length  $L$  is  $\frac{L}{\sqrt{\epsilon_r}}$  where  $\epsilon_r$  is the dielectric constant. Hence the extra target range of the dipole 3 path resulting from cable length  $L$  added is  $\Delta R = \frac{1}{2}c\frac{L}{\sqrt{\epsilon_r}} = \frac{1}{2}L\sqrt{\epsilon_r}$ . One can therefore estimate the effective dielectric constant (or ‘relative permittivity’) from the equation  $\epsilon_r = 4\left(\frac{\Delta R}{L}\right)^2$  where  $\Delta R$  is the measured dipole separation.

### 3.6.3 Summary of results

Trials data was successfully collected for all added cable lengths. For brevity let us simply compare Classical & Hybrid results for the dipole 1 reference and 58m dipole 1 & dipole 3 separation experiments. In figures 3.18 & 3.19 Hybrid results (blue) are overlaid with the Classical range profiles for on boresight (upper plot) and off boresight (lower plot) scenarios. For the dipole 1 reference result one can observe a total lack of Hybrid aliasing at integer intervals of  $\frac{c}{2\Delta f}$ . The Hybrid result appears to have significantly lower range sidelobes<sup>17</sup> than the Classical method. The latter are fixed at 40dB via the use of the Dolph-Chebyshev windowing function applied prior to the inverse Discrete Fourier Transform. Perhaps a more realistic result is the off boresight example. The remnants of aliasing can be seen at around 40dB below the peak and in the Classical region there is good agreement between profiles. However, as observed for the Pod recordings in fig 3.24, the Hybrid result is approximately 5dB worse in ‘close in’ sidelobe performance. Fig 3.19 illustrates a clear difference between Classical & Hybrid profiles. The Hybrid method enables both dipoles to be correctly separated using the HRR profile. In the Classical method, dipole 1 appears at an erroneously short range, with a reduction in gain of nearly 20dB. Signal to noise ratios of between 20 and 30dB are observed between on and off boresight scenarios. This result suggests a below-max length measurement threshold of between 20 and 25dB may be optimal for Waveform A.

---

<sup>17</sup>Although this statement requires some perspective: the Hybrid profile appears to have a noise floor at around 70dB below the peak, but the peak width increases significantly after about 40dB. So by peak width comparison, the Hybrid result and the Classical result are equivalent.



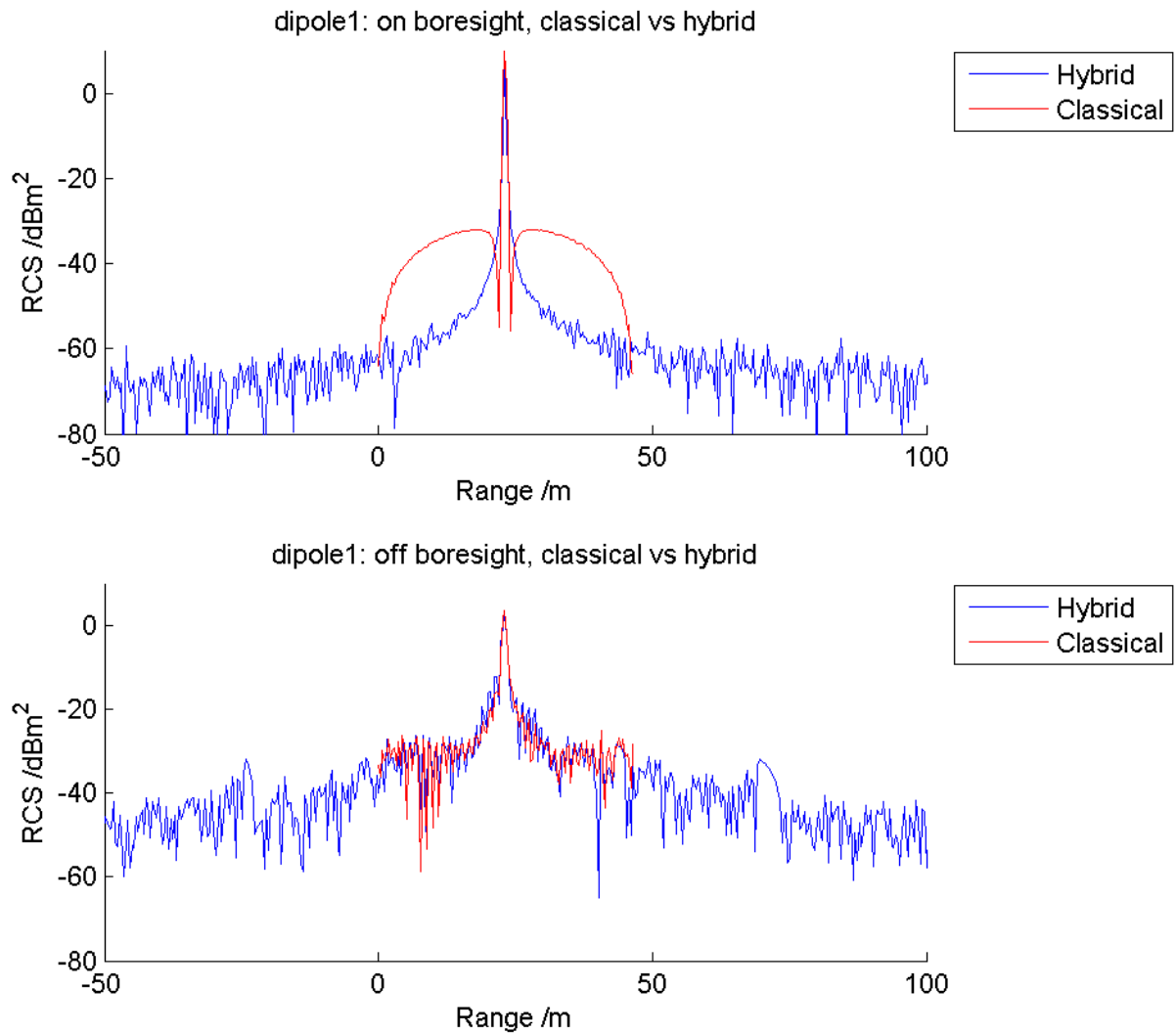


Figure 3.18: Hybrid (blue) and Classical (red) range profiles are compared for a single point target reflector. (Which is used to generate the pulse compression weights for Classical & Hybrid methods - i.e. this plot represents the autocorrelation function for these techniques). Waveform is A. In the upper graph the targets are positioned at boresight, i.e. aligned with the front face of the antenna as viewed from above. In the lower graph the targets are positioned 45 degrees left from this position. In order to illuminate the latter targets, MESAR2, being a fixed installation, was required to electronically scan its main beam by 45 degrees.

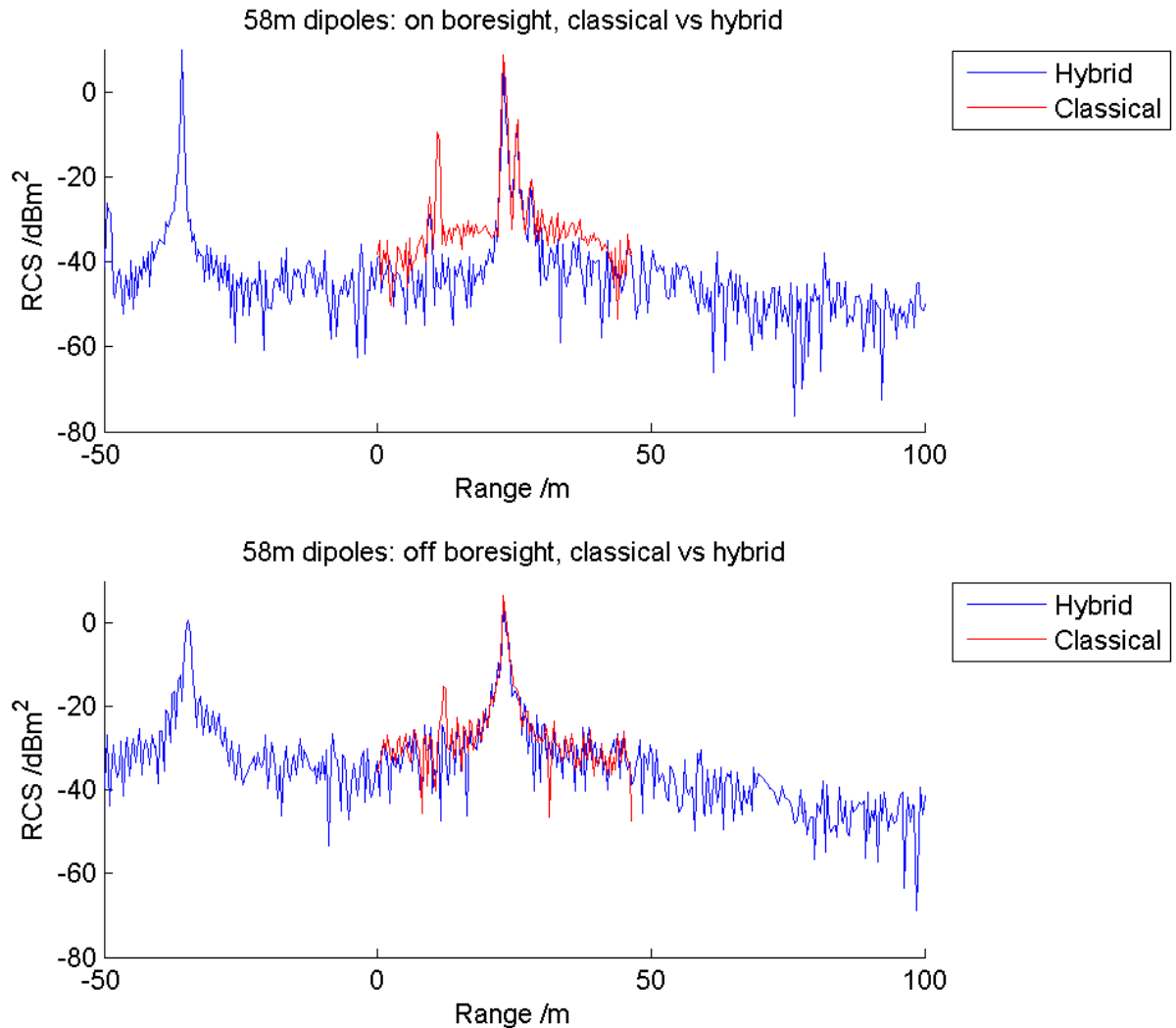


Figure 3.19: Hybrid (blue) and Classical (red) range profiles are compared for two static point target reflectors separated in range by 58m. In the upper graph the targets are positioned at boresight, i.e. aligned with the front face of the antenna as viewed from above. In the lower graph the targets are positioned 45 degrees left from this position. In order to illuminate the latter targets, MESAR2, being a fixed installation, was required to electronically scan its main beam by 45 degrees. The signal to noise ratio for the off boresight example is approximately 10dB less than the on boresight equivalent. This is more than might be expected from scanning loss alone:  $-10 \log_{10}(\cos \frac{\pi}{4}) \approx 3\text{dB}$ .

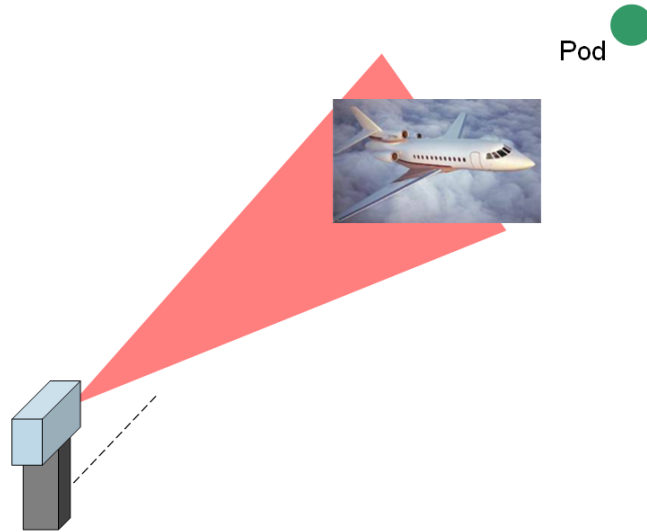


Figure 3.20: Cartoon of MESAR2 pod &amp; falcon trials

### 3.7 Pod & Falcon trials

#### 3.7.1 Trials description

Following successful On and Off-boresight static trials with MESAR2, a more complete test of the ‘Hybrid’ and ‘Classical’ stepped-frequency High Range Resolution processing techniques was performed in the actioning of NCTR looks upon a ‘Falcon’ jet aircraft. The Falcon contained a repeater ‘pod’ mounted in a missile-like container stored under one wing. The Pod is essentially a flight-worthy version of the False Target generator (FTG) used in the static experiments. Microwaves enter, propagate along several kilometers of cable before emerging and propagate back towards the source. From the perspective of a Radar system, the Pod will appear as a point target co-moving with the Falcon, as if connected by a rigid wire. The length of this imaginary wire is given by  $\frac{1}{2}c\Delta t_{pod}$  where  $\Delta t_{pod}$  is the time delay between microwaves exiting and entering the Pod.

In the context of the MESAR2 trial, which was conducted on Friday 14th October 2005 (with preliminary experiments conducted on Monday 10th October 2005) the Falcon and Pod were tracked as separate targets on an inbound trajectory between 50 and 20 km west of the Isle of Wight. (See fig 3.21) The tracks were established and maintained from plots obtained using the surveillance mode of MESAR2. NCTR waveforms were scheduled alongside these activities, and additional dedicated tracking tasks.

On Friday 14th October, 8 circuits were flown by the Falcon & Pod ensemble. NCTR waveforms were successfully delivered during the inbound sections of runs 1,3,4,5,6 and 8. In-phase (I) and Quadrature (Q) channel digital receiver samples were captured using the MESAR2 data logger. A sample rate of  $f_s = 5\text{MHz}$  was used in all instances. Data captured from all runs was converted into a human readable text-file format using software developed by BAE Systems. These files were then processed and visualized using MALAB.

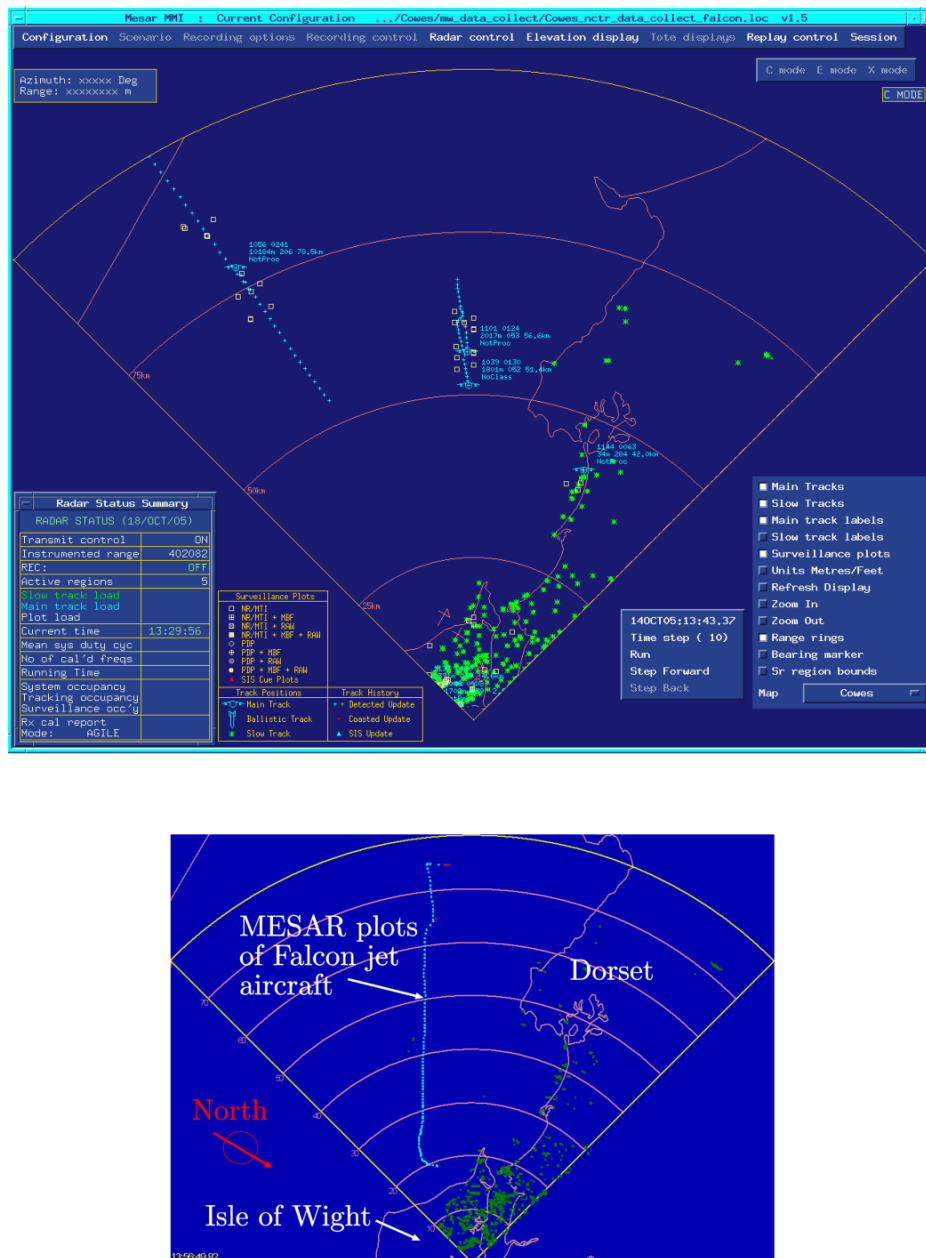


Figure 3.21: (Above) Screenshot of the MESAR2 ‘Man-Machine Interface’ (MMI). The Falcon and Pod targets are successfully tracked, and illuminated using NCTR waveforms, along inbound trajectories flying off the Dorset coast towards The Needles to the west of the Isle of Wight. In this figure, the Falcon (nearest) is at an altitude of 1801m and a slant range of 51.4km and is travelling with an (inbound) range-rate of  $\approx 130 \text{ ms}^{-1}$ . To the top left of the picture, a commercial airliner at altitude 10,184m and range 78.5km is also being successfully tracked. (Below) Tracks of the Falcon trials aircraft on an outbound (Westwards) trajectory from the Isle of Wight along the south coast of England. Blue dots indicate the position of the aircraft as determined by MESAR2. Range rings are km.

### 3.7.2 Summary of results

Fig 3.22 compares the receiver samples for pulse 1 of Waveform A (stacked over frequency steps) obtained for the Falcon and Pod targets. The interference effects caused by the multiple scatterers in the Falcon target are clearly evidenced by the non uniform power distribution with frequency step. Fig 3.23 compares the Classical & Hybrid range profiles of the Falcon & Pod targets, obtained using waveform A. Both targets are clearly displayed and it is possible to resolve four major Falcon scatterers and measure its length at approximately 17m. (The projected physical length was computed to be 17.8m). As suggested for the static targets, a below-maximum length threshold of 20 to 25dB appears to be appropriate for the Hybrid method. A lower threshold would cause aliases to corrupt the length measurement. By contrast, the Classical method appears to have a lower noise floor by approximately 5dB. (See fig 3.24). For targets which are genuinely shorter than  $\frac{c}{2\Delta f}$  it would appear the Classical result should yield a better length estimate. A full set of trials results are presented as target data sheets in the Appendix. These include HRR profiles using waveforms B & C plus Doppler profiles (which for both targets are devoid of JEM) using waveform D.

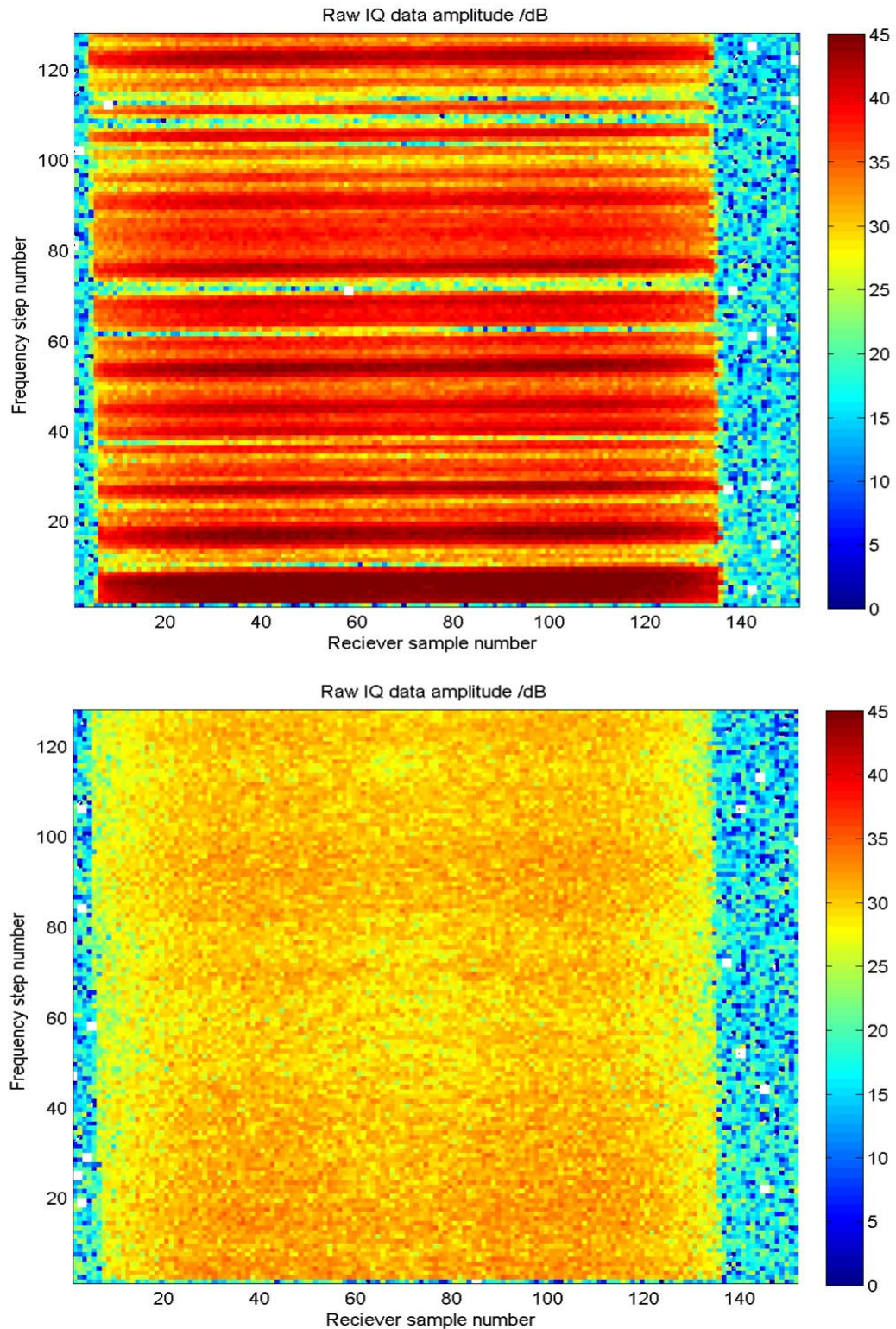


Figure 3.22: Stack of receiver sample power for burst 1 (of 8) using waveform A applied to Falcon (above) and Pod (below) targets. The stacking is over the 128 frequency steps (of 3.2MHz). In the Falcon example one can clearly see the result of interference effects due to multiple scatterers. In the Pod example (where the aim is for it to appear as a point target) there is much reduced variation with frequency.

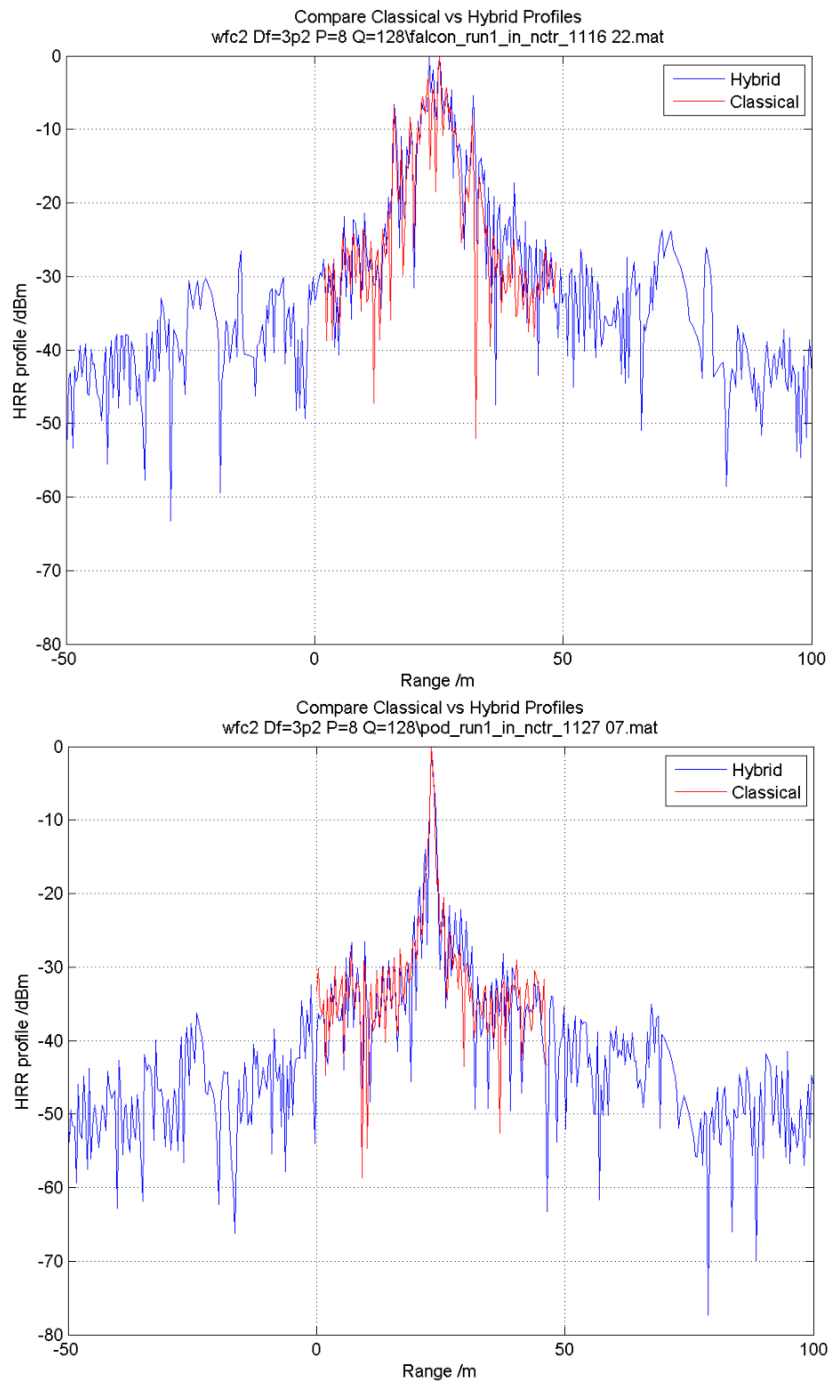


Figure 3.23: Overlay of Classical & Hybrid profiles for Falcon (above) and Pod (below). Hybrid aliases for the Falcon are approximately 25dB below the main return. In the Pod example, much more effective de-aliasing is in evidence, with levels down to 35dB below the peak. Waveform is A.



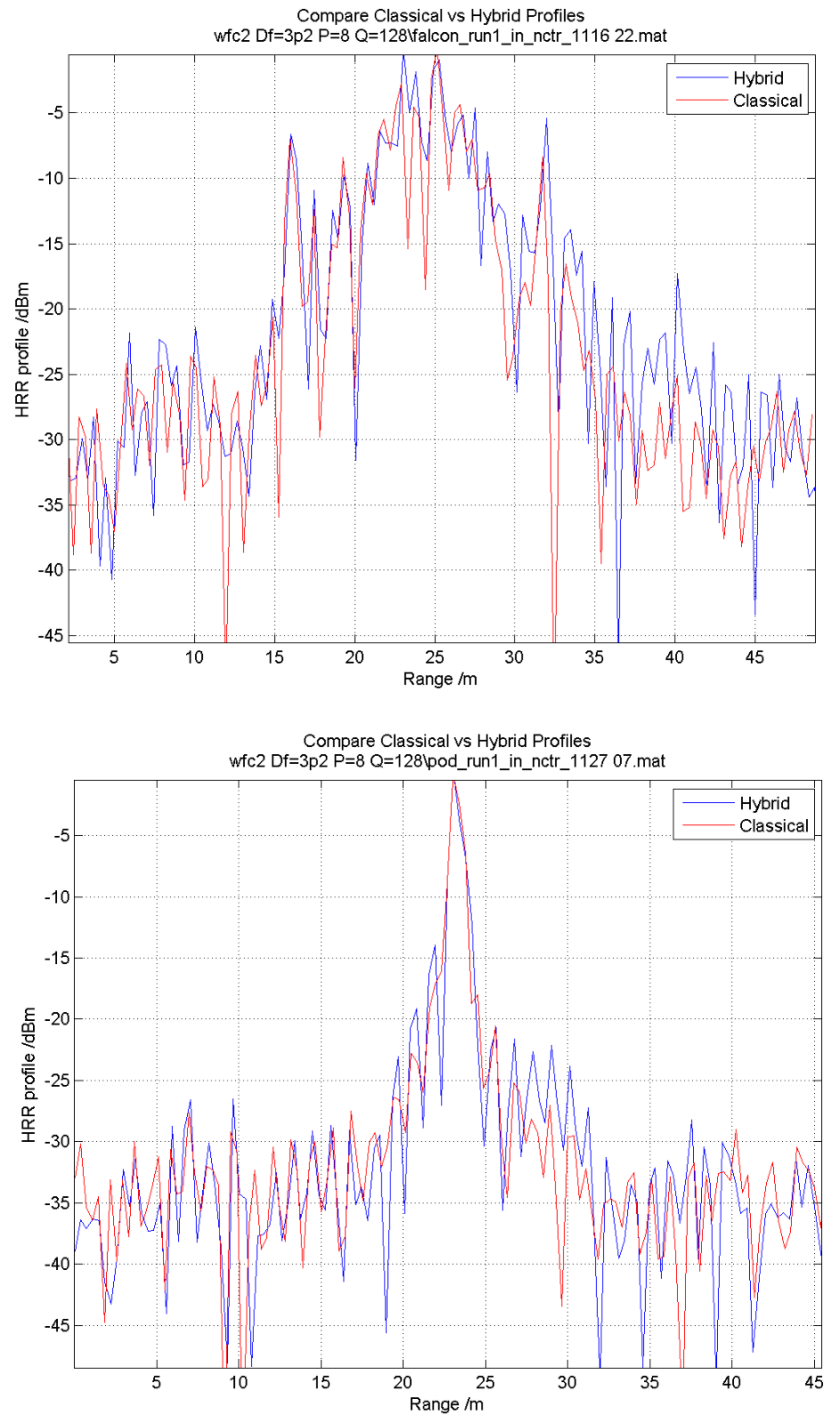


Figure 3.24: Close up view of Pod & Falcon data shown in fig 3.23. Although there is generally good agreement, there appears to be some asymmetry in the Hybrid result, causing the sidelobes to the right of the profile to rise above those of the Classical result by about 5dB.



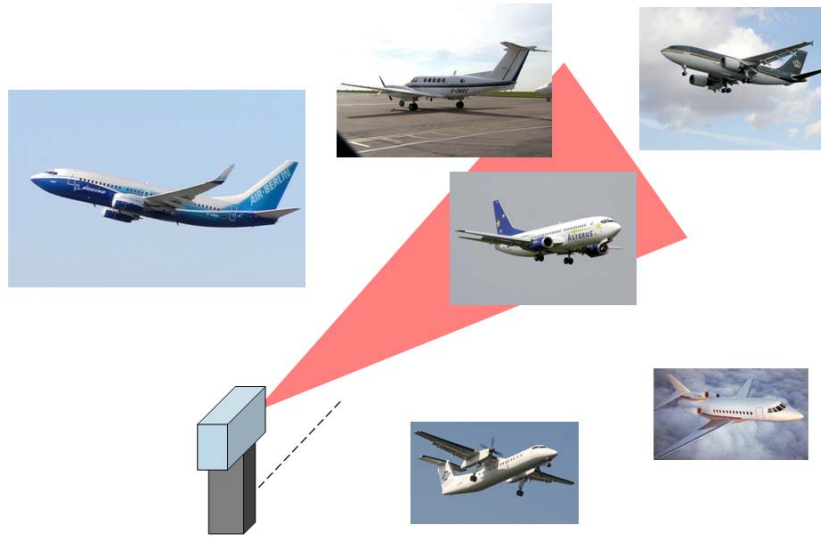


Figure 3.25: Cartoon of MESAR2 ‘Targets of Opportunity’ trial, in which 15 distinct aircraft were tracked over a (several hour) time interval. NCTR looks (waveforms A,B,C,E) were automatically actioned by MESAR2 against targets being tracked.

## 3.8 Targets of opportunity

### 3.8.1 Trials description

On July 4th 2006, MESAR2 automatically tracked and scheduled NCTR waveforms A,B,C,E onto targets of opportunity in the airspace of Southern England. MESAR2 operators at Cowes on the Isle of Wight were in telephone contact with colleagues at the National Air Traffic Service (NATS) in Swanwick to provide identification of aircraft associated with the tracks. In this way recordings of 15 types of known aircraft were made, starting with an Airbus A340 (callsign BWA900) at 0908 and ending with a Boeing 747 (callsign BAW207) at 1150. Permutations of NCTR waveforms A,B,C & E were automatically scheduled.

### 3.8.2 Summary of results

Following inspection of the individual range and Doppler profiles obtained during the targets of opportunity trial, there were four significant observations:

1. Using Waveform A, the Hybrid method can be used to generate a sub-metre range resolution profile of an inbound 747 aircraft. As shown in fig 3.26, this is not possible using the Classical method as the Classical HRR range window of waveform A is less than the length of the aircraft.
2. Waveform E, which uses a fourth of the frequency steps as waveform A, can (via the Hybrid method) also be used to accurately measure the (physical) length of an inbound 747. (See fig 3.27). In Chapter 6 we shall assess this statement in more detail.<sup>18</sup>
3. Jet Engine Modulation (JEM) has been observed (i.e. clearly distinguished from the skin echo) using waveform E. See fig 3.28.

<sup>18</sup>i.e. does the standard deviation in length feature measurements appear to scale linearly with overall bandwidth? If not, are their limits imposed by range sidelobes and tolerance of the waveform to errors in motion compensation and calibration errors, frequency jitter & noise? Is there an optimal scheme which can be used to choose between chirp type and processing method? i.e. non-linear chirp & Classical vs linear chirp & Hybrid?

4. A propeller driven aircraft (Dash8) can produce a Doppler spectrum which is different from those characterized by JEM. Rather than distinct lines, one observes more of a spectral continuum. In fig 3.29 one observes this continuum (resulting from a blade flash) punctuated by periodic nulls in what is effectively a frequency-time representation or ‘short time Fourier transform’. In this example one can infer the flash rate to be of the order of 750RPM. The differences in overall structure between the Doppler spectra of Jet aircraft with visible engines, propeller driven aircraft and aircraft with obscured jet engines (or none at all) could be used in classification. Given the PRFs for an S-band multifunction phased array Radar are likely to be too low to measure target internal motion induced modulation unambiguously<sup>19</sup>, this cruder form of spectral classification may well be a more productive strategy than attempting to make a direct measurement of specific engine rotational characteristics such as number of blades and spool rate, as described in Tait [103].

The opportunistic nature of this trial meant there was inherent uncertainty in the possible scope and quality of recordings. Indeed, many aircraft were on a crossing rather than radial trajectory. As a result, the numbers of inbound or outbound looks which could be readily classified using a simple length feature were modest (between 10 and 40 per waveform.<sup>20</sup>) However, since the overall goal is to develop Radar systems which are operationally useful rather than simply theoretically possible, an analysis of what could be observed in fairly realistic operating conditions is worthy of consideration. It is possibly more valid to state observed performance based upon a limited but uncontrived sample, and then infer what could be achieved with more looks, higher bandwidths etc; than report performance of a theoretically ideal situation and then try and infer what degradation is likely in an operational context. With this philosophy in mind, the classification performance reported (which is described in the following chapters) should be strongly linked to the target data sheets, which are presented in the Appendix. These describe the variability of the HRR and Doppler profiles for each target, and corresponding extracted features such as length.

---

<sup>19</sup>As described in section 2.4.2

<sup>20</sup>In this thesis the focus has been upon inbound aircraft, largely to make a fair comparison of targets of opportunity to the Pod & Falcon recordings (which were inbound). In the following Chapter, where Doppler analysis is discussed, outbound aircraft are also considered based upon the effect upon JEM and therefore Doppler spectra based classification. Given the wings of most commercial aircraft are perpendicular to the main fuselage, and wingspan is strongly correlated to length (but perhaps not linearly related since longer aircraft are heavier and therefore require more lift, but longer wings also have more mass) one might conjecture long aircraft could be discriminated from short even in a purely tangential aspect. This question is not explored in this thesis.

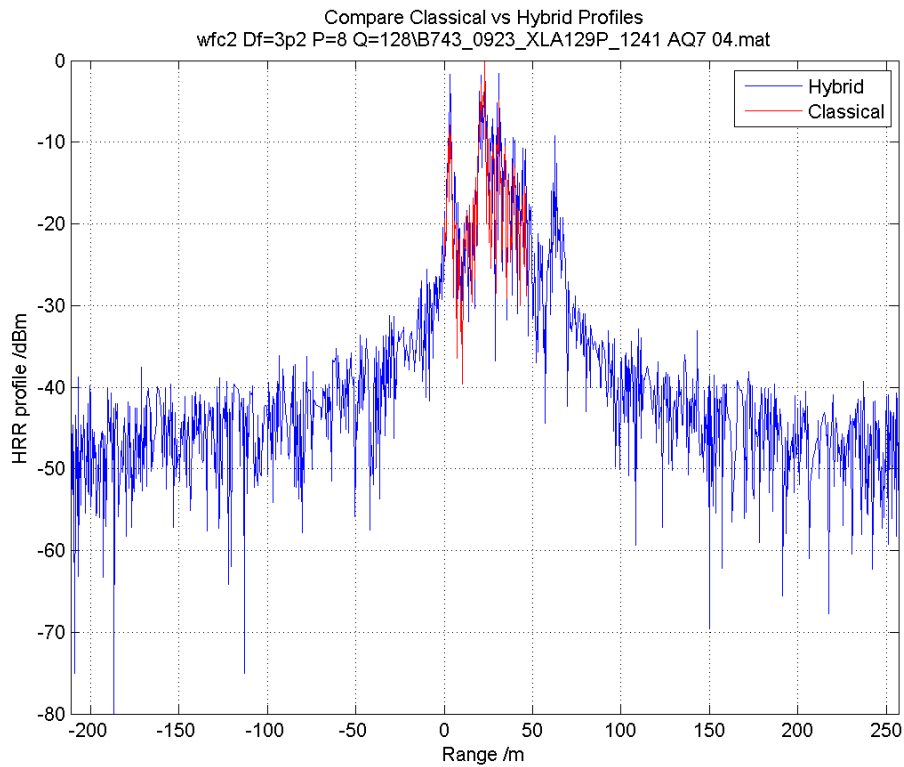


Figure 3.26: Overlay of Classical (red) and Hybrid (blue) high range resolution profiles of an inbound Boeing 747 (length = 70.6m). For the Hybrid result, a below-max length threshold of 25dB yields a radar length of 70.3m, which is in reasonable agreement with the optical length given the aircraft was observed at an aspect angle of approximately  $10^\circ$ , yielding a projected optical length of 69.5m. Since the aircraft projected length exceeds the Classical range window (for Waveform A it is 46.8m), the Classical method cannot be used to give a sensible measurement. Wrapping of the front of the aircraft to the rear is clearly evidenced.

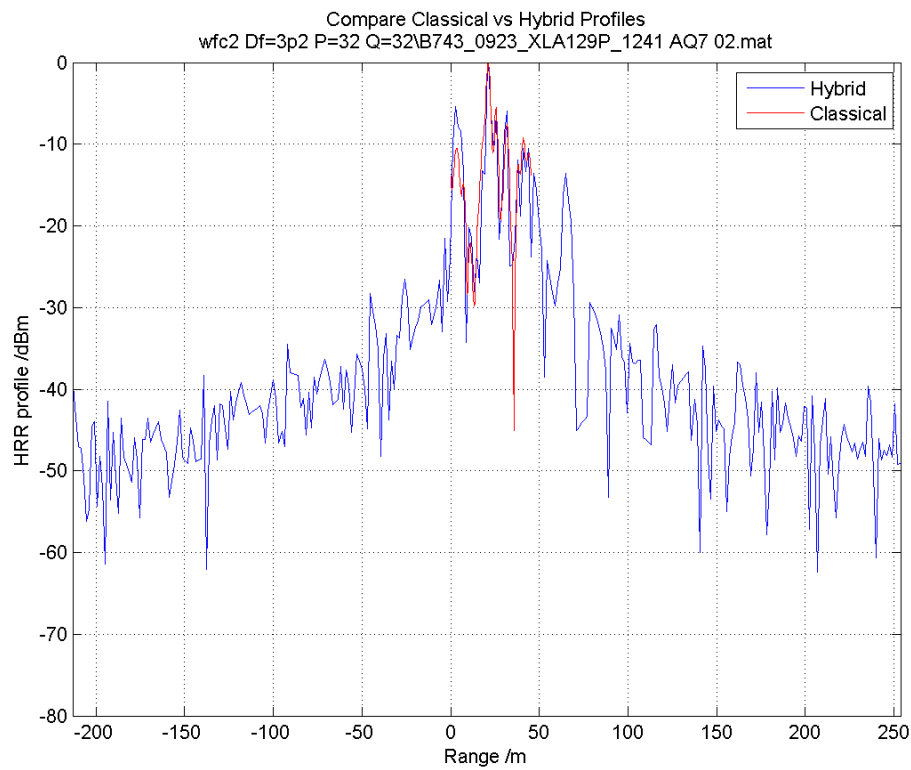


Figure 3.27: Classical & Hybrid HRRP overlays are presented for the same inbound Boeing 747 as illustrated in fig 3.26. In this case Waveform E is used, using only 32 frequency steps rather than the 128 of Waveform A. A 25dB below-max threshold yields a length of 71m.

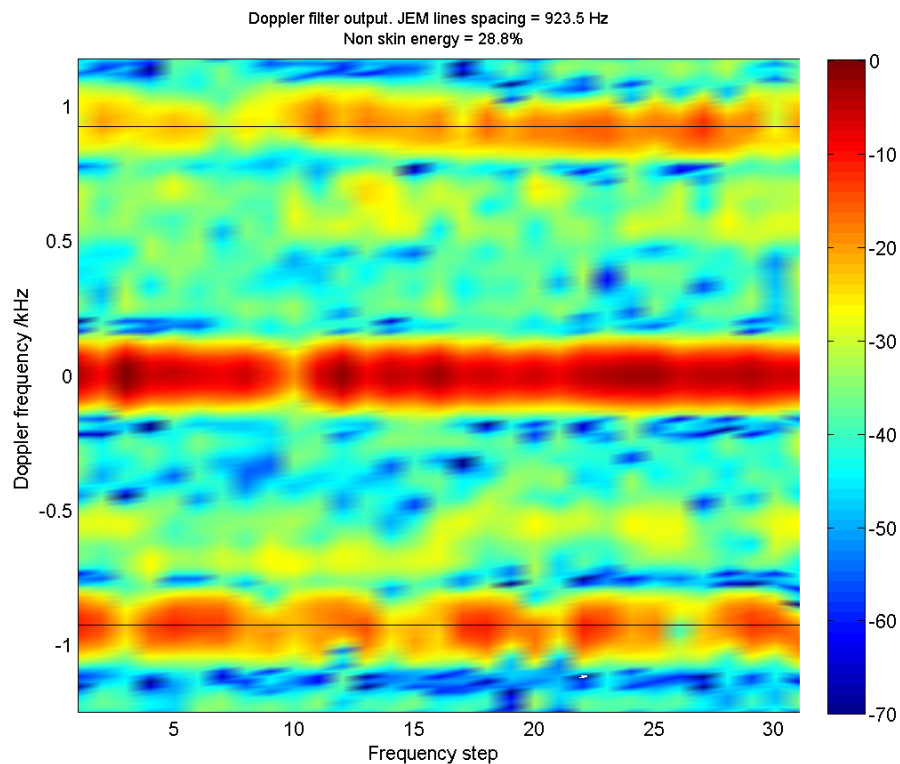


Figure 3.28: Stack of Doppler spectra /dBm for an inbound Boeing 747. Stack is over the 32 frequency steps of Waveform E. Jet Engine Modulation (JEM) is clearly present at  $\pm 1$  kHz. Although the limited PRF (2.5kHz) suggests this is likely to be an ambiguous result, and therefore little may be inferred with certainty about the number of blades or the spool rate, the presence of JEM is an identifying feature in itself (albeit for a wider class of targets than a 747).

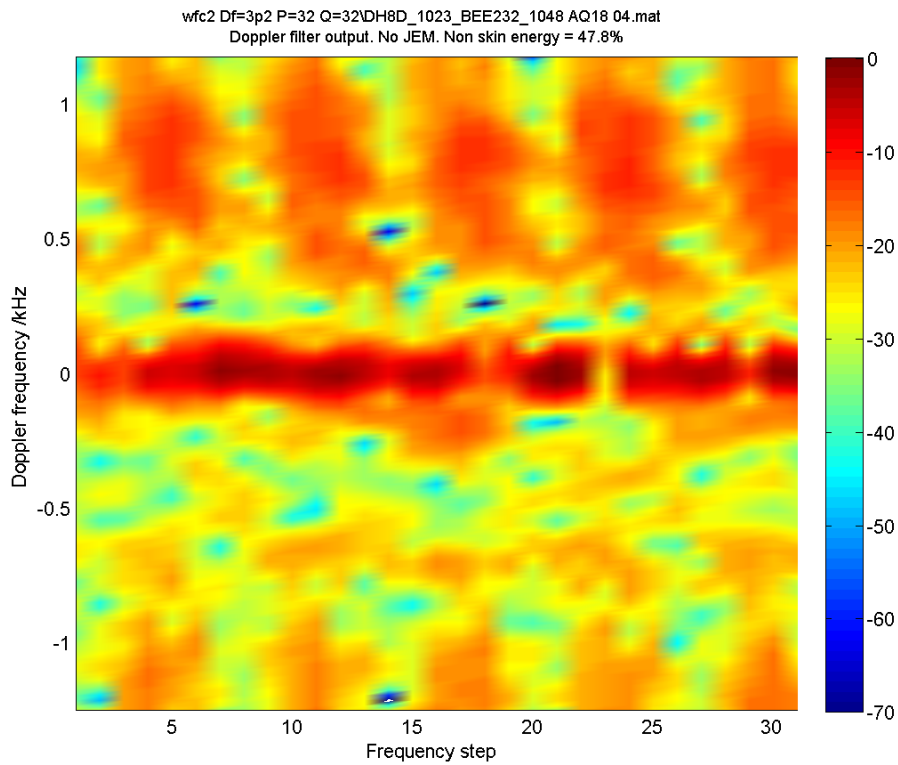


Figure 3.29: Stack of Doppler spectra /dBm for a inbound Dash8 propeller aircraft. Stack is over the 32 frequency steps used in Waveform E. Non-skin spectral features are not as localised into distinct peaks as in the 747 profile in fig 3.28, instead approaching a continuum at around -25dBm. Note in this example one can use the stack of spectra to estimate the blade flash rate. There appears to be roughly  $25/4 = 6.25$  frequency steps between flashes. Since there are 32 pulses per step and the PRF is 2.5kHz this implies 12.8ms per frequency step. Therefore flashes occur with a periodicity of 80ms which implies a flash rate of  $\approx 12.5\text{Hz}$  or 750RPM. This is a rather curious result. A Dash8 uses a six blade turboprop engine which typically rotates at 1500RPM. i.e.  $f_{rot} = 25\text{Hz}$  and  $Nf_{rot} = 150\text{Hz}$ . The observed flash rate therefore appears to correspond to once every two engine rotations. Intuitively one might conjecture an interference effect between the two propellers is responsible for this result.

### 3.9 Conclusions

Let us summarize the results presented in this chapter in the form of answers to the first key question posed in the introductory chapter.

1. *Can MESAR2 (and by inference other S-band multifunction phased array radars) be used to record robust range (and Doppler) profiles of air targets?*

- 1498 NCTR looks using 5 waveforms were scheduled by MESAR2 upon 17 different target classes. Based upon a ‘goodness’ criteria of  $> 30\text{dB}$  peak to median signal level of the pulse compressor output, 83% of recordings were ‘good.’
- On & off boresight static trials demonstrated that two static reflectors of separation 0 to 58m could be resolved unambiguously with a signal to noise ratio of between 20 and 30dB. The Hybrid technique allowed for an extension of the HRR profile window beyond the ‘Classical’ extent. In the trials this was 47m as a consequence of a 3.2MHz frequency stepped waveform being employed. (Waveform A). Signal processing refinements to the Hybrid technique helped to reduce aliases at intervals of the Classical window to negligible levels. Off boresight electronic scanning by MESAR2 did not corrupt the range profile to any significant degree.
- A ‘robust’ set of NCTR measurements were taken of a moving point target and a small jet (Falcon) aircraft during a fully operational MESAR2 trial; i.e. the NCTR looks were automatically scheduled between surveillance and tracking functions. 211 looks were recorded for the Falcon and 155 looks for the Pod, with approximately 40 looks for each of the four waveforms used. Overlays of range profiles (see sections K to N ) indicate a variation in signal strength of between 10 and 15dB, but overall a consistent range extent and distribution of major scattering centres.
- A limited set of measurements were taken of ‘targets of opportunity’, with measurements for Boeing B747, B757 & B777 and Dash8 aircraft presented in this thesis. In this uncontrolled experiment, approximately a quarter were ‘inbound’ ( $<20^\circ$  aspect), a quarter were ‘outbound’ ( $>160^\circ$  aspect) and half were of a ‘crossing aspect’. Between 10 and 40 looks per waveform were recorded for each aspect category and target data sheets were constructed for each waveform, aspect category<sup>21</sup> and aircraft. The plots of cumulative range and Doppler profiles (see Appendix) indicate an acceptable degree of stability could be achieved after around ten looks, assuming the target does not change aspect by a significant amount. (By significant I mean make the transition from an inbound to a crossing or an outbound aspect). The implication here, (which is alluded to by Zyweck & Bognor [118]) is that the spatial location of major scatterers is only significantly variable over a range of tens of degrees rather than degrees or fractions of a degree; i.e. classification of aircraft based upon simple features such as length measurement is unlikely to be a fruitless quest as long as multi-look averaging is done.
- The Doppler spectra of inbound jet aircraft consistently demonstrate the presence of Jet Engine Modulation (JEM). The difference between inbound and outbound target aspects is clearly evident in the Doppler spectra. The obscuration of the jet engines in the outbound

---

<sup>21</sup>Inbound aspect range profile and inbound and outbound aspect Doppler spectra data sheets are presented. Crossing aspect data is not presented.

example is consistent with a reduction in the presence of JEM in the Doppler spectra. The spectra of the propeller driven Dash8 is noticeably different from those arising from jet aircraft. Whereas the JEM spectra consist of well defined peaks which persist from burst to burst, the propeller modulations manifest as a spectral continuum, modulated on the burst timescale by periodic ‘blade flashes.’

- The Hybrid technique is able to yield an unambiguous range profile of an inbound Boeing 747 (length  $\approx 70\text{m}$ ) using a stepped frequency waveform (Waveform A) with a ‘Classical’ range window of 47m. (See Fig 3.26). Fig 3.26 (which corresponds to the 32 pulse waveform E) suggests that an accurate length measurement could be taken with a quarter of the frequency steps.



## Chapter 4

# Target classification using HRR profiles

### 4.1 Chapter summary

This Chapter describes classification of length and scattering center range feature measurements extracted from High Range Resolution profiles obtained via stepped frequency waveforms A,B & C. Six aircraft types are investigated (Pod, Falcon, Dash8, B747,B757 and B777). ‘Long or Short’, ‘Four Lengths’ and ‘Aircraft type’ class sets are used and classification performance is computed using Bayesian and Fuzzy Logic discriminant functions. Waveforms B and (Hybrid processed) A are used to help classify the aircraft which would normally exceed the 48m (3.2MHz) HRR window, whereas Waveform C is used to offer improved range profile sidelobe levels for shorter aircraft. Based upon the data set obtained, Long or Short classification offered high performance, with a confusion matrix Off Diagonal Extent (ODE)  $\xi$  of around 0.1. Four Lengths classification yielded a more modest performance with a  $\xi$  of around 0.3; the higher result being largely attributed to the misclassification of Long and Very Long classes. Scattering Center Model barcode matching (SCM compare classification) of Pod & Falcon was nearly perfect, but performance was poor ( $\xi \approx 0.6$ ) using all six aircraft classes. Whereas the Pod & Falcon length measurements are clearly distinguishable, the other aircraft length measurements were observed to vary significantly. The Dash8 length was observed to be systematically longer than physical dimensions would otherwise indicate. The presence of range sidelobes is the likely cause of these effects<sup>1</sup>, in particular for the Dash8 where the low frequency propeller modulations are likely to penetrate the eight pulse Doppler filters applied. In Chapter 6 we shall investigate the effect of raising<sup>2</sup> the length measurement threshold above the -20dBm used in this Chapter. Inspection of the Target data sheets constructed from the range profile information suggests that, in the absence of significant aspect angle change, a moving average of around eight HRR profiles can yield a stable range profile. In most examples quoted, profiles were aligned to the start of the length extent. However for the Dash8 example, (which suffers from high range sidelobes) alignment to the profile maximum was preferable.

### 4.2 Target data sheets of six aircraft types

To simplify analysis, the fifteen types of aircraft observed using MESAR2 during trials were reduced to six. Also, as discussed in the previous chapter, only inbound aircraft were used. The following target

---

<sup>1</sup>Since the Doppler spectra (see Appendix) indicates the other likely source of broadening and range profile corruption, that is poor motion compensation, is not really an issue.

<sup>2</sup>and lowering!

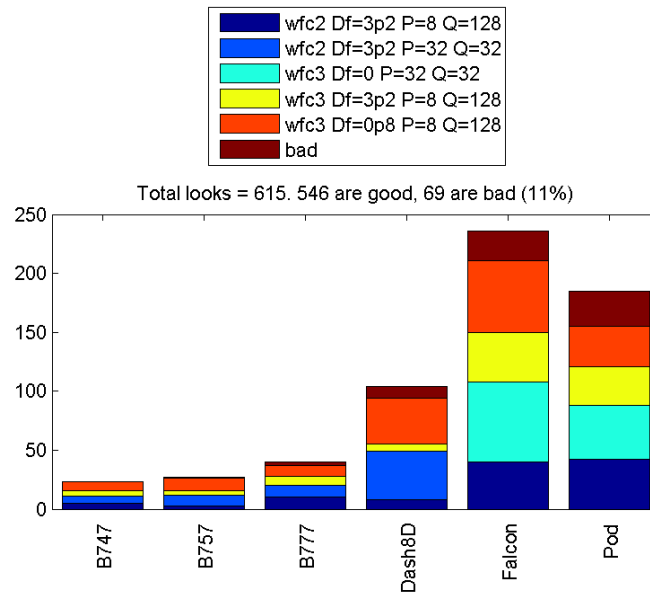


Figure 4.1: Total number of looks (by waveform) for the six aircraft used in classification analysis.

types were chosen to best capture the range of profiles obtained. In the table below, the number of looks (per waveform) is presented for each target type.

Aircraft	Why chosen?	A	B	C	D or E
Pod	1.5m/1.5m <sup>3</sup> moving point target	42	34	33	46
Falcon	17.15m/16.3m jet aircraft (2 engines, low profile)	40	61	42	68
Dash8	22.3m/25.9m turbo-prop aircraft (2 engines)	8	39	6	41
Boeing 757	47.32m/38.05m jet aircraft (2 engines)	3	10	4	9
Boeing 777	63.7m/60.9m jet aircraft (2 engines)	10	9	8	10
Boeing 747	70.6m/59.6m jet aircraft (4 engines)	5	7	5	6

In this chapter we shall focus upon classification performance based upon length feature measurements. Doppler spectra differences which result from no engines, low profile jet engines, propellers or jet engines will be discussed and exploited in the following chapter. In Chapter 6 we consider combinations of length *and* (Doppler) features.

As described in the table above and in fig 4.1, data is somewhat sparse for the Dash8, B757, B777 & B747 aircraft. However, given the operational context in which the data was collected one might actually regard the Pod & Falcon data set as being in excess! Either way, the small numbers are unlikely to yield robust statistics and therefore one must be cautious in the interpretation of abstracted measures such as overall classification performance. With this in mind, two styles of target data sheet have been created for each of the six aircraft to enable one to investigate the cause of the classification statistics. The first focusses on the range profile and the second upon the Doppler spectra. The target data sheets (which are listed in the Appendix by waveform and in figures 4.2 & 4.3) are a montage of the following:

1. Azimuth, elevation and aspect angle of target by look number

<sup>3</sup>The ratio X/Y corresponds to the length in proportion to the wingspan (in m); e.g. a Falcon is 17.15/16.3.

2. Stack of HRR profile power (normalized such that maximum is zero dB<sup>4</sup>) by look number and aligned in range either by (i) maximum or (ii) range of first length threshold crossing. Length bounds and front to back difference are overlaid upon this.
3. Same as (2), but computed as a cumulative mean.
4. Plan view of aircraft with (manually assigned) scattering centres indicated and numbered. Summary of parameters including target name, mean projected length<sup>5</sup>, thresholds used, alignment method etc.
5. Overlay of HRR profiles (normalized such that maximum is 0dB), length threshold, projected scattering center ranges, computed peak ranges and mean HRR profile (with length bounds). HRR profiles are colour coded by the product of the cosines of aspect and elevation angles; i.e. a value of unity indicates a purely radially inbound trajectory.
6. Radar lengths and projected physical lengths plotted against the product of the cosines of aspect and elevation angles.
7. Max and integrated RCS plotted against the product of the cosines of aspect and elevation angles.

Figures 4.2 & 4.3 display target data sheets for, respectively, Boeing 747 and Dash8 aircraft. Each figure is actually two representations of the same data. The upper is computed using range of first length threshold crossing (start) alignment of HRR profiles and the lower using alignment to the profile maxima.<sup>6</sup> As these examples illustrate, depending on the target type, either method may be preferable. In the 747 example, start alignment appears to yield a more consistent profile. Indeed we might speculate that after 7 to 10 looks one may (based on the cumulative HRR stack) be able to obtain a robust profile, assuming the target does not change aspect angle during this time. The converse is true of the Dash8. In this case (as illustrated in fig 4.4, which uses a greater range than the data sheets), range sidelobes exceeding the length threshold artificially extend the feature measurement. The likely cause of such sidelobes are low frequency propeller modulations which cannot be discriminated from the skin return via the 8 pulse Doppler filter employed with Waveform B.<sup>7</sup> The length feature measurement result will of course be the case for each profile regardless of range alignment method. However, as fig 4.3 demonstrates, the cumulative average plot with max alignment can enable a more reasonable length assessment when range sidelobes are a potential issue.

### 4.3 Range sidelobes resulting from low frequency propeller modulations

In fig 4.3 the range profile of the Dash8 aircraft exhibits significant sidelobes which give rise to an erroneously large length estimate. A model which predicts the spacing of these sidelobes can be

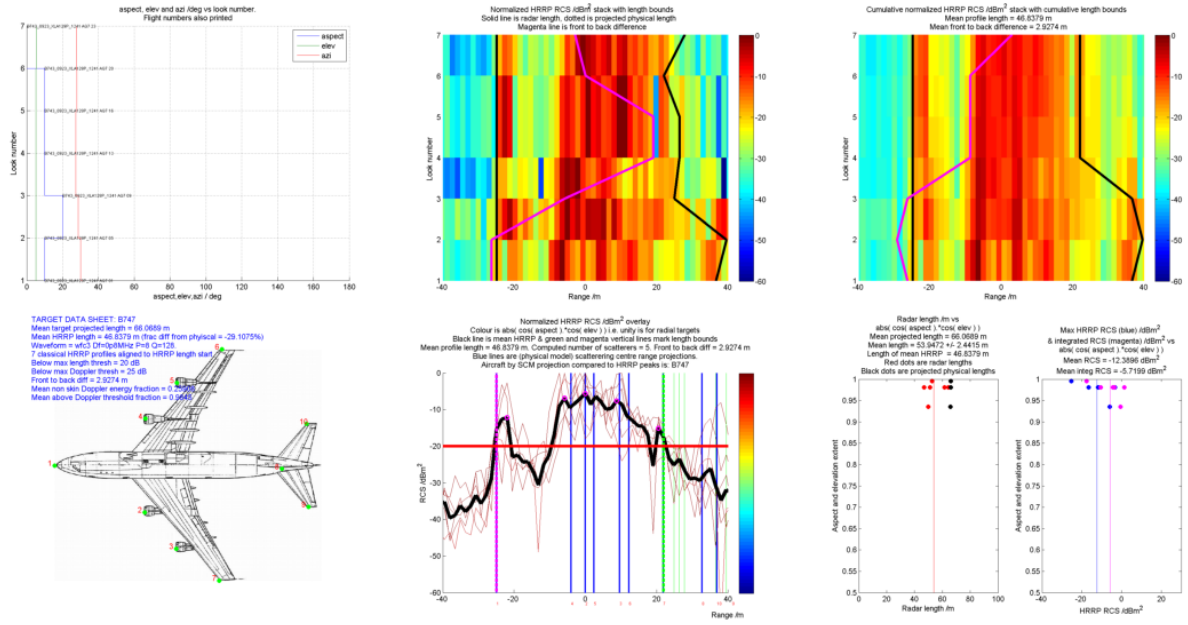
<sup>4</sup>Normalized power rather than RCS is used due to the observed variability in RCS discussed in section 2.5.3 and in the Appendix.

<sup>5</sup>This is the maximum range difference between the projections of the scattering centres upon the radial line, based upon estimation (via MESAR2) of the aspect angle of the target.

<sup>6</sup>The start range of the range profile is the range at which the range profile crosses the length threshold; e.g. 20dB below the maximum. ‘Start alignment’ is a lining up of consecutive range profiles such that the start range of each profile is set to be the same value. In contrast, ‘max’ alignment is when the range corresponding to the range profile maximum is set to the same value for all consecutive looks.

<sup>7</sup>See following section.

## Aligned to start of range profile



## Aligned to maximum of range profile

Figure 4.2: Target data sheets for an inbound Boeing 747 target illuminated with Waveform B. The upper graphs were created by aligning the HRR profiles to the start of the target length extent, using a threshold of 20dB. The lower graphs were aligned to the range of the maximum HRR power in each profile. In this case, a more stable range profile can be obtained by using the start alignment method.

## Aligned to start of range profile

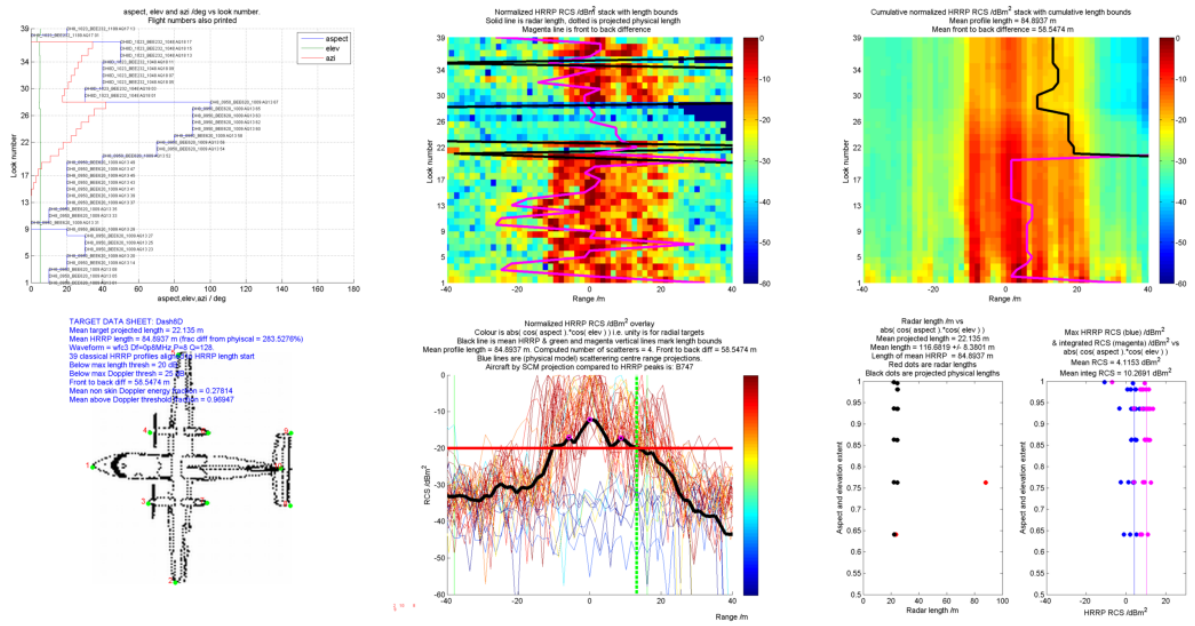


Figure 4.3: Target data sheets for a (mostly) inbound Dash8 target illuminated with Waveform B. The upper graphs were created by aligning the HRR profiles to the start of the target length extent, using a threshold of 20dB. The lower graphs were aligned to the range of the maximum HRR power in each profile. In this case, a more stable range profile can be obtained by using the max alignment method due to range sidelobes outside of the normal target range causing the start range to be offset. (Although in this case the likely cause is the change in aspect of the target to around 90 degrees between looks 22 to 29).

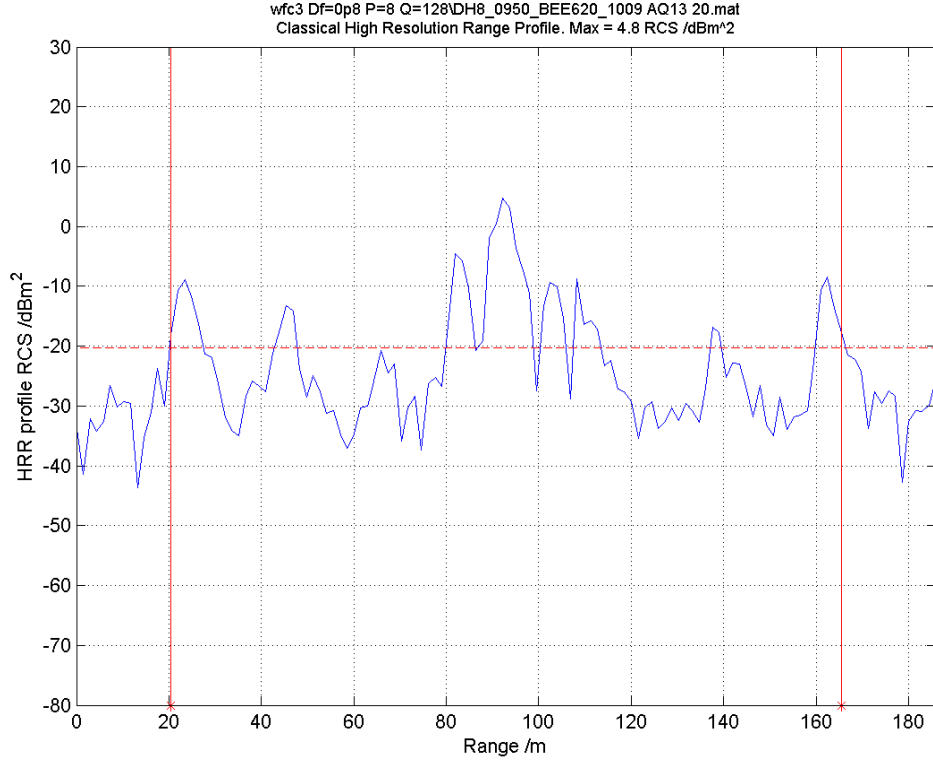


Figure 4.4: Classical HRR profile of a Dash8 aircraft using Waveform B ( $\Delta f = 0.8\text{MHz}$  frequency step with  $P = 8$  pulses per burst +  $G = 3$  guard pulses,  $2.5\text{kHz}$  PRF). Note the high range sidelobes (the aircraft is  $22\text{m}$  long) which exceed the  $20\text{dB}$  below-max length threshold, thereby artificially extending the length feature measurement. These sidelobes are likely to derive from low frequency propeller modulations which cannot be discriminated from the skin return via the  $P = 8$  pulse Doppler filter. A simple model of this effect suggests a range periodicity of  $\delta R = \frac{cNf_{rot}(P+G)}{2f_{PRF}\Delta f} \simeq 0.824Nf_{rot}$ . In this figure one might interpret three aliases of the target range profile with start ranges of  $22\text{m}$ ,  $80\text{m}$  and  $138\text{m}$ . Therefore we might conclude a  $\delta R$  of  $58\text{m}$  which implies  $Nf_{rot} \approx 70.4\text{Hz}$ . Since a Dash8 turboprop has six bladed engines, this predicts a rotation rate of  $704\text{RPM}$ . This seems to be about a half of what it should be (around  $1500\text{RPM}$ ). However, this result is consistent with the blade flash observations presented in fig 3.29

constructed as an extension to the Classical HRR theory described in section 2.2.1.

Using the same notation as in 2.2.1, a residual modulation of the (Doppler filtered) receiver samples by frequency  $jNf_{rot}$  (where  $j \in \mathbb{Z}$  is the modulation line number,  $N$  is the number of propeller blades and  $f_{rot}$  is the engine rotation frequency) will result in a modification of the ‘target sample’ for frequency step  $q$ .

$$\psi_q \rightarrow \psi_q e^{-2\pi i j N f_{rot} \frac{(G+P)}{f_{PRF}} (q-1)} \quad (4.1)$$

i.e. an additional phase shift of magnitude  $2\pi i j N f_{rot} \frac{(G+P)}{f_{PRF}}$  during inter-burst period  $\frac{(G+P)}{f_{PRF}}$ . Recall  $P$  is the number of pulses per burst used in Doppler processing and  $G$  is the number of guard pulses.

Following the same argument as in 2.2.1, one arrives at a modified expression for  $\psi_q$

$$\psi_q = \psi_0 e^{-\frac{4\pi i R_T (f_1 - \Delta f)}{c} + 2\pi i j N f_{rot} \frac{(G+P)}{f_{PRF}}} e^{\left[-\frac{4\pi i R_T \Delta f}{c} - 2\pi i j N f_{rot} \frac{(G+P)}{f_{PRF}}\right] q} \quad (4.2)$$

i.e. the impact of the propeller modulation in the term  $e^{[\dots]q}$  is the transformation

$$\frac{R_T \Delta f}{c} \rightarrow \frac{R_T \Delta f}{c} + \frac{j N f_{rot} (G+P)}{2 f_{PRF}} \quad (4.3)$$

Let us compute the Discrete Inverse Fourier Transform <sup>8</sup> (DIFT) of these samples to generate a  $Q$  component vector with elements  $\{y_n\}$ . For a derivation of the last step, see the Appendix C.

$$y_n = \frac{\psi_0}{Q} e^{-\frac{4\pi i R_T (f_1 - \Delta f)}{c} + 2\pi i j N f_{rot} \frac{(G+P)}{f_{PRF}}} \sum_{q=1}^Q e^{\frac{2\pi i (q-1)(n-1)}{Q} - 4\pi i \left(\frac{R_T \Delta f}{c} + \frac{j N f_{rot} (G+P)}{2 f_{PRF}}\right) q} \quad (4.4)$$

$$= \frac{\psi_0}{Q} e^{-\frac{4\pi i R_T (f_1 - \Delta f)}{c} + 2\pi i j N f_{rot} \frac{(G+P)}{f_{PRF}}} - \frac{2\pi i (n-1)}{Q} \sum_{q=1}^Q e^{\frac{2\pi i q}{Q} \left(n-1 - 2Q \left(\frac{R_T \Delta f}{c} + \frac{j N f_{rot} (G+P)}{2 f_{PRF}}\right)\right)} \quad (4.5)$$

$$= \frac{\psi_0}{Q} e^{-\frac{4\pi i R_T (f_1 - \Delta f)}{c} + 2\pi i j N f_{rot} \frac{(G+P)}{f_{PRF}}} - \frac{2\pi i (n-1)}{Q} \left( \frac{e^{ix} \sin \left\{ \left(1 + \frac{1}{Q}\right) x \right\}}{\sin \left(\frac{x}{Q}\right)} - 1 \right) \quad (4.6)$$

where  $\frac{x}{\pi} = n - 1 - 2Q \left(\frac{R_T \Delta f}{c} + \frac{j N f_{rot} (G+P)}{2 f_{PRF}}\right)$ . If range cells are defined

$$R(n) = \frac{c}{2Q\Delta f} (n - 1)$$

then

$$\begin{aligned} x(n) &= \pi \left( \frac{2Q\Delta f}{c} R(n) - 2Q \left( \frac{R_T \Delta f}{c} + \frac{j N f_{rot} (G+P)}{2 f_{PRF}} \right) \right) \\ &= \frac{2\pi Q\Delta f}{c} \left( R(n) - R_T - \frac{j c N f_{rot} (G+P)}{2 f_{PRF} \Delta f} \right) \end{aligned}$$

i.e. we should anticipate aliasing of the range profile at integer intervals<sup>9</sup> of

$$\delta R = \frac{c N f_{rot} (G+P)}{2 f_{PRF} \Delta f} \quad (4.7)$$

<sup>8</sup> A Discrete Inverse Fourier Transform (DIFT) is a linear filter of the form  $y_n = \sum_{q=1}^Q w_{n,q} \psi_q$  where  $\{\psi_q\}$  are the set of signal samples and  $w_{n,q} = \frac{1}{Q} e^{\frac{2\pi i (q-1)(n-1)}{Q}}$  are the filter weights.

<sup>9</sup> bounded by the maximum of JEM lines constrained by the JEM bandwidth defined in equation 2.51.

## 4.4 Target classes based on scalar HRR profile features

Analysis of classification performance using features obtained from HRR profiles was conducted using four sets of classes and (scalar) features. Given the aircraft type is known for all data recordings discussed in this thesis, one can assign a ‘truth’ classification for each aircraft type. The ‘Long or Short’ and ‘Four lengths’ truth classifications are determined using a physical length measure obtained from plan drawings of each aircraft. In all the examples discussed below, the wingspan has been used as this measure.<sup>10</sup>

### 4.4.1 Long or short (length)

Length measurement, based upon the range extent of the HRR profile exceeding a threshold defined to be a fixed number of decibels below the profile maximum power, is used to discriminate between two broad classes of aircraft ‘Long’ or ‘Short’. Note the Long class boundary is set to be below the HRR window for the 3.2MHz chirps (47m); i.e. we would expect all stepped frequency waveforms discussed in this thesis to be able to be used to enable ‘Long or Short’ class distinction.

Radar length	Class
< 30m	Short
$\geq$ 30m	Long

### 4.4.2 Four lengths (length)

Length measurement is used to discriminate between four broad classes: ‘Very Short’ (VS), ‘Short’ (S), ‘Long’ (L) and ‘Very Long’ (VL). The VL category takes advantage of the extended range capability of the 0.8MHz and Hybrid processed waveforms.

Radar length	Class
< 10m	VS
$\geq$ 10m, < 30m	S
$\geq$ 30m, < 50m	L
$\geq$ 50m	VL

### 4.4.3 Pod vs Falcon (SCM compare)

Pod and Falcon aircraft are compared using the ‘scattering center barcode matching’ algorithm discussed in section 2.5.5. Classes are aircraft type, e.g. Pod or Falcon.

### 4.4.4 Six aircraft types (SCM compare)

The six aircraft are compared using the ‘scattering center barcode matching’ algorithm discussed in section 2.5.5. Classes are aircraft type i.e. Pod, Falcon, Dash8, B747, B757 or B777.

---

<sup>10</sup>This option was set based upon the assumption that wingtip scatterers would be visible regardless of the aspect of the aircraft. Rather than attempting to scale the length measurement by the reciprocal of the cosine of the aspect angle (which  $\rightarrow \infty$  for the tangential case), the length measurement could be used as-is for all angles. In the case of the 747 (wingspan 59.6m and length 70.6m), one would therefore expect an underestimate for inbound trajectories. For the broad classifications discussed (long or short, four lengths), this makes no difference. However, for type classifications (used in conjunction with Doppler spectra features in Chapter 7), possible improvements could be made if the actual physical length is used. For example, this would enable better discrimination between the B777 and the B747. Their wingspans are equivalent (within a metre) but their lengths differ by over 10m.



## 4.5 Variation of length feature measurements

A qualitative assessment of likely (Long or Short, Four lengths) classification performance can be made by plotting the length feature measurements against overall target range<sup>11</sup>; i.e. if the feature data visually separates into classes, then high performance classification should be expected if the (*a priori* or ‘Expert’) inputs of the classifier are suitably tuned to reflect this natural segmentation.

Figures 4.5, 4.7, and 4.6 show these measurements of the six aircraft types using a below maximum length threshold of 20dB. In each figure the features obtained using Waveforms A, B & C (Classical processing) and Waveform A (Hybrid processing) are compared. Each figure displays the same measurements but the colour coding (based upon the truth classification) is different. Observations are the following:

1. As expected, the 47m length limit imposed by the 3.2MHz Classically processed waveforms cause a continuum of measurements above 30m for the B747, B757 and B777 aircraft, whereas a noticeable separation is observed for the Hybrid and 0.8MHz results.
2. The Pod and Falcon aircraft yield visually separable lines for all waveforms. Waveform C yields the most robust measurements, followed by Waveform A (Classical), Waveform A (Hybrid)<sup>12</sup> and then Waveform B. This is roughly consistent with the hierarchy of range resolutions associated with each waveform and the observation that the Hybrid method offers  $\approx 5$ dB less signal to noise ratio than its Classical equivalent.
3. The Dash8 aircraft, although less than 30m, yields length features which are comparable with the longer Boeing aircraft. These are considerably variable with Waveform B. One would therefore expect the Dash8 features to be misclassified on the basis of length and therefore degrade any overall classification performance. In the Appendix, (and fig 4.3) the Dash8 target data sheets for the 0.8MHz and Hybrid waveforms can explain these results. In both examples we see significant range sidelobes (above -20dBm) which extend the range artificially. After about 30 looks the cumulative (0.8MHz) profile appears to stabilize on a more reasonable length ( $\approx 25$ m), whereas the Hybrid profile (with only 8 looks) yields a value of around 50m. The range sidelobes can clearly be seen in the Hybrid profile, where a much larger (160m) range window is used. One may conjecture that the range sidelobes are due to the effects of lower frequency propeller modulations which are not effectively suppressed using the 8 pulse Doppler filter employed for both waveforms. Note the 0.8MHz result is additionally degraded by a change of aspect from  $\approx 20^\circ$  to a maximum of  $100^\circ$  (and back) between looks 20 and 28. The disappearance of the range profile in the Dash8 example can be explained by the use of the start alignment method, as discussed in the second section of this chapter.
4. Both 0.8MHz and Hybrid results demonstrate significant variability in the non Falcon & Pod results. Although one may expect acceptable Long or Short classification (Hybrid seems superior to 0.8MHz in this example), one might not expect clear distinctions between L and VL classes in the Four Lengths decomposition.

<sup>11</sup>i.e. the range of the target in km at the time of the first pulse of the waveform.

<sup>12</sup>If the effect of obvious outliers can be discounted. This analysis is based upon visual distribution rather than the mean and standard errors quoted in the figures.

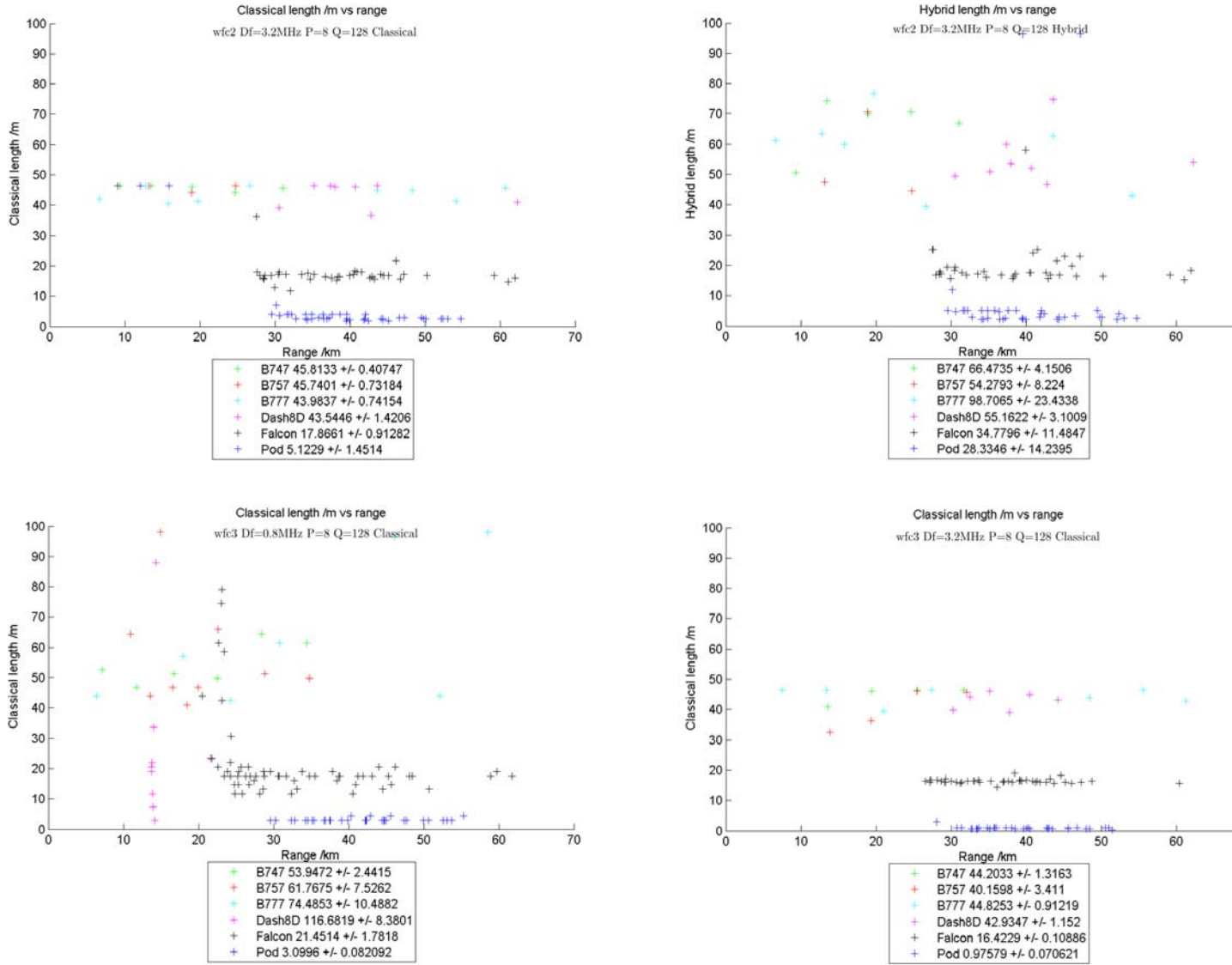


Figure 4.5: Target length feature vs range of target computed from HRR profiles using a below maximum threshold of 20dB. Each graph represents a different waveform. In this example, features are colour coded by aircraft name. The visual distribution of feature measurements (mean and standard errors are given in the legend) is a strong indicator of likely Classification performance. In this case Pod & Falcon aircraft have distinct, fairly stable lengths. This is not true of the other aircraft, hence one would predict poor overall classification performance.

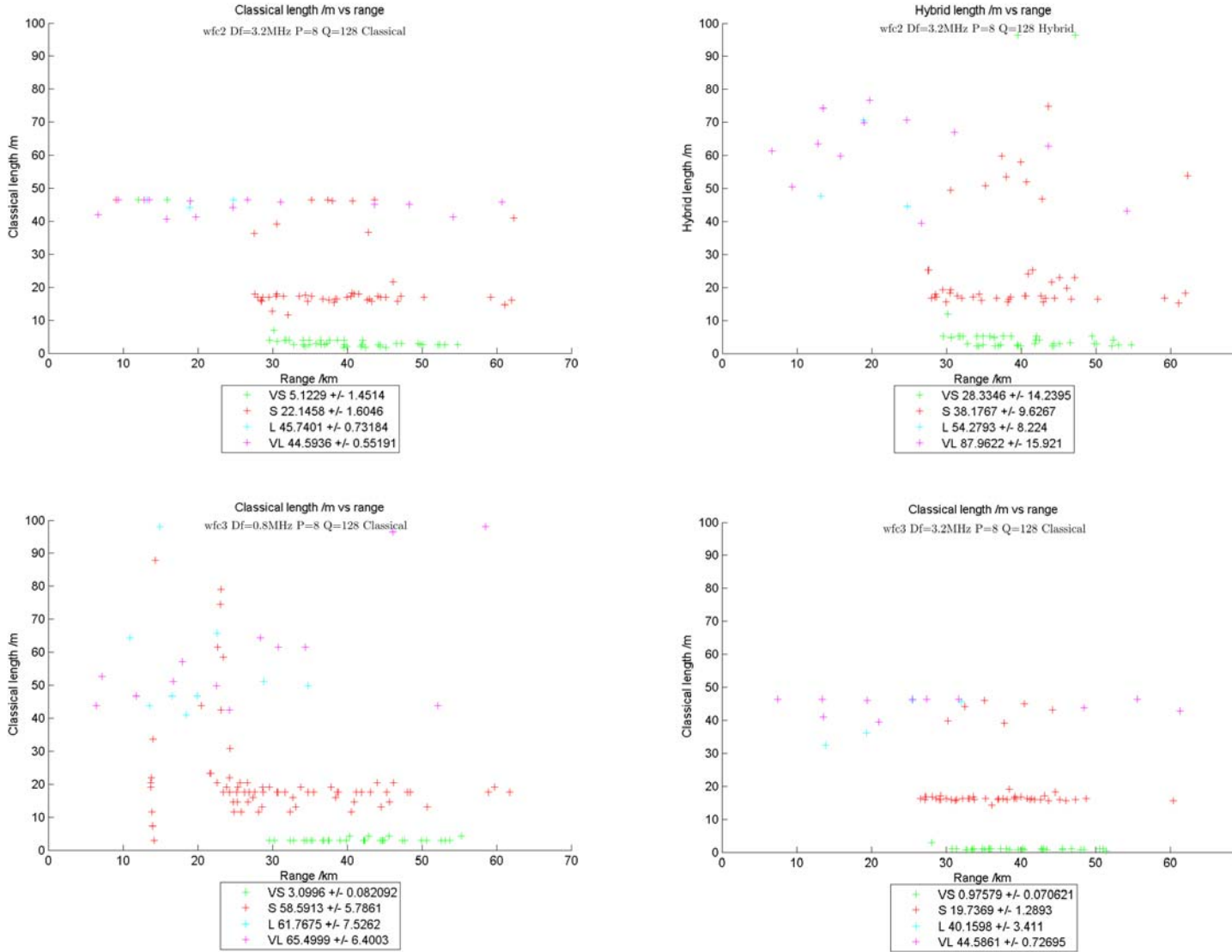


Figure 4.6: Target length feature vs range of target computed from HRR profiles using a below maximum threshold of 20dB. Each graph represents a different waveform. In this example, features are colour coded by one of four lengths. The visual distribution of feature measurements (mean and standard errors are given in the legend) is a strong indicator of likely Classification performance. In this case VS and S aircraft have distinct, fairly stable lengths. L & VL are less distinct. Note the Classical 3.2MHz maximum length of  $\frac{c}{2\Delta f} = 47\text{m}$  causes many of the L and VL aircraft to be set at this level. Hence the wfc2 Hybrid and wfc3 0.8MHz graphs are the only graphs which can offer useful L and VL measurements.

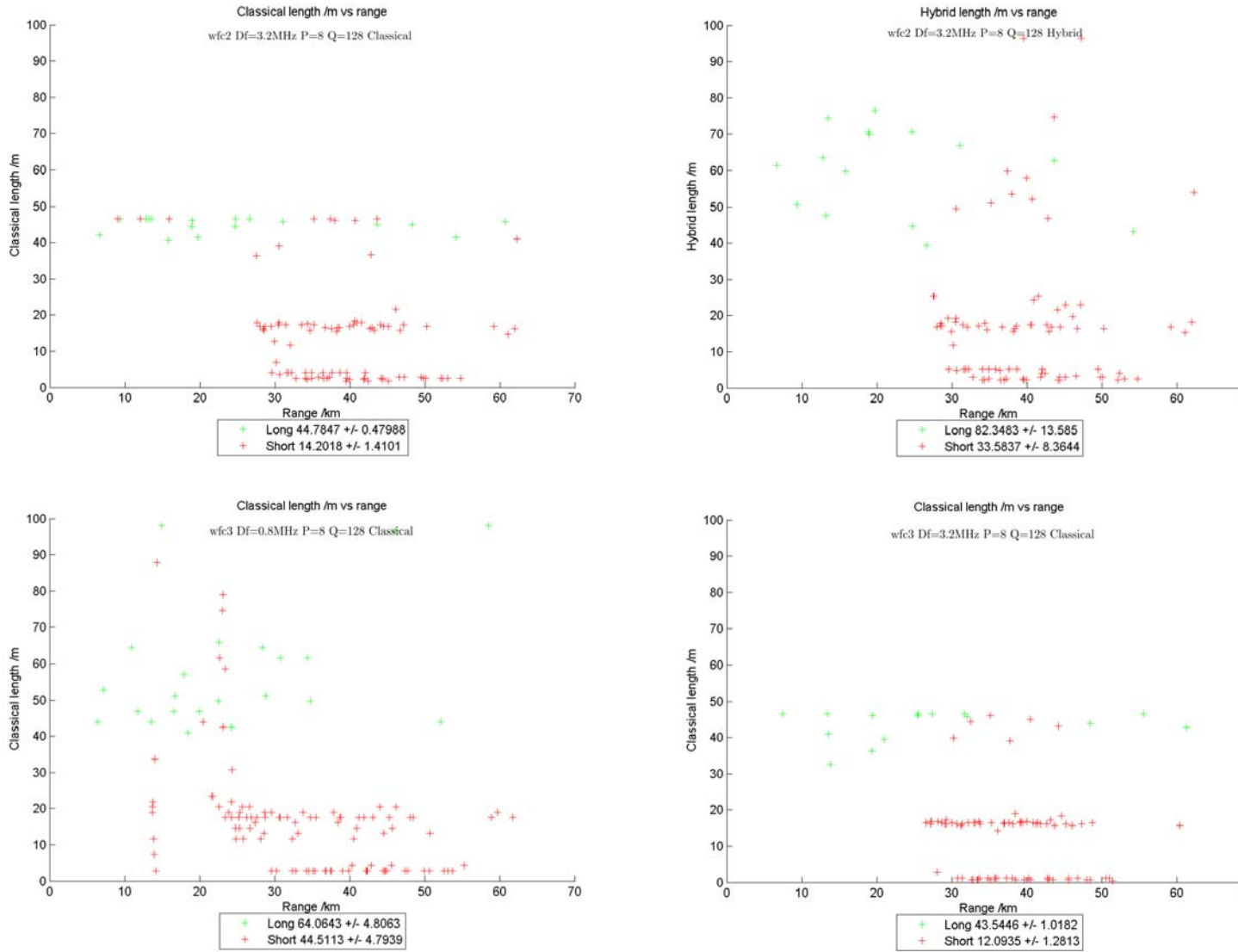


Figure 4.7: Target length feature vs range of target computed from HRR profiles using a below maximum threshold of 20dB. Each graph represents a different waveform. In this example, features are colour coded as Long or Short. The visual distribution of feature measurements (mean and standard errors are given in the legend) is a strong indicator of likely Classification performance. In this case we would expect low, but not zero, classification errors between classes due to the overlap between the data in a number of cases plus a number of obvious outliers.

## 4.6 Classification performance via range profiles of six aircraft

Bayesian and Fuzzy logic classifiers (see Background theory chapter sections 2.6.2 and 2.6.3) are used to assign Long or Short and Four Lengths classes to particular length feature measurements. These classifiers are trained using pre-determined ‘expert’ parameters which characterize the (respective) probability density or membership functions for each class as shown in figures 2.18 and 2.19. For the Bayesian classifier, the probability density functions are defined to be Gaussian distributions with means  $\mu$  and standard deviations  $\sigma$  as described in the tables below. (All length measurements are metres). The values assigned for  $\mu$  and  $\sigma$  for each class are motivated by the broad definitions above; i.e. they are ‘sensible guesses’ rather than parameters derived from the statistics of a training data set.<sup>13</sup> The standard deviation of 10m is set to reflect both the expected variations of feature measurements within each class (which could be estimated from figures 4.5, 4.7, & 4.6 ) and the variety of the actual aircraft lengths within each class.

Class	$\mu$	$\sigma$
Short	20	10
Long	50	10

Class	$\mu$	$\sigma$
VS	0.1	10
S	20	10
L	40	10
VL	50	10

Figures 4.8 and 4.9 represent a montage of bar charts and confusion matrices by waveform type for, respectively, Long or Short and Four Lengths classes. As predicted by the qualitative analysis of the features in the previous section, one can clearly observe clear distinctions between the Long or Short and VS, S, L/VL classes. However, there is significant misclassification of the L class as VL. In fig 4.10 the Scattering center Model (SCM) compare algorithm yields perfect classification of the Pod & Falcon data for Waveforms B & C and Off Diagonal Extents  $\xi$  (ODE) of 0.1 for the Waveform A data. However, this algorithm gives poor performance against the six aircraft data set as shown in fig 4.11. This observation may be explained by the variability of HRR profiles from look to look as evidenced in the target data sheets in the Appendix. The cumulative (aligned) set of HRR profiles indicates that an averaging of eight or more profiles, assuming aspect angle stability, may yield a more robust set of scattering center positions. In this thesis there are insufficient measurements to back up this claim. However, positive results using this approach have been published. (Zyweck & Bognor [118], Miller *et al* [71]). In [71]  $\xi$  values of below 0.1 are obtained for three aircraft classes, albeit using actual range profiles to derive the scattering center models. When "non Radar referents" (i.e. a scattering center model derived from aircraft plan views) were used,  $\xi$  values rise to 0.58, which is similar to the values computed here for six aircraft. Miller *et al* suggest the over emphasis of the tail scatterer (which may be obscured) is a possible factor. Indeed ignoring the tail scatterer lowered the  $\xi$  to 0.32.

Classification performance based on length and SCM features is summarized in figures 4.13, 4.14 and 4.12. In each case (which represents a different set of target data),  $\xi$  values are plotted against

<sup>13</sup>If a training data set were used then the  $\mu$  and  $\sigma$  parameters for each class would be computed directly from the data using the Friedman Regularized Discriminant method described in the Background Theory chapter.

waveform type for a variety of classifier. The following observations and inferences can be taken:

1. Bayesian and Fuzzy logic classifiers appear to offer very similar classification performance. This is not surprising given the form of the fuzzy membership functions (see fig 2.6.3) were designed to match those of the Bayesian probability density functions.
2. Long or Short classification is on average around 0.1, Four Lengths around 0.3 and SCM compare around 0.5 to 0.6. Outbound data adds around 0.1 to  $\xi$  and waveform choice can modify the result by a similar amount. This is most significant in the outbound example for the 0.8MHz Waveform B, which offers a 0.2 reduction in  $\xi$ . One may conjecture that the nose scatterer may be partially obscured in the outbound result, therefore yielding length measurements which are more variable than the inbound case. Due to the competing virtues of superior range resolution and sidelobe level of waveform C, and extended range of waveforms B and (Hybrid processed A), it is not clear at this level of analysis whether any one waveform offers the most overall benefit. We may conclude from this that an adaptive approach may be desirable. The length of an aircraft could be measured initially with a Hybrid 3.2MHz or Classical 0.8MHz waveform. If the measured length was less than, say, 40m (i.e. the 3.2MHz window minus a safety factor) one could switch to Waveform C.
3. Due to the modest data set, no averaging of HRR profiles was conducted prior to feature extraction.

In summary, Long or Short classification is high performance<sup>14</sup>, Four Lengths classification is viable but in need of optimization and SCM compare classification is poor (for six aircraft).

---

<sup>14</sup>One could quote 90% performance as a rough statistic, based upon the value of  $100 \times (1 - \xi)$

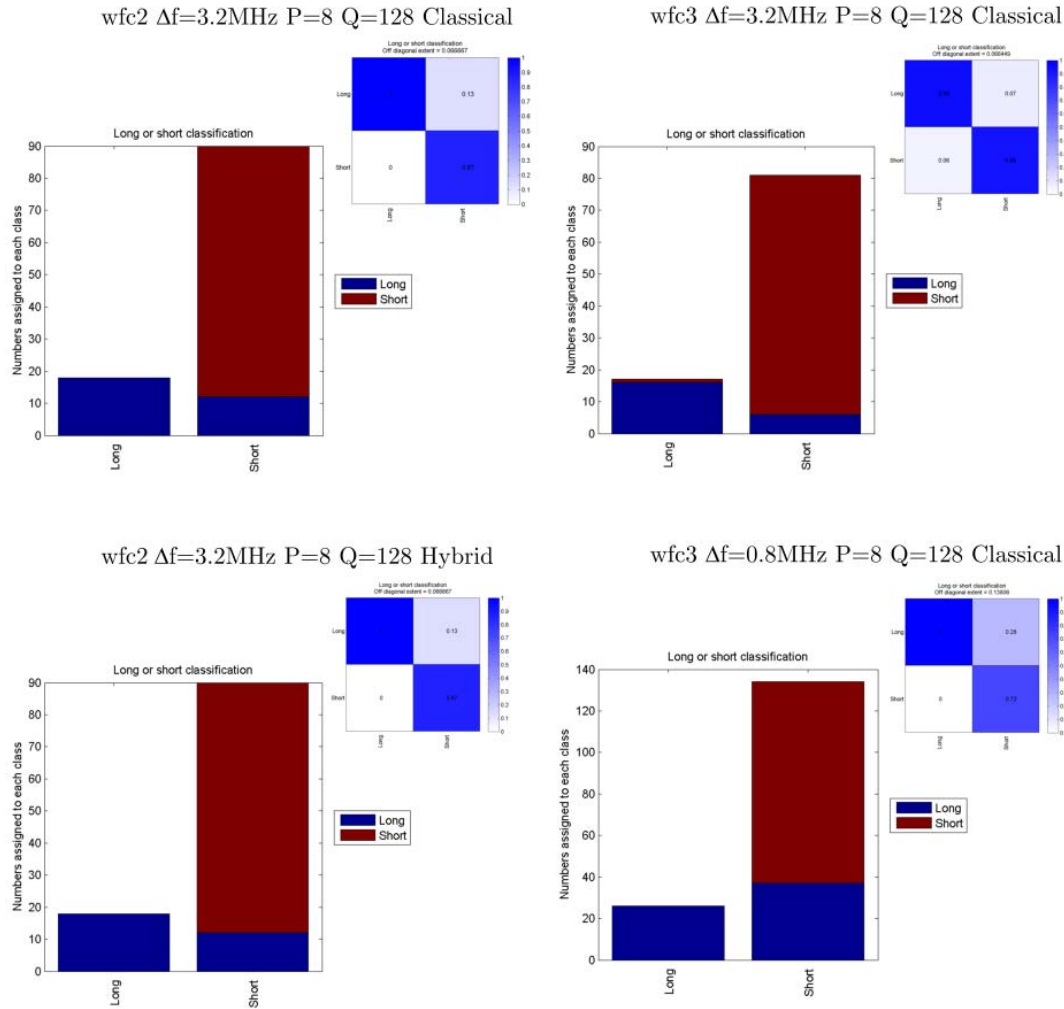


Figure 4.8: Long or Short classification of range profiles obtained from six different aircraft types, using waveforms A,B,C (Classical processing) and Waveform A (Hybrid processing). The bar charts show the absolute number of range profiles classified whereas the chequerboard above represents the associated confusion matrix (from which the off diagonal extent metric  $\xi$  is computed). The horizontal labels in both cases correspond to the asserted classification from knowledge of physical length; e.g a Falcon is Short and a 747 is Long. The bar charts and the columns of the confusion matrix describe the assignments of the classifier for each of these known results. If the confusion matrix has off diagonal elements, or the bar chart multi-coloured columns, this implies errors in classification.

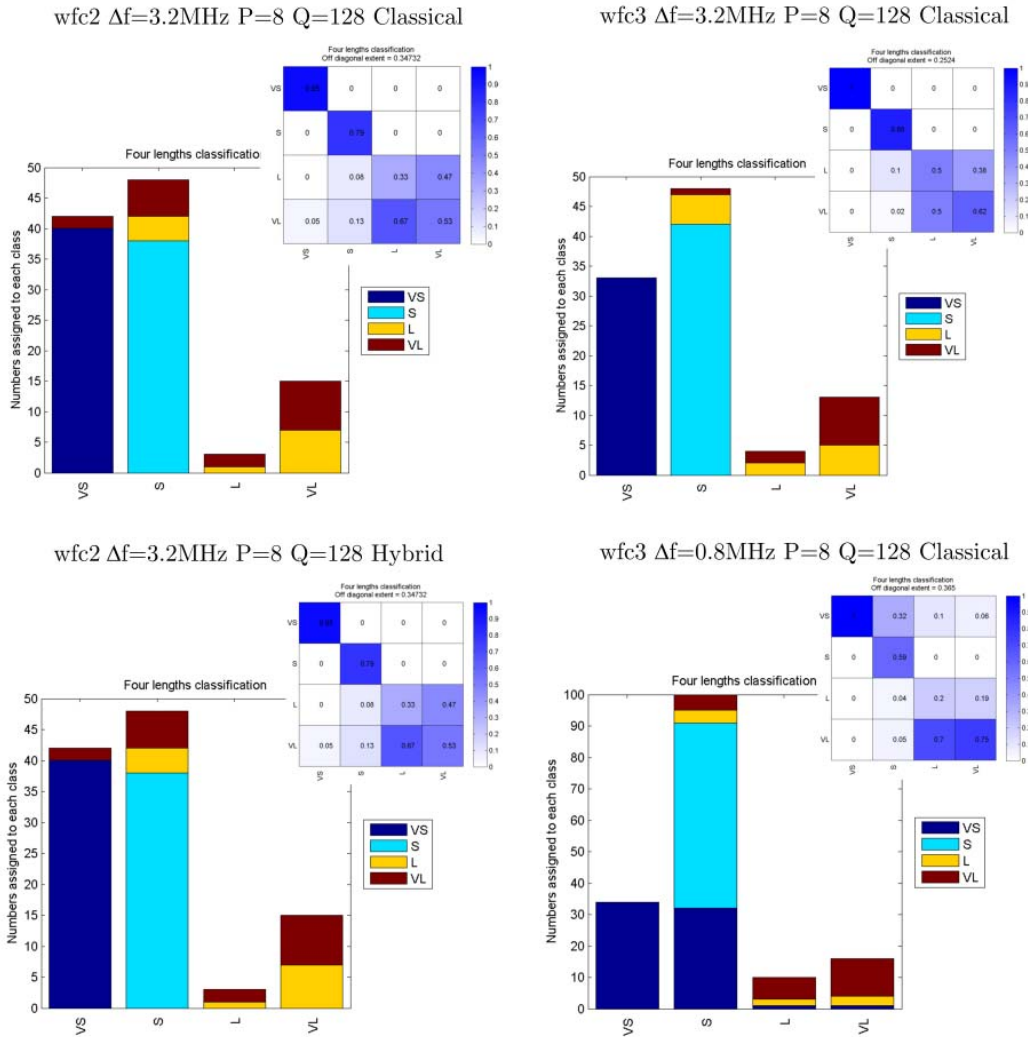


Figure 4.9: Four lengths classification of range profiles obtained from six different aircraft types, using waveforms A,B,C (Classical processing) and Waveform A (Hybrid processing). The bar charts show the absolute number of range profiles classified whereas the chequerboard above represents the associated confusion matrix (from which the off diagonal extent metric  $\xi$  is computed). The horizontal labels in both cases correspond to the asserted classification from knowledge of physical length; e.g a Pod is Very Short (VS) and a 747 is Very Long (VL). The bar charts and the columns of the confusion matrix describe the the assignments of the classifier for each of these known results. If the confusion matrix has off diagonal elements, or the bar chart multi-coloured columns, this implies errors in classification.



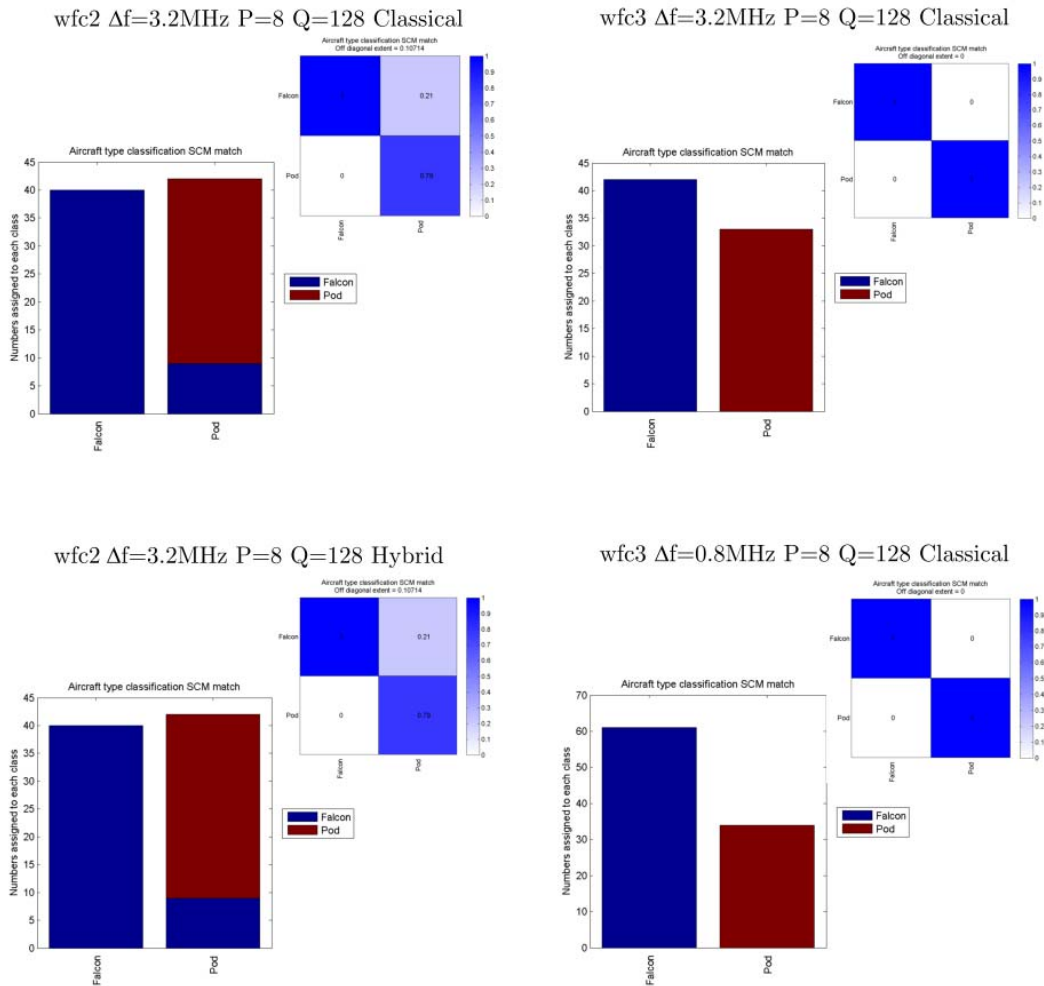


Figure 4.10: Pod or Falcon SCM classification using waveforms A,B,C (Classical processing) and Waveform A (Hybrid processing). The bar charts show the absolute number of range profiles classified whereas the chequerboard above represents the associated confusion matrix (from which the off diagonal extent metric  $\xi$  is computed).

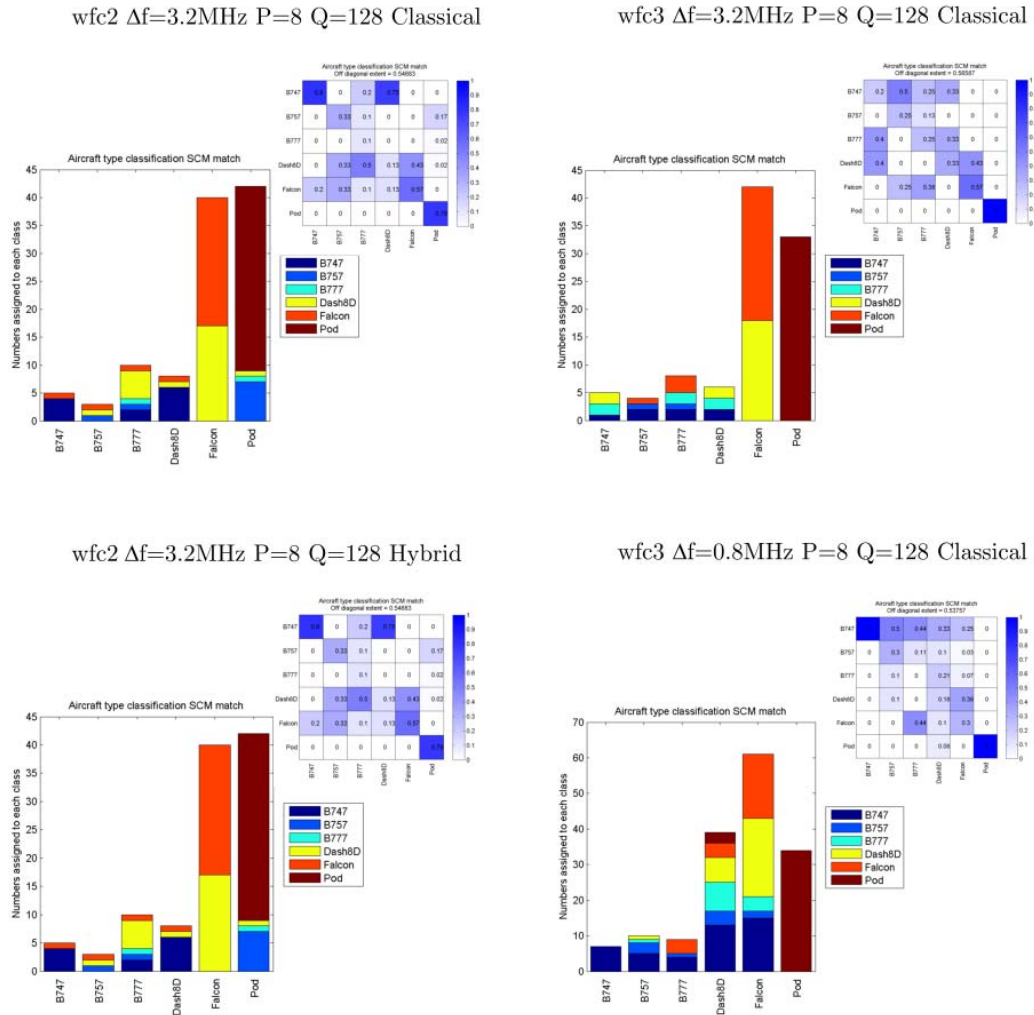


Figure 4.11: Scattering Centre Model (SCM) comparison classification obtained for six different (inbound) aircraft types, using waveforms A,B,C (Classical processing) and Waveform A (Hybrid processing). The bar charts show the absolute number of range profiles classified whereas the chequer-board above represents the associated confusion matrix (from which the off diagonal extent metric  $\xi$  is computed). The horizontal labels in both cases correspond to the actual aircraft types. The bar charts and the columns of the confusion matrix describe the assignments of the classifier for each of these known results. If the confusion matrix has off diagonal elements, or the bar chart multi-coloured columns, this implies errors in classification.

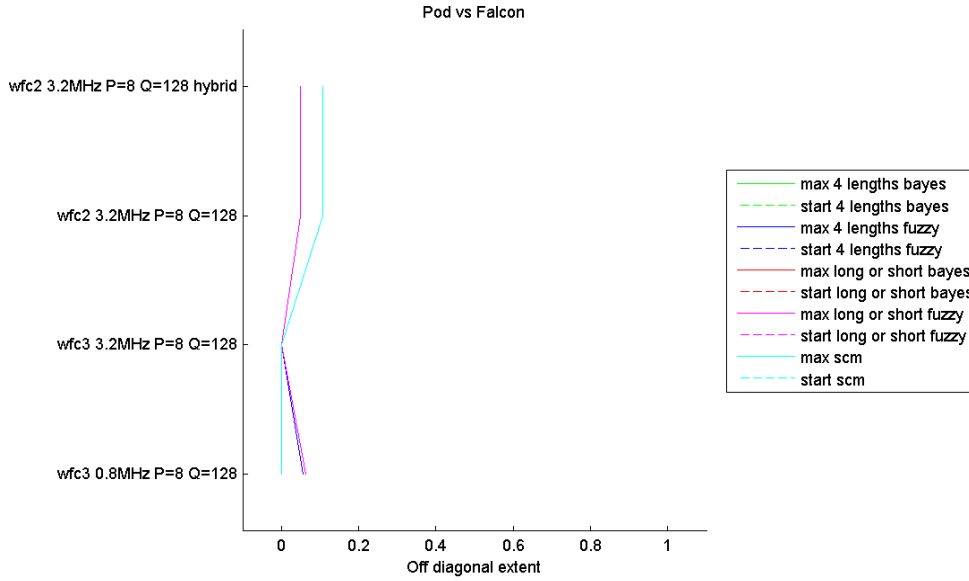


Figure 4.12: Classification performance (metricated by the off diagonal extent  $\xi$  of the class confusion matrix) using Pod & Falcon recordings for waveforms A,B,C (Classical processing) and Waveform A (Hybrid processing). Four Lengths, Long or Short & Scattering Centre Compare classification schemes are compared. ‘Max’ and ‘Start’ range alignment methods and Bayesian & Fuzzy Logic classifiers are compared.

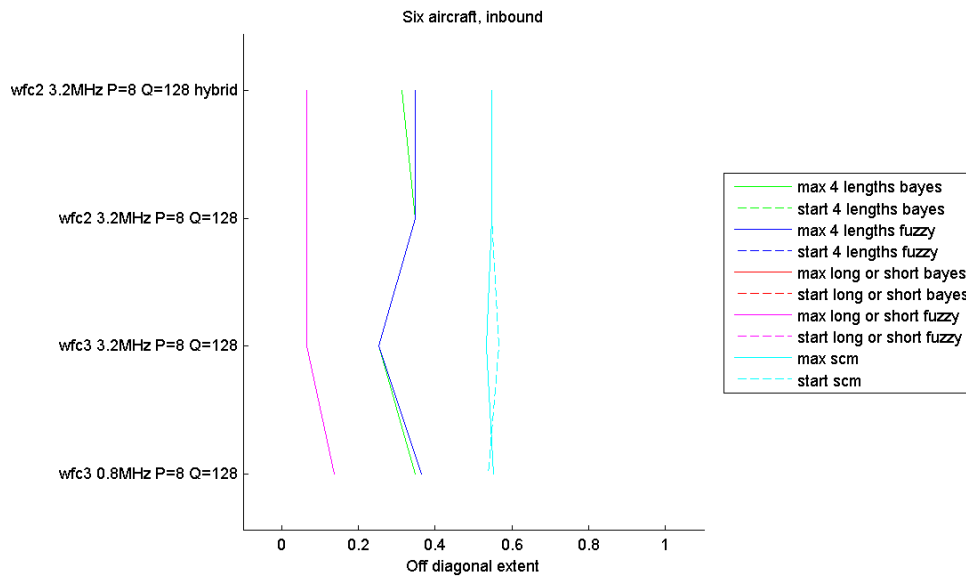


Figure 4.13: Classification performance (metricated by the off diagonal extent  $\xi$  of the class confusion matrix) using inbound Pod, Falcon, B747, B757, B777 & Dash8 recordings for waveforms A,B,C (Classical processing) and Waveform A (Hybrid processing). Four Lengths, Long or Short & Scattering Centre Compare classification schemes are compared. ‘Max’ and ‘Start’ range alignment methods and Bayesian & Fuzzy Logic classifiers are compared.

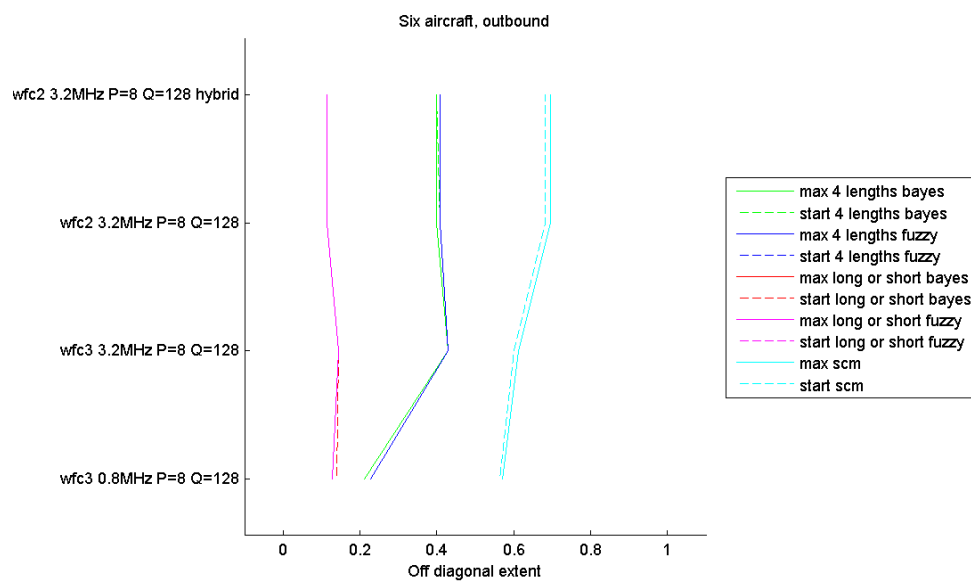


Figure 4.14: Classification performance (metricated by the off diagonal extent  $\xi$  of the class confusion matrix) using inbound Pod & Falcon + outbound B747, B757, B777 & Dash8 recordings for waveforms A,B,C (Classical processing) and Waveform A (Hybrid processing). Four Lengths, Long or Short & Scattering Centre Compare classification schemes are compared. ‘Max’ and ‘Start’ range alignment methods and Bayesian & Fuzzy Logic classifiers are compared.

## 4.7 Conclusions

Let us summarize the results presented in this chapter in the form of answers to the second and third key questions posed in the introductory chapter.

2. *How robust are feature measurements taken from the trials data set? Do feature measurements naturally segment into classes? Should certain features be combined, are they correlated?*

- Depending on processing method, length measurement errors varied (for the Falcon) between 0.1 and 11.5m, with the latter (using the Hybrid technique) distorted by outliers. Excluding outliers, errors of 2m are reasonable. (See fig 4.5). The average Radar length measurement of the Falcon aircraft matches, within the measurement errors, its physical length of 17.2m.
- Fig 4.5 demonstrates a significant variability in length measurements of the targets of opportunity, as might be expected from (i) the limited number of looks and (ii) variations in aspect angle.
- With the exception of Pod & Falcon data, the length measurements of aircraft do not naturally segment into aircraft type classes. However figures 4.7 and 4.6 demonstrate a good degree of segmentation into ‘Long’ and ‘Short’ classes and a moderate degree of segmentation into Four Length classes.<sup>15</sup>
- Length measurements of Dash8 aircraft are often erroneously high. (As measured using the Hybrid 3.2MHz waveform A and Classical 0.8MHz waveform B). The likely cause are high range sidelobes resulting from low frequency propeller modulations which penetrate the Doppler filter. Modelling suggests ‘propeller aliases’ of the target HRR profile occur at integer intervals of  $\delta R = \frac{cNf_{rot}(G+P)}{2f_{PRF}\Delta f}$ .
- Variation of target Radar Cross Section derived from range profiles were so variable for the measured data (around 20dB) as to be unhelpful as a feature measurement. Further work is required to understand why these RCS measurements should be so variable (see Recommendations).

3. *Can we achieve acceptable classifier performance based upon the extraction of various target features? How does the crudeness of class definition affect this result and how does performance depend upon (i) the proportion of total pulse cycles used to form the target data set (ii) thresholds used in feature measurement and (iii) the features used (and their possible combination) ?*

- ‘Long or Short’ classification of length feature measurements from six aircraft types yielded a confusion matrix off diagonal extent  $\xi$  of 0.1; i.e. high performance classification. Four lengths classification was more moderate (largely due to the misclassification of Long and Very Long classes) with a  $\xi$  of 0.3.
- Scattering Center Model (SCM) compare classification of Pod & Falcon was nearly perfect, but performance was poor ( $\xi \approx 0.6$ ) using all six aircraft classes.
- In all cases, Bayesian and Fuzzy logic classifiers (based upon ‘expert’ pre-defined probability density or membership functions) yielded consistent results as expected.

---

<sup>15</sup>Visual inspection seems to indicate three classes might be preferable to four. This is exemplified by the regular misclassification of L and VL classes.

## Chapter 5

# Range-Doppler profiling & Doppler spectra classification

### 5.1 Chapter summary

Classification of targets into No Non Skin Doppler (NNSD), Jet engine and Propeller classes is described using the *Doppler fraction* (dfrac) scalar feature obtained using waveforms D & E. For the inbound subset of the six aircraft under investigation, Bayesian and Fuzzy logic classifiers yield relatively high (and similar) performance results.<sup>1</sup> (A confusion matrix with an Off Diagonal Extent (ODE)  $\xi$  of below 0.2). Outbound data results in lower performance ( $\xi \approx 0.5$ ), a result which is consistent with full or partial obscuration of the rotating parts when viewed from the rear.

Up to this point we have considered methods of classification based upon features extracted from, respectively, High Range Resolution profiles and Doppler spectra. In this chapter we consider the feasibility of generating a range-Doppler image, i.e. combining these two ‘dimensions’. A benefit of this approach is the possibility of range localization of jet engines. However, stepped frequency waveforms cause a range-Doppler coupling effect; a JEM line of frequency  $f_{JEM}$  will be shifted in range by  $\delta R = \left(\frac{c}{2\Delta f}\right) \left(\frac{f_{JEM}P}{f_{PRF}}\right)$  where  $P$  is the number of pulses per burst,  $f_{PRF}$  is the PRF and  $\Delta f$  is the frequency step. This formula allows for JEM peaks in the range-Doppler profile to be shifted to the correct range if  $f_{JEM}$  is known unambiguously. Unfortunately this is typically unlikely to be the case since the PRF is often significantly less than the JEM bandwidth. (See section 2.4.2). A potential solution is to transmit two Doppler waveforms in quick succession using a PRF multiplied by an irrational number<sup>2</sup> such as  $\sqrt{2}$ . Comparison of the JEM lines ‘folded out’ by integer multiples of the PRF should yield the true value of  $f_{JEM}$ .

The chapter concludes with a comparison of measured Range-Doppler profiles of Boeing 777 and Dash8 aircraft with corresponding aircraft plan views. The latter are rotated by measured aspect angle and aligned with the first threshold crossing of the range profile. These Jet Engine and Propeller class examples describe two distinct manifestations of the stepped frequency range-Doppler coupling effect.

---

<sup>1</sup>In this chapter, the difference between ‘Prop’ class fuzzy membership and corresponding Gaussian PDF appears to make little difference to the overall classification performance. However, a noticeable difference is apparent when Prop, JEM or NNSD classification performance is evaluated for different number of pulses  $P$  per burst and different dfrac thresholds. This result is presented and discussed in the following chapter.

<sup>2</sup>An irrational number such as  $\sqrt{2}$  cannot be expressed as a fraction of integers, therefore the only possible alignment of (folded out) JEM lines is when the frequencies match the unambiguous value.

## 5.2 Prop, JEM and NNSD classes discriminated by the dfrac feature

Waveforms D & E offer 32 pulses per burst with a PRF of 2.5kHz. These are sufficient to generate Doppler power spectra from which discriminating characteristics can be obtained.<sup>3</sup>. The dfrac feature (see section 2.5.6) is used with a 25dB below maximum threshold. This value was chosen following initial inspection of a limited selection of Doppler spectra. In the following chapter classification performance is determined as a function of this threshold. Therefore at this point we should regard the figure of 25dB as semi-arbitrary rather than an optimal value, chosen merely to enable the methodology of classification via Prop, JEM or NNSD classes to be demonstrated by practical example.

The dfrac feature aims to discriminate between No Non Skin Doppler (NNSD) profiles, exemplific of targets without rotating elements, and targets with jet engines or propellers. In essence, a target with no moving parts should have a single ‘skin’ Doppler spectrum peak at 0Hz if bulk motion compensation is accurate. Any additional peaks are sidelobes resulting from the finite length of the Discrete Fourier Transform which constitutes the mathematical machinery of the Doppler filter<sup>4</sup>. As discussed in the Background theory chapter, one expects a number of distinct peaks in the spectra of a jet aircraft which result from Jet Engine Modulation. At the PRFs used one expects these peaks to be ambiguous; i.e. direct measurement of the JEM spacing will not yield the product of spool rate and number of blades. However, one should nonetheless expect a ‘spiky’ profile away from the skin return. As discussed in the Background theory section, propellers tend to cause a lower frequency modulation than jet engines (a combination of a smaller numbers of blades, lower spool rates and consequently lower airspeeds). The relatively small numbers of distinct blades (two for example) also means there will be a more significant modulation in reflectivity during each cycle of the propeller rotation. This amplitude modulation can cause a broadening of the Doppler spectra about the skin return. We can summarize these qualitative observations of Doppler spectra structure as follows:

Class	Qualitative description of spectra	dfrac
Prop	Continuum, or at least broad about 0Hz	Near unity
JEM	Spiky, i.e. a number of JEM peaks beyond skin return	<1, > 0
NNSD	Single peak at 0Hz	$\approx 0$

With this in mind, let us define mean and standard deviations of Bayesian classifier probability density functions (PDFs) for NNSD, JEM and Prop classes as follows.

Class	$\mu$	$\sigma$
Prop	0.7	0.1
JEM	0.4	0.2
NNSD	0.01	0.2

The actual PDFs are plotted in fig 5.2. Alternatively, let us define fuzzy membership functions (see fig 5.1) based along similar class distinctions. The shape of both fuzzy logic and Gaussian PDFs are defined as a ‘sensible guess’ based on the qualitative spectral descriptions above in conjunction with inspection of a plot of dfrac vs range (fig 5.3) for all the target measurements which are described

<sup>3</sup>Variation of dfrac classification performance with number of pulses shall be discussed in the following chapter. In this Chapter we use the maximum number for the MESAR2 trials data (which yields the most accurate resolution, which equals the PRF divided by the number of pulses).

<sup>4</sup>The length of the DFT being the number of pulses per burst.

in the following section.<sup>5</sup> An investigation of whether these initial definitions are typical, or indeed optimal, is beyond the scope of this thesis. As discussed in the previous chapter, the limited amount of observations has forced a decision to opt for an ‘expert’ classifier (rather than one whose discriminant functions are derived from training data) to enable a meaningful classification analysis to be conducted. An obvious recommendation from this research is that future trials include a training phase. An extension of the ‘targets of opportunity’ experiment could begin with a day of recordings used only for determining the PDFs of Prop, JEM and NNSD classes. This could be practically achieved using the Bayesian classifier recipe described in section 2.6.2. A following day of recordings could then be used for classification performance analysis without concern regarding any lack of independence between ‘training’ and ‘measurement’ data.

In the previous chapter, the intuitive but crude ‘fuzzy logic’ classifier was used as a check upon the implementation of the Bayesian Gaussian classifier. In this and subsequent chapters, the fuzzy logic classifier is used in a different role; to examine the impact upon classification performance when the fuzzy logic membership function differs in form from the Gaussian probability density functions (PDF) employed in the Bayesian classifier. For the Prop class, the fuzzy membership illustrated in fig 5.1 is a logical first approximation based on the qualitative spectral characteristics defined above. To achieve the same ‘leading edge’ for the Gaussian PDF, a mean of 0.7 and standard deviation of 0.1 were used. However, this results in an overall low probability density for dfrac values which approach unity. A more logical Prop PDF might be defined by a mean of 1 with a standard deviation of 0.2; i.e. symmetric with the NNSD definition and yielding a high Prop PDF for near unity dfrac values as required.

### 5.3 Classification performance using the dfrac feature

As in the previous chapter, data from six different aircraft types are used to determine classification performance. The following ‘truth’ classifications are used:

Aircraft type	Class
Pod	NNSD
Falcon <sup>6</sup>	NNSD
B747	JEM
B757	JEM
B777	JEM
Dash8	Prop

dfrac data from six aircraft are used to determine ‘Prop, JEM or NNSD’ classification performance. Fig 5.4 plots the off diagonal extent  $\xi$  of confusion matrices computed using the ‘Prop, JEM or NNSD’ classes and 25dB dfrac features by waveform and classifier method. The following observations and inferences can be made:

<sup>5</sup>Note: the ‘sensible guesses’ for the mean and standard deviation of the PDFs of Prop, JEM and NNSD classes were not totally independent of the measured data. The values for the means were indeed influenced by the mean dfrac with range for each Prop, JEM and NNSD class as illustrated in fig 5.3). Strictly speaking, this is a flawed analysis; a totally independent data set should have been used to assess classification performance. However, the measured data were not actually used in a direct sense in the generation of the covariance matrices employed by the Bayesian classifier. The fuzzy logic membership functions were similarly ‘defined’ rather than computed directly from measurements.

<sup>6</sup>No JEM effects were observed for the Falcon data, hence the NNSD truth classification. This is consistent with the Martin & Mulgrew JEM model [67] at a zero aircraft aspect angle. In the general case of ‘not purely radially inbound’ trajectories, one would expect to associate a jet aircraft such as the Falcon with the “JEM” class.



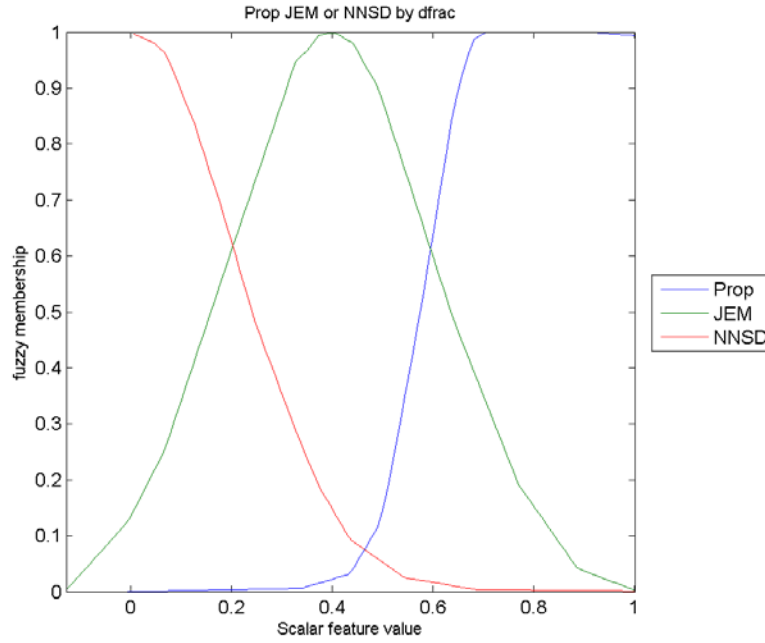


Figure 5.1: Fuzzy logic classifier membership functions for Prop (Propeller), JEM (Jet Engine Modulation) or NNSD (No Non Skin Doppler) classes. Scalar feature value is the proportion of the Doppler spectrum power over a defined (dB) threshold below the maximum spectral power.

1. Pod & Falcon (i.e. NNSD or not) classification is highly successful; almost a zero  $\xi$ .
2. Classification performance of the 6 aircraft inbound data is modest, with an  $\xi$  of less than 0.2. (See figures 5.6 and 5.5). The inbound result is not surprising given clear visual segmentation of classes in the dfrac vs range plot in fig 5.3. The individual Doppler spectra from which these measurements were taken are listed in the Appendix as Target data sheets (Doppler).
3. Classification performance of the six aircraft outbound<sup>7</sup> data is poor with an  $\xi$  of  $\approx 0.5$ .
4. Bayesian and Fuzzy logic methods yield very similar results.

The key message is that ‘Prop, JEM or NNSD’ classification is quite effective for inbound targets, where ‘inbound’ covers a range of angles about zero aspect such that JEM and propeller modulation effects can be measured. Outbound jet and propeller driven aircraft tend to be misclassified as NNSD (see figures 5.7 and 5.8). This makes sense as the rotating blades of the jet engine are likely to be obscured by the engine housing as viewed from behind. Similarly, propellers will be partially hidden by the engine unit and/or the main body of the aircraft.

<sup>7</sup>This includes the Pod & Falcon NNSD data to avoid numerical problems (in the confusion matrix) as a result of having no truth data from the NNSD class.

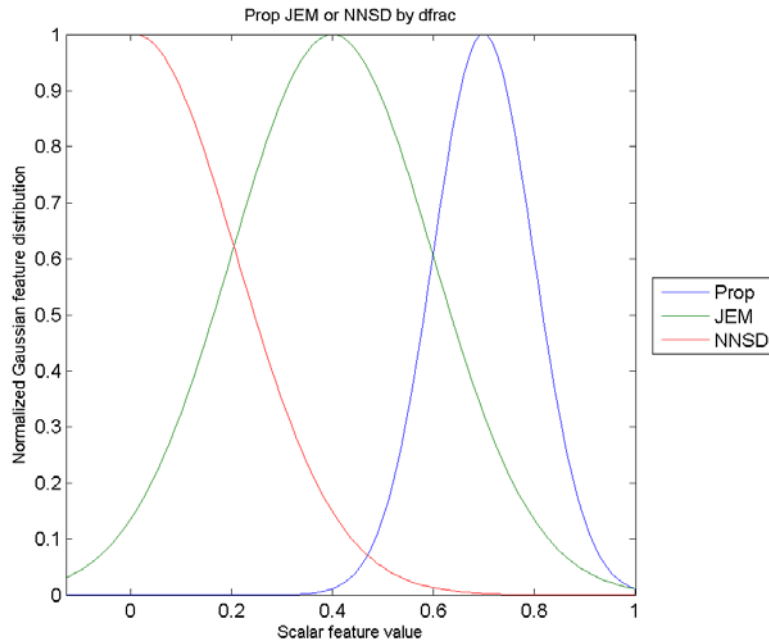


Figure 5.2: Bayesian classifier (Gaussian) un-normalized probability density functions for Prop (Propeller), JEM (Jet Engine Modulation) or NNSD (No Non Skin Doppler) classes. Scalar feature value is the proportion of the Doppler spectrum power over a defined (dB) threshold below the maximum spectral power.

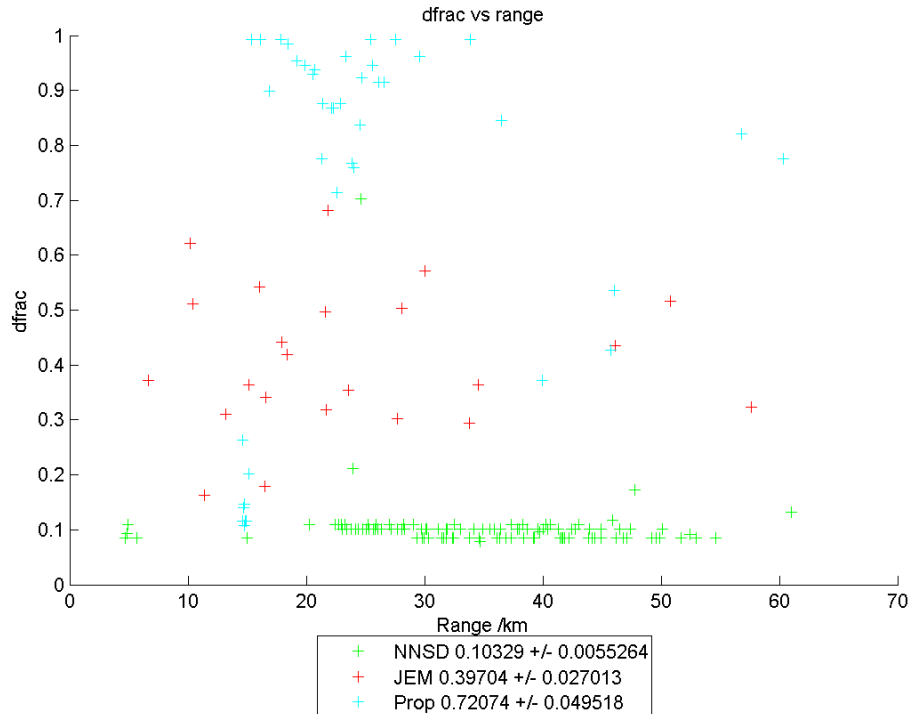


Figure 5.3: Doppler fraction (dfrac) feature is plotted vs target range from data derived from inbound Pod (NNSD), Falcon (NNSD), Dash8 (Prop), B747, B757 & B777 (Jet) aircraft. There appears to be clear segmentation between NNSD, Jet (i.e. JEM) and Propeller classes.

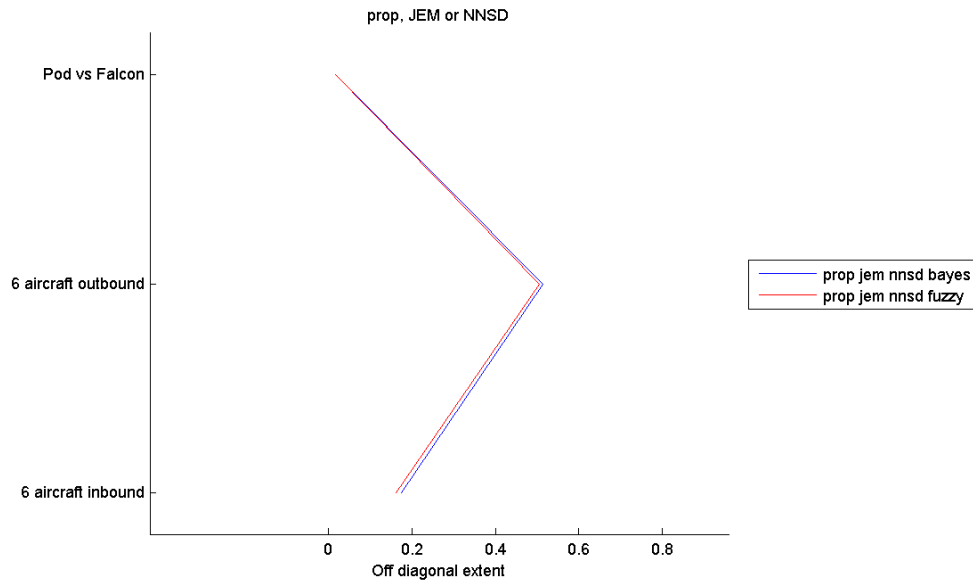


Figure 5.4: Prop, JEM or NNSD classification performance (metricated by the off diagonal extent  $\xi$  of the class confusion matrix) using recordings taken of Pod, Falcon, B747, B757, B777 & Dash8 aircraft. Waveform is D (wfc2  $\Delta f = 0\text{MHz}$ ,  $P = 32$ ,  $Q = 32$ ) for Pod and Falcon, and E for the others (wfc2  $\Delta f = 3.2\text{MHz}$ ,  $P = 32$ ,  $Q = 32$ ). Bayesian and Fuzzy logic classifiers are compared.

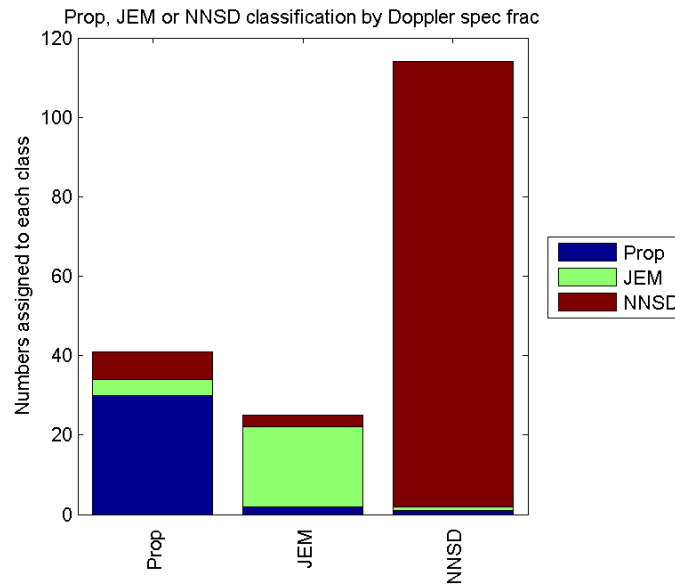


Figure 5.5: Bar chart describing numbers of Prop, JEM or NNSD assignments against actual assignments for six inbound aircraft (Prop : Dash8, JEM: B747,B757,B777, NNSD: Falcon, Pod). Classifier is Fuzzy Logic and waveforms are E/D. Feature is fraction of Doppler spectra above threshold, set at 25dB below the spectrum peak.

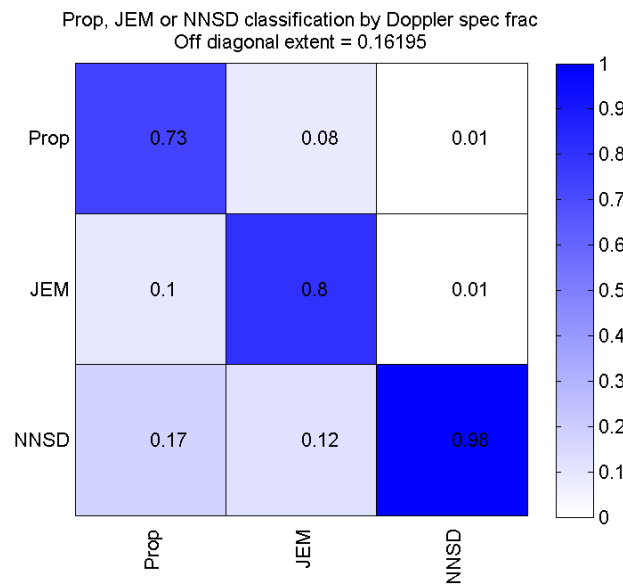


Figure 5.6: Confusion matrix describing fractions of Prop, JEM or NNSD assignments against actual assignments for six inbound aircraft (Prop : Dash8, JEM: B747,B757,B777, NNSD: Falcon, Pod). Classifier is Fuzzy Logic and waveforms are E/D. Feature is fraction of Doppler spectra above threshold, set at 25dB below the spectrum peak.

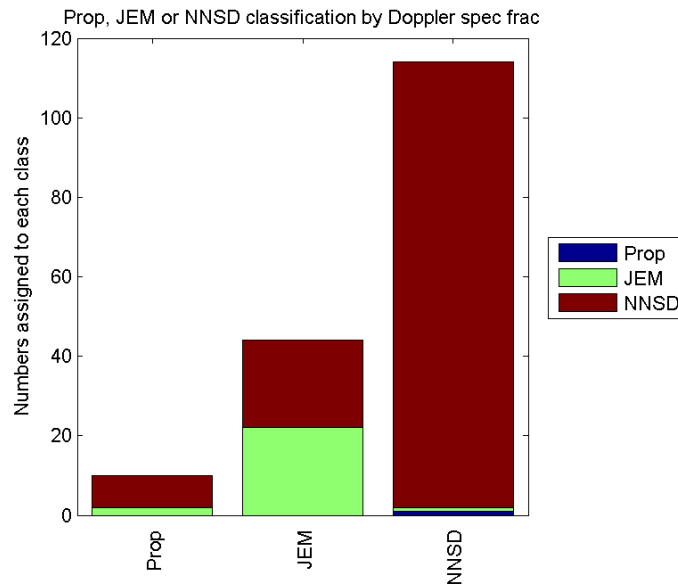


Figure 5.7: Bar chart describing numbers of Prop, JEM or NNSD assignments against actual assignments for four outbound and two inbound (NNSD) aircraft (Prop : Dash8, JEM: B747,B757,B777, NNSD: Falcon, Pod). Classifier is Fuzzy Logic and waveforms are E/D. Feature is fraction of Doppler spectra above threshold, set at 25dB below the spectrum peak.

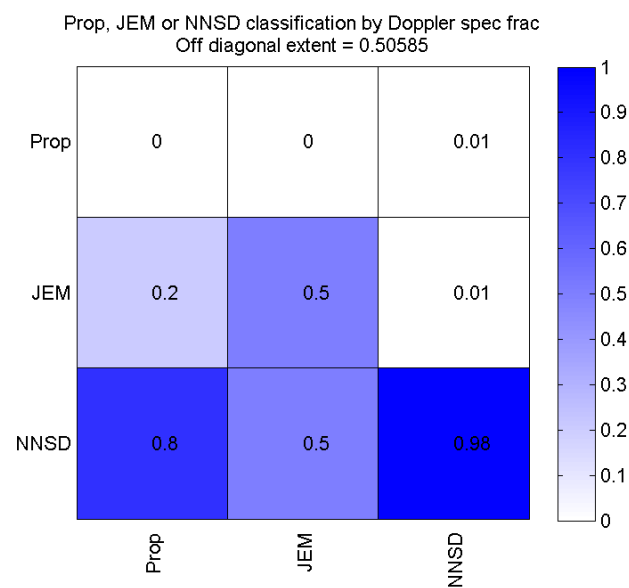


Figure 5.8: Confusion matrix describing fractions of Prop, JEM or NNSD assignments against actual assignments for two inbound and four outbound aircraft (Prop : Dash8, JEM: B747,B757,B777, NNSD: Falcon, Pod). Classifier is Fuzzy Logic and wavefoms are E/D. Feature is fraction of Doppler spectra above threshold, set at 25dB below the spectrum peak.

## 5.4 Range-Doppler profiles from stepped frequency waveforms

Up to this point we have considered HRR profiles and Doppler spectra as separate entities, each supplying its own set of features. In the NCTR processing chain described in Chapter 3, all outputs of the Doppler filtering process undergo stepped frequency range processing, not just the filter output corresponding to the skin return at 0Hz. This means we can form a single range-Doppler image of the target as an alternative to the separate Doppler power spectra and HRR profiles. This image could offer advantages over the latter if non-skin Doppler effects (e.g. JEM) could be localized in range as this would infer the positions of engines (i.e. the source of the rotational motion) in range. The scattering center decomposition could be appended with a ‘rotational part or non rotational part’ flag, which could aid classification by aircraft type.

However, the ambiguities caused by the PRF being less than the typical JEM bandwidth and the inherent HRR periodicity of  $\frac{c}{2\Delta f}$  can lead to range-Doppler coupling effects which can distort the range-Doppler image. To quantify these coupling effects let us extend the single scatterer model employed to explain the stepped frequency concept in section 2.2.1.

### 5.4.1 Classical stepped frequency model including JEM

The Martin & Mulgrew model [67] of JEM predicts spectral lines at  $f_{JEM} = jNf_{rot}$  within a bandwidth  $B_{JEM} = \frac{8\pi f_{rot}\Delta L \sin(a)}{c} f_{Tx}$  where  $f_{rot}$  is the engine spool rate,  $N$  is the number of blades,  $a$  is the aspect angle of the aircraft,  $f_{Tx}$  is the carrier frequency of the reflected waveform,  $\Delta L$  is the length of the engine blade (from the hub),  $c$  is the speed of light and  $j$  is an integer s.t.  $j \in [-J, J]$  where  $J = \text{ceil}\left(\frac{B_{JEM}}{2Nf_{rot}}\right)$ . If we imagine each JEM line to impart a modulation of frequency  $f_{JEM}$  to the waveform transmitted against the target, between pulses we would expect a phase shift of  $\Delta\phi_{JEM} = 2\pi \times f_{JEM} \times \frac{1}{f_{PRF}}$ . Therefore the total phase shift imparted upon pulse  $p$  from a burst of  $P$  pulses and frequency step  $q$  of  $Q$  steps is (for a motion compensated ‘JEM line reflector’  $j$  at range  $R_T$ )

$$\phi(p, q, j) = \underbrace{\frac{2\pi}{f_{PRF}} \{(q-1)P + p - 1\} jNf_{rot}}_{\text{JEM term}} + \underbrace{\frac{4\pi R_T}{c} (f_1 + (q-1)\Delta f)}_{\text{Range term}} \quad (5.1)$$

The resultant ‘target samples’ of the reflected signal are

$$\psi_{p,q} = \sum_{j=-J}^J \eta_j e^{-i\phi(p,q,j)} \quad (5.2)$$

A simple model of the skin return ( $j = 0$ ) and JEM lines ( $j \neq 0$ ) amplitudes could be parameterized by fixed constants

$$\eta_j = \begin{cases} a_+ & 0 < j \leq J \\ a_0 & j = 0 \\ a_- & -J \leq j < 0 \end{cases} \quad (5.3)$$

In the NCTR signal processing chain described in Chapter 3, the (Classical) range-Doppler profile is formed by firstly applying an inverse Discrete Fourier Transform over frequency steps and then a Doppler filter (a Discrete Fourier Transform) over pulses within each burst. In the exact implementation amplitude weighting functions are used. However, let us assume a uniform weighting to make

analytical progress towards our goal of deriving an expression for the range-Doppler coupling. The expression for the resulting range-Doppler profile  $\Theta(\alpha, \beta)$  is

$$\Theta(\alpha, \beta) = \sum_{p=1}^P \frac{1}{P} e^{\frac{-2\pi i(p-1)(\alpha-1)}{P}} \sum_{q=1}^Q \frac{1}{Q} e^{\frac{2\pi i(q-1)(\beta-1)}{Q}} \sum_{j=-J}^J \eta_j e^{-i\phi(p,q,j)} \quad (5.4)$$

where range  $R = \frac{c}{2Q\Delta f}(\beta - 1)$  and Doppler frequency is  $f = \frac{f_{PRF}}{P}(\alpha - 1)$ .  $\Theta(\alpha, \beta)$  can be rearranged to yield an expression which is the product of the function  $\chi(x, z) = \frac{e^{ix} \sin((1+z^{-1})x)}{\sin(z^{-1}x)} - 1$ , making use of the result (proved in the Appendix) : “if  $z \in \mathbb{Z}^+$ ,  $z \geq 1$  then  $\chi(x, z)$  is the summation of a geometric series of the form  $\sum_{n=1}^z e^{\frac{2in}{z}x} = \chi(x, z)$ .”

$$\begin{aligned} \Theta(\alpha, \beta) &= \frac{1}{PQ} \sum_{j=-J}^J \eta_j \sum_{p=1}^P e^{\frac{-2\pi i(p-1)(\alpha-1)}{P}} \sum_{q=1}^Q e^{\frac{2\pi i(q-1)(\beta-1)}{Q} - \frac{2\pi i}{f_{PRF}}\{(q-1)P+p-1\}jNf_{rot} - \frac{4\pi iR_T}{c}(f_1+(q-1)\Delta f)} \\ &= \frac{1}{PQ} \sum_{j=-J}^J \eta_j \sum_{p=1}^P e^{\frac{-2\pi i(p-1)(\alpha-1)}{P}} \sum_{q=1}^Q e^{\frac{2iq}{Q}x} e^v \\ &= \frac{1}{PQ} \sum_{j=-J}^J \eta_j \chi(x, Q) \sum_{p=1}^P e^{\frac{-2\pi i(p-1)(\alpha-1)}{P} + v} \end{aligned} \quad (5.5)$$

Where

$$\begin{aligned} \frac{x}{\pi} &= \beta - 1 - \frac{jPNf_{rot}Q}{f_{PRF}} - \frac{2R_TQ\Delta f}{c} \\ v &= -\frac{2\pi i(\beta-1)}{Q} - \frac{2\pi i}{f_{PRF}}(-P+p-1)jNf_{rot} - \frac{4\pi iR_T}{c}(f_1 - \Delta f) \end{aligned} \quad (5.6)$$

Hence

$$\begin{aligned} \Theta(\alpha, \beta) &= \frac{1}{PQ} \sum_{j=-J}^J \eta_j \chi(x, Q) \sum_{p=1}^P e^{\frac{-2\pi i(p-1)(\alpha-1)}{P} - \frac{2\pi i(\beta-1)}{Q} - \frac{2\pi i}{f_{PRF}}(-P+p-1)jNf_{rot} - \frac{4\pi iR_T}{c}(f_1 - \Delta f)} \\ &= \frac{1}{PQ} \sum_{j=-J}^J \eta_j \chi(x, Q) \sum_{p=1}^P e^{\frac{2ip}{P}v} e^w \\ &= \frac{1}{PQ} \sum_{j=-J}^J \eta_j e^{iw} \chi(x, Q) \chi(y, P) \end{aligned} \quad (5.7)$$

where

$$\begin{aligned} \frac{y}{\pi} &= -(\alpha - 1) - \frac{jNf_{rot}P}{f_{PRF}} \\ w &= \frac{2\pi(\alpha-1)}{P} - \frac{2\pi(\beta-1)}{Q} + \frac{2\pi}{f_{PRF}}(P+1)jNf_{rot} - \frac{4\pi R_T}{c}(f_1 - \Delta f) \end{aligned} \quad (5.8)$$

The major peaks of  $|\Theta(\alpha, \beta)|^2$  are likely to coincide with the maxima of the  $\chi(y, Q)$  and  $\chi(x, Q)$  functions. Appendix A shows this corresponds to

$$\begin{aligned} x &= \pi QX \\ y &= \pi PY \end{aligned} \quad (5.9)$$

where  $X, Y$  are integers. Using the expression derived above, and substituting for  $\beta - 1 = \frac{2Q\Delta f}{c}R$  and  $\alpha - 1 = \frac{Pf}{f_{PRF}}$

$$\begin{aligned} QX &= \frac{2Q\Delta f}{c}R_{peak} - \frac{jNf_{rot}Q}{f_{PRF}}P - \frac{2R_TQ\Delta f}{c} \\ PY &= -\frac{Pf_{peak}}{f_{PRF}} - \frac{PjNf_{rot}}{f_{PRF}} \end{aligned} \quad (5.10)$$

Hence<sup>8</sup>

$$\begin{aligned} R_{peak} &= R_T + \frac{c}{2\Delta f}X + \left(\frac{c}{2\Delta f}\right)\left(\frac{jNf_{rot}P}{f_{PRF}}\right) \\ f_{peak} &= jNf_{rot} + Yf_{PRF} \end{aligned} \quad (5.11)$$

i.e. the range peak ranges are ambiguous by integer steps of  $\frac{c}{2\Delta f}$  and the Doppler peaks by integer steps of  $f_{PRF}$ . This is consistent with the Background theory chapter relating to both the Classical technique & Doppler processing. However, we now have an additional range-Doppler coupling (i.e. a range offset) of

$$\delta R = \left(\frac{c}{2\Delta f}\right)\left(\frac{jNf_{rot}P}{f_{PRF}}\right) \quad (5.12)$$

for the  $j^{\text{th}}$  JEM line. This result is also consistent<sup>9</sup> with the prediction of range profile aliasing due to low frequency propeller modulations in section 4.3. Levanon & Mozeson [59], [58] derive the ambiguity function  $\chi(R, f_D)$  for a waveform based upon a ensemble of  $Q$  linear FM pulses stepped in carrier frequency by  $\Delta f$ . The ambiguity function yields the autocorrelation function of the waveform parameterized by range  $R$  and residual target Doppler  $f_D$ . In the expression below,  $\tau$  is the pulse length and  $B$  is the pulse bandwidth,

$$\chi(R, f_D) = \left(1 - \frac{1}{\tau} \left| \frac{2R}{c} \right| \right) \frac{\sin \left\{ \pi \tau \left( f_D + \frac{2R}{c} \frac{B}{\tau} \right) \left( 1 - \frac{1}{\tau} \left| \frac{2R}{c} \right| \right) \right\}}{\pi \tau \left( f_D + \frac{2R}{c} \frac{B}{\tau} \right) \left( 1 - \frac{1}{\tau} \left| \frac{2R}{c} \right| \right)} \times \dots \quad (5.13)$$

$$\dots \frac{\sin \left( \frac{Q\pi}{f_{PRF}} \left( f_D + \frac{2R}{c} f_{PRF} \Delta f \right) \right)}{Q \sin \left( \frac{\pi}{f_{PRF}} \left( f_D + \frac{2R}{c} f_{PRF} \Delta f \right) \right)} \quad (5.14)$$

In [58] the range-Doppler coupling for this waveform is effectively stated as (following a conversion of delay  $t$  into range via  $t = 2R/c$ )

$$\delta R = \frac{cf_D}{2f_{PRF}\Delta f} \quad (5.15)$$

If we let  $f_D = jNf_{rot}$  and  $P = 1$  then this result (which is computed assuming an analogue signal processing methodology) is also consistent with the derivation above. A plot of the Levanon & Mozeson ambiguity function is show in figures 5.9 and 5.10. Parameters for waveform E are used. In the second plot, the PRF is reduced by 32 to model the effect of using 32 coherent pulses in between frequency steps. In the first figure  $P$  should be taken as unity.

In principle, the analytic form of  $\delta R$  should mean that it is possible to correct for coupling effects and therefore generate a range-Doppler image which can, if JEM is present, enable engine localization

<sup>8</sup>Since  $Y$  and  $j$  are integers, and  $j \in [-J, J]$  the sign of  $Y$  and  $j$  can be exchanged without loss of generality.

<sup>9</sup>In section 4.3  $\delta R = \frac{cjNf_{rot}(P+G)}{2\Delta f f_{PRF}}$  is derived; i.e. the same as the result shown here except that the number of guard pulses  $G$  should also be taken into account.



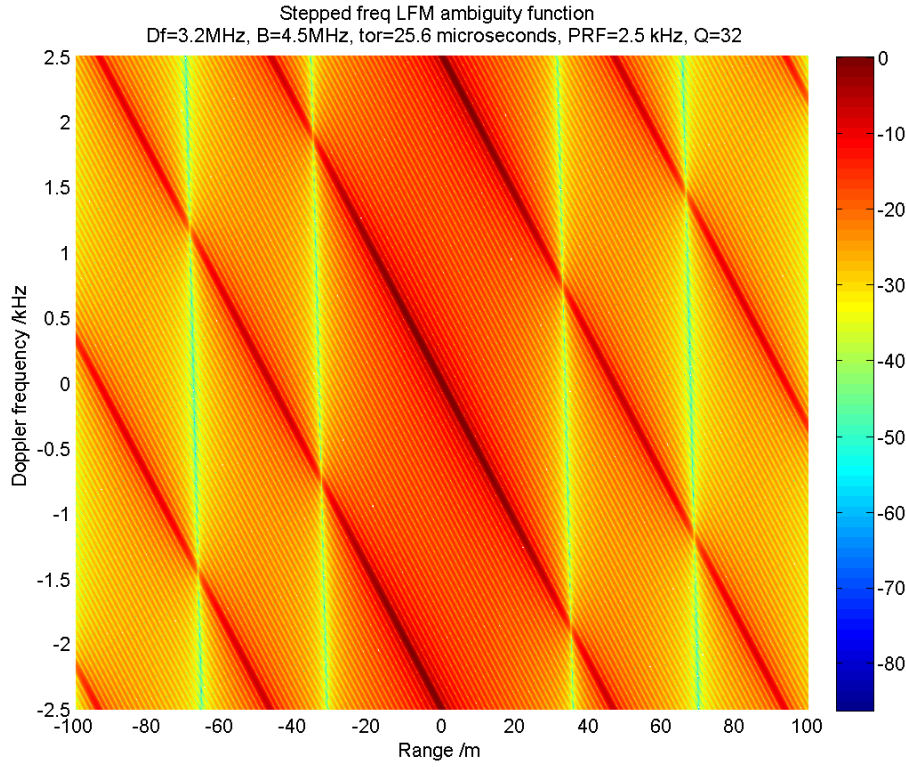


Figure 5.9: Ambiguity diagram of a stepped frequency linear FM waveform using  $Q = 32$  frequency steps. All other parameters are consistent with waveform E except there is no notion of a ‘burst’ of pulses between frequency steps.

in range. However, peak measurements are  $(R_{peak}, f_{peak})$ . Although  $c, \Delta f, P, f_{PRF}$  are known quantities, to compute  $\delta R$  one needs to calculate  $X, Y$  and  $jNf_{rot}$ . If the target length  $L$  is such that  $L \ll \frac{c}{2\Delta f}$ , or Hybrid processing is employed, then we may assume  $X = 0$ . To resolve the final two unknowns one needs to view the target with two waveforms of differing PRF. The true value of  $jNf_{rot}$  can be found by comparing the JEM lines following a ‘folding out’ of a spectra limited to the range  $\left[-\frac{f_{PRF}}{s}, \frac{f_{PRF}}{2}\right]$ . In order to ensure the only match is at the true value of  $jNf_{rot}$ , the PRFs should be in the ratio of an irrational number such as  $\sqrt{2}$  which cannot be expressed as a fraction of integers.<sup>10</sup>

<sup>10</sup>i.e. constructing a repeated stack of spectra. For example, if spectra #1 is constructed using a PRF of 5kHz and spectra #2 is constructed using a PRF of  $\sqrt{2} \times 5\text{kHz} = 7.07\text{kHz}$ ; a JEM line at 12kHz will appear at 4.93kHz in stack 2 of spectra #2 and 2kHz in stack 3 of spectra #1. Placing the stacks side by side will reveal the true JEM line frequency (12kHz in this case) since this will be the only mutual alignment. None of the ambiguities (i.e. integer multiples of the PRF) will align because the ratio of the two PRFs cannot be expressed as a fraction of integers.

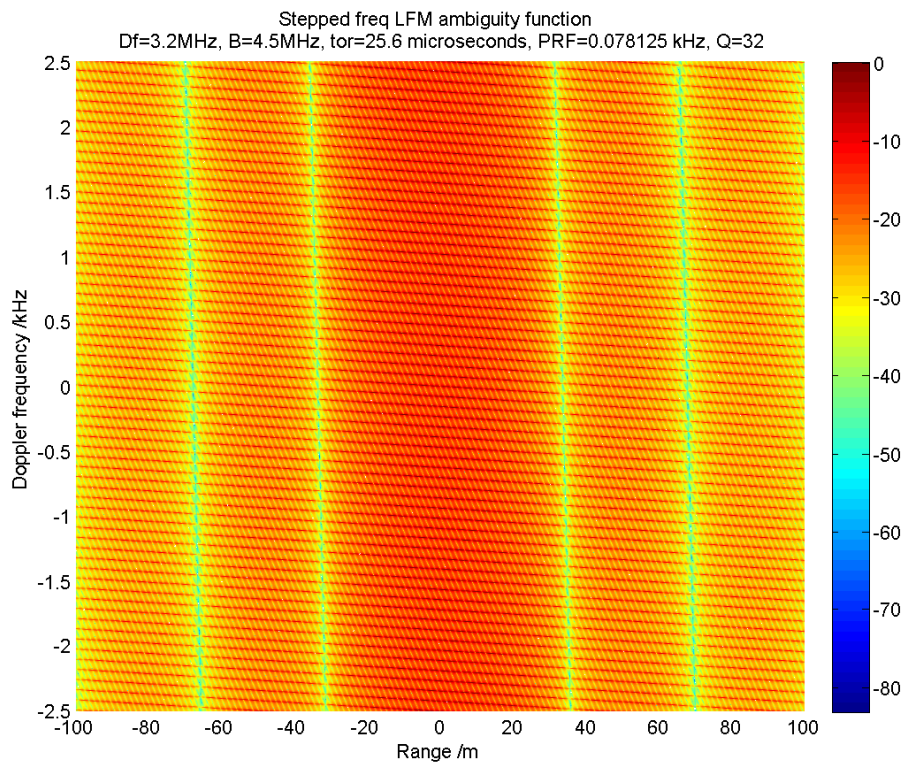


Figure 5.10: Ambiguity diagram of a stepped frequency linear FM waveform using  $Q = 32$  frequency steps. All other parameters are consistent with waveform E except there is no notion of a ‘burst’ of pulses between frequency steps. In this case the number of pulses per burst  $P = 32$  is ‘modelled’ by reducing the PRF by a factor of 32 from 2.5kHz to 0.078kHz.

### 5.4.2 Range-Doppler profiles from targets of opportunity

Typically,  $Nf_{rot}$  is quite different for Propeller driven engines and Jet engines. A turbo-prop engine<sup>11</sup> may typically rotate between 1500 and 2000RPM with a small number of blades. The Dash8 has  $N = 6$  blades yielding a typical value for  $Nf_{rot}$  of the order of 0.2kHz. A jet engine (see section 2.4.2) first stage may rotate at 12,000 RPM. An engine with 25 blades therefore yields a typical value of  $Nf_{rot}$  of 5kHz. This explains why we observe discrete lines (albeit ambiguous) in the Doppler spectra described in this thesis. The 32 pulse waveforms D and E have a PRF of 2.5kHz and therefore a Doppler resolution of 0.08kHz. One would therefore expect the propeller modulation to be very close to the skin return of the aircraft, whereas the JEM line is more likely to be clearly separated.<sup>12</sup> The difference in typical values of  $Nf_{rot}$  between Propeller and Jet engine aircraft is reflected in the structure of the range-Doppler profiles. Using  $f_{PRF} = 2.5\text{kHz}$ ,  $\Delta f = 3.2\text{MHz}$  and  $P = 32$  we can compute typical values for the coupling range offset  $\delta R$  for these two aircraft types. Note  $\frac{\delta R}{jNf_{rot}} = \frac{cP}{2f_{PRF}\Delta f} \approx 0.6 \text{ mHz}^{-1}$ .

Aircraft type	$Nf_{rot}$	$\delta R (j = 1)$
Prop	200Hz	120m
Jet	5,000Hz	3,000m

Fig 5.11 is a stack of Doppler spectra of an inbound Boeing 747. JEM lines are clearly evidenced. Waveform is E. Fig 5.12, is the corresponding Hybrid Range-Doppler profile and Fig 5.13, is the corresponding Classical Range-Doppler profile. Notice in the Classical profile (and also possibly in the Hybrid profile) how the coupling effects result in a complex dispersion of peaks away from 0Hz.

<sup>11</sup>Pratt & Whitney (Canada) construct the engine for the six blade turboprop used in the Dash8 aircraft. <http://www.pwc.ca/en/home>

<sup>12</sup>Unless  $\frac{Nf_{rot}}{f_{PRF}}$  is equal (or close to) an integer. In this case the JEM line would indeed be ‘wrapped’ onto the skin return.

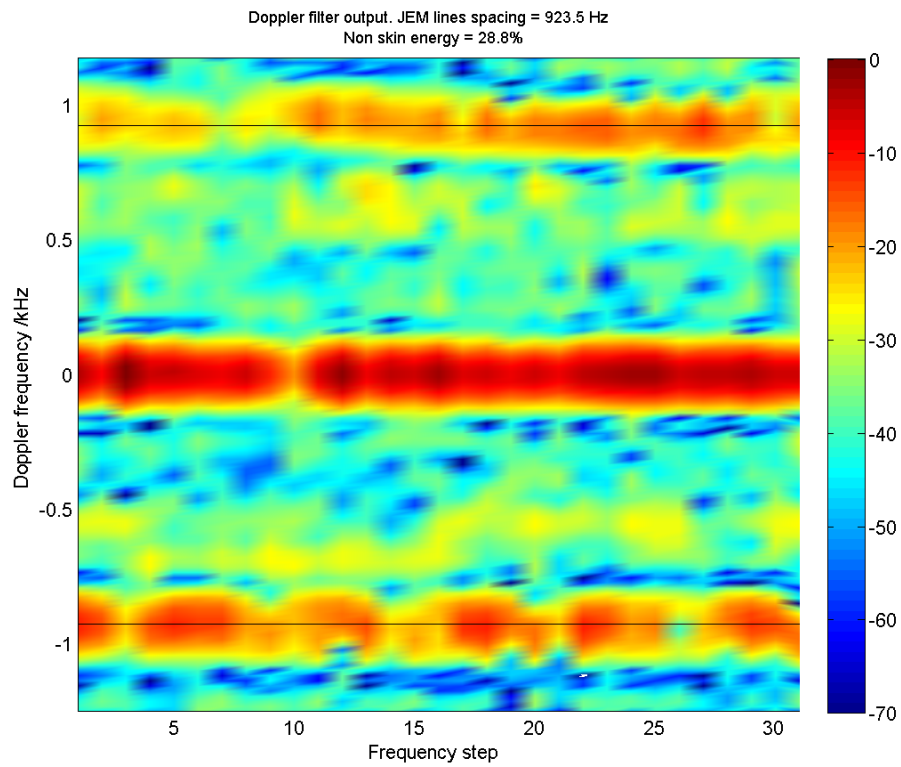


Figure 5.11: Doppler spectra of an inbound Boeing 747 observed using a 32 pulse waveform (E) with a PRF of 2.5 kHz. Notice the presence of JEM lines at  $\approx \pm 0.9\text{kHz}$

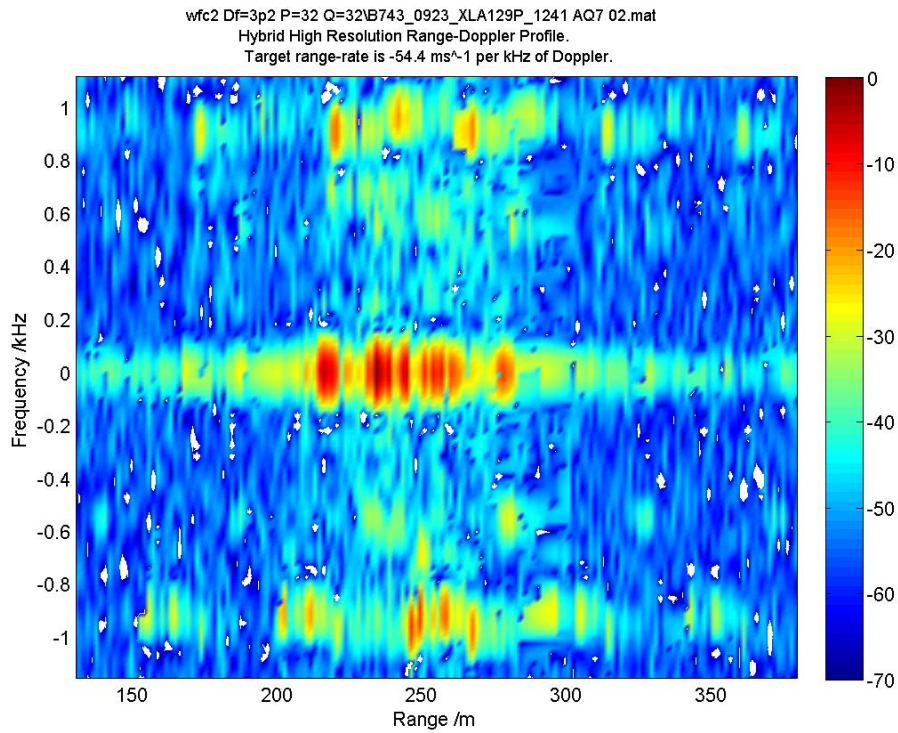


Figure 5.12: Hybrid range-Doppler profile of an inbound Boeing 747. Waveform is E. (32 pulses at a PRF of 2.5kHz and 32 frequency steps of 3.2MHz). The groups of peaks at  $\pm 0.9$  kHz are likely to be attributed to JEM effects resulting from the four jet engines. However, there is clear disagreement between the upper and lower Doppler frequencies with regard to the placement of these peaks. There is also some evidence that aliases at  $\frac{c}{2\Delta f}$  are not well suppressed beyond the skin return. Note: white spots on this figure indicate range-Doppler profile values  $< -70$  dBm.

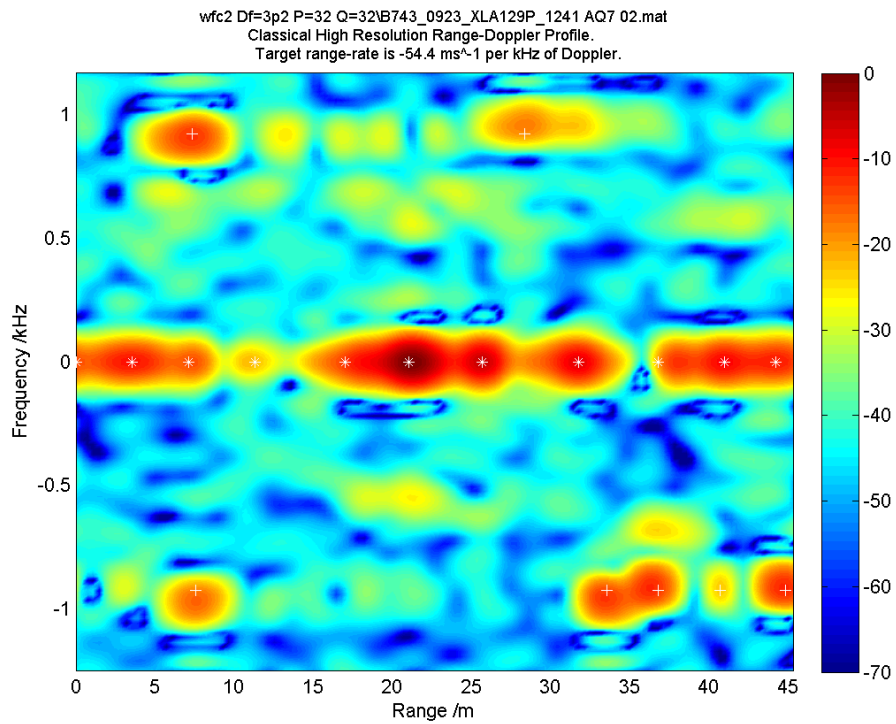


Figure 5.13: Classical Range-Doppler profile of a Boeing 747 constructed using waveform E. (32 pulses at a PRF of 2.5kHz and 32 frequency steps of 3.2MHz). The inherent ambiguities in range of  $\frac{c}{2\Delta f}$  coupled with the ambiguities of JEM peaks in Doppler due to the low PRF result in a complex arrangement of peaks which do not easily lead a casual observer to infer the range localization of jet engines.



One might think of a JEM or propeller modulation peak in the Range-Doppler profile to effectively sample the ambiguity function described above. We therefore might expect to see aliases of non-skin peaks occurring in bands of lines for turboprop aircraft, and sparsely separated peaks for jet aircraft. This result is consistent with the Dash8 and Boeing 747 profiles computed with waveform E in figures 5.15 and 5.14. However, in the Dash8 example, the gradient of the bands is not consistent with the expected formula  $\left| \frac{dR}{df_D} \right| \approx \frac{cP}{2f_{PRF}\Delta f}$ . The measured gradient is approximately  $-90\text{m} / 1.15\text{kHz} \approx 0.08 \text{ mHz}^{-1}$ . This result is nearly an order of magnitude smaller than the expected gradient. The interplay of the three ambiguity integers associated with propeller modulation, stepped frequency range and PRF offer a plausible explanation for the result. Fig 5.16 compares the Dash8 (Hybrid) Range-Doppler profile illustrated in fig 5.15 with all the possible peaks  $(R_{peak}, f_{peak})$  computed using

$$\begin{aligned} R_{peak} &= R_T + \frac{c}{2\Delta f}X + \left( \frac{c}{2\Delta f} \right) \left( \frac{jNf_{rot}P}{f_{PRF}} \right) \\ f_{peak} &= jNf_{rot} + Yf_{PRF} \end{aligned} \quad (5.16)$$

A spool rate of  $f_{rot} = 1650 \text{ RPM}$  is guessed to achieve the best match of gradient.<sup>13</sup> The maximum number of modulation lines is constrained by the modulation bandwidth  $B$ . As discussed in the Background theory section  $B \approx \frac{8\pi f_{rot}\Delta L \cos(\frac{\pi}{2}-a)}{c} f_{Tx}$  where  $a$  is the aspect angle and  $\Delta L$  is the propeller blade length. If  $\Delta L \approx 1\text{m}$ ,  $f_{Tx} = 3\text{GHz}$  and  $a \approx 45^\circ$ , the number of spectral lines is approximately  $2J + 1 \approx 15$  where

$$J \approx \text{floor} \left( \frac{4\pi f_{rot}\Delta L \cos(\frac{\pi}{2} - a) f_{Tx}}{Nf_{rot}c} \right) \quad (5.17)$$

---

<sup>13</sup>This is a valid procedure since the spool rate of the Dash8 turboprop is unknown. (Although one anticipates a maximum of 2000 RPM).

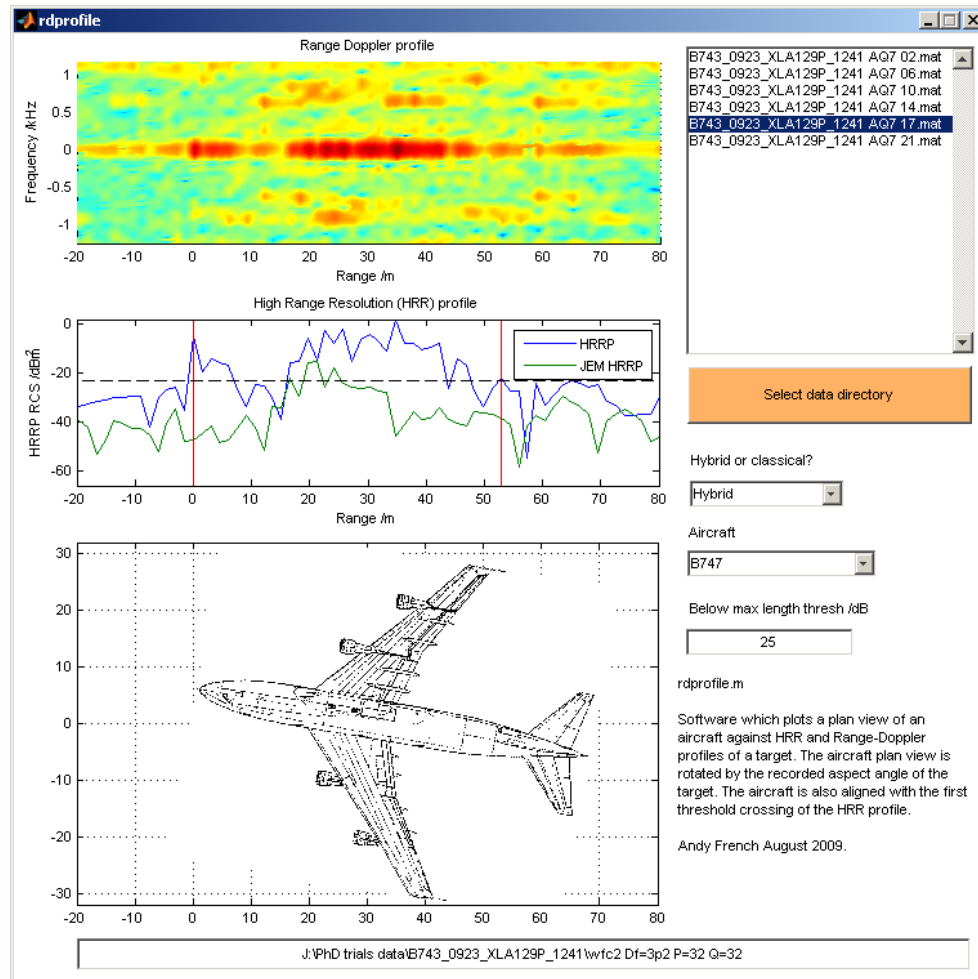


Figure 5.14: Hybrid range-Doppler profile of an inbound Boeing 747 observed using waveform E. This is compared with the Hybrid HRR profile (essentially a zero-Doppler cut of the Range-Doppler profile) and a HRRP formed using a Doppler filter tuned to the frequency of the 'loudest' JEM. A plan view of the B747 is presented incorporating a rotation via the inferred aspect angle. Whereas the range profile appears to correspond to the physical length, the 'JEM HRRP' is perhaps not so readily aligned to the physical positions of engines.



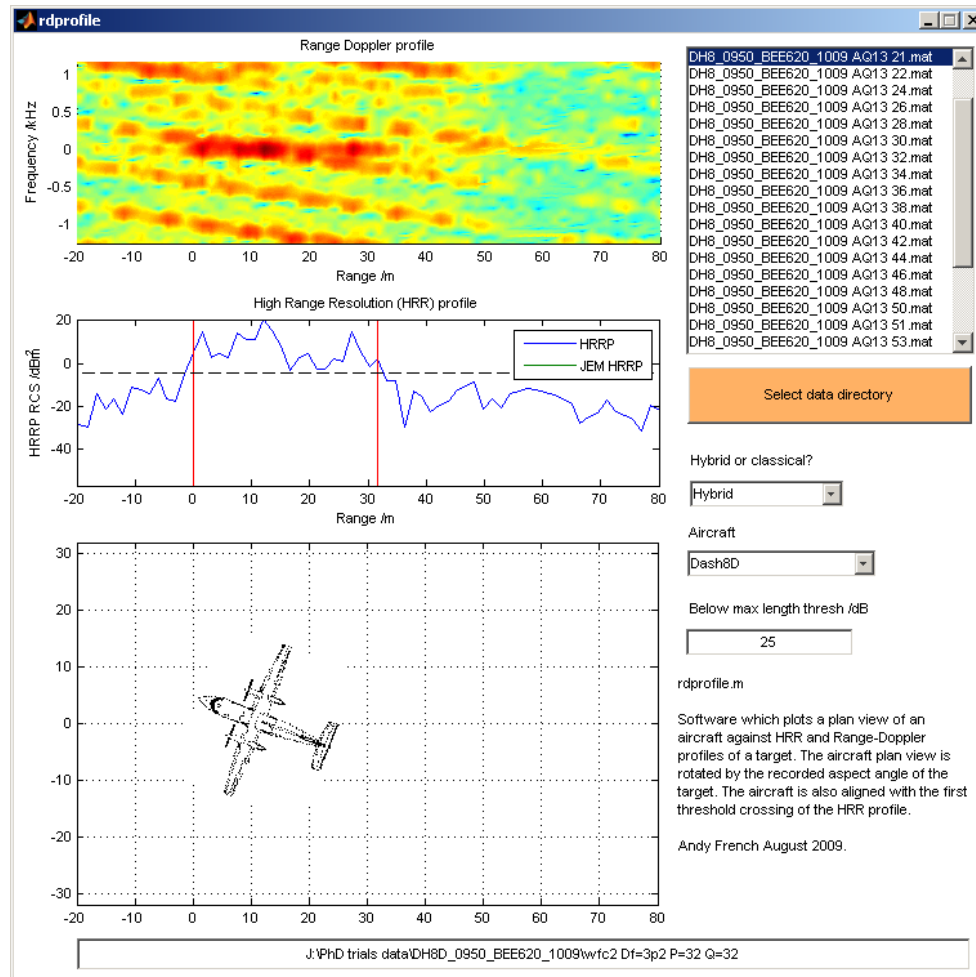


Figure 5.15: Hybrid range-Doppler profile of an inbound Dash8 turboprop aircraft observed using waveform E. This is compared with the Hybrid HRR profile (essentially a zero-Doppler cut of the Range-Doppler profile). In this case the Doppler signature resulting from propeller modulation manifests as a series of stripes of uniform gradient. This is quite different from the Range Doppler profiles of jet aircraft which do not have this feature.

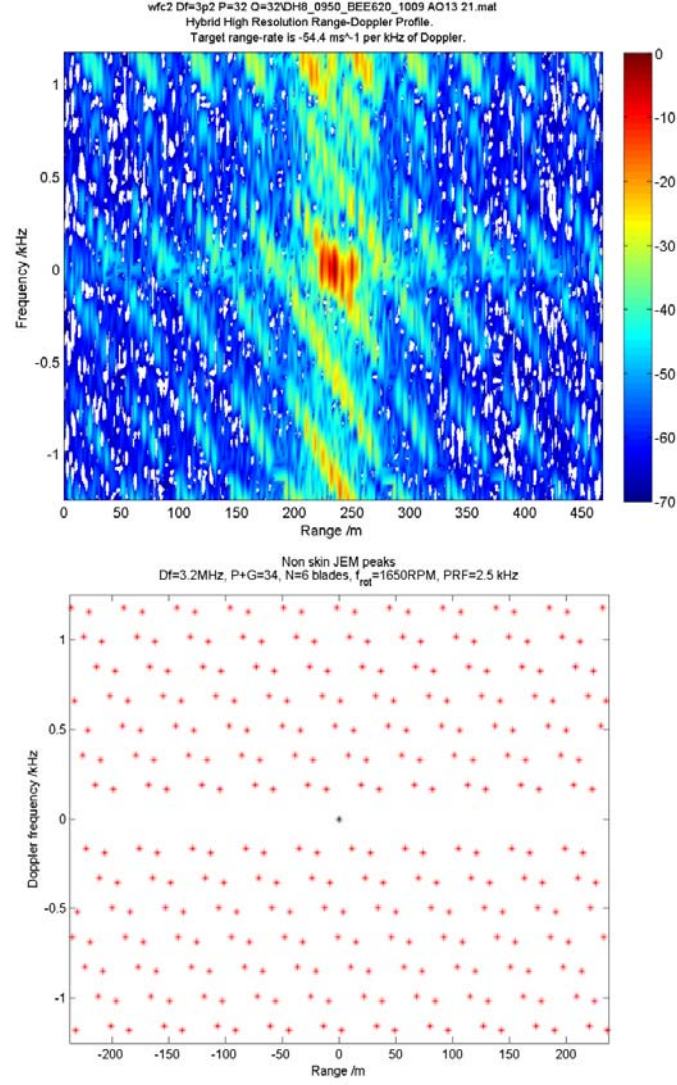


Figure 5.16: (Above) Hybrid range-Doppler profile of a Dash8 propeller aircraft generated using waveform E. The diagonal line ambiguities are consistent with theoretical predictions (see Lower plot) using the formulae  $R_{peak} = R_T + \frac{c}{2\Delta f}X + \left(\frac{c}{2\Delta f}\right)\left(\frac{jNf_{rot}P}{f_{PRF}}\right)$  and  $f_{peak} = jNf_{rot} + Yf_{PRF}$  for the (respective) range and Doppler peaks.  $X, N$  and  $Y$  are integers which define the ambiguities. In the lower plot, values of  $X, N$  and  $Y$  are set such that peaks fall into the range and Doppler bounds defined by the upper plot.

## 5.5 Conclusions

Let us summarize the results presented in this chapter in the form of (additional) answers to the first, second and third key questions posed in the introductory chapter.

1. *Can MESAR2 (and by inference other S-band multifunction phased array radars) be used to record robust range (and Doppler) profiles of air targets?*

- Both Pod & Falcon aircraft yielded consistent Doppler profiles which were devoid of JEM as expected due to (i) the Pod is a ‘point target’, (ii) the Falcon was observed at effectively zero aspect angle and (iii) the jet engines of a Falcon are somewhat obscured by engine cowlings.
- Range-Doppler profiles of aircraft can be formed using the 32 pulse, 32 frequency step waveform E. However, due to the low PRF and consequently ambiguous JEM modulation, the range-Doppler coupling effect resulting from the stepped frequency processing result in a confusing ensemble of peaks which do not allow for unambiguous localization of JEM (and therefore engines) in range. Unless the JEM ambiguity can be resolved (see Recommendations), separate stepped frequency HRR and single frequency high Doppler resolution looks appear to be superior than a single ‘range and Doppler’ look.
- Propeller aircraft, with modest modulation line periodicities  $Nf_{rot}$  have a characteristic ‘diagonal banding’ signature in the (Hybrid) range-Doppler profiles. The peaks within these bands manifest from the interplay of propeller modulation, stepped frequency range and PRF ambiguities. It is possible to derive  $Nf_{rot}$  from these bands using an iterative numerical method; i.e.  $Nf_{rot}$  is guessed and then the formulae derived in this chapter for peak coordinates are used to predict the band structure. Using a number of guesses, the best fit of the modelled result to the measured band structure yields  $Nf_{rot}$ . A recommendation from this thesis is an investigation into whether an efficient algorithm could be developed for this process.

2. *How robust are feature measurements taken from the trials data set? Do feature measurements naturally segment into classes? Should certain features be combined, are they correlated?*

- Fig 5.3 demonstrates that ‘Doppler fraction’ (dfrac) features segment into three natural classes: ‘No Non Skin Doppler’ (NNSD), (dfrac close to zero), ‘Propeller modulation’ (dfrac close to unity) and ‘JEM’ (dfrac somewhere between 0.3 and 0.7).

3. *Can we achieve acceptable classifier performance based upon the extraction of various target features? How does the crudeness of class definition affect this result and how does performance depend upon (i) the proportion of total pulse cycles used to form the target data set (ii) thresholds used in feature measurement and (iii) the features used (and their possible combination) ?*

- Prop, JEM or NNSD classification yielded a  $\xi$  of  $< 0.2$  for inbound aircraft. This rose to 0.5 for outbound aircraft, consistent with the obscuration of jet engines and propellers for the non-NNSD targets.
- In all cases, Bayesian and Fuzzy logic classifiers (based upon ‘expert’ pre-defined probability density or membership functions) yielded consistent results.

## Chapter 6

# Relationship between characteristics of stepped frequency methods and overall air target classification performance

### 6.1 Chapter summary

The variation of classification performance with parameters of the stepped frequency waveforms is assessed via the plotting of confusion matrix off diagonal extent  $\xi$  against characteristic variables. For the range profile and Doppler spectra based features and class assignments discussed in Chapters 5 and 6,  $\xi$  is plotted (as a surface) against, respectively, length measurement threshold and number of frequency steps, and Doppler fraction (dfrac) threshold and number of pulses per burst. To achieve these plots the entire data set was reprocessed using a different combination of  $P$  and  $Q$  values, and then post-processed for each permutation of the length and dfrac thresholds.  $P$  and  $Q$  could only be reduced from the values used during MESAR2 experiments; i.e. the analysis is of the classification response to degradation of the waveform rather than what could be achieved given more pulses and frequency steps.  $\xi$  is also plotted (for the non-degraded values of  $P$  and  $Q$ ) against a measure of carrier frequency jitter. An initial investigation into the possible combination of length *and* dfrac features in a joint (Bayesian) classifier is considered. Data from waveforms A, D & E are combined to form two dimensional feature vectors and used to classify against target types Pod, Falcon, B747, B757, B777 & Dash8. The (length,dfrac) data points are plotted to assess possible class segmentation and then used to generate a surface graph of classifier  $\xi$  plotted against length and dfrac thresholds.

### 6.2 Variation of $\xi$ with $P, Q$ and length and Doppler fraction feature thresholds

Figures 6.1 to 6.7 display the variation of confusion matrix off diagonal extent  $\xi$  as a function of number of pulses  $P$  (Prop, JEM or NNSD classification) or frequency steps  $Q$  (classification based upon range profiles) and either Doppler fraction or length feature *below max*<sup>1</sup> measurement thresholds. The idea is to assess (i) how classification performance varies with degradation in resolution of the profile used to derive the feature measurements and (ii) how classification performance varies with

---

<sup>1</sup>i.e. the threshold is defined as the signal power in dB *below* the maximum. Therefore a ‘high’ threshold will be a lower absolute value in dBm than a ‘low’ value.

the threshold levels used to determine the feature measurements. The figures were computed using 15 scales of  $P, Q$  degradation<sup>2</sup> and 15 levels of threshold between 15 and 35dB, resulting in a 225 point surface which could be smoothed via interpolation. As discussed in section 2.6.1, an ‘Expert’ Bayesian Gaussian classifier is chosen for the computation of classification performance. For the scalar feature data, the implementation of the classifier is checked via the intuitive but crude Fuzzy logic method. The following observations and conclusions may be inferred:

1. *Long or short classification* (figures 6.1 and 6.2)

$\xi \approx 0.1$  is achievable within the length threshold region of 20 to 25dB. This is largely independent of frequency steps within the range  $Q = 20 \dots 127$  shown. Above 25dB there is a ‘modest crisis’ which intriguingly extends to lower thresholds during the middle frequency step values ( $Q \sim 60$ ). Bayes and Fuzzy logic results are consistent.

2. *Four lengths classification* (figures 6.3 and 6.4)

A similar structure to the long or short case, except the crisis occurs at 2 or 3 dB lower in length threshold and is far less modest.  $\xi$  values of 0.4 are obtainable with a threshold of around 20dB. Intriguingly an ‘island of high performance’ exists within the range  $Q = 60 \dots 80$ . This result may be serendipitous given the inherent variability of the targets of opportunity data, i.e. it may not be a general result. However, it certainly proves that increasing the number of frequency steps may not always result in higher classification performance. Increasing the number of frequency steps, and therefore the resolution of the aircraft range profile, may expose scatterers which otherwise would be merged with more dominant ones. Given the high variability of a HRR profile with small changes in aspect angle (see Tait [103]), it is plausible that increased exposure of scatterers may actually cause greater variability in the HRR profile and therefore the length measurement. There might indeed be an optimum resolution for length measurement. In this case about 80cm. The same argument may also help to explain the ‘V’ shaped profile in all figures relating to features derived from the HRR profile. As  $Q$  increases, more scatterers are exposed and the inherent variability of the HRR profile could mean a greater possibility for classification performance degradation as the length threshold is increased in value. However, unlike the ‘island of high performance’ at thresholds of around 20dB, for higher thresholds the enhanced resolution with increased  $Q$  should eventually reduce the HRR variability (therefore enhancing performance) once all the major scatterers (and their sidelobes<sup>3</sup>) are resolved.

3. *Scattering center Model (SCM) compare classification* (figure 6.5)

SCM measurements are taken from the location of major peaks which are above the length threshold, hence the variation in both dimensions shown. Classification performance is universally poor. The trend of the crisis point being at lower threshold levels towards the middle of the range of frequency steps is evident.

4. *Prop, JEM or No Non Skin Doppler (NNSD)* (figures 6.6 and 6.7)

The crisis for these plots is in the opposite dimension to the length results; i.e. the number of pulses  $P$  is more significant than the dfrac threshold, certainly below  $P = 16$  pulses. This makes

<sup>2</sup>Which could be done independently on the same data set since length and dfrac measurements use different wave-forms.

<sup>3</sup>In the high performance region, the threshold is sufficient to capture the major scatterers (and thus infer a realistic target length), but not so high that sidelobes are exposed.

sense since JEM is likely to be masked by the sidelobes of the Doppler filter as  $P$  reduces. Below 16 pulses the ‘shape’ of the spectrum, which  $dfrac$  aims to characterize, is unlikely to change between classes. Fairly high performance classification ( $\xi < 0.2$ ) is obtainable above  $P = 27$  and within the threshold range of 22 to 30dB. This also makes sense: if the absolute threshold is too low then  $dfrac$  includes too much of the sidelobe region of the filter; variations due to JEM and Doppler modulation become less significant in terms of the overall amplitude sum since most of the spectrum will exceed the threshold. If the absolute threshold is too high then variations due to JEM and Doppler modulation may not be large enough (relative to the skin return) to be taken into account. In this example there is a significant difference between the Bayes and Fuzzy logic classifiers for higher below-max thresholds (i.e. lower absolute thresholds) when  $P$  is less than 16. This could be due to the fuzzy logic membership function (see fig 5.1) being different for Prop classes than the Gaussian Bayesian equivalent (see fig 5.2). When  $P$  is small and the absolute threshold is low, this will inevitably mean a higher  $dfrac$  value since more of the spectrum exceeds the threshold. Since the Fuzzy logic classifier assigns a unity value membership when  $dfrac$  is unity, this means many spectra will be ‘correctly’ classified as Prop. This means that genuine Prop classes are likely to be correctly classified whereas the Gaussian classifier could return random results given the probability density functions of all classes are small in value at unity  $dfrac$ .<sup>4</sup>

---

<sup>4</sup>This argument also implies the JEM and NNSD classes may be misclassified as Prop, raising the overall value of  $\xi$ . Therefore it is not surprising that the  $\xi$  values in the top left hand corner of the Fuzzy logic plot are of relatively modest values. (Around 0.4).

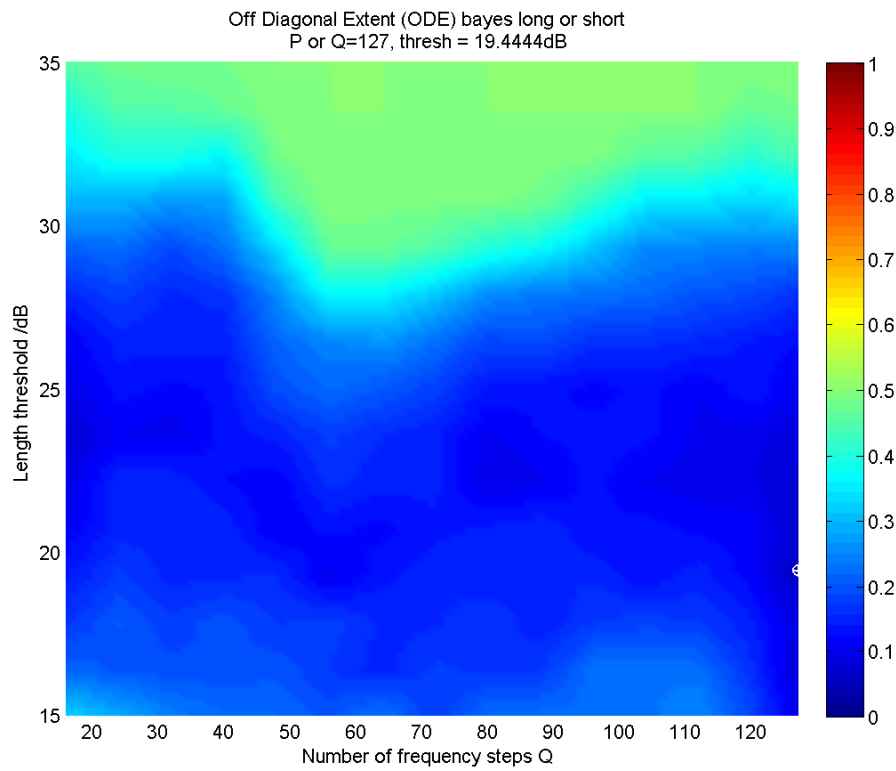


Figure 6.1: Surface plot of (Bayesian) classifier off diagonal extent (ODE) using a ‘Long or Short’ class assignment as a function of length threshold and number of frequency steps,  $Q$ . The global minimum ODE is marked with a white cross and corresponding  $Q$  and length threshold values are provided in the title.

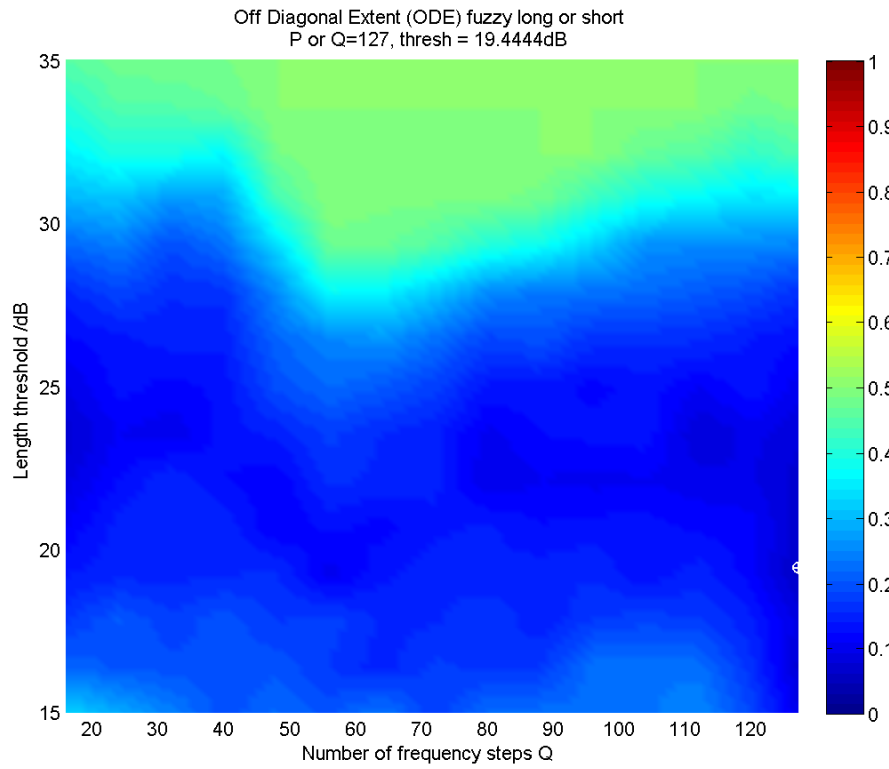


Figure 6.2: Surface plot of (Fuzzy logic) classifier off diagonal extent (ODE) using a ‘Long or Short’ class assignment as a function of length threshold and number of frequency steps,  $Q$ . The global minimum ODE is marked with a white cross and corresponding  $Q$  and length threshold values are provided in the title.



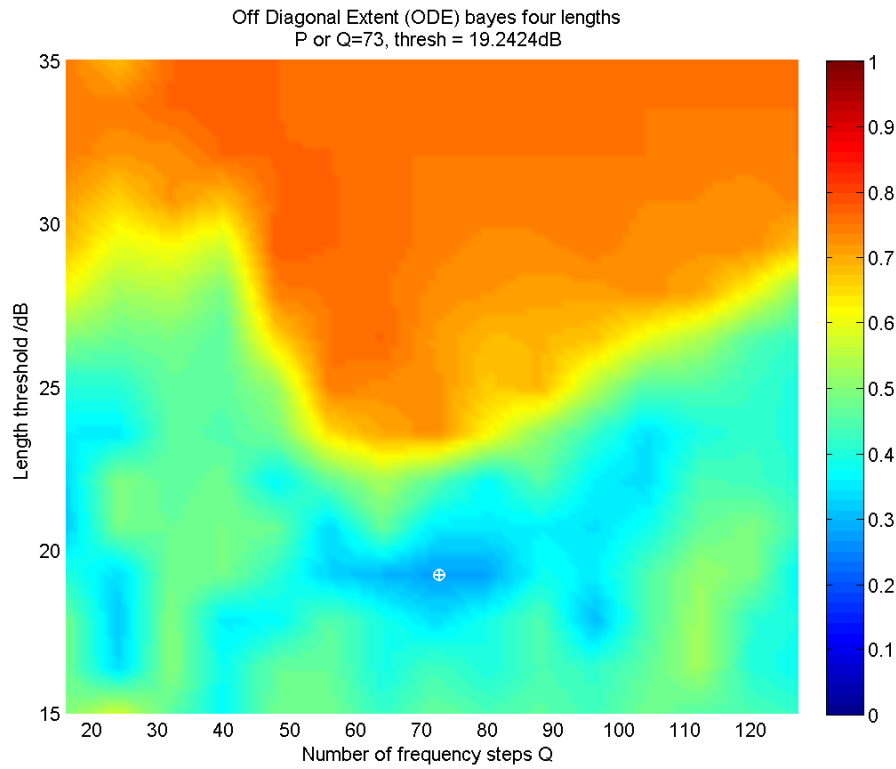


Figure 6.3: Surface plot of (Bayesian) classifier off diagonal extent (ODE) using a ‘Four Lengths’ class assignment as a function of length threshold and number of frequency steps,  $Q$ . The global minimum ODE is marked with a white cross and corresponding  $Q$  and length threshold values are provided in the title.

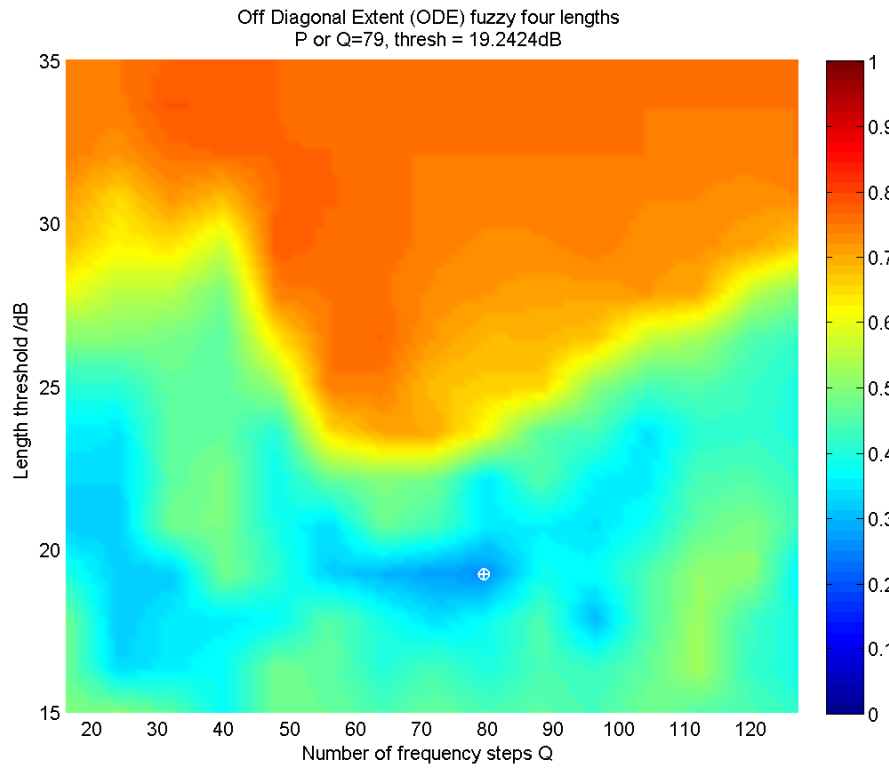


Figure 6.4: Surface plot of (Fuzzy logic) classifier off diagonal extent (ODE) using a ‘Four Lengths’ class assignment as a function of length threshold and number of frequency steps,  $Q$ . The global minimum ODE is marked with a white cross and corresponding  $Q$  and length threshold values are provided in the title.

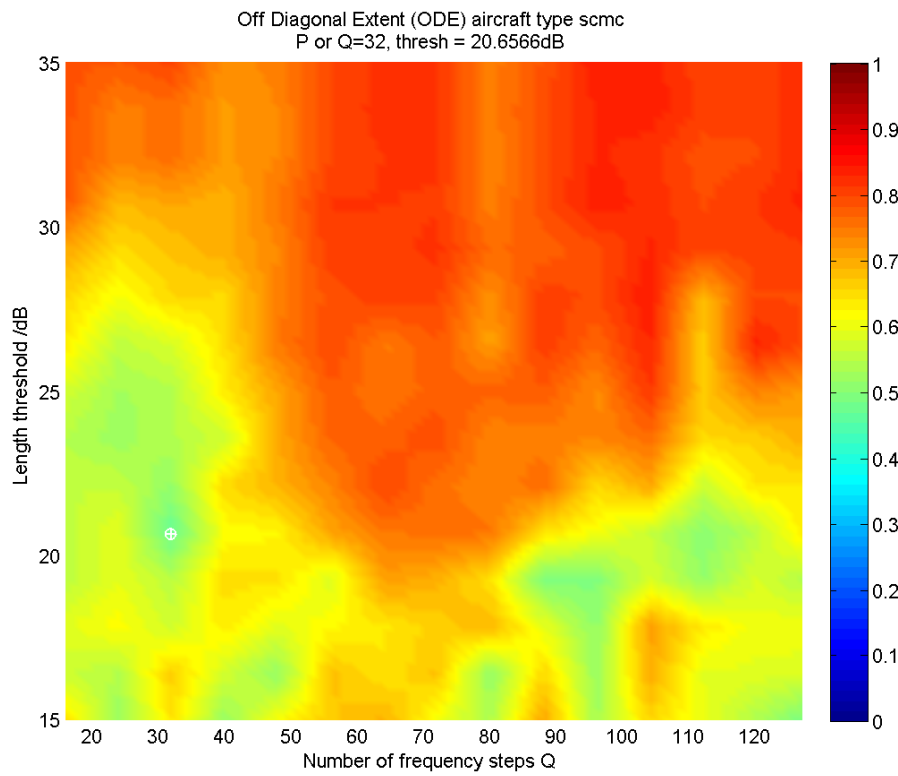


Figure 6.5: Surface plot of (Scattering Centre Model Compare) classifier off diagonal extent (ODE) using an 'Aircraft type' class assignment as a function of length threshold and number of frequency steps,  $Q$ . The global minimum ODE is marked with a white cross and corresponding  $Q$  and length threshold values are provided in the title.

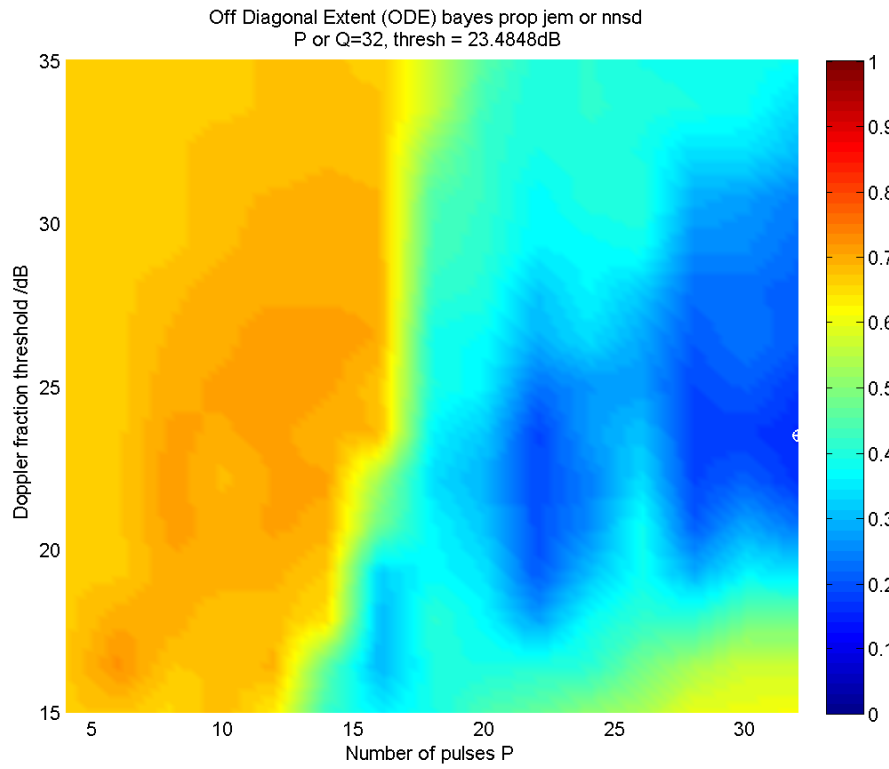


Figure 6.6: Surface plot of (Bayesian) classifier off diagonal extent (ODE) using a ‘Prop, JEM or NNSD’ class assignment as a function of Doppler fraction (dfrac) threshold and number of pulses per burst,  $P$ . The global minimum ODE is marked with a white cross and corresponding  $P$  and dfrac threshold values are provided in the title.

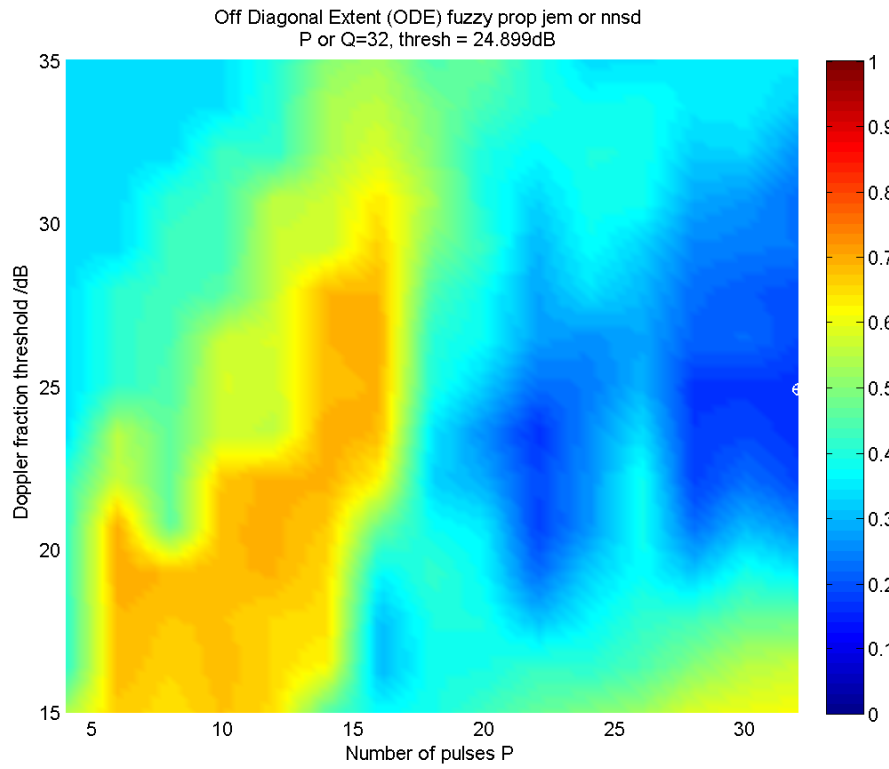


Figure 6.7: Surface plot of (Fuzzy Logic) classifier off diagonal extent (ODE) using a ‘Prop, JEM or NNSD’ class assignment as a function of Doppler fraction (dfrac) threshold and number of pulses per burst,  $P$ . The global minimum ODE is marked with a white cross and corresponding  $P$  and dfrac threshold values are provided in the title.

### 6.3 Variation of $\xi$ with carrier frequency jitter

Frequency jitter is defined to be the standard deviation  $\sigma_{f_{Tx}}$  of (zero mean) Gaussian errors imposed upon the carrier frequencies used in the stepped frequency waveforms discussed in this thesis. In section 2.7.2 the constraint  $\sigma_{f_{Tx}} \ll \frac{c}{4R}$  was suggested as a criteria of carrier frequency stability sufficient to enable the formation of HRR profiles using stepped frequency waveforms.  $c$  is the speed of light and  $R$  is the target range of interest.  $R = 100\text{km}$  gives  $\sigma_{f_{Tx}} \ll 750\text{Hz}$ . Since carrier frequencies are of the order of a few GHz at S-band, this implies a frequency stability requirement of better than 1 part in  $10^6$ .

The classification experiments described in Chapters 4 and 5 were re-run using twelve values of  $\sigma_{f_{Tx}}$  between 0Hz and 2,560Hz. This was achieved by modifying the stored carrier frequencies prior to NCTR signal processing; i.e. the effect of jitter should manifest in erroneous motion compensation. This is thought to be representative of a realistic system, whereby the received signal is correctly mixed down by the carrier, but the absolute value of the carrier may be different by  $\sigma_{f_{Tx}}$  from what is expected. In all cases length and dfrac thresholds were set at 25dB. Confusion matrix off diagonal extent  $\xi$  is plotted against  $\sigma_{f_{Tx}}$  in figure 6.8 for each experiment. Note for the length based classification, Hybrid processed waveform A was used. For the Doppler spectra based classification, waveforms D & E were used. The following observations can be made:

1. The imposed jitter (up to 2.56kHz) significantly affects classification performance based upon range profile derived features (i.e. length) but not Doppler spectra derived features. This is to be expected since the motion compensation algorithms always aspire to center the target skin return at 0Hz for each frequency step. However, significant phase errors between frequency steps will corrupt the HRR profile. Note carrier frequency jitter should not affect (motion compensated) Doppler spectra since JEM effects are independent of carrier frequency.
2. Bayesian and Fuzzy logic classifiers give very similar results. Unless both classifiers are erroneously implemented, this suggests the Bayesian result makes sense given the Fuzzy logic classifier is a crude but intuitive method.
3. The analysis suggests frequency jitter over 100Hz causes significant degradation in classifier performance. One may conclude frequency stability at S-band better than 1 part in  $10^8$  (i.e. a few tens of Hz) may be more appropriate. Is this requirement achievable? A modern 3GHz oscillator may be rated at -80dBc/Hz at 100Hz offset.<sup>5</sup> This statement refers to the ratio of oscillator spectral power density  $\eta$  (in dB) within a 1Hz bandwidth at 100Hz from the carrier, to a 1Hz bandwidth at the carrier. If the distribution of spectral power density  $p(f)$  is assumed to have the same (Gaussian) functional form as the predicted probability distribution of carrier

---

<sup>5</sup> [www.emresearch.com](http://www.emresearch.com)

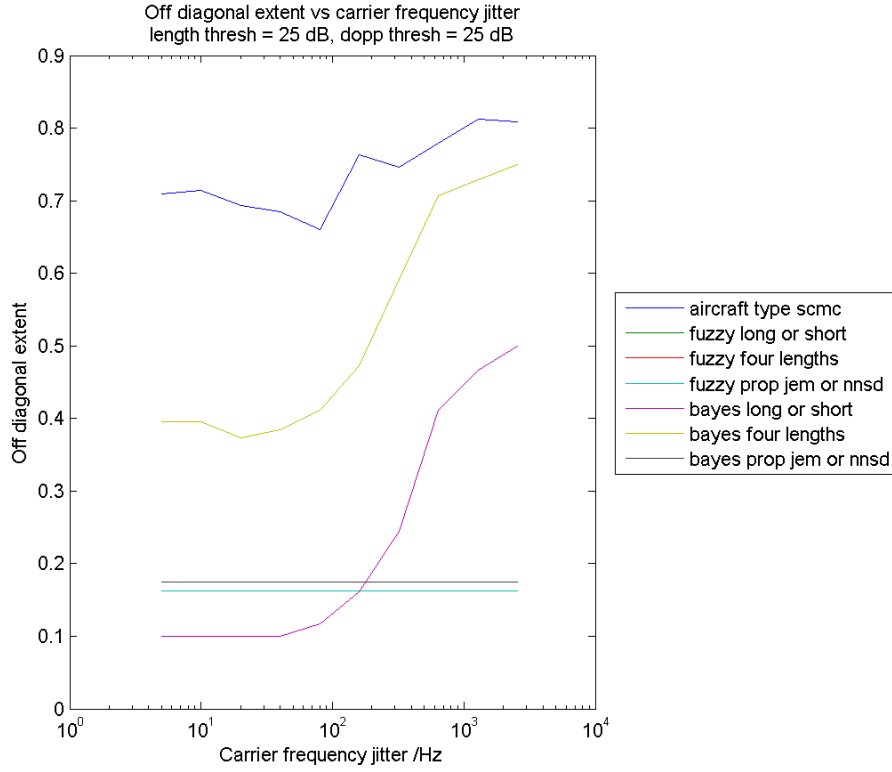


Figure 6.8: Plot of classifier off diagonal extent (ODE) vs frequency jitter for Bayesian & Fuzzy logic classifiers and for a number of different class assignments. Frequency jitter is defined to be the standard deviation of (zero mean) Gaussian errors imposed upon the carrier frequencies used in the stepped frequency waveforms. Note the imposed jitter (up to 2.56kHz) significantly affects classification performance based upon range profile derived features (i.e. length) but not Doppler spectra derived features. For the length based classification, Hybrid processed waveform A was used. For the Doppler spectra based classification, waveforms D & E were used.

frequencies<sup>6</sup> one can directly relate the frequency jitter standard deviation  $\sigma_{f_{Tx}}$  to  $\eta$ .

$$p(f_{offset}, \sigma_{f_{Tx}}) \approx \frac{1}{\sigma_{f_{Tx}} \sqrt{2\pi}} \exp\left(-\frac{f_{offset}^2}{2\sigma_{f_{Tx}}^2}\right) \quad (6.1)$$

$$\therefore \eta(f_{offset}, \sigma_{f_{Tx}}) \approx 10 \log\left(\frac{p(f_{offset})}{p(0)}\right) = -\frac{5f_{offset}^2}{\sigma_{f_{Tx}}^2} \log(e) \quad (6.2)$$

$$\therefore \sigma_{f_{Tx}} \approx \sqrt{-\frac{5f_{offset}^2}{\eta} \log(e)} \quad (6.3)$$

A graph (fig 6.9) of  $\sigma_{f_{Tx}}$  is plotted against  $\eta$  using an offset of 100Hz. A rating of -80dBc/Hz at 100Hz corresponds to a jitter of 16.5Hz. Therefore our requirement for a jitter less than a few tens of Hz is achievable with modern oscillators. Indeed this requirement could be satisfied with a poorer rating as -60dBc/Hz at 100Hz is equivalent to a 20Hz jitter.

<sup>6</sup>Note a Gaussian distribution is likely to be an approximation of the typical spectral density of an oscillator. Close to the carrier oscillators tend to exhibit a  $\frac{1}{f}$  (rather than an  $\exp(-f^2)$  functional form) (Skolnik [96] pp738) due to particular characteristics of the semiconductors employed. Away from the carrier the noise becomes somewhat independent of frequency, i.e. is broadband or 'shot' noise.

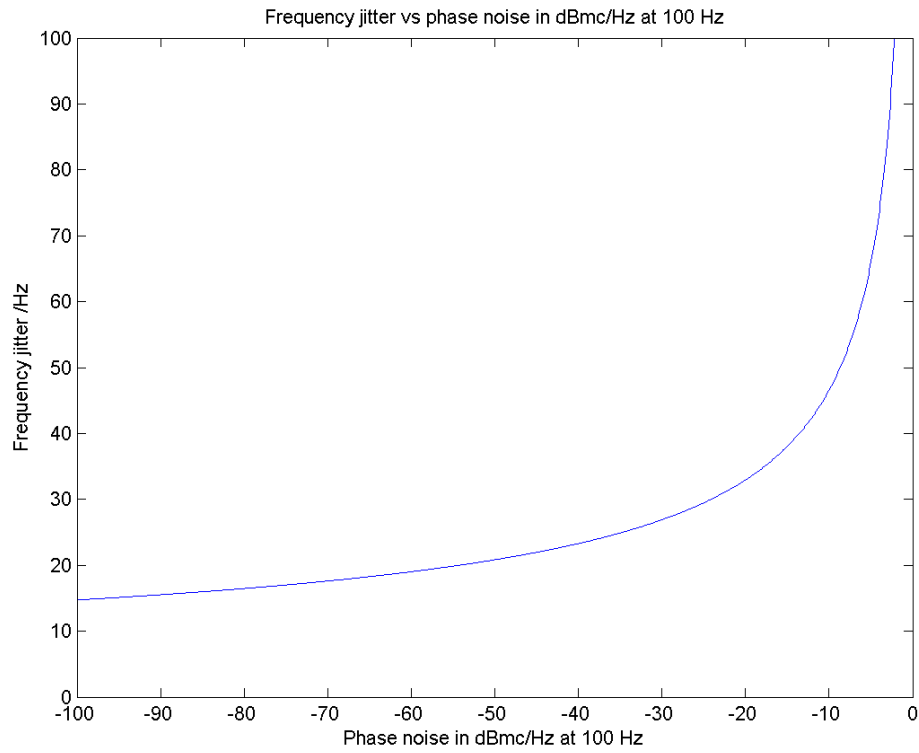


Figure 6.9: Oscillator frequency jitter standard deviation  $\sigma_{f_{Tx}}$  (Hz) is plotted against the ratio  $\eta$  (dBmc/Hz) of the oscillator spectral power density within a 1Hz bandwidth at  $f_{offset}=100\text{Hz}$  from the carrier, to the spectral power density within a 1Hz bandwidth at the carrier.



## Phase Noise

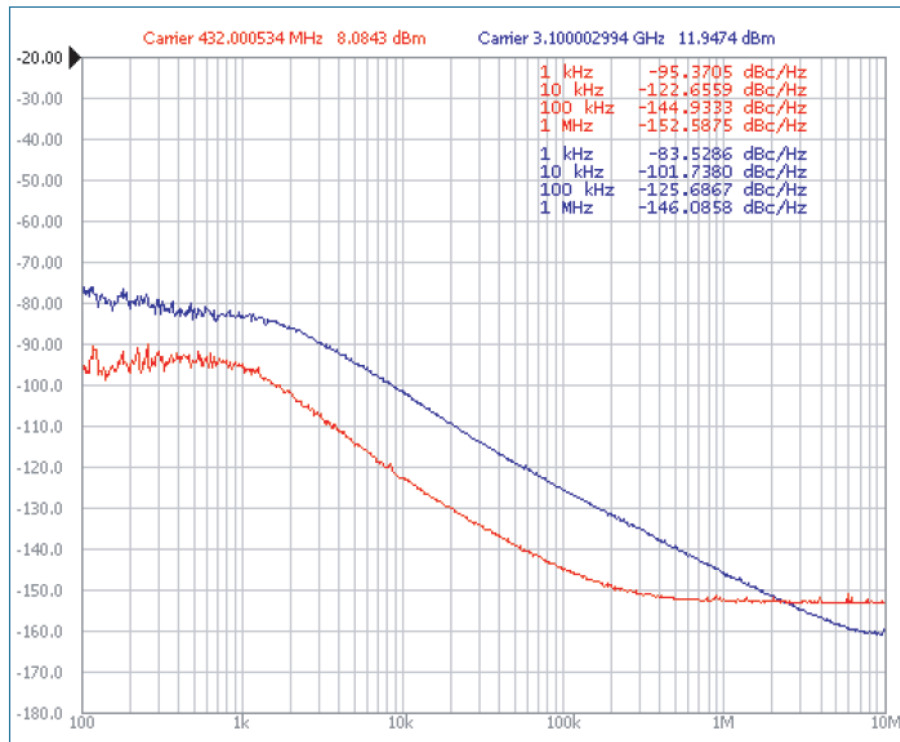


Figure 6.10: Phase noise of the CLX series semiconductor oscillators constructed by EM Research. [www.emresearch.com](http://www.emresearch.com). Specification is dated 19th June 2009. Up to a 1kHz offset the phase noise is relatively uniform for the 3GHz oscillator of interest (the blue trace). Between 1kHz and 1MHz the linear trace in the logarithmic space implies a power law phase noise frequency relationship  $\propto \frac{1}{f^\alpha}$ . The exponent  $\alpha$  is approximately  $\frac{146\text{dB} - 83\text{dB}}{60\text{dB} - 30\text{dB}} \approx 2.1$ . This possibly indicates some modern design improvements which better the expected  $\alpha$  of unity. The 432MHz oscillator exhibits a similar ‘flicker’ noise characteristic but then becomes frequency independent ‘shot noise’ beyond a 100kHz offset. One might assume a similar asymptotic behaviour for the 3GHz oscillator above a 10MHz offset.

## 6.4 Classification using combined length and Doppler fraction features

The Bayesian classifier<sup>7</sup> described in section 2.6.2 is designed to admit feature vectors of arbitrary dimensionality, assuming the distribution of all component features is Gaussian. Let us form a feature vector  $\mathbf{x}$  from both length  $L$  and Doppler fraction (dfrac)  $D$  measurements.

$$\mathbf{x} = \begin{pmatrix} L \\ D \end{pmatrix} \quad (6.4)$$

Using the MESAR2 recordings of Pod, Falcon, B747, B757 & B777 aircraft, let us assemble columns of feature vectors using dfrac measurements for waveforms D or E and length measurements for waveforms A,B or C. This data is plotted in figures 6.11 to 6.14 using colour coded ellipses for data from each aircraft type. The origin of the ellipses is set by the mean of the length and dfrac measurements whereas the ellipse width, in respective dimensions, is set by the standard error. The visual separation of the ellipses gives a clear indicator of likely performance of classification by aircraft type. In all cases there is some degree of separation, which suggests a type classification using length & dfrac will improve upon the somewhat poor performance observed using the Scattering center Model Compare algorithm. (See Chapter 4). However, the width of the ellipses (in particular the Hybrid example in figure 6.12) is somewhat large, characteristic of the spread in feature data from the targets of opportunity trials. As discussed above, we must therefore expect rather modest classification performance from such a limited, and inherently variable, data set.

The Classically processed waveform A and waveform C results in figures 6.11 & 6.14 offer limited range discrimination due to their range window being limited to 47m. However, the dfrac measurements clearly separate the aircraft.<sup>8</sup> In particular the Dash8 (dfrac near unity) is clearly distinguishable from the Boeing aircraft (dfrac 0.2 to 0.6) and Pod and Falcon (dfrac less than 0.2). The Hybrid processed waveform A data and Classically processed waveform B results in figures 6.12 & 6.13 demonstrate a greater separation in range, but also greater ellipse width in range. The waveform B range profiles of the Dash8 aircraft are corrupted by the effects of Propeller modulation, resulting in high range sidelobes which cause erroneous length measurements. The differences between these length feature measurements are discussed in section 4.5.

Figure 6.15 shows a surface of aircraft type classification confusion matrix off diagonal extent  $\xi$  plotted against length and dfrac thresholds. To generate the plot the classifier was applied 144 times, i.e. for each permutation of 12 values of length and dfrac thresholds. The plot implies classification performance is dominated by the length measurement. Indeed the surface is almost invariant with dfrac threshold. Above a length threshold of 25dB, classification performance rapidly becomes poor. To investigate whether the numerical differences between the features affected the classifier,<sup>9</sup> a scaling

<sup>7</sup>The k-means classifier described in section 2.6.4 would be an alternative to the Bayesian method. A benefit of k-means is that the assumption of Gaussian probability distributions of features is not required to be valid. However, k-means requires an amount of training data from which its ‘association hyperspheres’ can be formed via clustering. In this thesis the decision was made to opt for an ‘expert’ definition of what the feature probability distributions should look like; i.e. Gaussian in form, parameterized by *a-priori* defined means and standard deviations. This decision was largely forced given the data set was limited. In an operational system, which is able to run NCTR modes continuously, it is possible sufficient data may be collected to warrant a training subset. A k-means classifier could then be applied. The use of training data may also improve the performance of the Bayesian method.

<sup>8</sup>i.e. the ellipses formed from the mean and standard errors of the two dimensional (length & dfrac) feature data from each aircraft type are visually separable. Fig 4.5 demonstrates this was clearly not the case with length measurements alone.

<sup>9</sup>i.e. the apparent invariance of  $\xi$  with dfrac could be a spurious result, possibly an artifact of the finite precision

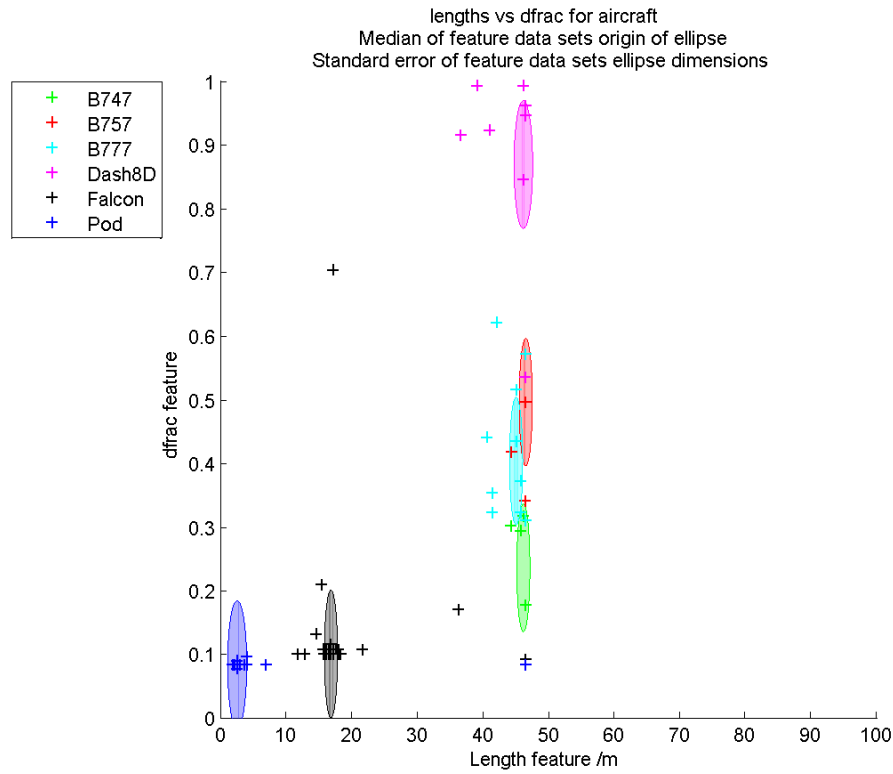


Figure 6.11: HRR profile Length feature measurements (using a below maximum threshold of 20dB) plotted against Doppler fraction (dfrac) features (using a threshold of -25dBm). Features are plotted for each six aircraft types. HRR waveform is A (wfc2  $\Delta f = 3.2\text{MHz}$ ,  $P = 8$ ,  $Q = 128$ ) and HRR processing method is Classical. Doppler waveform is D (32 pulse wfc3) for Pod/Falcon and E (32 pulse wfc2 stepped by  $\Delta f = 3.2\text{MHz}$ ) for others. Ellipses represent distribution of features. Ellipse origin is set to be the median feature value and ellipse height & width are defined to be the standard error in the (respective) feature measurements.

of 70m was applied to the length feature measurements; i.e. a 70m length (the approximate length of a Boeing 747) will yield a feature of 1 unit, numerically comparable with the highest dfrac value (which is unity). Fig 6.16 presents the same surface as 6.15, but this time with the length scaling applied. This plot shows a more understandable result. For very low ( $<15\text{dB}$ ) and very high ( $>45\text{dB}$ ) Doppler thresholds we see a degradation in classifier performance, as expected from the qualitative analysis in the previous section.

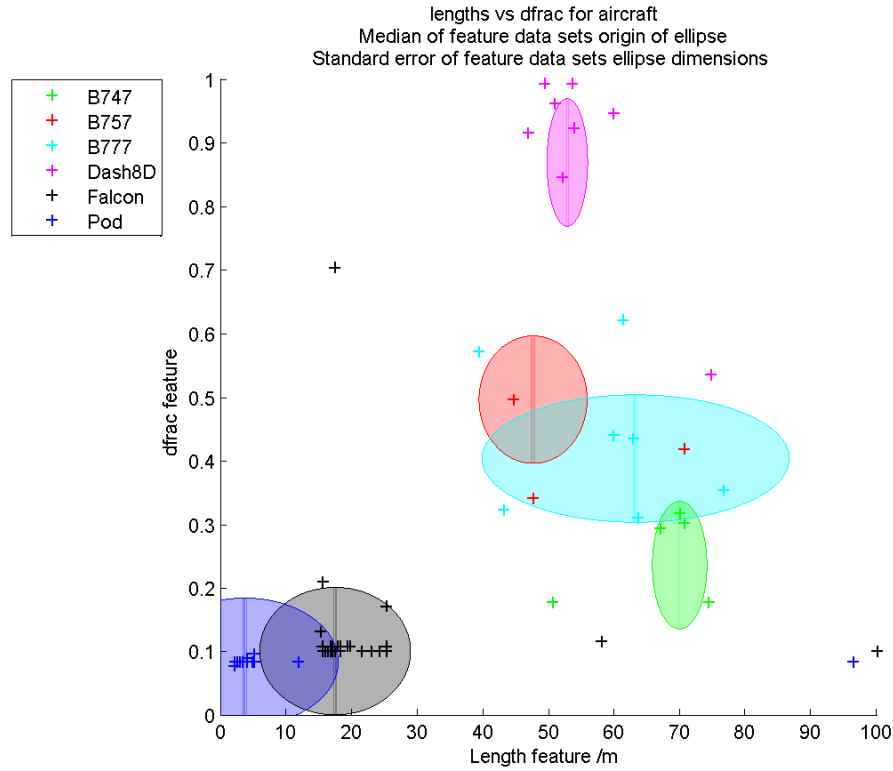


Figure 6.12: HRR profile Length feature measurements (using a below maximum threshold of 20dB) plotted against Doppler fraction (dfrac) features (using a threshold of -25dBm). Features are plotted for each six aircraft types. HRR waveform is A (wfc2  $\Delta f = 3.2\text{MHz}$ ,  $P = 8$ ,  $Q = 128$ ) and HRR processing method is Hybrid. Doppler waveform is D (32 pulse wfc3) for Pod/Falcon and E (32 pulse wfc2 stepped by  $\Delta f = 3.2\text{MHz}$ ) for others. Ellipses represent distribution of features. Ellipse origin is set to be the median feature value and ellipse height & width are defined to be the standard error in the (respective) feature measurements.

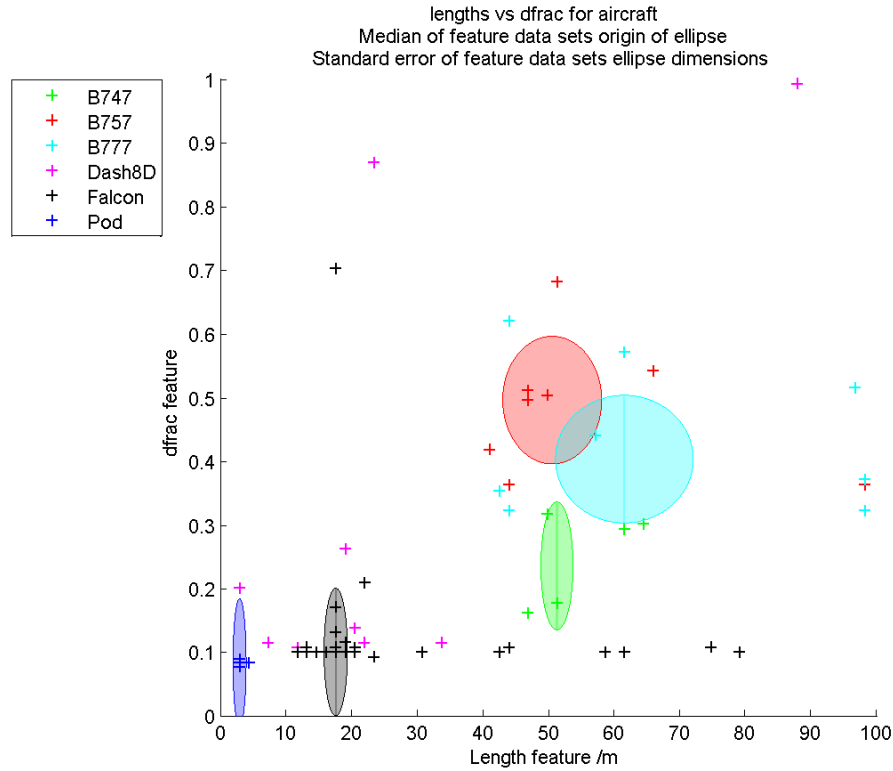


Figure 6.13: HRR profile Length feature measurements (using a below maximum threshold of 20dB) plotted against Doppler fraction (dfrac) features (using a threshold of -25dBm). Features are plotted for each six aircraft types. HRR waveform is B (wfc3  $\Delta f = 0.8\text{MHz}$ ,  $P = 8$ ,  $Q = 128$ ) and HRR processing method is Classical. Doppler waveform is D (32 pulse wfc3) for Pod/Falcon and E (32 pulse wfc2 stepped by  $\Delta f = 3.2\text{MHz}$ ) for others. Ellipses represent distribution of features. Ellipse origin is set to be the median feature value and ellipse height & width are defined to be the standard error in the (respective) feature measurements. Note the (erroneous) length measurement of the Dash8 resulting from the propeller modulation induced range sidelobes causes the Dash8 ellipse to not appear within the chosen plot range.

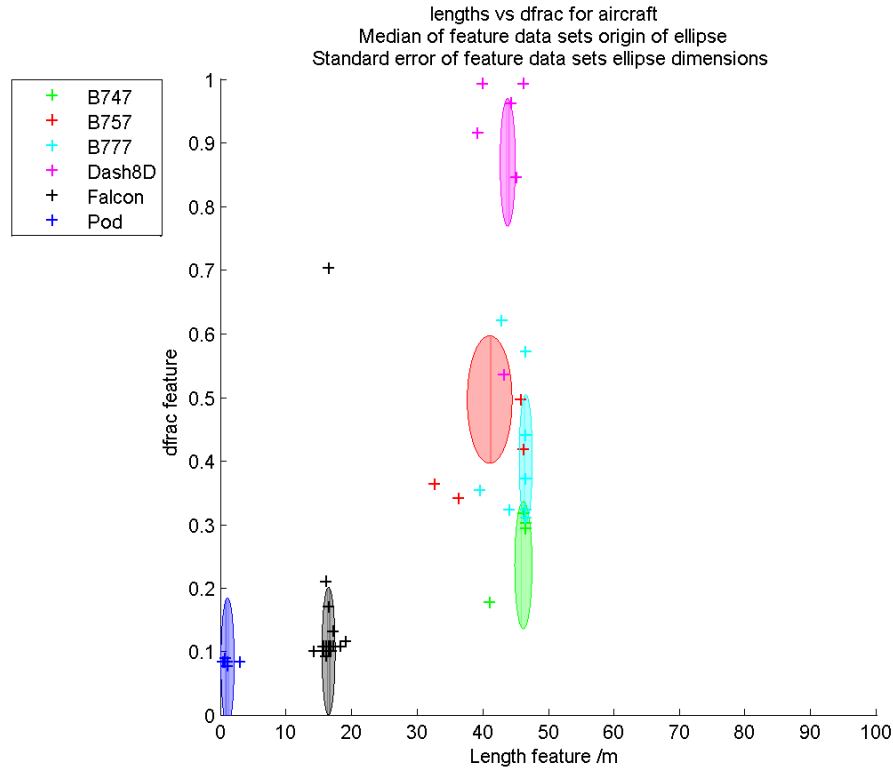


Figure 6.14: HRR profile Length feature measurements (using a below maximum threshold of 20dB) plotted against Doppler fraction (dfrac) features (using a threshold of -25dBm). Features are plotted for each six aircraft types. HRR waveform is C (wfc3  $\Delta f = 3.2\text{MHz}$ ,  $P = 8$ ,  $Q = 128$ ) and HRR processing method is Classical. Doppler waveform is D (32 pulse wfc3) for Pod/Falcon and E (32 pulse wfc2 stepped by  $\Delta f = 3.2\text{MHz}$ ) for others. Ellipses represent distribution of features. Ellipse origin is set to be the median feature value and ellipse height & width are defined to be the standard error in the (respective) feature measurements.

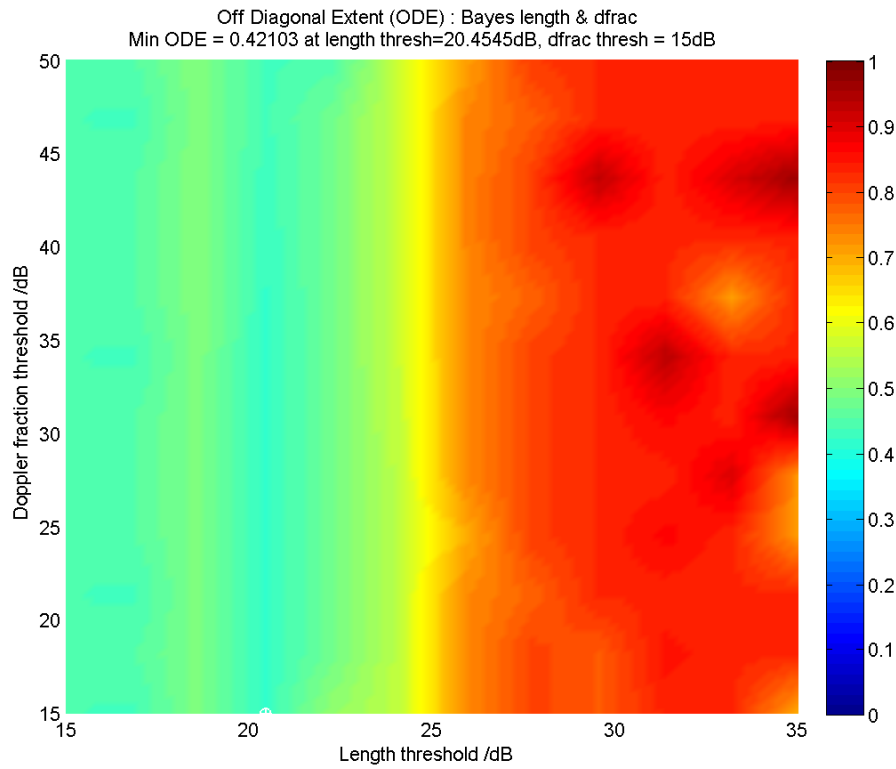


Figure 6.15: Bayesian classifier off diagonal extent (ODE) computed for feature vectors with elements of length and dfrac features. An ODE surface is plotted as a function of length and dfrac thresholds. Length features are obtained using Hybrid processed waveform A.

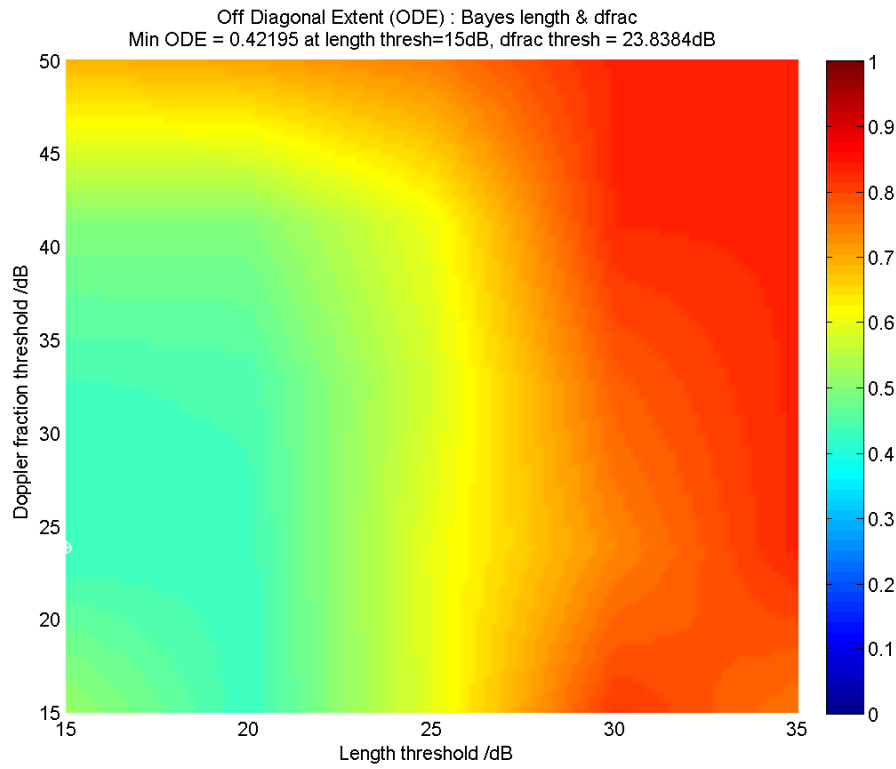


Figure 6.16: Bayesian classifier off diagonal extent (ODE) computed for feature vectors with elements of length and dfrac features. An ODE surface is plotted as a function of length and dfrac thresholds. Length features are obtained using Hybrid processed waveform A and are scaled by 70m; i.e. a 70m length is a 1 unit feature.



## 6.5 Conclusions

Let us summarize the results presented in this chapter in the form of (additional) answers to the second, third and fourth key questions posed in the introductory chapter.

2. *How robust are feature measurements taken from the trials data set? Do feature measurements naturally segment into classes? Should certain features be combined, are they correlated?*

- Figures 6.11 to 6.14 indicate the six aircraft chosen could be separately identified if length & dfrac features are combined into a feature vector. However, combination of scalar features to form other scalar features has not been explored. It is likely the aircraft airspeed is strongly correlated with spool rate via some functional relationship which is characteristic of a particular engine type. If spool rate could be obtained from the Doppler spectrum, its combination with airspeed may assist in classification via engine type. However, this is beyond the scope of the (ambiguous) Doppler spectral measurements reported in this thesis.

3. *Can we achieve acceptable classifier performance based upon the extraction of various target features? How does the crudeness of class definition affect this result and how does performance depend upon (i) the proportion of total pulse cycles used to form the target data set (ii) thresholds used in feature measurement and (iii) the features used (and their possible combination) ?*

- Long or short classification  $\xi$  is lowest for below-maximum length thresholds of between 20 and 25dB and is largely independent of numbers of frequency steps within the range  $20 < Q < 128$  studied. Classification performance drops dramatically for thresholds above 25dB as range sidelobes become exposed.
- Four length classification  $\xi$  appears to rise steeply from a plateau of 0.4 after thresholds of 23dB for intermediate values within the frequency step range. Interestingly, the lowest  $\xi$  is for 60 to 80 frequency steps with a threshold of 20dB. Although possibly a serendipitous result due to an inherent variability of measured HRR profiles, it does prove that increasing the number of frequency steps may not always result in higher classification performance.
- Prop, JEM or NNSD  $\xi$  is lowest for number of pulses  $P > 27$  with a 22 to 30dB dfrac threshold. Below  $P = 16$  classification performance drops rapidly with decreasing  $P$ , as expected due to the reduction in Doppler resolution.
- Combined length & dfrac measurements yield a  $\xi$  of 0.4 for aircraft type classification (i.e. similar to Four Lengths classification). Length thresholds of less than 25dB and Doppler thresholds between 20 and 40dB are required<sup>10</sup> to achieve this. Within this region,  $\xi$  is somewhat uniform.

4. *Based upon the learning obtained in conducting this research, what are the recommendations regarding the design of future NCTR modes?*

- Carrier frequency stability  $10 \log_{10} \left( \frac{\sigma_{f_{Tx}}}{f_{Tx}} \right)$  should be less than -80dB at S band (3GHz), i.e. a typical carrier frequency jitter  $\sigma_{f_{Tx}}$  of less than one part in  $10^8$ , which is a few tens of Hz.

---

<sup>10</sup>Following scaling of length features by 70m.

## Chapter 7

# NCTR waveform design recommendations

### 7.1 Chapter summary

This chapter endeavours to offer a ‘reality check’ upon the concepts previously discussed. It is effectively a response to the question: *"What is the parameter space for NCTR waveforms that could feasibly be used in an operational context?"*

From a list of generic operational requirements a set of constraints are derived which in turn enable an *NCTR waveform design chart* to be constructed. The chart is a colour coded surface plot of dwell time  $T_{dwell}$ , number of guard pulses  $G$  and expected target signal to noise ratio ( $S/N$ ) as a function of target range  $R$  and NCTR waveform PRF  $f_{PRF}$ . All other target, Radar, waveform and environmental parameters are held constant. Graphs of maximum viable PRF vs target range are derived from the chart. Charts are produced for waveform A and also for ‘candidate’ HRR and Doppler waveforms which represent the authors practical suggestions for viable NCTR modes.

### 7.2 Operational requirements of an NCTR waveform

The analysis presented to far is largely concerned with: (i) a discussion of NCTR waveforms A to E used in experiments with MESAR2 and (ii) the effect upon classification performance resulting from a degradation of these waveforms via the use of fewer pulses and frequency steps, and the ‘jittering’ of carrier frequencies. From (i) we may conclude the formation of high range resolution (HRR) profiles and Doppler spectra of aircraft targets is possible with a phased array system such as MESAR2, and from (ii) to what degree one can one ‘trim’ a waveform in terms of number of pulses (and therefore total duration) before classification performance becomes intolerable. The desire to reduce the dwell time of an NCTR waveform is an example of an operational need. If a viable NCTR waveform could be delivered in less time this means more time is available for (i) surveillance and tracking functions or (ii) further NCTR looks. As discussed above, more NCTR looks (of the same resolution) leads to improved classification. Let us qualitatively summarize the, possibly conflicting, operational requirements of an NCTR waveform, whose (single PRI) schematic is illustrated in fig 7.1.

1. The higher the PRF  $f_{PRF}$ , the reduction in potential ambiguity inherent in a target Doppler spectrum. If the PRF exceeds the JEM bandwidth for an aircraft, and the Doppler resolution is sufficiently fine, it may be possible to resolve both the spool rate and number of blades of a



interrogation time before a decision must be made whether to counter a perceived threat; e.g an incoming aircraft or missile.

7. The waveform must be designed such that the target (whose range and range rate is known from the tracking system) is not *eclipsed*, i.e. appears during the transmission phase of the pulse repetition interval.
8. The product of PRF and pulse length  $\tau f_{PRF}$  must not exceed the maximum duty cycle  $D_{\max}$  of the Radar. In the examples below a maximum duty of 0.2 is used, which is probably on the high side.<sup>3</sup>
9. The pulse repetition interval should be large enough to allow for a fixed extent  $\Delta R$  to be captured in receiver samples beyond the leading edge of the pulse reflection. In the examples below a  $\Delta R$  of 200m is used.
10. The PRF and number of pulses must be set such that the target Doppler response is: (i) not within  $\beta$  Doppler filter bins of the ‘edges’ of the filter and (ii) is sufficiently separable from any clutter, whose maximum range rate  $\dot{R}_c$  is specified. In the examples below,  $\beta$  is set as unity and  $\dot{R}_c$  is set at  $10\text{ms}^{-1}$ .

---

<sup>3</sup>The PAVE Phase Array Warning System (PAWS) long range ballistic missile defence radar is a non rotating planar phased array much like MESAR2, except is physically much larger (22.1m array face diameter) as a consequence of its operating frequency of 420 to 450MHz. PAVE PAWS has a duty cycle of 0.18 which can rise to a maximum of 0.25. <http://www.fas.org/spp/military/program/track/pavepaws.htm>

### 7.3 NCTR waveform design chart

The list above can be used to generate an ‘NCTR waveform design chart.’ The chart is a colour coded surface plot of dwell time  $T_{dwell}$ , number of guard pulses  $G$  and expected target signal to noise ratio  $(S/N)$  as a function of target range  $R$  and NCTR waveform PRF  $f_{PRF}$ . All other target, Radar, waveform and environmental parameters are held constant. Combinations of range and PRF which fail the requirements 6 to 10 above are not plotted, resulting in a series of ‘islands of possibility’ as indicated in fig 7.4, which is the chart for waveform A assuming a 20m<sup>2</sup> target with an inbound range rate of 200ms<sup>-1</sup>. Given it is desirable to maximize PRF, fig 7.3 illustrates the highest possible PRF for each range. If the Radar system is able to dynamically modify PRF prior to transmission of the NCTR look, an algorithm based upon the waveform design chart will be able to pick the optimum value.<sup>4</sup>

The recipe for construction of the design charts is as follows:

1. Construct vectors of range and PRF. In the examples below, ranges from 0 to 100km and PRF from 1 to 20kHz are defined in  $N = 200$  steps; i.e. define integer indices  $n, m = 1 \dots N$ .
2. Compute time  $t_T$  relative to the start of the PRI  $1/f_{PRF}(m)$  at which the leading edge of the target reflection at range  $R(n)$  will occur. Since the absolute range of the target is known prior to NCTR, the PRF need not be constrained to give an unambiguous range  $\frac{c}{2f_{PRF}}$  coverage, at minimum  $\Delta R$  beyond  $R(n)$ . Therefore  $t_T$  is computed from the formula

$$t_T = \frac{2R(n)}{c} - \frac{Y}{f_{PRF}(m)} \quad (7.1)$$

where  $Y$  is a positive integer to be found such that  $t_T \in [0, 1/f_{PRF}(m)]$ .

3. In a similar manner to the computation of  $t_T$  and  $Y$ , find the pulse number  $X$  such that the receiver samples from pulse  $X$  onwards contain clutter from the entire range  $R_c$  at which clutter is defined. In the examples below  $R_c$  is set at 100km.
4. Define the number of guard pulses  $G(n, m)$  to be the maximum of  $Y$  and  $X$ ; i.e. for any given burst we ignore the first  $G$  pulses, only taking data from the  $P$  pulses which follow.
5. Compute dwell time

$$T_{dwell}(n, m) = \frac{(P + G(n, m))Q}{f_{PRF}(m)} \quad (7.2)$$

6. Compute target signal to noise ratio via the Radar Equation, having previously defined antenna area  $A$ , antenna effectiveness  $\eta$ , integration efficiency<sup>5</sup>  $E_i$ , pulse length  $\tau$ , peak transmitted power  $P_t$ , target RCS  $\sigma$ , carrier frequency<sup>6</sup>  $f_{Tx}$ , propagation loss factor<sup>7</sup>  $|F^2|^2$ , system loss factor  $L$ , ambient temperature  $T_0$  and receiver noise figure  $N_f$

$$(S/N)_{n,m} = \frac{A^2 \eta^2 P E_i(P) \tau P_t \sigma f_{Tx}^2 |F^2|^2}{4\pi c^2 L k_B T_0 N_f R(n)^4} \quad (7.3)$$

<sup>4</sup>Note if the target range rate changes then a given chart will need to be recomputed.

<sup>5</sup>Typically for coherent (in-phase & quadrature) integration,  $E_i(P) = 1$ . For non-coherent integration  $E_i(P) = \frac{1}{\sqrt{P}}$ , i.e. such that  $E_i(P)P = \sqrt{P}$ .

<sup>6</sup>In a stepped frequency waveform the lowest frequency is used, thereby underestimating the signal to noise ratio.

<sup>7</sup>This is ignored, (i.e. set at 0dB) in the construction of the example waveform design charts.

7. Compute Doppler frequency  $f_D = -\frac{2\dot{R}}{c}f_{Tx}$  for target and (maximum) clutter range rates for highest and lowest frequencies used in the stepped frequency waveform. Determine (ambiguous) Doppler frequency  $f_{Da}$  ‘wrapped’ into extent  $[0, f_{PRF}(m)]$  via the computation of (positive or negative) integer  $Z$  such that  $f_{Da} = f_D + Zf_{PRF}(m)$
8. *Invalid test #1 (Eclipsing)* : if  $t_T < \tau + t_{switch} + \alpha\tau$  then set  $(S/N)_{n,m}$ ,  $T_{dwell}(n, m)$  and  $G(n, m)$  to be -1.  $t_{switch}$  is the switching time between transmit and receive modes of the Radar<sup>8</sup> and  $\alpha\tau$  is set to be the time either side of the target region of the receiver opening window. The receiver opening window (which must allow for pulse compression and a target extent of  $\Delta R$ ) is therefore of duration  $\frac{2\Delta R}{c} + (1 + 2\alpha)\tau$ . In the examples below  $\alpha = 0.25$ .
9. *Invalid test #2 (Duty)* : if  $f_{PRF}(m)\tau > D_{\max}$  then set  $(S/N)_{n,m}$ ,  $T_{dwell}(n, m)$  and  $G(n, m)$  to be -2.
10. *Invalid test #3 (Dwell)* : if  $T_{dwell}(n, m) > T_{\max}$  then set  $(S/N)_{n,m}$ ,  $T_{dwell}(n, m)$  and  $G(n, m)$  to be -3. The maximum dwell could be defined (e.g. for a fixed position antenna), or derived from the rotation rate  $\Omega_{rot}$  of the antenna and the maximum amount of angular scan  $\Delta\phi_{\max}$ , if this is appropriate to the Radar.<sup>9</sup> In the case of the latter  $T_{\max} = \frac{\Delta\phi_{\max}}{\Omega_{rot}}$ .
11. *Invalid test #4 (Insufficient PRI)* : if  $t_{close} + t_{switch} > \frac{1}{f_{PRF}(m)}$  then set  $(S/N)_{n,m}$ ,  $T_{dwell}(n, m)$  and  $G(n, m)$  to be -4. Define receiver opening time (relative to start of PRI) as

$$t_{open} = t_T - \alpha\tau \quad (7.4)$$

and receiver closing time as

$$t_{close} = t_{open} + \frac{2\Delta R}{c} + (1 + 2\alpha)\tau \quad (7.5)$$

12. *Invalid test #5 (Blind speed)* : set  $(S/N)_{n,m}$ ,  $T_{dwell}(n, m)$  and  $G(n, m)$  to be -5 if the following condition is not satisfied, using values for target ( $t$ ) and clutter ( $c$ ); Doppler frequencies  $f_D^{(t,c)}$  computed at *both* the smallest and largest of the carrier frequencies in the stepped frequency waveform must satisfy:

$$\max\left(\frac{\beta f_{PRF}}{P}, f_D^{(c)}\right) < f_D^{(t)} < \min\left(f_{PRF} - \frac{\beta f_{PRF}}{P}, f_{PRF} - f_D^{(c)}\right) \quad (7.6)$$

13. Unless an ‘invalid region’ graph is explicitly required, plot colour coded graphs of matrices  $S/N$ ,  $T_{dwell}$  and  $G$  for values of  $G \geq 0$ . For an invalid region graph (e.g. fig 7.2), only plot colour coded graphs of matrices  $S/N$ ,  $T_{dwell}$  and  $G$  for values of  $G < 0$ .<sup>10</sup>

To illustrate the use of the NCTR waveform design chart let us compare Waveform A with ‘candidate’ waveforms for optimized HRR and Doppler waveforms. It is the author’s suggestion<sup>11</sup> that *separate* range and Doppler waveforms be transmitted by a phased array system which employs stepped frequency techniques to achieve high range resolution. The parameters for each example are provided

<sup>8</sup>Which is assumed to be monostatic

<sup>9</sup>It is of course possible that a multi-face rotating phased array radar could ‘hand over’ NCTR activities between faces if the maximum scan angle of one face is exceeded.

<sup>10</sup>Note we could easily choose the sign of  $T_{dwell}$  for this test, but not  $S/N$  since this is expressed in dB and could in principle be negative. (Although this would not allow for a target detection!)

<sup>11</sup>Based upon the discussion of Range-Doppler profiles in the previous chapter.

in table 8.1 below. For the ‘candidate’ waveforms it is assumed a future operational system will have advanced beyond the capabilities of MESAR2. Hence a larger bandwidth (18MHz) and sample rate (20MHz) are used. This enables the HRR waveform to offer the same resolution as waveform A but with a factor of four less frequency steps and consequently lower dwell time. The initial carrier frequency is fixed at the same value as waveform A. There is nothing special about this frequency, apart from it should be characteristic of S-band; i.e. 3GHz would be equally acceptable at this level of analysis. Linear chirp pulses are assumed in order for Hybrid processing to be possible. Note the extra swept bandwidth will cause a squinting loss. However, as shown in fig 2.24, this should be a fraction of a dB. In both candidate waveforms, a reduced pulse length to  $10\mu s$  is used to raise the PRFs allowable given an assumed maximum duty of 20%. In order to compensate for a possible reduction in Doppler resolution caused by raising the PRF, the Doppler waveform is now  $P = 256$  pulses, and a single frequency step. Waveform E used a 2.5kHz PRF with 32 steps. If the PRF is increased to 20kHz, to achieve the same Doppler resolution  $\frac{f_{PRF}}{P}$  we must increase  $P$  by a factor of 8.

	Invalid regions example	Waveform A	HRR waveform	Doppler waveform
$\tau$	$25.6\mu s$	$25.6\mu s$	$10\mu s$	$10\mu s$
$B$	4.5MHz	4.5MHz	18MHz	18MHz
$f_1$	2.705GHz	2.705GHz	2.705GHz	2.705GHz
$P$	8	8	8	256
$Q$	128	128	32	1
$\Delta f$	3.2MHz	3.2MHz	12.8MHz	0MHz
$\Delta R$	200m	200m	200m	200m
$\alpha$	0.25	0.25	0.25	0.25
$\beta$	1	1	1	1
$\Omega_{rot}$	0	0	0	0
$\Delta\phi_{max}$	-	-	-	-
$T_{max}$	300	1000	100	100
$D_{max}$	0.2	0.2	0.2	0.2
$f_s$	5MHz	5MHz	20MHz	20MHz
$A$	$4m^2$	$4m^2$	$4m^2$	$4m^2$
$\eta$	0.5	0.5	0.5	0.5
$E_i$	1	1	1	1
$P_t$	12kW	12kW	12kW	12kW
$L$	10dB	10dB	10dB	10dB
$N_f$	1.68	1.68	1.68	1.68
$t_{switch}$	$5\mu s$	$5\mu s$	$5\mu s$	$5\mu s$
$\dot{R}$	$-200ms^{-1}$	$-200ms^{-1}$	$-200ms^{-1}$	$-200ms^{-1}$
$\sigma$	$20m^2$	$20m^2$	$20m^2$	$20m^2$
$R_c$	100km	100km	100km	100km
$\dot{R}_c$	$10ms^{-1}$	$10ms^{-1}$	$10ms^{-1}$	$10ms^{-1}$
$ F^2 ^2$	0dB	0dB	0dB	0dB
$T_0$	290K	290K	290K	290K

Table 8.1: input parameters for the creation of an NCTR waveform design chart. Parameters are

---

provided for the four examples in figures 7.2 to 7.8.



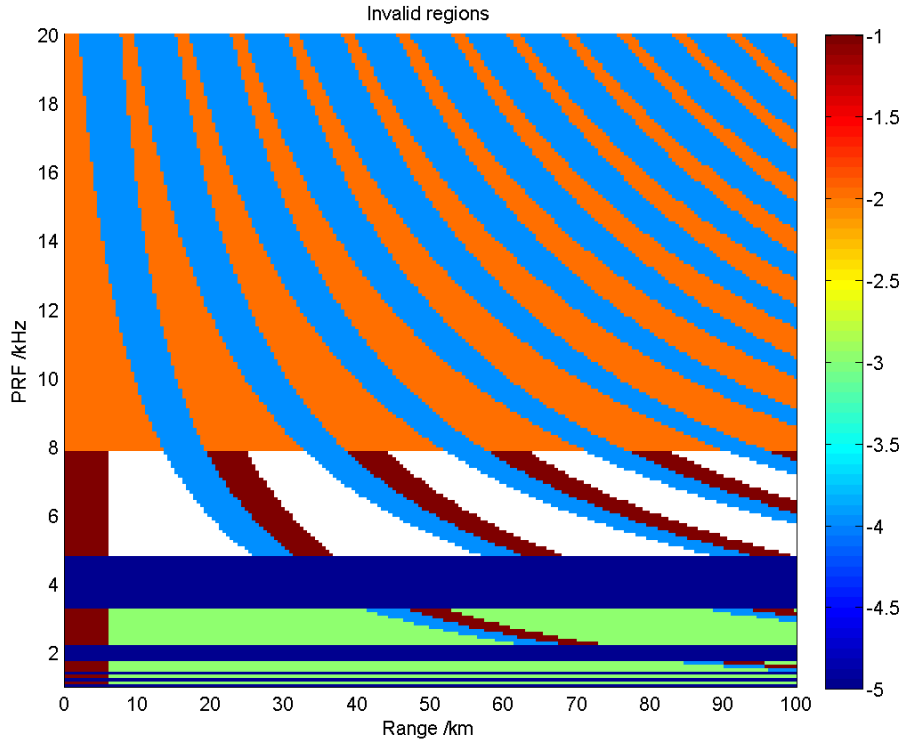


Figure 7.2: Example waveform design chart with invalid regions shown. Non-white regions correspond to invalid PRF and target range combinations due to failure of one (or more) of five tests: Eclipsed target (-1), Max duty cycle exceeded (-2), Max dwell time exceeded (-3), Required receiver closing time + switching time exceeds pulse repetition interval (-4), Target Doppler frequency is within clutter region or is within  $\frac{\beta f_{PRF}}{P}$  of edges of Doppler filter window  $[0, f_{PRF}]$  (-5).

Figures 7.3, 7.7 and 7.5 show the highest valid PRFs for a given target range (and corresponding dwell times, guard pulses and signal to noise ratio) for, respectively, waveform A, the candidate HRR waveform and the candidate Doppler waveform. One can immediately see that a reduction in dwell time is possible for waveform A from the 560-570ms in the experimental examples quoted in earlier chapters, to between 200 and 280ms depending on target range. PRFs are consequently enhanced to between 5 and 7.8 kHz. It is assumed the 8 pulse Doppler filter is still able to successfully filter JEM from the range profile given the effective resolution of the filter is now reduced by up to a factor of three. The candidate HRR waveform requires a much more reasonable dwell time of between 33 and 43ms owing to PRFs up to the maximum in the scale (20kHz) and the reduction in frequency steps resulting from the four fold increase in pulse bandwidth and receiver sampling rate. The Doppler waveform is even more modest with a dwell time of between 13 and 23ms.

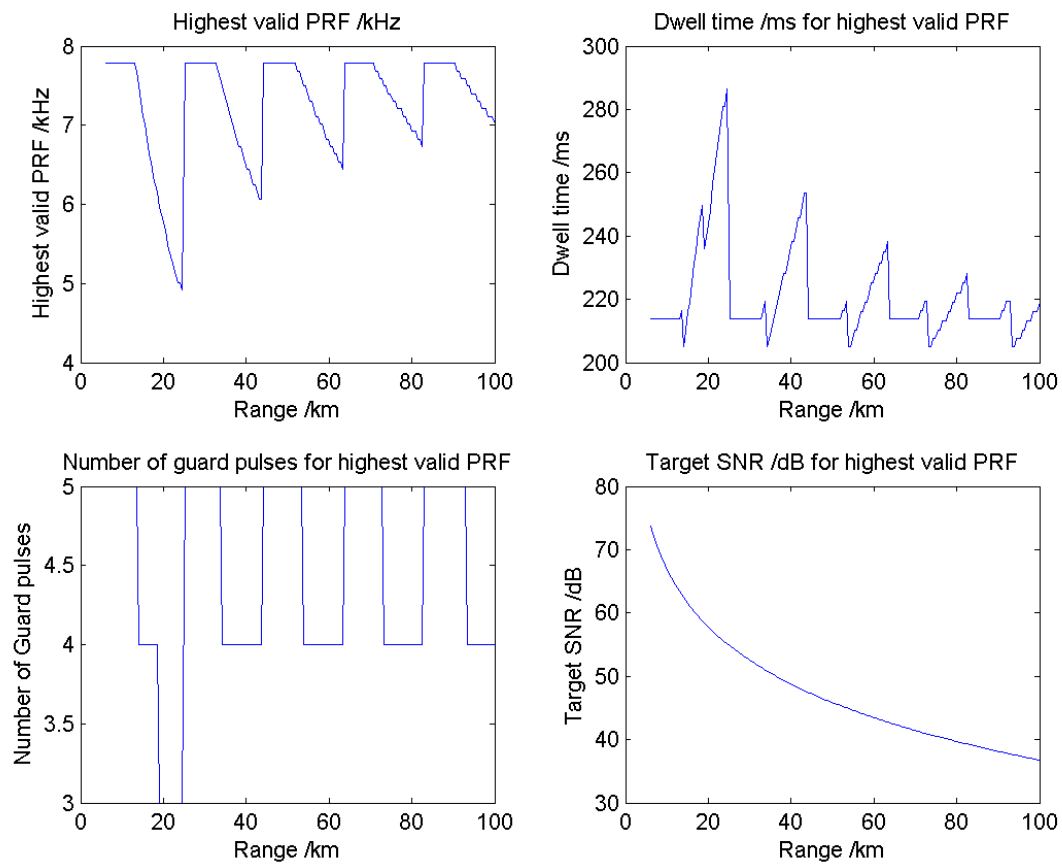


Figure 7.3: Highest valid PRF is plotted against target range for waveform A (see table 8.1). Corresponding target signal to noise ratio, number of guard pulses and waveform dwell time are also plotted.

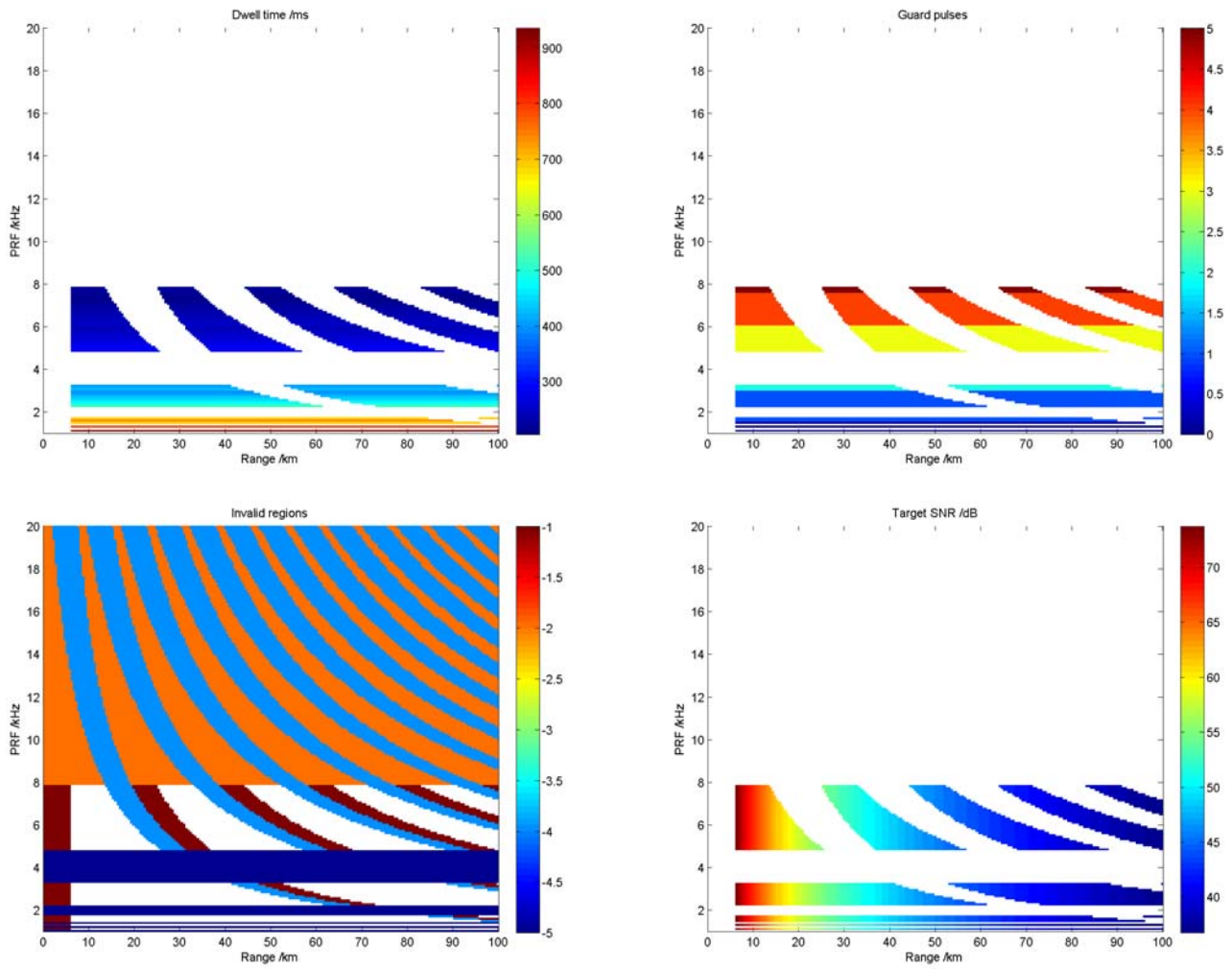


Figure 7.4: NCTR waveform design chart for waveform A. Coloured regions denote valid PRF and target range combinations given fixed target, environmental, waveform and radar parameters described in table 8.1.

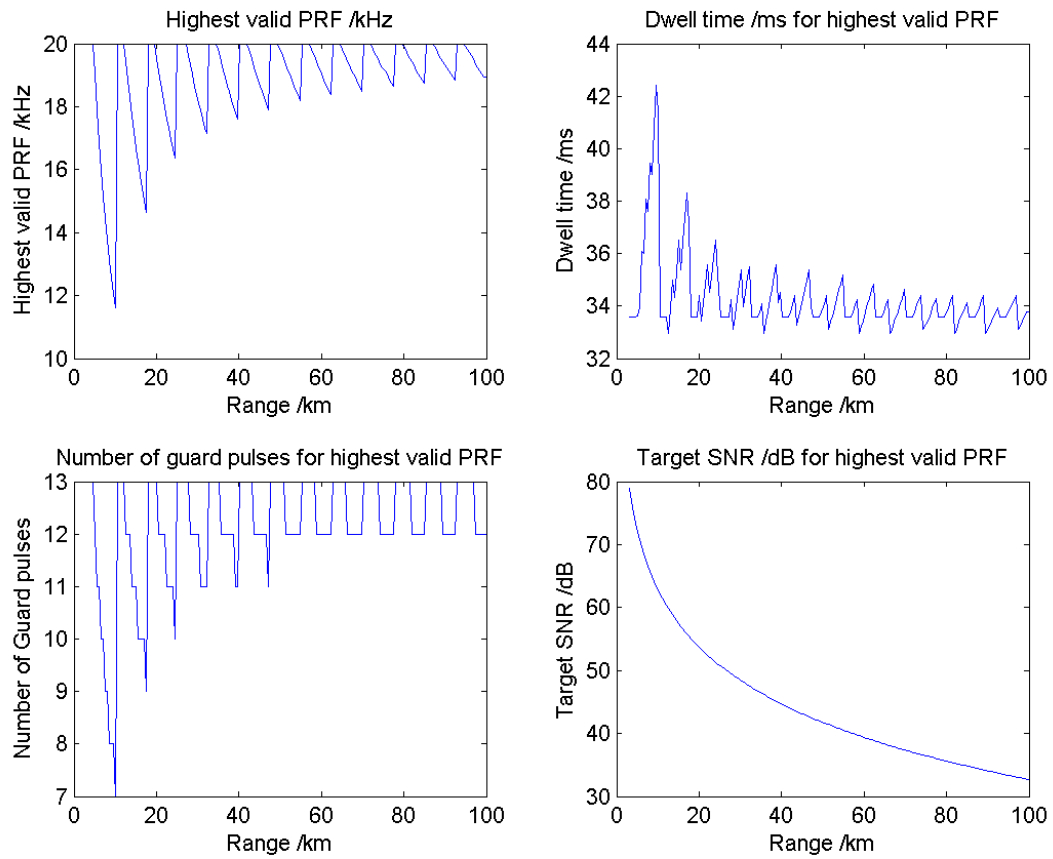


Figure 7.5: Highest valid PRF is plotted against target range for a candidate NCTR HRR waveform (see table 8.1). Corresponding target signal to noise ratio, number of guard pulses and waveform dwell time are also plotted.

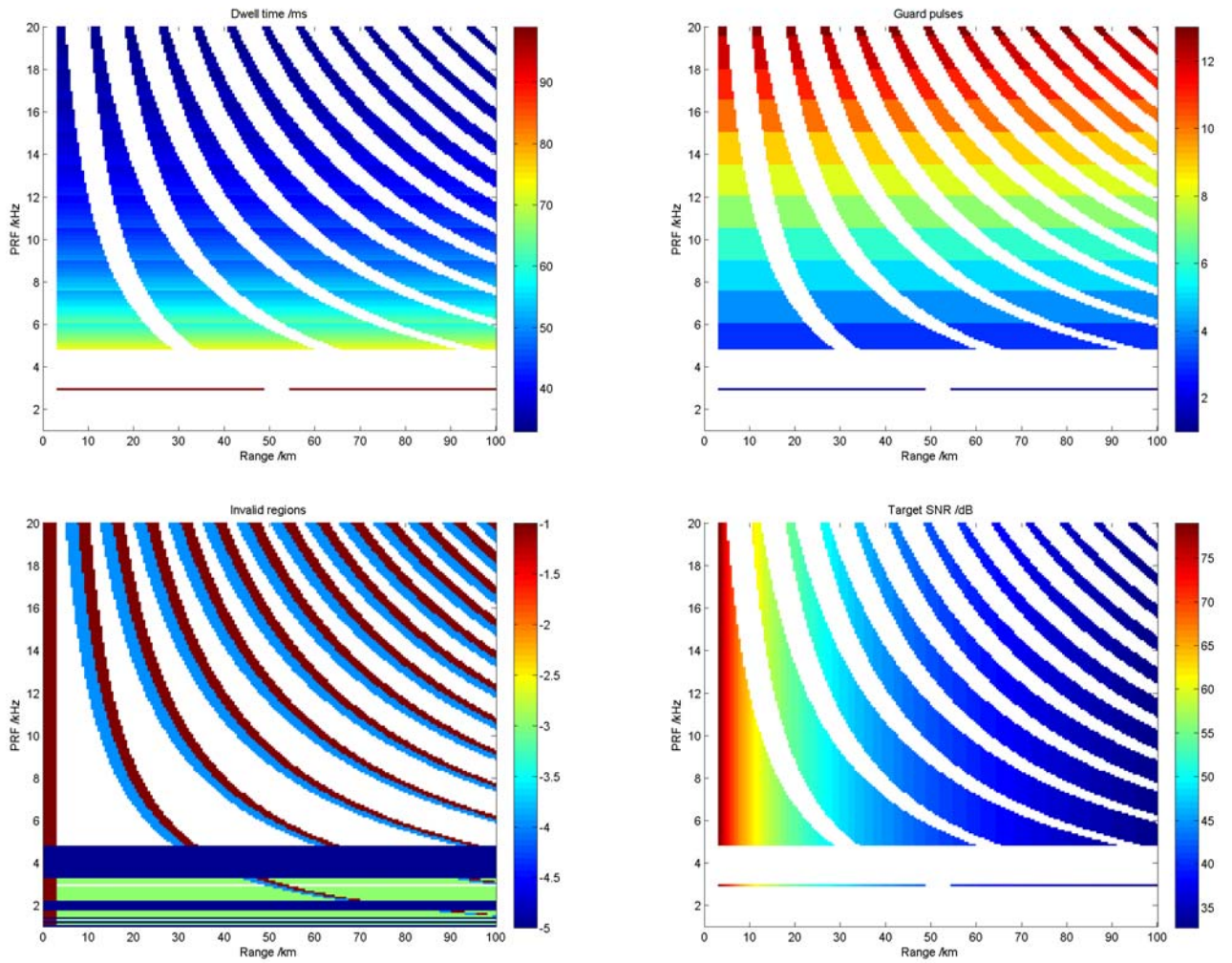


Figure 7.6: NCTR waveform design chart for a candidate HRR waveform. Coloured regions denote valid PRF and target range combinations given fixed target, environmental, waveform and radar parameters described in table 8.1.

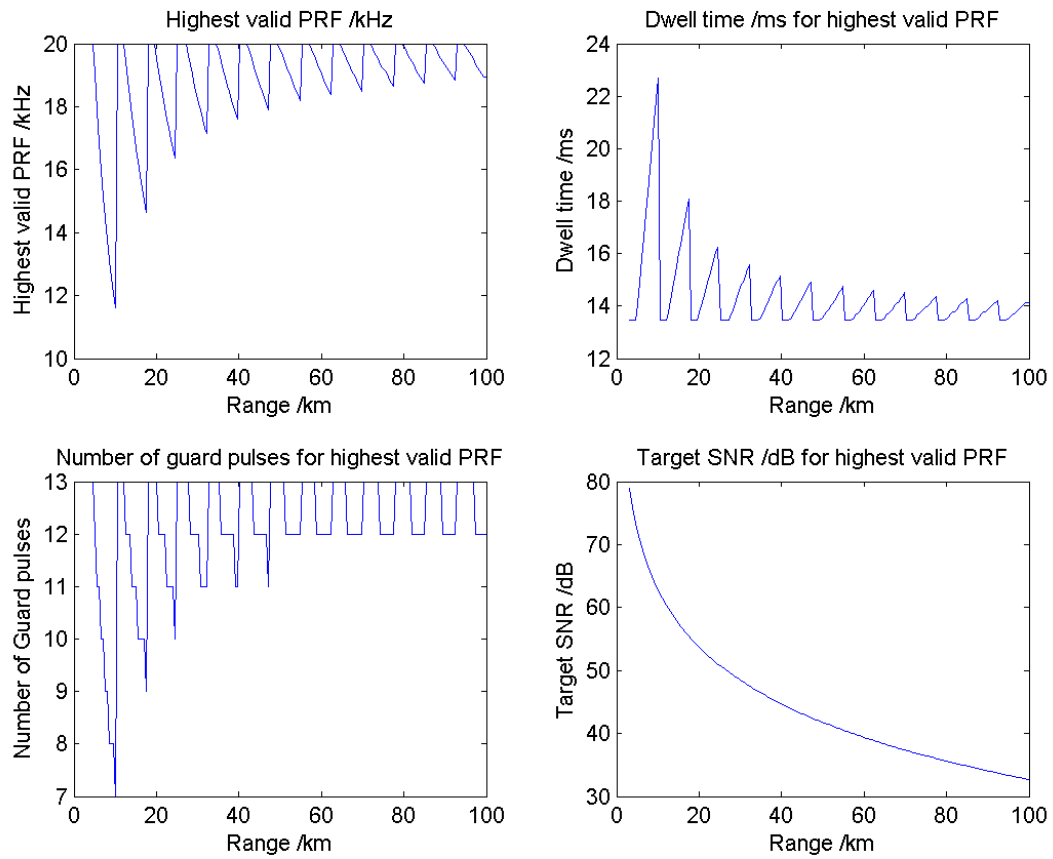


Figure 7.7: Highest valid PRF is plotted against target range for a candidate NCTR Doppler waveform (see table 8.1). Corresponding target signal to noise ratio, number of guard pulses and waveform dwell time are also plotted.



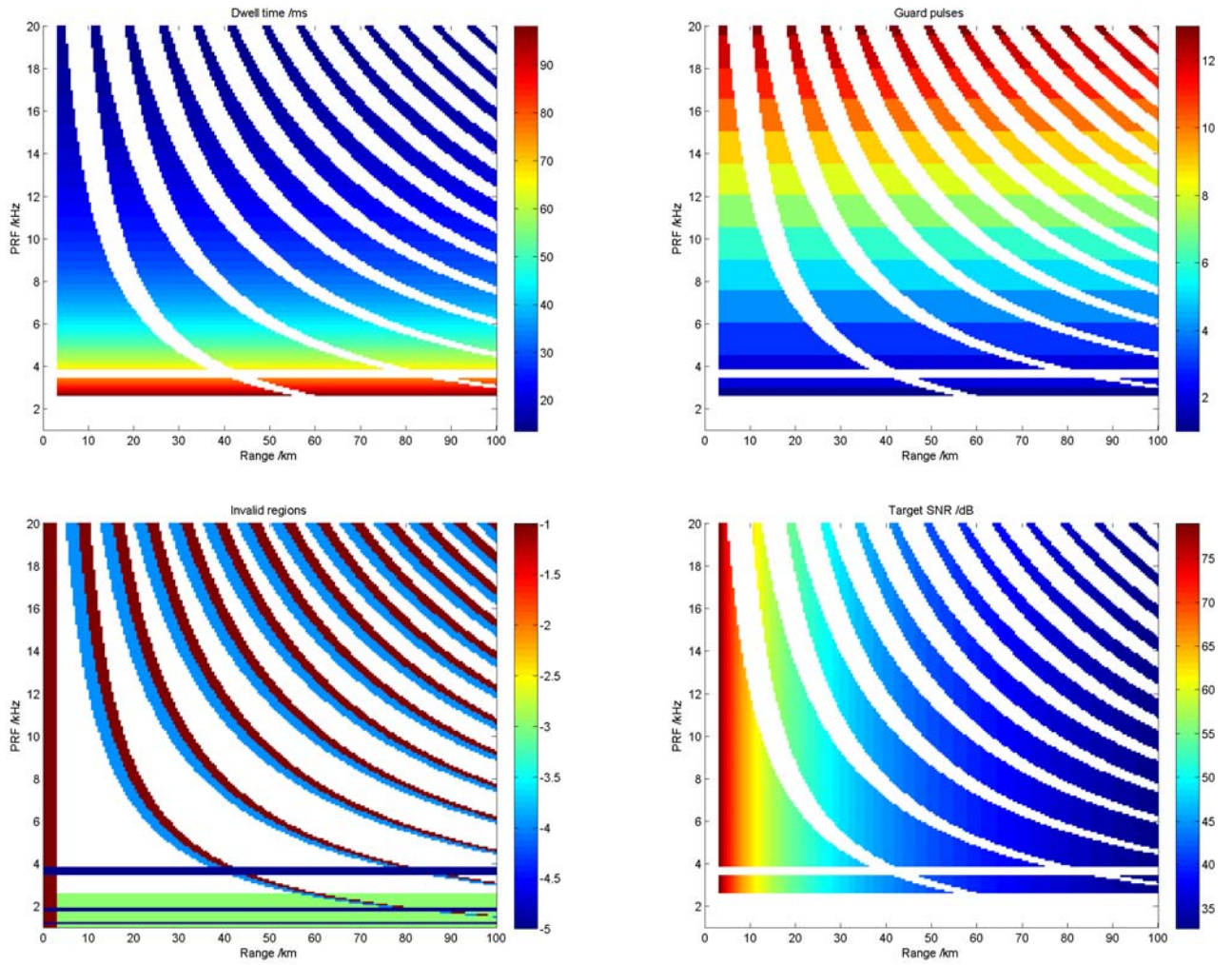


Figure 7.8: NCTR waveform design chart for a candidate Doppler waveform. Coloured regions denote valid PRF and target range combinations given fixed target, environmental, waveform and radar parameters described in table 8.1.

## 7.4 Conclusions

Let us summarize the results presented in this chapter in the form of (additional) answers to the fourth key question posed in the introductory chapter.

4. *Based upon the learning obtained in conducting this research, what are the recommendations regarding the design of future NCTR modes?*

The NCTR waveform design chart methodology described aims to embrace the operational requirements of an NCTR mode. To achieve high quality length and Doppler spectrum features one desires:

- A high PRF.  $\approx 30\text{kHz}$  is required for unambiguous JEM measurement;  $2.5\text{kHz}$  is sufficient to observe JEM, albeit ambiguously.
- A high number of pulses per burst to yield adequate Doppler resolution to resolve JEM lines from the skin return and its sidelobes. 32 pulses or higher seem adequate for a  $2.5\text{kHz}$  PRF. A practical Doppler waveform may be a single frequency burst of 256 pulses. To observe propeller blade flash, a 1024 pulse waveform at  $2.5\text{kHz}$  should be adequate based upon the recordings made with waveform E. If a single frequency burst is used there is the option of a high resolution Doppler spectrum or a  $(32 \text{ pulse spectrum} \times 32 \text{ time step})$  frequency-time representation which could be used to determine the flash rate.
- Frequency step size  $\Delta f$  and number of frequency steps  $Q$  to yield a range resolution fine enough to enable accurate length measurement. A resolution  $\frac{c}{2Q\Delta f}$  of around 1 metre appears to be sufficient.
- A lower pulse length (perhaps  $10\mu\text{s}$ ) is advisable to allow for higher PRFs given the duty cycle limitation.
- To enable scheduling in normal operation, practical NCTR waveforms for application in a multi-function phased array Radar should not have an excessive dwell time.  $< 100\text{ms}$  is likely to be acceptable, whereas the  $570\text{ms}$  duration of waveform A is likely to be unacceptable. Candidate HRR and Doppler waveforms proposed in this chapter have respective dwell times of between 33 to  $43\text{ms}$  and 13 to  $43\text{ms}$  respectively. To investigate propeller modulation or to generate a range-Doppler profile, one might require a dwell of  $172\text{ms}$ . (For  $P = 1024$  pulses).

Other practical considerations are:

- The algorithms used to calculate the maximum viable PRF from the NCTR waveform design chart should be used to adaptively set the PRF of each NCTR look in response to target range and range rate.
- If two or more Doppler spectra of a target with the same aspect angle are obtained using PRFs which are in irrational proportion (e.g.  $\sqrt{2}$ ) then it may be possible to resolve the JEM ambiguities. If this is achieved it may be possible to correct for the range-Doppler coupling effects and therefore localize engines in range in a range-Doppler profile. Therefore further constrain the maximum PRF such that both  $f_{PRF}$  and  $\frac{f_{PRF}}{\sqrt{2}}$  are not invalid for a given target range and range rate.



- 
- Extra pulses per burst should be provided if clutter filtering is required prior to NCTR signal processing. For example, a ground clutter filter should have two extra pulses since a typical filter produces a single output from three consecutive pulses.

## Chapter 8

# Conclusions & Recommendations

### 8.1 Revisit scope of thesis

As stated in section 1.4.2, this thesis aims to address two fundamental technical problems which constrain the ability of a multifunction radar to offer a Non Cooperative Target Recognition (NCTR) capability. These are: (i) limited transmitted pulse bandwidth and (ii) limited dwell time for a given look.

The notion of a multifunction Radar used here is that of a system with the capability to automatically schedule waveforms which enable surveillance and tracking of multiple targets. A practical system typically achieves this via the use of electronic scanning (as oppose to mechanical orientation of an antenna). A cost effective hardware implementation, which meets the resolution requirements of surveillance and tracking modes, is a phased array. Unfortunately a phased array operating at S-band (i.e. characteristic of MESAR2 and Sampson radars) will likely suffer from severe beam squint during pulse transmission if the pulse bandwidth is increased to meet the (typically sub-metre) range resolution requirements to yield NCTR via the provision of High Range Resolution (HRR) profiles. For example, the maximum pulse bandwidth of MESAR2 is approximately 5MHz, whereas the bandwidth required to yield one metre range resolution is 150MHz. A stepped frequency method is a simple mechanism to achieve sub-metre range resolution with a phased array *designed for surveillance and tracking* without expensive hardware modification<sup>1</sup> (e.g. via use of a stretch receiver processor, within pulse phase shifters, use of fibre optic true time delay ... ). The primary challenge of this research is to investigate whether stepped frequency waveforms can be used for NCTR in such a context. Given stepped frequency waveforms effectively trade time for bandwidth, attention is paid to the design of a compromise between resolution and dwell time. A secondary challenge is to investigate the additional benefits to overall target classification when the number of coherent pulses within an NCTR waveform is expanded to enable the extraction of spectral features which can help to differentiate particular classes of target. As with increased range resolution, the price for this extra information is a further increase in dwell time.

### 8.2 Summary of research achievements

The response to the primary and secondary challenges described above has involved the development of a number of novel techniques, which are summarized below.

---

<sup>1</sup> Although very stable oscillators are required - see the following conclusions summary section.

### 1. Design and execution of a series of experiments to further understanding of NCTR techniques applied using a multifunction phased array Radar

A progression of trials were devised to assess the benefits and limitations of the NCTR methodology within the design constraints imposed via the general characteristics of a multifunction phased array Radar, as exemplified by MESAR2. A trials data set of 1498 recordings of 17 aircraft using 5 waveforms is discussed in this thesis. The (four) trials were:

- Static on-boresight trials used to investigate the feasibility of sub-metre range resolution using stepped frequency waveforms. Initial investigation of the Hybrid technique (see below).
- Static off-boresight trials used to investigate the effect of electronic scanning upon the HRR profiles.
- An aircraft trial using a Falcon and a co-moving point target (achieved via a repeater pod mounted under the wing of the Falcon). NCTR waveforms were automatically scheduled against the targets and interleaved between surveillance and tracking functions.
- “Targets of opportunity” NCTR recordings of commercial aircraft combined with a positive type and flight number identification achieved via cooperation with the National Air Traffic Service (NATS) at Swanwick. Extended jet aircraft (Boeing 747 and 777) and propeller driven aircraft recordings (Dash8) are added to static, moving point target and small jet aircraft recordings already captured.

### 2. Hybrid stepped frequency technique: high resolution HRR profiles of extended aircraft

A suite of signal processing algorithms has been developed allowing enhanced HRR profile generation from stepped frequency waveforms. This represents a significant advance on current techniques. The Hybrid method enables sub-metre range resolution via stepped frequency waveforms but without the restricted unambiguous range window associated with ‘Classical’ Inverse Fourier Transform methods. The length of a Boeing 747 is measured directly using the Hybrid technique; this cannot be achieved using a Classical method based upon the same Radar waveform parameters. Improvements in signal processing are presented relative to the methodologies described in the open literature. (The most recent example being of Miller, Shephard & Newman [70], also of BAE Systems). Particular improvements, (the requirements for which were driven by the severe corruption of the range profiles obtained in the experiments above) focus on the reduction of range aliases using a combination of frequency domain weighting and signal power subtraction.

### 3. Development of an ‘end to end’ NCTR processing and visualization pipeline

An advanced NCTR processing and visualisation software pipeline has been developed. This captures the ‘end to end’ process of NCTR information capture from raw digital receiver samples through signal processing, feature extraction and target classification. The pipeline yields sub-metre range profiles and target Doppler spectra from the receiver samples plus kinematic information obtained from the Radar track extraction system. Aircraft length measurement and detection of principal scatterers is enabled using the High Range Resolution (HRR) profiles, whereas the Doppler spectra allow for a detection of the propulsion mechanism in three broad

classes. (Jet engine, propeller or no observable rotating blades). The pipeline includes comprehensive visualization techniques at all the major stages of processing to enable rapid fault finding and forensic analysis of derived results. Classification performance (quantified by the confusion matrix ‘off diagonal extent’ and visualized by the colour coded confusion matrix representation) can be understood by the distribution of (length and Doppler fraction) features, which in turn can be understood by the ensemble of range and spectral profiles in the ‘target data sheets’, which in turn can be understood by the various plots within the ‘target see’ tool. (See section 3.5).

**4. Use of ‘Doppler fraction’ spectral features to enable aircraft target classification via propulsion mechanism. Combination of Doppler fraction and physical length features to enable broad aircraft type classification.**

Doppler fraction (dfrac) is proposed as a characteristic to enable discrimination between ‘Jet engine’, ‘Propeller’ and ‘No-Non-Skin Doppler’ broad classes of propulsion system. The formation of two dimensional feature vectors from target length and dfrac can enable a simple but effective form of target classification without the need to resort to the intensive search of a high fidelity target database. For example, a classifier which can determine after a small number of looks that a target is likely to be “a propeller driven aircraft of between twenty and thirty metres long” may allow one to efficiently home in on a small subset of a high fidelity target feature database, which then might yield the refined result “Dash8.”

**5. Optimization of NCTR method classification performance as a function of feature and waveform parameters.**

Rather than attempt to develop and tune a novel classifier to the trials data recorded, the research focussed on the variation of performance of ‘standard’ classifiers (such as Bayes Gaussian, Fuzzy logic and k-means) with parameters associated with NCTR waveform design and feature extraction methods. Classification performance (characterized by the off diagonal extent of the associated confusion matrices) is computed as a function of pulses per burst, number of frequency steps, feature measurement thresholds and carrier frequency jitter for six aircraft type classes (Pod, Falcon, B757, B777, B747, Dash8) using length, dfrac and length & dfrac features. In addition to aircraft type classification, performance against more general distinctions is computed. (‘Long or Short’, ‘Four lengths’ and ‘Prop, JEM or NNSD’).

**6. Generic waveform design tools to enable delivery of time costly NCTR waveforms within operational constraints**

A novel ‘waveform design chart’ is developed as a tool for suggesting viable parameters which fit within general ‘operational’ constraints such as a maximum Radar duty cycle, desire to minimize dwell time, impact of clutter, range and range-rate of target. The tool includes a mechanism for deducing the highest viable pulse repetition frequency (PRF) for an NCTR waveform to be delivered upon a target at a given range.

### 8.3 Summary of results presented in this thesis

Recall the overall aim of the research is “to understand the relationship between characteristics of

the stepped frequency methods applied using MESAR2 and resulting air target classification performance”. Furthermore, “we shall seek to improve classification performance via optimization of the signal processing and feature extraction methods used.” The approach to achieving these aims is to provide answers to the four key questions posed in the introductory chapter. Let us summarize the research described in this thesis in the form of answers to these questions. Note these are high level conclusions and therefore a summary of the more detailed conclusions presented at the end of the preceding chapters.

1. *Can MESAR2 (and by inference other S-band multifunction phased array radars) be used to record robust range (and Doppler) profiles of air targets?*

- Radar data captured from MESAR2 of 17 aircraft classes using 5 NCTR waveforms. Out of 1498 looks, 83% were ‘good,’ i.e. the low resolution pulse compressor output was  $> 30\text{dB}$  in peak to median signal level.
- The ‘Hybrid’ technique allows for unambiguous lengths of extended aircraft (such as a Boeing 747) to be measured directly from range profiles.
- Although subject to 10 to 15dB of signal power variation, the major scatterers were clearly present within the Pod and Falcon range profiles; i.e. normalized range profiles can be thought of as ‘robust.’ Experiments suggest this result will be true for the more general case of ‘targets of opportunity’ following integration of eight to ten profiles.
- JEM, Propeller modulation and ‘No Non Skin Doppler’ (NNSD) spectral characteristics were observed as expected using the 32 pulse 2.5kHz PRF Doppler waveform E, albeit ambiguously.
- (Ambiguous) Range-Doppler coupling effects resulting from the use of the stepped frequency waveforms and relatively modest PRF (relative to the typical modulation bandwidths) imply separate range and Doppler waveforms may be optimal for an S-band multifunction Radar, rather than a combined HRR Range-Doppler waveform such as waveform E.
- Propeller modulation appears to result in a diagonal banding structure in the Range-Doppler profile. Using an iterative algorithm it is possible to guess the value of the product of number of blades and spool rate from this diagonal band.

2. *How robust are feature measurements taken from the trials data set? Do feature measurements naturally segment into classes? Should certain features be combined, are they correlated?*

- Length measurements derived from radially inbound Falcon aircraft range profiles were subject to errors of  $\approx 2\text{m}$ . In the case of the Falcon, the Radar length correlates strongly with physical (optical) length. Although a study of physical to Radar length correlation is outside the scope of this thesis, the experiments conducted imply modest classification performance can be achieved using ‘expert’ classifiers based upon Gaussian length feature distributions defined using a mean equal to the physical length.
- Strong aliases resulting from propeller modulation are observed in the range profiles of the Dash8 aircraft. Aliases can cause an erroneous increase in length measurement since the aliases often exceed the length measurement threshold. Alias positions appear consistent with theoretical predictions.

- The Radar Cross Section of aircraft observed using the MESAR2 NCTR waveforms appear to be highly variable (many tens of dB) and therefore are not used as additional ‘physical’ features.
  - Length features visually segment clearly into ‘Long or Short’ classes, and partially into ‘Four Lengths’ classes. Length measurements do not segment naturally into aircraft type, based on the six class example discussed.
  - Doppler fraction (dfrac) feature measurements appear to segment into Propeller, JEM and NNSD classes.
  - Segmentation into aircraft type classes is possible following the combination of length and dfrac features.
3. *Can we achieve acceptable classifier performance based upon the extraction of various target features? How does the crudeness of class definition affect this result and how does performance depend upon (i) the proportion of total pulse cycles used to form the target data set (ii) thresholds used in feature measurement and (iii) the features used (and their possible combination) ?*
- ‘Long or Short’ classification performance resulting in a confusion matrix ‘Off diagonal extent’  $\xi$  of 0.1 is achievable using length features extracted from the six aircraft experiment. Optimum classification appears to occur within below-max length thresholds 20 to 25dB. Within this region, classification performance is largely independent of the number of frequency steps within range  $20 < Q < 128$  which implies a smaller number of frequency steps could be adequate for such crude length classifications, rather than the 128 steps used in waveforms A, B and C.
  - $\xi \approx 0.3$  is achievable using ‘Four lengths’ classes. The impaired result largely results from a misclassification of the ‘Very Long’ (50m  $\pm$ 10m) aircraft wingspan. For example, erroneous Dash8 length measurements due to aliases resulting from Propeller Modulation. The Four Lengths example confirms that the increase of frequency steps does not necessarily correspond to an increase in classification performance.
  - Scattering center Model Comparison classification is very accurate in distinguishing Pod & Falcon targets. However, performance is poor against the six aircraft data set. Integration of range profiles may improve upon this method as one would predict the position of scattering centres to become more stabilized with integration, assuming no change of target aspect within the integration period.
  - Prop, JEM or NNSD classification has a low  $\xi$  of 0.2 using the dfrac feature for inbound targets. As expected, this rises (to 0.5) for outbound aircraft where engine intakes are more likely to be obscured. Optimum performance is achieved with  $P > 27$  pulses per burst and a 22 to 30dB dfrac threshold.
  - Six aircraft type classification performance of  $\xi \approx 0.4$  is achievable using combined length and dfrac physical features. It is recommended that length is pre-scaled by 70m (the maximum expected aircraft length) to yield feature dimensions of roughly the same expected size, given dfrac is by definition within the range 0...1.

4. *Based upon the learning obtained in conducting this research, what are the recommendations regarding the design of future NCTR modes?*

- The ‘NCTR waveform design chart’ is a proposed mechanism for selecting PRF as a function of target range.
- Alternate range and Doppler waveforms should be transmitted, rather than the four range and range-Doppler waveform cycles described in this thesis. (Waveforms A,B,C & D/E).
- A proposed HRR waveform should have smaller pulse length (e.g.  $10\mu\text{s}$ ), ideally wider pulse bandwidth (for example  $\Delta f = 12.8\text{MHz}$ ,  $B = 18\text{MHz}$ ), lower frequency steps (e.g.  $Q = 32$ ) and higher PRF (e.g. 12 to 20kHz). The example stated in Chapter 7 yields a more practical dwell time of between 33 and 43ms.
- A proposed Doppler waveform ( $\approx 200\text{ms}$  dwell) with PRF up to 20kHz should consist of  $P = 1024$  pulses using a single transmit frequency to enable the option of a 1024 bin high resolution spectra, or a  $32 \times 32$  bin time-varying spectra to record blade flash. These options could be processed in parallel.
- Transmission of alternate Doppler waveforms with a PRF in an irrational ratio such as  $\sqrt{2}$  might enable JEM ambiguity resolution.
- Carrier frequency stability  $10 \log \left( \frac{\sigma_{f_{Tx}}}{f_{Tx}} \right)$  should be  $< -80\text{dB}$  at S-band ( $f_{Tx} \sim 3\text{GHz}$ ); i.e. frequency jitter should be limited to a few tens of Hz.
- One might want to consider using the first few pulses of the range and Doppler waveforms to feed a conventional MTI filter (e.g. a three pulse ground clutter filter) to observe targets at low elevation which might be obscured by topographic reflections, rain etc. This step should be implemented prior to the NCTR signal processing discussed in this thesis, in particular the motion compensation algorithms. The HRR waveform might therefore use  $8 + 3 = 11$  pulses plus guards to enable ground clutter, then JEM filtering following motion compensation.

## 8.4 Recommendations for further study

The overall philosophy adopted in this thesis is to explore theoretical considerations of NCTR methods applicable to multifunction phased array radar via analysis of specific experimental results obtained via MESAR2. Although effort is made to derive generic mathematical statements to support the experimental analysis, there are clearly areas for further open investigative study (rather than ‘defined technique validation’) given the constraints imposed by: (i) the extent and content of the trials data set and (ii) the suite of waveforms offered by MESAR2 at the time of trials. Specifically, the line of research presented in this thesis might be further pursued via the following investigations:

### 1. Further experimental trials

- (a) In an operational implementation, provision should be made for the gathering of *training* length and dfrac feature measurements. These would be used to optimize the classifier employed. Bayesian and k-means could be implemented, with the latter as a backup if feature statistics appear to be non-Gaussian following long term data collection. A statistical test such as Kolmogorov-Smirnoff could be employed to assess this.

- (b) If possible, a greater number of looks upon each aircraft should be recorded to enable a quantitative study of the improvements upon classification performance which can be made through integration of range and Doppler profiles. The experiments described in this thesis suggest seven to ten looks might be an appropriate number. For further analysis one should therefore aim for upwards of fifty looks for each aircraft class to enable a representative data set; i.e. to yield several tens of integrated profiles. A practical improvement to an NCTR schedule (as exemplified with MESAR2 in this thesis) might be to reduce the waveforms to an optimized set as discussed in Chapters 6 and 7. Waveforms consisting of alternate Hybrid stepped frequency HRR followed by high resolution Doppler, with PRF optimized as suggested via the waveform design charts, might offer significantly more<sup>2</sup> target looks which can be directly compared.

## 2. Feature extraction

- (a) With a training data set, compare classification performance using ‘physical features’ such as length and dfrac with feature vectors derived from a Karhunen Loeve transform. An example recipe<sup>3</sup> might be as follows: (i) Following a range shift invariant transform such as a DFT or an alignment method, integrate profiles in batches; (ii) Treating the range & Doppler profiles (separately) as feature vectors, compute the covariance matrices for the training data for each (known) class; (iii) Determine the eigenvectors of these covariance matrices and construct ‘dimensionality reduced’ feature vectors from the first  $Z$  projections of the profile feature vectors along the eigenvalue ordered eigenvectors of the covariance matrices. (To begin with, start with a single scalar derived from range profiles and a single scalar from the Doppler profiles and combine these into a two dimensional feature vector).
- (b) Investigate from jet engine manufacturers whether there is a simple functional relationship between spool rate, number of blades, altitude and airspeed.
- (c) Investigate the causes for variation in target Radar cross section as computed from HRR profiles. Prior to future trials a series of calibration tests should be performed with all waveforms using a target of known RCS (e.g. a corner reflector).
- (d) Investigate whether kinematic information such as airspeed and/or acceleration could improve classification performance. Airspeed could be a useful discriminator between jet and propeller driven aircraft. The Dash8 turboprop has a cruising speed of  $149\text{ms}^{-1}$  whereas commercial jet aircraft typically have cruising speeds between  $200\text{ms}^{-1}$  and  $250\text{ms}^{-1}$ . An airspeed measurement could extend the two dimensional length and dfrac feature space by a third dimension, which may improve the inter-class distance between aircraft types which belong to ‘Prop’ and ‘JEM’ broad classes.

## 3. Signal processing algorithms

- (a) Investigate from a theoretical standpoint why the Hybrid method is approximately 5dB poorer in sidelobe performance than the Classical stepped frequency method.
- (b) Investigate the feasibility of computing the JEM ambiguities, thereby providing a mechanism for engine localization in range, using the method described in Chapter 5.

---

<sup>2</sup>i.e. at least a factor of two more than in the MESAR2 setup described, which used three distinct HRR waveforms and a Doppler waveform.

<sup>3</sup>Inspired by the practical methods of Zyweck & Bognor [118]



#### 4. Operational implementation

- (a) Validate the techniques described via real-time (or ‘nearly real time’) implementation in an operational Radar system.
- (b) Conduct an experiment whereby Radar operators are provided with graphical displays which visualize the target response to NCTR waveforms. The visualization tools developed for this research could be used as prototypes. (Target data sheets, features vs target range, length vs dfrac features, confusion matrix checkerboard...) Ideally a real-time processing chain of signal processing, feature extraction and classification should be implemented in hardware. Data at all stages should be available to the (experimental) operator to enable an optimum display to be configured given a realistic operational context. Given that human pattern recognition is still far in advance of artificial techniques, perhaps one should seek to optimize the display of NCTR data to take best advantage of the human element in the target recognition process.

### 8.5 List of publications arising from this thesis

- FRENCH, A., “Improved High Range Resolution Profiling of Aircraft using Stepped-Frequency Waveforms with an S-Band Phased Array Radar.” *2006 IEEE Radar Conference, Oneida Indian Reservation, Verona, NY, USA* April 2006, pp69 - 75.

*The paper “Improved High Range Resolution Profiling of Aircraft using Stepped-Frequency Waveforms with an S-band Phased Array Radar” was delivered orally at the Radar 2006 conference at Turning Stone Resort & Casino in the Oneida Indian Reservation, Verona, NY, USA between 24-27<sup>th</sup> April 2006. The paper describes experiments performed using the MESAR2 multi-function phased array Radar. ‘Classical’ and ‘Hybrid’ processing of NCTR stepped-frequency waveforms was achieved successfully using static and moving targets.*

# Bibliography

- [1] ANDERSON, S.J. "Target classification, recognition and identification with HF Radar." *RTO SET Symposium on "Target Identification and Recognition using RF Systems."* Oslo, Norway 11-13<sup>th</sup> Oct 2004. pp 25/1- 25/20.
- [2] ABBOTT, D.W., "Comparison of data analysis and classification algorithms for automatic target recognition." *IEEE International conference on systems, man and cybernetics.* 2-5 Oct 1994. Vol. 1. pp902-907.
- [3] ATROUZ, B., DUAZZOU, H.A., KIMOUCHE, H., "Features influence on targets classification performance using the high range resolution profiles (HRR profiles)." *Proc. IET International conference on Radar Systems.* 15-18 Oct 2007. pp1-4.
- [4] AXELSSON, S.R.J. "Analysis of random step frequency Radar and comparison with experiments." *IEEE Trans. on Geoscience and Remote Sensing.* Vol. 45. No. 4. April 2007.
- [5] BAI JIN LIANG, GUO MEI GUO, XU CHENG FA. "Method of stepped frequency signal processing based on fractional fourier transform." *Proc. ICSP 2008.* pp2550-2553.
- [6] BAKHTARI, A., et al. "Autonomous Surveillance of a Dynamic Multi-Subject Environment: An Implementation for Automatic Facial Recognition." *Measurement Systems for Homeland Security, Contraband Detection & Personal Safety Workshop.* 29-30<sup>th</sup> March 2005. pp 21-25.
- [7] BALANIS, C.A. Antenna Theory Analysis and Design. Harper & Row, Publishers Inc. 1982.
- [8] BALISE, P. (Rear Admiral. Director U.S. Navy Surface Warfare Division) Statement to the Seapower Subcommittee of the Senate Armed Services Committee on Surface Warfare Systems. 9 April 2002.
- [9] BASTIERE, A. & NIMIER, V., "MILORD, an application of multifeature fusion for Radar NCTR." *Proceedings of the Third International Conference on Information Fusion (ISIF) 2000.* 10-13 July. Vol 2. Wed1/17-Wed1/24.
- [10] BELL, M.R. & GRUBBS, R.A., "JEM modelling and measurement for target identification." *IEEE Transactions on Aerospace & Electronic Systems.* Vol 29, No. 1. January 1993.
- [11] BENITZ, G.R., "High Definition Vector Imaging." *MIT Lincoln Laboratory Journal.* 10 2 1997. pp147 -170.
- [12] BERIZZI, F., MARBRELLA, M. & BERNABO, M. "A range profiling technique for synthetic wideband Radar." *IET Radar, Sonar, Navig.* 2008. Vol 2. No 5. pp334-350.

- [13] BORRION, H. "Study of Processing Techniques for Radar Non-Cooperative Target Recognition." PhD Thesis. Department of Electronic & Electrical Engineering, University College London. September 2006.
- [14] BOWDEN, R. "Learning Non-linear Models of Shape and Motion." PhD thesis. Department of Systems Engineering, Brunel University. October 1999
- [15] CATTIN, V., CHAILLOUT, J.J., BLANPAIN, R., "Detection & localization with a step frequency Radar." *Detection of abandoned land mines*. 12-14th Oct 1998. Conference publication #458.
- [16] CHERNIAKOV, M., "Optimal step frequency signal for a ground penetrating Radar." *Electronics letters*. 4 Jan 1996. Vol **32**. No. 1. pp62-64.
- [17] CHING TAI LIN & BEN H. CANTRELL. "Synthesizing a wideband waveform by using a phased array." *Proc. 1998 IEEE National Radar conference. Dallas, Texas*. 12-13 May 1998. pp361-366.
- [18] CLARK, B.G., "A Efficient Implementation of the Algorithm CLEAN." *J. Astronomy & Astrophysics*. **89** pp377-378. 1980.
- [19] CLARK, M.E., "High range resolution techniques for ballistic missile targets." *High resolution Radar & sonar. IEE colloquium*. 11 May 1999. pp 6/1 - 6/13.
- [20] COHEN, M., "Radar & Multi-Sensor Target Recognition." Tutorial 3.4. *IEEE Radar Conference 2006*.
- [21] COHEN I AND GOLDSZMIDT M, 2004, Properties and benefits of calibrated classifiers, *Proc. 15th European Conference on Machine Learning and the 8th European Conference on Principles and Practice of Knowledge Discovery in Databases*. 20-24 September, Pisa, Italy. [www.hpl.hp.com/techreports/2004/HPL-2004-22R1.pdf](http://www.hpl.hp.com/techreports/2004/HPL-2004-22R1.pdf)
- [22] COLIN, N., MORUZZIS, M., "Radar target recognition by fuzzy logic." *IEEE AES Systems magazine*. July 1998. pp13-19.
- [23] COOK, C.E., PAOLILLO, J., BERNFELD, M. & PALMIERI, C.A. "Matched Filtering, Pulse Compression and Waveform Design." *Microwave Journal*. November 1964. pp 81-90.
- [24] CUOMO, S., PELLEGRINI, P.F. & PIAZZA, E., "Neural system for tracking & classification of primary Radar echo signals." *IEEE symposium on signals, systems & electronics*. 1995.
- [25] CUOMO, S., PELLEGRINI, P.F. & PIAZZA, E., "Model validation for Jet Engine Modulation." *Electronic Letters*. Vol **30**, issue 24. pp2073-2074. 24th November 1994.
- [26] DAS B, 1999, Representing Uncertainties Using Bayesian Networks, Defence Science and Technology Organisation (DSTO) Report, DSTO-TR-0918, Australia. <http://www.dsto.defence.gov.au/corporate/reports/DSTO-TR-0918.pdf>
- [27] DUDA, R.O., HART, P.E, STORK, D.G., *Pattern Classification*. 2<sup>nd</sup> Edition. John Wiley & Sons Inc. 2001.
- [28] EL-MATOUAT, F., COLOT, O., VANNOORENBERGHE, P., LABICHE, J., "Using optimal variables for Bayesian network classifiers." *Proc. Third International Conference on Information Fusion (FUSION) 2000*. 10-13 July 2000. Vol 1. pp18-23.

- [29] FOWLER, C.A., "Asymmetric Warfare: A Primer." <http://www.spectrum.ieee.org/print/3091>
- [30] FREEDMAN, A., BOSE, A., STEINBERG, B.D. "Thinned stepped frequency waveforms to furnish existing radars with imaging capability." *IEEE AES systems magazine*. Nov 1996. pp39-43.
- [31] FRENCH, A., "Improved High Range Resolution Profiling of Aircraft using Stepped-Frequency Waveforms with an S-Band Phased Array Radar." *2006 IEEE Radar Conference*. April 2006, pp69-75.
- [32] FREUNDORFER, A.P. & IIZUKA, K. "A study on the scattering of radio waves from buried spherical targets using the step frequency Radar." *Proc. IEEE Trans. on Geoscience & Remote Sensing*. Vol. **31**. No. 6. Nov 1993. pp1253-1255.
- [33] GERLACH, K. "Thinned spectrum ultrawideband waveforms using stepped frequency polyphase codes." *Proc. IEEE transactions on aerospace & electronic systems*. Vol. **34**. No. 4. October 1998. pp 1356-1361.
- [34] G.S. GILL & JEN-CHIH HUANG. "The Ambiguity Function of the Step Frequency Radar Signal Processor." *Proc. CIE International Conference of Radar*. 8-10 Oct 1996. pp 375 - 380
- [35] GILL, G.S. "Step frequency waveform design & processing for detection of moving targets in clutter." *Proc. IEEE International Radar Conference*. 8-11 May 1995. pp573-578.
- [36] GILL, G.S. "Simultaneous pulse compression and Doppler processing with step frequency waveform." *Electronics letters*. 7 Nov 1996. Vol. **32**. No. 23. pp2178-2179.
- [37] IRINA GLADKOVA & DMITRY CHEBANOV, "Suppression of grating lobes in stepped-frequency train." *2005 IEEE Radar Conference*. 9-12 May 2005, pp 371 – 376c
- [38] IRINA GLADKOVA, "A General Class of Stepped Frequency Trains", ' *2006 IEEE Radar Conference*. April 2006, pp 100 - 105.
- [39] GREEN, H.E. "Electromagnetic backscattering from a helicopter rotor in the decametric wave band regime." *IEEE trans. on Antennas and Propagation*. Vol. **42**. No. 4. April 1994. pp501-509.
- [40] HANSELMAN, D. & LITTLEFIELD, B., *Mastering MATLAB 6. A Comprehensive Tutorial and Reference*. Prentice Hall Inc. 2001.
- [41] HASPERT, K., HEAGY, J., SULIVAN, R., "Template-based target identification and confusion matrices." *IEEE A&E systems magazine*. Vol **21**. No. 6. June 2006. pp53-67.
- [42] HECKERMAN D, "A tutorial on learning with Bayesian networks." Microsoft Research Technical Report MSR-TR-95-06. March 1995. <ftp://ftp.research.microsoft.com/pub/tr/tr-95-06.pdf>
- [43] HECHT, E., "Optics." 3<sup>rd</sup> Edition. Adison Wesley Longman Inc. 1998.
- [44] HE SISAN, ZHU YONG-FENG, ZHAO HONG-ZHONG, ZHOU JIAN-XIONG, FU QIANG. "Analysis of rotating structures for stepped frequency Radar." *Proc. IEEE Radar 2008*. pp386-390.
- [45] HU, R., ZHU, Z., "Researches on Radar target classification based on high resolution range profiles." *Proc. IEEE National Aerospace and Electronics Conference. (NAECON)*. 14-18 July 1997. pp951-955.

- [46] HUDSON, S. & PSALTIS, D., "Correlation filters for aircraft identification from Radar range profiles." *IEEE Trans. Aerospace & Electronic systems*. Vol **29**. No. 3. July 1993. pp741-748.
- [47] HWANG, J. K., LIN, KUN-YO, DENG, J.H., "Automatic target recognition based on high resolution range profiles with unknown circular range shift." *Proc. IEEE Symposium on signal processing and information technology 2006*. pp283-288.
- [48] JAHANGIR, M., PONTING, K.M. & O'LOGHLEN, J.W., "Robust Doppler classification technique based on hidden markov models." *IEE Proc. Radar, Sonar & Navigation*. Vol. **150**. Issue 1. Feb 2003. pp33-36.
- [49] JAIN, A.K., DUIN, R.P.W., MAO, J., "Statistical pattern recognition: A review." *IEE Trans. on pattern analysis and machine intelligence*. Vol **32**. No. 1. Jan 2000. pp4-37.
- [50] JIN KAI, WANG WEI DONG & WANG DONG JIN. "The Study on a new Radar waveform with high range resolution." *IEEE ICSP 2004 proceedings*. pp 1957 - 1960.
- [51] KAHLER, B., BLASCH, E., "Robust multi-look HRR ATR Investigation through decision level fusion evaluation." *11<sup>th</sup> International conference on information fusion*. 30 June - 3 July 2008. pp1-8.
- [52] KASTELLA, K. AND ZATEZALO A. "A Nonlinear Filter for Real-Time Joint Tracking and Recognition." Institute for Mathematics and its Applications, University of Minnesota. 1998. <http://www.ima.umn.edu/preprints/APRIL98/1556.pdf>
- [53] KERR, D.E. *Propagation of Short Radio Waves*. McGraw Hill International. 1951.
- [54] KOTSIANTIS, S.B., "Supervised machine learning: A review of classification techniques." *Informatica*. Vol **31**. 2007. pp249-268.
- [55] KRIEG M.L., *A Tutorial on Bayesian Belief Networks*. Defence Science and Technology Organisation (DSTO) Report, DSTO-TN-0403, Australia. 2001. <http://www.dsto.defence.gov.au/corporate/reports/DSTO-TN-0403.pdf>
- [56] KULPA, K., CZEKALA, Z., MISUREWICZ, J., FALKIEWICZ, J. "Parametric detection of the helicopter hub echo." *Proc. IEEE Radar 2009*. pp262-266.
- [57] LANTERMAN A.D, Tracking and recognition of airborne targets via commercial television and FM radio signals, Coordinated Science Laboratory, Univ. of Illinois. (Abstract only). <http://citeseer.ist.psu.edu/correct/374167>
- [58] LEVANON, N., "Stepped Frequency Pulse Train Radar Signal." *IEE Proceeding of the Radar, Sonar & Navigation Group*. Vol. **149**. No 6. December 2002. pp 297-309
- [59] LEVANON, N. & MOZESON, E. "Nullifying ACF Grating Lobes in Stepped Frequency Train of LFM Pulses." *IEEE Transactions on Aerospace and Electronic Systems*. Vol. **39**. No. 2. April 2003. pp 694 - 703.
- [60] LEUNG H AND JIANGFENG W. "Bayesian and Dempster-Shafer target identification for Radar surveillance." *IEEE Transactions on Aerospace and Electronic Systems*. Vol. **36**. Issue 2, April 2000, pp 432 - 447. (Abstract only). <http://www.ewh.ieee.org/soc/aes/taes/aes362/3620432.htm>

- [61] LI HAIYING, YANG RULIANG. "Analysis of radial velocity effect on synthetic range profile of stepped frequency waveform." *IEEE International Geoscience & Remote sensing symposium. (IGARSS) 2002*. Vol 6. 24-28 June 2002. pp3689-3691.
- [62] LORD, R.T., INGG, M.R. "High resolution SAR processing using stepped frequencies." *IEEE International Geoscience and remote sensing symposium. (IGARSS) 1997*. Vol 1. 3<sup>rd</sup> Aug 1997. pp490-492.
- [63] LOZA, A. "Image Processing and Time-Frequency Transform Methods for Radar Characterisation and Recognition." PhD Thesis. center for Communications Research, University of Bristol. UK. March 2006.
- [64] LYNN, P.A., "Radar Systems." Macmillan New Electronics Introductions to Advanced Topics. Macmillan Education Ltd. 1987.
- [65] MCGROARY, F. & LINDELL, K., "A stepped chirp technique for range resolution enhancement." *Proc. National Telesystems Conference*. Vol.1, 26-27 March 1991, pp 121-126
- [66] MARON, D.E. "Frequency jumped burst waveforms with stretch processing." *Proc. IEEE International Radar conference*. 1990. pp274-279.
- [67] MARTIN, J. & MULGREW, B., "Analysis of the Theoretical Radar Return Signal from Aircraft Propeller Blades." *Proc. IEEE International Radar Conference* 1990. pp569 - 572.
- [68] MARTIN, J. & MULGREW, B., "Analysis of the Effects of Blade Pitch on the Radar Return Signal from Rotating Blades." *Proc. IEE RADAR -1992. Brighton, UK*. pp446.
- [69] MENDEL, J.M., "Fuzzy logic systems for engineering: A tutorial." *Proc. IEEE*. Vol. 83. No. 3. March 1995. pp345-377.
- [70] MILLER, R.J, SHEPARD, D., NEWMAN, M. "Aspects of NCTR for Near-Future Radar." *RTO SET Symposium "Target Identification and Recognition using RF Systems" held in Oslo, Norway*. 11-13<sup>th</sup> October 2004. Published in RTO-MP-SET-080 section 5.
- [71] MILLER, R.J., WYLLIE, C.B., SHEPHARD, D.J. "Advances in Radar NCTR using non-Radar referents". 2<sup>nd</sup> *EMRS DTC Technical Conference, Edinburgh* 2005.
- [72] MISIUREWICZ, J., KULPA, K., CZEKALA, Z. "Analysis of Radar echo from a helicopter rotor hub." *Proc. 12<sup>th</sup> International conference on microwaves and Radar (MIKON)*. 20-22 May 1998. Vol. 3. pp866-870.
- [73] MISIUREWICZ, J., KULPA, K., CZEKALA, Z. "Analysis of recorded helicopter echo." *Proc. RADAR 1997*. 14-16 Oct 1997. pp449-453.
- [74] MITCHELL, R.A., WESTERKAMP, J.J., "Statistical feature based target recognition." *Proc. IEEE National Conference of Aerospace & Electronics. (NAECON)* 1998. pp111-118.
- [75] MORUZZIS, M & COLIN, N., "Radar target recognition by fuzzy logic." *IEEE AES Systems Magazine*. July 1998. pp13-17

- [76] MURPHY K P. "A Brief Introduction to Graphical Models and Bayesian Networks." Departments of computer science and statistics, University of British Columbia. 1998 [http://www.cs.ubc.ca/~murphyk/Bayes/bayes\\_tutorial.pdf](http://www.cs.ubc.ca/~murphyk/Bayes/bayes_tutorial.pdf)
- [77] MURPHY, K.P. "An introduction to graphical models." Departments of computer science and statistics, University of British Columbia. 2001. [http://www.cs.ubc.ca/~murphyk/Papers/intro\\_gm.pdf](http://www.cs.ubc.ca/~murphyk/Papers/intro_gm.pdf)
- [78] NIEUWOUDT, C. & BOTHA, E.C., "Relative performance of correlation-based and feature-based classifiers of aircraft using Radar range profiles." *Proc. 14<sup>th</sup> International Conference on Pattern Recognition*. 16-20 Aug 1998. Vol **2**. pp1828-1832.
- [79] PELLEGRINI, P.F., CUOMO, S. & PIAZZA, E. "ATC Primary Radar signal analysis for target characterisation. A model validation." *Proc. IEEE Radar conference* 1995.
- [80] PELLEGRINI, P.F., CUOMO, S. & PARDINI, "Radar signals analysis oriented to target characterization applied to civilian ATC Radar." *Proc. IEEE Radar* 1992. pp 438-445.
- [81] PIERACCINI, M., FRATINI, M., PARNI, F., MACALUSO, G., ATZENI, C. "High speed CW step frequency coherent Radar for dynamic monitoring of civil engineering structures." *Electronics letters*. 8th July 2004. Vol. **40**. No. 14.
- [82] PHAM, D.T. "Applications of unsupervised clustering algorithms to aircraft identification using high range resolution Radar." *Proc. IEEE National conference of Aerospace & Electronics (NAECON)*. 13-17 July 1998. pp228-235.
- [83] PIAZZA, E., "Radar signals analysis & modulation in the presence of JEM: Application to civilian ATC radars." *IEEE AES Systems magazine*. January 1999.
- [84] POPSTEFANIJA, I., MCQUEEN, D.S., MCINTOSH, R.E. "A Stepped-Frequency Delta-K Microwave Radar for Oceanographic Studies." *IEEE Trans. on Geoscience & Remote Sensing*. Vol. **31**. No. 3. May 1993. pp681-691."
- [85] POULIGUEN, P., LUCAS, L., MULLER, F., QUETE, S., TERRET, C. "Calculation and analysis of electromagnetic scattering by helicopter rotating blades." *IEEE trans. on Antennas & Propagation*. Vol. **50**. No. 10. Oct 2002.
- [86] RA, B.S. & DURRANT-WHYTE H. "A decentralized Bayesian algorithm for identification of tracked targets", *IEEE Transactions on Systems, Man and Cybernetics*, Vol. **23**, Issue 6, Nov-Dec 1993. pp 1683 – 1698.
- [87] D.J. RABIDEAU. "Nonlinear synthetic wideband waveforms, Radar Conference." *Proceedings of the IEEE*, 22-25 April 2002. pp 212–219.
- [88] RICHARDS, M. A., *Fundamentals of Radar Signal Processing*. McGraw-Hill Inc. 2005.
- [89] RILEY, K.F., HOBSON, M.P. & BENICE, S.J., *Mathematical methods for physics and engineering*. Cambridge University Press. 1998.
- [90] ROSENBACH, K. & SCHILLER, J., "Non co-operative air target identification using Radar imagery: Identification rate as a function of signal bandwidth." *Proc. IEEE Radar conference 2000*. pp305-309.

- [91] ROSENBACH, K. & SCHILLER, J., "Identification of aircraft on the basis of 2D Radar images." *Proc. IEEE Radar conference 1995*. pp405-409.
- [92] SCHIMPF, H., WAHLEN, A. & ESSEN, H., "High range resolution by means of synthetic bandwidth generated by frequency-stepped chirps." *Electronics Letters*, Vol. **39**, Issue 18, 4 Sept. 2003, pp 1346 - 1348
- [93] SINHA, P., *et al*, "Face Recognition by Humans: 20 Results all Computer Vision Researchers Should Know About." Department of Brain and Cognitive Sciences, Massachusetts Institute of Technology.
- [94] TITIN-SCHNAIDER, C. & BROUARD, P., "Full-Polarimetric Analysis of MERIC Air Targets Data." *RTO SET Symposium "Target Identification and Recognition using RF Systems"* held in Oslo, Norway 11-13<sup>th</sup> October 2004. Published in RTO-MP-SET-080 section 39.
- [95] SKOLNIK, M.I., *Radar Handbook*. Second Edition. McGraw-Hill Inc. 1990.
- [96] SKOLNIK, M.I., *Introduction to Radar Systems*. Third Edition. McGraw-Hill Inc. 2001.
- [97] SORENSEN, H.B.D., JAKOBSEN, K.B., NYMANN, O. "Identification of mine shaped objects based on an efficient phase stepped frequency Radar approach." *Proc. International conference on image processing. 1997*. 26-29 Oct 1997. Vol. **3**. pp142-145.
- [98] STICKLEY, G.A., NOON, D.A., CHERNIAKOV, H., LONGSTAFF, I.D. "Preliminary field results of an ultra-wideband (10-620MHz) stepped frequency ground penetrating Radar." *Proc. International Geoscience and Remote Sensing Symposium (IGARSS) 1997*. Vol. **3**. 3 Aug 2007. pp1282-1284.
- [99] STORKEY A, Tutorial: "Introduction to Belief Networks." The Institute for Adaptive and Neural Computation, University of Edinburgh. <http://www.anc.ed.ac.uk/~amos/belief.html>
- [100] STOVE, A.G., SYKES, S.R. "A Doppler based automatic target classifier for a battlefield surveillance Radar." *Proc. RADAR 2002*. 15-17 Oct 2002. pp419-423.
- [101] STOVE, A.G., SYKES, S.R. "A Doppler-based target classifier using linear discriminants and principal components." *Proc. RADAR 2003*. pp171-176.
- [102] SUTHERLAND, K., "Automatic Face Recognition." *Proc. Conference of Intelligent Systems Engineering*. 19-21<sup>st</sup> August 1992. pp 29-24.
- [103] TAIT, P., *Introduction to Radar Target Recognition*. Published by the Institution of Electrical Engineers (IEE). London. 2005.
- [104] TEMPLE, M.A., SITLER, K.L., RAINES, R.A., HUGHES, J.A. "High range resolution (hRR) improvement using synthetic HRR processing and stepped-frequency polyphase coding." *Proc. IEE Radar. Sonar. Navig.* Vol. **151**. No. 1. Feb 2004. pp41-47.
- [105] TONG, C. *et al*, "Studies of modulation mechanism of Jet Engine Modulation effect." *Proc APMC 2005*.



- [106] VAN DER HEIDEN, R., ZWART, J.P., GELSEMA, S., GROEN, F., "Fast translation invariant classification of HRR range profiles in a zero phase representation." *IEE Proc. Radar. Sonar and Navigation*. 1 Dec 2003. pp411-418.
- [107] VAN DER WALT, C. & BARNARD, E., "Data characteristics that determine classifier performance." 2006.
- [108] VESPE, M., "Multi-Perspective Radar Target Classification." PhD thesis. Department of Electronic & Electrical Engineering, University College London. November 20, 2006.
- [109] WALBRIDGE, M.R. & CHADWICK, J., "Reduction of range ambiguities by using irregularly spaced frequencies in a synthetic wideband waveform." *High Resolution Radar and Sonar IEE Colloquium*. 11 May 1999, pp 2/1 - 2/6
- [110] WEBB, A., *Statistical Pattern Recognition*. 2<sup>nd</sup> Edition. John Wiley & Sons Ltd. 2002.
- [111] WEHNER, D.R., *High-Resolution Radar*. 2<sup>nd</sup> Edition. Artech House Inc. 1995.
- [112] WOAN, G., *The Cambridge Handbook of Physics Formulas*. Cambridge University Press. 2001.
- [113] CHING-CHANG WONG, CHIA-CHONG CHEN & SHIH-LIANG YEH, "K-Means-Based Fuzzy Classifier Design." *Ninth IEEE International Conference on Fuzzy Systems, FUZZ IEEE 2000*, Vol. **1**, 7-10 May 2000, pp 48-52.
- [114] YOON, S.H., KIM, B., KIM, Y.S., "Helicopter classification using time-frequency analysis." *Electronics letters*. 26th Oct 2000. Vol. **36**. No. 22. pp1871-1872.
- [115] YUAN HAOTIAN, CHENG ZHEN, WEN SCHULIANG, PENG JUN. "Study on Radar target imaging & velocity measurement simultaneously based on step frequency waveforms." *Proc. 1st Asian & Pacific conference on Synthetic Aperture Radar. (AP SAR) 2007*. 5-9 Nov 2007. pp404-407.
- [116] ZENG, D., LONG, T. "Study on the principle and implementation of a step frequency phased-array Radar." *7<sup>th</sup> International conference on signal processing. (ICSP'04)*. Aug 31-4 Sept 2004. Vol. **3**. Beijing. pp2037-2040.
- [117] ZHANG, Q.T., "Probability of Resolution of the MUSIC Algorithm." *IEEE Transactions on Signal processing*. **43** 4. April 1995. pp 978-987.
- [118] ZYWECK, A. & BOGNER, R.E., "Radar Target Classification of Commercial Aircraft." *IEEE Transactions on Aerospace & Electronic Systems*. Vol **32**, No 2. April 1996.
- [119] ZYWECK, A. & BOGNER, R.E., "Radar target recognition using range profiles." *Proc. International Conference on Acoustics, Speech and Signal Processing (ICASSP)*. Vol **2**, 19-22<sup>nd</sup> April 1994. pp373-376.
- [120] ZYWECK, A. & BOGNER, R.E., "High resolution Radar imagery of the Mirage III aircraft." *IEEE Trans. Antennas and Propagation*. Vol. **42**, Issue 9. September 1994. pp1356-1360.
- [121] ZYWECK, A. & BOGNER, R.E., "Coherent averaging of range profiles." *Proc. IEEE Radar conference 1995*. pp456-461.

## Appendix A

# The radiation pattern of a phased array Radar

A typical phased array is formed from a line or plane populated by identical radiators (i.e. ones that generate the same far field antenna pattern), but with controlled inter-element phase steps and amplitude scaling. Systems such as MESAR2 utilize large numbers of transmit-receive units (TRUs). These generate power in a distributed sense and thus offer a ‘soft failure’ feature; the loss of a single element will only marginally degrade the overall output field strength distribution. Other systems that are based on dipole arrays (e.g. Marconi Martello) or slotted waveguides (e.g. BAE Systems Commander) use a well designed microwave plumbing system to disperse a single high power source (such as a magnetron or solid state amplifier) such that the phase at each radiator is what is required.

In essence, the number of array elements (in conjunction with the antenna pattern of each element) constrains the width of the main beam, whereas the angular position of the beam (relative to the antenna geometry) is largely set by the phase differences between elements. As an example let us consider a series of  $N$  radiating elements arranged in a line. (fig A.1). Let coordinate  $x$  represent the position of the element along the line, measured from the centre point, i.e.  $x \in [-\frac{1}{2}L, \frac{1}{2}L]$  where  $L$  is the length of the line. Let us consider a point at range  $R$  from the centre point at azimuth  $\phi$  measured from the normal to the line. The  $\phi = 0$  direction shall be referred to as ‘boresight’ to the array. In the far-field<sup>1</sup> limit we can approximate wavefronts emanating from each element to be planar. Hence the net electric field strength  $\psi(R)$  can be expressed as

$$\psi(R) = \sum_{n=1}^N a_n e^{-\frac{2\pi i f}{c}(R - \delta R_n) + i\Omega_n} \quad (\text{A.1})$$

where  $f$  is the radiation frequency and  $\Omega_n$  is some additional phase supplied to element  $n$ . Using the plane-wave approximation we can further simplify by relating the range difference  $\delta R_n$  to the position of the radiating element. Using figure A.1

$$\delta R_n \approx x_n \sin \phi \quad (\text{A.2})$$

If the power output of each element is identical then  $a_n = a$  which gives

$$\psi(R) \approx a e^{-\frac{2\pi i f R}{c}} \sum_{n=1}^N e^{\frac{2\pi i f}{c} \left( x_n \sin \phi + \frac{c\Omega_n}{2\pi f} \right)} \quad (\text{A.3})$$

---

<sup>1</sup>See Appendix on derivation of the Martin & Mulgrew model of Jet Engine Modulation. In Far-Field “Fraunhofer” limit, range  $R \gg \frac{L^2}{\lambda}$ , and  $R \gg L$  where  $L$  is the size of the antenna and  $\lambda$  is the free space wavelength of the radiation being transmitted and received.

Let elements, and additional phases, be equally spaced

$$x_n = -\frac{L}{2} + \frac{n-1}{N-1}L \quad (\text{A.4})$$

$$\Omega_n = (n-1)\Delta\Omega \quad (\text{A.5})$$

Hence

$$\psi(R) \approx ae^{-\frac{2\pi if}{c}\left(R + \left(\frac{L}{2} + \frac{1}{N-1}L\right)\sin\phi + \frac{c\Delta\Omega}{2\pi f}\right)} \sum_{n=1}^N e^{\frac{2\pi ifL}{c}\left(\frac{\sin\phi}{N-1} + \frac{c\Delta\Omega}{2\pi fL}\right)n} \quad (\text{A.6})$$

Using the identity  $\sum_{n=1}^N e^{\frac{2i\omega n}{N}} = \frac{e^{i\omega} \sin\left(\frac{(1+N^{-1})\omega}{2}\right)}{\sin\left(\frac{\omega}{2}\right)} - 1$  this can be further simplified to

$$\psi(R) \approx ae^{-\frac{2\pi if}{c}\left(R + \left(\frac{L}{2} + \frac{1}{N-1}L\right)\sin\phi + \frac{c\Delta\Omega}{2\pi f}\right)} \left\{ \frac{e^{i\omega} \sin\left(\frac{(1+N^{-1})\omega}{2}\right)}{\sin\left(\frac{\omega}{2}\right)} - 1 \right\} \quad (\text{A.7})$$

where

$$\omega = \frac{\pi N f L}{c} \left( \frac{\sin\phi}{N-1} + \frac{c\Delta\Omega}{2\pi f L} \right) \quad (\text{A.8})$$

The peak of power  $|\psi(R)|^2$  occurs when  $\omega = \pi N Z$  where  $Z$  is an integer. (See Appendix C). Hence the peak angle(s) are at

$$\pi N Z = \frac{\pi N f L}{c} \left( \frac{\sin\phi_{peak}}{N-1} + \frac{c\Delta\Omega}{2\pi f L} \right) \quad (\text{A.9})$$

$\Rightarrow$

$$\Delta\Omega = -\frac{2\pi f}{c} \left( \frac{L}{N-1} \right) \sin\phi_{peak} + 2\pi Z = -\frac{2\pi f}{c} \left( \frac{L}{N-1} \right) \sin\phi_{peak}$$

since a phase rotation of  $2\pi Z$  has no effect upon the result.

It can be shown that inter-element spacing of half a wavelength yields the optimal beam. (Differences can result in a degradation of the beam pattern and the manifestation of grating lobes), i.e.

$$\frac{L}{N-1} = \frac{1}{2}\lambda = \frac{c}{2f}$$

Using a half wavelength spacing, the angular width of the peak is approximately  $\phi_{BW} \approx \frac{c}{fL}$  i.e the ratio of wavelength to length of array (or ‘aperture’). For an example of on-boresight and steered beamshapes see figures in the Background Theory section in the main thesis.

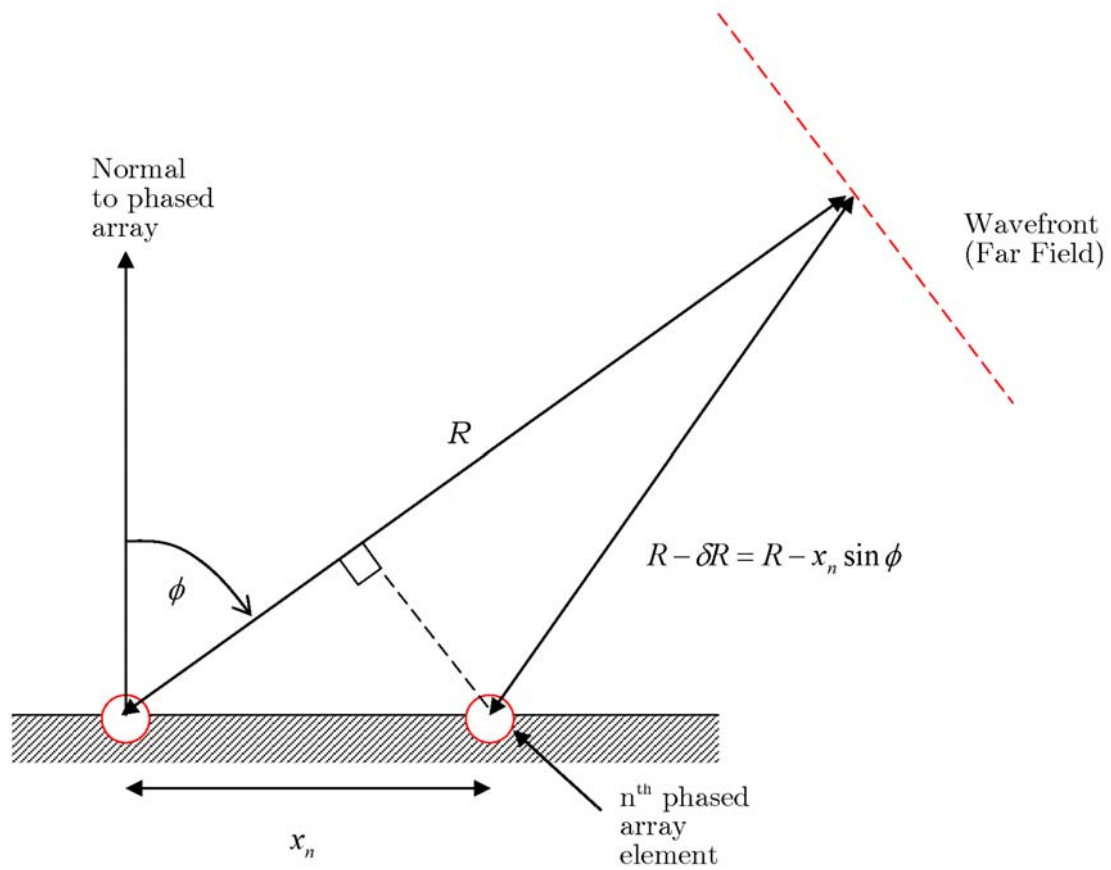


Figure A.1: Geometry of a linear phased array. The phase difference between two elements separated by  $x_n$  is  $\frac{2\pi}{\lambda} x_n \sin \phi$ .

## Appendix B

# The Radar Equation

Many Radar textbooks, for example Richards [88], Tait [103] and Skolnik [95], present slightly different versions of the *Radar Equation*, each using their own nomenclature. To avoid any confusion, the Radar Equation referred to in this thesis is derived below.

Let us assume a Radar which transmit electrical power  $P_t$  illuminates a target at range  $R$  of Radar cross section<sup>1</sup>  $\sigma$  with  $n$  pulses of duration  $\tau$  and bandwidth  $B$  transmitted using a carrier frequency  $f_{Tx}$ . The Radar transmits via an antenna of physical area  $A$  and therefore will offer a directional gain<sup>2</sup>  $G$  in the desired look direction (Tait [103] pp40), relative to an isotropic radiator.

$$G = \frac{4\pi A\eta}{\lambda^2} = \frac{4\pi A\eta}{c^2} f_{Tx}^2 \quad (\text{B.1})$$

Where  $\eta$  is the ‘antenna efficiency’ ( $\leq 1$ ),  $\lambda$  is the wavelength<sup>3</sup> and  $c$  is the speed of light. The electrical power backscatterered by the target in the direction of the Radar is therefore

$$P_s = G \frac{\sigma}{4\pi R^2} \frac{P_t}{L_t} = \frac{A\eta}{c^2} f_{Tx}^2 \frac{\sigma}{R^2} \frac{P_t}{L_t} \quad (\text{B.2})$$

where  $L_t$  is the combined loss factor upon transmission. (i.e. a practical antenna rated at  $P_t$  will not transmit all of this energy as electromagnetic radiation at the desired frequency), i.e. the backscattered power  $P_s$  is the target Radar cross section  $\sigma$  multiplied by the power flux at the target  $\frac{GP_t}{4\pi R^2 L_t}$ . The backscattered power  $P_r$  received at the Radar is therefore the power flux at the target  $\frac{P_s}{4\pi R^2}$  multiplied by the effective area of the antenna  $A\eta$  divided by the receiver losses  $L_r$ . We must also include the effects of propagation such as multipath and atmospheric loss. For single bounce multipath, the change in electric field strength resulting from the interference of direct and surface reflected paths is defined as  $F$ . The effect upon a Radar to target to Radar propagation (if both

---

<sup>1</sup>In the particular look direction. In general, targets such as an aircraft will not have an isotropic radar cross section (RCS) with look angle. However, as a first approximation one can use a ‘bulk RCS’ to estimate detection thresholds. Richards [88] pp65 suggests the following cross sections: Missile (0.5m<sup>2</sup>), Small aircraft (1m<sup>2</sup>), Jet airliner (20-40m<sup>2</sup>), Jumbo jet (100m<sup>2</sup>).

<sup>2</sup>Richards pp13 quotes the following approximate result for the antenna gain in terms of beamwidth:

$$G \approx \frac{26,000}{(\Delta\epsilon/\text{deg})(\Delta\phi/\text{deg})}$$

where  $\Delta\epsilon$  and  $\Delta\phi$  are the respective elevation and azimuth beamwidths in degrees. This formula is useful if the beamwidths, and therefore the gain is fixed. However, if a given antenna is used with a range of frequencies, the overall frequency dependence of the target signal to noise ratio in the Radar Equation can be misleading if the (inverse) frequency dependence of the beamwidths are not also stated explicitly.

<sup>3</sup>In this analysis the change of instantaneous carrier frequency from  $f_{Tx}$  over the pulse bandwidth  $B$  is ignored. The impact upon antenna gain, captured as a scanning loss, is discussed in section 2.7.3.

directions are assumed to be equal in propagation terms) is  $F^2$  and the effect upon received power is therefore  $|F^2|^2$ . Hence:

$$P_r = \frac{P_s}{4\pi R^2} \frac{A\eta}{L_r} |F^2|^2 = \frac{A^2 \eta^2 \sigma f_{Tx}^2}{4\pi R^4 c^2} \frac{P_t}{L_t L_r} |F^2|^2 \quad (\text{B.3})$$

Tait [103] pp 82 defines the receiver noise power to be

$$P_{noise} = k_B T_o B N_f \quad (\text{B.4})$$

where  $k_B$  is Boltzmann's constant,  $T_o$  is the ambient temperature in Kelvin,  $B$  is the bandwidth of the waveform being transmitted and  $N_f$  is the noise figure<sup>4</sup> of the receiver. In signal processing let us assume  $n$  pulses are integrated with efficiency  $E_i(n)$  and each pulse is cross-correlated with a copy of what was transmitted ('pulse compression'), yielding a gain of  $B\tau$ . If additional signal processing losses  $L_{sp}$  are incorporated into an overall loss product

$$L = L_r L_t L_{sp} \quad (\text{B.5})$$

then the signal to noise ratio  $S/N$  of the target signal can be expressed as

$$S/N = \frac{P_r}{P_{noise}} \frac{n E_i(n) B \tau}{L_{sp}} = \frac{A^2 \eta^2 n E_i(n) \tau P_t \sigma f_{Tx}^2 |F^2|^2}{4\pi c^2 L k_B T_o N_f R^4} \quad (\text{B.6})$$

Let us consider the following typical parameters, corresponding to a system similar to MESAR2 illuminating a modest airliner target with one burst of NCTR waveform A:

$A = 4\text{m}^2$ ,  $\eta = 0.5$ ,  $n = 8$ ,  $E_i(8) = 1$ ,  $\tau = 25.6\mu\text{s}$ ,  $P_t = 12\text{kW}$ ,  $\sigma = 20\text{m}^2$ ,  $f_{Tx} = 3\text{GHz}$ ,  $|F^2|^2 = 0\text{dB}$ ,  $k_B = 1.38 \times 10^{-23} \text{JK}^{-1}$ ,  $T_o N_f = 500\text{K}$ ,  $R = 50\text{km}$ ,  $L = 10\text{dB}$

The Radar Equation above yields  $S/N = 35.6\text{dB}$

For a measured  $S/N$ , one can estimate the target Radar cross section by using a rearrangement of the Radar Equation

$$\sigma = \frac{4\pi c^2 L k_B T_o N_f R^4}{A^2 \eta^2 n E_i(n) \tau P_t f_{Tx}^2 |F^2|^2} (S/N) \quad (\text{B.7})$$

---

<sup>4</sup>The noise figure, which is greater than unity, arises from the non-absolute zero temperature of the input terminals of the receiver amplifier. If the input terminals have temperature  $T_E$  then the noise power of the receiver + the noise power associated with the signal input at temperature  $T_0$  equates to a total noise power of  $G(T_E + T_0)k_B B$  where  $G$  is the gain of the amplifier. The noise figure is thus the ratio of this to the noise power due to the input i.e.

$$N_f = \frac{G(T_E + T_0)k_B B}{G T_0 k_B B} = 1 + \frac{T_E}{T_0}$$

## Appendix C

### The $\chi(x, z)$ function

Define the two parameter function

$$\chi(x, z) = \frac{e^{ix} \sin((1 + z^{-1})x)}{\sin(z^{-1}x)} - 1 \quad (\text{C.1})$$

*Conjecture:* if  $z \in \mathbb{Z}^+, z \geq 1$  then  $\chi(x, z)$  is the summation of a geometric series of the form

$$\sum_{n=1}^z e^{\frac{2ixn}{z}} = \chi(x, z) \quad (\text{C.2})$$

*Proof*

The sum of a geometric series of common ratio  $r$  has a well known closed form solution [112].

$$\sum_{j=0}^{N-1} r^j = \frac{1 - r^N}{1 - r} \quad (\text{C.3})$$

Setting  $z = N - 1$ ,  $n = j$  and taking the  $j = 0$  term outside the summation, this gives

$$\sum_{n=1}^z r^n = \frac{1 - r^{z+1}}{1 - r} - 1 \quad (\text{C.4})$$

The term  $\frac{1 - r^{z+1}}{1 - r}$  can be re-written as

$$\frac{1 - r^{z+1}}{1 - r} = \frac{r^{\frac{z}{2}} \left( r^{-\frac{z+1}{2}} - r^{\frac{z+1}{2}} \right)}{r^{-\frac{1}{2}} - r^{\frac{1}{2}}} = \frac{r^{\frac{z}{2}} \left( r^{\frac{z+1}{2}} - r^{-\frac{z+1}{2}} \right)}{r^{\frac{1}{2}} - r^{-\frac{1}{2}}} \quad (\text{C.5})$$

Now let  $r = e^{2ix/z}$ . This gives:

$$\frac{r^{\frac{z}{2}} \left( r^{\frac{z+1}{2}} - r^{-\frac{z+1}{2}} \right)}{r^{\frac{1}{2}} - r^{-\frac{1}{2}}} = \frac{e^{ix} \left( e^{ix(1+z^{-1})} - e^{-ix(1+z^{-1})} \right)}{e^{\frac{ix}{z}} - e^{-\frac{ix}{z}}} \quad (\text{C.6})$$

By De Moivre's theorem [112] we can write  $\sin \phi = \frac{1}{2i} (e^{i\phi} - e^{-i\phi})$  hence the above simplifies to

$$\frac{e^{ix} \left( e^{ix(1+z^{-1})} - e^{-ix(1+z^{-1})} \right)}{e^{\frac{ix}{z}} - e^{-\frac{ix}{z}}} = \frac{e^{ix} \sin((1 + z^{-1})x)}{\sin(z^{-1}x)} \quad (\text{C.7})$$

Using the form of the geometric progression summation above  $\sum_{n=1}^z r^n = \frac{1 - r^{z+1}}{1 - r} - 1$ , therefore

$$\sum_{n=1}^z e^{\frac{2ixn}{z}} = \frac{e^{ix} \sin((1 + z^{-1})x)}{\sin(z^{-1}x)} - 1 = \chi(x, z) \quad (\text{C.8})$$

as required.

Note the first derivative of  $\chi(x, z)$  is

$$\frac{\partial \chi(x, z)}{\partial x} = (1 + \chi(x, z)) \left( i + \frac{1 + z^{-1}}{\tan((1 + z^{-1})x)} - \frac{z^{-1}}{\tan(z^{-1}x)} \right) \quad (\text{C.9})$$

If  $z \in \mathbb{Z}^+, z \geq 1$  then  $\chi(0, z)$  can be evaluated using L'Hopital's rule [89] since  $\sin(0) = 0$ ,  $\cos(0) = 1$  and  $\frac{d}{dx} \sin(kx) = k \cos kx$

$$\chi(0, z) = \frac{1 + z^{-1}}{z^{-1}} - 1 = z \quad (\text{C.10})$$

Periodicity of this result occurs at  $x = z\pi Z$  where  $Z$  is an integer and is a local peak in  $|\chi(x, z)|^2$  which can be evaluated as

$$|\chi(x, z)|^2 = \left( \frac{e^{ix} \sin((1 + z^{-1})x)}{\sin(z^{-1}x)} - 1 \right) \left( \frac{e^{-ix} \sin((1 + z^{-1})x)}{\sin(z^{-1}x)} - 1 \right) \quad (\text{C.11})$$

$$= 1 + \frac{\sin^2((1 + z^{-1})x)}{\sin^2(z^{-1}x)} - \frac{2 \sin((1 + z^{-1})x)}{\sin(z^{-1}x)} \cos x \quad (\text{C.12})$$

$$\text{So } |\chi(z\pi Z, z)|^2 = 1 + \left( \frac{1+z^{-1}}{z^{-1}} \right)^2 - 2 \frac{1+z^{-1}}{z^{-1}} = 1 + (z+1)^2 - 2(1+z) = 1 + z^2 + 2z + 1 - 2 - 2z = z^2.$$

Secondary periodicity occurs when  $x = Z\pi$ , which is also approximately the peak width. For a complete analysis one needs to evaluate the Taylor series near  $x = z\pi Z$  i.e.

$$|\chi(x, z)|^2 \approx |\chi(z\pi Z, z)|^2 + (x - z\pi Z)^2 \frac{\partial^2 |\chi(x, z)|^2}{\partial^2 x} \Big|_{x=z\pi Z} \quad (\text{C.13})$$

and then compare this to the equation for determining the half width of an inverted parabola  $y = 1 - \frac{\alpha^2}{6} \Rightarrow y(\pm\sqrt{3}) = \frac{1}{2}$ , i.e.  $y = 1 - \frac{\alpha^2}{6}$  which has a half width of  $2\sqrt{3}$ . The task is to find the mapping between the above Taylor expansion and  $\alpha$ . This is left as an exercise for the reader!



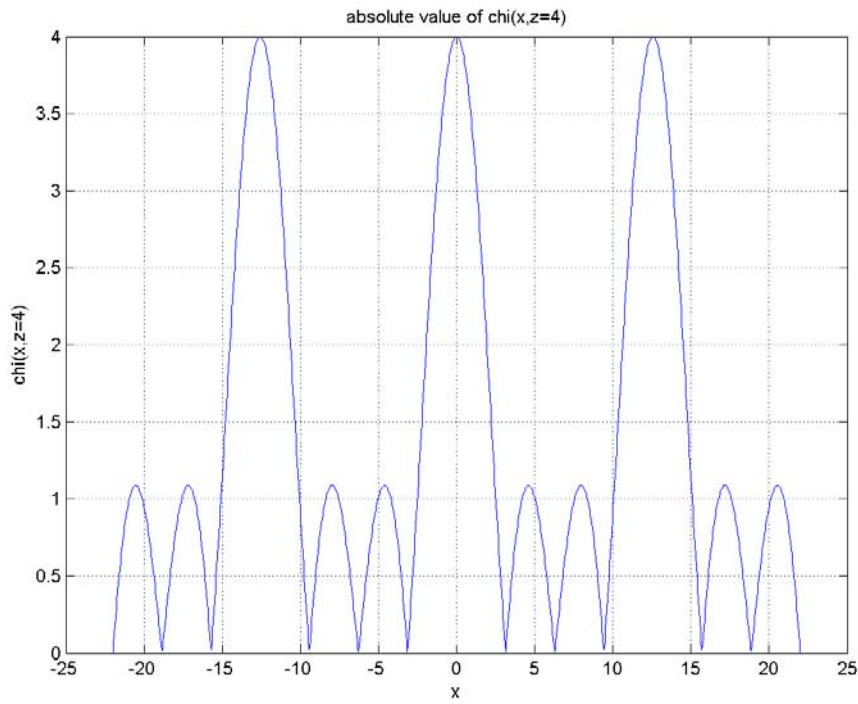


Figure C.1: Plot of magnitude of  $\chi(x, z) = \frac{e^{ix} \sin((1+z^{-1})x)}{\sin(z^{-1}x)} - 1$  where  $z = 4$ . Note peaks are of magnitude = 4 and peaks are separated by intervals of  $4\pi$ .

## Appendix D

# Fourier transform of a linear chirp waveform

### D.1 Definition of a linear chirp signal

A linear chirp pulse waveform  $\psi(t)$  is a rectangular envelope bounded signal with a frequency that increases in direct proportion to the time since the leading edge of the pulse. Let the chirp begin at time  $t_0$  and have duration  $\tau$ . Let the frequency range (bandwidth)  $B$  extend symmetrically about a mean  $\frac{c}{\lambda}$ . The chirp instantaneous frequency  $f(t)$  can be expressed

$$f(t) = \begin{cases} a + bt & t_0 < t < t_0 + \tau \\ 0 & t < t_0, \quad t > t_0 + \tau \end{cases} \quad (\text{D.1})$$

Now

$$f(t_0) = a + bt_0 = \frac{c}{\lambda} - \frac{1}{2}B \quad (\text{D.2})$$

$$\frac{df}{dt} = b = \frac{B}{\tau} \quad (\text{D.3})$$

Hence

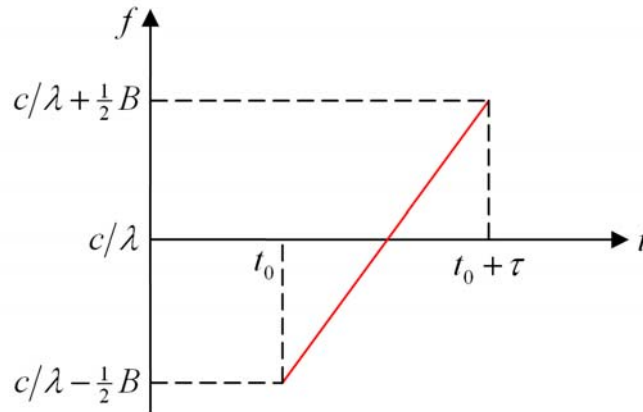


Figure D.1: Frequency vs time relationship for a linear chirp waveform.

$$a = \frac{c}{\lambda} - B \left( \frac{1}{2} + \frac{t_0}{\tau} \right) \quad (\text{D.4})$$

$$b = \frac{B}{\tau} \quad (\text{D.5})$$

Which gives

$$f(t) = \begin{cases} \frac{c}{\lambda} + B \left( \frac{t-t_0}{\tau} - \frac{1}{2} \right) & t_0 < t < t_0 + \tau \\ 0 & t < t_0, \quad t > t_0 + \tau \end{cases} \quad (\text{D.6})$$

The chirp signal amplitude  $\psi_{\text{real}}(t) = A \cos(\phi(t)) = A \text{Re} \{ e^{i\phi} \}$  where  $\phi$  is the phase of the waveform and  $A$  is defined to be a real constant. Let us define  $\psi(t)$  to be the unit amplitude complex part of the real signal. This shall be referred to as the ‘chirp signal’ from now on.

$$\psi(t) = e^{i\phi(t)} \quad (\text{D.7})$$

$$\psi_{\text{real}}(t) = A \text{Re} \{ \psi(t) \} \quad (\text{D.8})$$

The phase  $\phi$  is related to instantaneous frequency (in the continuous region of the pulse envelope  $t_0 < t < t_0 + \tau$ ) by

$$f(t) = \frac{1}{2\pi} \frac{d\phi}{dt} \quad (\text{D.9})$$

Hence

$$\phi(t) = 2\pi \int f(t) dt \quad (\text{D.10})$$

Conventionally [D.10] is an indefinite integral with constant of integration  $\gamma$  set such that the phase at the centre of the pulse is zero.

$$\phi(t_0 + \frac{1}{2}\tau) = 0 \quad (\text{D.11})$$

Using [D.6] and the above condition, the chirp phase can be evaluated analytically.

$$\phi(t) = 2\pi \int \left( \frac{c}{\lambda} + B \left( \frac{t-t_0}{\tau} - \frac{1}{2} \right) \right) dt \quad (\text{D.12})$$

$$= 2\pi \left[ \frac{c}{\lambda} t + Bt \left( \frac{\frac{1}{2}t - t_0}{\tau} - \frac{1}{2} \right) \right] + \gamma \quad (\text{D.13})$$

$$= 2\pi \left[ \frac{1}{2} \frac{B}{\tau} t^2 - \left( \frac{Bt_0}{\tau} + \frac{1}{2}B - \frac{c}{\lambda} \right) t \right] + \gamma \quad (\text{D.14})$$

Since  $\phi(t_0 + \frac{1}{2}\tau) = 0$

$$\gamma = -2\pi \left[ \frac{1}{2} \frac{B}{\tau} (t_0 + \frac{1}{2}\tau)^2 - \left( \frac{Bt_0}{\tau} + \frac{1}{2}B - \frac{c}{\lambda} \right) (t_0 + \frac{1}{2}\tau) \right] \quad (\text{D.15})$$

In summary, the linear chirp is described by the following system of equations

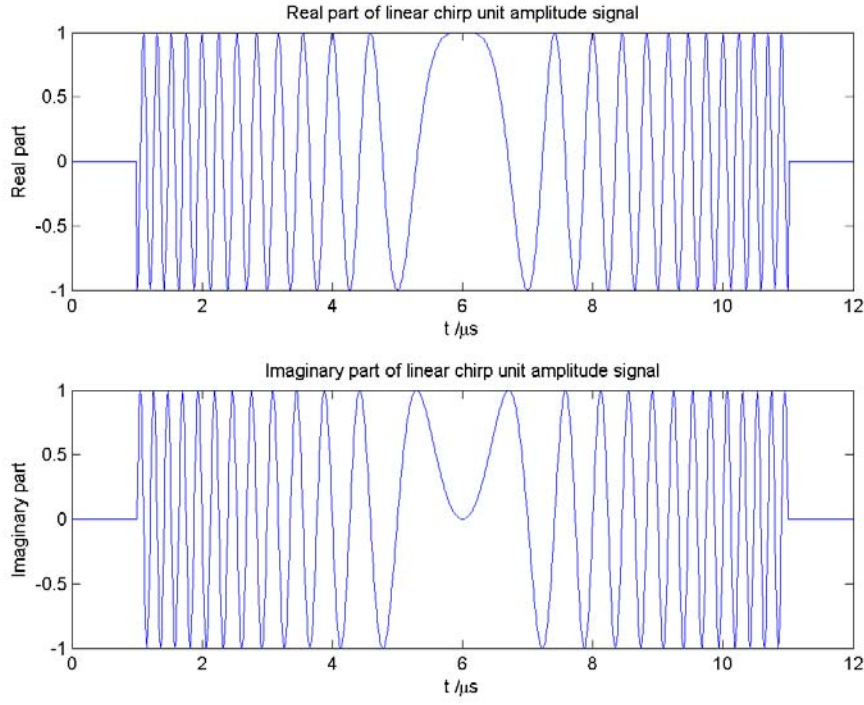


Figure D.2: Real and imaginary parts of a linear chirp waveform.

$$\begin{aligned}
 \psi_{\text{real}}(t) &= A \operatorname{Re} \{ \psi(t) \} \\
 \psi(t) &= \begin{cases} e^{i\phi(t)} & t_0 < t < t_0 + \tau \\ 0 & t < t_0, \quad t > t_0 + \tau \end{cases} \\
 \phi(t) &= \alpha t^2 + \beta t + \gamma \\
 \alpha &= \frac{\pi B}{\tau} \\
 \beta &= -2\pi \left( \frac{B t_0}{\tau} + \frac{1}{2} B - \frac{c}{\lambda} \right) \\
 \gamma &= -2\pi \left[ \frac{1}{2} \frac{B}{\tau} \left( t_0 + \frac{1}{2} \tau \right)^2 - \left( \frac{B t_0}{\tau} + \frac{1}{2} B - \frac{c}{\lambda} \right) \left( t_0 + \frac{1}{2} \tau \right) \right]
 \end{aligned}$$

(D.16)

Samples of the chirp (following analogue to digital conversion) occur after a mix down by some frequency  $f_{\text{mix}}$ . In this case

$$\beta \longrightarrow \beta - 2\pi f_{\text{mix}} \quad (\text{D.17})$$

If  $f_{\text{mix}} = \frac{c}{\lambda}$  then the signal is said to be converted down to baseband. In this case

$$\beta_{\text{baseband}} = -2\pi \left( \frac{B t_0}{\tau} + \frac{1}{2} B \right) \quad (\text{D.18})$$

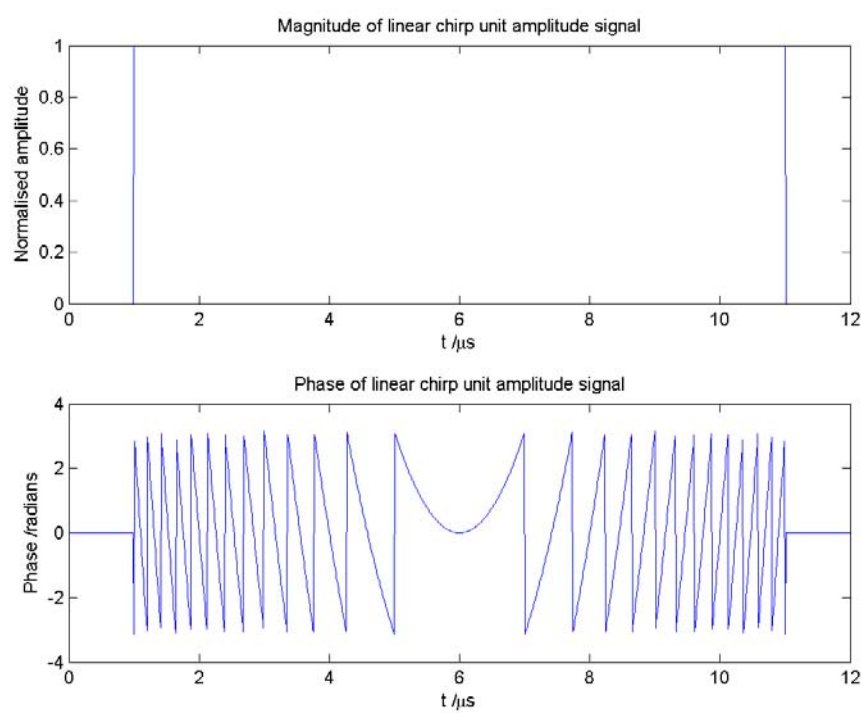


Figure D.3: Magnitude and phase of a linear chirp waveform.

## D.2 Fourier Transform of a linear chirp

The frequency spectrum of a linear chirp signal  $\psi(t)$  is defined by its Fourier Transform

$$\tilde{\psi}(f) = \int_{-\infty}^{+\infty} \psi(t) e^{-2\pi i f t} dt \quad (\text{D.19})$$

Using [D.16] this reduces to

$$\tilde{\psi}(f) = \int_{t_0}^{t_0+\tau} \exp [i (\alpha t^2 + (\beta - 2\pi f) t + \gamma)] dt \quad (\text{D.20})$$

Now define a set of dimensionless variables

$$\omega = \frac{f}{B} \quad (\text{D.21})$$

$$k = \frac{t - t_0}{\tau} - \frac{1}{2} \quad (\text{D.22})$$

Hence

$$t = k\tau + \frac{\tau}{2} + t_0 \quad (\text{D.23})$$

$$t^2 = k^2\tau^2 + 2\left(\frac{\tau}{2} + t_0\right)k\tau + \left(\frac{\tau}{2} + t_0\right)^2 \quad (\text{D.24})$$

$$k(t_0) = -\frac{1}{2} \quad (\text{D.25})$$

$$k(t_0 + \tau) = \frac{1}{2} \quad (\text{D.26})$$

The quadratic chirp phase transforms to

$$\begin{aligned} & \alpha t^2 + (\beta - 2\pi f) t + \gamma = \\ & \alpha \left\{ k^2\tau^2 + 2\left(\frac{\tau}{2} + t_0\right)k\tau + \left(\frac{\tau}{2} + t_0\right)^2 \right\} + (\beta - 2\pi B\omega) \left(k\tau + \frac{\tau}{2} + t_0\right) + \gamma \\ = & k^2 \{ \alpha\tau^2 \} + k \{ 2\alpha \left(\frac{\tau}{2} + t_0\right)\tau + (\beta - 2\pi B\omega)\tau \} + \alpha \left(\frac{\tau}{2} + t_0\right)^2 + (\beta - 2\pi B\omega) \left(\frac{\tau}{2} + t_0\right) + \gamma \end{aligned} \quad (\text{D.27})$$

This can be simplified slightly by recalling (using a general mixing down frequency  $f_{mix}$ )

$$\alpha = \frac{\pi B}{\tau} \quad (\text{D.28})$$

$$\beta = -2\pi \left( \frac{Bt_0}{\tau} + \frac{1}{2}B - \frac{c}{\lambda} + f_{mix} \right) \quad (\text{D.29})$$

$$\gamma = -2\pi \left[ \frac{1}{2} \frac{B}{\tau} \left( t_0 + \frac{1}{2}\tau \right)^2 - \left( \frac{Bt_0}{\tau} + \frac{1}{2}B - \frac{c}{\lambda} \right) \left( t_0 + \frac{1}{2}\tau \right) \right] \quad (\text{D.30})$$

and defining the pure number

$$n = B\tau\pi \quad (\text{D.31})$$

This gives

$$\alpha\tau^2 = n \quad (\text{D.32})$$

$$\begin{aligned} 2\alpha \left(\frac{\tau}{2} + t_0\right)\tau + (\beta - 2\pi B\omega)\tau &= 2n \left( \frac{1}{2} + \frac{t_0}{\tau} \right) - 2n \left( \frac{t_0}{\tau} + \frac{1}{2} - \frac{c}{\lambda B} + \frac{f_{mix}}{B} + \omega \right) \\ &= 2n \left( \frac{c}{\lambda B} - \frac{f_{mix}}{B} - \omega \right) \end{aligned} \quad (\text{D.33})$$

$$\begin{aligned} & \alpha \left( \frac{\tau}{2} + t_0 \right)^2 + (\beta - 2\pi B\omega) \left( \frac{\tau}{2} + t_0 \right) + \gamma = \\ & n \left( \frac{1}{2} + \frac{t_0}{\tau} \right)^2 - 2n \left( \frac{t_0}{\tau} + \frac{1}{2} - \frac{c}{\lambda B} + \frac{f_{mix}}{B} + \omega \right) \left( \frac{1}{2} + \frac{t_0}{\tau} \right) + \gamma \end{aligned} \quad (D.34)$$

Furthermore, define another dimensionless quantity

$$\eta = \frac{1}{2} + \frac{t_0}{\tau} \quad (D.35)$$

Hence

$$\begin{aligned} \gamma &= -2\pi \left[ \frac{B}{\tau} \left( t_0 + \frac{1}{2}\tau \right)^2 - \left( \frac{Bt_0}{\tau} + \frac{1}{2}B - \frac{c}{\lambda} \right) \left( t_0 + \frac{1}{2}\tau \right) \right] \\ &= -2\pi \left[ \frac{1}{2} \frac{B\tau^2}{\tau} \eta^2 - B\tau \left( \eta - \frac{c}{\lambda B} \right) \eta \right] \\ &= -n\eta^2 + 2n \left( \eta - \frac{c}{\lambda B} \right) \eta \\ &= n \left( \eta - \frac{2c}{\lambda B} \right) \eta \end{aligned} \quad (D.36)$$

$$\begin{aligned} & \alpha \left( \frac{\tau}{2} + t_0 \right)^2 + (\beta - 2\pi B\omega) \left( \frac{\tau}{2} + t_0 \right) + \gamma \\ &= n\eta^2 - 2n \left( \eta - \frac{c}{\lambda B} + \frac{f_{mix}}{B} + \omega \right) \eta + n \left( \eta - \frac{2c}{\lambda B} \right) \eta \\ &= -2n\eta \left( \omega + \frac{f_{mix}}{B} \right) \end{aligned} \quad (D.37)$$

Therefore

$$\alpha t^2 + (\beta - 2\pi f) t + \gamma = nk^2 + 2n \left( \frac{c}{\lambda B} - \frac{f_{mix}}{B} - \omega \right) k - 2n\eta \left( \omega + \frac{f_{mix}}{B} \right) \quad (D.38)$$

Since any quadratic polynomial  $P(k)$  can be written in ‘completed square’ form

$$Ak^2 + Bk + C \equiv \left( k\sqrt{A} + \frac{B}{2\sqrt{A}} \right)^2 - \frac{B^2}{4A} + C \quad (D.39)$$

we can redefine [D.20] to be

$$\tilde{\psi}(f) = \tau e^{-i \left\{ \left( \frac{c}{\lambda B} - \frac{f_{mix}}{B} - \omega \right)^2 + 2n\eta \left( \omega + \frac{f_{mix}}{B} \right) \right\}} \int_{-\frac{1}{2}}^{\frac{1}{2}} \exp \left[ i \left( k + \frac{c}{\lambda B} - \frac{f_{mix}}{B} - \omega \right)^2 n \right] dk \quad (D.40)$$

using

$$A = n \quad (D.41)$$

$$B = 2n \left( \frac{c}{\lambda B} - \frac{f_{mix}}{B} - \omega \right) \quad (D.42)$$

$$C = -2n\eta \left( \omega + \frac{f_{mix}}{B} \right) \quad (D.43)$$

This can be simplified further by adopting a change of integration variable

$$z\sqrt{\frac{\pi}{2}} = \left( k + \frac{c}{\lambda B} - \frac{f_{mix}}{B} - \omega \right) \sqrt{n} \quad (D.44)$$

$$\tilde{\psi}(f) = \tau \sqrt{\frac{\pi}{2n}} e^{-i \left\{ n \left( \frac{c}{\lambda B} - \frac{f_{mix}}{B} - \omega \right)^2 + 2n\eta \left( \omega + \frac{f_{mix}}{B} \right) \right\}} \int \sqrt{\frac{2n}{\pi}} \left( \frac{c}{\lambda B} - \frac{f_{mix}}{B} - \omega + \frac{1}{2} \right) \exp \left[ \frac{1}{2} i \pi z^2 \right] dz \quad (D.45)$$

The above result can now be expressed in terms of Fresnel Integrals. These can be easily evaluated using a numerical computation tool such as MATLAB.

$$C(x) = \int_0^x \cos \left( \frac{1}{2} i \pi z^2 \right) dz \quad (D.46)$$

$$S(x) = \int_0^x \sin \left( \frac{1}{2} i \pi z^2 \right) dz \quad (D.47)$$

Splitting the integral into two integrals from  $z = 0$

$$\int \sqrt{\frac{2n}{\pi}} \left( \frac{c}{\lambda B} - \frac{f_{mix}}{B} - \omega + \frac{1}{2} \right) e^{\frac{1}{2} i \pi z^2} dz = \int_0^{\sqrt{\frac{2n}{\pi}} \left( \frac{c}{\lambda B} - \frac{f_{mix}}{B} - \omega + \frac{1}{2} \right)} e^{\frac{1}{2} i \pi z^2} dz - \int_0^{\sqrt{\frac{2n}{\pi}} \left( \frac{c}{\lambda B} - \frac{f_{mix}}{B} - \omega - \frac{1}{2} \right)} e^{\frac{1}{2} i \pi z^2} dz \quad (D.48)$$

$$= C \left( \sqrt{\frac{2n}{\pi}} \left( \frac{c}{\lambda B} - \frac{f_{mix}}{B} - \omega + \frac{1}{2} \right) \right) + i S \left( \sqrt{\frac{2n}{\pi}} \left( \frac{c}{\lambda B} - \frac{f_{mix}}{B} - \omega + \frac{1}{2} \right) \right) \dots \quad (D.49)$$

$$- C \left( \sqrt{\frac{2n}{\pi}} \left( \frac{c}{\lambda B} - \frac{f_{mix}}{B} - \omega - \frac{1}{2} \right) \right) - i S \left( \sqrt{\frac{2n}{\pi}} \left( \frac{c}{\lambda B} - \frac{f_{mix}}{B} - \omega - \frac{1}{2} \right) \right) \quad (D.50)$$

We arrive at the readily evaluable result for the Fourier Transform of a linear chirp. Note both Fresnel functions are odd i.e.  $C(-x) = -C(x)$  and  $S(-x) = -S(x)$ . This allows the ‘Fresnel term’ to be written as a sum, which is better for numerical evaluation.

$$\tilde{\psi}(f) = \underbrace{\tau \sqrt{\frac{\pi}{2n}} e^{-i \left\{ n \left( \frac{c}{\lambda B} - \frac{f_{mix}}{B} - \omega \right)^2 + 2n\eta \left( \omega + \frac{f_{mix}}{B} \right) \right\}}}_{\text{Harmonic ‘phase’ term}} \underbrace{\{C_+ + C_- + iS_+ + iS_-\}}_{\text{‘Fresnel term’}}$$

$$\begin{aligned} C_+ &= C \left( \sqrt{\frac{2n}{\pi}} \left( \frac{1}{2} + w \right) \right) \\ S_+ &= S \left( \sqrt{\frac{2n}{\pi}} \left( \frac{1}{2} + w \right) \right) \\ C_- &= C \left( \sqrt{\frac{2n}{\pi}} \left( \frac{1}{2} - w \right) \right) \\ S_- &= S \left( \sqrt{\frac{2n}{\pi}} \left( \frac{1}{2} - w \right) \right) \end{aligned} \quad (D.51)$$

$$\begin{aligned} w &= \frac{c}{\lambda B} - \frac{f_{mix}}{B} - \omega \\ \eta &= \frac{1}{2} + \frac{t_0}{\tau} \\ n &= B\tau\pi \\ \omega &= \frac{f}{B} \end{aligned}$$



## Appendix E

# The Martin & Mulgrew model of Jet Engine Modulation

### E.1 Derivation of the Martin & Mulgrew model of JEM

A jet engine can be described as a series of propellers contained within a housing, with each of the propellers rotating about a central shaft. Since all parts are likely to be highly reflective at Radar frequencies, the electric field resulting from re-radiated energy will be extremely difficult to compute, even at ranges  $R \gg L_2$ , where  $L_2$  is the radius of the jet engine inlet.

However, it has been observed from experimental Radar studies than certain key features can be extracted from signals deriving from jet engine reflections. To attempt to explain these major features we shall consider a grossly simplified model which allows us to compute the received Radar signal analytically. If the model can be shown to predict the major features experimentally observed, then we can infer the assumptions upon which the model is based are valid. Hence by finding the various parameters of the model which reproduce a given signal, one can infer bulk characteristics of the jet engine. This could be extremely useful in target recognition applications.

Jet engine reflections are known to result in periodic amplitude and phase modulations upon the carrier signal. Hence the term ‘Jet Engine Modulation’ (JEM). The Martin & Mulgrew model [67],[68] is used to define these variations. A derivation is presented here and is founded upon the following assumptions:

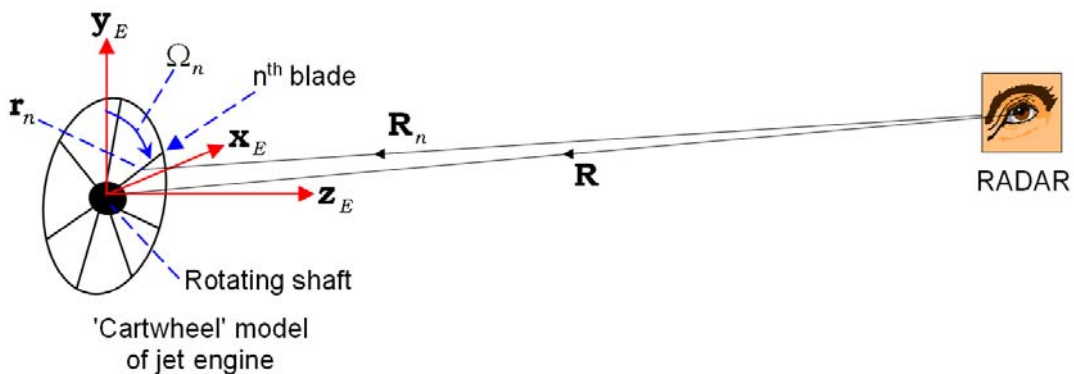


Figure E.1: A jet engine is modelled as a rotating “cartwheel” of reflecting blades. These act as line antennas which re-radiate energy imposed upon them by a Radar.

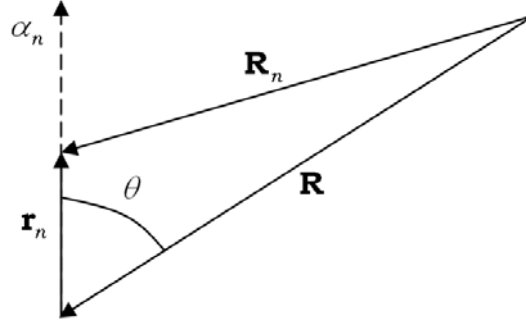


Figure E.2: The position vector of length  $\alpha_n$  along the  $n^{\text{th}}$  blade is given by  $\mathbf{r}_n$ . This vector has origin at the rotating shaft. In general the jet engine will not be oriented perpendicular to Radar line-of-sight along vector  $\mathbf{R}$ .

- Each engine blade acts as a homogeneous, linear, rigid antenna.
- The jet engine is in the far-field of the Radar, i.e.  $R \gg L_2$
- The only significant contributions to the received signal derive from reflections off the equi-spaced engine blades at the inlet. Hence the analysis is identical to that of a propeller. Reflections from the housing and rotating shaft are not considered since they will not result in any time varying effects, assuming the received signal is compensated for the bulk motion of the jet engine (i.e. the motion of the aircraft that bears it).
- The propeller model assumed is further simplified to a ‘cartwheel’ of radial line antennas. If parameter  $\alpha_n$  is used to define the distance from the centre of the rotating shaft along the  $n^{\text{th}}$  blade, then the blade shall be modelled as a uniform line antenna within the limits  $\alpha_n = [L_1, L_2]$ .  $L_1$  is the radius of the rotating shaft and  $L_1 - L_2$  is the length of the blade. Note the (far field) beamwidth (in radians) associated with an antenna dimension of width  $a$  is  $\approx \frac{\lambda}{a}$  where  $\lambda$  is the wavelength employed. If the jet engine blades are long and thin then the radiation pattern will be broad in the plane of the width dimension and narrow(er) in the plane of the length (radial) dimension. To resolve any time varying effect due to the jet engine blades the beamwidth of the blade antennas must be  $\leq$  Radar beamwidth  $\Delta\phi_{BW}$ . If the jet engine is observed with an S-band Radar, the carrier frequency  $f_{Tx} \approx 3$  GHz and thus the wavelength (strictly in vacuo but approximately correct in air)  $\lambda \approx 10$  cm. A typical Radar beamwidth  $\Delta\phi_{BW} \approx 2.5^\circ$ . Jet engine blades can be up to a few meters long and several centimeters wide. For the blades to have a significant effect upon the received signal then blade dimension  $a \gg \frac{\lambda}{\Delta\phi_{BW}}$ . For our typical S-band Radar,  $\frac{\lambda}{\Delta\phi_{BW}} \approx 2.2$  m. Hence we would expect the jet engine blades to only contribute to time-varying effects upon the received signal via their length dimension.
- Pitching and twisting of the blades is not considered. Blade pitching is known to have a significant effect upon JEM and will be considered in the next iteration of this model described in the following section.

The JEM signal as defined in the Martin & Mulgrew model can be derived using scalar wave theory and the above approximations. Let us start from some basic physics.

The Huygens-Fresnel Principle [43] states :

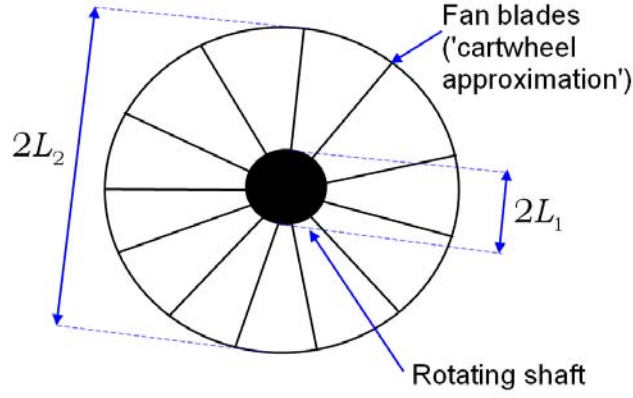


Figure E.3: “Cartwheel” model of a jet engine. The wheel spokes are line antennas.

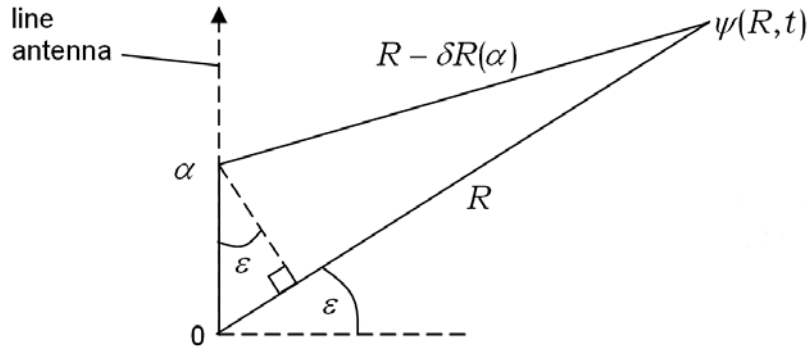


Figure E.4: Scalar wave-field resulting from superposition of spherical waves radiated by a line antenna.

*"Every unobstructed point of a wavefront, at a given instant, serves as a source of spherical secondary wavelets (with the same frequency as that of the primary wave). The amplitude of the optical field at any point beyond is the superposition of all these wavelets (considering their amplitudes and relative phases)."*

Using this principle we can express the (time varying) magnitude of the electric field  $\psi(R, t)$  resulting from a radiating line antenna element (extending from radial length  $\alpha$  from  $L_1$  to  $L_2$ ) as<sup>1</sup>

$$\psi(R, t) = \int_{L_1}^{L_2} \frac{A(\alpha)}{R + \delta R(\alpha)} e^{2\pi i f_{Tx} - ik(R - \delta R(\alpha))} d\alpha \quad (\text{E.1})$$

$R + \delta R(\alpha)$  is the displacement from the antenna (a distance  $\alpha$  along its length). We define  $\alpha = 0$  to correspond to  $\delta R(0) = 0$ .  $f_{Tx}$  is the carrier frequency of radiation and the corresponding wavenumber  $k = \frac{2\pi}{\lambda}$ .  $A(\alpha)$  is an illumination function which specifies the amplitude and phase distribution along the line antenna.

Using Pythagoras' theorem and trigonometric definitions one can relate the quantities  $\alpha, R, \delta R, \epsilon$  described in figure E.4

$$(R - \delta R)^2 = (R \sin \epsilon - \alpha)^2 + R^2 \cos^2 \epsilon \quad (\text{E.2})$$

Expanding the RHS and using the identity  $\sin^2 \epsilon + \cos^2 \epsilon = 1$  we find

$$1 - \frac{\delta R}{R} = \left( 1 + \frac{\alpha^2}{R^2} - \frac{2\alpha \sin \epsilon}{R} \right)^{\frac{1}{2}} \quad (\text{E.3})$$

<sup>1</sup>A more mathematically precise derivation of can be done using the Fresnel-Kirchoff diffraction integral

If we are in the far-field of the antenna then for all  $\alpha$ ,  $R \gg \alpha$ . Hence we can binomially expand the square root and take the first two terms to write

$$1 - \frac{\delta R}{R} \approx 1 + \frac{\alpha^2}{2R^2} - \frac{\alpha \sin \varepsilon}{R} \quad (\text{E.4})$$

Hence

$$\delta R \approx \alpha \sin \varepsilon - \frac{\alpha^2}{2R} \quad (\text{E.5})$$

The line antenna imposes little significant change upon the wave-field compared to a ‘point antenna’ if phase  $k\delta R \ll 2\pi$ . Using the above we can write this criterion as

$$\lambda \gg \alpha \sin \varepsilon - \frac{1}{2}\alpha \left( \frac{\alpha}{R} \right) \quad (\text{E.6})$$

Since the second term is much smaller than the first because  $R \gg \alpha$ ; if  $\max(\alpha) = L_2$ , the length of the line antenna, the antenna will behave like a point radiator if  $\lambda \gg L_2$ . If however  $\lambda \gg \frac{\alpha^2}{2R}$  but not the larger, linear term in  $\alpha$ , we can ignore the quadratic term in the phase expression. This is known as the ‘Fraunhofer limit’ and allows E.1 to be written as

$$\psi(R, t) \approx \frac{e^{2\pi i f_{Tx} t - ikR}}{R} \int_{L_1}^{L_2} A(\alpha) e^{ik\alpha \sin \varepsilon} d\alpha \quad (\text{E.7})$$

where  $R \gg \frac{L_2^2}{\lambda}$  and  $\lambda \gg L_2$ .<sup>2</sup>

Referring to fig E.1 and our JEM model assumptions, (extending ‘far-field’ to mean ‘Fraunhofer limit’) we may use the above to write down the wavefield resulting from a superposition of spherical waves radiated from all  $N$  line antennas.

Firstly note that  $(k\alpha \sin \varepsilon)_n = -\frac{2\pi}{R\lambda} \mathbf{r}_n \cdot \mathbf{R}$  and  $\sin \varepsilon = \cos \theta$ . Hence:

$$\psi(R, t) \approx \frac{e^{2\pi i f_{Tx} t - \frac{2\pi i R}{\lambda}}}{R} \sum_{n=0}^{N-1} \int_{L_1}^{L_2} A_n(\alpha_n) e^{-\frac{2\pi i}{R\lambda} \mathbf{r}_n \cdot \mathbf{R}} d\alpha_n \quad (\text{E.8})$$

The Radar illumination of the blades result in a linear phase ramp imposed upon them since, in our far field approximation, we can regard the wave front approaching (or re-radiated from) the line antenna/blade as being planar. The  $R^{-1}$  dependence is however still left to reflect the true spherical nature of the illumination signal (as viewed from the Radar). The wave-front approaching the jet engine can be thought to have negligible curvature on the length scale of the blades.

i.e.

$$A_n(\alpha_n) = \frac{\psi_0}{R} e^{-\frac{2\pi i}{\lambda} (R + \frac{\mathbf{r}_n \cdot \mathbf{R}}{R})} \quad (\text{E.9})$$

Therefore E.8 becomes

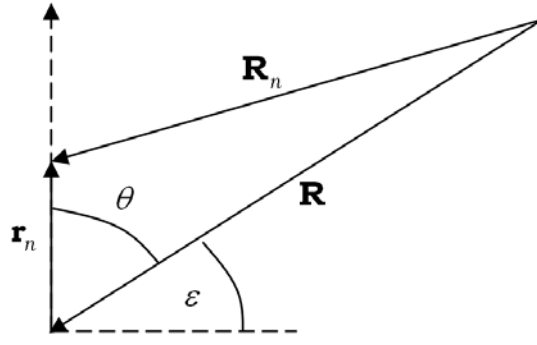
$$\psi(R, t) \approx \psi_0 \frac{e^{2\pi i f_{Tx} t - \frac{4\pi i R}{\lambda}}}{R^2} \sum_{n=0}^{N-1} \int_{L_1}^{L_2} e^{-\frac{4\pi i}{R\lambda} \mathbf{r}_n \cdot \mathbf{R}} d\alpha_n \quad (\text{E.10})$$

Using the diagram above we can express  $\mathbf{r}_n$  in terms of Cartesian unit-vectors  $\mathbf{x}_E$  and  $\mathbf{y}_E$ . These specify the orientation of the jet engine.

$$\mathbf{r}_n(\alpha) = \alpha_n (\mathbf{y}_E \cos \Omega_n + \mathbf{x}_E \sin \Omega_n) \quad (\text{E.11})$$

---

<sup>2</sup>Note the factor of 2 can be ‘safely’ neglected in the specification of this limit! If  $R \approx \frac{L_2^2}{\lambda}$  and  $\varepsilon \approx 0$  then the phase term in E.1 becomes purely quadratic in  $\alpha$ . This is known as the *Fresnel regime* and is extensively described in [43].

Figure E.5: Relationship between vector quantities  $\mathbf{r}_n$ ,  $\mathbf{R}_n$ ,  $\mathbf{R}$  and angles  $\varepsilon$  and  $\theta$ 

If the blades rotate at frequency  $f_{rot}$  about the central shaft (we will use the convention of a clockwise rotation being positive) then at time  $t$  the  $n^{\text{th}}$  blade will subtend angle  $\Omega_n$  from the  $\mathbf{y}_E$  axis. Recall the indexing of blades is  $n = 0 \dots N - 1$

$$\Omega_n = 2\pi \left( f_{rot} t + \frac{n}{N} \right) + \phi_0 \quad (\text{E.12})$$

$\phi_0$  is the initial angle of rotation corresponding to time origin  $t = 0$ .

In summary, the signal return received at the Radar due to a JEM reflection at range  $R$  will take the form (subject to the approximations above)

$$\psi(R, t) \approx \psi_0 \frac{e^{2\pi i f_{Tx} t - \frac{4\pi i R}{\lambda}}}{R^2} \sum_{n=0}^{N-1} \int_{L_1}^{L_2} e^{-\frac{4\pi i}{R\lambda} \mathbf{r}_n \cdot \mathbf{R}} d\alpha_n \quad (\text{E.13})$$

where

$$\mathbf{r}_n(\alpha) = \alpha_n (\mathbf{y}_E \cos \Omega_n + \mathbf{x}_E \sin \Omega_n) \quad (\text{E.14})$$

Define

$$\xi_n = -\frac{4\pi}{R\lambda} (\mathbf{y}_E \cos \Omega_n + \mathbf{x}_E \sin \Omega_n) \cdot \mathbf{R} \quad (\text{E.15})$$

This is a time varying quantity but is invariant with  $\alpha_n$ . The negative sign is used since  $\mathbf{R}$  points towards the jet engine. Hence:

$$\psi(R, t) \approx \psi_0 \frac{e^{2\pi i f_{Tx} t - \frac{4\pi i R}{\lambda}}}{R^2} \sum_{n=0}^{N-1} \int_{L_1}^{L_2} e^{i\alpha_n \xi_n} d\alpha_n \quad (\text{E.16})$$

The integral can be evaluated analytically and yields a sinc term<sup>3</sup> in multiplied by a harmonic term<sup>4</sup> in  $\xi_n$ .

$$\int_{L_1}^{L_2} e^{i\alpha_n \xi_n} d\alpha_n = \frac{1}{i\xi_n} \left[ e^{i\alpha_n \xi_n} \right]_{L_1}^{L_2} = \frac{1}{i\xi_n} \left( e^{iL_2 \xi_n} - e^{iL_1 \xi_n} \right) \quad (\text{E.17})$$

$$= \frac{1}{2} e^{\frac{1}{2} i(L_1 + L_2) \xi_n} 2(L_2 - L_1) \frac{1}{\frac{1}{2}(L_2 - L_1)} \frac{1}{2i} \left( e^{i\frac{(L_2 - L_1)}{2} \xi_n} - e^{-i\frac{(L_2 - L_1)}{2} \xi_n} \right) \quad (\text{E.18})$$

$$= (L_2 - L_1) e^{\frac{1}{2} i(L_1 + L_2) \xi_n} \text{sinc} \left( \frac{1}{2} (L_2 - L_1) \xi_n \right) \quad (\text{E.19})$$

<sup>3</sup>  $\text{sinc}(x) = \sin(x)/x$

<sup>4</sup> a function of the form  $f(x, a) = e^{iax}$

A closed form expression for the JEM signal can therefore be written as

$$\psi(R, t) \approx \frac{\psi_0 (L_2 - L_1)}{R^2} e^{2\pi i f_{Tx} t - \frac{4\pi i R}{\lambda}} \sum_{n=0}^{N-1} e^{\frac{1}{2} i (L_1 + L_2) \xi_n} \text{sinc} \left( \frac{1}{2} (L_2 - L_1) \xi_n \right) \quad (\text{E.20})$$

In the special case where  $\mathbf{R} = -R (\mathbf{z}_E \sin \theta + \mathbf{x}_E \cos \theta)$  i.e. the range vector  $\mathbf{R}$  is in the same plane as axis of jet engine rotation and the turbine body axis  $\mathbf{x}_E$ .

$$\xi_n = -\frac{4\pi}{R\lambda} (\mathbf{y}_E \cos \Omega_n + \mathbf{x}_E \sin \Omega_n) \cdot \mathbf{R} = \frac{4\pi}{\lambda} \sin \Omega_n \cos \theta \quad (\text{E.21})$$

Hence

$$\psi(R, t) \approx \frac{\psi_0 (L_2 - L_1)}{R^2} e^{2\pi i f_{Tx} t - \frac{4\pi i R}{\lambda}} \sum_{n=0}^{N-1} e^{\frac{2\pi i}{\lambda} (L_1 + L_2) \sin(2\pi (f_{rot} t + \frac{n}{N})) \cos \theta} \dots \quad (\text{E.22})$$

$$\times \text{sinc} \left( \frac{2\pi}{\lambda} (L_2 - L_1) \sin \left( 2\pi \left( f_{rot} t + \frac{n}{N} \right) \right) \cos \theta \right) \quad (\text{E.23})$$

Which is the same (apart from the sign in the harmonic term and a Doppler shift of carrier frequency) as that stated in [67].

Note we have set the unknown initial blade angle  $\phi_0 = 0$ . Since we have been precise in our definition of turbine body axis, this equivalence will not be true in the general case. A non-zero initial blade angle could be regarded as a constant time shift of  $\Delta t \approx \frac{\phi_0}{2\pi f_{rot}}$ .

This unknown blade angle should not pose much of a problem in the application of our JEM model since one will be utilizing the frequency spectrum of the JEM return rather than processing the signal in the time domain. The frequency spectrum is given by the magnitude of the Fourier Transform of signal  $\psi(R, t)$ .

$$\left| \tilde{\psi}(R, f) \right| = |\mathcal{F}[\psi(R, t)]| = \left| \int_{-\infty}^{\infty} \psi(R, t) e^{-2\pi i f t} dt \right| \quad (\text{E.24})$$

Using the Fourier shift theorem [112]

$$\mathcal{F}[\psi(t - \Delta t)] = e^{-2\pi i f \Delta t} \mathcal{F}[\psi(t)] \quad (\text{E.25})$$

Hence

$$\left| \tilde{\psi}(R, f) \right| = |\mathcal{F}[\psi(R, t)]| = |\mathcal{F}[\psi(R, t - \Delta t)]| \quad (\text{E.26})$$

since

$$|\mathcal{F}[\psi(R, t - \Delta t)]|^2 = e^{-2\pi i f \Delta t} \mathcal{F}[\psi(R, t)] e^{2\pi i f \Delta t} (\mathcal{F}[\psi(R, t)])^* = |\mathcal{F}[\psi(R, t)]|^2 \quad (\text{E.27})$$

i.e. the magnitude of the frequency spectrum of a signal is insensitive to any constant time shift of the signal.



Check:  $\mathbf{r}_n = r_n \hat{\mathbf{r}}_n$ ,  $\mathbf{c}_n$  and  $\mathbf{z}_E$  must form a right handed set of basis vectors so  $\hat{\mathbf{r}}_n \times \mathbf{c}_n = \mathbf{z}_E$

$$\hat{\mathbf{r}}_n \times \mathbf{c}_n = (\mathbf{y}_E \cos \Omega_n + \mathbf{x}_E \sin \Omega_n) \times (\mathbf{y}_E \sin \Omega_n - \mathbf{x}_E \cos \Omega_n) \quad (\text{E.31})$$

$$= (\mathbf{x}_E \times \mathbf{y}_E) \sin \Omega_n \sin \Omega_n - (\mathbf{y}_E \times \mathbf{x}_E) \cos \Omega_n \cos \Omega_n \quad (\text{E.32})$$

$$= (\sin^2 \Omega_n + \cos^2 \Omega_n) \mathbf{z}_E = \mathbf{z}_E \quad (\text{E.33})$$

Therefore:

$$\frac{\mathbf{a}_n}{a} = \mathbf{z}_E \cos \phi_P + (\mathbf{y}_E \sin \Omega_n - \mathbf{x}_E \cos \Omega_n) \sin \phi_P \quad (\text{E.34})$$

Hence the projected area is given by:

$$\zeta_n = -\frac{a}{R} (\mathbf{z}_E \cos \phi_P + (\mathbf{y}_E \sin \Omega_n - \mathbf{x}_E \cos \Omega_n) \sin \phi_P) \cdot \mathbf{R} \quad (\text{E.35})$$

Using the special case of

$$\mathbf{R} = -R (\mathbf{z}_E \sin \theta + \mathbf{x}_E \cos \theta) \quad (\text{E.36})$$

This gives

$$\zeta_n = -a (\mathbf{z}_E \cos \phi_P + (\mathbf{y}_E \sin \Omega_n - \mathbf{x}_E \cos \Omega_n) \sin \phi_P) \cdot (\mathbf{z}_E \sin \theta + \mathbf{x}_E \cos \theta) \quad (\text{E.37})$$

$$= a (\cos \phi_P \sin \theta - \cos \Omega_n \sin \phi_P \cos \theta) \quad (\text{E.38})$$

Using trigonometric identities  $2 \sin A \cos B = \sin(A + B) + \sin(A - B)$ ,  $\cos(-A) = \cos A$  and  $\sin(-A) = -\sin A$  ;

$$\frac{\zeta_n}{a} = \frac{1}{2} [\sin(\theta + \phi_P) + \sin(\theta - \phi_P)] - \frac{1}{2} [\sin(\theta + \phi_P) + \sin(\theta - \phi_P)] \cos \Omega_n \quad (\text{E.39})$$

$$= \frac{1}{2} [\sin(\theta + \phi_P) + \sin(\theta - \phi_P)] (1 - \cos \Omega_n) \quad (\text{E.40})$$

This result is very similar to the result stated in [68] which involves the factors  $\alpha$  and  $\beta$

$$\alpha = \sin(|\theta| + \phi_P) + \sin(|\theta| - \phi_P) \quad (\text{E.41})$$

$$\beta = \text{sign}(\theta) \sin(|\theta| + \phi_P) - \sin(|\theta| - \phi_P) \quad (\text{E.42})$$

This perhaps indicates [68] had a slightly different interpretation of the angle  $\theta$  to that specified here. However, since the adopted definition results in the same  $\cos \theta \sin \Omega_n$  variation of the sinc and harmonic terms as [68] and, unlike [68], refers to a properly defined geometry (in the basis  $\mathbf{x}_E, \mathbf{y}_E, \mathbf{z}_E$ ), we might use E.39 as a sound working hypothesis. To resolve any differences between E.39 and E.41, both 'blade pitch correction factors' should be tested against experimental data.

Incorporating the amplitude modulation due to blade pitch, the signal received resulting from JEM becomes:

$$\psi(R, t) \approx \frac{\psi_0 (L_2 - L_1)}{R^2} e^{2\pi i f_{Tx} t - \frac{4\pi i R}{\lambda}} \sum_{n=0}^{N-1} \zeta_n e^{\frac{1}{2} i (L_1 + L_2) \xi_n} \text{sinc}\left(\frac{1}{2} (L_2 - L_1) \xi_n\right) \quad (\text{E.43})$$

$$\zeta_n = -\frac{a}{R} (\mathbf{z}_E \cos \phi_P + (\mathbf{y}_E \sin \Omega_n - \mathbf{x}_E \cos \Omega_n) \sin \phi_P) \cdot \mathbf{R} \quad (\text{E.44})$$

$$\xi_n = -\frac{4\pi}{R\lambda} (\mathbf{y}_E \cos \Omega_n + \mathbf{x}_E \sin \Omega_n) \cdot \mathbf{R} \quad (\text{E.45})$$

$$\Omega_n = 2\pi \left( f_{rot} t + \frac{n}{N} \right) \quad (\text{E.46})$$



With the special case of  $\mathbf{R} = -R(\mathbf{z}_E \sin \theta + \mathbf{x}_E \cos \theta)$

$$\zeta_n = \frac{a}{2} [\sin(\theta + \phi_P) + \sin(\theta - \phi_P)] (1 - \cos \Omega_n) \quad (\text{E.47})$$

$$\xi_n = \frac{4\pi}{\lambda} \sin \Omega_n \cos \theta \quad (\text{E.48})$$

Since we would expect a target to be at fairly long range (i.e. 10 -100 km), and thus imply a small and fairly constant elevation, the ‘special case’ above may well be widely applicable. Hence the employment of this restricted theory in the Martin & Mulgrew model is justified.

The precise Martin & Mulgrew result presented in [68] is, using the same symbology as above

$$\begin{aligned} \psi_{M\&M}(R, t) \propto & e^{2\pi i f_{Tx} t - \frac{4\pi i R}{\lambda}} \sum_{n=0}^{N-1} \left( \alpha + \beta \cos \left\{ 2\pi \left( f_{rot} t + \frac{n}{N} \right) \right\} \right) \times \\ & \text{sinc} \left( \frac{4\pi}{\lambda} \frac{1}{2} (L_2 - L_1) \cos \theta \sin \left\{ 2\pi \left( f_{rot} t + \frac{n}{N} \right) \right\} \right) \times \\ & \exp \left( i \frac{4\pi}{\lambda} \frac{1}{2} (L_1 + L_2) \cos \theta \sin \left\{ 2\pi \left( f_{rot} t + \frac{n}{N} \right) \right\} \right) \end{aligned}$$

which could be written as (to enable visual comparison to the result derived above)

$$\psi_{M\&M}(R, t) \propto e^{2\pi i f_{Tx} t - \frac{4\pi i R}{\lambda}} \sum_{n=0}^{N-1} \zeta_n e^{\frac{1}{2} i (L_1 + L_2) \xi_n} \text{sinc} \left( \frac{1}{2} (L_2 - L_1) \xi_n \right) \quad (\text{E.49})$$

$$\zeta_n = \alpha + \beta \cos \Omega_n \quad (\text{E.50})$$

$$\xi_n = \frac{4\pi}{\lambda} \sin \Omega_n \cos \theta \quad (\text{E.51})$$

$$\Omega_n = 2\pi \left( f_{rot} t + \frac{n}{N} \right) \quad (\text{E.52})$$

$$\alpha = \sin(|\theta| + \phi_P) + \sin(|\theta| - \phi_P) \quad (\text{E.53})$$

$$\beta = \text{sign}(\theta) \sin(|\theta| + \phi_P) - \sin(|\theta| - \phi_P) \quad (\text{E.54})$$

## Appendix F

# The benefits and limitations of stretch processing

### F.1 Overview

An alternative to stepped frequency methods is the use of stretch processing. Rather than sampling the (mixed down) signal directly, the mixer itself is modified to be a replica of what was transmitted. The differential time delay (and thus range) between scatterers relative to some central reference point on the body of a target turns out to be proportional to a frequency modulation of the ‘stretch’ mixer output, if a linear frequency modulated waveform is used. If samples of this are taken and then processed using a Discrete Fourier Transform, the result will be a HRR profile of the target.

### F.2 The stretch mixer

A linear chirp signal  $\psi(t)$  is described by the following system of equations (see Appendix C for derivation).

$$\begin{aligned}\psi_{\text{real}}(t) &= A \operatorname{Re} \{ \psi(t) \} \\ \psi(t) &= \begin{cases} e^{i\phi(t)} & t_0 < t < t_0 + \tau \\ 0 & t < t_0, \quad t > t_0 + \tau \end{cases} \\ \phi(t) &= \alpha t^2 + \beta t + \gamma \\ \alpha &= \frac{\pi B}{\tau} \\ \beta &= -2\pi \left( \frac{B t_0}{\tau} + \frac{1}{2} B - f_{Tx} \right) \\ \gamma &= -2\pi \left[ \frac{1}{2} \frac{B}{\tau} \left( t_0 + \frac{1}{2} \tau \right)^2 - \left( \frac{B t_0}{\tau} + \frac{1}{2} B - f_{Tx} \right) \left( t_0 + \frac{1}{2} \tau \right) \right]\end{aligned}$$

$B$  is the chirp bandwidth,  $\tau$  is the pulse length,  $f_{Tx}$  is the carrier frequency and  $t_0$  is the time of the leading edge of the chirp. For a transmitted chirp  $\psi_{Tx}$ ,  $t_0 = 0$  and for a received chirp  $\psi_{Rx}$ ,  $t_0 = 2R/c$  where  $R$  is the target range. Let us define the stretch mixer to have the time variation  $M(t, R_0)$  where the output is  $y(t) = \psi_{Rx}(t)M(t, R_0)$ .  $R_0$  is the ‘central reference point’ and corresponds to

some position upon the main body of the target. This practically would be the target range provided by surveillance. Using the general form above

$$\begin{aligned}
 \psi_{Rx}(t) &= \begin{cases} e^{i\phi(t)} & t_0 < t < t_0 + \tau \\ 0 & t < t_0, \quad t > t_0 + \tau \end{cases} \\
 \phi(t) &= \alpha t^2 + \beta t + \gamma \\
 \alpha &= \frac{\pi B}{\tau} \\
 \beta &= -2\pi \left( \frac{Bt_0}{\tau} + \frac{1}{2}B - f_{Tx} \right) \\
 \gamma &= -2\pi \left[ \frac{1}{2} \frac{B}{\tau} \left( t_0 + \frac{1}{2}\tau \right)^2 - \left( \frac{Bt_0}{\tau} + \frac{1}{2}B - f_{Tx} \right) \left( t_0 + \frac{1}{2}\tau \right) \right] \\
 t_0 &= 2R/c
 \end{aligned} \tag{F.1}$$

$$\begin{aligned}
 M(t, R_0) &= e^{-i\phi(t)} \\
 \phi(t) &= \alpha t^2 + \beta t + \gamma \\
 \alpha &= \frac{\pi B}{\tau} \\
 \beta &= -2\pi \left( \frac{Bt_0}{\tau} + \frac{1}{2}B - f_{Tx} \right) \\
 \gamma &= -2\pi \left[ \frac{1}{2} \frac{B}{\tau} \left( t_0 + \frac{1}{2}\tau \right)^2 - \left( \frac{Bt_0}{\tau} + \frac{1}{2}B - f_{Tx} \right) \left( t_0 + \frac{1}{2}\tau \right) \right] \\
 t_0 &= 2R_0/c
 \end{aligned} \tag{F.2}$$

The stretch mixer output is therefore (note the quadratic time variation cancels)

$$y(t) = \psi_{Rx}(t)M(t, R_0) \tag{F.3}$$

$$= e^{i\xi} \exp \left\{ i \left[ -2\pi \left( \frac{2BR}{c\tau} + \frac{1}{2}B - f_{Tx} \right) + 2\pi \left( \frac{2BR_0}{c\tau} + \frac{1}{2}B - f_{Tx} \right) \right] t \right\} \tag{F.4}$$

$$= w(t)e^{i\xi}e^{\frac{4\pi i B(R_0 - R)}{c\tau}t} \tag{F.5}$$

where

$$\xi(R, R_0) = -2\pi \left[ \frac{1}{2} \frac{B}{\tau} \left( 2R/c + \frac{1}{2}\tau \right)^2 - \left( \frac{2BR}{c\tau} + \frac{1}{2}B - f_{Tx} \right) \left( 2R/c + \frac{1}{2}\tau \right) \right] \tag{F.6}$$

$$+ 2\pi \left[ \frac{1}{2} \frac{B}{\tau} \left( 2R_0/c + \frac{1}{2}\tau \right)^2 - \left( \frac{2BR_0}{c\tau} + \frac{1}{2}B - f_{Tx} \right) \left( 2R_0/c + \frac{1}{2}\tau \right) \right] \tag{F.7}$$

and

$$w(t) = \begin{cases} 1 & 2R/c < t < 2R/c + \tau \\ 0 & t < 2R/c, \quad t > 2R/c + \tau \end{cases} \tag{F.8}$$

The output of the stretch mixer has a linear phase variation with time, i.e. a fixed ‘beat’ frequency proportional to the differential target range  $R_0 - R$ . This means the magnitude of the Fourier Transform<sup>1</sup> the mixer output will yield a peak at  $R_0 - R$ .

<sup>1</sup>For simplicity of illustration let us take the analytical Fourier Transform and assume the sample rate of the (discrete) practical implementation is a good approximation. i.e. the sample rate is high enough to not produce aliases.

If a target can be thought of being comprised of a set of point scatterers, the received signal is actually a (weighted) sum of received chirps, each with a different range  $R_n$ . The output of the stretch mixer is thus

$$y(t) = \sum_n a_n w_n(t) e^{i\xi(R_n, R_0)} e^{\frac{4\pi i B(R_0 - R_n)}{c\tau} t} \quad (\text{F.9})$$

where the windowing function  $w_n(t)$  is

$$w_n(t) = \begin{cases} 1 & 2R_n/c < t < 2R_n/c + \tau \\ 0 & t < 2R_n/c, \quad t > 2R_n/c + \tau \end{cases} \quad (\text{F.10})$$

The Fourier Transform of  $y(t)$  will thus yield a range profile of the target with (magnitude) peaks at  $R_0 - R_n$ .

$$\tilde{y}(f) = \int_{-\infty}^{\infty} \left( \sum_n a_n w_n(t) e^{i\xi(R_n, R_0)} e^{\frac{4\pi i B(R_0 - R_n)}{c\tau} t} \right) e^{-2\pi i f t} dt \quad (\text{F.11})$$

$$= \sum_n a_n e^{i\xi(R_n, R_0)} \int_{2R_n/c}^{2R_n/c + \tau} e^{\frac{4\pi i B(R_0 - R_n)}{c\tau} t - 2\pi i f t} dt \quad (\text{F.12})$$

$$= \sum_n a_n \frac{e^{i\xi(R_n, R_0)}}{2\pi i \left( \frac{2B(R_0 - R_n)}{c\tau} - f \right)} \left[ e^{2\pi i t \left( \frac{2B(R_0 - R_n)}{c\tau} - f \right)} \right]_{2R_n/c}^{2R_n/c + \tau} \quad (\text{F.13})$$

$$= \sum_n a_n \frac{e^{i\xi(R_n, R_0) + i\pi(4R_n/c + \tau) \left( \frac{2B(R_0 - R_n)}{c\tau} - f \right)}}{\pi \left( \frac{2B(R_0 - R_n)}{c\tau} - f \right)} \sin \left( \frac{\tau}{2} \left( \frac{2B(R_0 - R_n)}{c\tau} - f \right) \right) \quad (\text{F.14})$$

where the last step makes use of the identity

$$e^{ia} - e^{ib} \equiv e^{\frac{i}{2}(a+b)} \left( e^{\frac{i}{2}(a-b)} - e^{-\frac{i}{2}(a-b)} \right) \equiv 2ie^{i\frac{a+b}{2}} \sin \left( \frac{1}{2}(a-b) \right) \quad (\text{F.15})$$

One can easily show the range resolution of such a profile (using the assignment of range  $R = \frac{c\tau}{2B} f$ ) is  $\delta R \approx \frac{c}{2B}$  i.e. the same resolution as if the chirp was pulse compressed in the conventional fashion.

### F.3 Benefits & limitations of stretch processing

The beat frequency (for target scattering center  $n$ ) of the output of the stretch mixer is

$$f_{sm} = \frac{2B(R_0 - R_n)}{c\tau} \quad (\text{F.16})$$

Let us define the HRR range window to be  $R_0 \pm \frac{1}{2}L$ . In order for peaks of the Fourier Transform of the stretch mixer output to appear correctly within this window, by the Shannon-Nyquist criterion the output must be sampled at a rate greater than or equal to the frequency difference between the component beats. Hence:

$$f_s \geq \frac{2B(R_0 + \frac{1}{2}L)}{c\tau} - \frac{2B(R_0 - \frac{1}{2}L)}{c\tau} \quad (\text{F.17})$$

$$\geq \frac{2BL}{c\tau} \quad (\text{F.18})$$

Note also that the stretch mixer must sweep for  $2L/c + \tau$  in order to collect the signal contributions from all scatterers in the HRR window and then compute the Fourier Transform of the mixer output samples. This means the mixer must be physically able to sweep through a bandwidth of

$$B_{sm} = \left(1 + \frac{2L}{c\tau}\right) B \quad (\text{F.19})$$

In summary, stretch processing allows for the production of a HRR target profile without necessarily having to sample at the bandwidth of the transmitted signal, as in conventional pulse compression. It therefore allows for high range resolution to be obtained from a single burst rather than having to wait for the transmission of an ensemble of burst stepped in frequency. To achieve  $\delta R = 1$  m range resolution, the bandwidth  $B = 149.9$  MHz. If a maximum sample rate of 5 MHz is possible, since  $L \leq \frac{c\tau}{2B} f_s$  this means the HRR window must be less than 100 m using a chirp pulse length of  $20 \mu\text{s}$ . Setting  $L = 100$  m gives a mixer sweep of  $B_{sm} = 154.9$  MHz. The outputs of the stretch mixer begin at time since transmission

$$t_{start} = \frac{2 \left(R_0 - \frac{L}{2}\right)}{c} \quad (\text{F.20})$$

and finish at time

$$t_{stop} = \frac{2 \left(R_0 + \frac{L}{2}\right)}{c} + \tau \quad (\text{F.21})$$

The potential limitations of stretch processing are:

1. Require modification to RF hardware to implement mixer. Mixer must be adaptive to changes in  $R_0$  which would vary as the target moves. The mixer must be able to sweep over  $\left(1 + \frac{2L}{c\tau}\right) B$ . The time variable in the mixer must be aligned with precision to that of the Radar clock which starts at the time of transmission, i.e. the mixer is phase locked to the transmitted signal.
2. Given a practical sample rate, to achieve finer range resolution will restrict the size  $L$  of the HRR window.
3. A separate mixer channel must be provided for each target, if separations are greater than  $L$ .
4. Since a stretch waveform is intrinsically wide bandwidth, an S-band phased array will sweep the beam significantly within the pulse. To alleviate this effect (and mitigate resulting losses of energy on target) true time delay corrections must be applied during pulse transmission and reception. This could be an expensive modification to the antenna!

## Appendix G

# Radar Cross Section measurements of aircraft

### G.1 All aircraft Max RCS of Classical HRR profiles

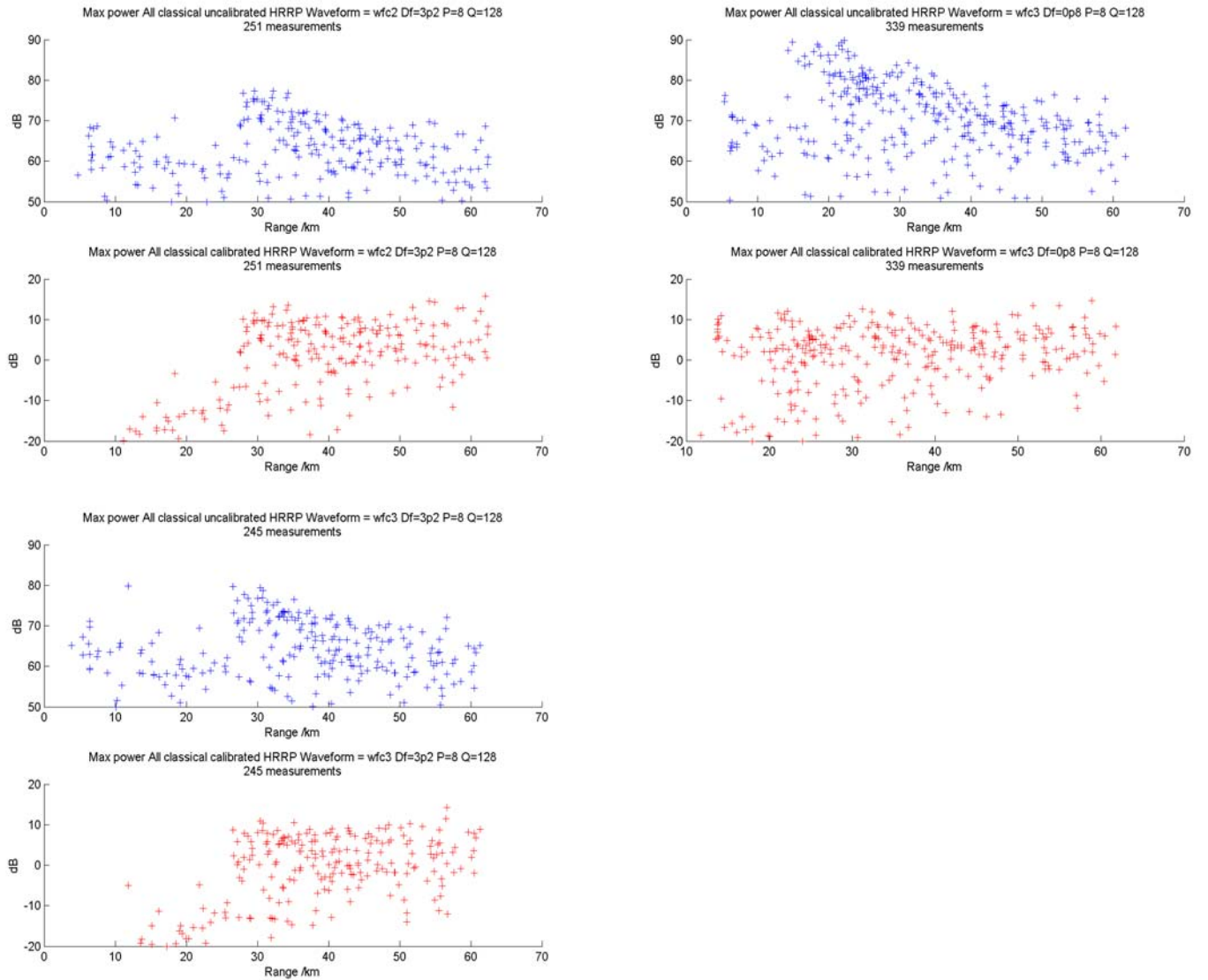


Figure G.1: Maximum Radar Cross Section (RCS) of Classical High Range Resolution profiles, plotted for all aircraft observed by MESAR2 during the pod/Falcon and targets of opportunity trials. The blue upper graphs show the (uncalibrated) maximum power /dB of the HRR profile. The red lower graphs show the same data following application of the Radar Equation. This has the effect of removing the negative trend resulting from the  $R^{-4}$  propagation loss. Each set of blue/red graphs represents a different waveform.

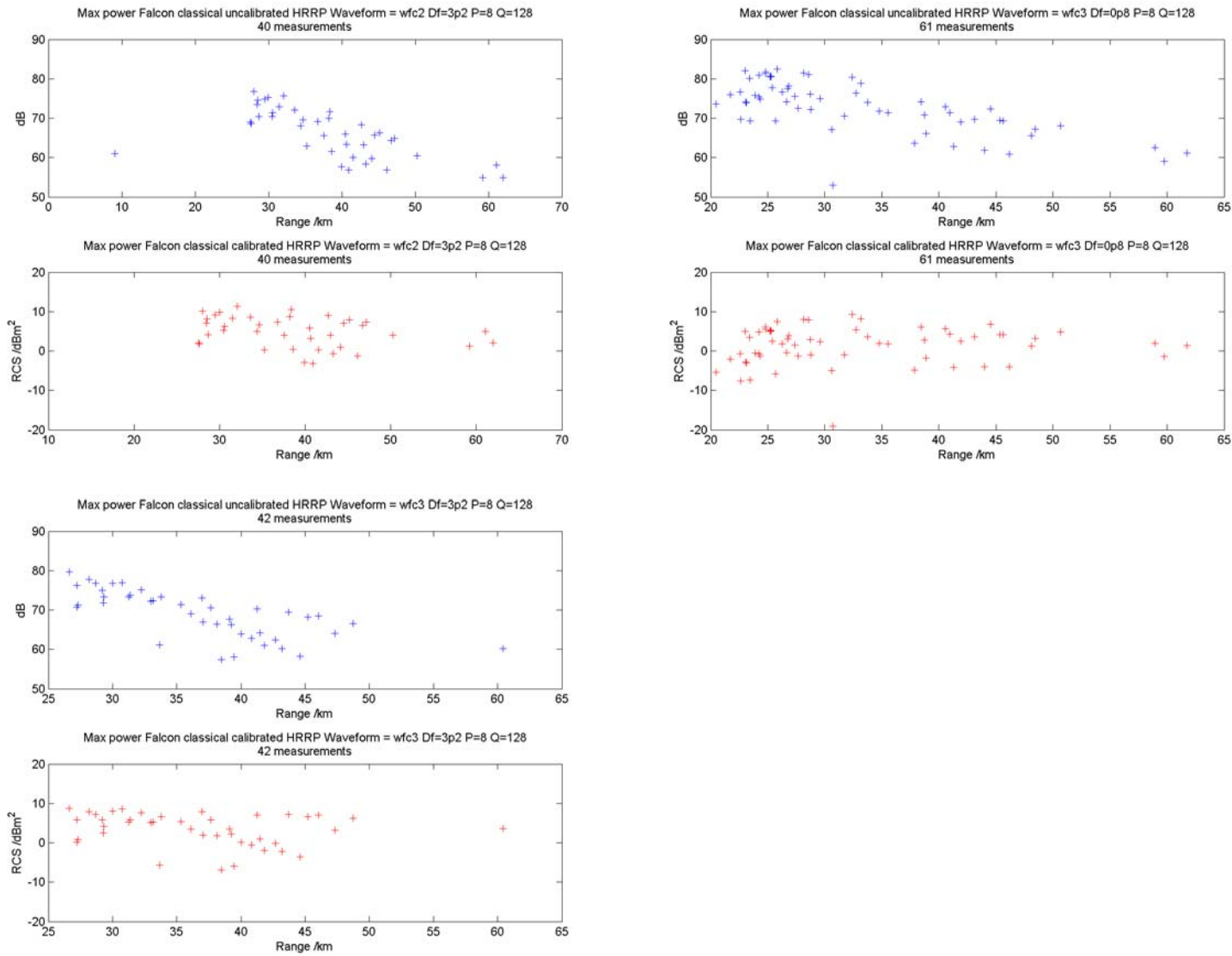


Figure G.2: Maximum Radar Cross Section (RCS) of Classical High Range Resolution profiles, plotted for an inbound Falcon aircraft observed by MESAR2 during trials. The blue upper graphs show the (uncalibrated) maximum power /dB of the HRR profile. The red lower graphs show the same data following application of the Radar Equation. This has the effect of removing the negative trend resulting from the  $R^{-4}$  propagation loss. Each set of blue/red graphs represents a different waveform. Despite the application of the radar equation, the RCS values are variable by the order of 10dBm<sup>2</sup>.



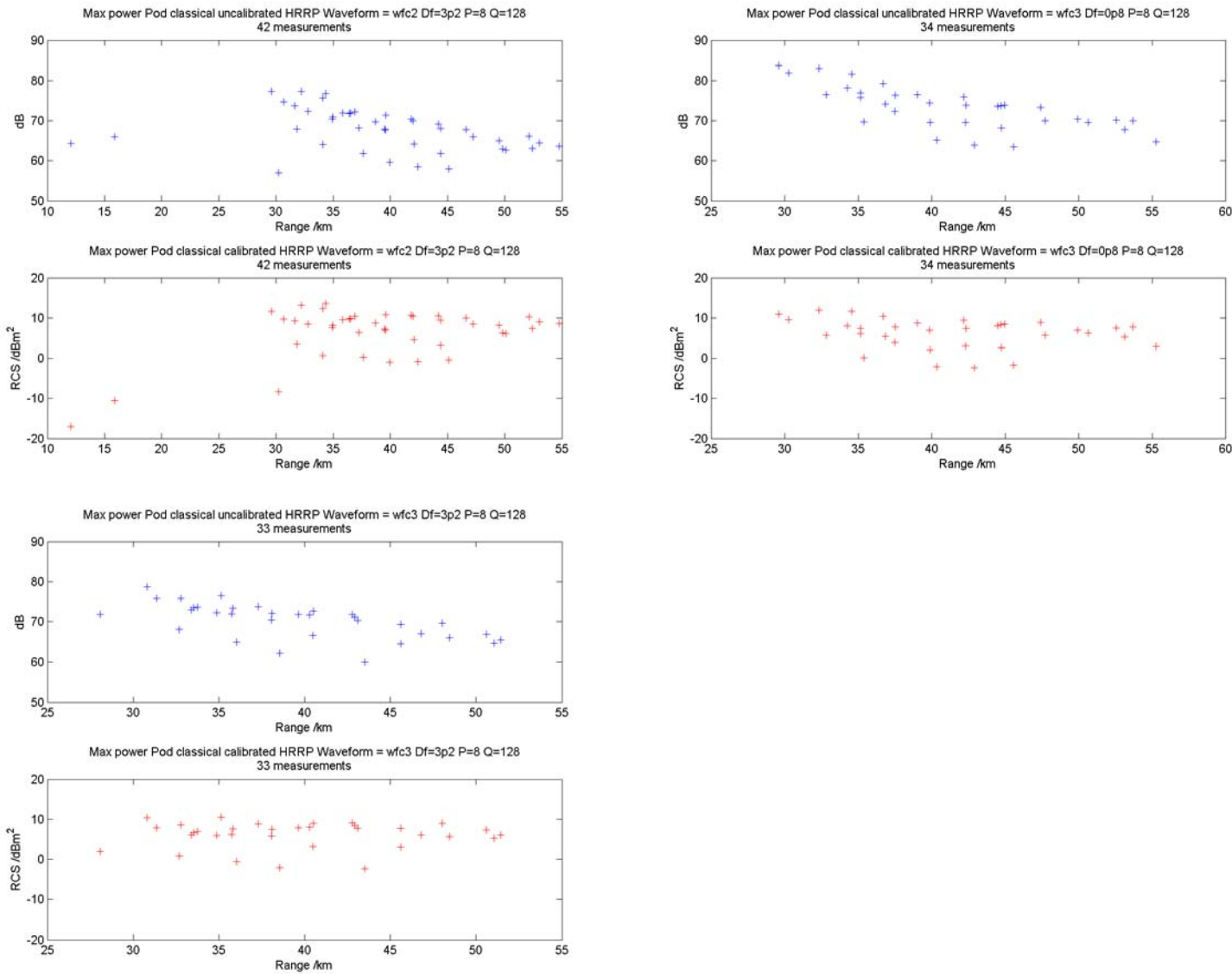


Figure G.3: Maximum Radar Cross Section (RCS) of Hybrid High Range Resolution profiles, plotted for an inbound Pod observed by MESAR2 during trials. The blue upper graphs show the (uncalibrated) maximum power /dB of the HRR profile. The red lower graphs show the same data following application of the Radar Equation. This has the effect of removing the negative trend resulting from the  $R^{-4}$  propagation loss. Each set of blue/red graphs represents a different waveform. Despite the application of the radar equation, the RCS values are variable by the order of 10dBm<sup>2</sup>.

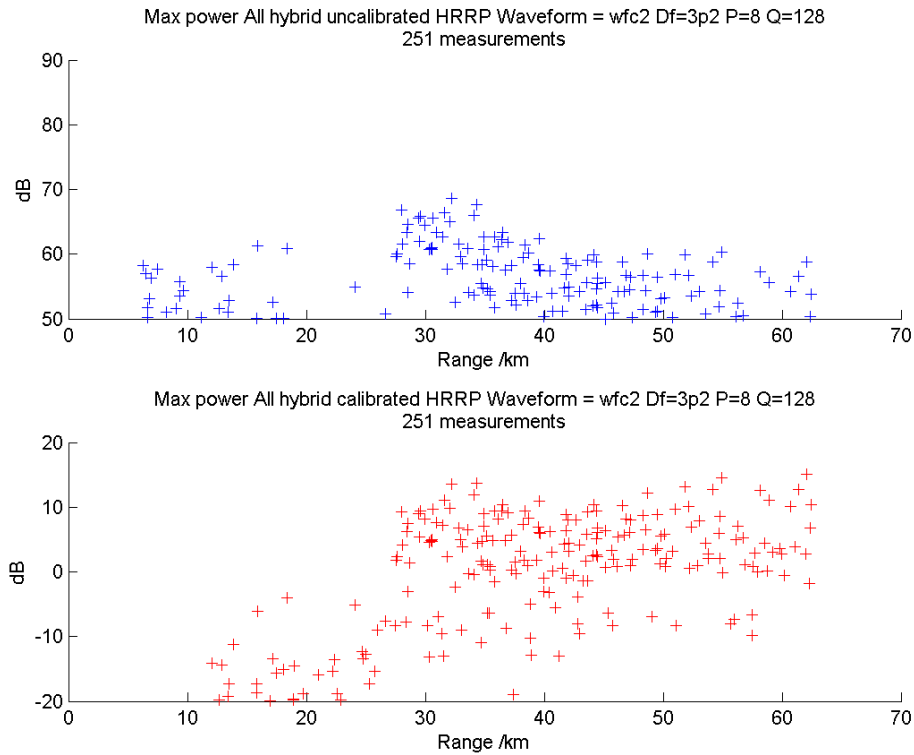


Figure G.4: Maximum Radar Cross Section (RCS) of Hybrid High Range Resolution profiles, plotted for all aircraft observed by MESAR2 during trials. The blue upper graphs show the (uncalibrated) maximum power /dB of the HRR profile. The red lower graphs show the same data following application of the Radar Equation. This has the effect of removing the negative trend resulting from the  $R^{-4}$  propagation loss. Each set of blue/red graphs represents a different waveform. Despite the application of the radar equation, the RCS values are variable by the order of  $10\text{dBm}^2$ .

## G.2 All aircraft Max RCS of Hybrid HRR profiles

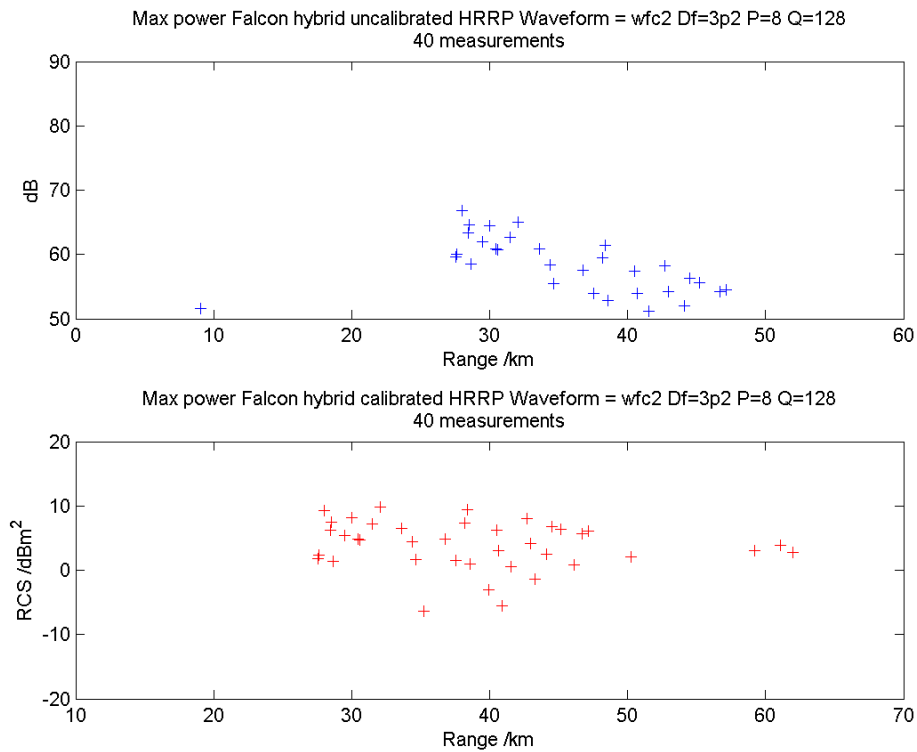


Figure G.5: Maximum Radar Cross Section (RCS) of Hybrid High Range Resolution profiles, plotted for an inbound Falcon aircraft observed by MESAR2 during trials. The blue upper graphs show the (uncalibrated) maximum power /dB of the HRR profile. The red lower graphs show the same data following application of the Radar Equation. This has the effect of removing the negative trend resulting from the  $R^{-4}$  propagation loss. Each set of blue/red graphs represents a different waveform. Despite the application of the radar equation, the RCS values are variable by the order of 10dBm<sup>2</sup>.

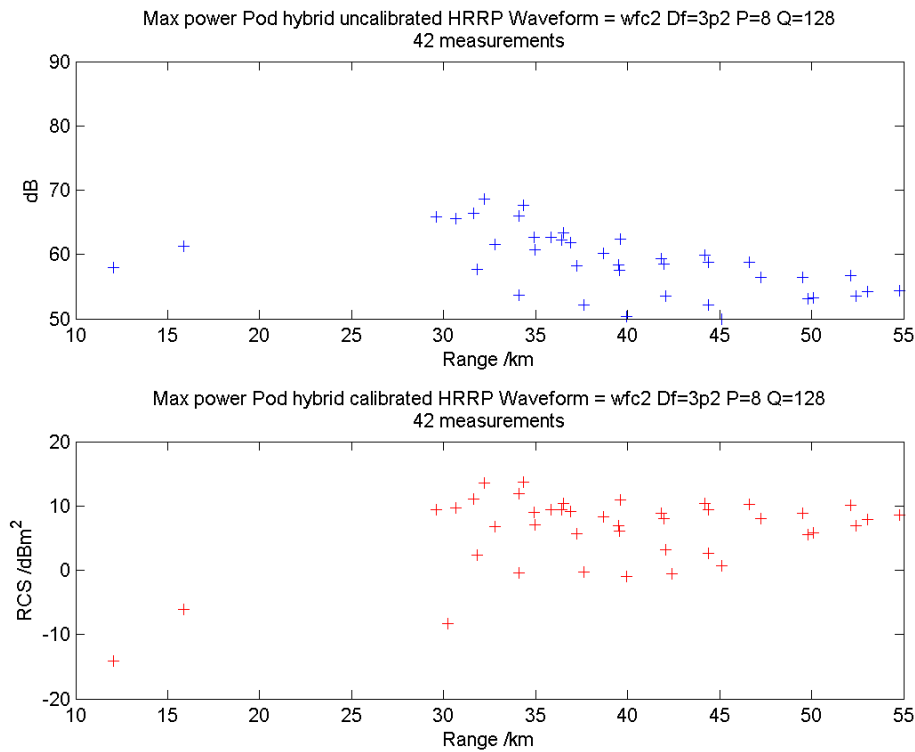


Figure G.6: Maximum Radar Cross Section (RCS) of Hybrid High Range Resolution profiles, plotted for an inbound Pod observed by MESAR2 during trials. The blue upper graphs show the (uncalibrated) maximum power /dB of the HRR profile. The red lower graphs show the same data following application of the Radar Equation. This has the effect of removing the negative trend resulting from the  $R^{-4}$  propagation loss. Each set of blue/red graphs represents a different waveform. Despite the application of the radar equation, the RCS values are variable by the order of 10dBm<sup>2</sup>.

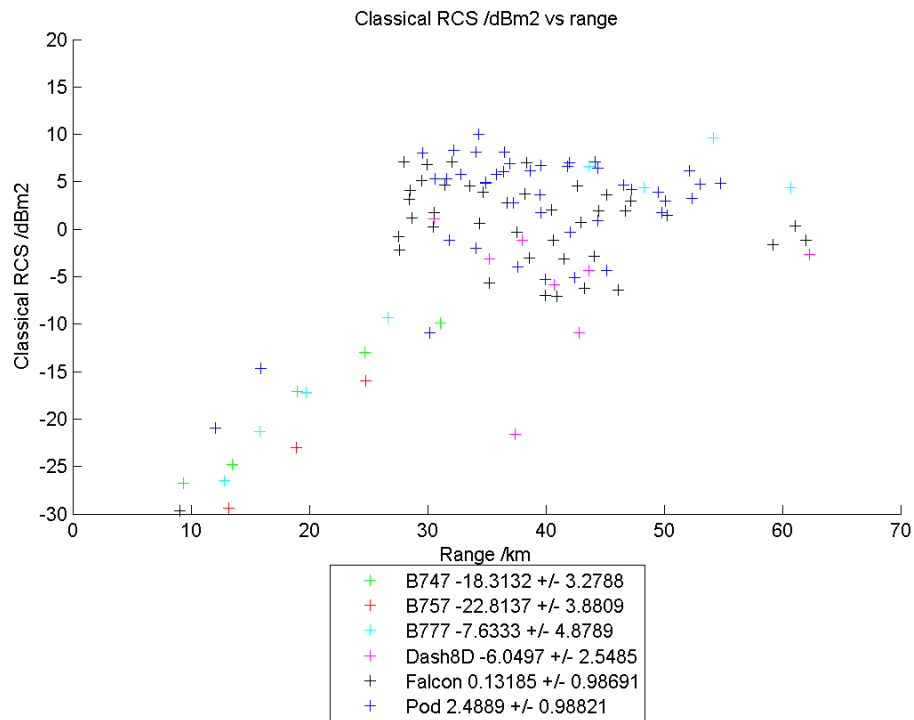


Figure G.7: Maximum (Classical) HRR profile RCS plotted against target range for six aircraft using Waveform A. Plots are colour coded by aircraft type.

### G.3 Six aircraft Max RCS Waveform A Classical

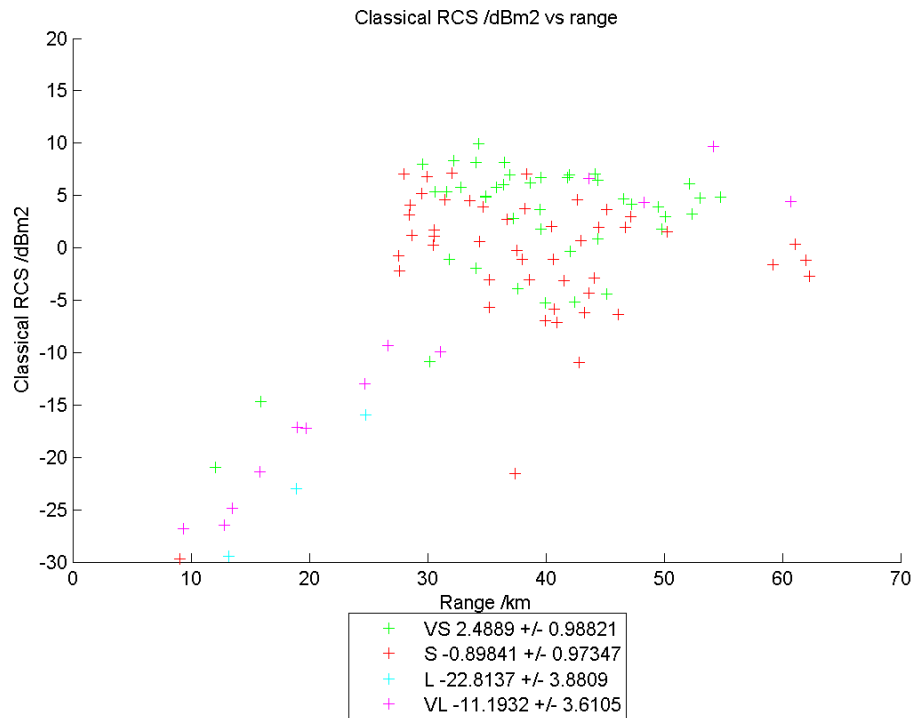


Figure G.8: Maximum (Classical) HRR profile RCS plotted against target range for six aircraft using Waveform A. Plots are colour coded by Four Lengths classes.

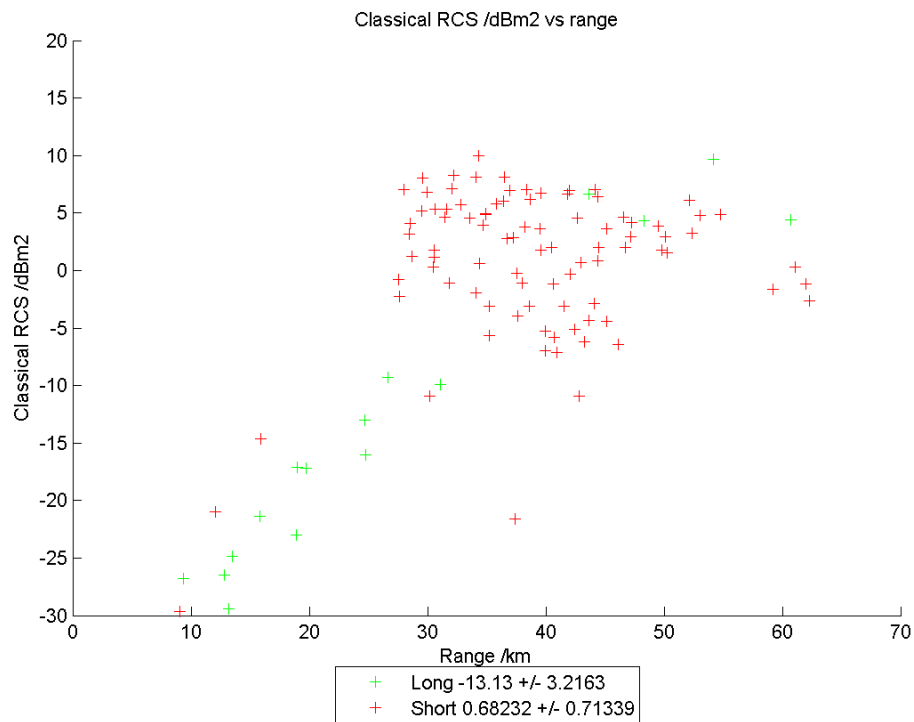


Figure G.9: Maximum (Classical) HRR profile RCS plotted against target range for six aircraft using Waveform A. Plots are colour coded by Long or Short classes.

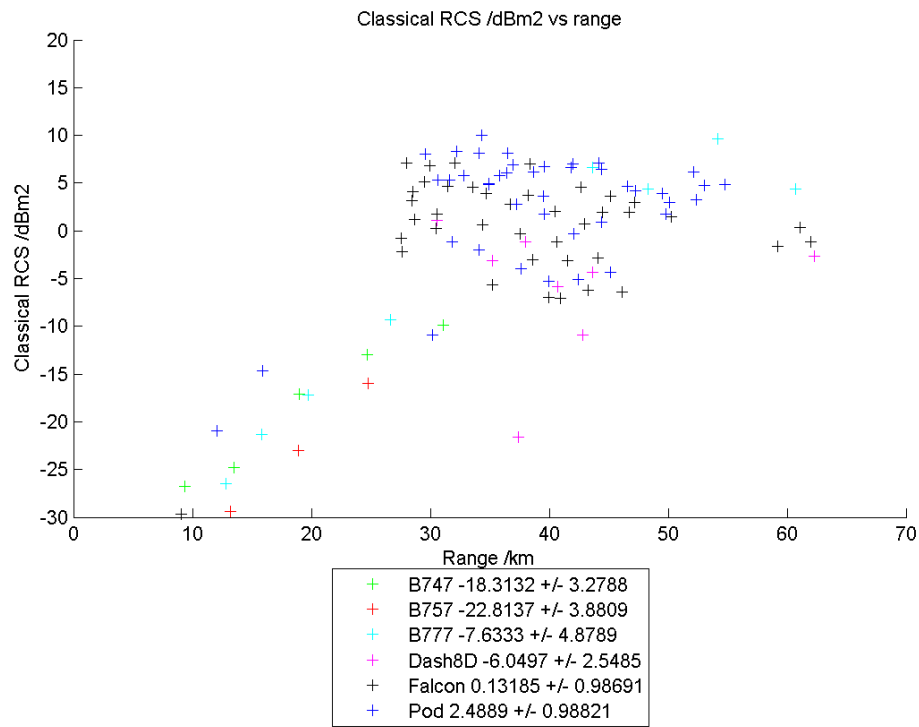


Figure G.10: Maximum (Hybrid) HRR profile RCS plotted against target range for six aircraft using Waveform A. Plots are colour coded by aircraft type.

#### G.4 Six aircraft Max RCS Waveform A Hybrid

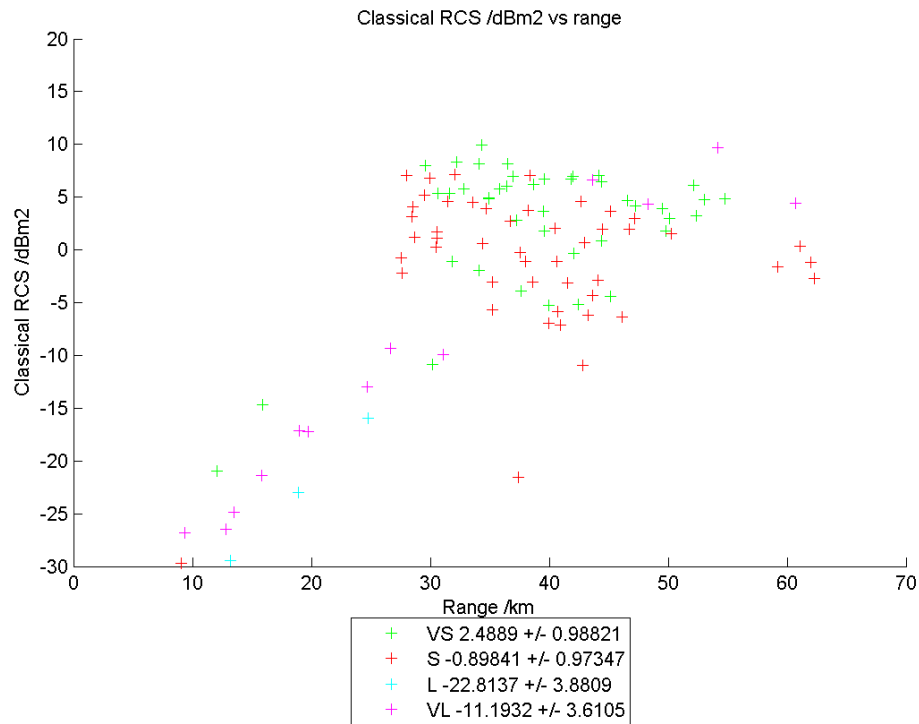


Figure G.11: Maximum (Hybrid) HRR profile RCS plotted against target range for six aircraft using Waveform A. Plots are colour coded by Four Lengths classes.

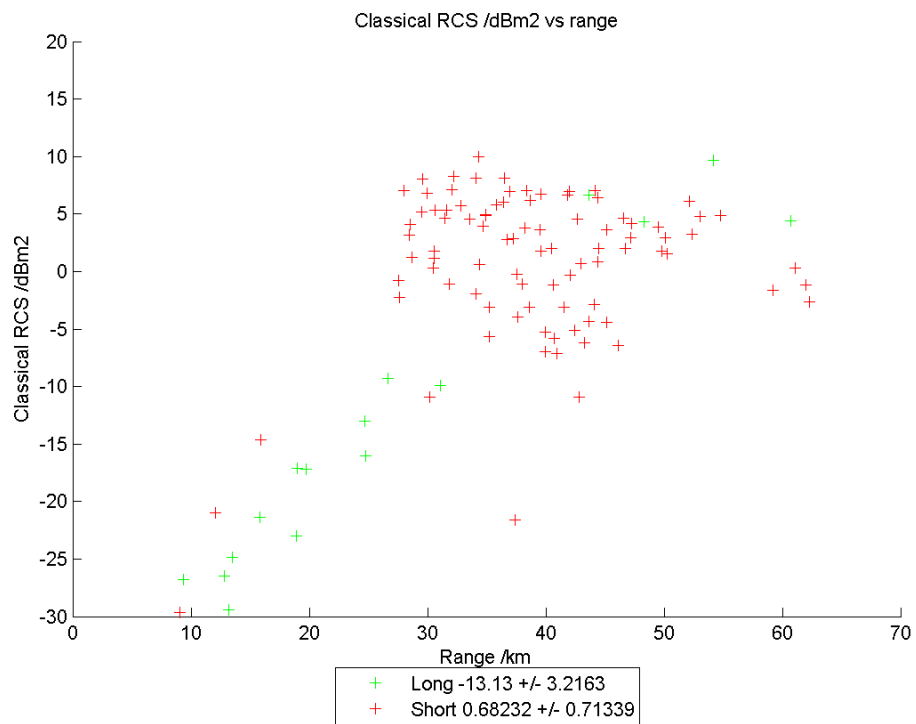


Figure G.12: Maximum (Hybrid) HRR profile RCS plotted against target range for six aircraft using Waveform A. Plots are colour coded by Long or Short classes.



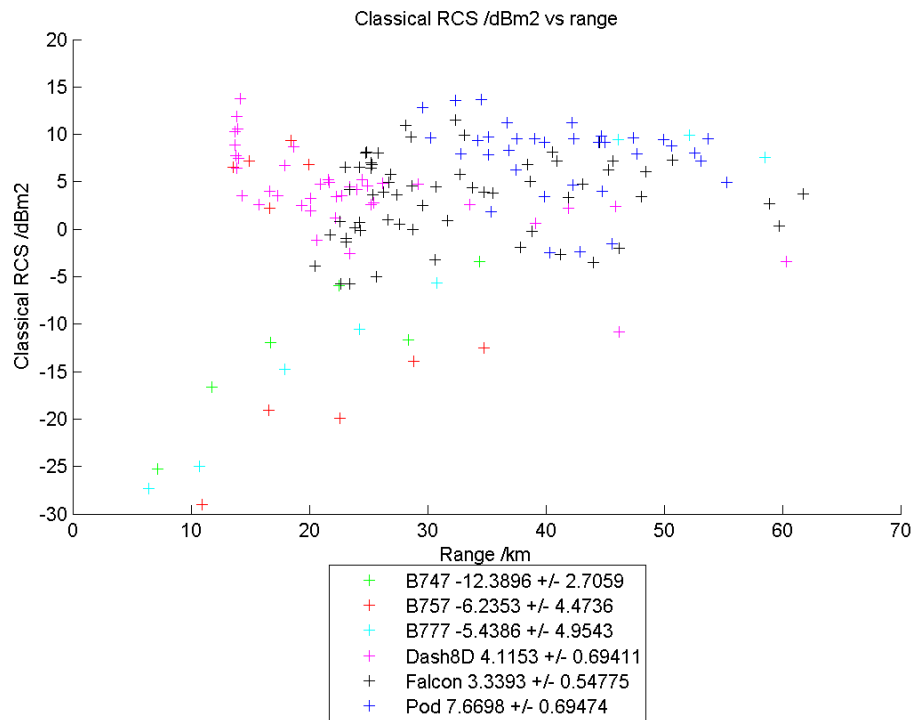


Figure G.13: Maximum (Classical) HRR profile RCS plotted against target range for six aircraft using Waveform B. Plots are colour coded by aircraft type.

## G.5 Six aircraft Max RCS Waveform B Classical

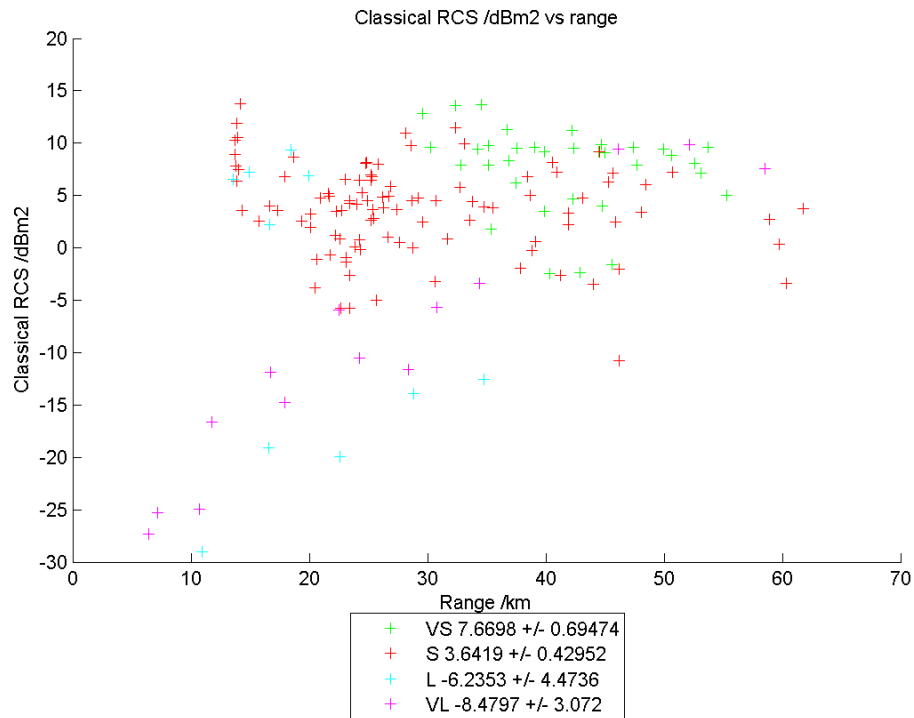


Figure G.14: Maximum (Classical) HRR profile RCS plotted against target range for six aircraft using Waveform B. Plots are colour coded by Four Lengths classes.

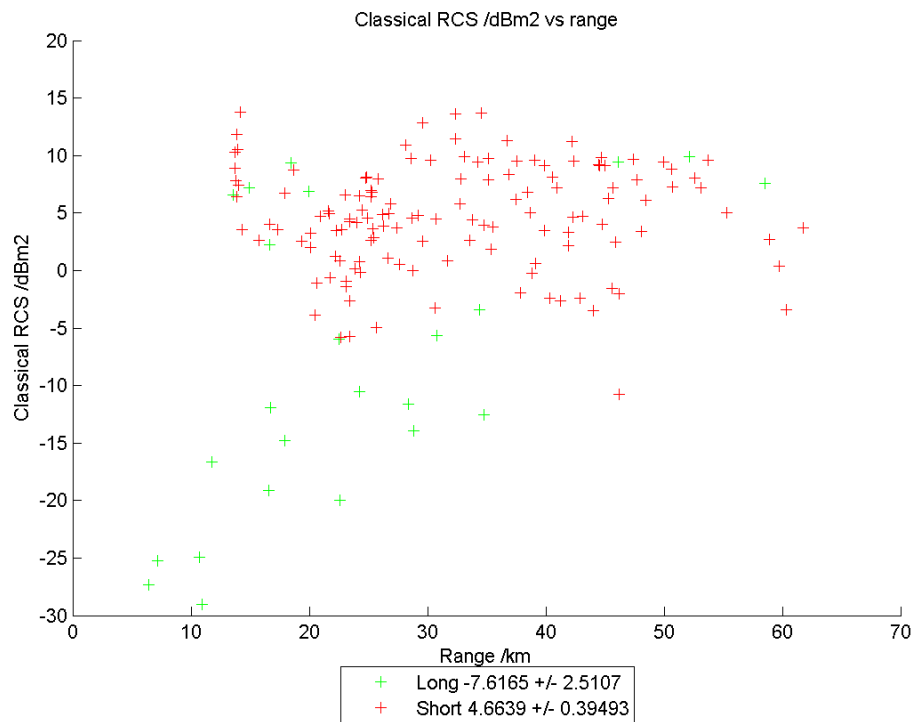


Figure G.15: Maximum (Classical) HRR profile RCS plotted against target range for six aircraft using Waveform B. Plots are colour coded by Long or Short classes.

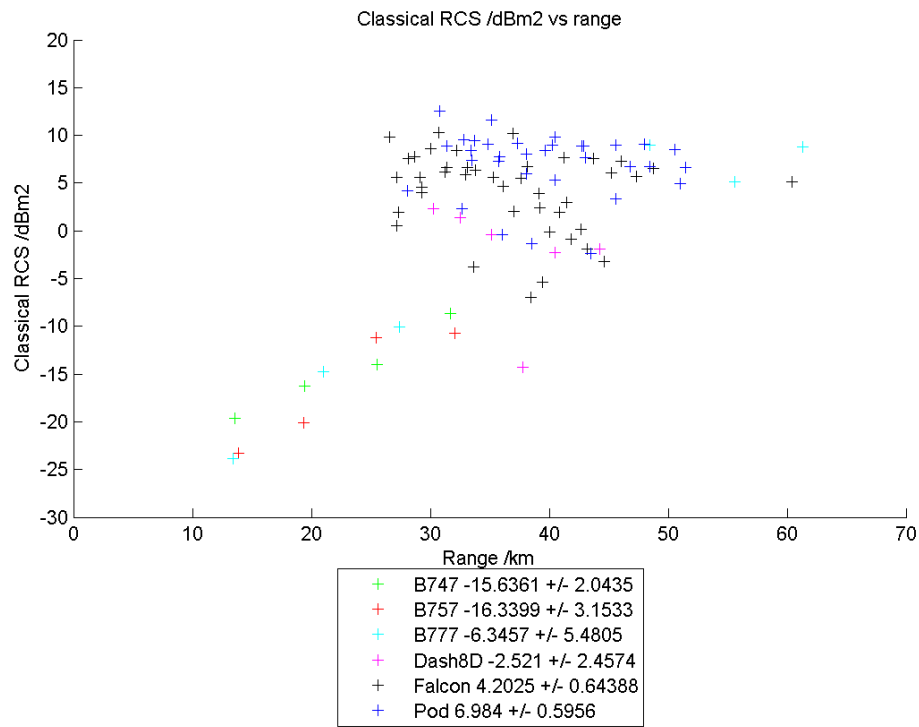


Figure G.16: Maximum (Classical) HRR profile RCS plotted against target range for six aircraft using Waveform C. Plots are colour coded by aircraft type.

## G.6 Six aircraft Max RCS Waveform C Classical

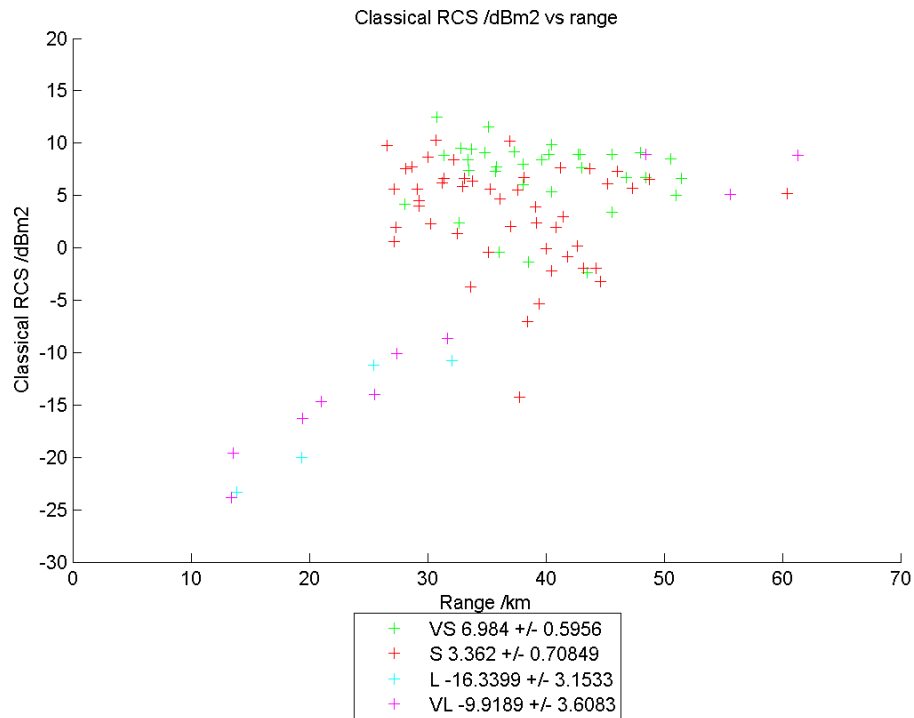


Figure G.17: Maximum (Classical) HRR profile RCS plotted against target range for six aircraft using Waveform C. Plots are colour coded by Four Lengths classes.

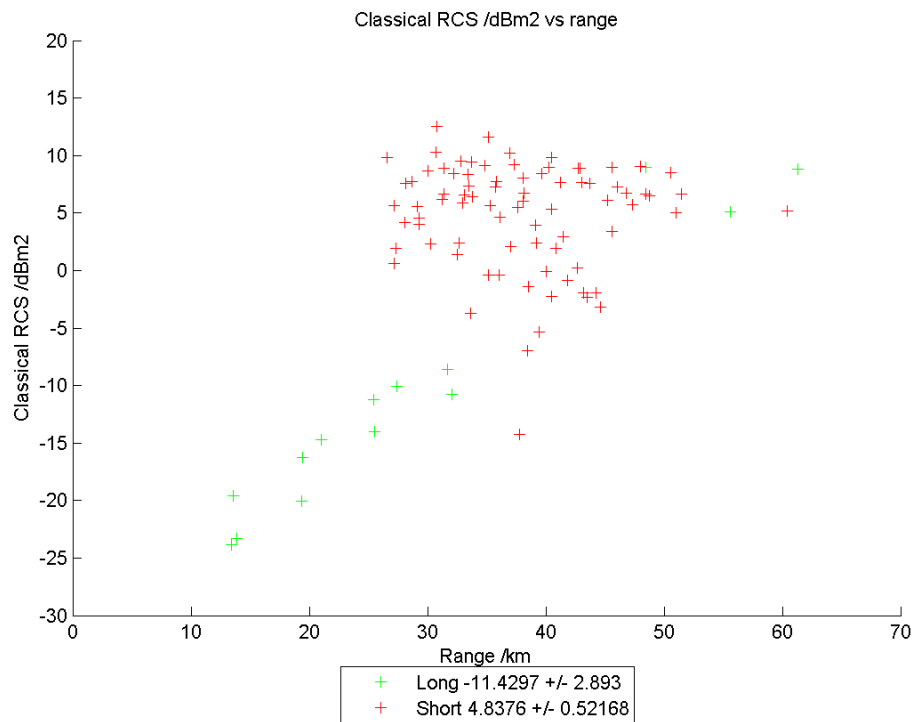


Figure G.18: Maximum (Classical) HRR profile RCS plotted against target range for six aircraft using Waveform C. Plots are colour coded by Long or Short classes.

## Appendix H

# Importing MESAR2 data: DRAS, M2DATS & MEROS import\_data\_gui

Recorded data was stored in the MESAR2 data logger in a proprietary format readable using the Roke Manor software package DRAS and could be extracted (either via dump to tape or via Ethernet connection) as a series of ‘acquisitions.’ These were often very large files (several GB) containing all the receiver samples data, indexed by waveform type, look type (e.g. “NCTR”) and track number. Once transferred to a standard PC, the data could be filtered by the track number assigned to each target. Track numbers were captured electronically during the trials and also by hand. The latter record was useful in overcoming problems of track dropping and seduction which might result in a change of track number for a given aircraft. For each experiment (most complicated in the Targets of Opportunity trial), a list of track numbers was noted against each named object, which was effectively tracked by eye.

For each aircraft (and each inbound run in the case of the Pod & Falcon trial) a set of files were saved, indexed by look number. This was a somewhat manual process, using DRAS as the filtering mechanism to extract the wanted data from the large acquisition file. DRAS files were then converted into human readable form using an in-house BAE Systems software package called ‘M2DATS’ (MESAR2 Data Analysis Toolset)<sup>1</sup>. Sub-array sum beam data was combined for each PRI of receiver samples. The resulting ASCII file comprised of a general header followed a header, receiver samples pairing for each burst of pulses. The header information comprised an extensive set of parameters defining each burst. From this the following attributes could be obtained:

- Carrier frequency
- Waveform type (from which pulse coding, pulse length, pulse bandwidth, frequency step, number of pulses and number of frequency stepped bursts are known)
- Start range of receiver samples
- Number of guard pulses
- Pulse Repetition Frequency (PRF)
- Timestamp of look
- U,V coordinates used to calculate target azimuth and elevation.

---

<sup>1</sup>Written by Graham Biggs.

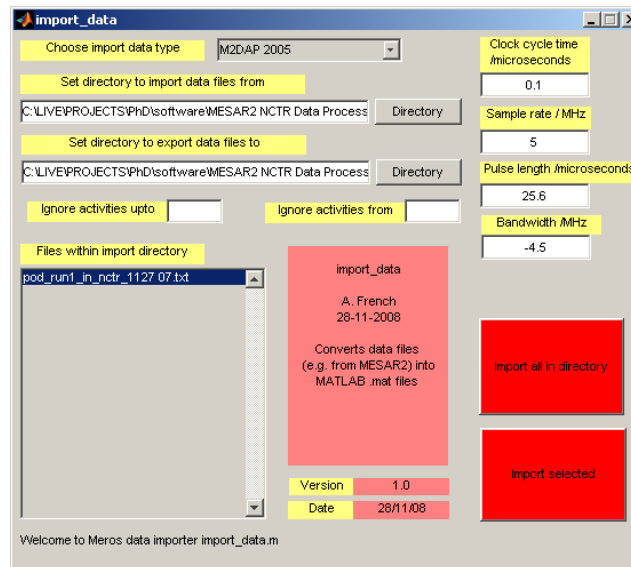


Figure H.1: Graphical user interface (GUI) to the MATLAB software `import_data_gui.m` written by the author to import ASCII files written out by M2DATS into structured arrays accessible within the MATLAB environment.

The ASCII files were then automatically sorted by waveform type using a MATLAB function `sort_wav.m`<sup>2</sup> and placed in a directory structure of hierarchy `<target name> \ <waveform type> \ <filename with look number>`. This was a useful innovation upon previous analysis as the exact cycle (and certainly the start type) of waveforms issued as NCTR looks was variable, as one might expect from the adaptive scheduling character of MESAR2. The ASCII data files were then imported into the MATLAB environment using the `import_data_gui.m` software (see figure H.1) created as part of the ‘Meros’ suite of applications. In the MATLAB environment, imported data is stored in a structured array `imported_data` with field names which easily identify the receiver samples and header entries. Each data type is converted into the most appropriate form for further use. For example, the receiver samples are stored in a three dimensional array with rows corresponding to pulses within each burst, columns corresponding to frequency steps and pages corresponding to samples within each receiver opening window. Hence each row and column index points to a unique vector of receiver samples, stored as complex numbers  $I + iQ$ .

<sup>2</sup>Written by the author & Mark Scott (2006)

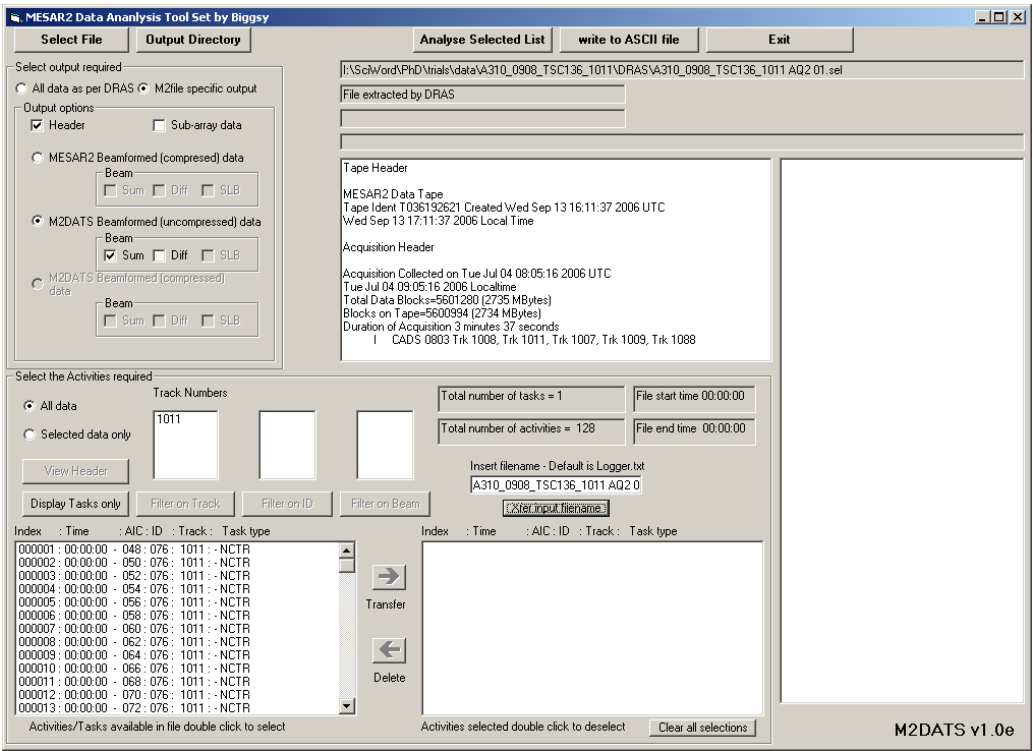


Figure H.2: MESAR2 Data Analysis Tool Set (M2DATS) written by Graham Biggs of BAE Systems to help extract easily importable (ASCII) data files from (binary) coded data read and written by the Roke Manor MESAR2 analysis software DRAS.

# Appendix I

## k-means classification

The *k-means fuzzy classifier* is a popular *non-parametric method* which is based upon the iterative Generalized Lloyd algorithm (Karayiannis 1995). The version described here is an application of the methods of Bezdeck, Ehrlich & Full cited in Bowden [14] and Wong [113] and clearly described (in the context of other clustering and classification techniques) in the textbooks by Webb [110] and Duda [27]. Unlike Bayesian methods, the k-means technique does not depend upon knowledge of the underlying likelihood probability distributions of the feature measurements.

### I.1 Clustering the training data

The inputs to the k-means classifier are  $i = 1...N$  sets of  $K$  hyperspheres of radii  $\{R_k^{(i)}\}$  and origin vectors  $\{\mathbf{c}_k^{(i)}\}$ . These are created from training data via the k-means clustering method:

1. Collect a training data set of  $z = 1...Z_i$  feature column vectors  $\{\mathbf{t}_z^{(i)}\}$  (consisting of  $M$  measurements, which are real numbers) known to derive from class  $w_i$  of a finite alphabet  $\{w_1...w_N\}$  of length  $N$ . Based on the recommendations of Zyweck & Bogdon [118] 40% of a total data set allocated to training might be an appropriate division. Otherwise proceed with a synthesis of training data using random number generators coupled with a probability distribution generating function and ‘expert’ parameters<sup>1</sup>. This of course breaks the assumption of no prior knowledge of the underlying feature statistical distribution.
2. Define a *feature membership* matrix  $\mathbf{U}$  of  $K$  rows and  $Z_i$  columns (such that  $K \ll Z_i$ ) and initialize its elements based on cluster assignment via permutation of  $1 \dots K$ , i.e. if  $K = 2$ , feature vectors  $\{\mathbf{t}_1^{(i)}, \mathbf{t}_2^{(i)}, \mathbf{t}_3^{(i)} \dots\}$  are assigned initial cluster memberships  $\{1, 2, 1, \dots\}$ . This would yield, (for even  $Z_i$ )  $\mathbf{U} = \begin{pmatrix} 1 & 0 & 1 & 0 \\ 0 & 1 & 0 & \dots & 1 \end{pmatrix}$ .
3. Compute a set of  $K$  ( $M$ -dimensional) hyperspheres of with origin vectors  $\{\mathbf{c}_k^{(i)}\}$

$$\begin{aligned} \mathbf{c}_k^{(i)} &= \frac{1}{\eta_k} \sum_{z=1}^{Z_i} U_{kz} \mathbf{t}_z^{(i)} \\ \eta_k &= \sum_{z=1}^{Z_i} U_{kz} \end{aligned} \tag{I.1}$$

---

<sup>1</sup>e.g. the class mean and standard deviation, if the underlying feature distribution was Gaussian.



4. Compute a matrix of *distances*  $\mathbf{D}$  from each of the feature vectors to each of the hypersphere centres. Let  $[\mathbf{D}]_{kz}$  be the Euclidean distance between the  $z^{\text{th}}$  feature vector and the  $k^{\text{th}}$  cluster centre.

$$[\mathbf{D}]_{kz} \equiv D_{kz} = \left| \mathbf{t}_z^{(i)} - \mathbf{c}_k^{(i)} \right| \quad (\text{I.2})$$

5. Compute hypersphere radii which bound the features to their assigned classes

$$R_k^{(i)} = \max [D_{k1}U_{k1} \dots D_{kZ_i}U_{kZ_i}] \quad (\text{I.3})$$

6. Compute cost function  $J$  which is the sum of the squares of distances between all feature vectors and their respective cluster centres.

$$J = \sum_{k=1}^K \sum_{z=1}^{Z_i} (D_{kz}U_{kz})^2 \quad (\text{I.4})$$

7. Update the feature membership matrix based upon the minimum feature to hypersphere centre distance, i.e. if hypersphere  $h$  satisfies  $D_{hz} = \min [D_{1z}, \dots, D_{Kz}]$

$$[\mathbf{U}]_{kz} \equiv U_{kz} \rightarrow \begin{cases} 1 & k = h \\ 0 & k \neq h \end{cases} \quad (\text{I.5})$$

An alternative ‘fuzzy’ update (see [110] pp380) is to allow for a non-binary membership of features with classes.

$$[\mathbf{U}]_{kz} \equiv U_{kz} \rightarrow \frac{1}{\sum_{v=1}^K \left( \frac{D_{kz}}{D_{vz}} \right)^{\frac{2}{F-1}}} \quad (\text{I.6})$$

$F$  is a ‘non linearity’ parameter in the range  $1 < F < \infty$

8. Store membership matrix, cost function, hypersphere centres and radii.  
9. Repeat from step 3.

After  $Q$  iterations (10 might be sufficient<sup>2</sup>) determine the hypersphere centres and radii which correspond to the minimum cost.

## I.2 Classifying features

Classification of a feature vector  $\mathbf{x}$  proceeds via evaluation of scalar discriminant functions  $g_i(\mathbf{x})$  for each class  $w_i$  of a finite alphabet  $\{w_1, \dots, w_N\}$ . The assigned class is that which corresponds to the maximum value of the set of discriminant functions  $\{g_1(\mathbf{x}), \dots, g_N(\mathbf{x})\}$ . The discriminant function  $g_i(\mathbf{x})$  is computed from the clusters formed from the training data set using the following formula:

$$g_i(\mathbf{x}) = \max_k \left\{ \exp \left( - \frac{\left| \mathbf{x} - \mathbf{c}_k^{(i)} \right|^2}{2R_k^{(i)} R_k^{(i)}} \right) \right\} \quad (\text{I.7})$$

---

<sup>2</sup>Alternatively, proceed until fractional change in the smallest two costs  $J$  is less than some set fraction e.g 0.01). If the cost minimum never reaches this stability, set an upper limit to the maximum number of iterations to allow the algorithm to complete in a timely fashion.

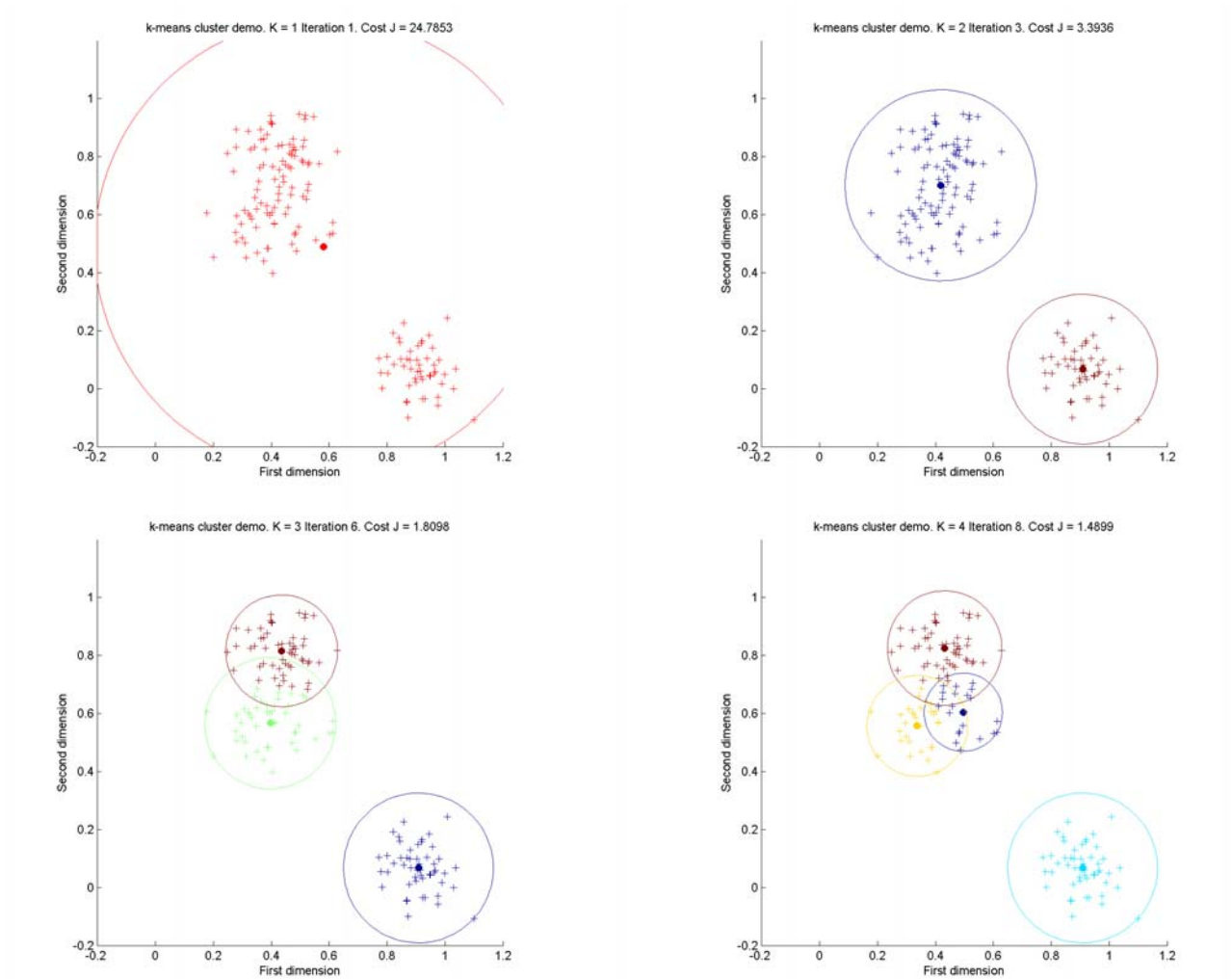


Figure I.1: An example application of the k-means clustering algorithm. Two dimensional feature data are clustered using  $K = 1, 2, 3$  & 4 clusters. The examples shown are for the minimum cost  $J$  after 10 iterations. From a visual perspective it is clear that the data separates into two classes. However,  $K > 2$  actually offers a marginal reduction in cost.

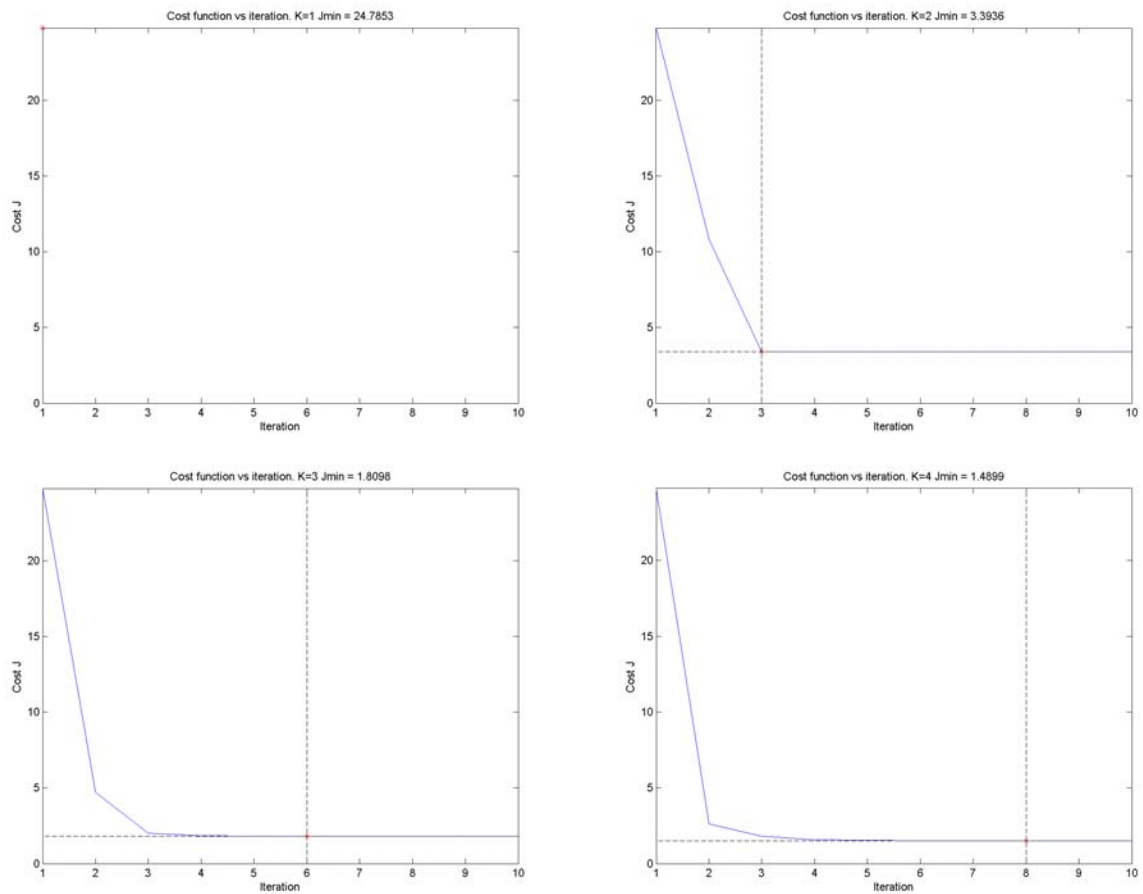


Figure I.2: Plot of k-means cost function  $J$  against iteration, for  $K = 1, 2, 3$  & 4 clusters. Note convergence in all cases is rapid. 4 iterations would have been sufficient.

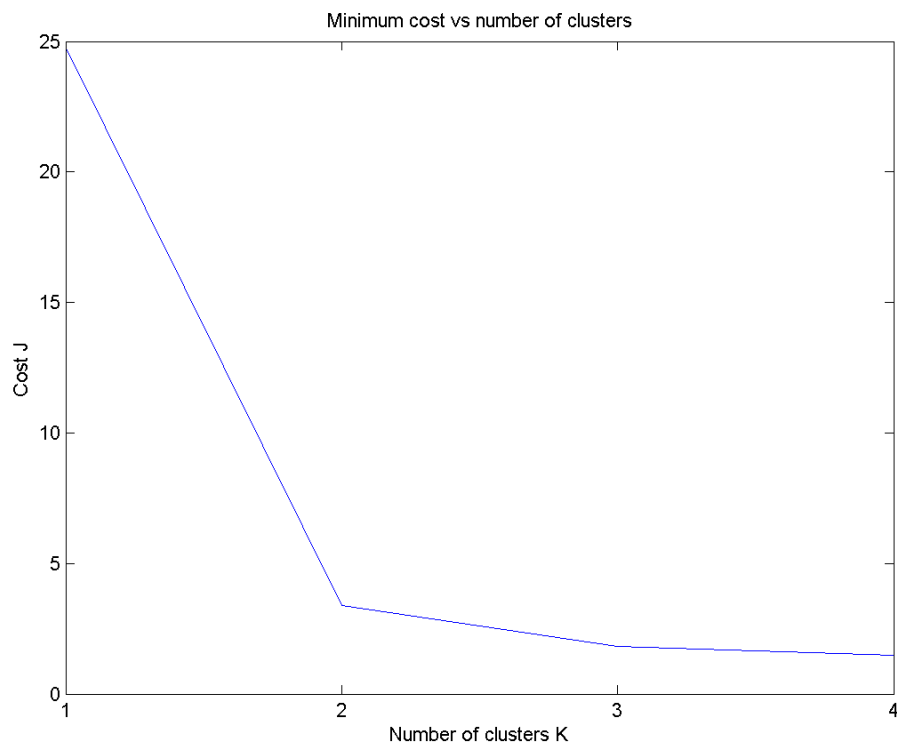


Figure I.3: Plot of minimum k-means cost vs number of clusters  $K$ . As one might expect, minimum cost appears to reduce with increased number of clusters. This is an obvious asymptotic result since if the number of clusters equals the number of data points, cluster centres at the data points will result in a zero distance matrix and therefore zero cost. However, this might not be a desirable result since it gives no information regarding how the data set is grouped.

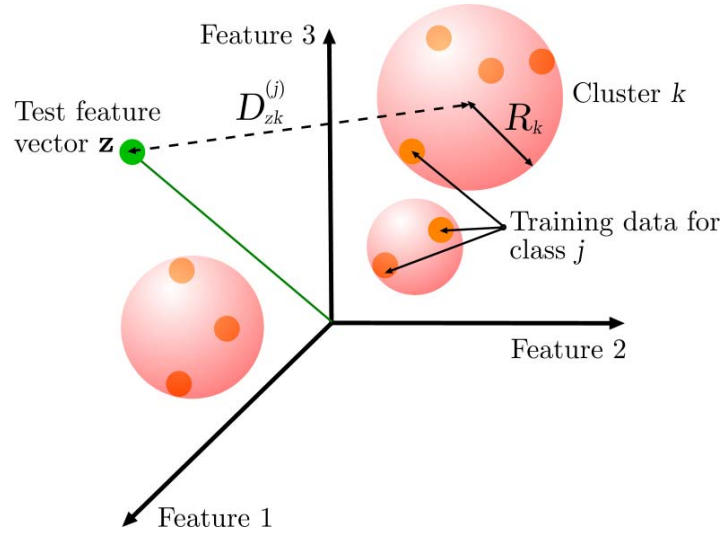


Figure I.4: Illustration of fuzzy k-means classification, using three feature dimensions. The training data set (orange points) are clustered into  $K = 3$  spherical regions. The *association*  $\exp\left(-\frac{|\mathbf{x} - \mathbf{c}_k^{(i)}|^2}{2R_k^{(i)}R_k^{(i)}}\right)$  between the test data point  $z$  is computed from the distance  $|\mathbf{x} - \mathbf{c}_k^{(i)}|$  to the centre of cluster  $k$  hypersphere, which has radius  $R_k^{(i)}$ .

i.e. find the maximum association  $\exp\left(-\frac{|\mathbf{x} - \mathbf{c}_k^{(i)}|^2}{2R_k^{(i)}R_k^{(i)}}\right)$  of the feature vector with each cluster hypersphere  $k$  (of  $K$ ) defined by radius  $R_k^{(i)}$  and origin vector  $\mathbf{c}_k^{(i)}$ , as illustrated in fig I.4.

Figures I.1, I.2 & I.3 illustrate the k-means clustering algorithm using two dimensional feature data. Note that the minimum value of the cost function  $J$  can reduce with increased number of clusters. However, from a visual perspective this is clearly not the ‘natural’ segmentation. A method to ‘optimize’ the value of  $K$  could be to add an additional condition of minimal hypersphere overlap. The optimum value of  $K$  in the context of the k-means classifier is even less clear. In this implementation we group training data from a particular class into a set of  $K$  hyperspheres and then derive a discriminant function based upon the maximum association with one of the hyperspheres. From a computational efficiency perspective, an excess of clusters is less desirable. However, if overlapping clusters map out a non-spherical training data distribution then the resulting classification performance should be higher. However, if the hypersphere radii are much smaller than the typical distance between classes, the discriminant function  $g_i(\mathbf{x})$  will use small numbers which could lead to unpredictable results given the finite precision of computational systems. A practical compromise could be to fix  $K$  at a relatively small value (e.g. 3 to 5) for the training data from each class.

## Appendix J

# Alternative Bayesian method of computing the confusion matrix

Define a set of classes defined by a finite alphabet  $\{c_1, c_2, \dots, c_N\}$  of length  $N$ . In the context of this research the class members correspond to target types such as Falcon, Pod, B747, or perhaps cruder distinctions such as ‘Long, but no JEM.’ Let each class have a corresponding set of  $M$  feature measurements  $\{m_1, m_2, \dots, m_M\}$ . Let these be weighted and normalized such that the numerical values of typical features are similar and, ideally, clustered around the interval  $[0,1]$ . This will remove any bias of a particular measurement. For example: target length, JEM spacing, maximum Radar Cross Section could be (respectively) divided by the length of the HRR window, the PRF and the maximum cross section observed in the target data set. The Bayesian classifier works by computing the *posterior probability*  $P(X|\{m_1, m_2, \dots, m_M\})$  of observing a particular class member  $X$ , given the entire set of feature measurements. Using Bayes rule [103], the single feature posterior probability  $P(X|m_j)$  can be expressed in terms of the *likelihood*  $P(m_j|X)$  of obtaining the feature measurement  $m_j$  given the assumption of a particular class, and the *prior* probability  $P(X)$  of choosing a particular class.

$$P(X|m_j) = \frac{P(m_j|X) P(X)}{\sum_{n=1}^N P(m_j|c_n) P(c_n)} \quad (\text{J.1})$$

Assuming each feature measurement is statistically independent, we can expand the joint probabilities defined by the combined feature posterior in terms of a product of single feature probabilities defined above. [103] pp 362.

$$P(X|\{m_1, m_2, \dots, m_M\}) = \frac{\prod_{j=1}^M P(X|m_j)}{\sum_{n=1}^N \prod_{j=1}^M P(c_n|m_j)} \quad (\text{J.2})$$

Tait [103] asserts a uniform prior  $P(X) = 1/N$  is often used without further justification. With this assumption we can therefore express the desired posterior probability in terms of likelihoods for

the individual features.

$$P(X|\{m_1, m_2 \dots m_M\}) = \frac{\prod_{j=1}^M \frac{P(m_j|X)}{\sum_{n=1}^N P(m_j|c_n)}}{\sum_{n=1}^N \prod_{j=1}^M \frac{P(m_j|c_n)}{\sum_{v=1}^N P(m_j|c_v)}} \quad (\text{J.3})$$

If each feature set  $\{m_1, m_2 \dots m_M\}$  derives from measurements from a known class  $k_j$ , which also belongs to the same alphabet  $\{c_1, c_2, \dots c_N\}$ , one can construct a *confusion matrix*  $\mathbf{C}$  with elements computed from the overall feature posterior defined above.

$$[C]_{ij} = P(c_i|\{m_1, m_2 \dots m_M\}_{k_j}) = \frac{\prod_{w=1}^M \frac{P(m_{wj}|c_i)}{\sum_{n=1}^N P(m_{wj}|c_n)}}{\sum_{n=1}^N \prod_{w=1}^M \frac{P(m_{wj}|c_n)}{\sum_{v=1}^N P(m_{wj}|c_v)}} \quad (\text{J.4})$$

i.e. the  $i^{\text{th}}$  row and  $j^{\text{th}}$  column correspond to the probability of class  $c_i$  based upon features  $\{m_{1j}, m_{2j} \dots m_{Mj}\}$  sourced from class  $k_j$ . An ideal classifier will have a very dominant (ideally unity) diagonal, i.e. when  $i = j$ , the class in question matches the source of the data.

The likelihoods can be computed from the probability distributions of the individual feature measurements. This is readily computable if such distributions are Gaussian. If this is the case then for each class of data, the feature measurements  $\{m_{1j}, m_{2j} \dots m_{Mj}\} \equiv \{m_1, m_2 \dots m_M\}_{k_j}$  will have an associated set of means  $\{\mu_{1j}, \mu_{2j} \dots \mu_{Mj}\}$  and standard deviations  $\{\sigma_{1j}, \sigma_{2j} \dots \sigma_{Mj}\}$ . The latter shall be obtained by prior knowledge of the data set ('Expert' prior knowledge) or via statistical calculation using a 'training' proportion of the data set. If there are  $Z$  sets of feature measurements  $\{m_{wj}^{(1)}, m_{wj}^{(2)}, \dots m_{wj}^{(Z)}\}$  contributing to the classification (for example, all the looks in a particular run) then one can apply a  $\chi^2$  test [89] to yield the required likelihood.

$$P(m_{wj}|c_n) = \int_{\chi_*^2}^{\infty} p(\chi^2, Z) d\chi^2 = 1 - \gamma\left(\frac{\chi_*^2}{2}, \frac{Z}{2}\right) \quad (\text{J.5})$$

where

$$\begin{aligned} \chi_*^2 &= \chi_*^2(w, j, n) = \sum_{z=1}^Z \frac{|m_{wj}^{(z)} - \mu_{wn}|^2}{\sigma_{wn}} \\ p(\chi^2) &= \frac{e^{-\frac{1}{2}\chi^2} \chi^{Z-2}}{2^{\frac{Z}{2}} \Gamma(\frac{Z}{2})} \\ \gamma(x, a) &= \frac{1}{\Gamma(a)} \int_0^x t^{a-1} e^{-t} dt \\ \Gamma(a) &= \int_0^{\infty} t^{a-1} e^{-t} dt \end{aligned} \quad (\text{J.6})$$

i.e.  $P(m_{wj}|c_n)$  is defined to be the probability of a  $\chi^2 \geq \chi_*^2$ . This has the desired properties since as  $\chi_{vj}^2$  becomes high,  $1 - \gamma\left(\frac{\chi_*^2}{2}, \frac{Z}{2}\right) \rightarrow 0$  and as  $\chi_{vj}^2 \rightarrow 0$ ,  $1 - \gamma\left(\frac{\chi_*^2}{2}, \frac{Z}{2}\right) \rightarrow 1$ . The key subtlety in  $P(m_{wj}|c_n)$  is that the means and standard deviations are taken from data corresponding to class  $c_n$

whereas the  $w = 1 \dots M$  sets of feature measurements are taken from class  $c_j$ . The functions  $\Gamma(a)$  and  $\gamma(x, a)$  are, respectively, ‘gamma’ and ‘lower incomplete gamma’ special functions, readily evaluatable using numerical software packages such as MATLAB.



## Appendix K

Target data sheets (Range profiles):

wfc2  $\Delta f=3.2\text{MHz}$   $P=8$   $Q=128$

(Waveform A). Classical method





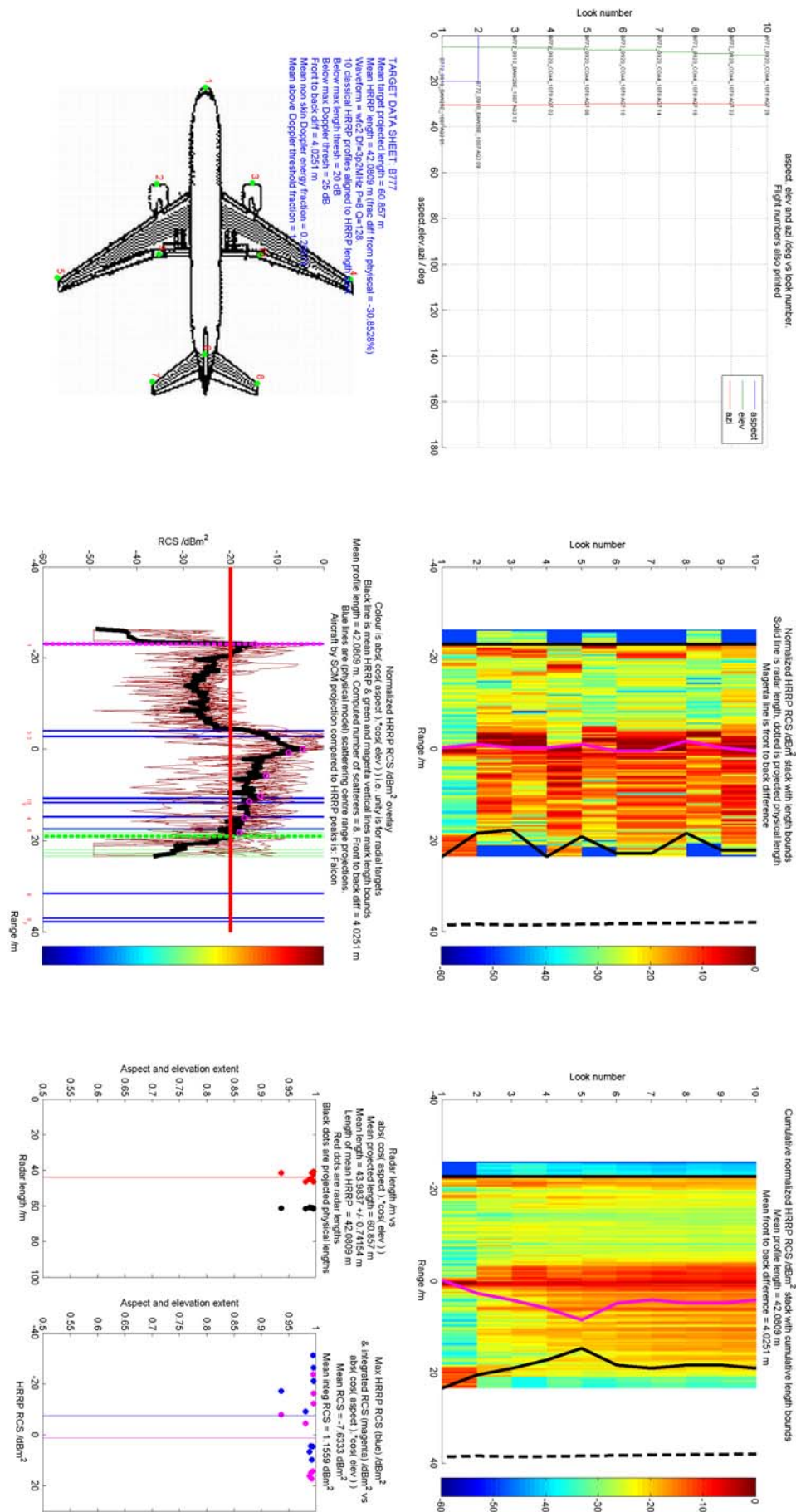
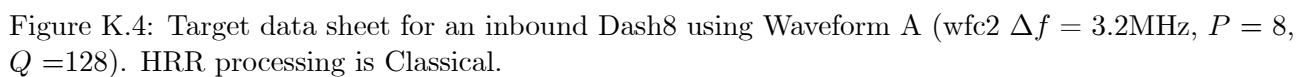
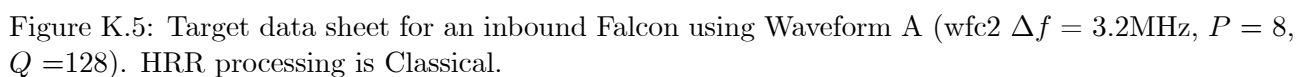


Figure K.3: Target data sheet for an inbound Boeing 777 using Waveform A (wfc2  $\Delta f = 3.2\text{MHz}$ ,  $P = 8$ ,  $Q = 128$ ). HRR processing is Classical.







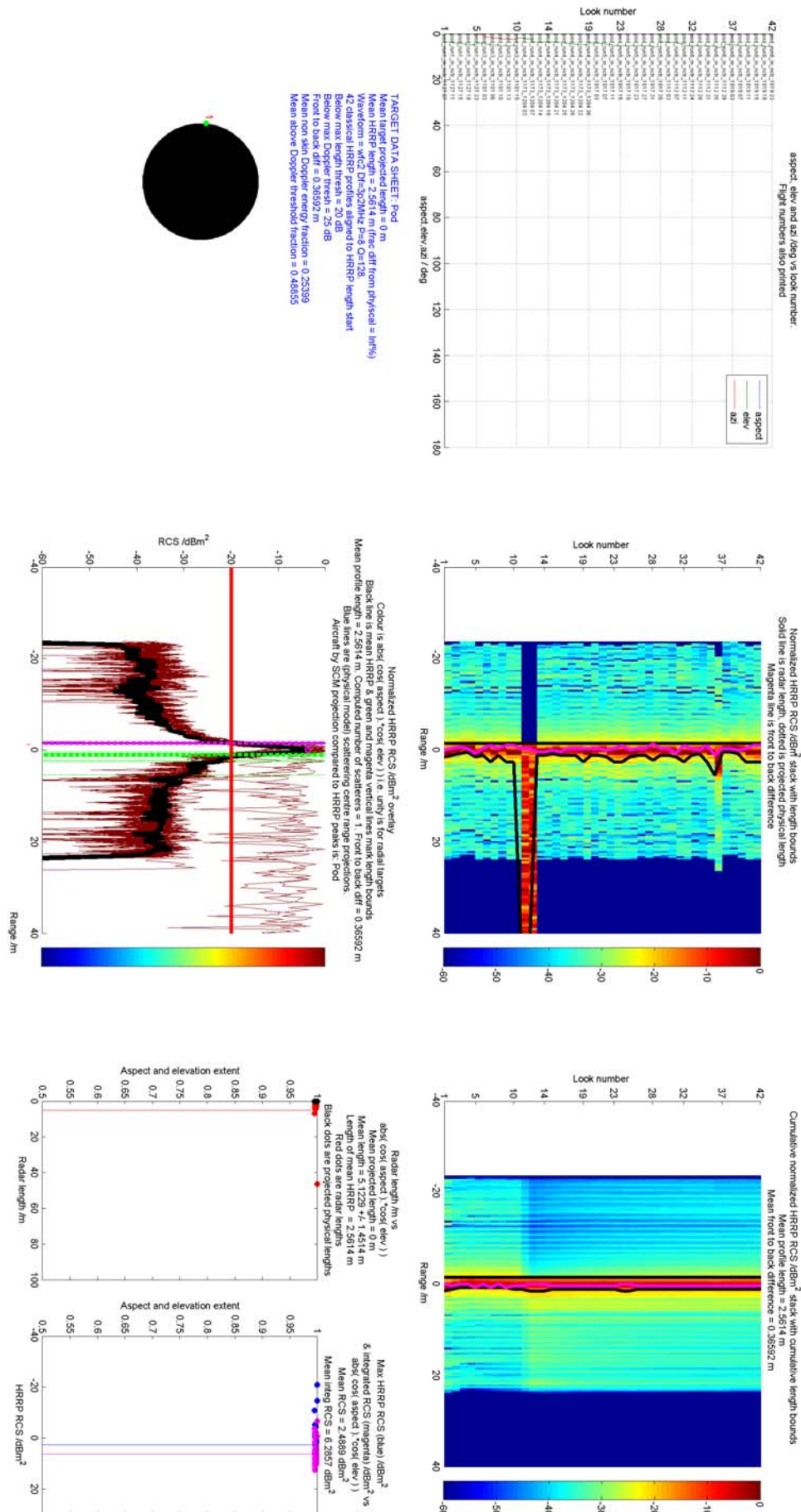


Figure K.6: Target data sheet for a repeater Pod (mounted upon the Falcon aircraft illustrated in fig K.5 using Waveform A (wfc2  $\Delta f = 3.2\text{MHz}$ ,  $P = 8$ ,  $Q = 128$ ). HRR processing is Classical.

## Appendix L

Target data sheets (Range profiles):

wfc2  $\Delta f=3.2\text{MHz}$   $P=8$   $Q=128$

(Waveform A). Hybrid method





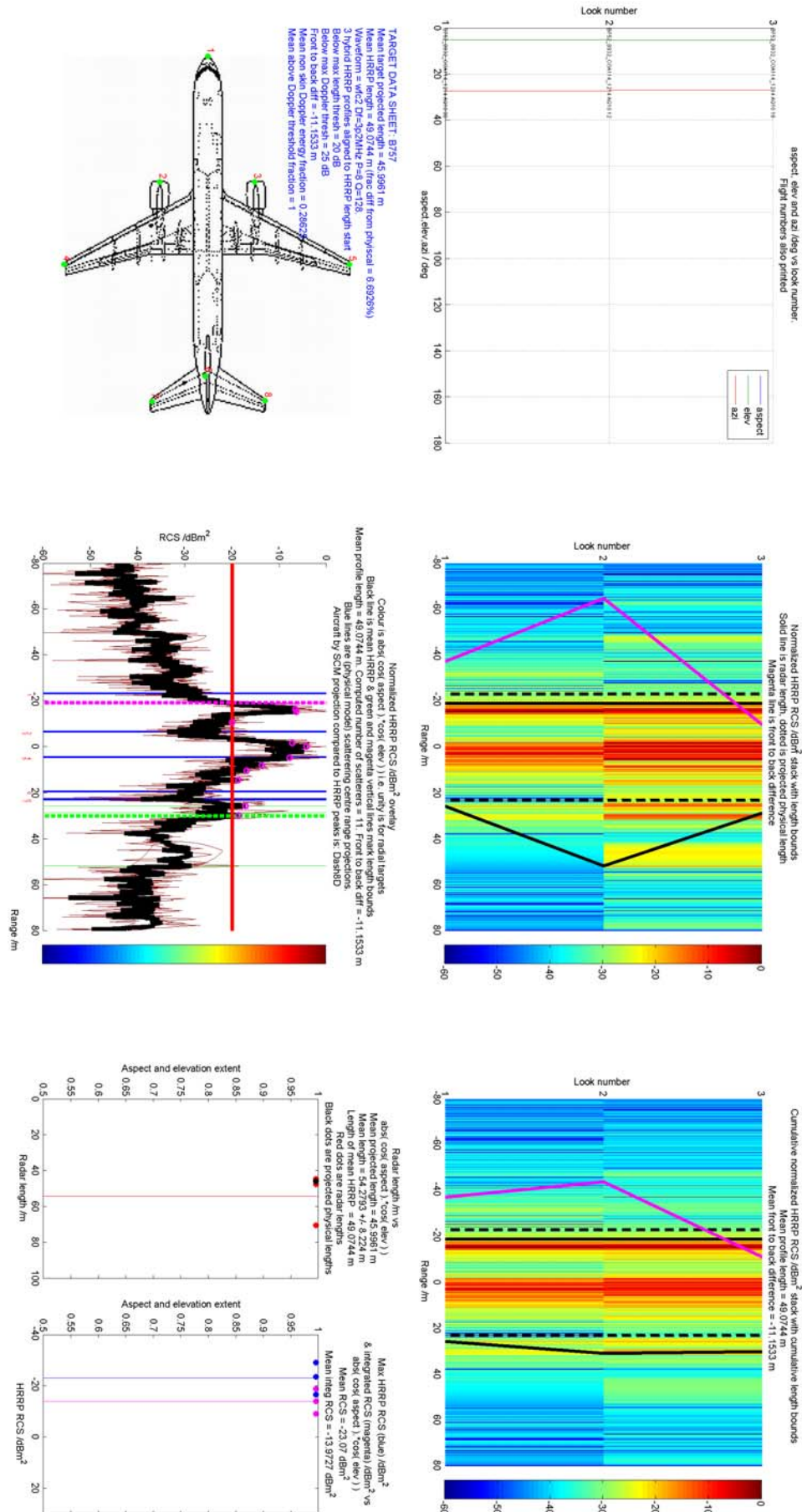
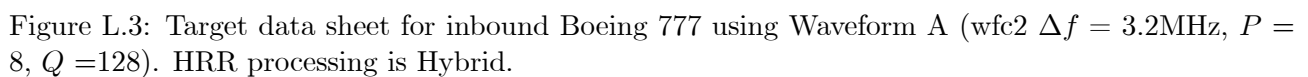
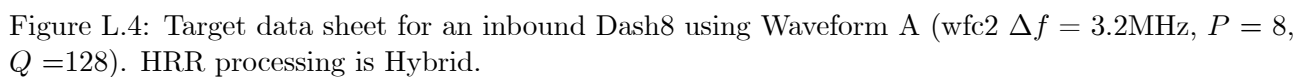


Figure L.2: Target data sheet for an inbound Boeing 757 using Waveform A ( $wfc2$   $\Delta f = 3.2\text{MHz}$ ,  $P = 8$ ,  $Q = 128$ ). HRR processing is Hybrid.









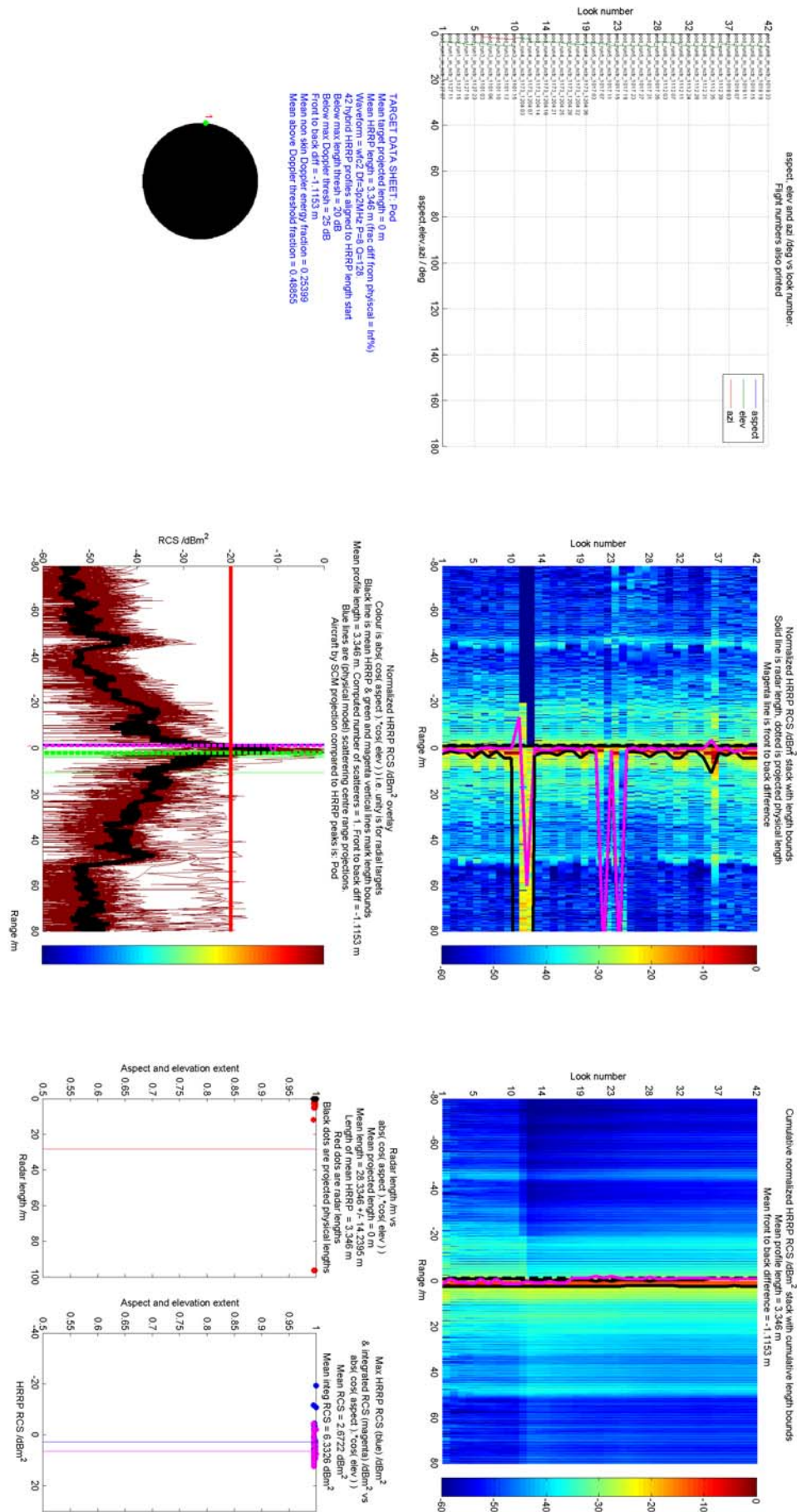


Figure L.6: Target data sheet for inbound Pod using Waveform A (wfc2  $\Delta f = 3.2\text{MHz}$ ,  $P = 8$ ,  $Q = 128$ ). HRR processing is Hybrid.

## Appendix M

Target data sheets (Range profiles):

wfc3  $\Delta f=0.8\text{MHz}$   $P=8$   $Q=128$

(Waveform B). Classical method



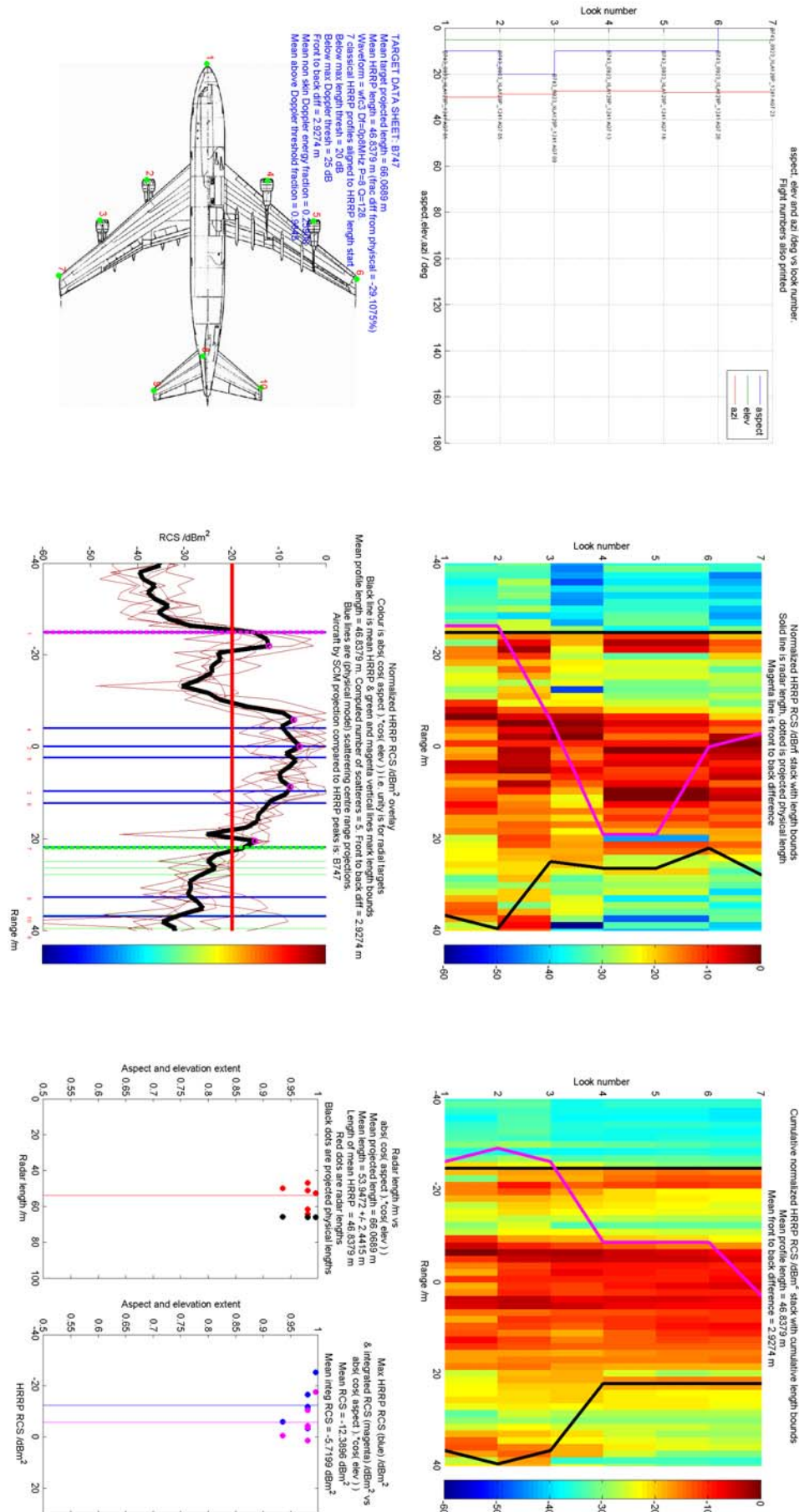


Figure M.1: Target data sheet for an inbound Boeing 747 using Waveform B (wfc3  $\Delta f = 0.8\text{MHz}$ ,  $P = 8$ ,  $Q = 128$ ). HRR processing is Classical.





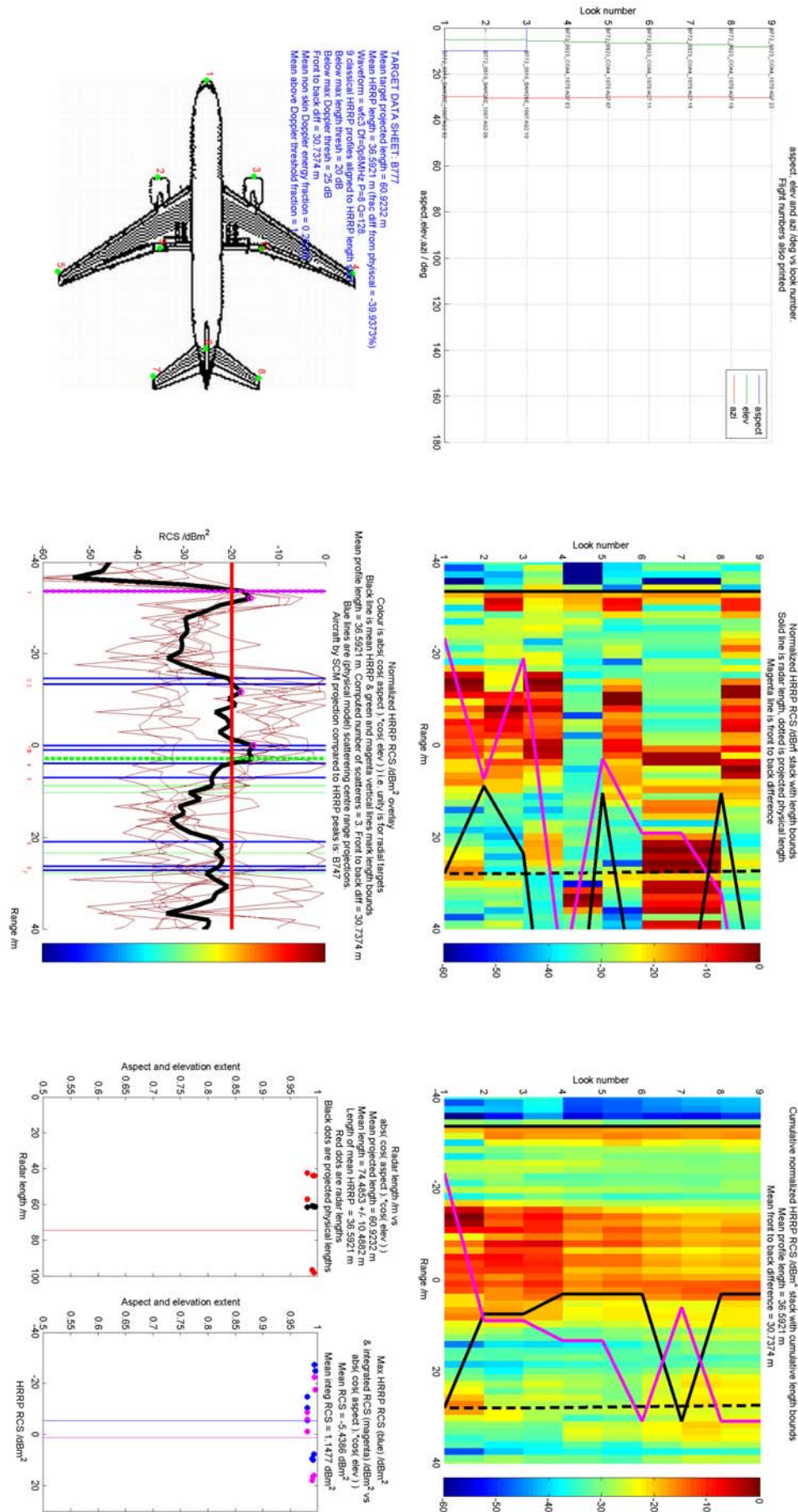


Figure M.3: Target data sheet for an inbound Boeing 747 using Waveform B (wfc3  $\Delta f = 0.8\text{MHz}$ ,  $P = 8$ ,  $Q = 128$ ). HRR processing is Classical.

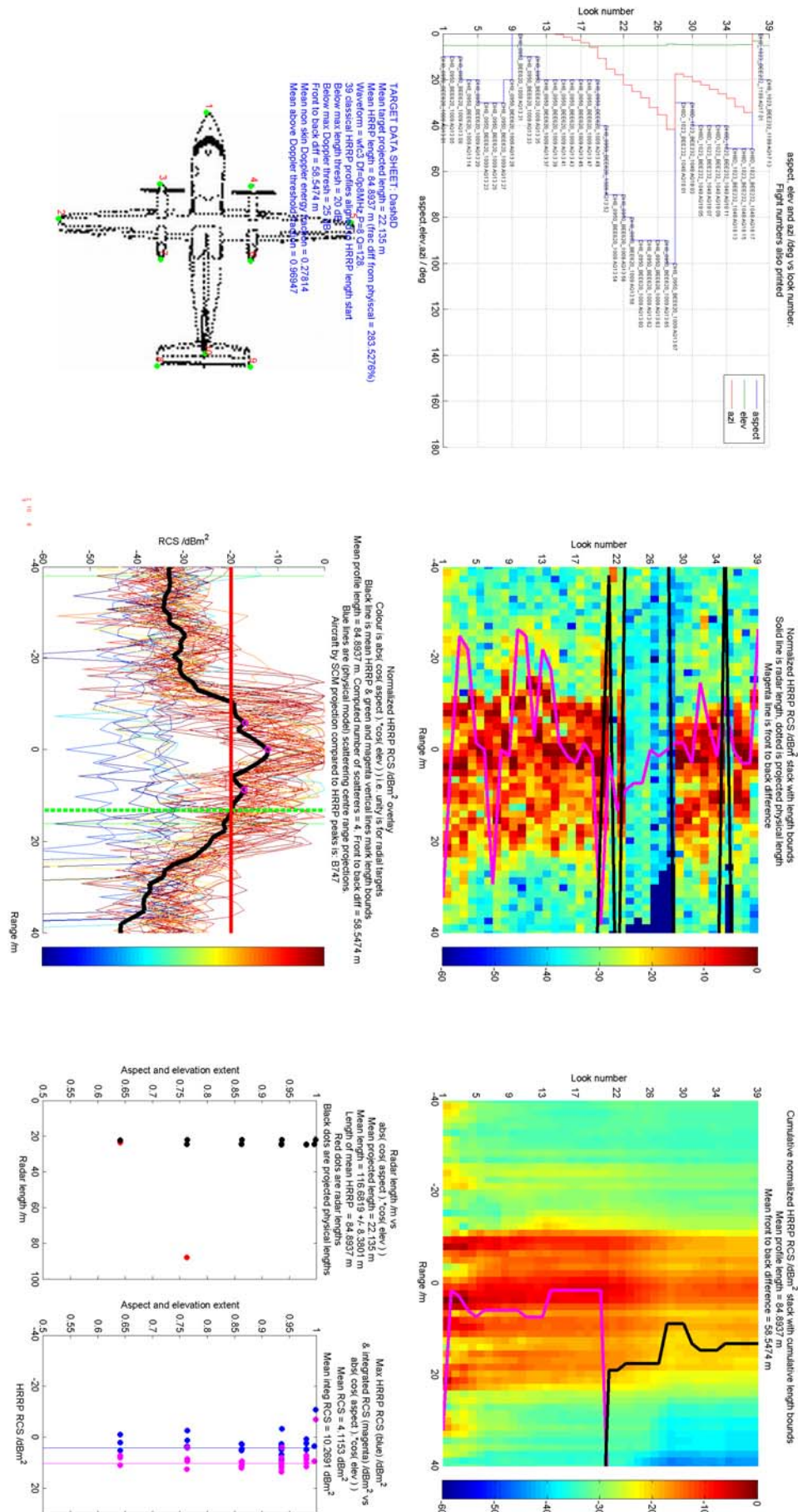


Figure M.4: Target data sheet for an inbound Boeing 747 using Waveform B (wfc3  $\Delta f = 0.8\text{MHz}$ ,  $P = 8$ ,  $Q = 128$ ). HRR processing is Classical.



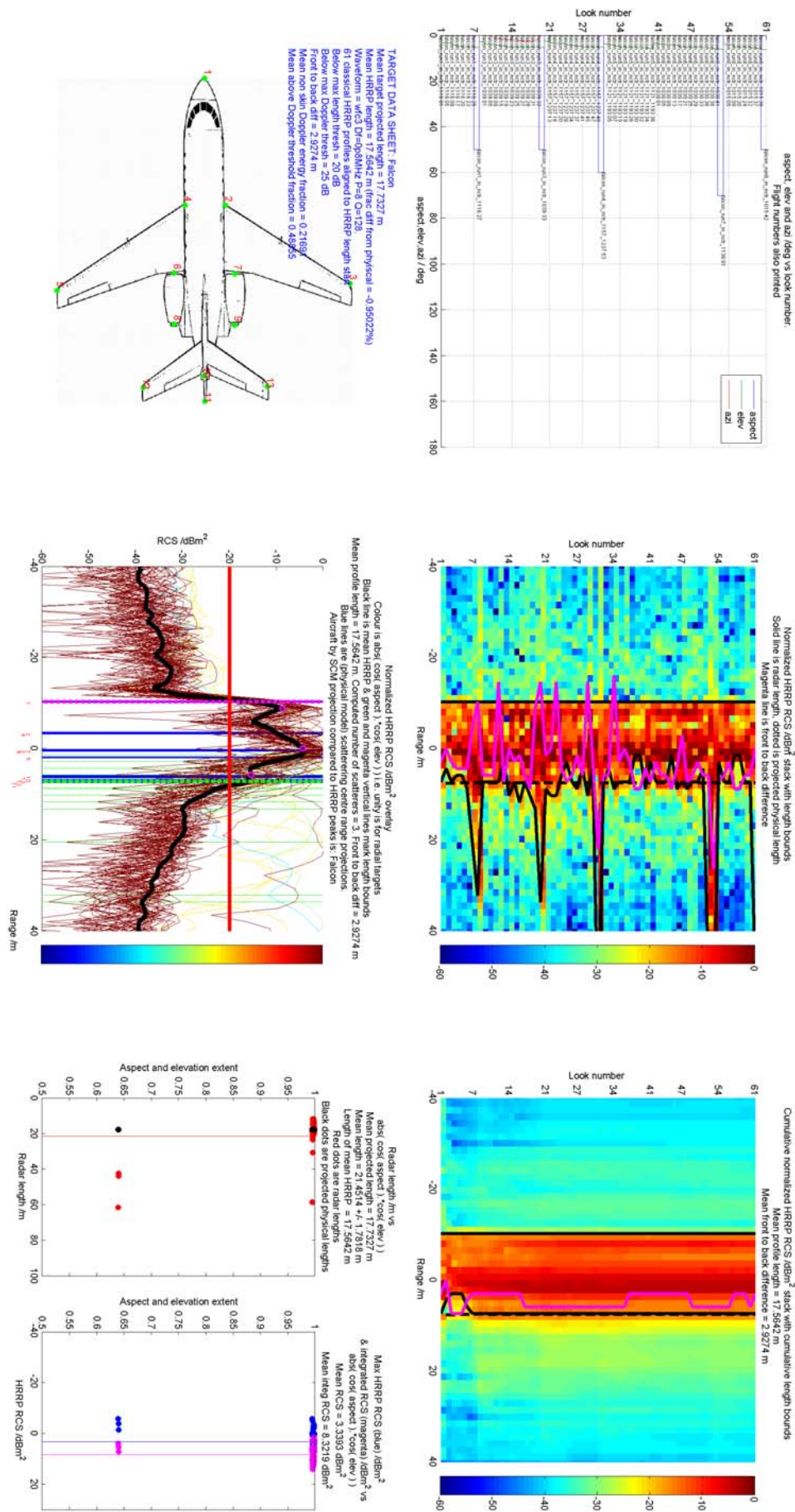


Figure M.5: Target data sheet for an inbound Boeing 747 using Waveform B ( $wfc3$   $\Delta f = 0.8\text{MHz}$ ,  $P = 8$ ,  $Q = 128$ ). HRR processing is Classical.



## Appendix N

Target data sheets (Range profiles):

wfc3  $\Delta f=3.2\text{MHz}$   $P=8$   $Q=128$

(Waveform C). Classical method

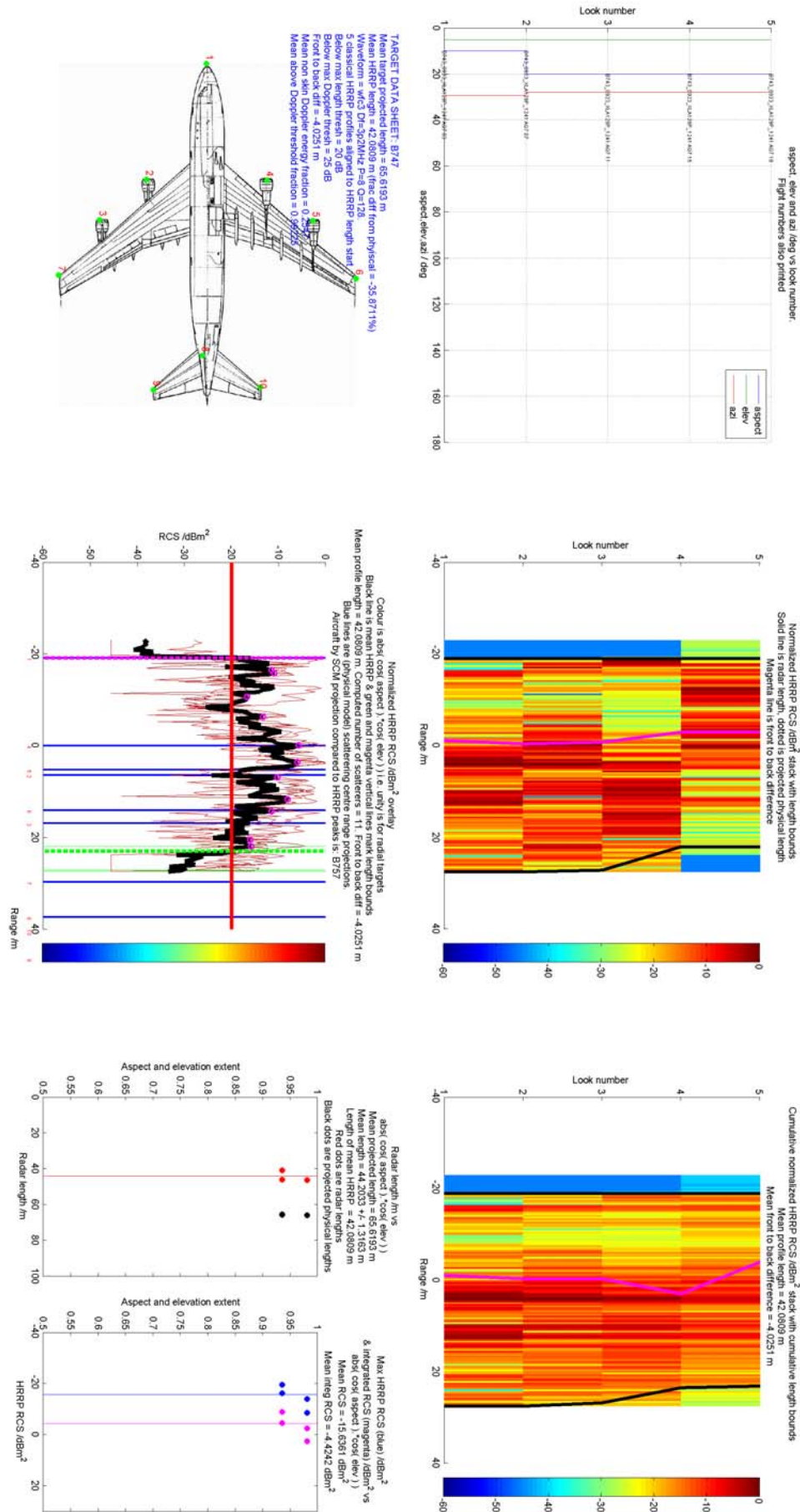


Figure N.1: Target data sheet for an inbound Boeing 747 using Waveform C (wfc3  $\Delta f = 3.2\text{MHz}$ ,  $P = 8$ ,  $Q = 128$ ). HRR processing is Classical.



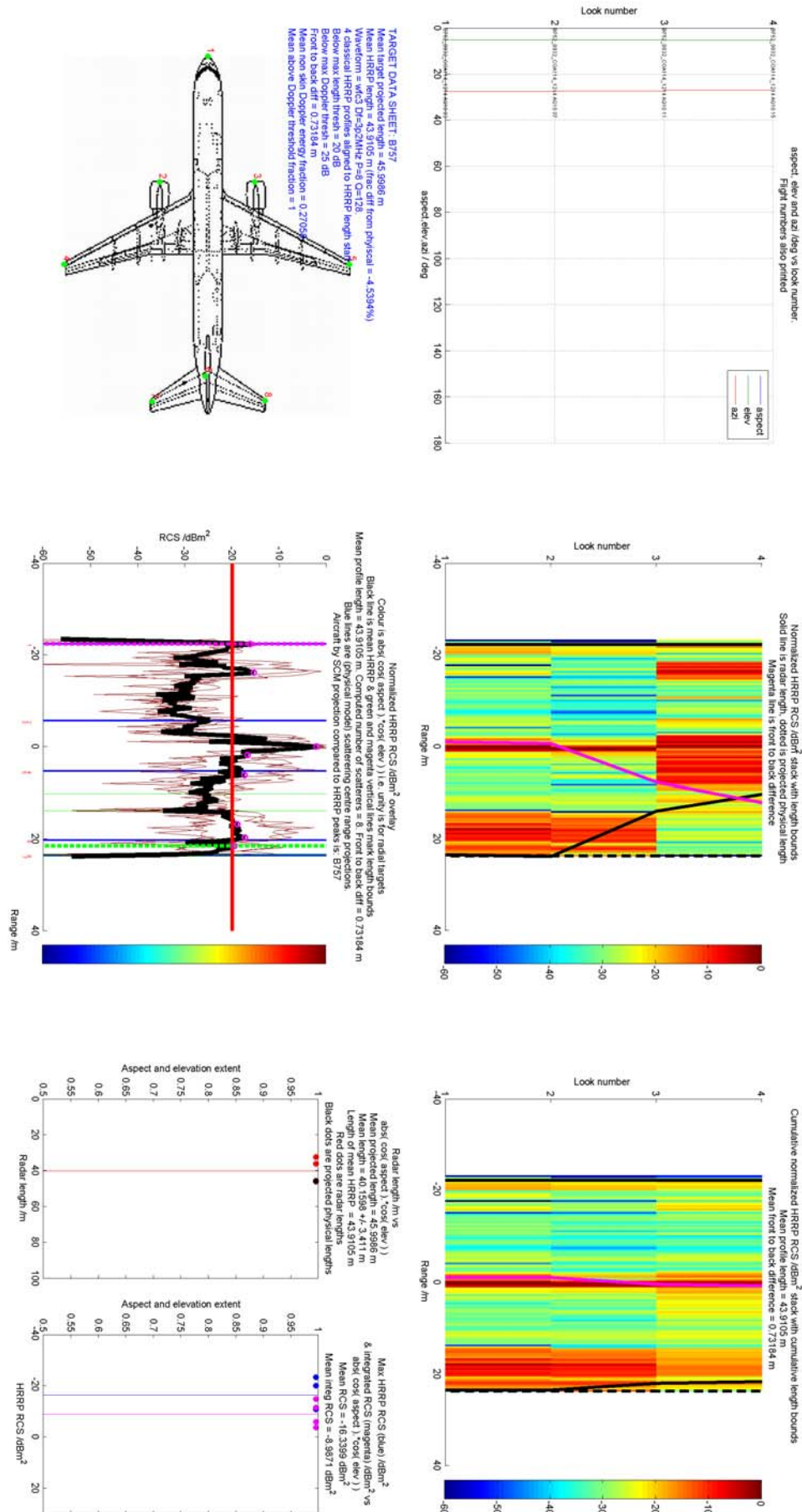


Figure N.2: Target data sheet for an inbound Boeing 757 using Waveform C (wfc3  $\Delta f = 3.2\text{MHz}$ ,  $P = 8$ ,  $Q = 128$ ). HRR processing is Classical.



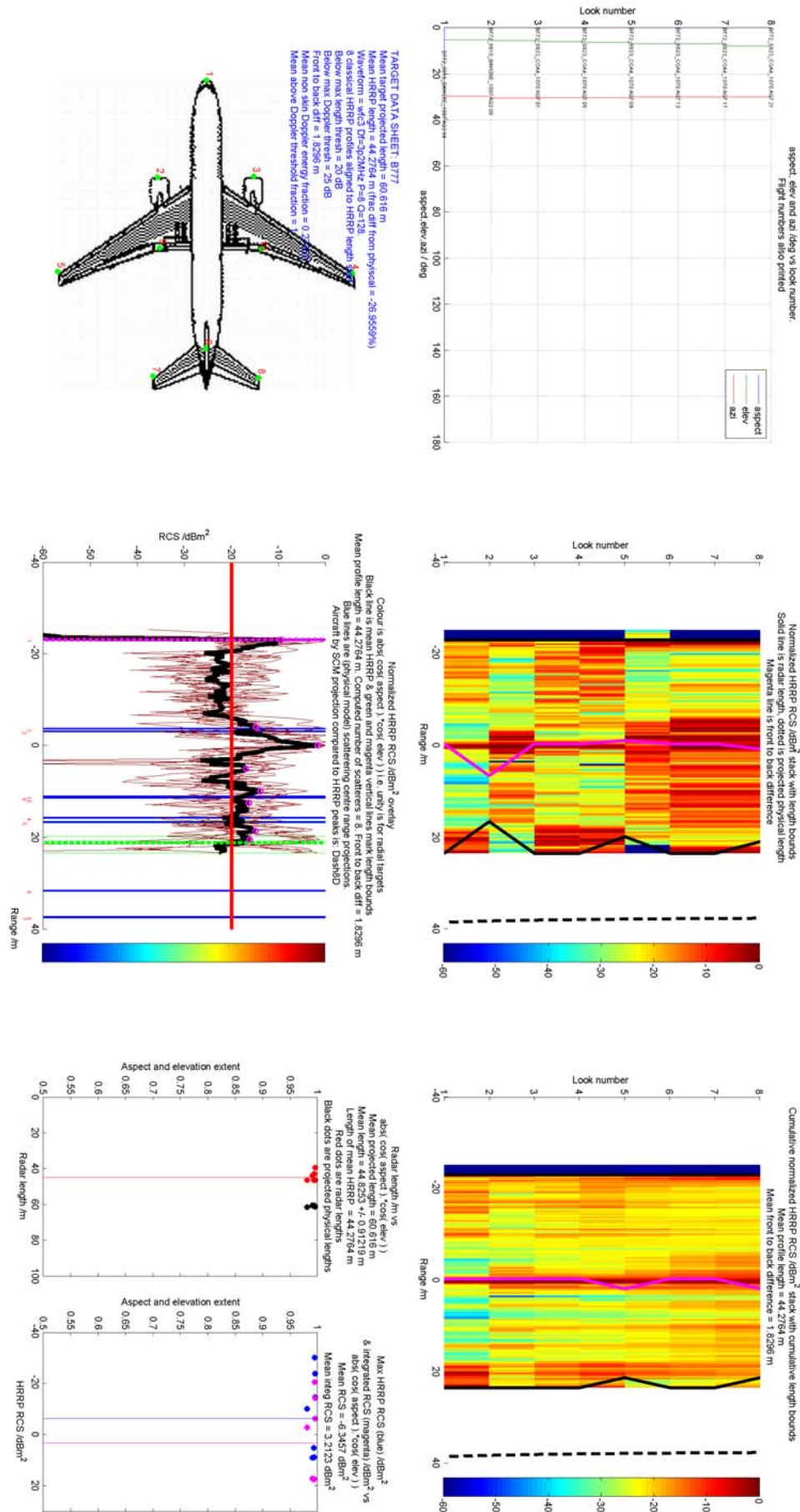
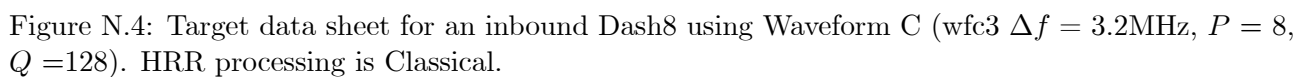


Figure N.3: Target data sheet for an inbound Boeing 777 using Waveform C (wfc3  $\Delta f = 3.2\text{MHz}$ ,  $P = 8$ ,  $Q = 128$ ). HRR processing is Classical.



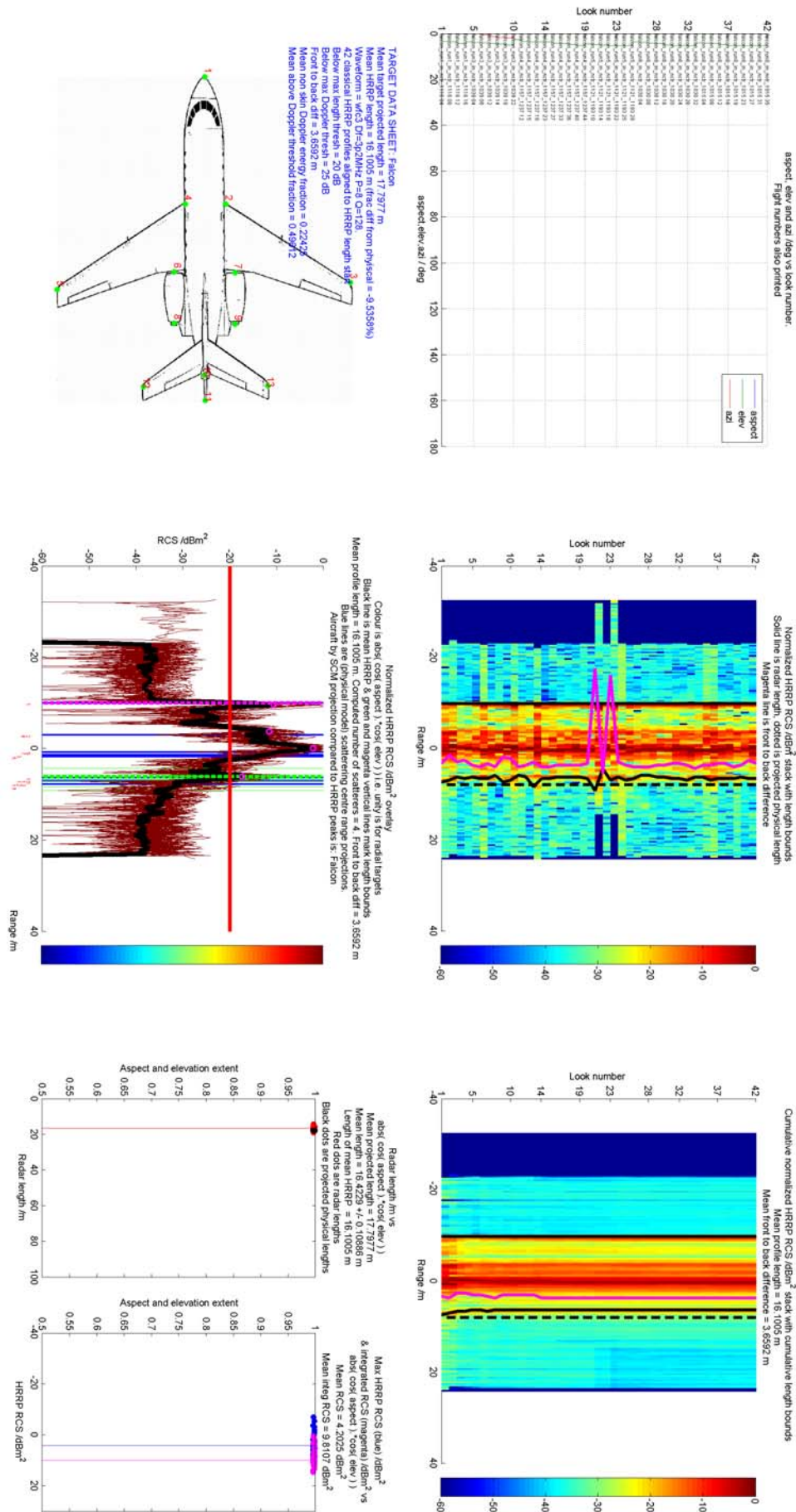


Figure N.5: Target data sheet for an inbound Falcon using Waveform C (wfc3  $\Delta f = 3.2\text{MHz}$ ,  $P = 8$ ,  $Q = 128$ ). HRR processing is Classical.



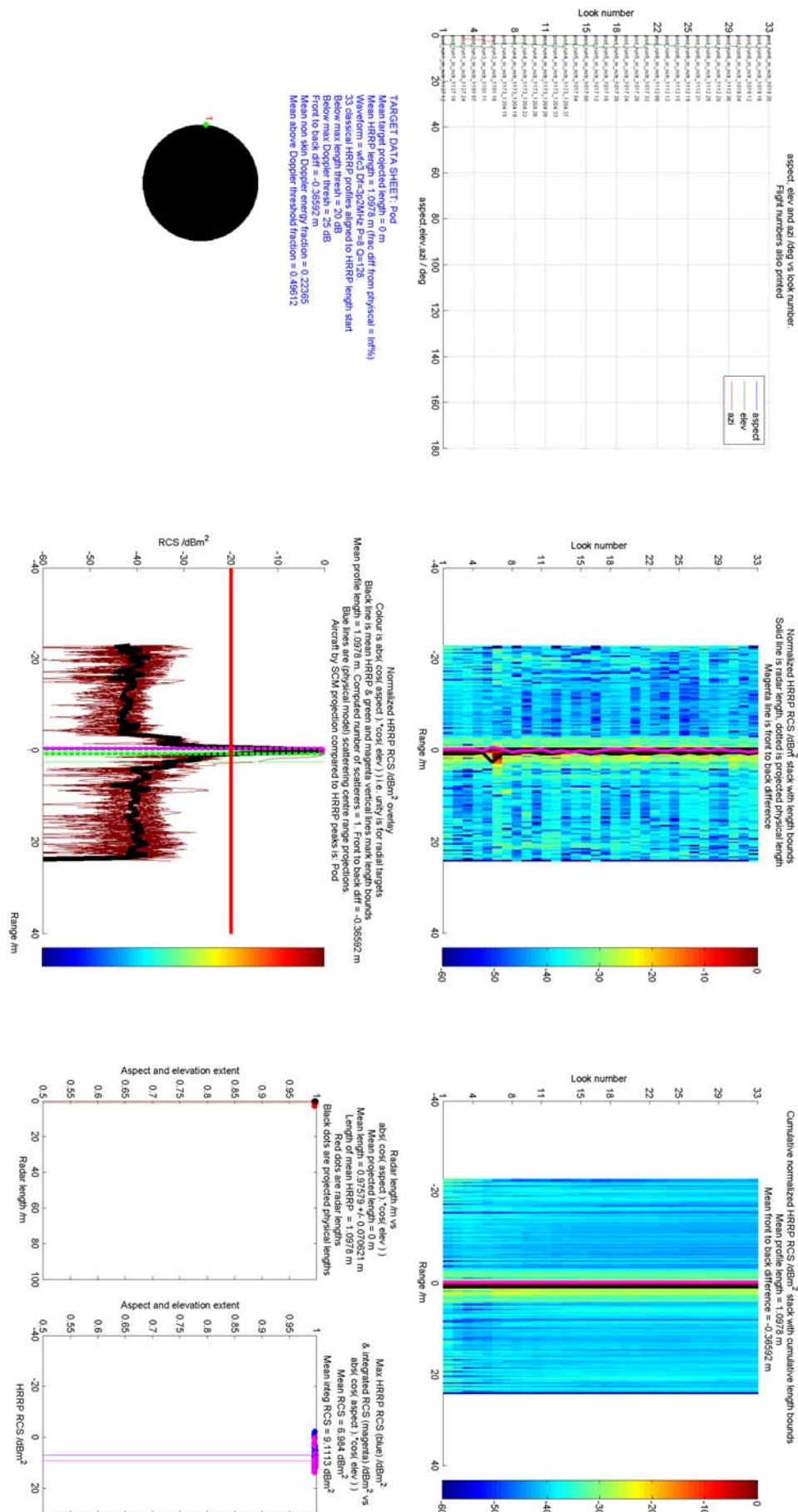


Figure N.6: Target data sheet for an inbound Pod using Waveform C (wfc3  $\Delta f = 3.2\text{MHz}$ ,  $P = 8$ ,  $Q = 128$ ). HRR processing is Classical.

## Appendix O

Target data sheets (Doppler): 6  
aircraft inbound

 $P = 32, Q = 32)$







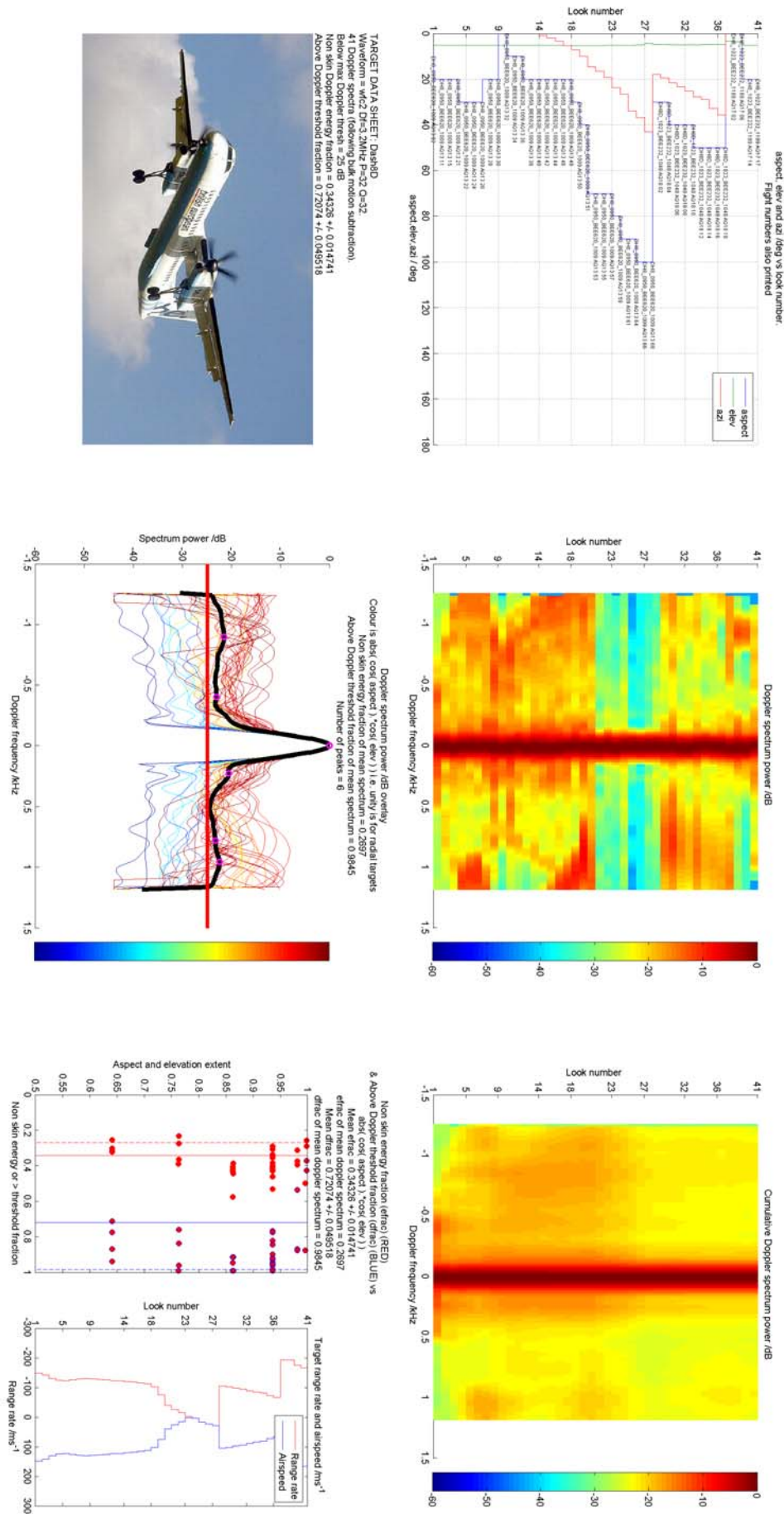


Figure O.4: (Doppler) target data sheet for inbound Dash8. Waveform is E (wfc2  $\Delta f = 3.2\text{MHz}$ ,  $P = 32$ ,  $Q = 32$ )

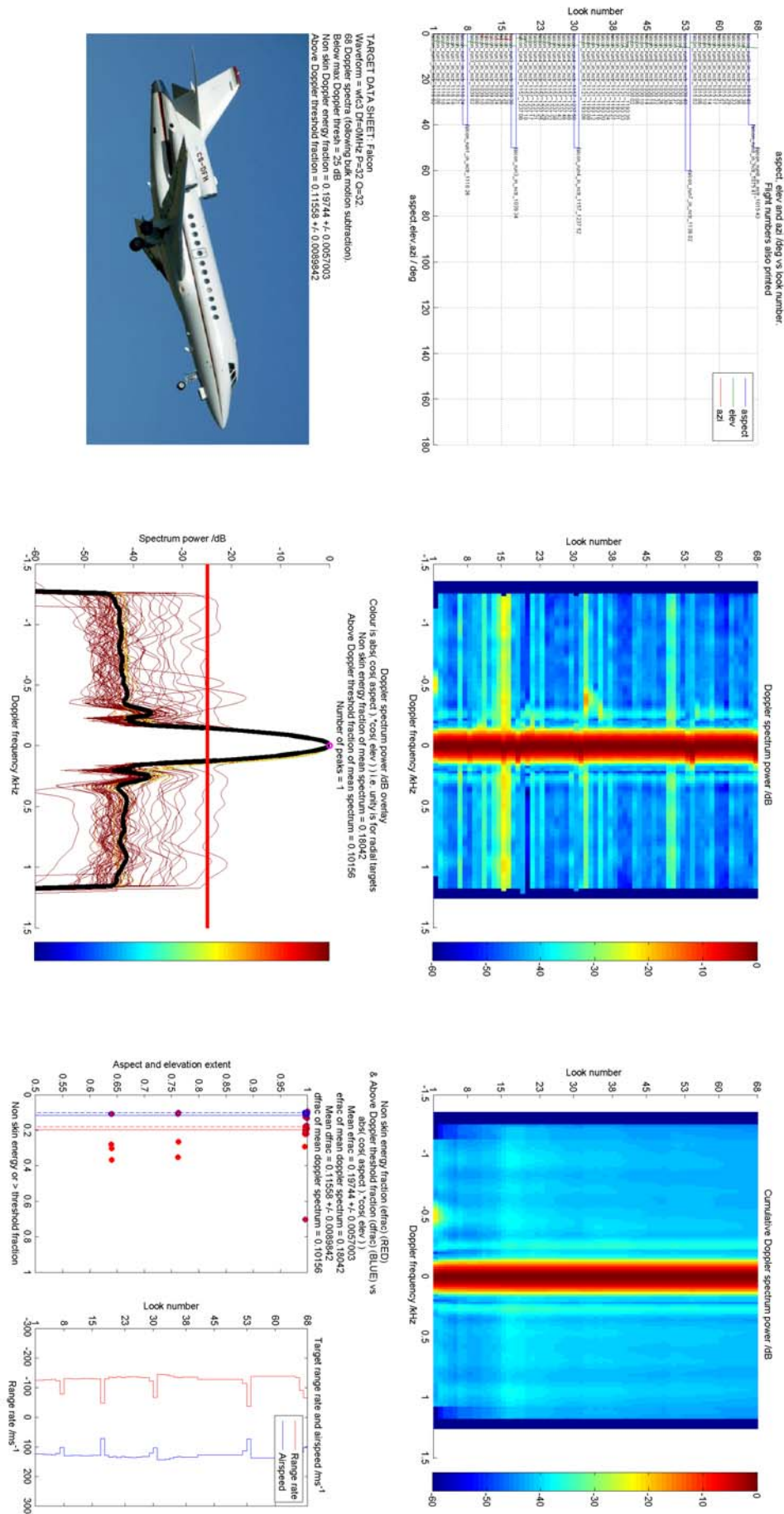


Figure O.5: (Doppler) target data sheet for inbound Falcon. Waveform is D ( $wfc2 \Delta f = 0\text{MHz}$ ,  $P = 32$ ,  $Q = 32$ )

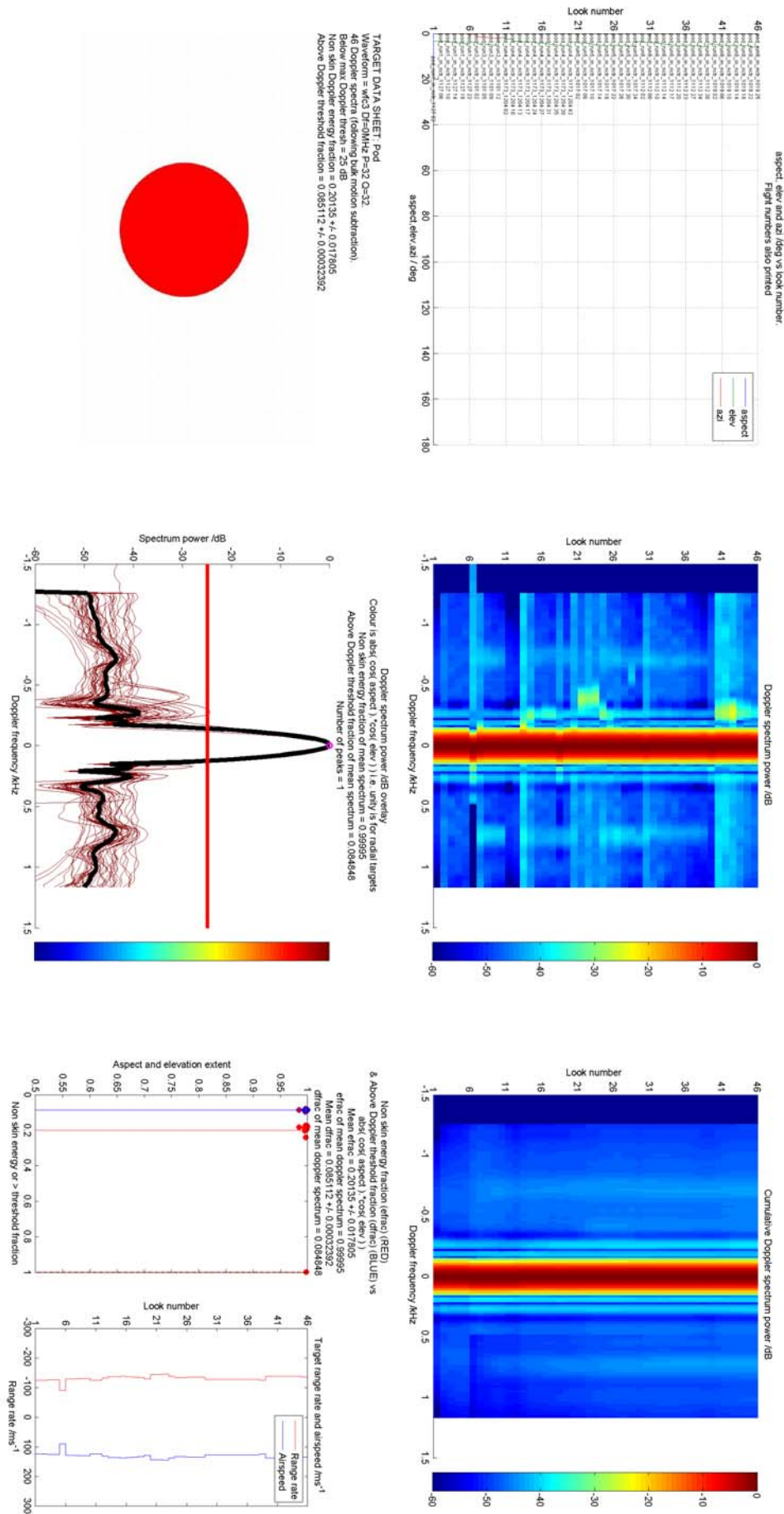
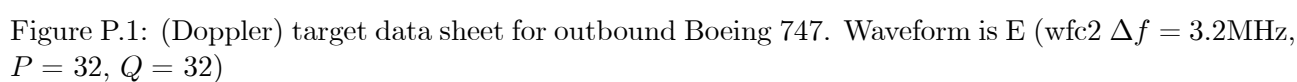


Figure O.6: (Doppler) target data sheet for inbound Pod. Waveform is D ( $wfc2$   $\Delta f = 0\text{MHz}$ ,  $P = 32$ ,  $Q = 32$ )

## Appendix P

Target data sheets (Doppler): 6  
aircraft outbound





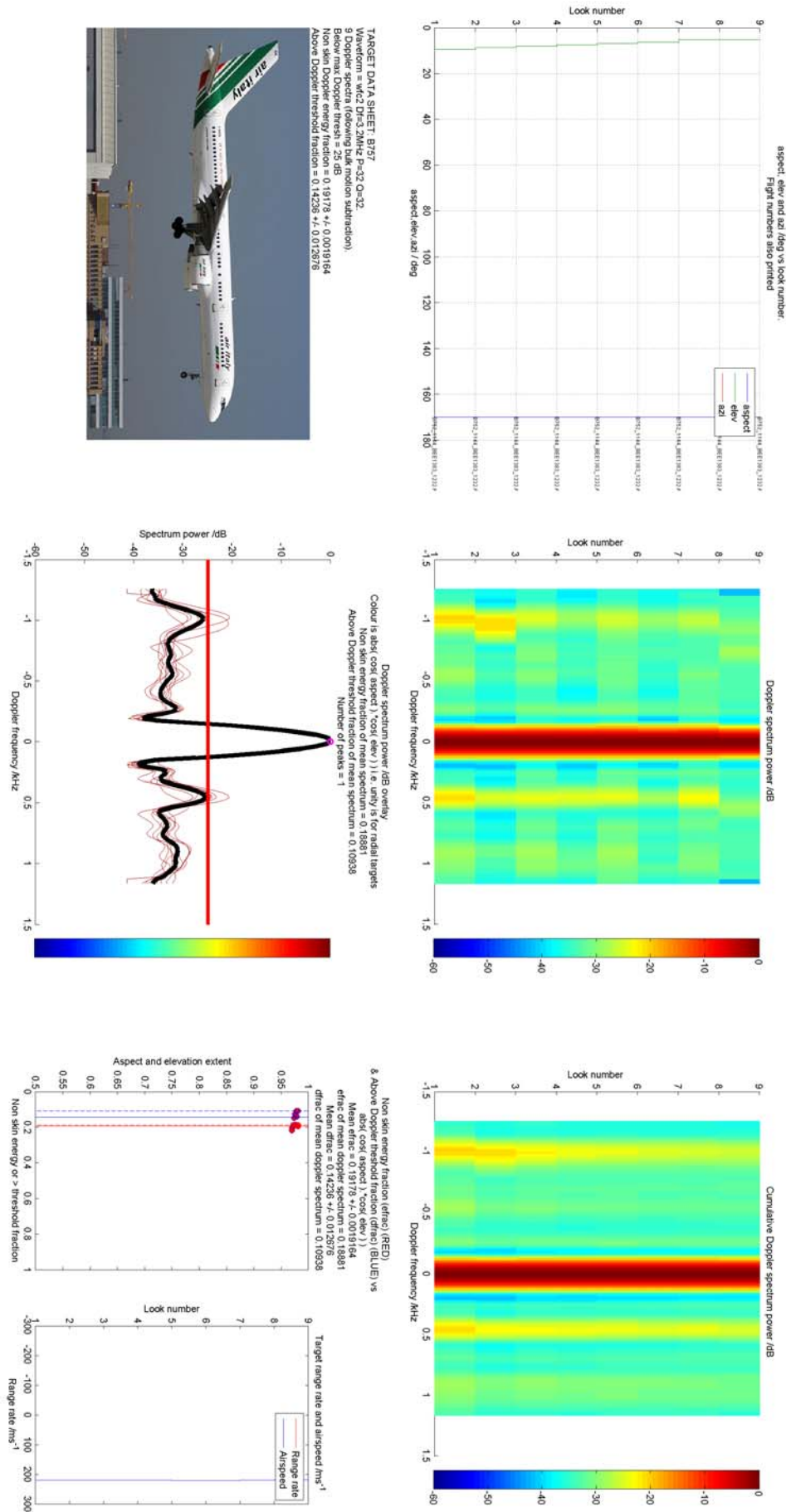


Figure P.2: (Doppler) target data sheet for outbound Boeing 757. Waveform is E ( $wfc2 \Delta f = 3.2\text{MHz}$ ,  $P = 32$ ,  $Q = 32$ )

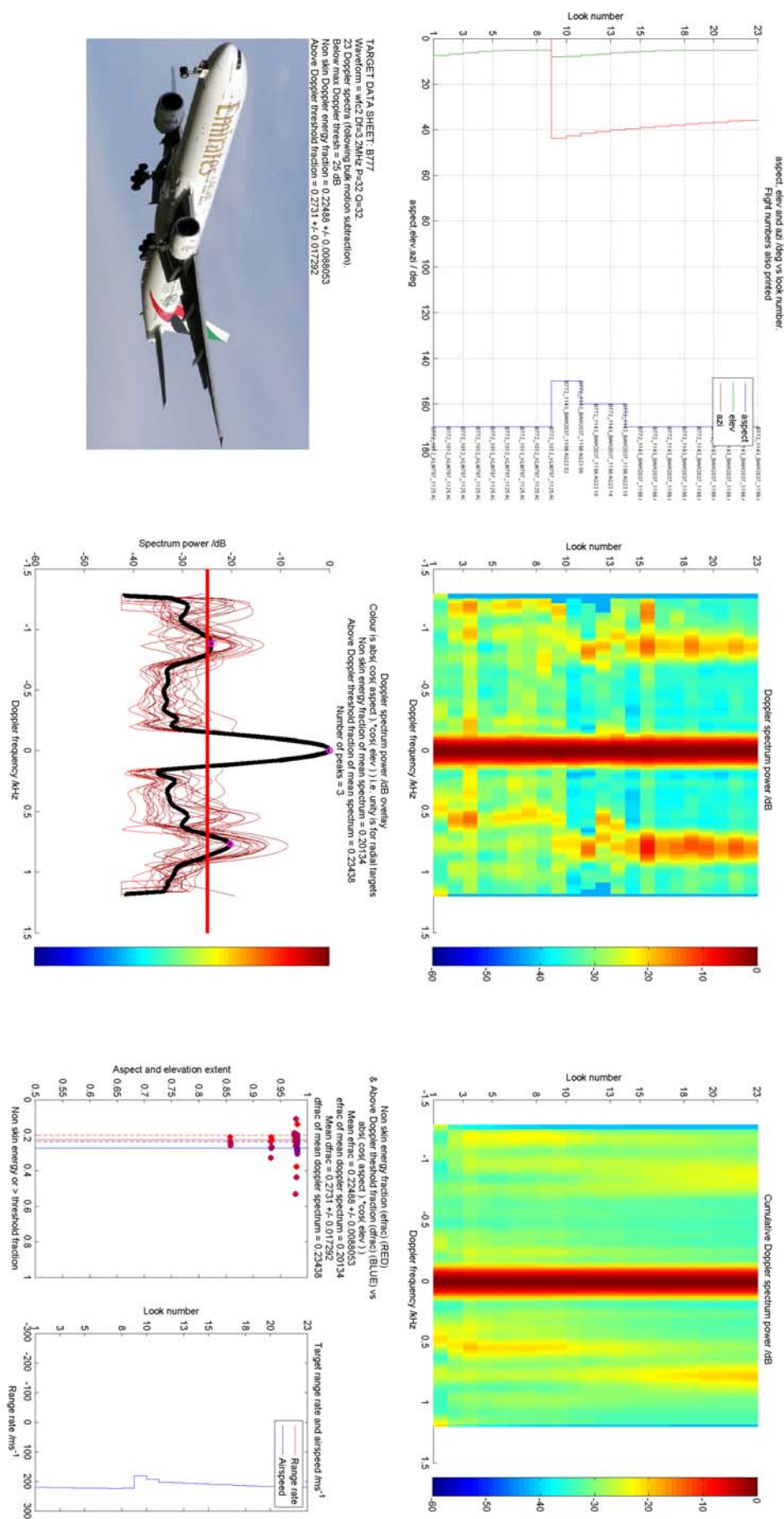


Figure P.3: (Doppler) target data sheet for outbound Boeing 777. Waveform is E (wfc2  $\Delta f = 3.2\text{MHz}$ ,  $P = 32$ ,  $Q = 32$ )

